

NASA/CR- 1998- 206995

A LONG-TERM SPACE ASTROPHYSICS RESEARCH PROGRAM

THE EVOLUTION OF THE QUASAR CONTINUUM

NASA Grant NAGW-2201

Final Report

For the Period 1 July 1990 through 31 December 1997

Principal Investigator

Dr. M. Elvis

January 1998

Prepared for:

National Aeronautics and Space Administration
Washington, DC 20546

Smithsonian Institution
Astrophysical Observatory
Cambridge, Massachusetts 02138

The Smithsonian Astrophysical Observatory
is a member of the
Harvard-Smithsonian Center for Astrophysics

The NASA Technical Officer for this grant is Darrell E. New, Code SZE, NASA Headquarters,
Washington, DC 20546.

FINAL
IN-90CR
OCIT
063074



The grant "The Evolution of the Quasar Continuum" resulted in over 53 published refereed papers and conference proceedings. The more significant of these papers are listed below, and abstracts are attached.

The papers address a wide range of issues involving the evolution of quasars, their electromagnetic emissions, and their environment, from nearby low luminosity Seyfert galaxies to quasars at the highest redshifts. Primarily observational in content the work nonetheless included theoretical studies of quasar accretion disks that attempt to explain the observed time variability of quasars, and the overall 'demographics' of the quasar population.

The work carried out under this grant has laid a strong foundation for ongoing and future research with AXAF, HST and other new facilities.

X-ray Spectral Survey of WGACAT Quasars I: Spectral Evolution & Low Energy Cut-Offs (F. Fiore, M. Elvis, P. Giommi, and P. Padovani), *Ap.J.*, **492**, in press (Jan 1, 1998).

X-ray Spectral Survey of WGACAT Quasars II: Optical and Radio Properties of Quasars with Low Energy X-ray Cut-Offs (M. Elvis, F. Fiore, P. Giommi, and P. Padovani), *Ap.J.*, **492**, in press (Jan 1, 1998).

The Origin of the Soft X-ray Excess in the Seyfert 2 Galaxy NGC2110 (K.A. Weaver, A.S. Wilson, M. Elvis, R.F. Mushotzky, and U. Briel) *BAAS*, **24**, No. 4, 1275.

A Search for Extended X-ray Emission in the Seyfert Galaxies NGC3516, NGC4151, and Markarian 3 (J.A. Morse, A.S. Wilson, M. Elvis, and K.A. Weaver), *Ap.J.*, **439**, 121.

An X-ray Image of the Seyfert Galaxy NGC 1068 (A.S. Wilson, M. Elvis, A. Lawrence, and J. Bland-Hawthorn), *Ap.J.(Letters)*, **391**, L75.

X-ray and Optical Continua of AGN with Extreme FeII Emission (A. Lawrence, M. Elvis, B.J. Wilkes, I. McHardy, and N. Brandt) *MNRAS*, **285**, 879.

X-ray Absorption by Ionized Oxygen in ASCA Spectra of the Infrared Quasar IRAS 13349+2438 (N. Brandt, S. Mathur, C.S. Reynolds, and M. Elvis), *MNRAS*, in press.

Testing Models for the Quasar Big Blue Bump via Color-Color Diagrams (A. Siemiginowska, O. Kuhn, M. Elvis, F. Fiore, J.C. McDowell, and B.J. Wilkes), *Ap.J.*, **454**, 77.

Star-Disk Collisions and the Origin of the Broad Lines in Quasars (W. H. Zurek, A. Siemiginowska, and S.A. Colgate), *Ap.J.*, **434**, 46.

The high-temperature big blue bump in the Seyfert galaxy RE J1034+396 (E.M. Puchnarewicz, K.O. Mason, A. Siemiginowska, and K.A. Pounds), *MNRAS*, **276**, 20.

The Complex Soft X-ray Spectrum of Low-Redshift Radio-Quiet Quasars I: The X-ray Data (F. Fiore, A. Siemiginowska, M. Elvis, B.J. Wilkes, and J.C. McDowell), *Ap.J.*, **431**, 515.

X-ray Selected Red, Absorbed Quasars (B.-W. Kim, M. Elvis), Proc. "X-ray Sky Surveys", ed. G. Hasinger, *Astr.Nachr.*, 319, ____.

- X-ray Color Selected Warm Absorbers (F. Nicastro, M. Elvis, and F. Fiore), Proc. "X-ray Sky Surveys", ed. G. Hasinger, *Astr.Nachr.*, 319, ____.
- Ten New BL Lac Objects Discovered by an Efficient X-ray/Radio/Optical Technique (J. Schachter, J. Stocke, E. Perlman, M. Elvis, A. Granados J. Luu, J.P. Huchra, R. Humphreys, R. Remillard, C.M. Urry, and J. Wallin), *Ap.J.*, **412**, 541.
- MgII Absorption in a Sample of 56 Quasars (T.L. Aldcroft, J. Bechtold, and M. Elvis), *Ap.J. Suppl.*, **93**, 1.
- A Sample of Lobe-Dominated Quasars for 21cm HI Absorption Line Study (T. Aldcroft, J. Bechtold, and M. Elvis) *BAAS*, **24**, No. 4, 1265.
- The Cambridge-Cambridge X-ray Serendipity Survey: I. X-ray Luminous Galaxies (B.J. Boyle, R.G. McMahon, B.J. Wilkes, and M. Elvis), *MNRAS*, **272**, 462.
- The Cambridge-Cambridge X-ray Serendipity Survey: II. Identification of X-ray Luminous Galaxies (B.J. Boyle, R.G. McMahon, B.J. Wilkes, and M. Elvis), *MNRAS*, **276**, 315.
- The Cambridge-Cambridge X-ray Serendipity Survey: III. VLA Observations and the Evolution of the Radio-Quiet and Radio-Loud Objects (P. Ciliegi, M. Elvis, B.J. Wilkes, B.J. Boyle, R.G. McMahon, and T. Maccacaro), *MNRAS*, **277**, 1463.
- The Cambridge-Cambridge X-ray Serendipity Survey: IV. The X-ray Properties (P. Ciliegi, M. Elvis, B.J. Wilkes, B.J. Boyle, R.G. McMahon, and T. Maccacaro), *MNRAS*, **284**, 401.
- The Cambridge-Cambridge X-ray Serendipity Survey: V. The Sample (B.J. Boyle, B.J. Wilkes, and M. Elvis), *MNRAS*, **285**, 511.
- Associated Absorption at Low and High Redshift (M. Elvis, S. Mathur, B.J. Wilkes, F. Fiore, P. Giommi, and P. Padovani) "Emission Lines in Active Galaxies New Methods and Techniques", IAU Colloquium 159, ed. B. Peterson, p.236.
- X-ray Absorption and High Redshift Quasars (M. Elvis) "Röntgenstrahlung From The Universe", eds. H.U. Zimmerman, J.E. Trümper, R.H. Yorke, [MPI Report 263] p.409.
- An Accurate Galactic N_H Map of the North Ecliptic Pole (M. Elvis, F.J. Lockman, and C. Fassnacht), *Ap.J. Suppl.*, **95**, 413.
- The Soft X-ray Properties of a Complete Sample of Optically Selected Quasars I: First Results (A. Laor, F. Fiore, M. Elvis, B.J. Wilkes, and J.C. McDowell), *Ap.J.*, **435**, 611.
- An Atlas of Quasar Energy Distributions. (M. Elvis, B.J. Wilkes, J.C. McDowell, R.P. Green, J. Bechtold, S.P. Willner, M.S. Oey, E. Polonski, and R. Cutri), *Ap.J. Suppl.*, **95** 1.
- The Origin of the Soft X-ray Excess in the Seyfert 2 Galaxy NGC2110 (K.A. Weaver, A.S. Wilson, R.F. Mushotzky, M. Elvis, and U.G. Briel), *Ap.J.*, **442**, 597.

- X-rays and High Redshift Quasars (M. Elvis), "New Horizon of X-ray Astronomy" [Tokyo: Universal Academy Press] eds. F. Makimo. and T. Ohashi, p.323.
- The Unusual Quasar PG1407+265 (J. McDowell, C. Canizares, M. Elvis, A. Lawrence, S. Markof, S. Mathur and B.Wilkes,), *Ap.J.*, **450**, 585.
- Testing Models for the Quasar Big Blue Bump via Color-Color Diagrams (A. Siemiginowska, O. Kuhn, M. Elvis, F.Fiore, J.C. McDowell, and B.J. Wilkes),1995 *Ap.J.*, **454**, 77.
- Associated X-ray Absorption in High Redshift Quasars (M. Elvis and F. Fiore), "Cold Gas at High Redshift", eds. M.N. Bremer, P.P. van der Werf, H.J.A. Röttgering, and C.L. Carilli [Dordrecht: Kluwer], p.239.
- X-ray Absorption in GPS and Red Quasars (M. Elvis, F. Fiore, P. Giommi, and P. Padovani), Second Workshop on Peaked Spectrum and Compact Steep Spectrum Radio Sources, 1996, eds. I.A.G. Snellen, B.T. Schilizzi, H.J.A. Röttgering & M.N. Bremer, [Leiden], p. 193.
- On the Observational Evidence for Accreting Black Holes in Quasars (F. Fiore and M. Elvis), Proc. *COSPAR*, "High Energy Radiation from Galactic and Extragalactic Black Holes", 1997, *Adv.Space Res.*, **19**, (1)85.
- The Soft X-ray Properties of a Complete Sample of Optically Selected Quasars II. Final Results (A. Laor, F. Fiore, M. Elvis, B.J. Wilkes, and J.C. McDowell), 1997 *Ap.J.*, **477**, 93.
- The X-ray Emission of NGC1068 (A.S. Wilson and M. Elvis), Proc. Ringberg Workshop on NGC1068, eds. 1997.
- Deriving the Quasar Luminosity Function from Accretion Disk Instabilities (A. Siemiginowska and M. Elvis), *Ap.J. Letters*, **482**, L9.
- X-raying a Galaxy: PHL6625 behind NGC247 (M. Elvis, F. Fiore, P. Giommi, and P. Padovani), *MNRAS (Letters)*, **291**, L49.
- ASCA and ROSAT X-ray Spectra of High Redshift Radio-Loud Quasars (M. Cappi, M. Matsuoka, A. Comastri, W. Brinkmann, M. Elvis, G.C.G. Palumbo, and C. Vignali) 1997, *Ap.J.*, **478**, 492.
- Science Driven Arguments for a 10 sq. meter, 1 arcsecond X-ray Telescope (M. Elvis and G. Fabbiano), 'Next Generation X-ray Observatories', eds. M.J.L. Turner and M.G. Watson [Leicester X-ray Astronomy Group Special Report, XRA97/02], p.33.
- The Einstein Slew Survey (M. Elvis, D. Plummer, J. Schachter, and G. Fabbiano), *Ap.J. Suppl.*, **80**, 257.
- The Einstein Slew Survey Sample of BL Lacs (E.S. Perlman, J.T. Stocke, J.F. Schachter, M. Elvis, E. Ellingson, C.M. Urry, C. Impey, and P. Klotzinsky), *Ap.J.Suppl.*, **104**, 251.

- X-ray Spectral Evolution of High Redshift Quasars (J. Bechtold, M. Elvis, F. Fiore, O. Kuhn, R. Cutri, J.C. McDowell, M. Rieke, A. Siemiginowska, and B.J. Wilkes), 1994, *A.J.*, **108**, 759.
- Deriving the Quasar Luminosity Function from Accretion Disk Instabilities (A. Siemiginowska and M. Elvis), *Ap.J. Letters*, **482**, L9.
- X-ray Constraints on the Intergalactic Medium (T.L. Aldcroft, M. Elvis, J.C. McDowell, and F. Fiore), 1994, *Ap.J.*, **437**, 584.
- The Spectral Energy Distribution of the $z = 3$ Quasar HS1946+7658 (O. Kuhn, J. Bechtold, R. Cutri, M. Elvis, and M. Rieke), *Ap.J.Letters*, **438**, 643.
- The Complex Soft X-ray Spectrum of Low-Redshift Radio-Quiet Quasars II. The Broad Band Spectral Energy Distribution (F. Fiore, A. Siemiginowska, M. Elvis, B.J. Wilkes, J.C. McDowell, and S. Mathur), *Ap.J.*, **449**, 74.
- The X-ray and Ultraviolet Absorbing Outflow in 3C351 (S. Mathur, B.J. Wilkes, M. Elvis, and F. Fiore), *Ap.J.*, **434**, 493.
- Testing Unified X-ray/UV Absorber Models with NGC5548 (S. Mathur, M. Elvis, and B.J. Wilkes), *Ap.J.*, **452**, 230.
- ASCA Observations of a BALQSO: PHL 5200 (S. Mathur, M. Elvis and K.P. Singh), *Ap.J.Letters*, **455**, L9.
- X-ray Continuum and Iron K Emission Line From the Radio Galaxy 3C390.3 (M. Inda, M. Tashiro, Y. Kohmura, T. Ohashi, K. Makishima, P. Barr, K. Hayashida, G.G. C. Palumbo, G. Trinchieri, M. Elvis, and G. Fabbiano), *Ap.J.*, **420**, 143.
- Interstellar Medium in the Seyfert Galaxy NGC7172 (G.C. Anupama, A.K. Kembhavi, M. Elvis, and R. Edelson), *MNRAS*, **276**, 125.
- An ASCA GIS Spectrum of S5 0014+813 at $z=3.384$ (M. Elvis, M. Matsuoka, A. Siemiginowska, F. Fiore, T. Mihara, and W. Brinkmann) *Ap.J.Letters*, **436**, L55.
- Galactic HI Column Densities toward Quasars and AGN (E.M. Murphy, F.J. Lockman, A. Laor, and M. Elvis) *Ap.J.Suppl.*, **105**, 369.

X-ray Spectral Survey of WGACAT Quasars, I: Spectral Evolution & Low Energy Cut-offs

Fabrizio Fiore^{1,2,3}, Martin Elvis¹, Paolo Giommi³,
Paolo Padovani⁴

¹ Harvard-Smithsonian Center for Astrophysics
60 Garden St, Cambridge MA 02138

²Osservatorio Astronomico di Roma, Monteporzio (Rm), Italy

³BeppoSAX Science Data Center, Roma, Italy

⁴Dipartimento di Fisica, II Università di Roma

version: 1pm June 24 1997

ABSTRACT

We have used the WGA catalog of ROSAT PSPC X-ray sources to study the X-ray spectrum of about 500 quasars in the redshift interval 0.1–4.1, detected with a signal to noise better than 7. We have parameterized the PSPC spectrum in terms of two ‘effective energy spectral indices’, α_S (0.1–0.8 keV), and α_H (0.4–2.4 keV), which allows for the different Galactic N_H along the quasars line of sight. We have used these data to explore the questions raised by the initial PSPC high redshift quasar studies, and in particular the occurrence of low X-ray energy cut-offs in high redshift radio-loud quasars. We have also studied the emission spectra of a large sample of radio-loud and radio-quiet quasars and studied their differences.

We find that low energy X-ray cut-offs are more commonly (and perhaps exclusively) found in radio-loud quasars. Therefore the low energy X-ray cut-offs are physically associated with the quasars, and not with intervening systems, since those would affect radio-quiet and radio-loud equally. We suggest that photoelectric absorption is a likely origin of these cut-offs.

The number of ‘cut-offs’ in radio-loud quasars significantly increases with redshift, rather than with luminosity. A partial correlation analysis confirms that α_S is truly anti-correlated with redshift at the 99.9% confidence level, indicating evolution with cosmic epoch, and not a luminosity effect. Conversely, for α_H the observed anti-correlation with redshift is mostly due to a strong dependence on luminosity.

We find marginal evidence for a flattening of α_H ($P=4.5\%$) going from $z<1$ to $z=2$, in radio-quiet quasars, in agreement with previous studies. On the other

ABSTRACT

We present and discuss an X-ray image and a medium resolution X-ray spectrum of the Seyfert 2 galaxy NGC 2110 obtained with the High Resolution Imager (HRI) on the *Rosat* X-ray Observatory (0.1–2.4 keV) and Goddard's Broad Band X-ray Telescope (BBXRT; 0.3–11 keV), respectively. Spatially resolved soft X-ray emission, which peaks 4'' to the north of the nucleus and near the position of the highest excitation optical emission line gas, is seen in the HRI observation. The extent has a flux of $\sim 3 \times 10^{-13}$ ergs cm $^{-2}$ s $^{-1}$ and accounts for $11 \pm 3\%$ of the total 0.1–2.4 keV flux. To model the BBXRT spectrum, a soft excess component is required which has a flux of $\sim 3.5 \times 10^{-13}$ ergs cm $^{-2}$ s $^{-1}$ and accounts for $\sim 14 \pm 6\%$ of the total 0.1–2.4 keV flux. In addition, BBXRT confirms the presence of an ~ 175 eV EW Fe K α fluorescence line in NGC 2110.

Because of the good agreement between their fluxes, we propose that the soft excess arises from the spatially resolved X-ray emission. This is contrary to previous suggestions that the spectral soft excess in NGC 2110 is due to leakage of the X-ray continuum through a patchy absorber. The temperature of the gas responsible for the soft excess is too high to be accounted for by local shock heating. In order to explain the soft excess and extent as either scattered continuum X-rays or fluorescence from gas photoionized by the nuclear source, the hard X-rays must be emitted anisotropically. However, the soft excess and extent can be well modeled as thermal emission from a hot, outflowing wind, which may also be responsible for confining at least some portion of the optical narrow line-emitting clouds.

Subject Headings: galaxies: individual (NGC 2110) - galaxies: interstellar matter - galaxies: nuclei - galaxies: Seyfert - X-rays: galaxies

X-ray Spectral Survey of WGACAT Quasars, II: Optical and Radio Properties of Quasars with Low Energy X-ray Cut-offs

Martin Elvis¹, Fabrizio Fiore^{1,2,3}, Paolo Giommi³,
Paolo Padovani⁴

¹ Harvard-Smithsonian Center for Astrophysics
60 Garden St, Cambridge MA 02138, USA

²Osservatorio Astronomico di Roma, Monteporzio (Rm), Italy

³BeppoSAX Science Data Center, Roma, Italy

⁴Dipartimento di Fisica, II Università di Roma "Tor Vergata", Via della Ricerca Scientifica
1, I-00133 Roma, Italy

(version: 11:45m, 2 June 1997, post-referee)

re-submitted 6/3/97

ABSTRACT

We have selected quasars with X-ray colors suggestive of a low energy cut-off, from the ROSAT PSPC pointed archive. We examine the radio and optical properties of these 13 quasars. Five out of the seven quasars with good optical spectra show associated optical absorption lines, with two having high Δv candidate systems. Two other cut-off quasars show reddening associated with the quasar. We conclude that absorption is highly likely to be the cause of the X-ray cut-offs, and that the absorbing material associated with the quasars, not intervening along the line-of-sight. The suggestion that Gigahertz Peaked Sources are associated with X-ray cut-offs remains unclear with this expanded sample.

Subject headings: quasars — absorption, X-rays

1. Introduction: Low Energy X-ray Cut-offs in Quasars

The first X-ray spectra of high z quasars showed strong, unanticipated, low energy cut-offs (Elvis et al., 1994). A tantalizing connection of these cut-offs with GPS quasars was also suggested, raising the possibility that these cut-offs were due to hot, galaxy-scale, medium that also confined the radio sources. If nuclear absorbing material produces the cut-offs a



Mark El

**THE ORIGIN OF THE SOFT X-RAY EXCESS
IN THE SEYFERT 2 GALAXY NGC 2110**

**K.A. Weaver, R.F. Mushotzky, P.J. Serlemitsos,
A.S. Wilson, M. Elvis, and U. Briel**



**LABORATORY FOR HIGH ENERGY
ASTROPHYSICS**

**National Aeronautics And Space Administration
Goddard Space Flight Center
Greenbelt, Maryland 20771**

EXTENDED SOFT X-RAY EMISSION IN SEYFERT GALAXIES: ROSAT HRI OBSERVATIONS OF NGC 3516, NGC 4151, AND MARKARIAN 3

JON A. MORSE AND ANDREW S. WILSON

Space Telescope Science Institute, 3700 San Martin Drive, Baltimore, MD 21218; morsey@stsci.edu, awilson@stsci.edu

MARTIN ELVIS

Harvard-Smithsonian Center for Astrophysics, 60 Garden Street, Cambridge, MA 02138; elvis@cfa.harvard.edu

AND

KIMBERLY A. WEAVER

Department of Astronomy and Astrophysics, 525 Davey Laboratory, Penn State University, University Park, PA 16802;
 kweaver@astro.psu.edu

Received 1994 May 26; accepted 1994 July 28

ABSTRACT

We have used the *ROSAT* High Resolution Imager (HRI) to examine the distribution of soft X-rays in three nearby Seyfert galaxies with $\sim 4''$ – $5''$ FWHM spatial resolution. A feature of our analysis is an attempt to remove errors in the aspect solution using a method developed by one of us (J. M.).

NGC 4151 shows resolved X-ray emission that is spatially correlated with the optical extended narrow-line region (ENLR), confirming the results obtained with the *Einstein* HRI by Elvis, Briel, & Henry. Image deconvolutions allow us to trace the extended X-rays along a position angle of $\sim 50^\circ/230^\circ$ as far as ~ 1.5 kpc southwest and ~ 0.5 kpc northeast of the nucleus (assuming a distance of 20 Mpc with $H_0 = 50 \text{ km s}^{-1} \text{ Mpc}^{-1}$). When a point source is subtracted from the nucleus of NGC 4151, the extended, bipolar X-rays peak in brightness ~ 425 pc southwest of the nucleus and ~ 280 pc northeast of the nucleus. The extended emission accounts for at least 31% of the total 0.1–2 keV *ROSAT* HRI flux (19% from the southwest quadrant, 12% from the northeast and constitutes roughly half of the total soft X-ray excess emission observed with other X-ray detectors. The soft X-ray excess in NGC 4151 has been modeled recently as containing both variable and constant flux components. We suggest that the constant flux component of the soft excess emission originates in the spatially extended regions we have resolved. If the extended X-rays result from electron-scattering of nuclear X-rays, the central source must emit anisotropically, and preferentially toward the extended X-rays and the ENLR. Alternatively, the extended X-rays may represent thermal emission from a hot ($T \sim 10^7$ K), outflowing wind which is in rough pressure equilibrium with the optical narrow-line-emitting clouds observed over the same spatial scale.

NGC 3516 is elongated along a position angle of $\sim 40^\circ/220^\circ$, similar to the direction of the Z-shaped narrow-line region. However, the azimuthally averaged radial brightness profile inside a radius of $10''$ is not distinguishable from a calibration point source. Much or all of the elongation may result from residual errors in the aspect solution, although an extended component associated with the ENLR is possible.

Mrk 3 is very faint in our HRI image and is probably spatially unresolved. We detect the faint X-ray source $\sim 2''$ west of the Mrk 3 nucleus previously found by Turner, Urry, & Mushotzky. It is not known whether this companion is physically associated with Mrk 3 although it does lie along a direction that is within $\simeq 1^\circ$ of the axis of the $2''$ nuclear radio jet.

We also detected the BL Lac object BL 1207+39 $\sim 5'$ north-northwest of NGC 4151. This object appears spatially unresolved, but some excess X-ray emission may be observed in the azimuthally averaged radial brightness profile of BL 1207+39 between radii of $10''$ and $30''$ when compared to a calibration source. A much deeper image is necessary to confirm this result.

Subject headings: galaxies: individual (NGC 3516, NGC 4151, Markarian 3) — galaxies: Seyfert — X-rays: galaxies

1. INTRODUCTION

Spatially extended X-ray emission may be a common feature among Seyfert galaxies (Elvis et al. 1990; Wilson et al. 1992; see Wilson 1994 for an overview). This is not surprising since high-velocity outflows from active galactic nuclei (AGNs) should generate hot gas behind shock waves that form in wind-cloud interactions or through entrainment of interstellar gas by the nuclear-driven jet. Gas may be heated to soft X-ray-emitting temperatures by the compact nuclear UV–X-ray source. Synchrotron emission or inverse Compton scattering by relativistic electrons may also produce extended X-rays. In

addition, X-rays generated in the compact active nucleus may be scattered by circumnuclear electrons and be seen as an X-ray “halo.” AGN outflows and nuclear radiation fields are often observed to be collimated, so any of the above mechanisms may generate extended X-ray distributions as well.

The interpretation of soft X-ray spectra and time variability of AGNs will be complicated by the presence of spatially extended X-rays. The spectra may reflect a composite of emission mechanisms and X-rays produced from outlying regions will “dilute” any variability of the compact source. It is valuable, therefore, to map the spatial structure of the X-ray-

AN X-RAY IMAGE OF THE SEYFERT GALAXY NGC 1068

A. S. WILSON¹

Astronomy Department, University of Maryland, College Park, MD 20742; and Space Telescope Science Institute, 3700 San Martin Drive,
 Baltimore, MD 21218

M. ELVIS¹

Harvard Smithsonian Center for Astrophysics, 60 Garden Street, Cambridge, MA 02138

A. LAWRENCE¹

Physics Department, Queen Mary and Westfield College, University of London, Mile End Road, London E1 4N2, England, UK

AND

J. BLAND-HAWTHORN¹

Department of Space Physics and Astronomy, Rice University, Houston, TX 77251-1892

Received 1992 January 21; accepted 1992 March 18

ABSTRACT

We present and discuss an image of NGC 1068 with resolution 4"–5" obtained with the High Resolution Imager on the *ROSAT* X-ray Observatory in the energy band 0.1–2.4 keV. The map shows a compact nuclear source, circumnuclear extended (diameter ≈ 1.5 kpc) emission, and emission on a scale (diameter ≈ 13 kpc) similar to the starburst disk. The circumnuclear emission extends preferentially toward the NE, the same direction as found in several other wavebands. We favor thermal emission from a hot (10^6 – 7 K), outflowing wind as the source of the nuclear and circumnuclear emission. This hot gas has a similar pressure to that of the optical line-emitting filaments in the lower density narrow-line region, and may be responsible for their confinement. The large-scale X-rays are probably dominated by emission from the starburst disk, although a contribution from an extension of the nucleus-driven wind to large radii is possible. The X-ray spectrum of the starburst disk is found to be harder than that of the nucleus. Emission from the starburst, rather than the electron-scattered Seyfert nucleus, may be responsible for much of the hard spectrum emission from NGC 1068 in the 2–10 keV band. Recent modeling of the electron-scattering cone in this galaxy has required the optical depth to photoelectric absorption near 1 keV to be ≤ 1 , but this constraint is unnecessary if most of the X-ray emission comes from spatial scales comparable to the starburst and the narrow-line region.

Subject headings: galaxies: individual (NGC 1068) — galaxies: interstellar matter — galaxies: jets — galaxies: nuclei — galaxies: Seyfert — X-rays: galaxies

1. INTRODUCTION

Studies of spatially extended, soft X-ray emission in active galaxies may yield valuable information about the interaction between the active galactic nucleus (AGN) and its surroundings. Thermal bremsstrahlung emission from hot gas should be ubiquitous, for such gas may be generated in shock waves produced through collisions between high-velocity clouds in the narrow-line region (NLR), or through entrainment of interstellar clouds in a radio jet, a radio lobe, or an outflowing wind. Extended X-ray emission associated with AGN can also result from synchrotron radiation or inverse Compton scattering. X-rays generated by the compact, nuclear X-ray source may be scattered by electrons in the interstellar medium and be seen as an X-ray "halo."

The nearby (15 Mpc, for $H_0 = 75 \text{ km s}^{-1} \text{ Mpc}^{-1}$), luminous $[(2-3) \times 10^{41} L_\odot]$ Seyfert galaxy NGC 1068 is an obvious candidate for extended X-ray emission, for it contains high-velocity (up to $\approx 1000 \text{ km s}^{-1}$) gas clouds in the inner $\approx 15''$ – $20''$ (1.1–1.5 kpc; e.g., Cecil, Bland, & Tully 1990) and a "linear" radio source, with extent 13" (950 pc), which is apparently fueled by collimated ejection from the active nucleus (Wilson & Ulvestad 1982). Further, X-rays should be produced by supernova remnants and X-ray binaries associated with the luminous, 30" (2.2 kpc) scale, disk "starburst" (e.g., Bruhweiler, Truong, & Altner 1991; Telesco et al. 1984). Although the

spectrum of the integrated X-ray emission of NGC 1068 has been measured (Monier & Halpern 1987; Elvis & Lawrence 1988), no studies of its spatial distribution have been published.

A quite different motivation for searching for extended, soft X-ray emission from NGC 1068 is related to the properties of the nuclear, electron scattering zone. Antonucci & Miller (1985) found that the spectrum of NGC 1068 (classically a Seyfert galaxy of type 2) in linearly polarized light resembles the spectrum of a Seyfert 1 galaxy. They proposed that the galaxy contains a Seyfert 1 nucleus blocked from direct view by a thick torus, but rendered visible through scattering by a cloud of electrons along the axis of the torus. Miller, Goodrich, & Mathews (1991) have inferred an electron temperature of less than $3 \times 10^5 \text{ K}$ for the scattering cloud from limits to broadening of $H\beta$ by the scattering. This low temperature must be reconciled with the high level of ionization implied by the absence of photoelectric absorption in the X-ray spectrum (Elvis & Lawrence 1988) and by the observed energy of the Fe $K\alpha$ line (Koyama et al. 1989). As described in detail by Miller, Goodrich, & Mathews (1991), models satisfying these contrasting constraints are possible, but the range allowed for the physical parameters describing the scattering zone is uncomfortably small. The constraints would be eased if some of the X-ray emission originates from larger scales than the scattering zone, and therefore does not have to pass through it.

In order to image NGC 1068 in soft X-rays, we have observed it with the High Resolution Imager (HRI) on the *ROSAT* X-Ray Observatory. The galaxy was observed

¹ Guest Observer, *ROSAT* Observatory.

X-ray and optical continua of AGN with extreme Fe II emission

Submitted to Monthly Notices of the RAS February 2 1996

A. Lawrence

Institute for Astronomy, University of Edinburgh
Royal Observatory, Blackford Hill, Edinburgh EH9 3HJ

M. Elvis, B.J. Wilkes

Center for Astrophysics

60 Garden St, Cambridge MA 02138, USA

I. McHardy

Physics Department, Southampton University
University Road, Southampton SO9 5NH

N. Brandt

Institute of Astronomy, University of Cambridge
Madingley Rd, Cambridge CB3 0HA

ABSTRACT

We present the results of ROSAT PSPC observations of three AGN with extremely strong Fe II emission (P111, 1092; IRAS 07598+6508; 1 Zw 1) and two AGN with very weak Fe II emission (MKN 10 and MKN 110). The weak Fe II emitters have X-ray spectra typical of Type 1 AGN ($\alpha \approx 1.35$ and 1.41, where α is the spectral energy index). Of the strong Fe II emitters, two have steep spectra (P111, 1092 has $\alpha \approx 3.5$ and 1 Zw 1 has $\alpha \approx 2.0$) and the third, IRAS 07598+6508 is barely detected and so is extremely X-ray quiet ($\alpha_{\text{Fe}} = 2.45$). During our observations, P111, 1092 varied by a factor of four, unusually fast for such a high luminosity object, and requiring an efficiency of matter-to-energy conversion of 2% or more. Compiling recently published data on other strong Fe II emitters we find that they are *always* X-ray quiet, and usually X-ray steep.

Adding these data to the complete UVX selected quasar sample of Laor et al (1994) we find a correlation of Fe II/H β with α_{Fe} in the sense of a strong statistical connection, but not a simple relationship: weak Fe II emitters always have flat spectra, but strong Fe II emitters can be either flat or steep. A much cleaner relationship exists between Fe II strength and X-ray loudness, as quantified by α_{Fe} , the spectral index between 1 μ m and 2 keV. We also confirm that Fe II/H β anti-correlates with Balmer line velocity width, which

in turn correlates well with both α_{Fe} and α_{Fe} in the sense that AGN with narrow lines are X-ray quiet. We also show that Fe II/H β correlates with both optical continuum slope, and the curvature of the optical-UV-X-ray continuum: strong Fe II objects have steeper continua and weaker "H δ bumps". The amount of extinction required to explain the optical steepening compared to normal quasars (E(B-V) in the range 0.2 to 0.6) suggests absorbing columns in the range $1 - 3 \times 10^{21} \text{ cm}^{-2}$, just about the right amount to reduce the ROSAT band X-ray flux by enough to explain the correlation with α_{Fe} . However the spectral shapes observed in the ROSAT band are not consistent with a simple absorption model.

Three objects in our total sample of 19 stand out persistently in all correlations: MKN 231, IRAS 07598+6508, and MKN 507. Interestingly, two out of three are known to have low ionisation broad absorption lines in the UV, and the third (MKN 507) has no UV spectrum available. Furthermore low-ionisation broad absorption lines are at least an order of magnitude more common in strong Fe II emitters than in quasars in general. Overall, continuum slope and blue shifted absorption should be added to the intriguing cluster of properties which all vary loosely together, and which has been isolated as "eigen vector 1" by Boroson and Green (1992): Fe II strength, velocity width, narrow line strength, and line asymmetry. We suggest that the underlying parameter is the density of an outflowing wind.

1 Introduction

The Fe II emission lines which dominate the optical-UV spectra of many AGN present a worrying puzzle in several ways: (i) The total luminosity in Fe II emission often exceeds the available ionising luminosity implied by the strength of Ly α (Netzer 1985; Collin-Souffrin 1986). (ii) All photo-ionisation models attempted so far have failed to replicated the strength of Fe II relative to the Balmer lines (see July 1993 and references therein). (iii) The relative strength of Fe II emission varies widely amongst different AGN, and shows intriguing correlations with other AGN properties: X-ray slope (Wilkes Elvis and McHardy 1988), Balmer line velocity width (Gaskell 1985; Zheng and O'Brien 1990; Boroson and Green 1992), radio loudness (Osterbrock 1977, Grandi and Osterbrock 1978, Bergeron and Kuntz 1984), and, within radio band objects, core dominance (July 1991). These correlations have been questioned however (e.g. Boroson 1989, Zheng and O'Brien 1990), and are perhaps not simple dependencies, but rather, statistical tendencies. As they seem to be important clues to the AGN phenomenon, it is important to clarify their reality and nature.

Over the last decade a handful of objects have been discovered which have "super-strong" Fe II emission (Bergeron and Kuntz 1980; Lawrence et al 1988; Lippart et al 1991). We quantify Fe II strength throughout this paper by the quantity $\text{Fe II } 4570/\text{H}\beta$, i.e. the relative fluxes in the 4570 \AA feature (made up of transitions from multiplets 37 and 38), and in H β . Because standard photo-ionisation models tend to have Fe II and Balmer lines tracking each other (e.g. July 1987), this is the most challenging quantity to test.

X-ray absorption by ionized oxygen in *ASCA* spectra of the infrared quasar IRAS 13349+2438

W.N. Brandt,^{1*} S. Mathur,¹ C.S. Reynolds² and M. Elvis¹

¹ *Harvard-Smithsonian Center for Astrophysics, 60 Garden Street, Cambridge, Massachusetts 02138, USA*

² *JILA, University of Colorado, Boulder, Colorado 80309-0440, USA*

18 July 1997

ABSTRACT

We present evidence for X-ray absorption by ionized oxygen in *ASCA* spectra of the prototype infrared quasar IRAS 13349+2438. This powerful ($L_{\text{bol}} \gtrsim 2 \times 10^{46} \text{ erg s}^{-1}$) quasar was studied in detail with *ROSAT*, and the combination of the X-ray data and optical/near-infrared spectropolarimetry strongly suggested the presence of a dusty ionized ('warm') absorber along the line of sight to the central X-ray source. The *ASCA* spectra, in contrast to an earlier claim, show evidence for ionized oxygen edges, and the presence of such edges appears to provide the most physically plausible interpretation of the data. Thus, the *ASCA* spectra support the dusty warm absorber hypothesis. The *ASCA* data also allow the physical properties of the warm absorber to be constrained far better than before. A one-zone warm absorber model indicates the ionized column to be in the range $(2\text{--}6) \times 10^{21} \text{ cm}^{-2}$, and it gives an ionization parameter of $\xi = 31_{-12}^{+12} \text{ erg cm s}^{-1}$. The dusty warm absorber appears to have a density of $\lesssim 3 \times 10^8 \text{ cm}^{-3}$, and it is probably located outside the broad-line region. The dust in the warm absorber does not appear to have been heavily sputtered or destroyed via other means. Based on the *ASCA* fitting, we suggest that ultraviolet absorption lines from the warm absorber may be detectable and discuss how they can be used to further constrain the warm absorber properties. We compare and contrast the X-ray properties of IRAS 13349+2438 with those of broad absorption line quasars. We comment on the steep $> 2 \text{ keV}$ continuum of IRAS 13349+2438 and examine the relevance to some models of radiative Fe II formation.

Key words: galaxies: individual: IRAS 13349+2438 – galaxies: active – X-rays: galaxies.

1 INTRODUCTION

IRAS 13349+2438 ($z = 0.107$) is the prototype infrared quasar with high polarization (Beichman et al. 1986; Wills et al. 1992, hereafter W92). It is radio quiet and has a bolometric luminosity of $\gtrsim 2 \times 10^{46} \text{ erg s}^{-1}$. W92 presented a detailed model for the optical and near-infrared light paths in IRAS 13349+2438 in which we are viewing the combination of a direct, but attenuated, quasar spectrum and a scattered spectrum. They found an attenuation of at least $E(B - V) = 0.3$, which corresponds to an X-ray absorption column density of $\gtrsim 1.7 \times 10^{21} \text{ cm}^{-2}$ assuming the mean Galactic dust-to-gas ratio (see equation 7 of

Burstein & Heiles 1978). Brandt, Fabian & Pounds (1996, hereafter BFP96) used *ROSAT* Position Sensitive Proportional Counter (PSPC) and Wide Field Camera (WFC) data to test the W92 model. IRAS 13349+2438 was very bright for the PSPC, being seen at up to 5 count s^{-1} . BFP96 found large-amplitude X-ray variability and a high X-ray luminosity which argued against the possibility that most of the X-rays were scattered to Earth around the attenuating matter of W92 (barring an extremely unusual X-ray scattering 'mirror'). Furthermore, they found that the *ROSAT* spectrum constrained the intrinsic X-ray absorption column of neutral matter to be about 35 times smaller than expected based on the optical/near-infrared extinction. To reconcile this large discrepancy, BFP96 invoked a dusty warm absorber, in which the dust causing the optical extinction is embedded in ionized, rather than neutral, gas. This reduced the expected X-ray absorption greatly and thereby allevi-

* Current address: The Pennsylvania State University, Department of Astronomy and Astrophysics, 525 Davey Lab, University Park, Pennsylvania 16802, USA

Abstract

We discuss several models of quasar *big blue bump* emission in color-color and color-luminosity diagrams. We define several broad passbands: IR ($0.8 - 1.6\mu\text{m}$), VIS ($4000 - 8000\text{\AA}$), UV ($1000 - 2000\text{\AA}$), UV1 ($1400 - 2000\text{\AA}$) and UV2 ($1000 - 1400\text{\AA}$), SX ($0.2 - 0.4\text{ keV}$). The colors have been chosen to investigate characteristics of the big blue bump: (1) IR/VIS color represents the importance of the IR component and shows the contribution around $\sim 1\mu\text{m}$; (2) UV/VIS color shows the slope of the big blue bump: in a region where it dominates a higher value means the bump gets steeper; (3) the combination of IR/VIS/UV colors shows the relative strength of the big blue bump and the IR component; (4) UV1/UV2 color is important as an indicator of a flattening of the spectrum in this region and the presence of the far-UV turn-over. (5) UV/SX tests the relationship between the big blue bump and the soft X-ray component. All colors are needed to investigate the range of model parameters.

We describe the colors for several models: accretion disk models in Schwarzschild and Kerr geometries, single temperature optically thin emission, combination of the main emission model and non-thermal power law or dust, irradiation of the disk surface. We test models against the sample of 47 low redshift quasars from Elvis et al. (1994, Paper I). We find: (1) modified blackbody emission from an accretion disk in a Kerr geometry can successfully reproduce both the luminosities and colors of the quasars except for the soft X-ray emission; (2) no additional components (hot dust or power law) are needed to fit the optical-UV colors when the irradiation of the surface of the disk is included in the model; (3) even modest (10%) irradiation of the surface of the disk modifies significantly the optical colors; (4) the simplest, single temperature, free-free models need either an additional component or a range of temperatures to explain the observations.

Tables of predicted colors for each model family are provided on the AAS CD-ROM.

The high-temperature big blue bump in the Seyfert galaxy RE J1034 + 396

E. M. Puchnarewicz,¹ K. O. Mason,¹ A. Siemiginowska² and K. A. Pounds³

¹Mullard Space Science Laboratory, University College London, Holmbury St. Mary, Dorking, Surrey RH5 6NT

²Harvard-Smithsonian Center for Astrophysics, 60 Garden Street, MS-4, Cambridge, MA 02138, USA

³X-ray Astronomy Group, University of Leicester, University Road, Leicester LE1 7RH

Accepted 1995 February 24. Received 1995 February 15; in original form 1994 December 2

ABSTRACT

X-ray, UV and optical spectra are presented for a rare, EUV-bright Seyfert galaxy RE J1034 + 396 ($z=0.042$). When combined, these data describe a very-high temperature big blue bump (BBB; $kT_{\text{eff}} \sim 100$ eV) whose high energy turnoff is observed in soft X-rays. The soft X-ray/UV flux ratio is extremely high, $L_{0.2\text{keV}}/L_{1200\text{\AA}} \sim 10$, compared to AGN in general whose ratio is usually less than 1. The optical/UV continuum betrays no trace of the BBB or the host galaxy. It rises steeply to the red, and is consistent with an underlying far-IR to X-ray power law with an index of ~ 1.3 . This may represent the first direct identification of an optical power law component in a non-blazar AGN. We compare the optical to soft X-ray spectrum of RE J1034 + 396 with three mechanisms for the production of the BBB: an optically thick accretion disc (AD); optically thin emission from a hot plasma; and reprocessing in cool clouds. A thin AD can reproduce the observed spectrum of RE J1034 + 396, but a free-free spectrum predicts too much flux in the UV. The reprocessing of a non-thermal continuum is only possible if there is a steep break between ~ 60 and 1000 Å; a reprocessed free-free spectrum is an alternative. We compare the data with those of the high-redshift quasar E1346 + 266, whose BBB component is similar in shape, but 200 times stronger than that of RE J1034 + 396. A simple, thin AD is *not* appropriate for E1346 + 266 because of its high luminosity, but, when electron scattering is taken into account, an adequate representation is obtained for a black hole mass $M = 2.3 \times 10^8 M_{\odot}$ with an accretion rate of $2.7 M_{\odot} \text{ yr}^{-1}$ ($L/L_{\text{Edd}} \sim 2$). Optically thin ($T_{\text{brem}} = 7 \times 10^6 \text{ K}$) emission and reprocessed free-free are also possible for E1346 + 266.

Key words: accretion, accretion discs – line: formation – galaxies: active – galaxy individual: RE J1034 + 396 – galaxies: Seyfert – X-rays: galaxies.

1 INTRODUCTION

A universally acceptable explanation for the origin of the ‘big blue bump’ (BBB) in active galactic nuclei (AGN) has proved to be elusive. This feature dominates the spectra of most non-blazar AGN (e.g. Edelson & Malkan 1986; Elvis et al. 1994). It is usually seen rising through the optical and UV, and the soft X-ray excess (e.g. Turner & Pounds 1989; Walter & Fink 1993; Thompson & Córdova 1994) is believed to be its high-energy tail. It contains the bulk of the bolometric luminosity of the spectrum, therefore understanding its origin and its effect on the environment are essential for developing realistic models of the central engine in AGN.

A complete description of the BBB has been frustrated by the lack of data in the extreme ultraviolet (EUV), where the peak lies. EUV photons are very readily absorbed by the neutral and ionized gas that lies in our own Galaxy and in the regions local to the AGN themselves. Detections of AGN by the ROSAT Wide Field Camera (WFC; Wells et al. 1990) which is sensitive between ~ 60 and 200 eV, were restricted to Galactic column densities below $2 \times 10^{20} \text{ cm}^{-2}$. Nonetheless, five Seyferts, RE J1034 + 396, Mrk 478 (QS 1440 + 356), RE J1237 + 267 (IC3599, Zw 159.034), R J2248 – 511 and RE J1337 + 243 were observed (Pounds et al. 1993; Mason et al. 1995).

We present observations of one of these rare EUV-bright

Abstract

Eight high signal to noise ROSAT PSPC observations of six low-redshift ($0.048 < z < 0.155$) radio-quiet quasars have been analyzed to study any soft excess. All the spectra can, at least roughly, be described in the 0.1-2.5 keV band by simple power laws reduced at low energies by Galactic absorption. The strong oxygen edges seen in the PSPC spectra of several Seyfert galaxies and quasars are not observed in this sample. The limits implied for the amount of absorbing gas intrinsic to the quasars are particularly tight: of the order of $\sim 10^{20} \text{ cm}^{-2}$. The range of energy indices is broad: $1.3 < \alpha_E < 2.3$. The energy indices are systematically steeper than those found in the same sources at higher energies (by $\Delta\alpha_E \sim 0.5 - 1$ with respect to *Ginga* or EXOSAT - 2-10 keV - measurements, and by $\Delta\alpha_E \sim 0.5$ with respect to IPC - 0.2-3.5 keV - measurements). This suggests a break between the hard and soft components in the "keV" region, and therefore that the PSPC spectra are strongly dominated by the soft components. In fact, a fit to the composite, high signal-to-noise, spectrum reveals a significant excess above ~ 1 keV with respect to the simple power law model. No evidence for strong emission lines is found in any of the quasars. This argues against emission from an ionized plasma as the main contributor to the soft X-ray component unless there is a distribution of temperatures. If the soft X-ray spectrum of these quasars is dominated by radiation reflected by the photoionized surface of an accretion disk, the absence of strong emission lines suggests high ionization parameters and therefore high accretion rates.

We include in two Appendices a comparison of the two official PSPC resolution matrices, those released on March 1992 and on January 1993, a discussion of the amplitude of the residual systematic uncertainties in the January 1993 matrix, and a comparison between the PSPC and IPC spectra of a sample of sources.

Subject headings: Quasars - X-ray: Spectra

**THE COMPLEX OPTICAL TO SOFT X-RAY
SPECTRUM OF LOW-REDSHIFT RADIO-QUIET
QUASARS. I: THE X-RAY DATA**

Fabrizio Fiore¹ , Martin Elvis, Jonathan C. McDowell, Aneta Siemiginowska
and Belinda J. Wilkes

Harvard-Smithsonian Center for Astrophysics
60 Garden St, Cambridge MA 02138

March, 7, 1994

¹Present address: Osservatorio Astronomico di Roma, via dell'Osservatorio 5, Monteporzio-
Catone (Rm), I00040 Italy

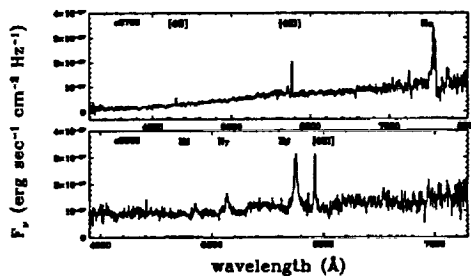
X-ray Selected Red, Absorbed Quasars

DONG-WOO KIM^{1,2} AND MARTIN ELVIS¹¹ Harvard-Smithsonian Center for Astrophysics 60 Garden Street, Cambridge, MA 02138, USA² Department of Astronomy and Space Science, Chungnam National University, Taejeon 305-764 Korea

We have performed optical spectroscopy to search for a hidden population of red, absorbed quasars. Bright, radio-quiet, optically-red X-ray sources were selected from the ROSAT WGA catalog, and the APM Catalog. Of 52 objects observed, we have found 5 red quasars with $\alpha_{opt} > 2$. They have moderate redshifts ($0.06 < z < 0.31$) and luminosities. These red quasars provide the first evidence for a radio-quiet population that is the counterpart of the radio-loud red quasars found by Smith and Spinrad (1980), and Webster et al. (1995). For all these red quasars, $H\alpha/H\beta > 5$ suggesting that they are absorbed ($A_V > 2$), rather than having intrinsically steep spectra. Even this moderate amount of extinction hides $\sim 10\%$ of quasars. Red quasars appears to be more frequent in fainter sources and so it is likely that there exists a larger population of more absorbed, fainter quasars.

Sample Selection

From the WGA catalog (White et al. 1995), we selected sources that are (1) X-ray bright ($f_X > 10^{-13}$ erg sec⁻¹ cm⁻²), (2) well-detected with SNR > 10 and DQFLAG > 5 , (3) within $r=18'$ from the detector center, (4) $|b| > 20^\circ$, and (5) unidentified. To effectively exclude Galactic sources, we required $\alpha_{ox} > 1.8$ and finally selected only those with red optical APM counterparts ($O - E > 2$). Of $\sim 70,000$ sources in WGACAT, 970 sources ($\sim 1\%$) satisfy the 5 criteria listed above. 10% of them, a mere 0.1% of WGACAT sources, also have $\alpha_{ox} > 1.8$ and $O - E > 2$. We have observed and identified 52 of these red sources.



Observations and Results

Of 52 sources observed 7 are quasars with red optical colors. Although all the sources were selected based on optical $O - E$ color, 2 quasars have relatively flat optical continuum shapes, either because of line emission, or uncertainties on the APM magnitudes. We measured the

optical continuum power law slopes, excluding strong emission lines, and found values of α_{opt} ($F_\nu \sim \nu^{-\alpha_{opt}}$) from 0.9 to 2.6. Five quasars have steep optical continuum spectra ($\alpha_{opt} > 2$), while the remaining 2 quasars are intermediate ($\alpha_{opt} = 1 - 1.5$). Figure 1 shows the mean spectra of two groups (the top one with $\alpha_{opt} > 2$ and the bottom one with $\alpha_{opt} < 2$).

These two groups also differ in their $H\beta$ line strengths (see Figure 1). The group with the steep optical continuum have strikingly weak $H\beta$ line or an upper limit, whereas the group with a relatively flat continuum show strong $H\beta$ emission. For all 5 quasars with $\alpha_{opt} > 2$, $H\alpha/H\beta > 5$, whereas the line ratios of the remaining 2 quasars are smaller. Using $H\alpha/H\beta$ as a measure of optical extinction, we find $A_V > 2$.

Discussion

Both the continuum slopes and the $H\alpha/H\beta$ ratios of these red quasars suggest that they are absorbed ($A_V > 2$ mag), rather than having intrinsically steep spectra. Moreover, the occurrence of red quasars appears to be 3-4 times higher for $O > 19$ mag than for $O < 19$ mag, as would be expected if they are absorbed.

The five reddest quasars are all radio-quiet and provide the first evidence for a radio-quiet population that is the counterpart of the radio-loud red quasars found by Smith and Spinrad (1980) and Webster et al. (1995).

Webster et al. (1995) suggested that 80% of radio-loud quasars had been missed by optical surveys, due to dust absorption. In our small sample, we estimate that the red quasars consists of about 4% of AGN ($F_X < 10^{-13}$ erg cm⁻² sec⁻¹ and $O \lesssim 20$ mag), increasing to $\sim 10\%$ at the same *unabsorbed* X-ray flux (assuming the ROSAT logN-logS curve, Hasinger et al. 1993). Apparently even a moderate amount of extinction ($A_V > 2$ mag) already hides 10% of quasars from optical color surveys. ASCA source counts in harder X-rays (e.g., Ueda 1997) indicate that larger A_V is common. To estimate an accurate fraction of this hidden population, particularly as a function of redshift and luminosity, needs study of more heavily absorbed and fainter objects. Potentially, red quasars could dominate all quasar populations, regardless of radio-loudness.

References

- Webster, R. L., Francis, P. J., Peterson, B. A., Drinkwater, M. J., & Mascl, F. J. 1995, *Nature*, 375, 469
 Smith, H. E. & Spinrad, H. 1980 *ApJ*, 236, 419.

X-ray Color Selected Warm Absorbers

FABRIZIO NICASTRO³, MARTIN ELVIS¹, AND FABRIZIO FIORE^{1,2}¹ Harvard-Smithsonian Center for Astrophysics 60 Garden St, Cambridge MA 02138² Osservatorio Astronomico di Roma via Osservatorio, Monteporzio-Catone (RM), I00040 Italy³ Istituto di Astrofisica Spaziale (CNR) Via Fosso del Cavaliere, Rome, 00131 Italy

1. Introduction

Absorption features from ionized gas are common in the X-ray spectra of *Seyfert* galaxies (Reynolds, 1997), but rare in the higher redshift, higher luminosity quasars (Laor et al., 1997). Main characteristic of warm absorber are strong OVII and OVIII edges at 0.74 and 0.87 keV (rest frame). The absence of absorption (either “cold” or “warm”), in high luminosity quasars could reveal an intrinsic property of this class of AGN. For example, AGN absorbers may all lie at a similar distance from the central source, so that the brighter UV-X-ray continuum in quasars photoionizes the gas, making it more transparent in the X-rays.

In this work we analyze the X-ray colors of a large sample of sources from the WGACAT, to select new warm absorbed quasar candidates. In both identified and unidentified source samples we search for sources with a deficit of counts in the 0.5-1 keV energy range. We look for possible optical and radio counterparts of these sources, in the POSS, UK Schmidt, NVSS and FIRST surveys. We use the optical and radio data to further screen the sample of unidentified sources from stars and galaxies.

1.1. Sample Selection

We selected from the WGACAT (White, Giommi & Angelini, 1994) well detected sources in two radial bands, an inner region (avoiding the target) for which good X-ray positions can be found, and an outer band in which a radio identification can pinpoint the optical counterpart. We used only sources that: (a) have good detection quality (i.e. QFLAG ≥ 5); (b) are far from the PSPC support structures and at offaxis angles smaller than 40' (i.e. excluding detections with $18' < \theta_{off} < 24'$ and $\theta_{off} > 40'$); (c) have a signal to noise ratio (SNR) greater than 15. This gives two samples of 773 AGN and 1530 UNIDENTIFIED sources.

We examined the two ROSAT-PSPC energy spectral indices α_S (0.1 – 0.8 keV), and α_H (0.9 – 2.4 keV) (obtained correcting the respective colors for the vignetting, PSF effects and Galactic absorption). We then selected sources with: $0 < \alpha_H < 1.1$, $\alpha_S > 1.3$, $\Delta\alpha_{S,H} < 0.2$, ($\theta_{off} < 18'$), $\Delta\alpha_{S,H} < 0.3$, ($24' < \theta_{off} < 40'$). There are 27 AGN, and 54 UNIDENTIFIED sources which satisfy these criteria. AGN: $\sim 50\%$ of the sources in our AGN sample are well known warm absorbers, and 3 out of the 13 remaining sources are new warm absorber candidates (see Table 1). UNIDENTIFIED: 5 out of the 54 sources have both optical and radio counterparts

in the POSS, UK Schmidt, NVSS and FIRST surveys. All these candidates have high X-ray to optical ratios indicative of AGN (Maccacaro et al., 1988).

1.2. Spectral Fits

We performed full spectral fit analysis of the 5 radio-loud unidentified sources and of 3 AGN not previously recognized as warm absorbers, using first a simple power law model (Model 1), and then adding either a physical warm absorber model (built with CLOUDY, Ferland, 1996), or an absorption line (Model 2). In all but one case the addition of a warm absorption component improves the χ^2 .

1.3. Conclusion

We used the X-ray color technique to select objects with PSPC spectral shapes markedly departing from a simple power law, and suggesting the presence of absorption edge features in the 0.5-1 keV energy range. We searched for optical and radio counterparts of the unidentified sources, and used these data to screen the sample from stars and normal galaxies. We found 5 unidentified sources with a radio counterpart (and quasar candidates on the basis of their X-to-optical ratio), and 3 not yet X-ray studied AGN. All these sources but 1 show absorption features by warm gas in their PSPC spectra, thus greatly expanding the sample of already known warm absorbed quasars.

References

- Ferland G.J., 1996: *CLOUDY 90.01*
 Laor A., Fiore F., Elvis M., Wilkes B.J., McDowell J.C., 1997, *ApJ* 477, 93
 Maccacaro T., Gioia I.M., Wolter A., Zamorani G., Stocke J.T., 1988, *ApJ* 326, 680
 Reynolds C.S., 1997, *MNRAS* 286, 513
 White N.E., Giommi P., & Angelini L., 1994, *IAUC* 6100

1 but-bl

TEN NEW BL LACERTAE OBJECTS DISCOVERED BY AN EFFICIENT X-RAY/RADIO/OPTICAL TECHNIQUE

JONATHAN F. SCHACHTER,² JOHN T. STOCKE,² ERIC PERLMAN,² MARTIN ELVIS,² RON REMILLARD,³
ARNO GRANADOS, JANE LUU,⁴ JOHN P. HUCHRA, ROBERTA HUMPHREYS,⁵
C. MEGAN URRY,⁶ AND JOHN WALLIN⁷

Harvard-Smithsonian Center for Astrophysics, MS 4, 60 Garden Street, Cambridge, MA 02138; and
University of Colorado, Department APAS, Campus Box 391, Boulder, CO 80309

Received 1992 August 31; accepted 1993 February 2

ABSTRACT

We report the recent discovery of 10 BL Lac objects in the *Einstein* IPC Slew Survey by means of X-ray/radio versus X-ray/optical color-color diagrams and confirming optical spectroscopy. These 10 BL Lac objects were discovered using a technique proposed by Stocke et al. which exploits the characteristic broad-band spectra of BL Lac objects. New VLA detections provide accurate fluxes [limiting $f(6\text{ cm}) \sim 0.5\text{ mJy}$] and $\sim 1''$ positions, facilitating the determination of an optical counterpart. All 10 new BL Lac objects show essentially featureless optical spectra and lie within the range of radio/X-ray/optical colors of known X-ray-selected BL Lac objects, when $\sim 1\text{ mag}$ optical variability is included. We expect ~ 50 new BL Lac objects in total, from complete optical follow-up of our now completed VLA work and recent Australia Telescope observations, yielding a complete Slew Survey sample of ~ 90 BL Lac objects.

Subject headings: BL Lacertae objects: general — galaxies: active — galaxies: nuclei —
methods: observational — X-rays: galaxies — surveys

1. INTRODUCTION

BL Lac objects have been hard to find: in the 20 years following the discovery of the first example (Schmitt 1968), their numbers grew by only a factor ~ 10 (Véron-Cetty & Véron 1991). By comparison, in the 20 years following the discovery of quasars (Schmidt 1963) their numbers grew 500-fold (Véron-Cetty & Véron 1991). The elusiveness of BL Lac objects is due to the very lack of strong emission lines that make BL Lac objects interesting. BL Lac objects account for $\sim 2\%$ (162 out of 7765) of sources in the Véron-Cetty & Véron (1989) AGN catalog.

In the last few years, the nearly complete identification of the *Einstein* Medium Sensitivity Survey (EMSS; Gioia et al. 1990; Stocke et al. 1991) has allowed the discovery of three dozen new BL Lac objects (Morris et al. 1991; Stocke et al. 1991). Through this work, a reliable and efficient technique for identifying new BL Lac objects from X-ray survey data was developed (Stocke et al. 1989). This paper reports the extension of this technique to the *Einstein* Slew Survey (Elvis et al. 1992). Using this technique, 10 BL Lac candidates were identified, all 10 of which have now been confirmed spectroscopically. These

are the first results of a new, uniformly selected, sample of 85–90 bright BL Lac objects.

2. AN X-RAY/RADIO/OPTICAL TECHNIQUE FOR IDENTIFYING BL LAC OBJECTS

The key to finding BL Lac objects is to exploit their salient characteristics:

First, all BL Lac objects are radio-loud [$\alpha_{RO} > 0.3$, i.e., $f(6\text{ cm}) > 1\text{ mJy}$ for $V \leq 20$; Stocke et al. 1990]. For this reason, radio surveys with follow-up optical spectroscopy (e.g., Kühr et al. 1981), have been considerably more efficient than optical surveys ($\sim 1\%$). Also, based upon X-ray observations of many BL Lac objects, there is strong evidence that all BL Lac objects are X-ray-loud (e.g., Schwartz & Ku 1983). Thus, X-ray surveys can be similar to radio surveys in their efficiency at finding BL Lac objects (Stocke et al. 1991; Schwartz et al. 1989).

Second, all BL Lac objects have distinctive X-ray/radio/optical colors (Stocke et al. 1991). Thus, X-ray surveys, combined with radio and optical data, have been shown to be the best approach thus far to find BL Lac objects ($\sim 80\%$ efficiency; Stocke et al. 1989, 1991; Morris et al. 1991).

Third, the surface density of X-ray-selected BL Lac objects flattens at fluxes below $10^{-12}\text{ ergs s}^{-1}\text{ cm}^{-2}$ (Wolter et al. 1991). Therefore, wide-angle (all-sky) surveys are better for detecting BL Lac objects than narrow-beam, deep surveys. Because the EMSS covers only 2% of sky, a shallower, wide-angle X-ray survey, e.g., the *Einstein* Slew Survey, would be expected to find more BL Lac objects. The Slew Survey, constructed from 2799 individual slews of the *Einstein* Imaging Proportional Counter (IPC), covers 50% of sky at an exposure time of 6 s (Elvis et al. 1992). The Slew Survey contains 819 total sources, having 1/2 positional uncertainty (90% confidence), most of which (78%) are identified with stars, emission-line AGNs, BL Lac objects, and clusters. Of the 193

¹ Research reported here used the Multiple Mirror Telescope Observatory, which is a joint facility operated by the Smithsonian Institution and the University of Arizona.

² Visiting Astronomer at the National Radio Astronomy Observatory (NRAO), which is operated by Associated Universities, Inc., under contract with the National Science Foundation (NSF).

³ Postal address: Massachusetts Institute of Technology, Center for Space Research, Room 37-595, Cambridge, MA 02139.

⁴ Smithsonian Fellow.

⁵ Postal address: University of Minnesota, School of Physics & Astronomy, Minneapolis, MN 55455.

⁶ Postal address: Space Telescope Science Institute, 3700 San Martin Drive, Baltimore, MD 21218.

⁷ Postal address: Naval Research Laboratory, Code 4129 6, 4555 Overlook Avenue SW, Washington, DC 20375.

ABSTRACT

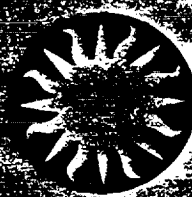
We present an analysis of the statistical properties of Mg II absorbers found in the spectra of 56 intrinsically faint, steep-spectrum radio quasars. We observe for the first time a significant excess of associated Mg II absorbers over the number expected from cosmologically distributed absorbers. This result is in contrast to previous Mg II surveys in which the QSOs were optically selected. This distinction is similar to the result for associated C IV absorbers, in which intrinsically faint, steep-spectrum quasars show excess associated absorption and intrinsically bright QSOs (both radio-loud and radio-quiet) do not show an excess.

From our spectra a statistically complete list of absorption lines is derived and we find 29 Mg II absorbers, 18 of which have not been previously reported. We also determine several characteristics of the quasar emission lines in our spectra. The Mg II absorber distribution as a function of redshift and equivalent width is calculated for our sample alone and from our sample combined with spectra from other surveys. For the redshift distribution $n(z) = n(1+z)^\gamma$, we obtain using the combined sample the values $\gamma = 1.11 \pm 0.46$ for $W_{min} = 0.6 \text{ \AA}$ and $\gamma = 2.47 \pm 0.68$ for $W_{min} = 1.0 \text{ \AA}$. We find that the distribution of strong absorbers is inconsistent with no evolution at a confidence between 2.2 to 2.9- σ , depending on the deceleration parameter q_0 . The discrepancy from no evolution is similar what had been previously reported.

Subject headings: quasars: absorption lines



Harvard-Smithsonian Center for Astrophysics



Preprint Series

Preprint 85-012
(Received June 5, 1985)

TESTING MODELS FOR THE QUASAR BIG BLUE BUMP VIA COLOR-COLOR DIAGRAMS

Anda Siemiginowska, Olga Kuhn, Martin Elvis, Fabrizio Fiore,
Jonathan McDowell, and Belinda J. Wilkes
Harvard-Smithsonian Center for Astrophysics

To appear in
The Astrophysical Journal
November 20, 1985

HARVARD COLLEGE OBSERVATORY

SMITHSONIAN ASTROPHYSICAL OBSERVATORY

20 Garden Street, Cambridge, Massachusetts 02138

MG II ABSORPTION IN A SAMPLE OF 56 STEEP-SPECTRUM QUASARS

Thomas L. Aldcroft¹

Department of Physics, Stanford University, Stanford, CA 94305-4060

Jill Bechtold

Steward Observatory, University of Arizona, Tucson, AZ 85721

and

Martin Elvis

Harvard-Smithsonian Center for Astrophysics, 60 Garden Street, Cambridge, MA 02138

Received _____; accepted _____

1994 Ap. J. Suppl. 93, 1.

¹Now at Center for Astrophysics, 60 Garden St., Cambridge, MA 02138

The Cambridge-Cambridge *ROSAT* Serendipity Survey – I. X-ray-luminous galaxies

B.J. Boyle,^{1,2} R.G. McMahon,¹ B.J. Wilkes³ and M. Elvis³

¹ Institute of Astronomy, University of Cambridge, Madingley Road, Cambridge CB3 0HA

² Present address: Royal Greenwich Observatory, Madingley Road, Cambridge CB3 0EZ

³ Center for Astrophysics, 60 Garden St, Cambridge, MA 21260, USA

Accepted 1994 September 20. Received 1994 September 19; in original form 1994 February 2

ABSTRACT

We report on the first results obtained from a new optical identification programme of 123 faint X-ray sources with $S(0.5\text{--}2\text{ keV}) > 2 \times 10^{-14} \text{ erg s}^{-1} \text{ cm}^{-2}$ serendipitously detected in *ROSAT* PSPC pointed observations. We have spectroscopically identified the optical counterparts to more than 100 sources in this survey. Although the majority of the sample (68 objects) are QSOs, we have also identified 12 narrow emission line galaxies which have extreme X-ray luminosities ($10^{42} < L_X < 10^{43.5} \text{ erg s}^{-1}$). Subsequent spectroscopy reveals them to be a mixture of starburst galaxies and Seyfert 2 galaxies in approximately equal numbers. Combined with potentially similar objects identified in the *Einstein* Extended Medium Sensitivity Survey, these X-ray-luminous galaxies exhibit a rate of cosmological evolution, $L_X \propto (1+z)^{2.5 \pm 1.0}$, consistent with that derived for X-ray QSOs. This evolution, coupled with the steep slope determined for the faint end of the X-ray luminosity function ($\Phi(L_X) \propto L_X^{-1.9}$), implies that such objects could comprise 15–35 per cent of the soft (1–2 keV) X-ray background.

Key words: galaxies: active – quasars: general – galaxies: Seyfert – galaxies: starburst – X-rays: galaxies.

1 INTRODUCTION

The launch of *ROSAT* has provided a new opportunity to resolve the soft (0.5–2 keV) X-ray background (XRB) down to flux levels five times fainter than achieved with the deepest pointings performed by the *Einstein* satellite (Griffiths et al. 1992). At these levels ($S \sim 2 \times 10^{-15} \text{ erg s}^{-1} \text{ cm}^{-2}$) almost 60 per cent of the XRB is resolved (Hasinger et al. 1993) and, at the current limit of the follow-up optical identification programmes ($S \sim 4 \times 10^{-15} \text{ erg s}^{-1} \text{ cm}^{-2}$, Georgantopoulos et al. 1995), QSOs account for the majority (~75 per cent) of the extragalactic sources. However, fluctuation analyses (Hasinger et al. 1993; Georgantopoulos et al. 1993) and differences between the X-ray spectra of QSOs and that of the background (Georgantopoulos et al. 1995) suggest that these QSOs are unlikely to contribute more than ~50 per cent of the 1-keV background and probably do not comprise more than ~20 per cent of the XRB at harder energies (2–10 keV), the energy range at which the XRB was first discovered (Giacconi et al. 1962). Indeed, at faint flux levels, $S < 10^{-14} \text{ erg s}^{-1} \text{ cm}^{-2}$, the spectroscopic observations of Georgantopoulos et al. (1995) tentatively identify an increasingly large fraction of galaxies as counterparts to X-ray sources.

Unfortunately the low flux levels currently employed in both the X-ray and optical regimes make optical identification difficult and positional coincidence hard to establish conclusively (e.g. Georgantopoulos et al. 1995). By slightly increasing

the flux limit and extending any survey over a wider area, it may be possible to identify the brighter members of any new class. We have therefore carried out an optical identification programme of X-ray sources detected by *ROSAT* at a level intermediate in flux, $S(0.5\text{--}2\text{ keV}) = 2 \times 10^{-14} \text{ erg s}^{-1} \text{ cm}^{-2}$, between the deepest *ROSAT* surveys and the Extended Medium Sensitivity Survey (EMSS, see Stocke et al. 1991) performed with the *Einstein* satellite at a flux limit $S(0.3\text{--}3.5\text{ keV}) \sim 1 \times 10^{-13} \text{ erg s}^{-1} \text{ cm}^{-2}$. The sources in our survey were detected ‘serendipitously’ in existing PSPC fields available in the *ROSAT* archive, originally taken to study the X-ray properties of known targets (QSOs/CVs/galaxies). The optical counterparts of these X-ray sources were identified spectroscopically with the William Herschel Telescope (WHT). A full description of the survey and catalogue will appear elsewhere (McMahon et al., in preparation, hereafter M95). In this paper we report on the discovery of a significant number of narrow emission line galaxies in the survey. In Section 2 we briefly describe the selection of the X-ray sources, the optical identification procedure and the spectroscopic observations. We discuss our results in Section 3 and present our conclusions in Section 4.

2 OBSERVATIONS

2.1 X-ray source detection

Objects in the Cambridge-Cambridge *ROSAT* Serendipity Survey (CRSS) were detected as serendipitous X-ray sources in

The Cambridge–Cambridge *ROSAT* Serendipity Survey – II. Classification of X-ray-luminous galaxies

B.J. Boyle,¹ R.G. McMahon,² B.J. Wilkes³ and Martin Elvis³

¹ Royal Greenwich Observatory, Madingley Road, Cambridge CB3 0EZ

² Institute of Astronomy, University of Cambridge, Madingley Road, Cambridge CB3 0HA

³ Center for Astrophysics, 60 Garden St, Cambridge, MA 02138, USA

Accepted 1995 April 20. Received 1995 March 27

ABSTRACT

We present the results of an intermediate-resolution (1.5 Å) spectroscopic study of 17 X-ray-luminous narrow emission-line galaxies previously identified in the Cambridge–Cambridge *ROSAT* Serendipity Survey and the *Einstein* Extended Medium Sensitivity Survey. Emission-line ratios reveal that the sample is composed of ten Seyfert and seven starburst galaxies. Measured linewidths for the narrow H α emission lines lie in the range 170–460 km s^{−1}. Five of the objects show clear evidence for asymmetry in the [O III] λ 5007 emission-line profile. Broad H α emission is detected in six of the Seyfert galaxies, which range in type from Seyfert 1.5 to 2. Broad H β emission is detected in only one Seyfert galaxy. The mean full width at half maximum for the broad lines in the Seyfert galaxies is FWHM = 3900 ± 1750 km s^{−1}. Broad (FWHM = 2200 ± 600 km s^{−1}) H α emission is also detected in three of the starburst galaxies. This emission could originate from stellar winds or supernova remnants. The mean Balmer decrement for the sample is H α /H β = 3, consistent with little or no reddening for the bulk of the sample. There is no evidence for any trend with X-ray luminosity in the ratio of starburst galaxies to Seyfert galaxies. Based on our previous observations, it is therefore likely that both classes of object comprise ~ 10 per cent of the 2-keV X-ray background.

Key words: galaxies: active – quasars: general – galaxies: Seyfert – galaxies: starburst – X-rays: general.

1 INTRODUCTION

A number of recent spectroscopic surveys of soft (0.5–2 keV) X-ray sources detected at faint fluxes with the *ROSAT* mission (Boyle et al. 1995; Georgantopoulos et al. 1995) have all confirmed that, while QSOs comprise in excess of 50 per cent of the total X-ray population down to these flux levels, an increasingly large number of X-ray-luminous, narrow (FWHM < 1000 km s^{−1}) emission-line galaxies (NLXGs) are identified as counterparts to faint X-ray sources with fluxes $S(0.5–2 \text{ keV}) < 10^{-13} \text{ erg s}^{-1} \text{ cm}^{-2}$. These galaxies have X-ray luminosities in the range $10^{42}–10^{43.5} \text{ erg s}^{-1}$, over 100 times more luminous than late-type galaxies (Fabbiano 1989) which exhibit similar low-resolution optical spectra. In a previous paper in this series (Boyle et al. 1995; hereinafter Paper I), we have demonstrated that, based on their space density and cosmological evolution, these emission-line galaxies could comprise between 15 and 30 per cent of the soft 0.5–2 keV X-ray background. This is entirely consistent with the upper limit of ~ 50 per cent for the contribution of QSOs to the 0.5–2 keV X-ray background, based on their luminosity function (Boyle et al. 1994), clustering properties (Georgantopoulos et al. 1993) and X-ray spectra (Georgantopoulos et al. 1995).

Unfortunately, due to the poor quality of many of the

identification spectra, little is known about the precise nature of this population. In particular, it is not clear whether these emission-line galaxies are examples of starburst galaxies or ‘hidden’ active galactic nuclei (e.g. Seyfert 2 galaxies), both of which have previously been suggested as possible significant contributors to the X-ray background (Griffiths & Padovani 1990; Fabian & Barcons 1992) and are known to exist in X-ray surveys (e.g. Böller et al. 1992), albeit at much higher X-ray flux levels and lower space densities.

In order to understand the origin of this potentially significant population of X-ray sources, we report in this paper on a detailed intermediate-resolution spectroscopic study of 17 NLXGs, 10 of which have been identified in the Cambridge–Cambridge *ROSAT* Serendipity Survey (CRSS, see Paper I), and a further 7 objects selected at random from the *Einstein* Extended Medium Sensitivity Survey (EMSS, Stocke et al. 1991) which we suspect are similar (Paper I). This sample comprises all but two of the NLXGs identified in the CRSS (CRSS1514.4+5627 and CRSS1605.9+2554), which were not observed due to lack of time.

In Section 2 we report on the observation and analysis of the NLXG spectra. Based on the results obtained from these spectra, we discuss the properties and classification of the NLXGs in Section 3, including the implications for the

A SAMPLE OF LOBE-DOMINATED QUASARS WITH Mg II ABSORPTION LINES

THOMAS L. ALDCROFT

Department of Physics, Stanford University, Stanford, California 94305-4060
 Electronic mail: tla@egret.stanford.edu

MARTIN ELVIS

Harvard-Smithsonian Center for Astrophysics, 60 Garden Street, Cambridge, Massachusetts 02138
 Electronic mail: elvis@cfa.harvard.edu

JILL BECHTOLD

Steward Observatory, University of Arizona, Tucson, Arizona 85721
 Electronic mail: jill@astro.as.arizona.edu

Received 1993 January 19; revised 1993 February 12

ABSTRACT

We present a sample of quasars which are lobe-dominated in their radio emission and contain Mg II absorption line systems. This sample will be useful in a search for redshifted H I 21 cm absorbers which are along lines of sight different from the optical. These systems will allow the measurement of the linear size and related physical parameters of the absorption line clouds. Since quasars appropriate for this study are rare, building this sample requires a substantial database of radio and optical observations. We have defined a set of criteria for selecting these objects and obtained the necessary data, from the literature and from new optical and Very Large Array (VLA) observations, to assemble a sample based on these criteria. Out of 4234 Quasi Stellar Objects (QSOs), we find 31 lobe-dominated quasars which are appropriate for optical and radio absorption line study in the Northern hemisphere. We have obtained or located optical spectra for 29 of these 31 quasars. In the optical spectra we find 17 Mg II absorption systems, with redshifts between 0.3 and 1.4 and Mg II $\lambda 2796$ rest equivalent widths between 0.3 and 2.0 Å. Based on statistics of 21 cm absorption in Mg II selected QSOs we expect this sample of 17 systems to yield one or two new H I absorbers. In this paper we give an analysis of our criteria, discuss the sample, and present new VLA observations of 16 quasars.

1. INTRODUCTION

It is now widely accepted that Quasi Stellar Object (QSO) metal line, damped Ly α , and H I 21 cm absorption systems arise primarily from clouds associated with intervening galaxies. These systems exhibit a range of neutral hydrogen column densities from less than 10^{17} cm^{-2} to more than 10^{21} cm^{-2} (Petitjean *et al.* 1993, and references therein). Comparing these column densities to values observed in our Galaxy and nearby galaxies suggests that 21 cm absorption is most likely to occur in the disk whereas metal line absorption can occur in the disk or extended halo (Briggs & Wolfe 1983, hereafter BW). Statistical correlations between Mg II and 21 cm lines as well as cloud properties such as spin temperature, ionization levels, and component line profiles corroborate this picture (Savage & Jeske 1981; BW).

Despite the general success of this galactic absorption interpretation, there still exist problems and questions to be addressed. Foremost among these is the result that the mean free path for absorption is much shorter than expected based on statistical studies and models of the properties of the absorbing galaxies. Even after adopting the most extreme parameter values, the mean free path is still three times too short for C IV (Sargent *et al.* 1988) and two times too short for Mg II (Sargent 1988) and damped Ly α (Lanzetta *et al.* 1991). This is interpreted to imply either that galaxy halos are much larger than convention-

ally thought or that the number density of galaxies has evolved. Recent work on imaging the absorbing galaxies for redshifts less than about one (Bergeron & Boissé 1991; Bergeron *et al.* 1992; Steidel & Dickinson 1992) indicates directly the existence of very large halos.

In addition to imaging techniques, one can learn about the linear size of absorbers at any redshift when there are two or more lines of sight intersecting the same system. This is generally not the case, but quasars with lobe-dominated extended radio emission provide distinct lines of sight in the optical and radio. If we observe H I 21 cm absorption at the same redshift as a known optical absorber we can then begin to define the absorber properties. This method is particularly useful because the typical angular scales of extended radio emission are well matched to galactic angular scales. For instance, at $z \approx 1.5$ ($H_0 = 100h \text{ km s}^{-1} \text{ Mpc}^{-1}$ and $q_0 = 0$), 5 arcsec corresponds to $\sim 30 h^{-1} \text{ kpc}$. In addition to probing the overall size of halo absorbers, the presence of 21 cm absorption in a resolved background provides a means of measuring the sizes of individual absorbing clouds. This is done by analyzing the absorbed 21 cm flux in relation to the radio source surface brightness. In the case of 3C 196, Brown *et al.* (1988) were able to conclude that the absorbing cloud is at least $2.25h^{-1} \text{ kpc}$ across, which is surprisingly large.

To make efficient use of radio telescope time, the absorbing system redshifts should be determined optically.

STAR-DISK COLLISIONS AND THE ORIGIN OF THE BROAD LINES IN QUASARS

WOJCIECH H. ZUREK¹, ANETA SIEMIGINOWSKA,² AND STIRLING A. COLGATE¹

Received 1993 August 16; accepted 1994 April 20

ABSTRACT

Quasars and other active galactic nuclei (AGNs) are most likely powered by a massive black hole surrounded by an accretion disk and inhabiting the core of a dense stellar cluster. Star orbits intersect the disk. Hence, star-disk collisions are a daily (if not more frequent) occurrence. We consider the consequences of such collisions and show that the “star tails” of the disk material, accelerated by the encounter with the passing star, can travel well above the disk and, therefore, are a natural candidate for the observed broad emission-line regions.

Subject headings: galaxies: active — line: formation — quasars: general — radiation mechanisms: nonthermal

1. INTRODUCTION

Broad emission lines are one of the most conspicuous features of nearly all active galactic nuclei (AGNs) (Krolik 1992; Netzer 1990; Peterson 1988; Collin-Souffrin & Lasota 1988; Krolik, McKee, & Tarter 1981). They must originate close to the central powerhouse, in clumps of relatively dense, cool gas irradiated by UV and X-ray continuum and located within a fraction of a parsec from the massive black hole. This upper limit on the distance is implied by the delay between the changes of the continuum and the lines (Krolik 1992; Peterson 1988). It is also consistent with their width which is attributed to the Doppler broadening due to the motion in the black hole potential. Properties of the emitted radiation (Netzer 1990; Peterson 1988) imply that the emitting clouds have densities of 10^{10} cm^{-3} , are only partially ionized (i.e., have temperatures of $\sim 10^4 \text{ K}$) and have sizes of $\sim 10^{13} \text{ cm}$. They obscure and reradiate $\sim 10\%$ of the original output in a typical AGN.

The similarity of the properties of the broad-line emission regions (BLR) observed in many different AGNs seems surprising: AGNs differ by orders of magnitude in the total power outputs, variability timescales, spectral features, etc., and, therefore, are likely to be characterized by a wide range of physical conditions in the central region. What process could be immune to such a diversity of the environments?

The standard AGN paradigm (Holt, Neff, & Urry 1991; Blandford 1990; Miller 1985) is focused on the “power house”—the central black hole with a mass $M \sim 10^6 M_\odot$ (Schwarzschild radius $R_{\text{BH}} \sim 1.5 \times 10^{13} M_8 \text{ cm}$), and an accretion disk with a mass of $\sim 10^4\text{--}10^5 M_\odot$ and a radius $\sim 10^4 R_{\text{BH}}$. Moreover, it is often assumed, especially in the discussions of fueling of AGNs (see, e.g., Blandford 1990; Binney & Tremaine 1987 [§ 8.4], and references therein) that the AGN engine exists in the center of a dense cluster with stellar densities as large as $N_* \sim 10^7\text{--}10^8$ stars per cubic parsec. Of course, neither this assumption, nor the other elements of the standard paradigm can be verified directly. However existence of dense clusters in the AGNs is supported by persuasive indirect evidence: nearby galaxies have central star clusters with densities $10^6\text{--}10^8 M_\odot \text{ pc}^{-3}$ (Lauer 1989; Lauer et al. 1992; Fabbiano, Fassnacht, & Trinchieri 1994, and references therein) and often with a velocity distribution which suggests a

central black hole which might be a remnant of the “burned out” AGN. Moreover, formation of black holes is difficult to imagine unless the environment is rich enough to precipitate collapse (Quinlan & Shapiro 1990). Thus, while existence of dense stellar clusters enveloping the central powerhouse is an assumption, of the three elements (black hole, disk, cluster) of the model we shall discuss below, the star cluster is perhaps least exotic and most directly supported by the observations.

Collisions between the cluster stars and the disk are not only inevitable, but must be quite frequent ($\nu \sim 10^4 \text{ yr}^{-1}$). Their consequences for the angular momentum of the disk (Ostriker 1983), for the luminous output of the AGN (Zentsova 1983), as well as for the decay of stellar orbits intersecting the disk (Syer, Clarke, & Rees 1991) were already investigated. Here we shall pursue the ideas sketched by Zurek, Siemiginowska, & Colgate (1991) and consider the fate of the disk material shocked and accelerated by the passing star. We shall show that much of it rises in a comet-like fashion as a *star tail* above the surface of the disk. There the star tails evolve under the influence of the gravitational pull of the black hole and the radiative push of the emitted radiation. In this model the similarity of the properties of the broad-line regions in different AGNs can be therefore understood in part as a consequence of their common origin, which is in turn tied to the relatively invariant components of the AGN models.

Once above the disk, star tails will move under the influence of gravity and radiation pressure. These two forces may alter the distribution of velocities of the star tail matter—and, hence, the shape of the broad lines—but as we shall see below, they are unlikely to significantly change their spatial distribution: it is difficult to imagine that star tails will be sufficiently long lived to travel far in radius from where they were pulled out from the disk. In the absence of any confining medium, their lifetime will be of the order of the sound crossing time, as star tails will expand and gradually become too tenuous for the recombination to be effective. This expansion might be slowed down or even halted in the hot medium presumably filling the space above the disk, which may help confine them to the sizes inferred from the observations. Magnetic fields—these permeating the space as well as those pulled out by the star tail out of the disk—may also play a role. Alternatively—given their “birthrate” and distribution as a function of the radius—one may consider the possibility that the star tails are destroyed as a consequence of expansion to densities at which the rate of ionization by the flux from the central source can be

¹ Theoretical Astrophysics, T-6, MS B288, LANL, Los Alamos, NM 87545.

² Center for Astrophysics, Cambridge, MA 02138.

Abstract

We present results of the modeling of thermal-viscous ionization instabilities in accretion disks in AGN. This instability, analogous to the instability which drives outbursts in cataclysmic variables (Smak 1984b) or X-ray transients (see Mineshige & Kusunose 1993, for review), is expected also to occur in accretion disks around supermassive black holes (Lin & Shields, 1986; Clarke & Shields 1989; Mineshige & Shields 1990) unless self-gravity effects or irradiation prevent the existence of the partial ionization zone (which causes the instability). We assume that viscosity scales with the gas pressure (β -viscosity). We discuss in detail evolution of the accretion disk around a $M_{bh}=10^8 M_\odot$ black hole mass, assuming a range of accretion rates corresponding to luminosities between $10^{-5} - 1$, in Eddington units.

We show that the ionization instability does operate in such disks. Depending on the viscosity, the instability can develop in a very narrow unstable zone thus causing a flickering, or can propagate over the entire disk resulting in the large amplitude outbursts on the timescales of order 10^3 - 10^5 years. As a consequence: (1) AGN are not always in their active state; and (2) the emitted optical-UV spectra are quite different from the spectrum of a thin stationary accretion disk. External irradiation is shown to have a large effect on the instability and on the emitted optical-UV spectra. We briefly consider observational consequences.

Subject headings: accretion, accretion disks - galaxies: active - quasars



Harvard-Smithsonian Center for Astrophysics



Preprint Series

No. 4402

(Received September 10, 1996)

THE CAMBRIDGE-CAMBRIDGE ROSAT SERENDIPITY SURVEY - IV. THE X-RAY PROPERTIES

P. Ciliegi, M. Elvis, B.J. Wilkes, B.J. Boyle, and R.G. McMahon

To appear in
Monthly Notices of the Royal Astronomical Society

Center for Astrophysics
Preprint Series No. 4402

**THE CAMBRIDGE-CAMBRIDGE *ROSAT* SERENDIPITY SURVEY –
IV. THE X-RAY PROPERTIES**

P. Ciliegi, M. Elvis, B.J. Wilkes, B.J. Boyle, and R.G. McMahon

The Cambridge-Cambridge *ROSAT* Serendipity Survey - IV. The X-ray properties

P.Ciliegi,^{1,2,3} M.Elvis,¹ B.J.Wilkes,¹ B.J.Boyle,⁴ and R.G. McMahon,⁵

1. Harvard-Smithsonian Center for Astrophysics 60 Garden St, Cambridge MA 02138, USA

2. Dipartimento di Fisica dell'Università di Milano, Italy

3. Osservatorio Astronomico di Brera, Via Brera 28, I-20121 Milano, Italy

4. Royal Greenwich Observatory, Madingley Road, Cambridge, CB3 0EZ

5. Institute of Astronomy, University of Cambridge, Madingley Road, Cambridge, CB3 0HA, UK

Submitted September 1995

ABSTRACT

We present a detailed X-ray spectral analysis in the 0.1–2.4 keV *ROSAT* band of a complete sample of X-ray selected AGN using the 80 AGNs in the Cambridge-Cambridge *ROSAT* Serendipity Survey (68 QSOs and 12 narrow emission line galaxies, NLXGs). We have also made a comparison between the X-ray spectral properties of QSOs and NLXGs. For 36 objects we have enough net counts to allow an X-ray spectral fit, while for the other sources we have characterized the spectrum using the hardness ratio technique. A maximum-likelihood analysis was used to find the mean power-law energy spectral index $\langle \alpha_x \rangle$ and the standard deviation σ for QSOs and NLXGs, assuming the intrinsic distribution to be Gaussian. We found no difference between QSOs and NLXGs: $\langle \alpha_x \rangle = 1.32$ with dispersion $\sigma = 0.33$ for the QSOs and $\langle \alpha_x \rangle = 1.30$ with $\sigma = 0.49$ for the NLXGs. A single power-law with a Galactic absorbing column density yields a good representation of the X-ray spectra for the majority of the sources. Only three objects show a significant deviation from this model. There is evidence in the NLXG sample for a flattening of the spectral slope α_x with increasing redshift and for a steepening of α_x with increasing $(L_{2500\text{\AA}}/L_x)$. For the QSO sample we found no significant correlation. The lack of correlation between α_x and z suggests that for the CRSS QSOs the power-law spectrum in the QSO rest frame extends from the soft (~ 0.1 –2.4 keV) into the harder X-ray band (~ 0.3 –7.3 keV) with the same slope.

Key words: galaxies:active – galaxies:nuclei – quasars:general – radio continuum: galaxies – X-ray: galaxies

1 INTRODUCTION

The spectral properties of QSOs in the X-ray band have been studied extensively over the last decade (e.g. Wilkes and Elvis 1987, Canizares and White 1989, Comastri et al. 1992, Williams et al. 1992, Fiore et al. 1994, Laor et al. 1994). However, these studies were limited to optical and radio selected QSOs and were generally not of complete samples. Although the *Einstein* and *ROSAT* satellites have produced large samples of X-ray selected QSOs, no detailed information is available about their X-ray spectral properties. For the *Einstein* Extended Medium Sensitivity Survey (EMSS) sample (Gioia et al. 1990, $f_{\text{lim}}(0.3 - 3.5 \text{ keV}) \sim 1.0 \times 10^{-13} \text{ erg cm}^{-2} \text{ s}^{-1}$) Maccacaro et al. (1988) gave only a mean spectral index for the whole sample determined from the hardness ratio.

The improved X-ray sensitivity of the *ROSAT* satellite

(Trümper, 1983) allows us, for the first time, to study the X-ray spectral properties of a complete sample of X-ray selected AGN. A new, fully identified sample of X-ray selected AGN, the Cambridge-Cambridge *ROSAT* Serendipity Survey (CRSS, Boyle et al. 1995a) has been obtained. This is a well defined sample of 80 X-ray selected AGN discovered serendipitously with the *ROSAT* PSPC at fluxes 5–10 times fainter than the EMSS. Of the 80 AGN, 68 were classified as QSOs from the presence of broad emission lines with full width half maximum (FWHM) $> 1000 \text{ km s}^{-1}$, while 12 were classified as narrow emission line X-ray galaxies (NLXGs, see Boyle et al. 1995a). A detailed intermediate-resolution (1.5Å) spectroscopic follow-up of 10 CRSS NLXGs has shown that the NLXG sample appears to be a heterogeneous mix of Seyfert (Sy) and starburst galaxies (HII) (Boyle et al. 1995b). Based on their emission line ratios, the 10 re-observed CRSS NLXGs comprise five starburst galaxies, two

Sy 1.5, one Sy 1.8 and two Sy 2 galaxies. In this paper we report the analysis of the X-ray spectra of these X-ray selected QSOs and NLXGs together with a comparison of their X-ray spectral properties. In section 2 we describe the analysis of the spectra. We report our results in section 3, give a discussion in section 4 and we conclude in section 5 with a summary of our main results. In Appendix A we describe the hardness ratio technique used to characterize the spectra of those sources with few net counts.

Throughout the paper a Hubble constant of $H_0 = 50 \text{ km s}^{-1} \text{ Mpc}^{-1}$ and a deceleration parameter $q_0 = 0$ are assumed.

2 DATA ANALYSIS

The 20 CRSS *ROSAT* PSPC fields are all at high Galactic latitude ($|b^{II}| \geq 30^\circ$). The source selection criteria were an X-ray flux $f_x(0.5 - 2.0 \text{ keV}) > 2 \times 10^{-14} \text{ erg cm}^{-2} \text{ s}^{-1}$ and an off-axis angle $\theta \leq 15'$ in the *ROSAT* Position Sensitive Proportional Counter (PSPC) field. Radio observations of the CRSS AGN sample (Ciliegi et al. 1995) have shown that seven objects have detectable radio emission at the 5σ level and only two ($2.5^{+4.0}_{-1.7}\%$) qualify as radio-loud objects using a standard radio to optical spectral index criterion ($\alpha_{ro} \geq 0.35$).

All the PSPC observations were performed with PSPC-B. Because all the sources have an off-axis angle $\theta < 15'$ there are no problems of obscuration by the window support structure and the effects of vignetting are negligible (Hasinger et al. 1994). For each source we fitted the X-ray image with a two-dimensional gaussian to determine its centroid. Subsequently we extracted the source counts in the $0.1 - 2.4 \text{ keV}$ band using a circle centered on the source centroid. To optimize signal to noise ratio the extraction radius r was chosen to be the distance from the centroid at which the radial profile of the point source meets the background level. All the extraction radii lay in the range $1.5 \text{ arcmin} \leq r \leq 2.5 \text{ arcmin}$. The background counts were estimated in an annulus centered on the source with inner radius 3 arcmin and outer radius 5 arcmin . When detected, other sources within the source or background region were removed using a 2 arcmin radius circle chosen to contain at least 95% of the source counts (Turner and George 1992). Table 1 lists the sources in the sample, including their classification as QSO (Q), Seyfert galaxy (Sy) starburst galaxy (HII) or narrow emission line galaxies (NLXG), redshift, observation date, extraction radius r (arcmin), off-axis angle θ (arcmin), the net counts detected within the circle of radius r in the soft ($S = 0.1 - 0.4 \text{ keV}$), hard ($H = 0.5 - 2.0 \text{ keV}$) and broad ($B = 0.1 - 2.4$) band and the *ROSAT* sequence number.

The 34 energy channels from the MPE standard analysis software system (SASS) pipeline processing were used for the spectral analysis, excluding the first two channels ($< 0.1 \text{ keV}$) and the last channel ($> 2.4 \text{ keV}$) because the response of the instrument is not well-defined at the extremes of the energy range. Finally the spectrum was binned to obtain a signal to noise ratio $S/N \geq 3$ per bin so that the χ^2 statistic could be applied. When it was not possible to obtain at least 6 bins with $S/N \geq 3$, we used the simple hardness ratio HR ($HR = [H - S]/[H + S]$, see Appendix A for

a complete description of this technique) to characterize the spectrum.

For 36 sources we obtained an X-ray spectrum with 6 or more channels with $S/N \geq 3$ each, while for 42 objects we have computed the energy spectral index α_{eHR} of the power-law using the HR and fixing N_H at the Galactic value.

For only two sources (the QSOs CRSS1429.2+0120 and CRSS1545.5+4847) did the few net counts detected (< 20) preclude any spectral analysis. For the 36 sources with enough net counts, we made two different power-law fits (1) with N_H fixed at Galactic value and (2) with N_H as free parameter. Throughout this paper all the N_H Galactic values are from Stark et al. (1992). To test the reliability of the hardness ratio technique we also calculated α_{eHR} for the 36 sources for which we made a spectral analysis (see Appendix for details).

Model fits were carried out using the XSPEC software package, and the best fit model parameters were obtained by χ^2 minimization. Following Fiore et al. (1994), we have used the 1992 March response matrix for observations made before October 1991 and the 1993 January response matrix for observations made after October 1991.

3 RESULTS

The results of the spectral fits are given in Table 2 with errors quoted at the 1σ level for a single interesting parameter when N_H is fixed (fit 1) and for two interesting parameters when both the X-ray energy spectral index α_x and N_H are free to vary (fit 2). For each source we report the hardness ratio HR , the energy spectral index α_{eHR} obtained from the HR fixing $N_H = N_{H_{Gal}}$, and the results of both spectral fits. For each fit we give the best fitting spectral slope α_x , the N_H value ($N_{H_{Gal}}$) for fit 1 and for the sources analyzed only with the HR statistic, and the best fitting N_H for fit 2, the χ^2 of the fit (χ^2_{FIT}), the number of degrees of freedom (dof), the probability for $\chi^2 \geq \chi^2_{FIT}$, $P(\chi^2 > \chi^2_{FIT})$. In column 9 we report the F-test probability (Bevington and Robinson 1992) that the reduction in χ^2_{FIT} with the addition of N_H as a free parameter is not statistically significant, $P(F > F_{FIT})$. In columns 10 and 11 we give respectively the X-ray flux, the logarithm of the X-ray luminosity in the $0.5 - 2.0 \text{ keV}$ band obtained from fit 1 (i.e. $N_H = N_{H_{Gal}}$) and the logarithm of the monochromatic luminosities at 2500\AA . These latest are based on the optical Palomar sky survey O magnitudes (Boyle et al. 1996, in preparation) with a typical error of $\sim 0.2 \text{ mag}$ which corresponds to an error on the logarithm of the 2500\AA luminosity of $\sim 0.1 \text{ erg s}^{-1} \text{ Hz}^{-1}$. For the sources without spectral information (see below) we computed the X-ray flux and luminosity using a power-law model with $N_H = N_{H_{Gal}}$ and $\alpha_x = 1.3$ (this value represents the mean spectral index both for QSOs and NLXGs, see section 4.2).

A comparison of fit 1 and 2 allows us to determine whether there is evidence for a significant intrinsic excess absorption or excess emission relative to a single power law fit with $N_H = N_{H_{Gal}}$. As shown in Table 2, in three of the 36 objects for which we have enough net counts to allow a spectral fit, there are significant deviations from a simple power-law fit (i.e. $P(F > F_{FIT}) < 0.01$). The QSOs CRSS0008.4+2034 and CRSS0030.6+2620 show a best fit

value of N_H lower than Galactic value at 90% and 99% confidence level respectively, indicating a soft emission excess relative to a single power-law fit with $N_H = N_{H_{Gal}}$. The Sy1.8 CRSS1412.5+4355 shows excess absorption ($N_H > N_{H_{Gal}}$), although only at 68 per cent confidence level. We find that the soft excess in the two QSOs is well parameterized by fitting the data with a broken power-law with N_H fixed at the Galactic value. The absorption excess in the Sy1.8 CRSS1412.5+4355 can also be well parameterized by fitting the data with a power-law including a $z = 0$ absorption fixed at the Galactic value plus another absorption component at the redshift of the source. In Table 3 we report the results for these spectral models.

Of the 42 sources analyzed with the hardness ratio technique, four (the three QSOs CRSS0029.7+2603, CRSS1429.0+0122, CRSS1605.2+2541 and the Sy2 CRSS0030.7+2616) have $HR = 1.00$ (i.e. zero net counts detected in the soft band) and three (the QSOs CRSS0008.6+2045, CRSS1416.2+1131 and CRSS1545.4+4838) have $HR < 1$ but $HR + HR_{ERROR} > 1.00$. For these seven sources with very hard (or heavily absorbed) spectra we cannot obtain a reliable value of the spectral index α_{eHR} (see Appendix). Also the analysis of the average spectrum obtained by combining the seven spectra of these sources does not allow us to distinguish the origin of their extremely high hardness ratio values.

In summary, of the 78 AGN in our sample of 80 for which some spectral information can be obtained, 9% (6 QSOs and 1 NLXGs) have an extremely high value of HR , 3% (2, both QSOs) show significant soft excess above a simple power law with $N_H = N_{H_{Gal}}$, 1% (1 NLXG) shows excess absorption ($N_H > N_{H_{Gal}}$), while 87% (58 QSOs and 10 NLXGs) have well constrained values of the energy spectral index α_x fitting the spectra with a simple power law.

Similar examples of X-ray luminous narrow emission line galaxies were also identified in the EMSS by Stocke et al. (1991). In order to increase the NLXG sample, we searched in the Public *ROSAT* Archive the *ROSAT*/PSPC data containing "serendipitous" observations of EMSS NLXGs. We find good *ROSAT* data for 5 EMSS NLXGs. We retrieved the observations from the archive and we analyzed the data as described in section 2. Because we detected few net counts (< 220) from each source, we have computed the energy spectral index of the power-law using the hardness ratio technique. In Table 4 we report the data for these 5 EMSS NLXGs. No intermediate-resolution optical spectra are available for these sources.

4 DISCUSSION

4.1 High Hardness Ratio

As discussed above, 7 of the 42 objects analyzed with the hardness ratio technique have $HR = 1$ or $HR + HR_{ERROR} > 1$. High HR values may be the result of truly hard X-ray spectra but they could be also the result of the presence of a significant amount of intrinsic absorption. We have checked if these seven objects show some peculiar characteristic suggestive of intrinsic absorption. Elvis et al. (1994) have shown using *ROSAT* data that X-ray absorption is common in high

redshift ($z \approx 3$) QSOs. Earlier work found that the least luminous AGN more often show X-ray absorption (Lawrence and Elvis 1982). Absorption would also be likely to redden the ultraviolet "Big Bump" continuum. Therefore we have checked if these seven "hard" objects have higher redshift lower luminosity or obvious optical reddening. In Figure 1 we plot the X-ray luminosity, redshift and optical $O - E$ colour (Boyle et al. 1996, in preparation) distributions the whole CRSS sample with the distribution of the seven objects superimposed. A Kolmogorov-Smirnov test shows that in all the cases the seven objects have the same distribution of the whole sample with a confidence level greater than 99 per cent, excluding any peculiarity. All but one of the "hard" sample show clear broad optical emission lines. This is quite unlike the situation for the heavily absorbed hard X-ray selected AGN where some 50% of the AGN show large absorbing column densities ($\sim 10^{22} \text{ cm}^{-2}$) and these are found primarily among the type 1.8, 1.9 or 2 Seyferts (Turner and Pounds 1989).

4.2 Power-law Spectral index

To study the X-ray spectral properties of QSOs and NLXGs separately, we used the 68 CRSS sources (58 QSOs and 10 NLXGs) for which we have well-constrained values of the energy spectral index α_x . In order to obtain an homogeneous sample of narrow emission line galaxies we excluded from the CRSS NLXG sample the two Seyfert 1.5 galaxies reported by Boyle et al. (1995b, see Table 1). The two NLXG not observed at intermediate-resolution (CRSS1514.4+5627 and CRSS1605.9+2554) and the NLXG which still has an uncertain classification (CRSS1705.3+6049, see Boyle et al. 1995b) were included in the sample. In figure 2 we show the distribution of the energy spectral index for the 58 QSOs, the 8 NLXGs and the 2 Seyfert 1.5 galaxies.

The distribution in the slope values is quite broad, both for QSOs and NLXGs. Some extreme objects have well-determined slopes (e.g. CRSS1418.3+0637 $\alpha_x = 2.56 \pm 0.10$; CRSS1654.5+3954 $\alpha_x = 0.90 \pm 0.10$ see Figure 4a). If the assumption is made that both the measurements and the underlying spectral index distribution is normal, then the mean spectral index ($\bar{\alpha}$) and the intrinsic spread in spectral slope (σ_{int}) of each class of objects can be quantified using Maximum-Likelihood (ML) analysis (Worrall and Wilkes 1990, Maccacaro et al. 1988). Table 5 and Figure 3 give the results of the ML analysis. In the table we report for each class of objects the mean spectral index $\bar{\alpha}_{ML}$ and the intrinsic dispersion σ_{int} obtained with the ML analysis and, for comparison, the mean index $\bar{\alpha}_{WM}$ and relative dispersion σ obtained by simply weighting the same data.* For the QSO and NLXG of the CRSS sample the 90% confidence contour for two interesting parameters is plotted in Figure 3. As shown in Table 5 and Figure 3 there is no significant difference between the mean spectral index of QSOs and NLXGs.

* In the analysis the weighted mean value of each quantity has been obtained using the formula $\bar{x} = \Sigma(x_i/\sigma_i^2)/\Sigma(1/\sigma_i^2)$ where x_i is the single measurement value and σ_i is the associated error, whereas the relative dispersion has been obtained using the formula $\sigma^2 = 1/(N-1) \times \Sigma(x_i - \bar{x})^2$ (Bevington and Robinson 1992).

Instead the mean spectral index of EMSS NLXGs is significantly flatter ($> 95\%$ confidence level) than the mean value of the CRSS NLXGs (see Table 5). This difference is not present in the QSO population. A detailed study of the *ROSAT*/PSPC X-ray spectra of the EMSS AGN has shown that the mean X-ray spectral index $\bar{\alpha}_{\text{ML}}$ in the *ROSAT* band of 50 radio-quiet EMSS AGN is $\bar{\alpha}_{\text{ML}} \sim 1.5$ with $\sigma_{\text{int}} \sim 0.4$ (Ciliegi and Maccacaro 1996). Therefore the spectral difference can not be attributed to the harder selection band of the EMSS sources (the 0.3–3.5 keV *Einstein*/IPC band) compared to the CRSS sources (the 0.5–2 keV *ROSAT*/PSPC band). Given the uncertainty on the real nature of the EMSS NLXG and the differences between the mean spectral index of these objects and that of the CRSS NLXG, we did not combine these two small samples of NLXG to obtain a mean value of their spectral index. A classification based on higher resolution optical spectra of the EMSS NLXG (are they objects with HII-like spectra or with AGN-like spectra?) would give us useful information on the nature of the difference in the spectral index between CRSS NLXG and EMSS NLXG.

Excluding the two radio-loud QSOs (CRSS1705.5–6042 and CRSS2250.0+1407) makes a negligible difference in mean spectral index or dispersion (Table 5) so we have used the whole sample for the correlation analysis described below.

Our values of the mean spectral index for QSOs and NLXGs are consistent with previous values for optically selected AGN. Laor et al. (1994) and Walter and Fink (1993) using samples of optically selected AGN find a mean value of the *ROSAT*/PSPC spectral index of 1.50 ($\sigma = 0.40$) and 1.57 ($\sigma = 0.30$) respectively. Recently, Schartel et al. (1995) using the *ROSAT* All-Sky Survey (RASS) data for the QSOs in the Large Bright QSO Survey (LBQS) find a mean energy spectral index of $\alpha_x = 1.70 \pm 0.20$ for RQ and 1.00 ± 0.30 for RL QSOs.

Note that these values of $\bar{\alpha}_x$ obtained from *ROSAT*/PSPC are significantly steeper than the mean spectral index of the EMSS AGN obtained by Maccacaro et al. (1988) with the *Einstein* IPC, who find $\bar{\alpha}_x = 1.03^{+0.05}_{-0.06}$ with a dispersion $\sigma = 0.36$. This difference may be real, reflecting a “soft excess” in the *ROSAT*/PSPC band ($\sim 0.1 - 2.4$ keV) compared to the *Einstein* IPC band ($\sim 0.3 - 3.5$ keV), or may be due to calibration error in the PSPC and/or IPC instruments (see Appendix B in Fiore et al. 1994 for more details). However, in their analysis, Maccacaro et al. (1988) did not separate radio-loud from radio-quiet AGNs (there are 43 radio-loud and 363 radio-quiet AGNs in the EMSS). Considering that radio-loud AGNs show flatter spectra than radio-quiet AGNs (Wilkes and Elvis 1987, Schartel et al. 1995) the steeper mean spectral index in the CRSS sample may be due to its lack of radio-loud objects.

4.3 Correlation Analysis

We searched for correlations between α_x and other physical parameters of the sources, in particular redshift z , optical and X-ray luminosity (L_{2500} and L_x) and the ratio between optical and X-ray luminosities (L_{2500}/L_x).

Given the dependence of the monochromatic flux (and luminosity) at 2 keV on the energy spectral index α_x (Ulrich and Molendi 1995), in our correlation analysis we used the

broad band (0.5 – 2.0 keV) X-ray flux (f_x) and luminosity (L_x), which are much less sensitive to change in α_x . For this reason we did not use the usual two point spectral index α_{ox} but instead used the ratio between the optical (at 2500Å) and broad band X-ray luminosities (L_{2500}/L_x).

The correlation significance was tested using the Spearman Rank correlation coefficient r_s and the relative probability P_r that an observed correlation could occur by chance for uncorrelated data sets (see Press et al. 1992). A correlation was taken to be significant when $P_r \leq 0.01$. A summary of all the correlation coefficients and their significance is given in Table 6, while Figures 4a, 4b, 4c and 4d show redshift (z), X-ray luminosity (L_x), optical luminosity (L_{2500}) and L_{2500}/L_x , respectively, as a function of the X-ray energy spectral index α_x .

Table 6 shows that we find a flattening of the CRSS NLXGs spectral slope with increasing redshift (~ 99 per cent significance, see Figure 4a) and a steepening of the spectral index with increasing optical/X-ray luminosity ratio (~ 99.97 per cent significance, see Figure 4d). The same correlation between α_x and the optical/X-ray luminosity ratio was found by Laor et al. (1994) for a sample of 10 QSOs and subsequently confirmed for a complete sample of 23 optically selected QSOs from the Bright QSO Survey (BQS, Laor et al. in preparation). It is puzzling that, in our survey, this correlation appears only for narrow line objects, those in the CRSS sample least like the PG QSOs in Laor et al.

The lack of correlation between α_x and z for the CRSS QSOs suggests that the power-law spectrum in the QSO rest frame extends from the soft ($\sim 0.1 - 2.4$ keV) into the hard X-ray band (for the highest redshift objects the observed energy range corresponds to the range $\sim 0.3 - 7.3$ keV) with the same slope. The same result was obtained for radio-loud and radio-quiet optically-selected QSOs by Canizares and White (1989) using *Einstein*/IPC data and by Williams et al. (1992) with the *Ginga* data. The most directly comparable studies, however, are those of Schartel et al. (1992, 1995). Using the *ROSAT* All-Sky Survey data for 162 strongly-detected optically-selected QSOs (Schartel et al. 1992) they found a flattening of the spectral slope with increasing redshift from $\alpha_x \sim 1.5$ to $\alpha_x \sim 0.8$ between $z = 0.2$ and $z \sim 2$. The LBQS QSOs showed a much weaker effect over the same redshift range (from $\alpha_x = 1.5 \pm 0.1$ to $\alpha_x = 1.3 \pm 0.2$). As with the EMSS, Schartel et al. did not make a distinction between radio-loud (RL) and radio-quiet (RQ) objects. However, there is some evidence (e.g. Hooper et al. 1995) that RL QSOs may represent an increasing fraction of all QSOs at high redshift. This effect might be responsible for the observed flattening at higher redshift. For example the *Ginga* data (Williams et al. 1992) appear to show a flattening with redshift but, as Williams et al. show, this is a secondary effect of the well-known difference in mean slope between RL and RQ QSOs (Wilkes and Elvis 1987). The flattening, in fact, disappears when RL and RQ are considered separately. Therefore, as noted also by Schartel et al. (1995), the observed flattening at higher redshift in the Schartel et al. (1992) sample might be due to an increased fraction of RL QSOs.

Finally, the lack of correlation between α_x and optical and X-ray luminosities (both for QSOs and NLXGs) is in

agreement with the results obtained by Laor et al. (1994) for 23 BQS QSOs.

5 CONCLUSIONS

We have analyzed the X-ray properties of the Cambridge-Cambridge *ROSAT* sample of 80 X-ray selected AGN. This is the first detailed X-ray spectral analysis of a complete sample of X-ray selected AGN, and the first comparison between the X-ray spectral properties of QSOs and narrow emission line galaxies. The most important results of our analysis can be summarized as follows:

1. The Maximum-Likelihood analysis show no difference between the mean spectral index of QSOs and NLXG. We find $\langle \alpha_x \rangle = 1.32$ with dispersion $\sigma = 0.33$ for the sample of 58 QSOs and $\langle \alpha_x \rangle = 1.64$ with $\sigma = 0.34$ for the sample of 8 NLXGs.

2. A single power-law with an absorbing column density fixed at Galactic value yields a good representation of the X-ray spectra for $\sim 90\%$ of the 36 CRSS AGNs for which we can fit the spectra with two free parameters (the spectral index α and N_H). Only three objects show a significant deviation from this model. Two of them (both QSOs) show a soft emission excess relative to a single power law fit with $N_H = N_{H_{Gal}}$ and their spectra are well represented by a broken power law with a break point at 0.5-0.6 keV. The other object (a Sy1.8 galaxy) shows a significant absorption excess ($N_H > N_{H_{Gal}}$) and its spectrum is well represented by a power-law with Galactic absorption plus an intrinsic absorption component N_H of $1.42^{+1.07}_{-0.90} \times 10^{20} \text{ cm}^{-2}$.

3. Seven of the 42 sources analyzed with the hardness ratio technique show an extremely high value HR value ($HR = 1$ or $HR + HR_{\text{ERROR}} > 1$) indicating hard X-ray spectra or the presence of intrinsic absorption. We checked for possible evidence of intrinsic absorption, but given the few net counts detected from each sources it was not possible to determine the origin of these extremely high hardness ratio values.

4. The mean spectral index of EMSS NLXGs is significantly flatter than the mean value of the CRSS NLXGs. A classification based on higher resolution optical spectra of the EMSS NLXGs would give us useful information on the nature of this spectral difference.

5. There is evidence in the NLXG sample for a correlation between spectral index α_x and redshift and between α_x and the ratio between optical (2500Å) and broad band X-ray luminosity (L_{2500}/L_x). We find a flattening of the CRSS NLXG spectral slope with increasing redshift and a steepening of α_x with increasing (L_{2500}/L_x).

6. For the QSO sample we found no significant correlations. The lack of correlation between α_x and z suggests that for the CRSS QSOs the power-law spectrum in the QSO rest frame extends from the soft ($\sim 0.1 - 2.4 \text{ keV}$) into the hard X-ray band ($\sim 0.3 - 7.3 \text{ keV}$) with the same slope.

ACKNOWLEDGMENTS

The optical identifications of the CRSS were made at the William Herschel Telescope at the Observatorio del Roque de los Muchachos operated by the Royal

Greenwich Observatory. P.C. acknowledges partial financial support from a Smithsonian Predoctoral Fellowship. This work has received partial financial support from NASA contracts NAGW-2201(LTSA), NAS8-39073(ASC) and NASA5-30934(RSDC).

APPENDIX A

In order to obtain spectral information on objects with a limited number of net counts (\lesssim a hundred photons), we have used the hardness ratio (*HR*), an "x-ray color" defined as :

$$HR = \frac{H-S}{H+S}$$

$$HR_{\text{ERR}} = 2 \times \frac{\sqrt{(S \cdot H_{\text{ERR}})^2 + (H \cdot S_{\text{ERR}})^2}}{(H+S)^2}$$

where S is the number of net counts detected in the channels 11-42 ($\sim 0.11 - 0.43 \text{ keV}$), H is the number of net counts detected in the channels 51-201 ($\sim 0.51 - 2.02 \text{ keV}$) and S_{ERR} and H_{ERR} are the errors on S and H respectively, computed as the square root of the total counts. These colours are similar to those used by Hasinger (1992), but with slightly different boundaries for the soft and hard band to maximize the S/N ratio for faint sources. Because of its definition, the hardness ratio has values confined between -1 and $+1$ (inclusive). Values close to -1 indicate that the source has an extremely soft spectrum; while very hard or heavily absorbed sources, are characterized by an HR value close to $+1$. If we assume that the spectrum of the sources can be represented by a power-law model with N_H fixed at the Galactic value, then there exists a one to one relationship between power-law spectral index α_x and the measured hardness ratio. The correspondence between HR and the slope of the power-law for a set of values of the equivalent hydrogen column density N_H is shown in Figure A1. Uncertainties in the exact value of N_H contribute, in principle, an additional uncertainty in the resulting value of α_x . In practice, the uncertainty in α_x due to the uncertainty in N_H is negligible when compared to the uncertainty resulting from the errors on the HR itself (see also Maccacaro et al. 1988 for a description of the hardness ratio technique used to analyse the EMSS AGN observed with the IPC or the *Einstein* satellite).

To test the reliability of the hardness ratio technique we have compared the value of the spectral index $\alpha_{x,HR}$ derived from the hardness ratio with those derived from the detailed spectral analysis for the 36 CRSS sources with enough net counts (see section 3 and Table 1 and 2). In order to assure consistency with the hardness ratio results, we used the best fit slopes obtained with fit 1 (N_H fixed at Galactic value). The result is illustrated in Figure A2. The slopes derived through the two methods (hardness ratio and spectral analysis) are very well correlated through the entire range of values ($\alpha_x \sim 0.6 - 2.6$), with a typical differences of 0.1 or less in α_x .

REFERENCES

Bevington P.R. and Robinson D.K. 1992, *Data Reduction and Error Analysis for the Physical Sciences*. McGraw-Hill, New York.

- Boyle B.J., McMahon R.G., Wilkes B.J. and Elvis M., 1995 a, MNRAS, 272, 462
- Boyle B.J., McMahon R.G., Wilkes B.J. and Elvis M., 1995 b, MNRAS in press.
- Canizares C.R., and White J.L., 1989, ApJ, 339, 27.
- Cilieggi P., Elvis M., Wilkes B.J., Boyle B.J., McMahon R.G and Maccacaro T., 1995, MNRAS, 277, 1463.
- Cilieggi P. and Maccacaro T., 1996, MNRAS, submitted.
- Comastri A., Setti G., Zamorani G., Elvis M., Giommi P., Wilkes B.J. and McDowell J.C., 1992, ApJ, 384, 62.
- Elvis M., Fiore F., Wilkes B.J., McDowell J., and Bechtold J., 1994, ApJ, 422, 60.
- Fiore F., Elvis M., McDowell J., Siemiginowska A. and Wilkes B.J., 1994, ApJ, 431, 515.
- Gioia I.M., Maccacaro T., Schild R.E., Wolter A., Stocke J.T., Morris S.L., and Henry J.P., 1990, ApJS, 72, 567.
- Hasinger G., 1992, MPE Report n. 235, p. 321.
- Hasinger G., Boese G., Predehl P., Turner T.J., Yusaf R., George I.M. and Rohrbach G., 1994, MPE/OGIP Calibration Memo CAL/ROS/93-015.
- Laor A., Fiore F., Elvis M., Wilkes B.J. and McDowell J.C., 1994, ApJ, 435, 611.
- Hooper E., Impey C.D., Foltz C. and Hewett P., 1995, ApJ, 445, 62.
- Lawrence A. and Elvis M., 1982, ApJ, 256, 410.
- Maccacaro T., Gioia I.M., Wolter A., Zamorani G., and Stocke J.T., 1988, ApJ, 326, 680.
- Masnou J.L., Wilkes B.J., Elvis M., McDowell J.C. and Arnaud K.A., 1992, A&A, 253, 35.
- Press W.H., Teukolsky S.A., Vetterling W.T. and Flannery B.P., 1992, *Numerical Recipes, Second Edition*, Cambridge: Cambridge Univ. Press.
- Reichert G.A., Mushotzky R.F., Petre R. and Holt S.S., 1985, ApJ, 296, 69.
- Schartel N., Fink H., Brinkmann W., and Trümper J., 1992, MPE Report no. 235 1992, p. 195.
- Schartel N. et al., 1995, ApJ, submitted
- Stark A.A., Gammie C.F., Wilson R.W., Bally J., Linke R., Heiles C., and Hurwitz M., 1992, ApJS, 79, 77.
- Stocke J.T., Morris S.L., Gioia I.M., Maccacaro T., Schild R.E., Wolter A., Fleming T.A., and Henry J.P., 1991, ApJS, 76, 813.
- Trümper J., 1983, Adv. Space Res., 2, No.4 241.
- Turner T.J. and Pounds K.A., 1989, MNRAS, 240, 833.
- Turner T.J. and George I.M., 1992, OGIP Calibration Memo.
- Ulrich M.N. and Molendi S., 1995, ApJ, December 95, in press.
- Walter R. and Fink H., 1993, A&A, 274, 105.
- Wilkes B.J. and Elvis M., 1987, ApJ, 323, 243.
- Williams O.R. et al., 1992, ApJ, 389, 157.
- Worrall D.M., and Wilkes B.J., 1990, ApJ, 360, 396.

Figure 3. Mean energy spectral index and intrinsic dispersion obtained from the Maximim-Likelihood analysis for CRSS QSOs (thick line) and CRSS NLXGs (thin line). The confidence contours correspond to 90 per cent level for two interesting parameters.

Figure 4. (a) Redshift, (b) X-ray broad-band (0.5 – 2.0 keV) luminosity L_x , (c) optical luminosity at 2500Å and (d) L_{2500}/L_x as a function of the X-ray energy spectral index for CRSS radio-quiet QSOs (open squares), CRSS radio-loud QSOs (filled circles) CRSS starburst HII objects (filled squares), CRSS Seyfert Galaxies 1.5 (open circles) and EMSS NLXGs (open stars).

Figure A1. PSPC hardness ratio for power-law spectra as a function of the energy spectral index α_X and of the hydrogen column density N_H .

Figure A2. Upper panel: Comparison between the spectral slope α determine

Figure Captions

Figure 1. (a) X-ray luminosity, (b) redshift, (c) color $O - E$ distributions of the whole CRSS sample (open) and of the 7 sources with $HR = 1$ or $HR + HR_{\text{ERROR}} > 1$ (shaded).

Figure 2. Energy spectral index distributions of the CRSS QSOs (open), of the CRSS NLXGs (HII, Sy1.8, Sy 2 and NLXG not observed at intermediate resolution, shaded) and of the CRSS Sy 1.5 galaxies (filled).

TABLE 1 : CRSS Sources

| SOURCE | Type ¹ | <i>z</i> | Date | <i>r</i> (<i>l</i>) | <i>θ</i> (<i>l</i>) | Net Counts ² | | | Sequence number |
|-----------------|-------------------|----------|--------------|--------------------------|--------------------------|-------------------------|------------|-------------|--------------------|
| | | | | | | S | H | B | |
| CRSS0007.3+2042 | Q | 0.769 | 1991 June 30 | 1.8 | 13.5 | 47.8±12.7 | 91.5±11.4 | 149.6±17.0 | 700101 |
| CRSS0007.7+2050 | Q | 1.396 | " | 1.7 | 12.9 | 32.7± 8.9 | 47.4± 8.2 | 86.6±12.8 | " |
| CRSS0008.0+2043 | Q | 1.381 | " | 1.5 | 5.0 | 19.4±11.6 | 57.7± 9.9 | 90.6±16.7 | " |
| CRSS0008.4+2034 | Q | 0.389 | " | 1.6 | 6.7 | 123.2±14.8 | 315.4±19.3 | 464.7±26.0 | " |
| CRSS0008.4+2042 | Q | 1.710 | " | 1.5 | 2.4 | 9.7± 7.8 | 38.1± 7.7 | 50.9±11.1 | " |
| CRSS0008.6+2045 | Q | 0.752 | " | 1.5 | 6.9 | 1.75±10.7 | 48.8± 9.5 | 52.5±16.2 | " |
| CRSS0009.0+2041 | HII | 0.189 | " | 1.7 | 9.8 | 20.3±11.4 | 48.1± 9.7 | 75.8±16.3 | " |
| CRSS0029.7+2606 | Q | 1.094 | 1991 July 5 | 2.0 | 11.8 | 0.0± 7.1 | 35.2± 7.2 | 37.8±11.3 | 300016 |
| CRSS0030.2+2611 | HII | 0.077 | " | 1.6 | 6.3 | 105.9±13.0 | 72.9±10.1 | 197.7±17.0 | " |
| CRSS0030.6+2620 | Q | 0.492 | " | 1.6 | 8.4 | 327.0±21.6 | 377.8±19.4 | 730.7±31.5 | " |
| CRSS0030.7+2616 | Sy 2 | 0.246 | " | 1.7 | 9.4 | 0.0±11.1 | 64.4±10.6 | 67.0±17.9 | " |
| CRSS0030.8+2628 | Q | 1.372 | " | 2.4 | 14.7 | 40.6±12.2 | 56.2± 9.9 | 96.8±17.7 | " |
| CRSS1406.7+2827 | Q | 0.878 | 1991 July 13 | 1.5 | 3.1 | 114.5±19.0 | 51.4±12.2 | 167.3±24.0 | 700061 |
| CRSS1406.7+2838 | HII | 0.331 | " | 2.3 | 12.2 | 106.8±28.8 | 61.8±17.8 | 175.2±43.9 | " |
| CRSS1407.3+2818 | Q | 1.121 | " | 1.7 | 9.9 | 400.4±25.5 | 294.4±19.2 | 721.9±32.6 | " |
| CRSS1407.3+2814 | Q | 0.728 | " | 2.3 | 12.9 | 72.2±17.5 | 71.0±12.3 | 155.4±23.0 | " |
| CRSS1407.6+2825 | Q | 1.222 | " | 1.8 | 8.9 | 95.6±13.4 | 17.9± 7.2 | 118.1±13.9 | " |
| CRSS1407.7+2830 | Q | 0.642 | " | 2.0 | 10.9 | 680.5±30.7 | 623.7±23.7 | 1360.2±42.1 | " |
| CRSS1407.7+2824 | Q | 1.127 | " | 1.9 | 10.7 | 76.2±13.7 | 84.4±11.3 | 164.0±18.3 | " |
| CRSS1412.5+4355 | Sy 1.8 | 0.094 | 1991 June 26 | 2.5 | 14.4 | 386.7±22.7 | 303.9±18.6 | 742.8±31.6 | 700248 |
| CRSS1413.3+4405 | Sy 1.5 | 0.136 | " | 1.6 | 7.5 | 91.6±18.5 | 119.7±12.6 | 211.6±24.7 | " |
| CRSS1413.4+4358 | Q | 0.950 | " | 1.5 | 3.9 | 85.6±18.4 | 40.3± 9.9 | 136.1±23.7 | " |
| CRSS1413.8+4406 | Q | 0.978 | " | 1.6 | 6.7 | 129.8±18.3 | 72.8±11.1 | 229.1±24.8 | " |
| CRSS1413.8+4402 | Q | 1.347 | " | 1.5 | 2.6 | 52.0±16.8 | 52.3±10.1 | 120.8±17.6 | " |
| CRSS1414.2+4354 | Q | 1.197 | " | 1.6 | 7.4 | 152.0±19.6 | 75.4±11.4 | 255.6±25.5 | " |
| CRSS1415.0+4402 | Sy 1.5 | 0.136 | " | 2.0 | 13.0 | 62.7±16.6 | 74.1±11.2 | 149.3±19.7 | " |
| CRSS1415.0+1119 | Q | 0.538 | 1991 July 21 | 2.5 | 14.4 | 98.0±18.8 | 103.3±14.8 | 202.6±26.1 | 700122 |
| CRSS1415.1+1140 | Q | 2.353 | " | 2.1 | 13.3 | 58.6±17.4 | 55.9±12.7 | 123.2±23.8 | " |
| CRSS1415.2+1123 | Q | 1.230 | " | 2.0 | 9.6 | 97.1±23.7 | 37.7±15.7 | 139.9±35.4 | " |
| CRSS1415.5+1127 | Q | 1.412 | " | 1.5 | 4.4 | 44.4±12.7 | 60.6± 8.4 | 119.8±17.3 | " |
| CRSS1415.5+1131 | Q | 0.256 | " | 1.5 | 4.2 | 214.7±21.8 | 286.3±20.4 | 542.0±32.7 | " |
| CRSS1415.5+1128 | Q | 0.359 | " | 1.8 | 3.4 | 98.2±18.4 | 28.0±12.2 | 131.8±23.2 | " |
| CRSS1415.7+1116 | Q | 1.257 | " | 2.2 | 13.4 | 58.9±22.5 | 30.9±15.8 | 93.3±31.3 | " |
| CRSS1416.2+1131 | Q | 1.429 | " | 1.7 | 7.5 | 3.5±10.9 | 38.9± 9.7 | 46.2±14.4 | " |
| CRSS1416.3+1124 | Q | 1.673 | " | 1.9 | 10.3 | 76.7±17.9 | 31.8±12.2 | 115.2±23.1 | " |
| CRSS1418.3+0637 | Q | 0.328 | 1992 July 25 | 2.5 | 14.6 | 1100.8±35.3 | 190.5±15.3 | 1366.5±39.5 | 700865 |
| CRSS1419.2+5429 | Q | 0.722 | 1990 July 22 | 1.7 | 7.4 | 62.0±10.3 | 28.5± 6.2 | 105.8±12.9 | 150046 |
| CRSS1419.3+5424 | Q | 0.785 | " | 1.5 | 4.1 | 29.5± 9.0 | 10.6± 5.0 | 45.5±10.6 | " |
| CRSS1419.8+5433 | Q | 0.367 | " | 2.1 | 10.4 | 27.3±10.9 | 24.1± 6.6 | 58.9±14.0 | " |
| CRSS1419.9+5430 | Q | 2.257 | " | 1.6 | 7.0 | 64.6±12.5 | 38.2± 8.0 | 111.5±16.1 | " |
| CRSS1420.1+5426 | Q | 0.583 | " | 1.5 | 4.7 | 186.7±17.2 | 79.9±10.4 | 281.0±20.6 | " |
| CRSS1428.3+4231 | Q | 2.170 | 1992 Jan 24 | 1.8 | 8.5 | 34.7±11.9 | 16.0± 6.9 | 55.2±13.1 | 700535 |

TABLE 1 : Continued

| SOURCE | Type ¹ | z | Date | r (ν) | θ (ν) | S | Net Counts ² H | B | Sequence number |
|-----------------|-------------------|-------|--------------|------------------|-----------------------|------------|------------------------------|-------------|--------------------|
| CRSS1429.0+0122 | Q | 0.416 | 1990 July 19 | 1.5 | 4.3 | 0.0± 5.3 | 21.0± 8.3 | 22.6± 8.4 | 150007 |
| CRSS1429.0+0120 | HII | 0.102 | " | 1.5 | 2.6 | 27.6± 8.5 | 12.4± 5.5 | 42.0± 9.4 | " |
| CRSS1429.1+0128 | Q | 1.131 | " | 2.0 | 10.2 | 21.6± 8.3 | 15.4± 5.3 | 37.4±10.0 | " |
| CRSS1429.2+0120 | Q | 1.127 | " | 1.5 | 4.1 | 0.0± 6.8 | 12.1± 5.3 | 14.0± 5.3 | " |
| CRSS1429.7+4240 | Q | 1.672 | 1991 Jan 24 | 1.6 | 8.5 | 86.0±16.2 | 94.1±12.0 | 185.4±23.3 | 700535 |
| CRSS1514.4+5627 | NLXG | 0.446 | 1992 Jan 13 | 2.5 | 14.7 | 89.6±22.5 | 56.8±12.2 | 159.7±14.7 | 600190 |
| CRSS1514.7+3641 | Q | 1.219 | 1992 Aug 12 | 1.8 | 9.2 | 19.2± 6.8 | 26.8± 2.6 | 48.6± 9.4 | 700807 |
| CRSS1515.0+3657 | Q | 0.253 | " | 1.6 | 7.6 | 82.6±10.6 | 45.9± 7.3 | 137.0±13.4 | " |
| CRSS1515.1+5628 | Q | 0.723 | 1992 Jan 13 | 1.9 | 11.4 | 49.6±10.8 | 80.6± 9.9 | 135.9±15.1 | 600190 |
| CRSS1515.4+3652 | Q | 0.893 | 1992 Aug 12 | 1.7 | 8.8 | 33.1± 7.8 | 27.2± 5.9 | 69.3±10.6 | 700807 |
| CRSS1515.5+3655 | Q | 0.812 | " | 2.0 | 11.5 | 59.0± 9.4 | 34.1± 6.6 | 98.1±12.0 | " |
| CRSS1515.7+5610 | Q | 0.296 | 1992 Jan 13 | 2.3 | 8.6 | 127.1±23.3 | 68.9±13.2 | 204.8±33.8 | 600190 |
| CRSS1516.3+5611 | Q | 1.167 | " | 1.6 | 8.1 | 45.4±10.8 | 24.9± 6.4 | 77.4±13.2 | " |
| CRSS1517.0+5623 | Q | 0.434 | " | 1.7 | 10.6 | 68.8±15.2 | 103.8±12.0 | 177.3±20.8 | " |
| CRSS1545.4+4838 | Q | 0.937 | 1992 Aug 22 | 1.7 | 8.0 | 3.0± 6.8 | 16.1± 4.7 | 20.1± 9.2 | 700809 |
| CRSS1545.5+4858 | Q | 0.666 | " | 2.0 | 11.8 | 43.6± 9.0 | 10.1± 4.4 | 56.4±10.8 | " |
| CRSS1545.5+4847 | Q | 1.403 | " | 1.5 | 1.2 | 5.1±12.3 | 12.4± 4.4 | 19.0± 8.0 | " |
| CRSS1545.9+4849 | Q | 0.154 | " | 1.5 | 5.2 | 14.7± 7.5 | 22.0± 5.2 | 37.2± 9.4 | " |
| CRSS1604.8+2549 | Q | 0.426 | 1991 Aug 27 | 2.2 | 12.4 | 43.1±15.1 | 24.6± 9.0 | 69.4±17.4 | 300021 |
| CRSS1605.2+2541 | Q | 1.071 | " | 2.2 | 12.3 | 0.0±19.0 | 88.8±13.7 | 90.2±26.4 | " |
| CRSS1605.6+2543 | HII | 0.278 | " | 1.7 | 8.5 | 21.4±15.1 | 83.8±11.8 | 114.8±20.6 | " |
| CRSS1605.9+2554 | NLXG | 0.151 | " | 1.5 | 3.9 | 52.7±16.2 | 70.3±11.8 | 128.4±21.8 | " |
| CRSS1606.6+2542 | Q | 1.436 | " | 2.3 | 14.3 | 16.3±14.2 | 46.5±10.0 | 74.9±19.3 | " |
| CRSS1618.4+0558 | Q | 0.406 | 1991 Feb 20 | 1.9 | 11.6 | 20.4± 8.2 | 32.4± 7.5 | 52.9±11.2 | 700213 |
| CRSS1620.1+1724 | Q | 0.114 | 1991 Feb 19 | 1.5 | 0.3 | 271.4±17.6 | 738.1±27.5 | 1065.7±33.7 | 700022 |
| CRSS1653.3+3951 | Q | 0.692 | 1991 Feb 26 | 1.7 | 8.2 | 58.6±11.5 | 52.8± 8.9 | 120.6±15.7 | 700130 |
| CRSS1654.5+3954 | Q | 0.340 | " | 1.8 | 11.4 | 75.0±10.3 | 115.6±11.3 | 203.0±15.8 | " |
| CRSS1704.1+6047 | Q | 1.361 | 1991 Oct 30 | 1.5 | 5.4 | 93.3±14.4 | 63.8±10.9 | 166.8±20.0 | 700439 |
| CRSS1705.3+6049 | Sy 2? | 0.572 | " | 2.0 | 7.1 | 46.5± 7.6 | 53.5± 5.2 | 105.0± 9.4 | " |
| CRSS1705.3+6044 | Q | 1.416 | " | 1.5 | 5.3 | 24.3±11.7 | 35.8± 9.5 | 66.6±17.5 | " |
| CRSS1705.4+6031 | Q | 0.375 | " | 2.2 | 14.4 | 117.5±17.8 | 86.7±13.7 | 221.2±26.1 | " |
| CRSS1705.5+6042 | Q | 0.280 | " | 2.3 | 6.9 | 472.6±28.0 | 506.6±25.4 | 1028.4±42.6 | " |
| CRSS1706.4+6042 | Q | 1.142 | " | 2.1 | 13.2 | 55.3±12.7 | 20.1± 8.8 | 87.3±17.3 | " |
| CRSS2235.3+1340 | Q | 1.021 | 1991 Nov 24 | 2.0 | 12.5 | 10.1± 5.2 | 43.5± 7.0 | 56.9± 9.2 | 700438 |
| CRSS2250.0+1407 | Q | 1.159 | 1991 Nov 26 | 2.2 | 13.5 | 20.5± 6.3 | 29.3± 6.2 | 51.7± 9.3 | 700254 |
| CRSS2251.0+1418 | Q | 0.962 | " | 1.7 | 9.2 | 7.2± 4.0 | 42.6± 6.8 | 52.1± 8.1 | " |
| CRSS2324.7+2315 | Q | 1.828 | 1991 June 29 | 1.9 | 12.1 | 20.1± 9.8 | 71.8±10.7 | 100.1±15.7 | 200322 |
| CRSS2324.8+2321 | Q | 0.447 | " | 1.6 | 7.8 | 51.0±11.3 | 125.0±13.0 | 193.7±18.7 | " |

¹ Q = Quasar , Sy = Seyfert Galaxies , HII = Starburst galaxies

NLXG = narrow line X-ray galaxies not observed at intermediate-resolution

² Net counts in the Soft (S = 0.1-0.4 keV), Hard (H = 0.5-2.0 keV) and Broad band (B = 0.1-2.4 keV)

TABLE 2: X-ray properties of the CRSS sample

| HR ANALYSIS | | | | SPECTRAL ANALYSIS | | | | | | | Log $L_{0.5-2.0 \text{ keV}}^b$ Log $L_{2500 \text{ \AA}}^c$ |
|-----------------|------------|--|-----|--|--|---------------------------|----------------------------|----------------------|-----------|-------|---|
| SOURCE | HR | α_{HR} | FIT | α_z | N_H | χ^2_{FIT}/dof | $P(\chi^2 > \chi^2_{FIT})$ | $P(F > F_{FIT})$ | ξ_z^a | | |
| 1 | 2 | 3 | 4 | 5 | 6 | 7 | 8 | 9 | 10 | 11 | |
| CRSS0007.3+2042 | 0.31±0.13 | 1.46 ^{+0.26} _{-0.28} | 1 | 1.53 ^{+0.24} _{-0.29} | 4.07 | 1.25/5 | 0.94 | | 0.51±0.06 | 44.40 | |
| CRSS0007.7+2050 | 0.18±0.16 | 1.69 ^{+0.26} _{-0.27} | 2 | 1.26 ^{+1.09} _{-1.02} | 3.19 ^{+4.04} _{-2.69} 4.07 | 1.12/4 | 0.89 | 0.53 | 0.28±0.04 | 30.57 | |
| CRSS0008.0+2043 | 0.50±0.23 | 1.12 ^{+0.43} _{-0.61} | | | 4.07 | | | | 0.33±0.06 | 44.83 | |
| CRSS0008.4+2034 | 0.44±0.05 | 1.20 ^{+0.13} _{-0.13} | 1 | 1.08 ^{+0.12} _{-0.14} | 4.01 | 18.8/20 | 0.53 | | 1.71±0.01 | 30.50 | |
| CRSS0008.4+2042 | 0.59±0.27 | 0.89 ^{+0.62} _{-0.79} | 2 | 0.45 ^{+0.36} _{-0.34} | 1.69 ^{+1.12} _{-0.90} 4.07 | 10.5/19 | 0.94 | 9.7×10 ⁻⁴ | 0.21±0.05 | 44.89 | |
| CRSS0008.6+2045 | 0.93±0.41 | <1.11 | | | 4.06 | | | | 0.28±0.10 | 31.10 | |
| CRSS0009.0+2041 | 0.41±0.25 | 1.28 ^{+0.44} _{-0.58} | | | 4.07 | | | | 0.29±0.10 | 44.11 | |
| CRSS0029.7+2606 | 1.00±0.40 | <0.81 | | | 3.75 | | | | 0.19±0.06 | 29.79 | |
| CRSS0030.2+2611 | -0.18±0.09 | 2.10 ^{+0.18} _{-0.18} | 1 | 2.31 ^{+0.19} _{-0.15} | 3.83 | 10.1/6 | 0.12 | | 0.37±0.03 | 42.73 | |
| CRSS0030.6+2620 | 0.07±0.04 | 1.79 ^{+0.07} _{-0.07} | 2 | 3.23 ^{+0.15} _{-0.15} | 9.82 ^{+4.60} _{-3.97} | 4.8/5 | 0.44 | 0.06 | 0.28±0.10 | 28.05 | |
| CRSS0030.7+2616 | 1.00±0.34 | <0.71 | 1 | 1.75 ^{+0.08} _{-0.08} | 3.91 | 38.4/24 | 0.03 | | 0.19±0.06 | 44.37 | |
| CRSS0030.8+2628 | 0.16±0.17 | 1.68 ^{+0.27} _{-0.29} | 2 | 0.84 ^{+0.26} _{-0.25} | 1.33 ^{+0.66} _{-0.55} 3.90 | 13.8/23 | 0.93 | 1.6×10 ⁻⁶ | 0.37±0.03 | 30.78 | |
| CRSS1406.7+2827 | -0.38±0.12 | 1.50 ^{+0.19} _{-0.19} | 1 | 1.68 ^{+0.30} _{-0.38} | 3.97 | 8.9/4 | 0.30 | | 0.23±0.10 | 42.04 | |
| CRSS1406.7+2836 | -0.27±0.18 | 1.31 ^{+0.29} _{-0.26} | 2 | 0.37 ^{+1.38} _{-0.29} | 1.60 ^{+1.60} _{-1.60} | 6.0/3 | 0.11 | 0.31 | 0.32±0.06 | 29.42 | |
| CRSS1407.3+2818 | -0.15±0.04 | 1.16 ^{+0.07} _{-0.07} | 1 | 1.52 ^{+0.26} _{-0.19} | 1.38 | 2.8/4 | 0.58 | | 0.23±0.03 | 44.51 | |
| CRSS1407.3+2818 | -0.15±0.04 | 1.16 ^{+0.07} _{-0.07} | 2 | 1.07 ^{+1.18} _{-0.62} | 0.47 ^{+2.46} _{-0.10} 1.35 | 2.3/3 | 0.51 | 0.47 | 0.32±0.08 | 30.68 | |
| CRSS1407.3+2818 | -0.15±0.04 | 1.16 ^{+0.07} _{-0.07} | 1 | 1.17 ^{+0.18} _{-0.08} | 1.41 | 24.0/16 | 0.09 | | 0.23±0.05 | 42.89 | |
| CRSS1407.3+2818 | -0.15±0.04 | 1.16 ^{+0.07} _{-0.07} | 2 | 1.29 ^{+0.37} _{-0.33} | 1.69 ^{+0.89} _{-0.72} | 23.7/15 | 0.07 | 0.67 | 1.28±0.05 | 28.09 | |
| CRSS1407.3+2818 | -0.15±0.04 | 1.16 ^{+0.07} _{-0.07} | | | | | | | 0.32±0.06 | 44.87 | |
| CRSS1407.3+2818 | -0.15±0.04 | 1.16 ^{+0.07} _{-0.07} | | | | | | | 0.23±0.03 | 30.91 | |
| CRSS1407.3+2818 | -0.15±0.04 | 1.16 ^{+0.07} _{-0.07} | | | | | | | 0.32±0.08 | 44.20 | |
| CRSS1407.3+2818 | -0.15±0.04 | 1.16 ^{+0.07} _{-0.07} | | | | | | | 1.28±0.05 | 30.02 | |
| CRSS1407.3+2818 | -0.15±0.04 | 1.16 ^{+0.07} _{-0.07} | | | | | | | 0.32±0.08 | 43.31 | |
| CRSS1407.3+2818 | -0.15±0.04 | 1.16 ^{+0.07} _{-0.07} | | | | | | | 1.28±0.05 | 28.44 | |
| CRSS1407.3+2818 | -0.15±0.04 | 1.16 ^{+0.07} _{-0.07} | | | | | | | 1.28±0.05 | 45.23 | |
| CRSS1407.3+2818 | -0.15±0.04 | 1.16 ^{+0.07} _{-0.07} | | | | | | | 1.28±0.05 | 31.42 | |

TABLE 2 : Continued

| HR ANALYSIS | | | | SPECTRAL ANALYSIS | | | | | | | | Log L _{0.5-2.0 keV} Log L _{2500 Å} |
|-----------------|------------|--|-----|--|--|------------------------------------|--|--------------------------|----------------|-------|--|---|
| SOURCE | HR | α _{HR} | FIT | α _z | N _H | χ ² _{FIT} /dof | P(χ ² > χ ² _{FIT}) | P(F > F _{FIT}) | Γ _z | | | |
| 1 | 2 | 3 | 4 | 5 | 6 | 7 | 8 | 9 | 10 | 11 | | |
| CRSS1415.5+1131 | 0.15±0.06 | 0.92 ^{+0.09} _{-0.08} | 1 | 0.97 ^{+0.08} _{-0.09} | 1.80 | 11.7/17 | 0.82 | | 1.28±0.08 | 43.68 | | |
| CRSS1415.5+1128 | -0.56±0.16 | 2.02 ^{+0.97} _{-0.54} | 2 | 1.18 ^{+0.39} _{-0.36} | 2.43 ^{+1.12} _{-0.97} | 10.9/16 | 0.82 | 0.28 | 0.10±0.02 | 29.06 | | |
| CRSS1415.7+1116 | -0.31±0.29 | 1.28 ^{+0.50} _{-0.41} | | | 1.80 | | | | 0.20±0.07 | 42.89 | | |
| CRSS1416.2+1131 | 0.83±0.47 | <0.68 | | | 1.80 | | | | 0.15±0.05 | 28.65 | | |
| CRSS1416.3+1124 | -0.41±0.19 | 1.75 ^{+0.32} _{-0.30} | | | 1.80 | | | | 0.16±0.03 | 44.56 | | |
| CRSS1418.3+0637 | -0.70±0.02 | 2.45 ^{+0.11} _{-0.09} | 1 | 2.56 ^{+0.10} _{-0.10} | 2.14 | 15.2/14 | 0.37 | | 2.25±0.07 | 30.98 | | |
| | | | 2 | 3.15 ^{+0.30} _{-0.30} | 3.29 ^{+0.80} _{-0.80} | 10.2/13 | 0.68 | 0.03 | 0.30±0.04 | 44.29 | | |
| CRSS1419.2+5429 | -0.37±0.12 | 1.45 ^{+0.19} _{-0.19} | 1 | 1.49 ^{+0.17} _{-0.17} | 1.32 | 2.8/6 | 0.83 | 0.08 | 0.13±0.03 | 30.24 | | |
| | | | 2 | 2.35 ^{+1.84} _{-1.11} | 3.37 ^{+4.82} _{-2.48} | 1.4/5 | 0.92 | | 0.33±0.08 | 44.09 | | |
| CRSS1419.3+5424 | -0.47±0.22 | 1.57 ^{+0.43} _{-0.33} | | | 1.31 | | | | 0.16±0.06 | 30.06 | | |
| CRSS1419.8+5433 | -0.06±0.24 | 1.00 ^{+0.35} _{-0.34} | | | 1.33 | | | | 0.43±0.06 | 43.83 | | |
| CRSS1419.9+5430 | -0.26±0.13 | 1.26 ^{+0.20} _{-0.19} | 1 | 1.21 ^{+0.18} _{-0.19} | 1.32 | 3.9/7 | 0.79 | | 0.23±0.08 | 29.95 | | |
| | | | 2 | 0.99 ^{+1.43} _{-0.66} | 0.83 ^{+3.67} _{-0.10} | 3.8/6 | 0.70 | 0.90 | 0.31±0.08 | 43.44 | | |
| CRSS1420.1+5426 | -0.40±0.07 | 1.50 ^{+0.11} _{-0.11} | 1 | 1.52 ^{+0.12} _{-0.12} | 1.31 | 4.3/10 | 0.93 | 0.57 | 0.43±0.06 | 28.85 | | |
| | | | 2 | 1.63 ^{+0.62} _{-0.49} | 1.55 ^{+1.41} _{-0.95} | 4.1/9 | 0.90 | | 0.86±0.06 | 45.63 | | |
| CRSS1428.3+4231 | -0.37±0.23 | 1.47 ^{+0.57} _{-0.46} | | | 1.40 | | | | 0.16±0.06 | 32.23 | | |
| CRSS1429.0+0122 | 1.00±0.50 | <0.74 | | | 2.75 | | | | 0.23±0.08 | 44.32 | | |
| CRSS1429.0+0120 | -0.38±0.23 | 2.09 ^{+0.51} _{-0.36} | | | 2.75 | | | | 0.13±0.03 | 29.15 | | |
| CRSS1429.1+0128 | -0.17±0.25 | 1.77 ^{+0.40} _{-0.40} | | | 2.75 | | | | 0.31±0.08 | 45.04 | | |
| | | | | | | | | | | 32.31 | | |
| | | | | | | | | | | 43.38 | | |
| | | | | | | | | | | 29.44 | | |
| | | | | | | | | | | 41.79 | | |
| | | | | | | | | | | 28.83 | | |
| | | | | | | | | | | 44.62 | | |
| | | | | | | | | | | 30.03 | | |

TABLE 2: Continued

| HR ANALYSIS | | | | SPECTRAL ANALYSIS | | | | | | | |
|-----------------|------------|--|-----|--|--|---------------------------|----------------------------|------------------|-----------|---|--|
| SOURCE | HR | α_{HR} | FIT | α_z | N_H | χ^2_{FIT}/dof | $P(\chi^2 > \chi^2_{FIT})$ | $P(F > F_{FIT})$ | t^*_z | $\text{Log } L^b_{0.8-2.0 \text{ keV}}$ $\text{Log } L^c_{2500 \text{ \AA}}$ | |
| | 2 | 3 | 4 | 5 | 6 | 7 | 8 | 9 | 10 | 11 | |
| CRSS1604.8+2549 | -0.27±0.23 | 2.61 ^{+0.50} _{-0.45} | | | 4.61 | | | | 0.15±0.04 | 43.25 | |
| CRSS1605.2+2541 | 1.00±0.43 | < 1.30 | | | 4.62 | | | | 0.32±0.11 | 29.12 44.57 | |
| CRSS1605.6+2543 | 0.59±0.23 | 1.05 ^{+0.49} _{-0.84} | 1 | 1.36 ^{+0.33} _{-0.43} | 4.60 | 3.5/6 | 0.74 | | 0.45±0.08 | 30.91 43.30 | |
| | | | 2 | 1.19 ^{+1.19} _{-1.15} | 3.85 ^{+7.25} _{-3.55} | 3.3/5 | 0.65 | 0.62 | | 29.00 | |
| CRSS1605.9+2554 | 0.14±0.17 | 1.90 ^{+0.27} _{-0.30} | 1 | 1.93 ^{+0.31} _{-0.40} | 4.54 | 7.0/4 | 0.13 | | 0.39±0.06 | 42.64 | |
| | | | 2 | 0.28 ^{+1.24} _{-0.35} | 1.00 ^{+1.90} _{-1.00} | 3.1/3 | 0.38 | 0.15 | | 28.23 | |
| CRSS1606.6+2542 | 0.48±0.34 | 1.30 ^{+0.64} _{-1.15} | | | 4.57 | | | | 0.30±0.08 | 44.90 | |
| CRSS1618.4+0558 | 0.23±0.22 | 1.77 ^{+0.36} _{-0.41} | | | 4.57 | | | | 0.48±0.11 | 31.21 43.70 | |
| CRSS1620.1+1724 | 0.46±0.03 | 1.19 ^{+0.06} _{-0.06} | 1 | 1.13 ^{+0.06} _{-0.06} | 4.09 | 31.5/25 | 0.17 | | 16.2±0.51 | 29.27 43.97 | |
| | | | 2 | 1.00 ^{+0.21} _{-0.21} | 3.62 ^{+0.70} _{-0.65} | 30.5/24 | 0.17 | 0.38 | | 29.89 | |
| CRSS1653.3+3951 | -0.05±0.13 | 1.11 ^{+0.19} _{-0.18} | 1 | 1.07 ^{+0.20} _{-0.20} | 1.64 | 2.1/4 | 0.72 | | 0.88±0.11 | 44.51 | |
| | | | 2 | 0.87 ^{+1.00} _{-0.75} | 1.15 ^{+2.51} _{-1.15} | 1.9/3 | 0.59 | 0.62 | | 29.77 | |
| CRSS1654.5+3954 | 0.21±0.08 | 0.76 ^{+0.12} _{-0.12} | 1 | 0.90 ^{+0.11} _{-0.11} | 1.70 | 9.8/10 | 0.46 | | 1.77±0.13 | 44.08 | |
| | | | 2 | 1.08 ^{+0.51} _{-0.53} | 2.24 ^{+1.94} _{-1.42} | 9.5/9 | 0.39 | 0.64 | | 29.55 | |
| CRSS1704.1+6047 | -0.19±0.11 | 1.62 ^{+0.18} _{-0.16} | 1 | 1.54 ^{+0.18} _{-0.18} | 2.33 | 3.2/4 | 0.52 | | 0.64±0.08 | 45.16 | |
| | | | 2 | 1.67 ^{+0.33} _{-0.33} | 2.67 ^{+3.92} _{-2.62} | 3.2/3 | 0.36 | 0.90 | | 31.52 | |
| CRSS1705.3+6049 | 0.07±0.10 | 1.24 ^{+0.31} _{-0.32} | | | 2.33 | | | | 0.52±0.04 | 44.08 | |
| CRSS1705.3+6044 | 0.19±0.26 | 1.03 ^{+0.40} _{-0.46} | | | 2.33 | | | | 0.36±0.09 | 29.10 44.96 | |
| CRSS1705.4+6031 | -0.15±0.11 | 1.55 ^{+0.16} _{-0.16} | 1 | 1.60 ^{+0.17} _{-0.16} | 2.33 | 6.1/4 | 0.19 | | 0.99±0.11 | 31.09 43.94 | |
| | | | 2 | 2.31 ^{+1.33} _{-1.32} | 3.97 ^{+3.69} _{-2.53} | 5.3/3 | 0.15 | 0.55 | | 30.09 | |
| CRSS1705.5+6042 | 0.03±0.04 | 1.28 ^{+0.07} _{-0.06} | 1 | 1.30 ^{+0.06} _{-0.06} | 2.33 | 28.3/25 | 0.29 | | 4.85±0.20 | 44.33 | |
| | | | 2 | 1.32 ^{+0.29} _{-0.28} | 2.38 ^{+0.81} _{-0.72} | 28.1/24 | 0.26 | 0.70 | | 28.98 | |
| CRSS1706.4+6042 | -0.47±0.19 | 2.05 ^{+0.35} _{-0.30} | | | 2.33 | | | | 0.23±0.22 | 44.50 31.05 | |

TABLE 2 : Continued

| HR ANALYSIS | | | | SPECTRAL ANALYSIS | | | | | | |
|-----------------|-----------------|------------------------|-----|------------------------|------------------------|--------------------|----------------------------|------------------|-----------------|---|
| SOURCE | HR | α_{eHR} | FIT | α_z | N_H | χ^2_{FIT}/dof | $P(\chi^2 > \chi^2_{FIT})$ | $P(F > F_{FIT})$ | χ^2_z | $\log L^b_{0.5-2.0 \text{ keV}}$ $\log L^c_{2500 \text{ \AA}}$ |
| 1 | 2 | 3 | 4 | 5 | 6 | 7 | 8 | 9 | 10 | 11 |
| CRSS2235.3+1340 | 0.62 ± 0.17 | $1.06^{+0.40}_{-0.61}$ | | | 4.88 | | | | 1.04 ± 0.17 | 45.03 |
| CRSS2250.0+1407 | 0.18 ± 0.18 | $1.90^{+0.29}_{-0.32}$ | | | 4.69 | | | | 0.62 ± 0.11 | 30.46 |
| CRSS2251.0+1418 | 0.71 ± 0.14 | $0.79^{+0.49}_{-0.69}$ | | | 4.78 | | | | 0.71 ± 0.12 | 44.95 |
| CRSS2324.7+2315 | 0.56 ± 0.17 | $1.16^{+0.36}_{-0.50}$ | | | 4.70 | | | | 0.13 ± 0.02 | 30.22 |
| CRSS2324.8+2321 | 0.42 ± 0.10 | $1.47^{+0.19}_{-0.21}$ | 1 | $1.44^{+0.18}_{-0.21}$ | 4.70 | 3.5/5 | 0.62 | | 0.79 ± 0.08 | 44.79 |
| | | | 2 | $1.21^{+0.68}_{-0.63}$ | $3.80^{+2.53}_{-2.01}$ | 2.0/4 | 0.74 | 0.55 | | 30.73 |
| | | | | | | | | | | 44.84 |
| | | | | | | | | | | 31.53 |
| | | | | | | | | | | 44.01 |
| | | | | | | | | | | 29.65 |

^a X-ray flux between 0.5-2.0 keV in unit of $10^{-13} \text{ erg cm}^{-2} \text{ s}^{-1}$ ^b X-ray luminosity between 0.5-2.0 keV (erg s^{-1})^c Monochromatic luminosity at 2500 Å ($\text{erg s}^{-1} \text{ Hz}^{-1}$).

Table 3
Spectral models for the CRSS sources with a significant deviation from a power-law fit with $N_H = N_H \text{ Gal.}$

| Sources with "soft-excess" | | | | | | |
|----------------------------------|-------------------------------------|---------------------|----------------------------|---|------------------------|-----------------|
| SOURCE | Model | χ^2/dof | $P(\chi^2 > \chi^2_{FIT})$ | E_{break} (keV) | α_{SOFT} | α_{HARD} |
| CRSS0008.4+2034 | Broken power-law | 6.95/18 | 0.99 | 0.52 ± 0.20 | 2.03 ± 0.76 | 0.50 ± 0.34 |
| CRSS0030.6+2620 | Broken power-law | 12.41/22 | 0.95 | 0.59 ± 0.19 | 2.52 ± 0.56 | 0.74 ± 0.25 |
| Sources with "absorption excess" | | | | | | |
| SOURCE | Model | χ^2/dof | $P(\chi^2 > \chi^2_{FIT})$ | N_H^{int} ($\times 10^{20} \text{ cm}^{-2}$) | α_x | |
| CRSS1412.5+4355 | Power-law + Intrinsic Absorption | 9.64/19 | 0.96 | $1.42^{+1.58}_{-1.27}$ | $1.51^{+0.54}_{-0.46}$ | |

Table 4 : ROSAT data of the EMSS NLXGs

| Source | ROSAT ROR | Exp Time (s) | θ^a (l) | Net Counts | HR | α_{eHR} | f_z^b | $\text{Log } L_z^c$ | $\text{Log } L_{2500}^d$ |
|---------------|-----------|-----------------|-----------------------|------------------|------------------|-----------------|-----------------|---------------------|--------------------------|
| MS1114.4+1801 | RP600263 | 23865 | 18.3 | 211.9 \pm 34.6 | 0.38 \pm 0.17 | 0.45 \pm 0.29 | 0.84 \pm 0.13 | 42.50 | 29.22 |
| MS1253.6-0539 | RP700305 | 8513 | 8.7 | 101.0 \pm 20.8 | 0.37 \pm 0.21 | 0.70 \pm 0.37 | 1.01 \pm 0.21 | 44.05 | 29.30 |
| MS1412.8+1320 | WP700549 | 3313 | 16.9 | 77.9 \pm 20.4 | -0.16 \pm 0.21 | 1.24 \pm 0.31 | 1.32 \pm 0.34 | 43.11 | 28.75 |
| MS1414.8-1247 | WP700527 | 9109 | 24.3 | 134.5 \pm 33.2 | 0.85 \pm 0.25 | 0.72 \pm 1.00 | 1.05 \pm 0.26 | 43.34 | 28.82 |
| MS2348.6+1956 | WP701217 | 7655 | 7.2 | 210.7 \pm 20.9 | 0.75 \pm 0.07 | 0.54 \pm 0.28 | 3.16 \pm 0.32 | 42.35 | 28.25 |

^a Off-axis angle in the ROSAT/PSPC field

^b X-ray flux between 0.5-2.0 keV in unit of $10^{-13} \text{ erg cm}^{-2} \text{ s}^{-1}$

^c X-ray luminosity between 0.5-2.0 keV (erg s^{-1})

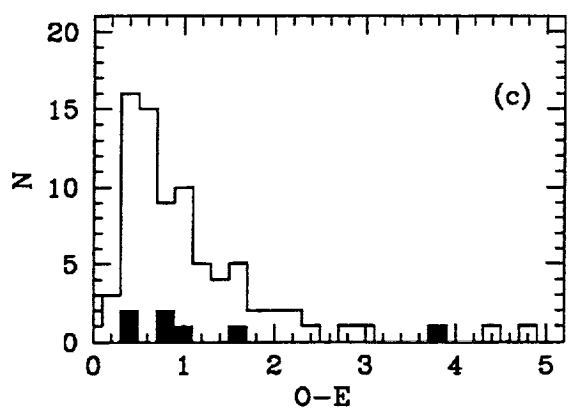
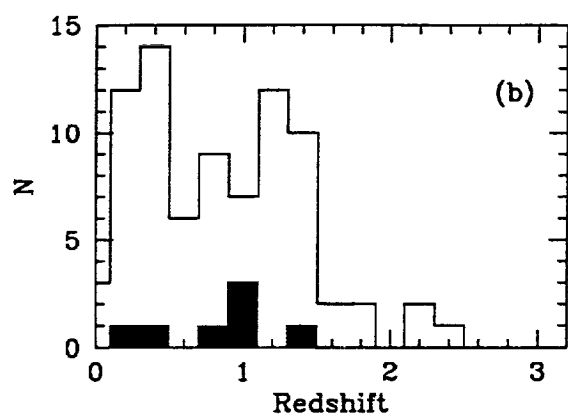
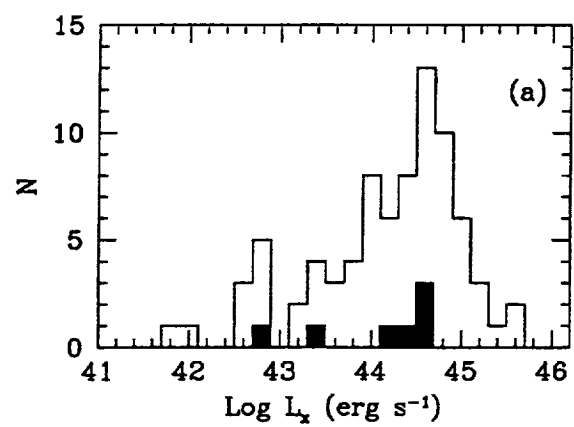
^d Monochromatic luminosity at 2500 Å ($\text{erg s}^{-1} \text{ Hz}^{-1}$). Optical data from Stocke et al. (1991)

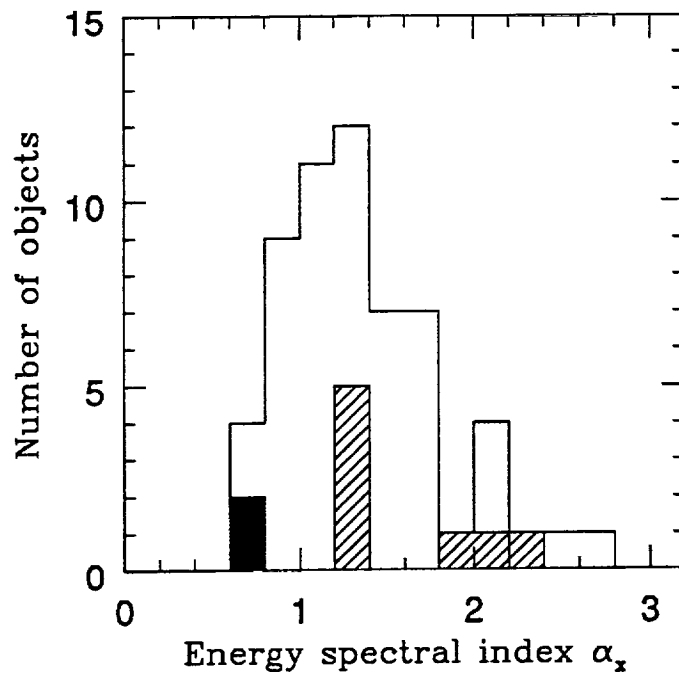
Table 5
 Weighted Mean X-ray spectral index and Maximum Likelihood analysis

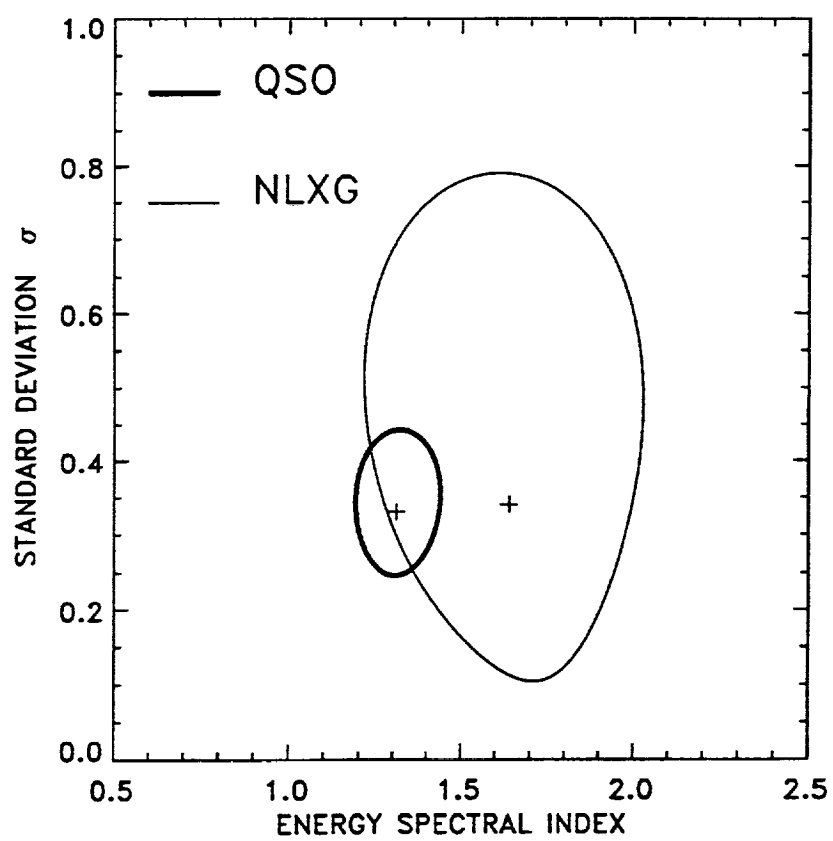
| | Maximum Likelihood | | Weighted Mean | | Number Objects |
|--------------|---------------------------------|-----------------------|---------------------------------|----------|----------------|
| Sample | $\overline{\alpha}_{\text{ML}}$ | σ_{int} | $\overline{\alpha}_{\text{WM}}$ | σ | |
| CRSS QSOs | 1.32 | 0.33 | 1.27 | 0.43 | 58 |
| CRSS RQ QSOs | 1.31 | 0.33 | 1.25 | 0.43 | 56 |
| CRSS NLXGs | 1.64 | 0.34 | 1.74 | 0.43 | 8 |
| EMSS NLXGs | 0.72 | 0.06 | 0.71 | 0.31 | 5 |

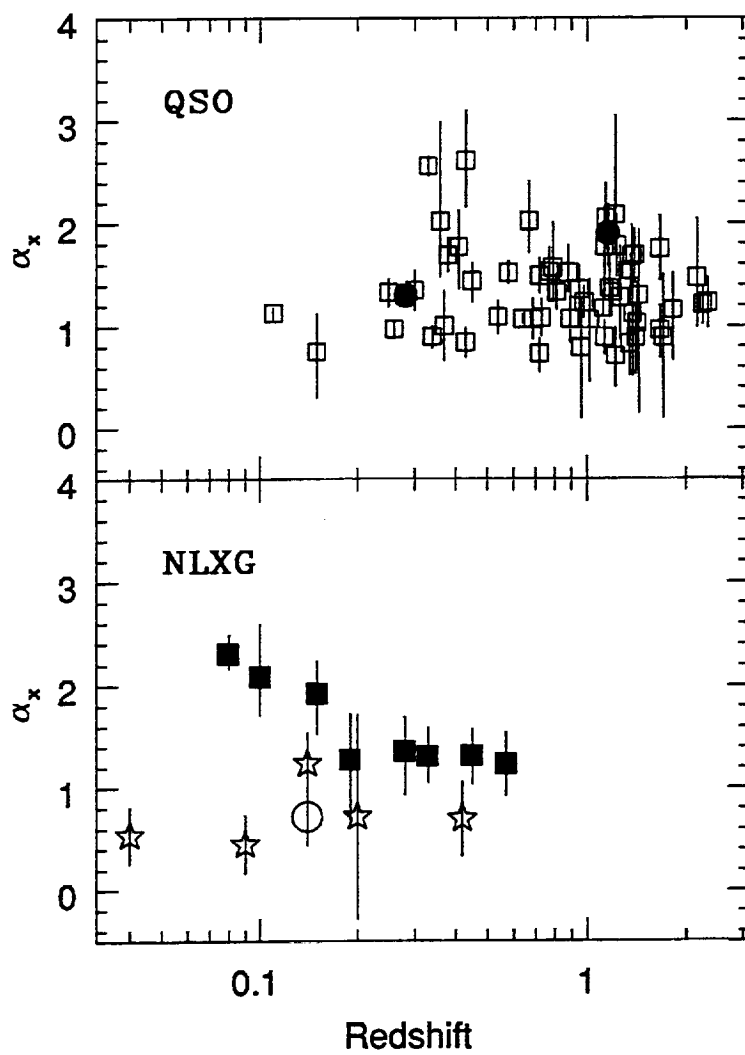
Table 6
Significance of Spearman Rank Correlation Analysis

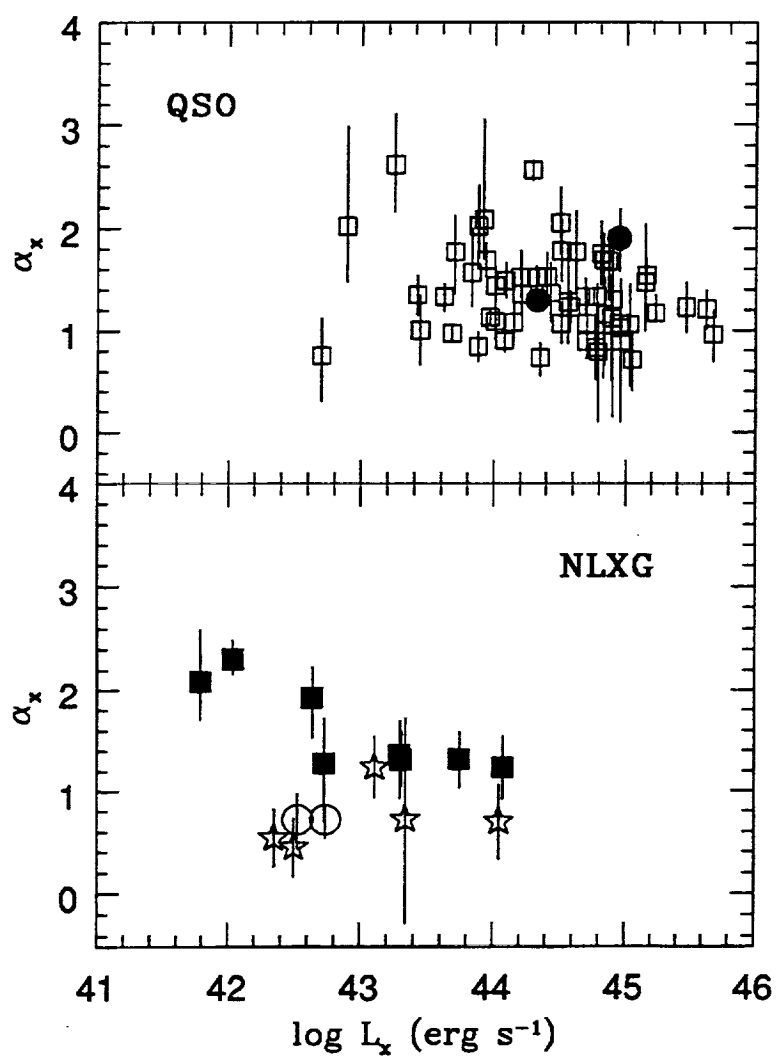
| Variables Correlated | Rs | Pr | d.o.f |
|--------------------------------------|--------|----------------------|-------|
| CRSS Quasars | | | |
| α_x, z | -0.032 | 0.810 | 56 |
| α_x, L_x | -0.232 | 0.078 | 56 |
| $\alpha_x, L_{2500 \text{ \AA}}$ | 0.050 | 0.710 | 56 |
| $\alpha_x, L_{2500 \text{ \AA}}/L_x$ | 0.311 | 0.018 | 56 |
| CRSS NLXGs | | | |
| α_x, z | -0.833 | 0.010 | 6 |
| α_x, L_x | -0.810 | 0.015 | 6 |
| $\alpha_x, L_{2500 \text{ \AA}}$ | 0.286 | 0.490 | 6 |
| $\alpha_x, L_{2500 \text{ \AA}}/L_x$ | 0.952 | 2.6×10^{-4} | 6 |

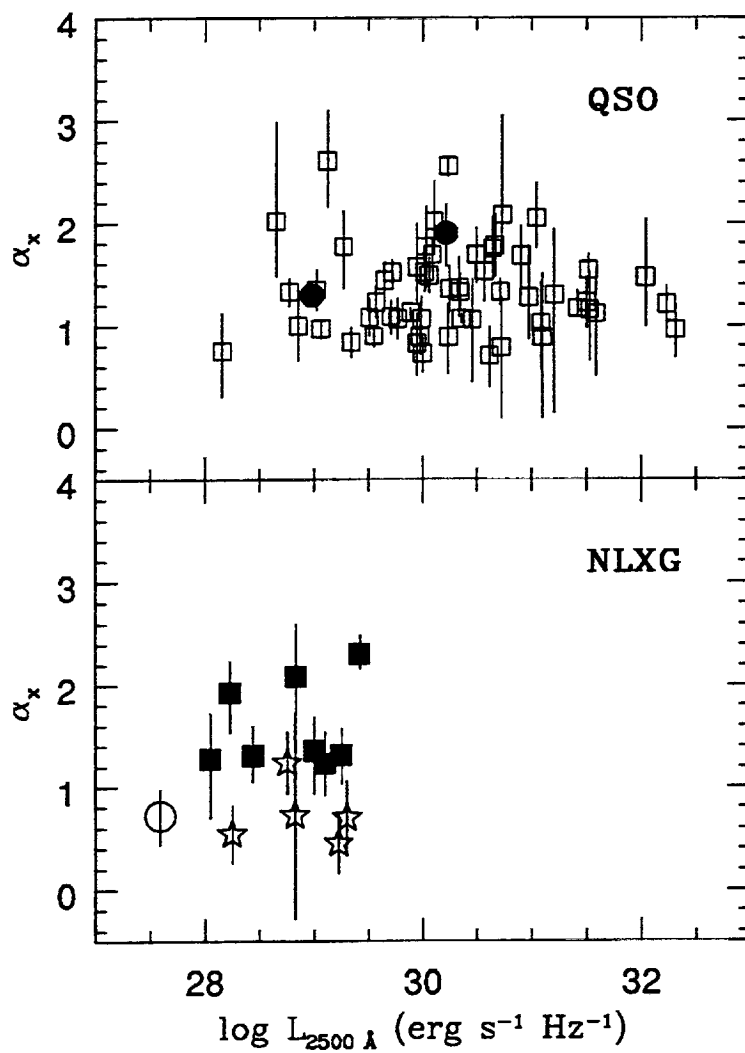


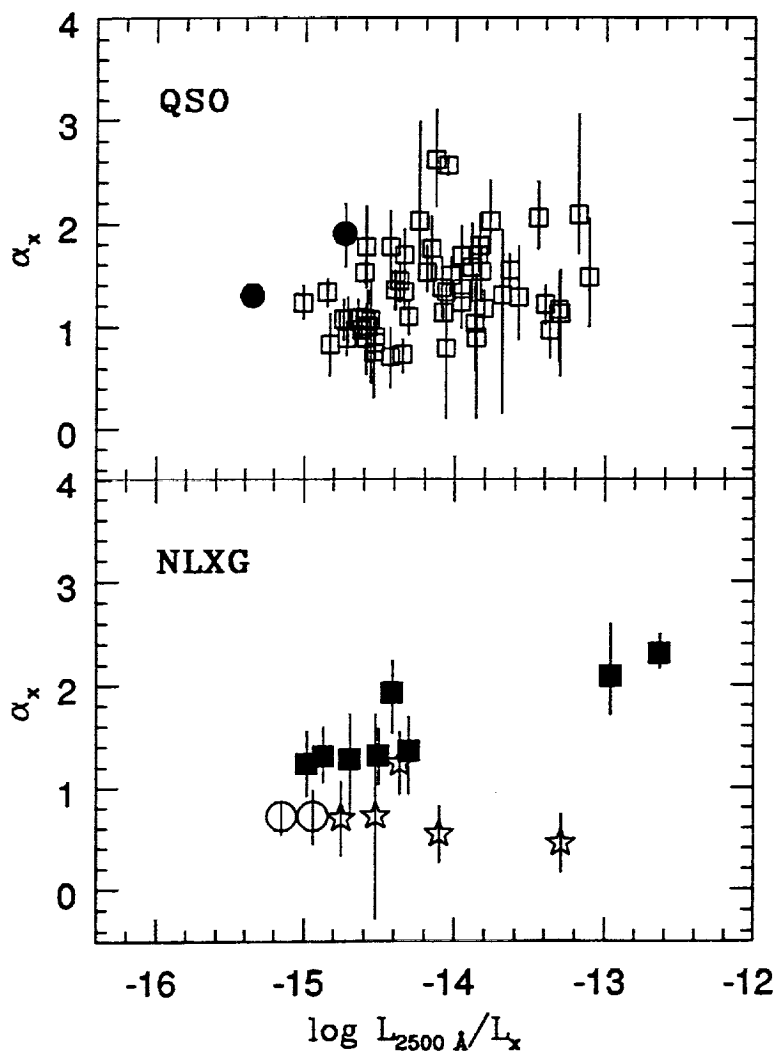












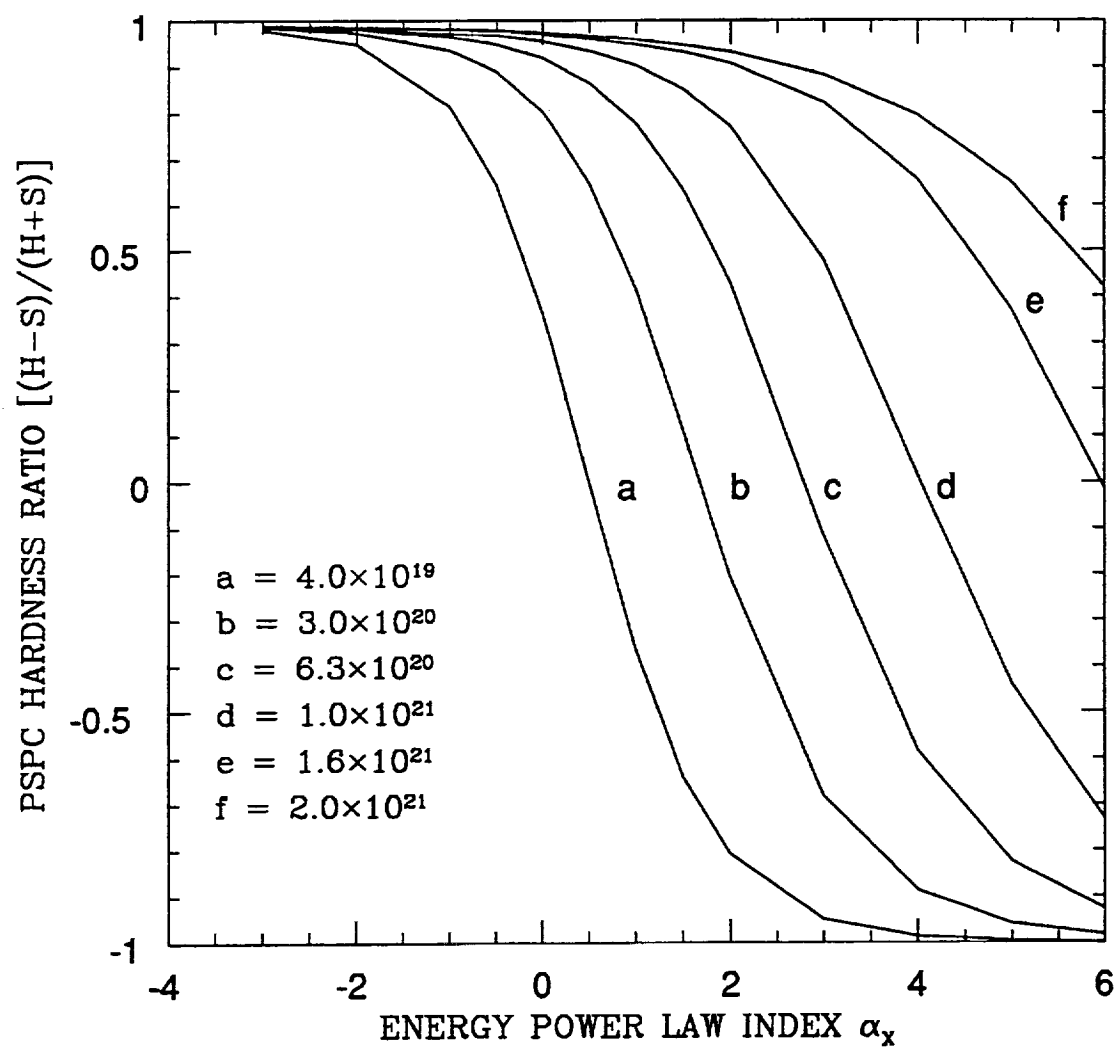


Figure A1

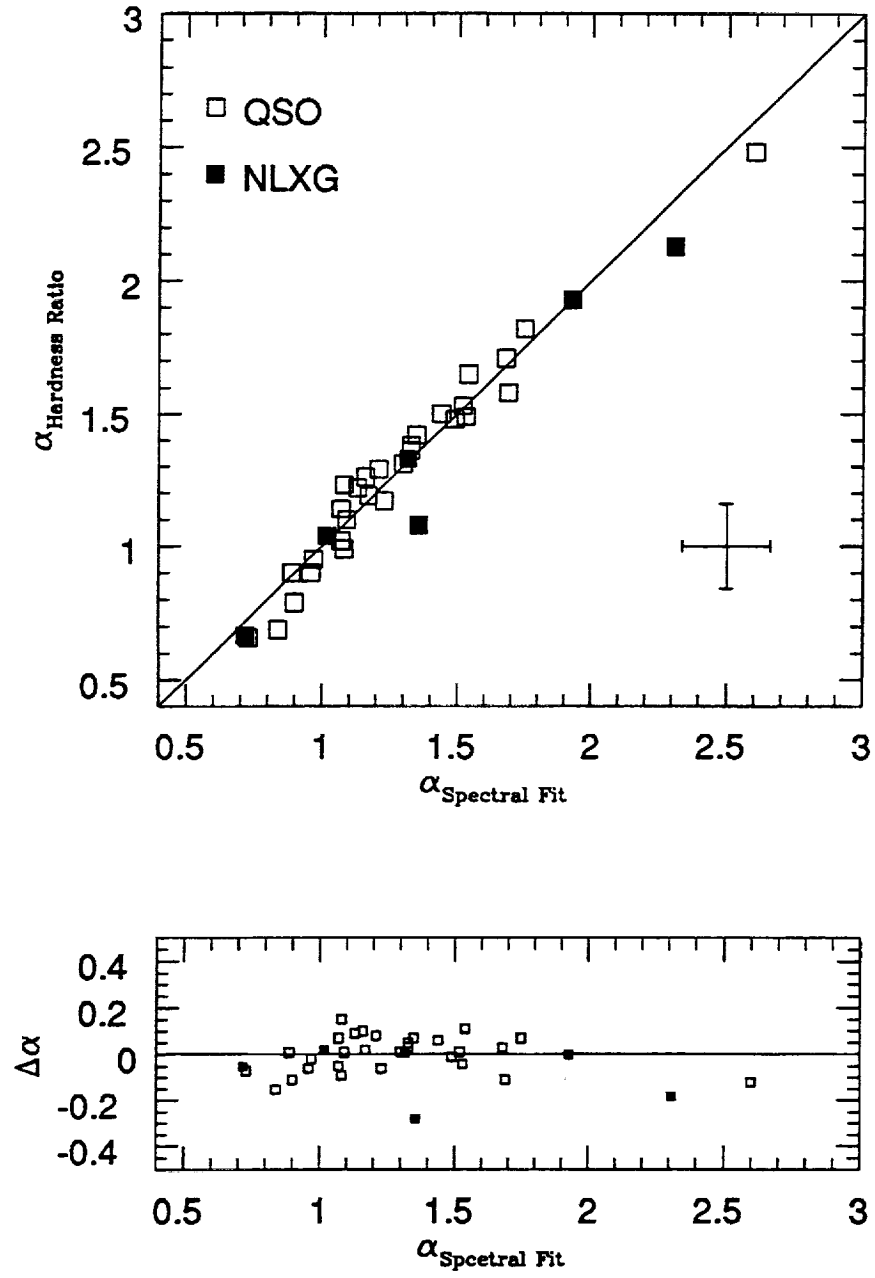


Fig. A2

The Cambridge-Cambridge *ROSAT* Serendipity Survey - III. VLA observations and the evolution of Radio-quiet and Radio-loud objects

P. Ciliegi¹, M. Elvis, B.J. Wilkes

Harvard-Smithsonian Center for Astrophysics 60 Garden St, Cambridge MA 02138.

¹ also Dipartimento di Fisica dell'Università di Milano, Italy and
Osservatorio Astronomico di Brera, Via Brera 28, I-20121 Milano, Italy.

B.J. Boyle

Royal Greenwich Observatory, Madingley Road, Cambridge, CB3 0EZ

R.G. McMahon

Institute of Astronomy, University of Cambridge, Madingley Road, Cambridge, CB3 0HA, UK

T. Maccacaro

Osservatorio Astronomico di Brera, Via Brera 28, I-20121 Milano, Italy.

Accepted for publication in the MNRAS

ABSTRACT

We present the results of the VLA Radio observations at 1.475 GHz (20 cm) of the Active Galactic Nuclei (AGN) in the Cambridge-Cambridge *ROSAT* Serendipity Survey (CRSS), a sample of 123 faint X-ray sources with $f_x(0.5-2.0 \text{ keV}) \geq 2 \times 10^{-14} \text{ erg s}^{-1} \text{ cm}^{-2}$. Of the 80 AGN in the sample, seven show radio emission at 5σ level and only two ($2.5^{+4.0}_{-1.7} \%$) qualify as Radio-Loud (RL) objects ($\alpha_{ro} \geq 0.35$). This result, compared with 13% RL in the *Einstein Observatory* Extended Medium Sensitivity Survey (EMSS) sample of AGN (flux limit $f_x(0.3-3.5 \text{ keV}) \sim 2 \times 10^{-13} \text{ erg s}^{-1} \text{ cm}^{-2}$) confirms that the fraction of X-ray selected RL AGN drops rapidly as the X-ray flux limit is lowered.

Combining the CRSS AGN sample with that extracted from the EMSS we have studied the X-ray Luminosity Function (XLF) and evolutionary properties for Radio-Quiet (RQ) and Radio-Loud separately. We find that the RQ and RL AGN population show the same cosmological evolution within the errors. In fact, when the luminosity evolution is parameterised with a power law of the form $L_X^*(z) = L_X^*(0)(1+z)^k$, we find $k = 2.43 \pm 0.26$ and $k = 2.71 \pm 0.10$ for RL and RQ AGN populations respectively. In addition, the shape of the de-evolved XLF of the two classes appears to be different both at the low luminosity ($L_X < 10^{44} \text{ erg s}^{-1}$) and high luminosity ends. These results are robust for different cosmological models (using $q_0=0.0$ and $q_0=0.5$) and for different value of the threshold α_{ro} used to distinguish between RQ and RL objects.

Finally we find that the differences in the shape of the XLF of RQ and RL AGN can be explained by introducing an X-ray beaming model to separate the observed X-ray luminosity of radio quasars into relativistically beamed and isotropic contributions.

The Cambridge-Cambridge ROSAT Serendipity Survey – V: Catalogue and Optical Identifications

B.J.Boyle¹, B.J.Wilkes², M.Elvis²

¹ Royal Greenwich Observatory, Madingley Road, Cambridge, CB3 0EZ

² Harvard-Smithsonian Center for Astrophysics, 60 Garden St, Cambridge, MA 02138, USA.

ABSTRACT

We report the results of a medium-depth X-ray survey of 20 *ROSAT* PSPC fields. 123 X-ray sources were detected down to a flux limit of $S(0.5 - 2 \text{ keV}) > 2 \times 10^{-14} \text{ ergs}^{-1} \text{ cm}^{-2}$ lying between that of the *Einstein* Extended Medium Sensitivity Survey and the deepest *ROSAT* surveys. Optical identifications of 110 of these sources have revealed 68 QSOs, 12 NLXGs, 24 stars, 2 BL Lac objects, 2 galaxies and two clusters. CCD imaging reveals the possible presence of galaxy groups or clusters at the positions of a further 4 X-ray sources. The number-redshift and $\log N - \log S$ relations of the 68 QSOs are in better agreement with the faster rate of cosmological evolution for X-ray QSOs derived from *ROSAT* deep surveys ($L_X \propto (1+z)^{3.34 \pm 0.1}$, $z_{\text{max}} = 1.79$) than with the evolution obtained from the EMSS ($L_X \propto (1+z)^{2.55 \pm 0.1}$), the latter being rejected at greater than the 3σ level as a model for the current sample. We present the optical spectra and measurements of the emission lines. The equivalent width distributions are consistent with those of QSO samples selected in other wavebands. We find no evidence for an inverse correlation between line width and X-ray spectral slope as recently reported for other *ROSAT* QSO samples.

Key words: X-rays: general – galaxies: active – quasars: general

1 INTRODUCTION

The high sensitivity of the *ROSAT* PSPC has allowed a number of X-ray surveys to be made to significantly fainter flux levels than was previously possible (e.g. Shanks et al. 1991, Hasinger et al. 1993, Branduardi-Raymont et al. 1994), shedding new light on the nature of faint X-ray sources and their cosmological evolution. Results from one deep *ROSAT* survey (Boyle et al. 1994) have previously implied significantly faster QSO evolution than had been deduced from earlier surveys at somewhat higher energies such as the *Einstein* Medium Sensitivity Survey (Maccacaro et al. 1991). This discrepancy is not well understood, possible explanations include the different energy ranges of the *Einstein* IPC (0.3–3.5 keV) and *ROSAT* PSPC (0.5–2 keV), which can result in different spectral components dominating the QSO X-ray spectra (see Ciliegi et al. 1995), and the inclusion of the redshift cut-off in the modelling procedure (Jones et al. 1996).

However, the EMSS and *ROSAT* deep survey also have different characteristics. This can be seen from the X-ray luminosity-redshift diagram for QSOs selected from the two samples (Fig. 1). There is little or no overlap between the distribution of QSO X-ray luminosities at a given redshift in the two surveys and thus they are sampling different parts of the QSO population. In an attempt to fill in the gap in the luminosity-redshift plane between these two

surveys, we made a survey of 20 medium-depth (5000 – 30000 sec) PSPC observations (the Cambridge-Cambridge *ROSAT* serendipity survey, CRSS). The resulting sample, with a flux limit between the EMSS ($S(0.3 - 3.5 \text{ keV}) > 1 \times 10^{-13} \text{ ergs}^{-1} \text{ cm}^{-2}$, Gioia et al. 1990) and the *ROSAT* deep survey ($S(0.5 - 2 \text{ keV}) > 4 \times 10^{-15} \text{ ergs}^{-1} \text{ cm}^{-2}$, Boyle et al. 1994), results in continuous coverage of the L, z plane and overlaps with both the other samples, facilitating a significantly improved comparison between the samples (see Fig. 1). Other X-ray samples currently near completion, e.g. the *ROSAT* International X-ray Optical Survey (RIXOS, see Page et al. 1996) will also help to fill this important gap.

In this paper we report the X-ray source positions and fluxes, the optical identifications and make a comparison between this survey and the EMSS and *ROSAT* deep surveys discussed above. In associated papers we also discuss the nature of the significant subset of narrow emission-line X-ray-luminous galaxies (NLXGs) found in this sample (Boyle et al. 1995a: Paper I, Boyle et al. 1995b: Paper II), the X-ray spectral properties of the QSOs in the sample (Ciliegi et al. 1996, Paper IV), and the radio fluxes of the sample (Ciliegi et al. 1995, Paper III).

2 OBSERVATIONS

2.1 X-ray source detection

Associated Absorption at Low and High Redshift

Martin Elvis¹, Smita Mathur¹, Belinda J. Wilkes¹, Fabrizio Fiore^{1,2},
Paolo Giommi² & Paolo Padovani²

1: *Harvard-Smithsonian Center for Astrophysics, 60 Garden St.,
Cambridge, MA 02138, USA*

2: *SAX Data Center, Roma, Italy*

Abstract. Combining information on absorbing material in AGN from X-ray and the UV creates a powerful investigative tool. Here we give examples from both low and high redshift.

1. Introduction

At low redshift we have found that the ionized (“warm”) X-ray absorbers and the associated UV absorbers in two radio-loud quasars were due to the same material: an X-ray quiet quasar 3C351 (Mathur et al. 1994) and a red quasar 3C212 (Elvis et al., 1994, Mathur 1994). In both cases the absorber is situated outside the broad emission line region (BELR), is outflowing, and is highly ionized. This delineates a new nuclear component in lobe-dominated, radio-loud quasars. Could the same component explain all the X-ray and UV absorption in AGN seen over the past 20 years and more (Anderson 1974, Ulrich 1988)?

We have recently tested this generalization using the best studied of all AGN, NGC5548. We applied the same photoionization modeling method (Mathur et al., 1994) to the X-ray and UV absorbers in NGC5548 to determine whether consistent values for the abundances of all the observed ions could be obtained. In NGC5548 the model must meet two extra requirements: it must not lead to a density for the absorber in conflict with its recombination time; and the distance of the absorber from the continuum source must not conflict with the well-determined BELR size.

At high redshifts X-ray absorption and rest frame UV absorption have been found together in a number of radio-loud quasars. The low energy X-ray cut-offs in these objects are likely to be due to their environment. The absorption seen in the high- z quasars may be similar to the low- z ‘X/UV’ absorption, but on a larger scale.

2. Testing the X/UV models with NGC5548

ASCA observations confirm the presence of an ionized absorber in NGC5548 with equivalent $N_H = 3.8 \times 10^{21} \text{cm}^{-2}$ (Fabian et al. 1994a), and resolving the OVII and OVIII absorption edges. An Fe-K edge is not detected ($\tau_{\text{Fe-K}} \leq 0.1$). HST finds blueshifted UV absorption lines (Korista et al. 1995). The CIV and

Martin Elvis

X-ray Absorption and High Redshift Quasars

Martin Elvis

Harvard-Smithsonian Center for Astrophysics, 60 Garden St., Cambridge MA 02138, USA

Abstract. X-ray absorption now seems to be common among several different types of high redshift ($1 < z < 4$) quasar. We discuss (1) 'low energy cut-offs' toward $z > 2$ radio-loud quasars; (2) Red Quasars; and (3) Broad Absorption Line quasars.

1. Introduction - the value of high redshift

ROSAT's capability to study fainter X-ray sources than ever before opened up the range of AGN quasars that could be reached to virtually the whole span of their properties. Rather than revisiting the objects made famous by earlier missions, we therefore adopted a strategy of exploring this new parameter space (Elvis 1994), with the high redshift range ($1 < z < 4$) being a major focus. ASCA is now allowing us to slowly extend these studies, primarily to higher energies. Redshift 3 quasars were the most distant for which we could obtain ROSAT spectra.

High redshifts objects are faint. Why should we try hard to study them? Apart from their 'headline' appeal there are 4 reasons: (1) *Time*: we can probe the earliest epochs, about 1 Gyr after the big bang, when the first star and galaxy formation is likely to be occurring; (2) *Distance*: they can be background light sources and so enable "We X-ray the Universe"¹ and let us see dark intervening material; (3) *Volume*: Rare, extreme objects can turn up in the 100-fold larger sample of the Universe accessible; (4) *Redshifting*: makes new features technologically accessible. Here we illustrate three of these reasons.

Our original goal was to study changes of quasars' emission as a function of their evolution (Bechtold et al., 1995a, b). Instead unexpected *absorption* has become a theme of these studies. I will only discuss absorption in this presentation.

2. Cut-offs in $z=3$ Quasars - the value of time

The ROSAT PSPC spectra of $z=3$ quasars immediately surprised us by often showing strong low energy cut-offs (Elvis et al., 1994a), far larger than those expected due to

absorption by our galaxy. We now believe that these cut-offs are associated with the quasars because they are only seen in radio-loud quasars. The horizontal lines in figure 1 are the expected PSPC colors for quasars with the measured *Ginga* low z slopes (2-10 keV, rest frame, Williams et al., 1992). Absorbed quasars would lie below this line. (Two of the quasars with measured low-energy cut-offs do in fact lie in this region.) Only the radio-loud population has a population of quasars below the line. The difference is significant at the 99.5% level for quasars with $z > 2$. Immediately this tells us the crucial point: *The low energy cut-offs are associated with the quasars themselves.* With WGACAT (White, Giommi & Angelini, 1995) we are at the limit of detecting this effect. For $z > 2.5$ this difference is 89%, so a few more objects at $z > 2.5$ would strengthen this results greatly. Note that the X-ray cut-off quasars have normal strong UV continua (Kuhn et al., 1996) so reddening by dusty intervening material (e.g. Fall 1995), which would bias us toward radio-loud objects having X-ray cut-offs, is ruled out.

Although the Poisson error bars are large, there is a strong hint that the cut-off fraction of quasars rises rapidly from $z \sim 2$ (figure 2a, b). This indicates that the cut-offs are more common in the past than now, i.e. *cut-offs are an evolutionary effect.* As in quasar population evolution (Boyle et al., 1987), $z \sim 2$ is special, which may not be a coincidence.

Knowing that the cut-offs are at the redshift of the quasar allows us to begin interpreting the results. If we also assume absorption is the cause, then we can constrain the physical conditions of the absorbers. If we fit this cut-off with absorption at the quasar we find we need column densities of order 10^{22} atoms cm^{-2} . For Milky Way dust-to-gas ratios this would produce $A_V = 4.2$ (Jenkins & Savage 1974, Seaton 1979). The strong UV bumps in these quasars limits $A_V < 1$ (Kuhn et al., 1996), so the absorber must have a low dust-to-gas ratio, as in the BALQSO PHL5200 (see §4, Mathur, Elvis & Singh, 1995), but unlike the Red Quasar 3C212 (see §3, Elvis et al., 1994b, Mathur 1994).

Absorption by a neutral hydrogen column would produce strong absorption in the optical/UV spectrum of these quasars. At 10^{22} atoms cm^{-2} damped Lyman- α absorption should be found, which is not seen; nor is Lyman-limit absorption near the quasar redshift seen, so the neutral hydrogen column must be below $10^{17.5}$ atoms cm^{-2}

¹ ©'Roentgenstrahlung in the Universe' conference organizers.

AN ACCURATE GALACTIC NH MAP OF THE NORTH ECLIPTIC POLE

Martin Elvis
Harvard-Smithsonian Center for Astrophysics
Felix J. Lockman
NRAO, Green Bank
C. Fasnacht
Harvard-Smithsonian Center for Astrophysics

May 26, 1994

Abstract

The Galactic HI column density was measured at $21'$ angular resolution over an $8^\circ \times 9^\circ$ region centered on the North Ecliptic Pole. Over the region N_H varies smoothly between 3×10^{20} atoms cm^{-2} and 8×10^{20} atoms cm^{-2} ; some structure is seen over most of the map on an 0.5 to 1 degree scale. There are other possible sources of interstellar opacity in this direction which may add an equivalent 10^{20} cm^{-2} of HI. We evaluate the effect of uncertainties in the HI column density on implied X-ray fluxes of extragalactic objects.

1. Introduction

The North Ecliptic Pole (NEP) has a special significance for space observatories. All earth-orbiting satellites with fixed solar panels must keep them pointed at the Sun, and because the Earth is in the ecliptic, the free axis about which these satellites can rotate sweeps out circles of almost constant ecliptic longitude which pass through the north and south ecliptic poles. The South Ecliptic Pole coincides with the Large Magellanic Cloud, but the NEP lies on an undistinguished piece of sky at moderately high Galactic latitude ($l = 96^\circ$, $b = +29^\circ$). The combination of ready access and

AN ACCURATE GALACTIC NH MAP OF THE NORTH ECLIPTIC POLE

Martin Elvis
Harvard-Smithsonian Center for Astrophysics
Felix J. Lockman
NRAO, Green Bank
and
C. Fasnacht
Harvard-Smithsonian Center for Astrophysics

THE SOFT X-RAY PROPERTIES OF A COMPLETE SAMPLE OF OPTICALLY SELECTED QUASARS. I. FIRST RESULTS

ARI LAOR,¹ FABRIZIO FIORE,^{2,3} MARTIN ELVIS,² BELINDA J. WILKES,² AND JONATHAN C. McDOWELL²

Received 1993 October 21; accepted 1994 May 11

ABSTRACT

We present the results of *ROSAT* PSPC observations of 10 quasars. These objects are part of our *ROSAT* program to observe a complete sample of optically selected quasars. This sample includes all 23 quasars from the bright quasar survey with a redshift $z \leq 0.400$ and a Galactic H I column density $N_{\text{HI}}^{\text{Gal}} < 1.9 \times 10^{20} \text{ cm}^{-2}$. These selection criteria, combined with the high sensitivity and improved energy resolution of the PSPC, allow us to determine the soft (~ 0.2 – 2 keV) X-ray spectra of quasars with about an order of magnitude higher precision compared with earlier soft X-ray observations.

The following main results are obtained: Strong correlations are suggested between the soft X-ray spectral slope α_x and the following emission line parameters: H β FWHM, $L_{\text{[O III]}}$, and the Fe II/H β flux ratio. These correlations imply the following: (1) The quasar's environment is likely to be optically thin down to ~ 0.2 keV. (2) In most objects α_x varies by less than $\sim 10\%$ on timescales shorter than a few years. (3) α_x might be a useful absolute luminosity indicator in quasars. (4) The Galactic He I and H I column densities are well correlated.

Most spectra are well characterized by a simple power law, with no evidence for either significant absorption excess or emission excess at low energies, to within $\sim 30\%$. We find $\langle \alpha_x \rangle = -1.50 \pm 0.40$, which is consistent with other *ROSAT* observations of quasars. However, this average is significantly steeper than suggested by earlier soft X-ray observations of the *Einstein* IPC. The 0.3 keV flux in our sample can be predicted to better than a factor of 2 once the $1.69 \mu\text{m}$ flux is given. This implies that the X-ray variability power spectra of quasars flattens out between $f \sim 10^{-5}$ and $f \sim 10^{-8}$ Hz.

A steep α_x is mostly associated with a weak hard X-ray component, relative to the near-IR and optical emission, rather than a strong soft excess, and the scatter in the normalized 0.3 keV flux is significantly smaller than the scatter in the normalized 2 keV flux. This argues against either thin or thick accretion disks as the origin of the soft X-ray emission. Further possible implications of the results found here are briefly discussed.

Subject headings: accretion, accretion disks — ISM: abundances — quasars: general — X-rays: galaxies

1. INTRODUCTION

Despite 30 years of intensive research the energy source of quasars is not yet established. Quasars have been detected over a very wide energy range, from the radio to hard γ -rays. However, more than half of their extreme power is typically concentrated over a relatively small energy range, from the optical to soft X-rays (e.g., Sanders et al. 1989). The UV power generally rises with increasing energy, while the soft X-ray power (below ~ 1 keV) generally falls with increasing energy, indicating that the peak power of quasars is emitted somewhere in the extreme UV (a few hundred angstroms). An accurate determination of the continuum emission of quasars near their power peak energy is important for testing and constraining possible emission mechanisms.

The large Galactic opacity prevents a direct observation of the extreme UV in quasars. One alternative is to observe the UV spectra of very high redshift quasars (e.g., Reimers et al. 1992); however, this approach is limited by the high abundance

of Lyman limit systems at $z \gtrsim 3$. The other alternative, adopted here, is to go to the other side of the Galactic opacity barrier and to observe low-redshift quasars in very soft X-rays.

The X-ray properties of quasars have been studied extensively over the last decade using *HEAO-1*, *Einstein*, *EXOSAT*, and *Ginga* (e.g., Mushotzky 1984; Wilkes & Elvis 1987; Canizares & White 1989; Comastri et al. 1992; Lawson et al. 1992; Williams et al. 1992; and a recent review by Mushotzky, Done, & Pounds 1993). These observations indicate that the X-ray emission above 1–2 keV is well described by a power law with a spectral slope $\alpha_x = d \ln f_x / d \ln \nu$ of about -0.5 for radio-loud quasars and about -1.0 for radio-quiet quasars.

As mentioned above, X-ray observations below 1 keV indicate a spectral steepening, or equivalently an excess emission, relative to the flux predicted by an extrapolation of the hard X-ray power law (e.g., Arnaud et al. 1985; Wilkes & Elvis 1987; Turner & Pounds 1989; Masnou et al. 1992; Comastri et al. 1992). In some objects the excess can be described as a very steep and soft component, which is consistent with the Wien tail of a hot thermal component dominating the UV emission. However, these studies were limited by the low signal-to-noise ratio (S/N) and energy resolution of the *Einstein* IPC and the *EXOSAT* LE detectors, in particular in the crucial energy range below 0.5 keV. This prevented an accurate determination of the soft X-ray emission spectrum of quasars. Furthermore, the objects studied do not form a complete sample, and these results are likely to be biased by various selection effects

¹ School of Natural Sciences, Institute for Advanced Study; Current address: Theoretical Astrophysics, Caltech 130-33, Pasadena, CA 91125; laor@tapir.caltech.edu.

² Harvard-Smithsonian Center for Astrophysics, 60 Garden Street, Cambridge, MA 02138; elvis@cfa222.harvard.edu, belinda@cfa222.harvard.edu, mcdowell@urania.harvard.edu.

³ Current address: Osservatorio Astronomico di Roma, via dell'Osservatorio 5, Monteporzio-Catone (RM), 00040 Italy; fiore%astrmp.deinet@cfa.harvard.edu.

ATLAS OF QUASAR ENERGY DISTRIBUTIONS¹

MARTIN ELVIS,² BELINDA J. WILKES,² JONATHAN C. McDOWELL,² RICHARD F. GREEN,³ JILL BECHTOLD,⁴
 S. P. WILLNER,² M. S. OEY,^{2,4} ELISHA POLOMSKI,^{2,5} AND ROC CUTRI⁴

Received 1993 June 1; accepted 1994 April 21

ABSTRACT

We present an atlas of the spectral energy distributions (SEDs) of normal, nonblazar, quasars over the whole available range (radio to 10 keV X-rays) of the electromagnetic spectrum. The primary (UVSX) sample includes 47 quasars for which the spectral energy distributions include X-ray spectral indices and UV data. Of these, 29 are radio quiet, and 18 are radio loud. The SEDs are presented both in figures and in tabular form, with additional tabular material published on CD-ROM. Previously unpublished observational data for a second set of quasars excluded from the primary sample are also tabulated. The effects of host galaxy starlight contamination and foreground extinction on the UVSX sample are considered and the sample is used to investigate the range of SED properties. Of course, the properties we derive are influenced strongly by the selection effects induced by quasar discovery techniques. We derive the mean energy distribution (MED) for radio-loud and radio-quiet objects and present the bolometric corrections derived from it. We note, however, that the dispersion about this mean is large (~one decade for both the infrared and ultraviolet components when the MED is normalized at the near-infrared inflection). At least part of the dispersion in the ultraviolet may be due to time variability, but this is unlikely to be important in the infrared. The existence of such a large dispersion indicates that the MED reflects only some of the properties of quasars and so should be used only with caution.

Subject headings: atlases — galaxies: photometry — quasars: general

1. INTRODUCTION

One of the reasons that main-sequence stars are much better understood than quasars is that they radiate (almost) blackbody spectra with temperatures between ~4000 and ~30,000 K, so that their blackbody peak moves conveniently through the optical band. The resulting strong color changes allowed the early recognition of the main sequence in the Hertzsprung-Russell diagram. By showing that most stars lie in a restricted band of color and luminosity, this diagram provided a crucial input to theories of stellar structure. The current lack of understanding of quasars may correspondingly be due to the distribution of their continuum light. Because the quasar phenomenon covers an extremely broad range of wavelengths, it is hard to see continuum features analogous to the blackbody peak in normal stars. Quasars emit almost constant power per decade of frequency from 100 μ m to at least 100 keV (see, e.g., Fig. 1 of Carleton et al. 1987). While this equipartition is surprising and may be to some extent an observational artifact (Brissenden 1989; Elvis 1991), it contains too little information to constrain theoretical ideas. Overcoming this problem requires

the assembly of spectral energy distributions (SEDs) for sizeable samples of quasars over the whole accessible range of the electromagnetic spectrum from radio to hard X-rays (and in the future, gamma rays).

In this paper we present SEDs for a sample of 47 quasars. We concentrate on "normal" quasars with little or no polarization and no dramatic optical variability. Our primary selection criteria were (1) existing *Einstein* observations at good signal-to-noise ratio (to ensure good X-ray spectra), and (2) an optical magnitude bright enough to make an *IUE* spectrum obtainable. Making the primary selection at these wavelengths means that not all the sample are detected in the *IRAS* data.

Several previous studies of quasar SEDs have been published. Each emphasized a particular region, and none considered the X-rays in detail. Early work included SEDs for *IRAS*-bright AGNs by Edelson & Malkan (1986), and for hard X-ray-selected Seyfert galaxies by Ward et al. (1987). Infrared to optical SEDs for the PG quasars were presented by Sanders et al. (1989) with an emphasis on explaining the infrared. Near-infrared to ultraviolet SEDs for *IUE* observed quasars were presented by Sun & Malkan (1989). Our study is different in that it includes X-ray data, divided into three energy bands in many cases, for all the objects, and includes both *IUE* and *IRAS* data. The X-rays are important to define the total luminosity and are crucial in overall modeling as they seem to come most directly from the central source. The sample is fairly evenly divided between radio-quiet and radio-loud objects.

We present the data in § 4 and the necessary corrections for reddening, variability and, importantly, host galaxy contributions in § 5. Section 6 discusses the properties of the SEDs, including their mean and dispersion. First, however, we out-

¹ Based in part on data acquired with the *International Ultraviolet Explorer* satellite, operated at the Goddard Space Flight Center for the National Aeronautics and Space Administration, the Multiple Mirror Telescope (MMT), a joint facility of the Smithsonian Institution and the University of Arizona, and the Infrared Telescope Facility (IRTF), a joint facility of NASA and the University of Hawaii.

² Center for Astrophysics, 60 Garden Street, Cambridge, MA 02138.

³ National Optical Astronomy Observatories, Kitt Peak National Observatory, Tucson, AZ 85726. KPNO is operated by the Association of Universities for Research in Astronomy, Inc., under contract with the NSF.

⁴ Steward Observatory, University of Arizona, Tucson, AZ 85721.

⁵ Center for EUV Astrophysics, Berkeley, CA.

THE ORIGIN OF THE SOFT X-RAY EXCESS IN THE SEYFERT 2 GALAXY NGC 2110

K. A. Weaver^{1,2}, R. F. Mushotzky, P. J. Serlemitsos

NASA/Goddard Space Flight Center, Code 666, Greenbelt, MD 20771

A. S. Wilson²

Space Telescope Science Institute, 3700 San Martin Drive, Baltimore MD 21218

M. Elvis

Harvard Smithsonian Center for Astrophysics, Cambridge, MA 02138

and

U. Briel

Max-Planck Institute, Garching, Germany

To be published in the Astrophysical Journal

¹ Presently at the Department of Astronomy and Astrophysics, 525 Davey Lab,
Penn State University, University Park, PA, 16802

² Also Astronomy Department, University of Maryland, College Park, MD 20742

ABSTRACT

We present and discuss an X-ray image and a medium resolution X-ray spectrum of the Seyfert 2 galaxy NGC 2110 obtained with the High Resolution Imager (HRI) on the *Rosat* X-ray Observatory (0.1–2.4 keV) and Goddard's Broad Band X-ray Telescope (BBXRT; 0.3–11 keV), respectively. Spatially resolved soft X-ray emission, which peaks 4'' to the north of the nucleus and near the position of the highest excitation optical emission line gas, is seen in the HRI observation. The extent has a flux of $\sim 3 \times 10^{-13}$ ergs cm $^{-2}$ s $^{-1}$ and accounts for $11 \pm 3\%$ of the total 0.1–2.4 keV flux. To model the BBXRT spectrum, a soft excess component is required which has a flux of $\sim 3.5 \times 10^{-13}$ ergs cm $^{-2}$ s $^{-1}$ and accounts for $\sim 14 \pm 6\%$ of the total 0.1–2.4 keV flux. In addition, BBXRT confirms the presence of an ~ 175 eV EW Fe K α fluorescence line in NGC 2110.

Because of the good agreement between their fluxes, we propose that the soft excess arises from the spatially resolved X-ray emission. This is contrary to previous suggestions that the spectral soft excess in NGC 2110 is due to leakage of the X-ray continuum through a patchy absorber. The temperature of the gas responsible for the soft excess is too high to be accounted for by local shock heating. In order to explain the soft excess and extent as either scattered continuum X-rays or fluorescence from gas photoionized by the nuclear source, the hard X-rays must be emitted anisotropically. However, the soft excess and extent can be well modeled as thermal emission from a hot, outflowing wind, which may also be responsible for confining at least some portion of the optical narrow line-emitting clouds.

Subject Headings: galaxies: individual (NGC 2110) - galaxies: interstellar matter - galaxies: nuclei - galaxies: Seyfert - X-rays: galaxies

X-RAYS AND HIGH REDSHIFT QUASARS

Martin Elvis

Harvard-Smithsonian Center for Astrophysics, Cambridge, MA 02138, USA

(*internet: elvis cfa.harvard.edu*)

ABSTRACT

X-ray observations of high redshift ($z \sim 3$) quasars have yielded a wealth of surprises, both in their emission spectra, and in their absorption properties. The same observations can place limits on a hot diffuse IGM (the "X-ray Gunn-Peterson test"), and on physical conditions in damped Lyman- α absorbers. This paper reviews the current status of the ROSAT observations, and looks forward to the diagnostics that will be provided by ASCA and other spectroscopy missions, such as AXAF.

1. The Moving Frontier

At the Nagoya meeting on 'Frontiers of X-ray Astronomy' in 1991 I showed the X-ray frontier for quasars in several observable dimensions, e.g. α_{OX} , redshift (Elvis 1991), and speculated on how our ideas of what was true for quasars in general may be biased by our limited observing capabilities.

Since then we have pursued a strategy with ROSAT that explores the whole parameter space of quasars - high redshift, X-ray quiet (Fiore et al 1993, Mathur et al 1994), optically-quiet (Elvis et al 1994a, Mathur 1994), IR-quiet and radio-silent (Aldcroft et al 1994 in preparation), high signal-to-noise (Fiore et al 1994), and low Galactic N_H (Laor et al 1994). Figure 1 shows the 1991 frontier projected into (α_{OX}, z) space. Our new ROSAT PSPC points are superposed, showing how far we have reached beyond our knowledge of 3 years ago.

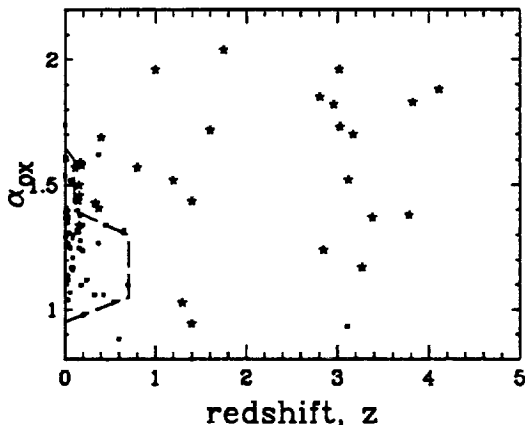


Figure 1: Observed regions in (α_{OX}, z) space. Stars show our ROSAT points, filled squares the IPC spectral observations, defining the 1991 'frontier'- approximated by the dashed line.

THE UNUSUAL QUASAR PG1407+265

Jonathan C. McDowell¹, Claude Canizares³, Martin Elvis¹, Andrew Lawrence², Sera Markoff^{3,4}, Smita Mathur¹, Belinda J. Wilkes¹

Astrophysical Journal, 1995 Sep 10, in press

ABSTRACT

PG1407+265, discovered in the Palomar-Green Survey (Schmidt and Green 1983), was identified as a redshift one radio-quiet quasar on the basis of a single weak line. Further observations over a wide wavelength range confirm the identification, but reveal the object to have unusual emission line properties. Broad $H\alpha$ is the only strong emission line, with $H\beta$ and Lyman α almost undetectably weak. The emission lines show a range in redshift of over 10000 km/s, systematically decreasing with ionization potential, or almost equivalently, increasing to longer wavelengths. $z = 0.94 \pm 0.02$ is a reasonable statement of our knowledge of the quasar's redshift. However, the object's continuum properties are those of a normal radio-quiet quasar. We discuss a number of possible models for the object, but its nature remains puzzling.

Subject headings: Galaxies: Quasars

¹Center for Astrophysics, 60 Garden Street, Cambridge, MA 02138

²University of Edinburgh

³Massachusetts Institute of Technology, Cambridge MA

⁴Dept. of Physics and Steward Observatory, University of Arizona

**TESTING MODELS FOR THE QUASAR BIG BLUE
BUMP VIA COLOR-COLOR DIAGRAMS.**

Aneta Siemiginowska, Olga Kuhn, Martin Elvis, Fabrizio Fiore*
Jonathan McDowell and Belinda J. Wilkes
Harvard-Smithsonian Center for Astrophysics
60 Garden St, Cambridge MA 02138

* Present address: Osservatorio Astronomico di Roma
via dell'Osservatorio 5, Monteporzio-Catone (RM), I00040 Italy

May 31, 1995

Abstract

We discuss several models of quasar *big blue bump* emission in color-color and color-luminosity diagrams. We define several broad passbands: IR ($0.8 - 1.6\mu\text{m}$), VIS ($4000 - 8000\text{\AA}$), UV ($1000 - 2000\text{\AA}$), UV1 ($1400 - 2000\text{\AA}$) and UV2 ($1000 - 1400\text{\AA}$), SX ($0.2 - 0.4\text{ keV}$). The colors have been chosen to investigate characteristics of the big blue bump: (1) IR/VIS color represents the importance of the IR component and shows the contribution around $\sim 1\mu\text{m}$; (2) UV/VIS color shows the slope of the big blue bump: in a region where it dominates a higher value means the bump gets steeper; (3) the combination of IR/VIS/UV colors shows the relative strength of the big blue bump and the IR component; (4) UV1/UV2 color is important as an indicator of a flattening of the spectrum in this region and the presence of the far-UV turn-over. (5) UV/SX tests the relationship between the big blue bump and the soft X-ray component. All colors are needed to investigate the range of model parameters.

We describe the colors for several models: accretion disk models in Schwarzschild and Kerr geometries, single temperature optically thin emission, combination of the main emission model and non-thermal power law or dust, irradiation of the disk surface. We test models against the sample of 47 low redshift quasars from Elvis et al. (1994, Paper I). We find: (1) modified blackbody emission from an accretion disk in a Kerr geometry can successfully reproduce both the luminosities and colors of the quasars except for the soft X-ray emission; (2) no additional components (hot dust or power law) are needed to fit the optical-UV colors when the irradiation of the surface of the disk is included in the model; (3) even modest (10%) irradiation of the surface of the disk modifies significantly the optical colors; (4) the simplest, single temperature, free-free models need either an additional component or a range of temperatures to explain the observations.

Tables of predicted colors for each model family are provided on the AAS CD-ROM.

ASSOCIATED X-RAY ABSORPTION IN HIGH REDSHIFT QUASARS

MARTIN ELVIS AND FABRIZIO FIORE
Harvard-Smithsonian Center for Astrophysics
60 Garden St., Cambridge MA 02138 USA

1. Introduction

When ROSAT was launched in June 1990 it provided X-ray astronomy with the capability to study fainter sources that had hitherto been accessible. This opened up the range of AGN quasars that could be reached to virtually the whole span of their properties. So, instead of revisiting the same objects made famous by earlier missions, we adopted a strategy of exploring this new parameter space (Elvis 1994). The most obvious of the parameters to push was redshift, since almost no X-ray spectra of quasars at $z > 0.5$ were then available. Redshift three quasars were the most distant for which we could obtain strong ROSAT detections.

The ROSAT PSPC spectra of $z = 3$ quasars immediately surprised us by often showing strong low energy cut-offs (Elvis *et al.*, 1994), far larger than those expected due to absorption by our galaxy. We now believe that these cut-offs are associated with the quasars. Assuming photoelectric absorption by cold gas¹ to be the cause this proximity allows us to derive some properties of the absorber.

2. Low Energy Cut-offs in High z Quasars

The signature of these low energy cut-offs is not subtle. Figure 1a shows a PSPC pulse height spectrum of a high z quasar with only absorption due to our galaxy. Figures 1b,c show two other quasars in which the low energy counts are clearly missing.

If we fit this cut-off with absorption at the quasar we find we need column densities of order 10^{22} atoms cm^{-2} , however we cannot determine the absorber redshift from the PSPC data. If the absorber is closer to us

¹“Cold gas” is a relative term. For an X-ray astronomer it means, roughly $< 10^6 \text{K}$, so that metal atoms are not fully stripped.

X-ray Absorption in GPS and CSS Quasars

Martin Elvis, Fabrizio Fiore,
Harvard-Smithsonian Center for Astrophysics, Cambridge MA 02138, USA

Paolo Giommi, Paolo Padovani
SAX Data Center

ABSTRACT

We have selected quasars with X-ray colors suggestive of a low energy cut-off, from the ROSAT PSPC pointed archive. We examine the radio and optical properties of these quasars. All seven (non-blazar) quasars with good optical spectra show optical absorption lines and/or reddening associated with the quasar. We conclude that absorption is highly likely to be the cause of the X-ray cut-offs, and that the absorbing material associated with the quasars, not intervening along the line-of-sight.

Almost all of the high redshift objects are Gigahertz Peaked Spectrum radio sources or candidates. The link with GPS sources strongly suggests that the absorption is extended on the scale of the radio sources (i.e. pc - kpc). These observations show that more detailed X-ray observations, using e.g. AXAF, are likely to reveal much about quasar environments at high redshift.

1. Introduction

The first X-ray spectra of high z quasars showed strong low energy cut-offs and a tantalizing connection of these with GPS quasars (Elvis et al., 1994). We have now scoured the 60,000 sources in the ROSAT pointed PSPC database (using 'WGACAT', White, Giommi & Angelini 1995) to gather more statistics on this. WGACAT contains 456 PSPC X-ray sources identified with known quasars at $z > 0.1$ and with signal-to-noise > 7 .¹ Of these quasars 21 have $z > 2$. While this is not a large number, it is a big increase over earlier work. However only four quasars with $z > 2.5$ are radio-quiet. The soft X-ray color (S/M) was converted into an effective low energy power-law slope, α_S , by making a small correction for counts missed by the WGACAT selection process, and assuming absorption by the Galactic column density.

We find (Fiore et al., 1996, Paper I):

¹The redshift cut avoids Seyfert galaxies, for which nuclear absorption is common, Lawrence & Elvis 1982). The minimum signal-to-noise gives two X-ray 'colors' from three bands: soft ($S=0.1-0.39$ keV), medium ($M=0.40-0.86$ keV), and hard ($H=0.87-2.0$ keV).



ON THE OBSERVATIONAL EVIDENCE FOR ACCRETING BLACK HOLES IN QUASARS

Fabrizio Fiore*,** and Martin Elvis**

* *Osservatorio Astronomico di Roma*

** *Harvard-Smithsonian Center for Astrophysics*

ABSTRACT

We review (mainly high energy) observations which could lend support to (or dismiss) the hypothesis of an accreting central black hole in quasars. Direct imaging is not powerful (1). We focus on three main topics: 2) variability as a constraint of the quasar compactness; 3) X-ray continuum; 4) X-ray spectral features, expected from reprocessing of the X-ray radiation from matter near the X-ray source. We argue that the above observations provide a weaker evidence than once thought for a black hole as the engine of quasars. New tests will come from (5) the study of the evolution of the quasar Spectral Energy Distribution (SED) in the framework of models of quasar physical evolution. We present some new results, obtained comparing ROSAT X-ray observations of $z=2-3$ quasars with previous monitoring of low- z quasars, which represent a first step in this direction.

© 1997. Published by Elsevier Science Ltd on behalf of COSPAR. All rights reserved

1. DO WE HAVE DIRECT PROOFS FOR A BLACK HOLE IN QUASARS?

The longstanding 'best buy' model for the underlying power source in quasars¹ is accretion onto a massive black hole. There are four traditional main areas of observational support for the black hole theory:

- (1) IMAGING: VLBI sizes; stellar cusps.
 - (2) VARIABILITY: X-ray compactness; microlensing.
 - (3) GALACTIC ANALOGS: similarity with Galactic black hole candidates (BHC).
 - (4) DYNAMICS: Fe-K line profiles; H- α line profiles; HST stellar velocity dispersions (e.g. M87).
- To which we may now add:
- (5) EVOLUTION: a new family of tests using characteristic break luminosities and redshifts.

We are not going to give a complete review of all above observational efforts, rather we will focus on a few topics, most of which related with high energy observations, organized in order of decreasing 'strength'. We think that, in order to understand how constraining the observations truly are on the black hole model, it is instructive to compare it to an alternative. The Starburst model of quasars /1/, where the central engine is not a compact object but the core of an elliptical galaxy, is the most developed of competing quasar models. So we use this as our 'sparring partner' throughout.

2. VARIABILITY

The strongest tests and constraints on quasar compactness come from observations of microlensing in the optical band and fast variations in the X-ray band. We discuss these next. But first we must dispense with the false clues introduced by relativistic beaming.

Beamed Sources

¹we shall use 'quasars' to refer to all types of activity including all active galactic nuclei, Seyferts, and both radio-loud and radio-quiet objects. We will distinguish only BL Lacs as a separate class in this papers.

THE SOFT X-RAY PROPERTIES OF A COMPLETE SAMPLE OF OPTICALLY SELECTED QUASARS. II. FINAL RESULTS

ARI LAOR

Theoretical Astrophysics, Caltech 130-33, Pasadena, CA 91125; current address: Physics Department, Technion, Haifa 32000, Israel;
 laor@physics.technion.ac.il

FABRIZIO FIORE

Osservatorio Astronomico di Roma, via dell'Osservatorio 5, Monteporzio-Catone (RM) 00040, and SAX Scientific Data Center,
 via Corcolle 19, I-00131, Rome, Italy; fiore@susy.mporzio.astro.it

AND

MARTIN ELVIS, BELINDA J. WILKES, AND JONATHAN C. MCDOWELL

Harvard-Smithsonian Center for Astrophysics, 60 Garden Street, Cambridge, MA 02138;
 elvis@cfa.harvard.edu, belinda@cfa.harvard.edu, mcdowell@cfa.harvard.edu

Received 1996 June 6; accepted 1996 September 19

ABSTRACT

We present the final results of a *ROSAT* PSPC program to study the soft X-ray emission properties of a complete sample of low- z quasars. This sample includes all 23 quasars from the Bright Quasar Survey with $z \leq 0.400$ and $N_{\text{HI}}^{\text{Gal}} < 1.9 \times 10^{20} \text{ cm}^{-2}$. Pointed *ROSAT* PSPC observations were made for all quasars, yielding high signal-to-noise (S/N) spectra for most objects, which allowed an accurate determination of the spectral shape. The following main results were obtained:

1. The spectra of 22 of the 23 quasars are consistent, to within $\sim 30\%$, with a single power-law model at rest-frame 0.2–2 keV. There is no evidence for significant soft excess emission with respect to the best-fit power law. We place a limit (95% confidence) of $\sim 5 \times 10^{19} \text{ cm}^{-2}$ on the amount of excess foreground absorption by cold gas for most of our quasars. The limits are $\sim 1 \times 10^{19} \text{ cm}^{-2}$ in the two highest S/N spectra.
2. The mean 0.2–2 keV continuum of quasars agrees remarkably well with an extrapolation of the mean 1050–350 Å continuum recently determined by Zheng et al. (1996) for $z > 0.33$ quasars. This suggests that there is no steep soft component below 0.2 keV.
3. Significant X-ray absorption ($\tau > 0.3$) by partially ionized gas (“warm absorber”) in quasars is rather rare, occurring for $\leq 5\%$ of the population, which is in sharp contrast to lower luminosity active galactic nuclei (AGNs), where significant absorption probably occurs for $\sim 50\%$ of the population.
4. Extensive correlation analysis of the X-ray continuum emission parameters with optical emission-line parameters indicates that the strongest correlation is between the spectral slope α_x and the H β FWHM. A possible explanation for this remarkably strong correlation is a dependence of α_x on L/L_{Edd} , as seen in Galactic black hole candidates.
5. The strong correlations between α_x and $L_{[\text{O III}]}$, Fe II/H β , and the peak [O III] to H β flux ratio are verified. The physical origin of these correlations is still not understood.
6. There appears to be a distinct class of “X-ray-weak” quasars, which form $\sim 10\%$ of the population (three out of 23), where the X-ray emission is smaller, by a factor of 10–30, than expected based on their luminosity at other bands and on their H β luminosity. These may be quasars in which the direct X-ray source is obscured and only scattered X-rays are observed.
7. Thin accretion disk models cannot reproduce the observed 0.2–2 keV spectral shape, and they also cannot reproduce the tight correlation between the optical and soft X-ray emission. An as yet unknown physical mechanism must be maintaining a strong correlation between the optical and soft X-ray emission.
8. The H I/He I ratio in the high Galactic latitude ISM must be within 20%, and possibly within 5%, of the total H/He ratio of 10, which indicates that He in the diffuse H II gas component of the interstellar medium is mostly ionized to He II or He III.

We finally note the intriguing possibility that although $\langle \alpha_x \rangle$ in radio-loud quasars (-1.15 ± 0.14) is significantly flatter than in radio-quiet quasars (-1.72 ± 0.09) the X-ray emission may not be related to the presence of radio emission. The difference in $\langle \alpha_x \rangle$ may result from the strong α_x versus H β FWHM correlation and the tendency of radio-loud quasars to have broader H β .

Subject headings: galaxies: active — galaxies: nuclei — quasars: general — X-rays: galaxies

1. INTRODUCTION

Quasars emit most of their power in the ultraviolet to soft X-ray regime. The position-sensitive proportional counter (PSPC) detector aboard *ROSAT* allowed a significantly improved study of the soft X-ray emission of quasars com-

pared with earlier missions (some of which were not sensitive below 2 keV), such as *HEAO-1*, *Einstein*, *EXOSAT*, and *Ginga* (e.g., Mushotzky 1984; Wilkes & Elvis 1987; Canizares & White 1989; Comastri et al. 1992; Lawson et al. 1992; Williams et al. 1992; and a recent review by

THE X-RAY EMISSION OF NGC 1068

A. S. WILSON

*Astronomy Department
University of Maryland
College Park, MD 20742*

AND

M. ELVIS

*Harvard-Smithsonian Center for Astrophysics
60 Garden St.
Cambridge, MA 02138*

Abstract. This paper summarises the X-ray properties of NGC 1068 from the observers perspective and reports new observations with the *ROSAT* HRI. Below $\simeq 2$ keV, the spectrum is steep and probably represents thermal emission from gas with temperature $kT \simeq 0.1 - 0.6$ keV. Above $\simeq 2$ keV, the spectrum is much flatter and may be described by a power-law with energy index $\alpha \simeq 0.3$. Images with the *ROSAT* HRI reveal that about half the X-ray flux in the 0.1 – 2.4 keV band is extended on scales $> 5''$ (360 pc). Recent *ROSAT* PSPC observations of starburst galaxies show integrated soft X-ray spectra which are very similar to that of NGC 1068 below 2 keV. The spatially extended, steep, soft X-ray emission of NGC 1068 probably originates through thermal emission from a hot wind driven by the disk starburst, the Seyfert nucleus or a combination of the two. On the other hand, the hard emission above 2 keV is almost certainly dominated by the Seyfert nucleus.

1. Introduction

There are many reasons to be interested in the X-ray properties of NGC 1068. If the galaxy contains a hidden Seyfert 1 nucleus (Antonucci & Miller, 1985), we may hope to see the associated compact hard X-ray source either directly or after scattering by electrons. In the latter case, the X-rays must

DERIVING THE QUASAR LUMINOSITY FUNCTION FROM ACCRETION-DISK INSTABILITIES

ANETA SIEMIGINOWSKA AND MARTIN ELVIS

Harvard-Smithsonian Center for Astrophysics 60 Garden Street, MS-70, Cambridge, MA 02138; asiemiginowska@cfa.harvard.edu

Received 1997 January 24; accepted 1997 March 24

ABSTRACT

We have derived the quasar luminosity function assuming that the quasar activity is driven by a thermal-viscous unstable accretion disk around a supermassive black hole. The instabilities produce large amplitude, long-term variability of a single source. We take a light curve of a single source and calculate the luminosity function from the fraction of time it spends at each luminosity. Convolving this with an assumed mass distribution we were able to fit well the observed optical luminosity function of quasars at four redshifts. As a result we obtain the evolution of the mass distribution between redshifts 2.5 and 0.5.

The main conclusions are as follows: (1) the quasar long-term variability due to the disk thermal-viscous instabilities provides a natural explanation for the observed quasar luminosity function; (2) the peak of the mass function evolves toward lower black hole masses at lower redshifts by a factor ~ 10 ; (3) the number of high-mass sources declines rapidly, so low-mass sources become dominant at lower redshift; (4) outbursts of activity appear as long as the matter is supplied to the accretion disk; (5) since the time-averaged accretion rate is low, the remnant sources (or sources in the low activity phase) do not grow into very massive black holes; and (6) a continuous fuel supply at a relatively low accretion rate (~ 0.01 – $0.1 \dot{M}_{\text{Edd}}$) for each single source is required over the lifetime of the entire quasar population.

Subject heading: accretion: accretion disks — cosmology: theory — quasars: general

1. INTRODUCTION

The quasar luminosity function has been studied for the last three decades and is observationally now quite well determined as a function of redshift for $z < 4$ (see, e.g., Boyle et al. 1991). However, there have been few attempts to derive the luminosity function from physical models of the quasar power engine. There are three possible phenomenological scenarios (Cavaliere & Padovani 1988): long-lived objects, recurrent objects (possibly related to galaxy mergers), and a single short event over the whole host galaxy lifetime. Continuous models imply masses for the remnant black holes that are too large, and accretion rates that are too low (Cavaliere et al. 1983; Cavaliere & Szalay 1986; Cavaliere & Padovani 1988, 1989; Caditz, Petrosian, & Wandel 1991).

Short-lived models have been studied more recently. Haehnelt & Rees (1993) assumed that new quasars were born at successive epochs with a short active phase followed by a rapid exponential fading because of exhaustion of fuel. They used the cold dark matter formalism (Press & Schechter 1974) to estimate the number of newly forming dark matter halos at different cosmic epochs. Small & Blandford (1992) suggested a scenario involving a mixture of continuous and recurrent activity. They assumed that newly formed sources achieve the Eddington luminosity quickly such that the accretion rate is limited by radiation pressure. The break in the luminosity function is related to the boundary between the continuous and intermittent accretion phases originating in the amount of fuel supply to the black hole.

However, none of these models relate directly to the physical processes responsible for powering a quasar. They simply invoke sources that emit at the Eddington luminosity for a certain time and then fade below an observational threshold. Here we describe a scenario which for the first time derives the luminosity function from a specific physical process.

The time evolution of an accretion disk around a supermassive black hole (the main components of the standard quasar paradigm) exhibits large variations on long timescales because of thermal-viscous instabilities (Siemiginowska, Czerny, & Kostyurin 1996, hereafter SCK96; Mineshige & Shields 1990). Depending on the assumed disk model, variations of up to a factor $\sim 10^4$ can be produced on timescales of 10^4 – 10^6 years. Here, we assume that all quasars are subject to this variability. We then take the light curve of a single source and calculate the luminosity function of a population of identical sources from the fraction of time it spends at each luminosity. Convolving this with an assumed mass distribution, we fitted the observed quasar luminosity function at four redshifts. As a result, we obtain the evolution of the mass distribution between redshifts 2.5 and 0.5.

2. EVOLUTION OF AN ACCRETION DISK

Accretion onto a supermassive black hole is the leading model for powering quasars (see, e.g., Rees 1984). The accretion process is frequently described using the model of a stationary thin disk (Lynden-Bell 1969; Shakura & Sunyaev 1973). However, there are both observational and theoretical arguments indicating that time-dependent effects in the accretion process are of extreme importance. Observationally, the evidence for global evolutionary effects is compelling in accretion disks around Galactic X-ray sources. Outbursts (by factors $> 10^4$) of cataclysmic variables or X-ray novae last for weeks or months and happen every few months to years. The outbursts are essentially caused by the disk thermal instability in the partial ionization zone (Meyer & Meyer-Hoffmeister 1982; Smak 1982; see also Cannizzo 1993 for review). There is a strong similarity between Galactic X-ray sources and active galactic nuclei (AGNs) both in spectral behavior and in overall variability (Fiore & Elvis 1997; Tanaka & Lewin 1995), which leads us to expect similar accretion-disk behavior in AGNs.

X-raying a galaxy: PHL 6625 behind NGC 247

Martin Elvis,¹ Fabrizio Fiore,^{1,2,3} Paolo Giommi³ and Paolo Padovani^{4,5}

¹Harvard-Smithsonian Center for Astrophysics, 60 Garden Street, Cambridge, MA 02138, USA

²Osservatorio Astronomico di Roma, Via dell'Osservatorio 2, I-00040, Monteporzio (Rm), Italy

³BeppoSAX Science Data Center, Via Corcolle 19, I-00131, Roma, Italy

⁴Dipartimento di Fisica, II Università di Roma, 'Tor Vergata', Via della Ricerca Scientifica 1, I-00133 Roma, Italy

⁵Space Telescope Science Institute, ESA Space Science Department, 3700 San Martin Drive, Baltimore MD 21218, USA

Accepted 1997 August 19. Received 1997 August 18; in original form 1997 April 21

ABSTRACT

PHL 6625, a $z=0.38$, radio-quiet quasar, shows a clear excess of low-energy absorption in its *ROSAT* PSPC soft X-ray spectrum. This absorption is almost certainly produced by the interstellar medium in NGC 247, a foreground spiral galaxy, which lies ~ 3.4 kpc (4.6 arcmin) away in projection. Comparison of the X-ray absorption and the 21-cm H I column density through NGC 247 suggests a larger than expected effect in X-rays. Several possibilities are considered to explain this apparent discrepancy. Additional high-velocity H I components of the interstellar medium are currently the most plausible cause. PHL 6625 also clearly decreased in its soft X-ray flux by a factor of 2 in 6 months.

Key words: galaxies: active – galaxies: individual: NGC 247 – galaxies: ISM – quasars: individual: PHL 6625 – X-rays: galaxies.

1 INTRODUCTION

Probes of the interstellar medium (ISM) of galaxies via absorption in the spectra of background quasars have proven valuable in the ultraviolet, the radio and, more recently, the millimetre bands (Savage et al. 1993; Braun 1995; Combes & Wiklind 1996). In principle, X-ray absorption spectra can also provide valuable diagnostics of metal abundances and other properties, especially for partially ionized components of the ISM. Up to now, X-ray instruments have not been powerful enough to be used in this way. Here we present the first clear example, other than the Milky Way, of X-ray absorption of a quasar by a foreground galaxy.

X-ray absorption in quasars is rare (Wilkes & Elvis 1987; Laor et al. 1997), unlike the situation in the lower luminosity Seyfert galaxies (Turner & Pounds 1989). Recent work has shown that some radio-loud quasars, particularly at high redshift, do show X-ray absorption (Elvis et al. 1994, 1998; Fiore et al. 1998) but that radio-quiet quasars do not.

There was only one clear exception to this rule in a survey of 298 radio-quiet quasars (Fiore et al. 1997), the quasar PHL 6625. Clearly PHL 6625 must in some way be unusual. In fact PHL 6625 lies only 4.6 arcmin north-west of the line of sight through the centre of NGC 247 (see Fabbiano, Kim & Trinchieri 1992, fig. 7). This is a projected distance of 3.4 kpc at the 2.5-Mpc distance of NGC 247 (Carignan & Puche 1990).

In this paper we present a full analysis of the *ROSAT* X-ray spectrum and compare the observed absorption with that expected from NGC 247.

2 PSPC OBSERVATIONS OF PHL 6625

As part of an unbiased search for absorbed active galactic nuclei (AGN) in the *ROSAT* (Trümper 1983) Position Sensitive Proportional Counter (PSPC: Pfefferman et al. 1987) pointed archive (using WGACAT: White, Giommi & Angelini 1994), Fiore et al. (1997) found PHL 6625 to have X-ray colours suggesting absorption.

The source was observed twice: for 9460 s between 1991 December 21 and 1992 January 6 (RP600159AO0) and for 9456 s on 1992 June 11–13 (RP600159AO1). The PSPC source position lies 2.5 arcsec from the optical position (Véron-Cetty & Véron 1996). We have retrieved the two data sets from the *ROSAT* archive at the HEASARC and have re-extracted the pulse height spectrum using IRAF/PROS for the quasar PHL 6625. We used a 2 arcmin radius circle.

NGC 247 is X-ray-faint [$L_x = 10^{38.3}$ erg s⁻¹ (0.3–2.5 keV)] with almost all the flux coming from a few bright sources (Fabbiano et al. 1992; Mackie et al. 1998). Nevertheless, the vicinity of the galaxy NGC 247 offers the possibility of both a larger background [owing to soft emission from the galaxy: e.g. NGC 33 (Trinchieri, Fabbiano & Peres 1988; see also Fabbiano 1996)] and of a smaller background [owing to

ASCA AND ROSAT X-RAY SPECTRA OF HIGH-REDSHIFT RADIO-LOUD QUASARS

M. CAPPI,^{1,7} M. MATSUOKA,¹ A. COMASTRI,² W. BRINKMANN,³ M. ELVIS,⁴
 G. G. C. PALUMBO,^{5,6} AND C. VIGNALI⁵

Received 1996 June 20; accepted 1996 October 17

ABSTRACT

Results are presented on the X-ray properties of 9 high-redshift ($1.2 < z < 3.4$) radio-loud quasars (RLQs) observed by the *Advanced Satellite for Cosmology and Astrophysics* (ASCA; 10 observations) and *ROSAT* (11 observations, for a subset of six quasars). New ASCA observations of S5 0014+81 ($z = 3.38$) and S5 0836+71 ($z = 2.17$) and *ROSAT* observations of PKS 2126–158 for which results were never presented elsewhere are included.

A simple model consisting of a power law plus cold, uniform absorption gives acceptable fits to the spectra of all sources. The ASCA spectra of the six brightest objects show evidence for absorption in excess of the Galactic value at a $\geq 99\%$ confidence level. Comparison with the *ROSAT* data suggests that absorption has significantly varied ($\Delta N_H \sim 8 \times 10^{20} \text{ cm}^{-2}$) in the case of S5 0836+71, on a time-scale of approximately 0.8 yr in the quasar frame. For the remaining five sources for which *ROSAT* spectra were available, the two instruments gave consistent results, and the data were combined yielding unprecedented spectral coverage (typically about 0.4–40 keV in the quasar frame) for high- z quasars. This allows us to put severe limits on several different descriptions of the continuum (e.g., broken power law, bremsstrahlung, reflection component). No Fe K α emission line is detected in any of the ASCA spectra. An absorption edge consistent with Fe K α at the quasar redshift is marginally detected in S5 0014+81. Possible origins for the observed low energy absorption are discussed. In particular, contributions from the molecular clouds and dust present in our Galaxy (usually disregarded) are carefully considered. In light of the new results for S5 0836+71 and S5 0014+81, absorption intrinsic to the quasars is considered and discussed.

The average slope obtained from the eight ASCA spectra in the observed ~ 0.5 –10 keV energy band is $\langle \Gamma_{0.5-10 \text{ keV}} \rangle \simeq 1.61 \pm 0.04$, with a dispersion $\sigma_{0.5-10 \text{ keV}} \simeq 0.10 \pm 0.03$. The average photon index in the observed 2–10 keV band, where the effect of absorption is negligible, is $\langle \Gamma_{2-10 \text{ keV}} \rangle \simeq 1.53 \pm 0.05$, with a dispersion $\sigma_{2-10 \text{ keV}} \lesssim 0.12$. Furthermore, the implications of the present results on the calculations of the contribution of quasars to the cosmic X-ray and γ -ray backgrounds are briefly discussed.

Subject headings: galaxies: active — quasars: general — radiation mechanisms: nonthermal — X-rays: galaxies

1. INTRODUCTION

Quasars are the most powerful objects in the whole universe. This is especially true in the X-ray band, where luminosities can reach 10^{47} – $10^{48} \text{ ergs s}^{-1}$. However, how quasars produce such a large amount of energy remains a challenging astrophysical problem. Certainly, because of their extreme conditions, quasars provide a powerful test for models of emission mechanisms of active galactic nuclei (AGNs) (Rees 1984). Quasars show strong continuum emission over the entire electromagnetic spectrum, from radio through the X-ray and even γ -ray region (Sanders et al. 1989; Elvis et al. 1994a; Thompson et al. 1995). Optically selected samples of quasars indicate that approximately

90% of them are radio quiet (RQQs) and approximately 10% are radio-loud (RLQs).

X-ray quasar spectral observations are crucial for two main reasons: first, X-rays carry a large amount of the total quasar luminosity; second, as demonstrated by observations of rapid X-ray variability, X-rays originate from the innermost regions of the quasar (Mushotzky, Done, & Pounds 1993). Most X-ray spectral observations have included mainly low-redshift ($z < 1$) quasars; the poor energy resolution generally limited the analysis to a simple parameterization of the spectrum with a single power law. In the ~ 0.1 –4 keV energy range, previous *Einstein* IPC and *ROSAT* Position Sensitive Proportional Counter (PSPC) observations have shown that RLQs have significantly flatter X-ray spectra than RQQs (Wilkes & Elvis 1987; Brunner et al. 1992) and that, for a given optical luminosity, RLQs are on average approximately 3 times brighter in X-rays than RQQs (Zamorani et al. 1981). Studies at higher energies (~ 2 –10 keV) with *EXOSAT* and *Ginga* have confirmed the dichotomy, with a clear correlation between spectral index and radio loudness (Williams et al. 1992; Lawson et al. 1992). Whether differences in the observed X-ray properties should be attributed to either intrinsically different properties of the sources or inclination effects and/or host galaxy properties is not yet well understood. Also, selection effects and/or complex spectral structures (e.g., soft-excess emission, ionized absorption) may compli-

¹ The Institute of Physical and Chemical Research (RIKEN), 2-1, Hiro-sawa, Wako, Saitama 351-01, Japan.

² Osservatorio Astronomico di Bologna, via Zamboni 33, I-40126 Bologna, Italy.

³ Max-Planck-Institut für Extraterrestrische Physik, D-85748 Garching bei München, Germany.

⁴ Harvard-Smithsonian Center for Astrophysics, 60 Garden Street, Cambridge, MA 02138.

⁵ Dipartimento di Astronomia, Università di Bologna, via Zamboni 33, I-40126 Bologna, Italy.

⁶ Istituto per le Tecnologie e Studio Radiazioni Extraterrestri, ITESRE/CNR, via Gobetti 101, I-40129 Bologna, Italy.

⁷ Present address: Istituto per le Tecnologie e Studio Radiazioni Extraterrestri, ITESRE/CNR, via Gobetti 101, I-40129 Bologna, Italy; mcappi@tesre.bo.cnr.it.

Science Driven arguments for a 10 sq.meter, 1 arcsecond X-ray Telescope

Martin Elvis and Giuseppina Fabbiano

Harvard-Smithsonian Center for Astrophysics, Cambridge Mass USA

Abstract.

X-ray astronomy needs to set bold, science driven goals for the next decade. Only with defined science goals can we know what to work on, and a funding agency appreciate the need for significant technology developments. To be a forefront science the scale of advance must be 2 decades of sensitivity per decade of time. To be stable to new discoveries these should be general, discovery space, goals.

A detailed consideration of science goals leads us to propose that a mirror collecting area of 10 sq.meters with arcsecond resolution, good field of view (>10 arcmin), and with high spectral resolution spectroscopy ($R=1000-10,000$) defines the proper goal. This is about 100 times AXAF, or 30 times XMM. This workshop has shown that this goal is only a reasonable stretch from existing concepts, and may be insufficiently bold.

An investment of $\sim \$10$ M/year for 5 years in X-ray optics technologies, comparable to NASA's investment in ASTRO-E or a SMEX, is needed, and would pay off hugely more than any small X-ray mission.

1. Long Term Goals for X-ray Astronomy

Any big undertaking, such as X-ray astronomy ¹ surely is, must set long range goals. With clear long-term science goals in place we can see which developments are essential, and which are mere sidelines - amusing, but dead ends. Daniel Goldin, the NASA Administrator, urged astronomers (San Antonio AAS meeting, January 1996) to make decade length plans, even if the plan changes in a few years time. This is what we do here.

The goals we shall describe are deliberately ambitious. We propose that X-ray astronomers should aim to reach sensitivities 100 times beyond AXAF, while retaining high angular resolution and achieving high dispersion spectroscopy (Table 1) ². This does not mean that the very next mission we design should necessarily have all these capabilities. Nor does it rule out smaller missions with different goals. It does mean that the next major mission we design should at least be a deliberate and significant step toward these capabilities. To some

¹We discuss only the standard 0.1-10 keV band of X-ray astronomy, in which grazing incidence optics work efficiently.

²These numbers describe quite well Hale's Mt. Wilson 100-inch telescope (Osterbrock 1995), so we are suggesting that X-ray astronomy try to equal the state of optical astronomy in 1917.

THE EINSTEIN SLEW SURVEY

MARTIN ELVIS, DAVID PLUMMER, JONATHAN SCHACHTER, AND G. FABBIANO

Harvard-Smithsonian Center for Astrophysics, 60 Garden Street, Cambridge, MA 02138

Received 1991 May 31; accepted 1991 August 15

ABSTRACT

A catalog of 819 sources detected in the *Einstein* IPC Slew Survey of the X-ray sky is presented; 313 of the sources were not previously known as X-ray sources. Typical count rates are $0.1 \text{ IPC count s}^{-1}$, roughly equivalent to a flux of $3 \times 10^{-12} \text{ ergs cm}^{-2} \text{ s}^{-1}$. The sources have positional uncertainties of 1.2 (90% confidence) radius, based on a subset of 452 sources identified with previously known pointlike X-ray sources (i.e. extent less than $3'$).

Identifications based on a number of existing catalogs of X-ray and optical objects are proposed for 637 of the sources, 78% of the survey, (within a $3'$ error radius) including 133 identifications of new X-ray sources. A public identification data base for the Slew Survey sources will be maintained at CfA, and contributions to this data base are invited.

Subject headings: BL Lacertae objects: general — catalogs — quasars: general — X-rays: general — X-rays: stars — surveys

1. INTRODUCTION

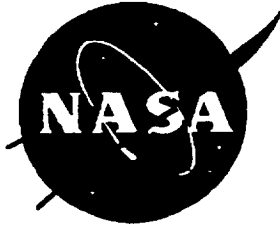
Sky surveys have always played a major role in astronomy. In the present era in astronomy, we are rapidly accumulating new sky surveys across the whole spectrum. In particular, the advent of imaging telescopes has made X-ray surveys possible that are comparable in sensitivity to those at other wavelengths. The *Einstein* Observatory (*HEAO 2*; Giacconi et al. 1979a) was the first imaging X-ray astronomy satellite, and many papers have reported on surveys of restricted regions of the sky made using pointed observations taken with the Imaging Proportional Counter (IPC, Gorenstein, Harnden, & Fabricant 1981) on board *Einstein*. (The "Medium Survey," e.g. Gioia et al. 1990; the "Deep Survey," e.g. Primiini et al. 1991; Table 1). As a result we are in the peculiar position in the soft X-ray band covered by *Einstein* ($\sim 0.2\text{--}3.5 \text{ keV}$), of knowing more about the faint sources than about the bright sources. The limited sky coverage of the Medium and Deep Surveys results in their having effective *upper* limits to their sensitivity as well as lower limits since bright sources are rare on the sky (Fig. 1; Table 1). This limitation complicates $\log N\text{--}\log S$ and source evolution studies (Fig. 1) since for bright source counts we have to refer to the hard X-ray surveys, usually to the Piccinotti et al. (1982) *HEAO A-2* survey which covered the $2\text{--}10 \text{ keV}$ energy band. For example, Schmidt (1990) has emphasized how the Piccinotti et al. and the Medium Survey source counts are in contradiction for AGNs and clusters of galaxies (although evolution may explain these problems; Gioia et al. 1990). What is needed is a $\log N\text{--}\log S$ with the same instrument over the whole X-ray flux range. A survey of the bright sources in the soft X-ray range is thus important, and only a survey covering most of the sky can find the relatively rare bright sources. A survey using the same instrument as used for the *Einstein* Medium and Deep Surveys would greatly simplify interpretation. Samples of bright sources selected uniformly by their X-ray properties are also valuable for follow-up detailed work with other instruments, e.g., *ROSAT*, *ASTRO-D*.

We have constructed a survey of the sky with the *Einstein* IPC using the "Slew" data taken when the satellite was moving ("slewing") from one target to the next. By co-adding all these slews, we have achieved a useful sensitivity over a large solid angle, some 50% of the sky. The main properties of the *Einstein* IPC Slew Survey are given in Table 2. Because it was not clear that this survey could be constructed successfully, it was not attempted earlier. The resources needed to process the data were large, making the effort too large for the uncertain payoff. Computer processing power and on-line storage capacity have grown by orders of magnitude in the last few years so that it is now possible for projects of this size to be carried out experimentally by a small team relatively quickly, and thus at low risk. This paper describes the *Einstein* Slew Survey and presents the resulting catalog of X-ray sources.

The complete information content of the Slew Survey is more than the source catalog. A CD-ROM issued by SAO (Plummer et al. 1991) contains the full data on the individual photons in the Slew Survey and the aspect solution file for each slew. This enables a user to derive fluxes and upper limits for any position on the sky covered by the Slew Survey. The CD-ROM also contains more information on the source detections (see "lists/unix/srcs.lis," "lists/vms/srcs.lis," etc.). The CD-ROM is available from SAO (send requests by e-mail to the *Einstein* Data Products Office, edpo@cfa.harvard.edu), or via the *Einstein* On-Line Information System, *einline* (Harris et al. 1991).

2. DATA SELECTION

For the survey we selected all the data taken while the *Einstein* satellite was slewing with the IPC at the focus ("SLEW" mode data—hence the survey name). Only the IPC data is valuable for this survey. Table 3 compares a "figure of merit" for this type of work for the four focal plane instruments on *Einstein*. The combination of wide field of view, high quantum efficiency, and large fraction of time in the focal plane make



The *Einstein* Slew Survey Sample of BL Lacs

Eric S. Perlman, John T. Stock, Jonathan F. Schachter, Martin Elvis, Erica
Ellingson, C. Megan Urry, Michael Potter, Chris D. Impey and Peter Kolchinsky

Laboratory for High Energy
Astrophysics



High Energy Astrophysics Science
Archive Research Center

NASA Goddard Space Flight Center
Greenbelt, MD 20771

Abstract

We have used an efficient method of finding new BL Lacertae objects in the *Einstein* Slew Survey suggested by Stocke et al. By exploiting the unique broad-band (radio/optical/X-ray) spectra of X-ray selected BL Lacs, we have identified 29 new BL Lacs out of 32 candidates observed, effectively doubling the size of the Slew Survey BL Lac sample, which now includes 62 objects. Six more BL Lac candidates have yet to be observed, and seven blank field radio sources cannot be ruled out as optically faint BL Lacs, although this is unlikely. The correct identification of one BL Lac candidate remains uncertain. We present finding charts, optical spectroscopy, radio images, and optical polarimetry for these new BL Lacs. Based upon nearly complete radio imaging and optical spectroscopy observations, we present the northern, high-latitude Slew Survey BL Lac sample, in the area bounded by $\delta \geq -40^\circ$ and $|b_{II}| \geq 15^\circ$, and excluding the region within 5° of M31. This sample contains 48 BL Lacs, four BL Lac candidates, and five blank fields which may contain possible BL Lac candidates. This is considerably larger than any previous complete sample of BL Lacs. We compare this sample with the X-ray selected EMSS sample of BL Lacs as well as the radio-selected 1 Jy sample.

X-RAY SPECTRAL EVOLUTION OF HIGH REDSHIFT QUASARS

JILL BECHTOLD

Steward Observatory, University of Arizona, Tucson, Arizona 85721
Electronic mail: jbechtold@as.arizona.edu

MARTIN ELVIS, FABRIZIO FIORE, AND OLGA KUHN

Harvard-Smithsonian Center for Astrophysics, 60 Garden Street, Cambridge, Massachusetts 02138
Electronic mail: elvis@cfa.harvard.edu

ROC M. CUTRI

Steward Observatory, University of Arizona, Tucson, Arizona 85721
Electronic mail: rcutri@as.arizona.edu

JONATHAN C. McDOWELL

Harvard-Smithsonian Center for Astrophysics, 60 Garden Street, Cambridge, Massachusetts 02138
Electronic mail: mcdowell@as.arizona.edu

MARCIA RIEKE

Steward Observatory, University of Arizona, Tucson, Arizona 85721
Electronic mail: mrieke@as.arizona.edu

ANETA SIEMIGINOWSKA AND BELINDA J. WILKES

Harvard-Smithsonian Center for Astrophysics, 60 Garden Street, Cambridge, Massachusetts 02138
Electronic mail: aneta@miles.harvard.edu

Received 1994 February 14; revised 1994 April 26

ABSTRACT

At $z \approx 3$, the x-ray spectra of radio-loud and radio-quiet quasars are different. High-redshift radio-quiet quasars either have large absorbing columns, N_H , and steeper power law spectral indices, α_E , than low redshift quasars, or no absorption and similar α_E 's. In contrast, the radio-loud quasars at high redshift have substantial absorption and similar α_E 's to low redshift quasars. Implications for the interpretation of the evolution of the luminosity function of quasars are discussed. If the absorption arises outside the central engine for both radio-loud and radio-quiet quasars, then radio-quiet quasars differ from the radio-loud quasars in that their emitted power law spectrum has evolved with redshift. We argue that this favors models where quasars are numerous and short-lived, rather than rare and long-lived.

1. INTRODUCTION

A basic characteristic of quasars is the scale-free nature of their emission. From the lowest luminosity AGN (e.g., M81) to the highest redshift, most luminous quasars, the quasar continuum and emission lines scale almost linearly with luminosity, regardless of redshift (e.g., Netzer 1990; Blandford 1990, and references therein). This is true within both the radio-loud and the radio-quiet classes of quasar. There are small deviations from this pattern, e.g., the Baldwin effect (Baldwin 1977), and the slowly decreasing x-ray loudness of higher luminosity quasars (Avni & Tananbaum 1986; Trull et al. 1987). Even these, however, are continuous changes in the sense that there is no characteristic redshift or luminosity at which they occur.

By contrast, evolution studies show that quasars evolve strongly with redshift, and that $z \sim 2$ is a characteristic redshift for the quasar population. The break point, L^* , of their luminosity function shifts to higher luminosities by a factor 40–50 between $z=0.1$ and $z=2$ (Boyle et al. 1987). There are two extreme possibilities for the physical evolution that

causes the observed population evolution: individual objects are long-lived or short-lived. In the long-lived case, quasars are intrinsically rare, their present-day remnants have very high masses from the integrated accretion of mass over a Hubble time, and today they should emit at less than 1% of the Eddington luminosity, L_{Edd} (Cavaliere & Padovani 1988). In the alternative short-lived case, quasars are common, so that most large galaxies had one at one time, but each is active only for a short time ($\sim 10^8$ yr). In order not to require too much mass tied up in black holes, these quasars must be accreting close to their Eddington limits while they are active (Small & Blandford 1992; Chokshi & Turner 1992).

Physical evolution models could be more easily distinguished if there were characteristic luminosities or redshifts at which the properties of individual quasars changed. Recent results presented by Elvis et al. (1994) and Bechtold et al. (1994) suggest that the continuum spectral energy distributions of quasars are in fact changing at $z \sim 2$. They find:

- (1) Radio-loud quasars become strongly x-ray absorbed

between $z=0.5$ and $z=3$, whereas radio-quiet quasars probably do not.

(2) Steep spectrum radio-loud quasars do not continue to follow the correlation of α_{ox} increasing with L_{opt} at high redshift; they are too x-ray bright. Radio-quiet quasars instead continue to follow the correlation of α_{ox} increasing with increasing L_{opt} seen at lower redshift.

These observations suggest that breaks in the scaling laws for quasars are beginning to appear which may be related to the evolution of the quasar population as a whole. In this paper we review the data supporting these claims, and then discuss their potential value for understanding quasar emission mechanisms.

2. X-RAY SPECTRA AND HARDNESS RATIOS

Obtaining x-ray spectra of high redshift quasars has become feasible with the *ROSAT* (Trümper 1983) Position Sensitive Proportional Counter (PSPC, Pfefferman *et al.* 1987). Elvis *et al.* (1994, hereafter referred to as Paper I) presented x-ray spectra of several radio-loud high-redshift quasars. Bechtold *et al.* (1994, hereafter referred to as Paper II) derived hardness ratios for a dozen $z \sim 3$ quasars, six of them radio-quiet. Although the small number of counts in these detections render their hardness ratios ambiguous, they nevertheless add significantly to our knowledge of quasar spectra at high redshift.

Since Paper II was completed, other PSPC data on high redshift quasars have been published (Fink & Briel 1993; Henry *et al.* 1994; Molthagen *et al.* 1994; Band *et al.* 1994). This allows us to expand on the results given in Paper II. In Table 1, we list the x-ray results derived in Paper I and Paper II. We also give the results for OQ 172, which we reanalyzed in order to ensure uniformity of treatment, since the PSPC data have now become public. The $z=4.5$ quasar 0953+47 observed by Molthagen *et al.* (1994) was not detected in the PSPC, but we include their limit for α_{ox} below.

The PSPC hardness ratio, defined as

$$R = (H - S) / (H + S),$$

is given in Table 1 for each quasar. Here H is the number of counts in a hard band defined as PI channels 41–245, or 0.41 to 2.48 keV in the observed frame; S is the number of counts in a soft band defined as PI channels 11–40, or observed energies of 0.11 to 0.40 keV. Note that for an object at $z=3$, these channels correspond to 1.64–9.92 keV and 0.44–1.60 keV, respectively. In addition to the high-redshift quasars, we include four intermediate redshift, radio-quiet quasars with $1.5 < z < 2.2$ found in the PSPC field of Q0130–403 (see Paper II; Hoag & Smith 1977; Osmer 1977).

Figure 1 is a plot of R for the quasars in our sample. Clearly, there is a systematic difference between the radio-loud and radio-quiet quasars. Omitting the three cases where the galactic column density is larger than 7×10^{20} atoms cm^{-2} (implying transmission of only 10% at the carbon edge and hence a large effect on R), the mean R for radio-quiet quasars is -0.018 ± 0.110 , while for the radio-loud quasars the mean R is 0.78 ± 0.03 , a 7.2σ difference.

TABLE 1. X-ray and hardness ratios.

| quasar | z_{em} | N_{HGal}^a | R^b | Case A | Case B |
|-----------|-----------------|---------------------|---------------------|--------------------------|-------------------------|
| | | | | α_E | α_E |
| 0000-263 | 4.11 | 1.60 | -0.065 ± 0.183 | $1.30^{+0.23c}_{-0.23}$ | $2.20^{+0.27d}_{-0.30}$ |
| 0130-403 | 3.03 | 2.30 | -0.170 ± 0.372 | $1.69^{+0.71c}_{-0.60}$ | $2.30^{+0.80d}_{-0.55}$ |
| 0207-398 | 2.81 | 1.53 | 0.128 ± 0.216 | $0.90^{+0.34c}_{-0.36}$ | $1.60^{+0.30d}_{-0.40}$ |
| 1107+481 | 2.96 | 1.40 | 0.066 ± 0.257 | $0.93^{+0.39c}_{-0.39}$ | $1.61^{+0.39d}_{-0.48}$ |
| 1208+101 | 3.82 | 1.70 | -0.249 ± 0.346 | $1.54^{+0.73c}_{-0.53}$ | $2.05^{+0.70d}_{-0.60}$ |
| 1946+768 | 3.02 | 7.50 | 0.935 ± 0.157 | $1.00^{+0.28c}_{-0.32}$ | $1.23^{+0.37d}_{-0.39}$ |
| 0130-401 | 1.73 | 2.30 | -0.154 ± 0.269 | $1.66^{+0.51c}_{-0.44}$ | $3.88^{+0.60e}_{-0.60}$ |
| 0130-404 | 2.16 | 2.30 | 0.081 ± 0.465 | $1.27^{+0.79c}_{-0.80}$ | $2.88^{+0.93e}_{-0.99}$ |
| 0131-401A | 1.83 | 2.30 | -0.249 ± 0.204 | $1.83^{+0.38c}_{-0.36}$ | $3.93^{+0.47e}_{-0.43}$ |
| 0131-401C | 1.65 | 2.30 | 0.129 ± 0.339 | $1.20^{+0.53c}_{-0.59}$ | $3.40^{+0.67e}_{-0.70}$ |
| 0014+813 | 3.38 | 14.4 | 0.962 ± 0.077 | $0.82^{+0.19c}_{-0.19}$ | $0.97^{+0.20d}_{-0.20}$ |
| 0420-388 | 3.12 | 1.91 | 0.406 ± 0.074 | $0.73^{+0.10c}_{-0.10}$ | $1.24^{+0.48d}_{-0.48}$ |
| 0438-436 | 2.85 | 1.50 | 0.903 ± 0.071 | $0.61^{+0.22f}_{-0.22}$ | $0.61^{+0.22f}_{-0.22}$ |
| 0636+680 | 3.17 | 5.70 | 1.140 ± 0.276^g | $-0.24^{+0.50c}_{-0.44}$ | $0.04^{+0.50d}_{-0.54}$ |
| 1442+101 | 3.54 | 1.73 | 0.480 ± 0.067 | $0.45^{+0.09c}_{-0.09}$ | $0.45^{+0.10f}_{-0.10}$ |
| 1745+624 | 3.87 | 3.40 | — | $0.30^{+0.60f}_{-0.60}$ | $0.30^{+0.60f}_{-0.60}$ |
| 2000-330 | 3.78 | 7.50 | 0.721 ± 0.242 | $1.61^{+0.71c}_{-0.92}$ | $1.49^{+0.53d}_{-0.57}$ |
| 2126-158 | 3.27 | 4.85 | 0.963 ± 0.041 | $0.52^{+0.25f}_{-0.21}$ | $0.52^{+0.25f}_{-0.21}$ |

Notes to TABLE 1

^aIn units of 10^{20} atoms cm^{-2} . ^bHardness ratio, $R = H - S / H + S$; for 1745+624 the PSPC data are not available. ^c N_{H} fixed to the galactic value. ^dAdditional N_{H} at $z = z_{\text{em}}$ fixed to 10^{22} atoms cm^{-2} . ^eAdditional N_{H} at $z = z_{\text{em}}$ fixed to 5×10^{21} atoms cm^{-2} . ^fBest fit additional N_{H} at $z = z_{\text{em}}$. ^gFormally, $R > 1$ since $S = -4.8 \pm 6.5$ after background subtraction. Only values of $R < 1$ and $S > 0$ are physical, however.

The dashed and dotted lines in Fig. 1 represent the expectation for radio-loud and radio-quiet quasars, respectively, using the mean spectral index found at low redshift by *Ginga* (0.71 for radio-loud and 1.03 for radio-quiet, Williams *et al.* 1992) and the minimum and maximum galactic N_{H} values in our samples (1.4 – 2.3×10^{20} atoms cm^{-2} for the radio-quiet quasars and 1.5 – 5.7×10^{20} atoms cm^{-2} for the radio-loud quasars). The radio-quiet quasars have R compatible with the low redshift predictions, while at least some of the radio-loud quasars have R definitely greater than predicted. We compare our results to the *Ginga* data for low redshift quasars, since for $z \sim 3$ the PSPC bandpass corresponds to rest frame energies of ~ 1 – 10 keV, similar to the *Ginga* bandpass for low redshift objects. For the $z \sim 2$ quasars, the PSPC bandpass corresponds to ~ 0.6 – 7 keV, between the harder x-rays observed by *Ginga* (2–10 keV) and the softer x-rays observed by the IPC (0.1–3.5 keV) for low redshift objects. However, this energy difference is probably not important for these comparisons since the *Ginga* and IPC measured slopes are similar (Fiore *et al.* 1994).

The difference in R between low and high redshift radio-loud quasars, can be interpreted in different ways. The two

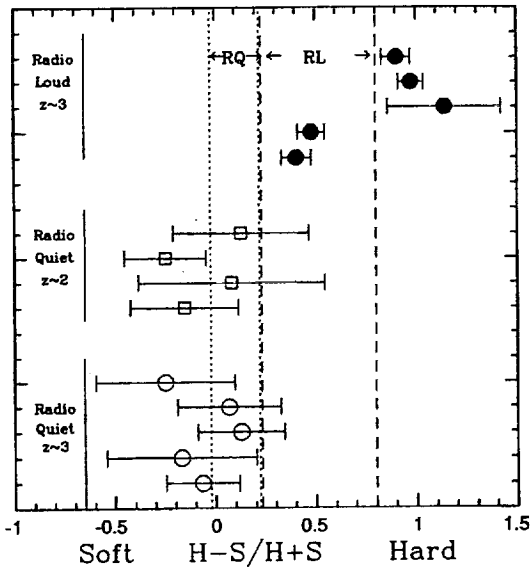


FIG. 1. The *ROSAT* PSPC hardness ratio for a sample of high-redshift quasars. Open symbols identify radio-quiet quasars, filled symbols identify radio-loud quasars: circles correspond to $2.8 < z < 4.1$ quasars; squares corresponds to $1.6 < z < 2.2$ quasars. The dotted and dashed lines show the range of hardness ratio expected from the low z *Ginga* observations. H —number of counts in the hard PSPC band (0.41–2.48 keV); S —number of counts in the soft PSPC band (0.11–0.40 keV).

most simple and extreme possibilities are (A) a difference in emitted power law index, in the sense that the high-redshift quasars are flatter than the low redshift ones, or (B) a difference in absorbing column density, in the sense that the high z quasars have a larger absorbing column than at low z . Of course intermediate situations, where both the emitted power law index and the absorption properties of high z quasars are different, are also possible. In Table 1, we list the spectral index α_E obtained for both cases (A) and (B) using the hardness ratio diagrams discussed in Paper II, for the radio-quiet quasars Q0130–403, Q0207–398, Q1107+481 and Q1208+101, and for the intermediate redshift radio-quiet quasars in the field of Q0130–403. For the other quasars, the α_E obtained from normal spectral fitting is given (Paper I).

For case (A), N_H was assumed to be equal to the galactic N_H value in all the objects for which this assumption is statistically consistent with the observed spectrum (i.e., all radio-quiet quasars, and all the radio-loud quasars with the exception of PKS 0438–436, PKS 2126–158, see Papers I, II). For case (B), an absorber with the best fit N_H at $z = z_{\text{em}}$ (as given in Paper I) was assumed for PKS 0438–436 and PKS 2126–158. Otherwise, a column of $N_H = 10^{22}$ atoms cm^{-2} at z_{em} was assumed in addition to the galactic N_H . In these cases, the statistics of the data are not good enough to constrain the intrinsic N_H (this includes all the radio-quiet quasars and the radio-loud quasars Q0014+813, Q0420–388, Q0636+680, and PKS 2000–330). In both cases the absorbers were assumed to have cross sections given by Morrison & McCammon (1983) with solar metal abundance. We note that two of the eight radio-loud quasars, Q1745+624 (Fink & Briel 1993) and OQ 172, do not show evidence for intrinsic absorption. The limit for intrinsic absorption quoted by Fink & Briel for the first object is 2×10^{20}

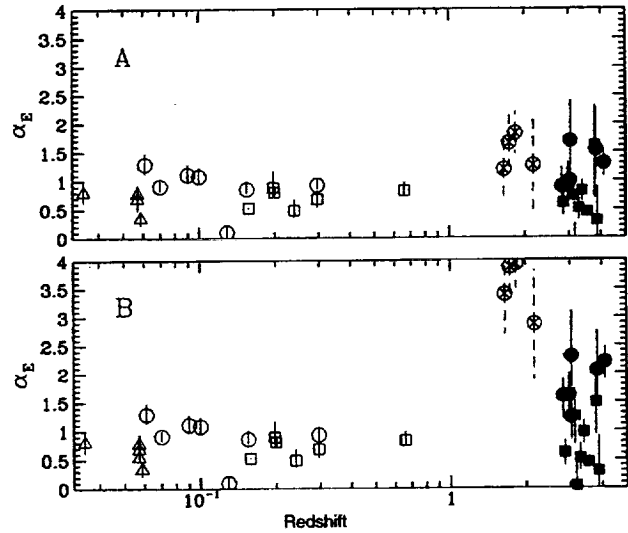


FIG. 2. X-ray energy spectral index in the 1–10 keV *emitted* frame vs redshift when assuming: (a) N_H at $z = z_{\text{em}}$ of 10^{22} atoms cm^{-2} for $z \sim 3$ quasars and 5×10^{21} atoms cm^{-2} for $z \sim 2$ quasars; (b) N_H fixed at the galactic value. Squares=radio-loud quasars, circles=radio-quiet quasars; triangles=radio galaxies; filled symbols=*ROSAT* PSPC $z \sim 3$ quasars; open circles with crosses=quasars with $1.6 < z < 2.2$. Open symbols and triangles=*Ginga* results.

atoms cm^{-2} , while for the second object we found a 99% limit of 0.5×10^{22} atoms cm^{-2} .

3. X-RAY SPECTRAL EVOLUTION

How does α_E evolve with redshift?

Figures 2 and 3 show α_E as a function of redshift (Fig. 2) and luminosity (Fig. 3) for the objects in this sample,

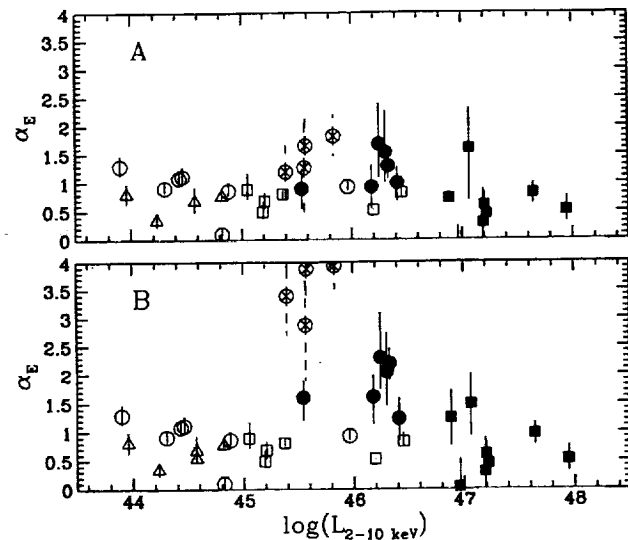


FIG. 3. X-ray energy spectral index in the 1–10 keV *emitted* frame vs 2–10 keV luminosity when assuming: (a) N_H at $z = z_{\text{em}}$ of 10^{22} atoms cm^{-2} for $z \sim 3$ quasars and 5×10^{21} atoms cm^{-2} for $z \sim 2$ quasars; (b) N_H fixed at the galactic value. Squares=radio-loud quasars, circles=radio-quiet quasars; triangles=radio galaxies; filled symbols=*ROSAT* PSPC $z \sim 3$ quasars; open circles with crosses=quasars with $1.6 < z < 2.2$. Open symbols and triangles=*Ginga* results.

and for a low redshift comparison, quasars observed with *Ginga*. Note that the sizes of the low redshift and high redshift samples are similar. Figures 2 and 3 are updated versions of those in Paper I. Note that the PSPC spectral index covers 0.4–9.4 keV for the lowest redshift object ($z=2.81$), and 0.6–12.7 keV for the highest redshift object ($z=4.11$). This introduces some ambiguity, although not a large one if the *Ginga* low z spectra are a reliable guide (Williams *et al.* 1992). We note also that the high redshift quasars in our sample are also the most luminous, so it is hard to distinguish whether the x-ray spectral properties depend primarily on z or L_x . In the remainder of the discussion we consider the dependence of α_E on z , for case (A) and case (B).

Case (A): Only radio-loud high z quasars are absorbed [Figs. 2(a), 3(a)]. In this case, the difference in slope between radio-loud and radio-quiet quasars which was found at low redshifts (Wilkes & Elvis 1987; Williams *et al.* 1992) persists at $z \sim 3$, radio-quiet quasars having steeper slopes. The weighted mean spectral slope of the radio-quiet quasars is 1.15 ± 0.14 (the error represents the error on the mean), consistent with the $\langle \alpha_E \rangle = 1.03$, for a sample of six low redshift radio-quiet quasars (Williams *et al.* 1992; excluding the peculiar object PG 1416–129, which has a best fit 2–10 keV slope of only 0.1). The constraint on any change of α_E with z is no more than 0.3 (99% confidence). For the radio-loud quasars the weighted mean spectral slope is 0.59 ± 0.06 , comparable with the $\langle \alpha_E \rangle = 0.71$ for a sample of five low-redshift radio-loud quasars (Williams *et al.* 1992).

In case (A) then radio-quiet quasars show no change in either emitted slope or absorption out to $z=4$, while radio-loud quasars commonly exhibit strong x-ray absorption at $z=3$, with no change in intrinsic slope. This immediately implies that the absorption in radio-loud $z \sim 3$ quasars (Paper I) is primarily intrinsic to the quasars, since intervening absorbers would be found independently of the radio properties of the quasar. (The number of objects is still small, however.)

The slope obtained for the intermediate redshift quasars, assuming galactic N_H (case A), is steeper than the IPC and *Ginga* slopes and is similar to those found in the PSPC spectra of low-redshift radio-quiet quasars (Walter & Fink 1993; Laor *et al.* 1994; Fiore *et al.* 1994), despite the significantly lower energy range covered by the PSPC. In this case then the major evolution in x-ray slope occurs between $z \sim 0$ and $z \sim 2$, with little change thereafter up to $z \sim 3$. This behavior would be similar to the evolution of the quasar luminosity function (e.g., Boyle *et al.* 1993).

Case (B): All high z quasars are absorbed [Figs. 2(b), 3(b)]. No matter where the absorbers are located, the x-ray hardness ratios of the radio-quiet quasars imply α_E 's which are steeper by ~ 0.7 than the no absorption case (see Table 1).

Figures 2(b) and 3(b) shows α_E as a function of x-ray luminosity and redshift for case (B). The mean α_E for the high-redshift radio-quiet quasars is $\langle \alpha_E \rangle = 1.82 \pm 0.17$. This is significantly steeper than $\langle \alpha_E \rangle = 1.03$ for the similar low-redshift quasars observed with *Ginga*. The two distributions of low and high redshift radio-quiet quasars spectral indices are different at the 97% confidence level (using the Kolmogorov–Smirnov test). The high-redshift radio-quiet

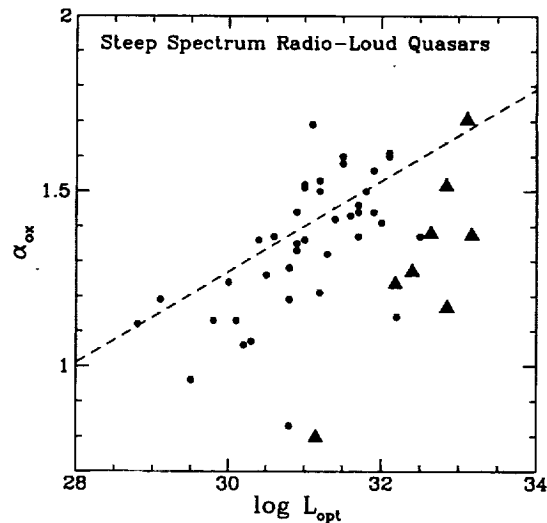


FIG. 4. α_{ox} vs $\log L_{opt}$ in erg s^{-1} , for steep spectrum, radio-loud quasars. Filled circles are quasars detected with the *Einstein* IPC (Wilkes *et al.* 1994; Paper II) with $\alpha_{radio} > 0.8$. Triangles are $z \sim 3$ quasars reported in Papers I and II. The dashed line is the predicted relation for steep spectrum radio sources from Worrall *et al.* (1987). The high redshift quasars are more x-ray bright than the low redshift relation predicts.

mean slope is also different from that of high-redshift radio-loud quasars which demonstrably show absorption ($\langle \alpha_E \rangle = 0.52 \pm 0.16$), and that of all high-redshift radio-loud quasars ($\langle \alpha_E \rangle = 0.57 \pm 0.08$).

The intermediate redshift quasars would have steeper slopes $\alpha_E \sim 4$ on this assumption. They would then be steeper at $z \sim 1.5$ than at either $z \sim 0$ or $z \sim 3$. This seems unlikely, but is not ruled out. We note that the path length for absorption, X (Bahcall & Peebles 1969), is half as large at the mean redshift of the quasars in the field of Q0130–403 ($z=1.84$) than of the absorbed quasars in Paper I, so the chance of intervening absorbers is similarly reduced.

In summary, in either case (A) or (B), the x-ray colors and spectra suggest that radio-quiet and radio-loud objects have evolved differently since $z \approx 3$. If the radio-quiet objects have, on average, as much absorption as the radio loud quasars, their power laws must be steeper than their low redshift counterparts, indicating evolution in the emission spectrum with redshift. If only radio-loud quasars have absorption, then the high-redshift radio-loud objects differ from both their low z counterparts and from the radio-quiet quasars in that they have substantial absorbing material.

4. X-RAY LOUDNESS (α_{ox}) VERSUS L_{opt}

The plots of x-ray loudness, α_{ox} (e.g., Tananbaum *et al.* 1979), versus L_{opt} in Figs. 4 and 5 are updated versions of that in Paper II. The triangles mark the high redshift quasars from Paper II, Band *et al.* (1994), and Molthagen *et al.* (1994); the small circles show the quasars from the *Einstein* IPC survey (Wilkes *et al.* 1994) which are predominantly at low ($z < 1$) redshift. Figure 5 shows only radio-quiet quasars, while Fig. 4 contains only radio-loud quasars. Moreover, we have restricted the radio-loud quasars to those in which beaming is not likely to be important, i.e., lobe-dominated or

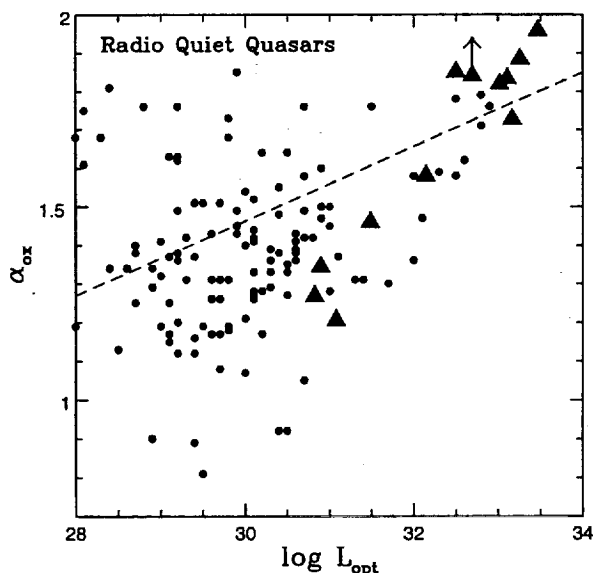


FIG. 5. α_{ox} vs $\log L_{\text{opt}}$ in erg s^{-1} for radio-quiet quasars. Filled circles are quasars detected with the *Einstein* IPC (Wilkes *et al.* 1994; Paper II). Triangles are radio-quiet quasars presented in Paper II. The dashed line is the predicted relation for radio-quiet quasars from Worrall *et al.* (1987). The high redshift quasars are consistent with the low redshift relation.

steep spectrum radio sources ($\alpha_{\text{radio}} > 0.8$). Beaming is not thought to be important in GPS sources and therefore in most of our high-redshift, radio-loud quasars.

The dashed lines show the predicted relations from Worrall *et al.* (1987) for each class of quasar. The high-redshift, radio-quiet quasars are consistent with the extrapolation from low redshift, and may even be slightly x-ray quiet (cf. Pickering & Impey 1994). In contrast, for steep-spectrum radio-loud quasars, the high redshift quasars lie systematically below the prediction. They are too x-ray loud for their optical luminosity. Note that despite the relatively small number of quasars detected in the IPC, the uncertainty in the predicted line is small on this scale.

While the range of observed α_{ox} of the high z radio-loud quasars in Paper I ranges between 1.1 and 1.6, they are bunched toward small values of α_{ox} (Fig. 5). There are three cases with $\alpha_{\text{ox}} < 1.3$ and only one with $\alpha_{\text{ox}} \sim 1.6$. This is S4 0636+680 which interestingly is also the most radio-quiet quasar in the radio-loud sample. A $\Delta\alpha_{\text{ox}}$ of 0.3 corresponds to a factor ~ 6 in x-ray to optical flux ratio, so that this is a large effect.

This break in the predictive power of the α_{ox} vs L_{opt} relations indicates a characteristic luminosity at $\log L_{\text{opt}} \sim 32\text{--}33 \text{ erg s}^{-1} \text{ Hz}^{-1}$, for steep-spectrum radio-loud quasars.

5. DISCUSSION

One can use these observations to speculate on the physical nature of the evolution of quasars in different scenarios. As mentioned briefly in the introduction there are two extreme possibilities: individual quasars are long-lived or short-lived. In the long-lived case, quasars are intrinsically rare, their present day remnants have very high masses from

the integrated accretion of mass over a Hubble time, and today they should emit at less than 1% of the Eddington luminosity, L_{Edd} (Cavaliere & Padovani 1988). Since there is no evidence for very large black hole masses in nearby Seyferts or ellipticals and since there are indications that the ratio of the luminosity to its Eddington value in nearby Seyferts and intermediate redshift quasars is between 0.01 and 0.1 (Wandel & Mushotzky 1986; Padovani & Rafanelli 1988; Chokshi & Turner 1992; Small & Blandford 1992), it seems unlikely that the evolution of the luminosity function could be explained by the gradual decline in luminosity of individual, rare objects. A further test for the long-lived option is the evolution of the quasar continuum, since as the quasar black holes grow larger and become more starved of accreting matter, the continuum they produce is likely to change in form.

Alternatively, in the short-lived case, quasars are common (so that most large galaxies had one at one time), but each is active only for a short time ($\sim 10^8 \text{ yr}$). In order not to require too much mass tied up in black holes, these quasars must be accreting close to their Eddington limits while they are active (Small & Blandford 1992). Haehnelt & Rees (1993) have discussed the formation of such black holes in the context of the hierarchical collapse of cold dark matter fluctuations. At high redshifts only the most massive fluctuations can collapse; as time goes on, and the universe expands, less overdense structures collapse. Thus, the black hole mass of a typical quasar should strongly *decrease* with redshift, rather than slowly increase by mass accretion. This gives rise to opposite expectations about the quasar continuum evolution compared to the long-lived model. Any systematic differences in the spectral energy distributions of high and low redshift quasars could therefore guide and constrain models for the evolution of the quasar luminosity function.

5.1 X-ray Spectral Evolution

In Sec. 2, we have shown that radio-loud and radio-quiet quasars at high redshift have different x-ray colors, but whether this is the result of different intrinsic x-ray power laws or different absorbing columns cannot be determined from the present data. We discuss the implications of both possibilities.

How does the x-ray spectral index depend on physical models of evolution? In the standard accreting massive black hole model, simple assumptions can give the sense of the dependence of α_{E} on the black hole mass and accretion rate.

Comptonization of soft photons by a population of thermal electron in a hot corona above a layer of cold reflecting matter has been proposed as the origin of the 2–10 keV spectrum in radio-quiet quasars (Haardt & Maraschi 1993). In this model sources powered by accretion onto large black holes ($\sim 10^{10} M_{\odot}$, such as those needed at the center of these luminous $z \sim 3$ quasars) result in 2–10 keV spectra which are significantly *steeper* than those of sources with smaller black holes. This holds for a range of corona optical depths, and therefore luminosities (Haardt & Maraschi 1993).

If the evolution of the quasar luminosity function results

from the slow evolution of a few, long-lived quasars, then one expects that the black hole masses *increase* with decreasing z , with $L/L_{\text{Edd}} \sim 1$ at $z=3$, and $L/L_{\text{Edd}} \ll 1$ at $z=0$. The Haardt & Maraschi (1993) models would then predict that α_E would steepen with decreasing z . On the other hand, if quasars are numerous, short-lived, and result from collapsing CDM halos in the Haehnelt & Rees (1993) picture, then a typical quasar black hole mass will *decrease* with z . Then the x-ray spectra will be steeper with increasing z .

In case (B), where all quasars are absorbed, radio-quiet quasars are steeper at higher z . This is opposite to the expectations for rare, long-lived quasars, but in agreement with the short-lived quasars in the Haehnelt and Rees picture.

In this case, the lack of evolution of the emitted x-ray power law for the radio-loud quasars is also significant. It would imply that their x-ray emission is not closely related to the black hole mass. In fact, at low redshift, radio-loud quasars are also more x-ray loud (i.e., have smaller α_{ox}) than radio-quiet quasars. This supports the notion that there is an "extra" component of the x-ray emission related to the radio source. We return to this in our discussion of α_{ox} vs L_{opt} in the next section.

In case (A), where only high z radio-loud quasars are absorbed, neither the radio-quiet nor radio-loud quasars have changed their x-ray spectral indices with redshift. Then one is forced to conclude that the x-ray emission is not related in a direct way to black hole mass for either radio-quiet or radio-loud quasars, or that the number of quasars studied is so small that only the most extreme members of the population, all with nearly the same black hole mass, have been sampled.

Case (A) has other strong implications. Since soft x-ray absorption appears at high redshift only for the radio-loud quasars then (1) quasar radio emission results from a different environment in the high-redshift objects; (2) a dust shrouded phase of quasar development may be associated with radio-emission and be short-lived, having the same fractional life as the ratio of radio-loud to radio-quiet quasars. Some support for the second hypothesis comes from the fact that about 50% of the high-redshift radio-loud quasars are GHz Peaked Spectrum (GPS) sources, while the fraction is much reduced at low redshift (O'Dea *et al.* 1991). In fact five of the eight radio-loud quasars in our sample are candidate GPS sources in the list of O'Dea *et al.* (1991; Q0420-388, Q0636+680, OQ 172, PKS 2000-330, and PKS 2126-158). PKS 0438-436 also has a radio spectrum that resembles that of GPS sources. GPS sources are unusually compact (~ 10 milliarcsec, ~ 100 pc at $z=3$, Pearson & Readhead 1984). This compactness could be evidence for a dense surrounding medium which confines the radio source. This hypothesis is discussed in more detail in Paper I.

5.2 X-ray Loudness (α_{ox})

The presence of a critical luminosity above which radio-loud quasars have a smaller optical to x-ray luminosity ratio than the less luminous, low-redshift ones (Sec. 4) suggests that the x-ray emission of these objects becomes dominated

by some mechanism not directly connected with the accretion rate, or limited by the Eddington luminosity.

An oft-suggested mechanism of this kind is the electromagnetic extraction of the black hole rotational energy (Blandford & Znajek 1977), which would be converted into x-rays through the SSC mechanism. Blandford (1990) gives the electromagnetic luminosity, L_{em} , as

$$L_{\text{em}} \approx 10^{45} \mathcal{M}_8^2 \left(\frac{a}{m} \right)^2 B_4^2 \text{ erg s}^{-1},$$

where \mathcal{M}_8 is the black hole mass in units of $10^8 \mathcal{M}_{\odot}$, B is the magnetic field in units of 10^4 G, a is the specific angular momentum, and $m = GM/c^2$. The x-ray luminosity in high luminosity radio-loud quasars could therefore be proportional to L_{em} , say a fraction g of L_{em} : $L_{\text{xem}} = g L_{\text{em}}$.

The luminosity due to the extraction of the gravitational energy of accreting gas, L_{accr} , in both radio-quiet and radio-loud quasars has a different, linear, dependence on the black hole mass (Blandford 1990):

$$L_{\text{opt}} \approx L_{\text{accr}} \sim 1.3 \times 10^{46} \mathcal{M}_8 \frac{L_{\text{accr}}}{L_{\text{Edd}}} \text{ erg s}^{-1}.$$

We may identify L_{accr} with the optical-UV luminosity, with the x-ray luminosity in radio-quiet quasars, and with some part of the x-ray luminosity of radio-loud quasars, say a fraction f of L_{accr} : $L_{\text{xaccr}} = f L_{\text{accr}}$.

Comparing these two equations then defines a critical mass for radio-loud quasars at which L_{xem} equals L_{xaccr} . This mass is

$$\mathcal{M}_8 \sim \frac{f}{g} 13 \frac{L_{\text{accr}}}{L_{\text{Edd}}} \left(\frac{a}{m} \right)^{-2} B_4^{-2}.$$

We can now interpret the critical luminosity of $\log L_{\text{opt}} \sim 32-33 \text{ erg s}^{-1} \text{ Hz}^{-1}$ (Fig. 4) as corresponding to this critical mass for steep spectrum radio-loud quasars. For an Eddington limited source this corresponds to a black hole mass of $10^9-10^{10} \mathcal{M}_{\odot}$, since the luminosity per decade, $L_{\text{opt}} = 10^{47}-10^{48} \text{ erg s}^{-1}$.

Then,

$$\frac{f}{g} \sim 0.077 \mathcal{M}_8 \left(\frac{L_{\text{accr}}}{L_{\text{Edd}}} \right)^{-1} \left(\frac{a}{m} \right)^2 B_4^2 \sim 0.2-2,$$

if $a/m = 0.5$ and $L_{\text{accr}} = L_{\text{Edd}}$, i.e., g is the order of f .

f can be estimated from the α_{ox} measured in high z radio-quiet quasars. The observed α_{ox} of ~ 1.8 corresponds to a ratio of optical to x-ray luminosity per decade of ~ 100 , i.e., $f \sim 0.01$.

In this scenario the energy connected with the extraction of the black hole rotational energy is only inefficiently converted into x-ray photons, or into any photons at all. Thus, the bulk ($\sim 99\%$) of the power extracted from the spin of the black hole must go into kinetic energy of accelerated particles or be carried far away from the x-ray emission region by the electromagnetic field.

Following Blandford (1990), the lifetime of a quasar powered only by the extraction of the spin of the black hole is:

$$t_{\text{em},8} \approx 16.7 \mathcal{M}_8^{-1} B_4^{-2},$$

where t_8 is the time in units of 10^8 yr. For the range of masses we considered before we have $t_8=0.2-2$. This is actually a lower limit, since the accreting gas could deposit angular momentum into the black hole and spin it up. The corresponding accretion time scale, or Eddington, time is: $t_{\text{Edd},8} \approx 4$, so that $t_{\text{em},8} < t_{\text{Edd},8}$ for $M_8 > 4$. In this scenario some of the high luminosity radio-quiet quasars could be objects which were powerful radio sources in the past, but whose central black hole has in the meantime completely slowed down.

6. CONCLUSIONS

In summary, *ROSAT* PSPC colors of 17 high-redshift quasars show that the x-ray spectral properties of radio-loud and

radio-quiet quasars at $z \approx 3$ have evolved differently: *either* only radio-loud quasars show absorption, *or* only radio-quiet quasars change their emitted power law spectrum. This implies different changes in the environment or emission mechanism of the two types of quasar. Distinguishing the two spectral possibilities should be straightforward with more high energy measurements.

Some of the data reported in this paper came from the *ROSAT* data bank. This work was supported by NASA Grants NAGW-2201 (LTSARP), NAG5-1872, NAG5-1536, and NAG5-1680 (*ROSAT*), and NASA contracts NAS8-39073 (ASC) and NAS5-30934 (RSDC). This work was also supported by NSF Grants RII-8800660, INT-9010583, and AST-9058510, and a gift from Sun Microsystems.

REFERENCES

- Avni, Y., & Tananbaum, H. 1986, *ApJ*, 305, 83
 Bahcall, J., & Peebles, J. 1969, *ApJ*, 156, L7
 Baldwin, J. 1977, *MNRAS*, 178, 67P
 Band, D. L., Cohen, R. D., Blanco, P. R., Junkkarinen, V. T., Burbidge, E. M., Rothschild, R. T., & Reichert, G. A. 1994, in *Multi-Wavelength Continuum Emission of AGN*, edited by T. J.-L. Courvoisier and A. Blecha (Kluwer, Dordrecht), p. 318
 Bechtold, J., et al. 1994, *AJ*, 108, 374 (Paper II)
 Blandford, R. D. 1990, *Active Galactic Nuclei*, Saas-Fee Advanced Course 20, edited by T. J.-L. Courvoisier and M. Mayor (Springer, Berlin)
 Blandford, R. D., & Znajek, R. L. 1977, *MNRAS*, 179, 433
 Boyle, B. J., Fong, R., & Shanks, T. 1987, *MNRAS*, 227, 717
 Boyle, B. J., Griffiths, R. E., Shanks, T., Stewart, G. C., & Georgantopoulos, I. 1993, *MNRAS*, 260, 49
 Cavaliere, A., & Padovani, P. 1988, *ApJ*, 315, 411
 Chokshi, A., & Turner, E. L. 1992, *MNRAS*, 259, 421
 Elvis, M., Fiore, F., Wilkes, B. J., McDowell, J., & Bechtold, J. 1994, *ApJ*, 422 (Feb. 10) (in press) (Paper I)
 Fiore, F., Elvis, E., Siemiginowska, A., Wilkes, B. J., & McDowell, J. C. 1994, *ApJ* (submitted)
 Fink, H. H., & Briel, U. G. 1993, *A&A*, 274, L45
 Haardt, F., & Maraschi, L. 1993, *ApJ*, 413, 507
 Haehnelt, M. G., & Rees, M. J. 1993, *MNRAS*, 263, 168
 Henry, P., et al. 1994, *A. J.*, 107, 1270
 Hoag, A. A., & Smith, M. G. 1977, *ApJ*, 217, 362
 Laor, A., Fiore, F., Elvis, M., Wilkes, B. J., & McDowell, J. C. 1994, *ApJ* (submitted)
 Møllthagen, K., Wendker, H. J., & Briel, U. G. 1994, *A&A* (in press)
 Morrison, R., & McCammon, D. 1983, *ApJ*, 270, 119
 Netzer, H. 1990, *Active Galactic Nuclei*, Saas-Fee Advanced Course 20, edited by T. J.-L. Courvoisier and M. Mayor (Springer, Berlin)
 O'Dea, C. P., Baum, S. A., & Stanghellini, C. 1991, *ApJ*, 380, 66
 Osmer, P. 1977, *ApJ*, 214, 1
 Padovani, P., & Rafanelli, P. 1988, *A&A*, 205, 53
 Pearson, T. J., & Readhead, A. C. S. 1984, in *VLBI and Compact Radio Sources*, IAU Symposium No. 110 (Reidel, Dordrecht), p. 15
 Pfefferman, E., et al. 1987, *Proc. SPIE*, 733, 519
 Pickering, T., & Impey, C. 1994 (in preparation)
 Small, T., & Blandford, R. 1992, *MNRAS*, 259, 725
 Tananbaum, H., et al. 1979, *ApJ*, 234, L9
 Trümper, J. 1983, *Adv. Space Res.*, 2, 241
 Walter, R., & Fink, H. H. 1993, *A&A*, 274, 105
 Wandel, A., & Mushotzky, R. F. 1986, *ApJ*, 339, 674
 Wilkes, B. J., & Elvis, M. 1987, *ApJ*, 323, 243
 Wilkes, B. J., Tananbaum, H., & Worrall, D. M. 1994, *ApJS*, 92, 53
 Williams, O. R., et al. 1992, *ApJ*, 389, 157
 Worrall, D. M., Giommi, P., Tananbaum, H., & Zamorani, G. 1987, *ApJ*, 313, 596

DERIVING THE QUASAR LUMINOSITY FUNCTION FROM ACCRETION-DISK INSTABILITIES

ANETA SIEMIGINOWSKA AND MARTIN ELVIS

Harvard-Smithsonian Center for Astrophysics 60 Garden Street, MS-70, Cambridge, MA 02138; asiemiginowska@cfa.harvard.edu

Received 1997 January 24; accepted 1997 March 24

ABSTRACT

We have derived the quasar luminosity function assuming that the quasar activity is driven by a thermal-viscous unstable accretion disk around a supermassive black hole. The instabilities produce large amplitude, long-term variability of a single source. We take a light curve of a single source and calculate the luminosity function from the fraction of time it spends at each luminosity. Convolution with an assumed mass distribution we were able to fit well the observed optical luminosity function of quasars at four redshifts. As a result we obtain the evolution of the mass distribution between redshifts 2.5 and 0.5.

The main conclusions are as follows: (1) the quasar long-term variability due to the disk thermal-viscous instabilities provides a natural explanation for the observed quasar luminosity function; (2) the peak of the mass function evolves toward lower black hole masses at lower redshifts by a factor ~ 10 ; (3) the number of high-mass sources declines rapidly, so low-mass sources become dominant at lower redshift; (4) outbursts of activity appear as long as the matter is supplied to the accretion disk; (5) since the time-averaged accretion rate is low, the remnant sources (or sources in the low activity phase) do not grow into very massive black holes; and (6) a continuous fuel supply at a relatively low accretion rate ($\sim 0.01\text{--}0.1 \dot{M}_{\text{Edd}}$) for each single source is required over the lifetime of the entire quasar population.

Subject heading: accretion: accretion disks — cosmology: theory — quasars: general

1. INTRODUCTION

The quasar luminosity function has been studied for the last three decades and is observationally now quite well determined as a function of redshift for $z < 4$ (see, e.g., Boyle et al. 1991). However, there have been few attempts to derive the luminosity function from physical models of the quasar power engine. There are three possible phenomenological scenarios (Cavaliere & Padovani 1988): long-lived objects, recurrent objects (possibly related to galaxy mergers), and a single short event over the whole host galaxy lifetime. Continuous models imply masses for the remnant black holes that are too large, and accretion rates that are too low (Cavaliere et al. 1983; Cavaliere & Szalay 1986; Cavaliere & Padovani 1988, 1989; Caditz, Petrosian, & Wandel 1991).

Short-lived models have been studied more recently. Haehnelt & Rees (1993) assumed that new quasars were born at successive epochs with a short active phase followed by a rapid exponential fading because of exhaustion of fuel. They used the cold dark matter formalism (Press & Schechter 1974) to estimate the number of newly forming dark matter halos at different cosmic epochs. Small & Blandford (1992) suggested a scenario involving a mixture of continuous and recurrent activity. They assumed that newly formed sources achieve the Eddington luminosity quickly such that the accretion rate is limited by radiation pressure. The break in the luminosity function is related to the boundary between the continuous and intermittent accretion phases originating in the amount of fuel supply to the black hole.

However, none of these models relate directly to the physical processes responsible for powering a quasar. They simply invoke sources that emit at the Eddington luminosity for a certain time and then fade below an observational threshold. Here we describe a scenario which for the first time derives the luminosity function from a specific physical process.

The time evolution of an accretion disk around a supermassive black hole (the main components of the standard quasar paradigm) exhibits large variations on long timescales because of thermal-viscous instabilities (Siemiginowska, Czerny, & Kostyunin 1996, hereafter SCK96; Mineshige & Shields 1990). Depending on the assumed disk model, variations of up to a factor $\sim 10^4$ can be produced on timescales of $10^4\text{--}10^6$ years. Here, we assume that all quasars are subject to this variability. We then take the light curve of a single source and calculate the luminosity function of a population of identical sources from the fraction of time it spends at each luminosity. Convolution with an assumed mass distribution, we fitted the observed quasar luminosity function at four redshifts. As a result, we obtain the evolution of the mass distribution between redshifts 2.5 and 0.5.

2. EVOLUTION OF AN ACCRETION DISK

Accretion onto a supermassive black hole is the leading model for powering quasars (see, e.g., Rees 1984). The accretion process is frequently described using the model of a stationary thin disk (Lynden-Bell 1969; Shakura & Sunyaev 1973). However, there are both observational and theoretical arguments indicating that time-dependent effects in the accretion process are of extreme importance. Observationally, the evidence for global evolutionary effects is compelling in accretion disks around Galactic X-ray sources. Outbursts (by factors $> 10^4$) of cataclysmic variables or X-ray novae last for weeks or months and happen every few months to years. The outbursts are essentially caused by the disk thermal instability in the partial ionization zone (Meyer & Meyer-Hoffmeister 1982; Smak 1982; see also Cannizzo 1993 for review). There is a strong similarity between Galactic X-ray sources and active galactic nuclei (AGNs) both in spectral behavior and in overall variability (Fiore & Elvis 1997; Tanaka & Lewin 1995). This leads us to expect similar accretion-disk behavior.

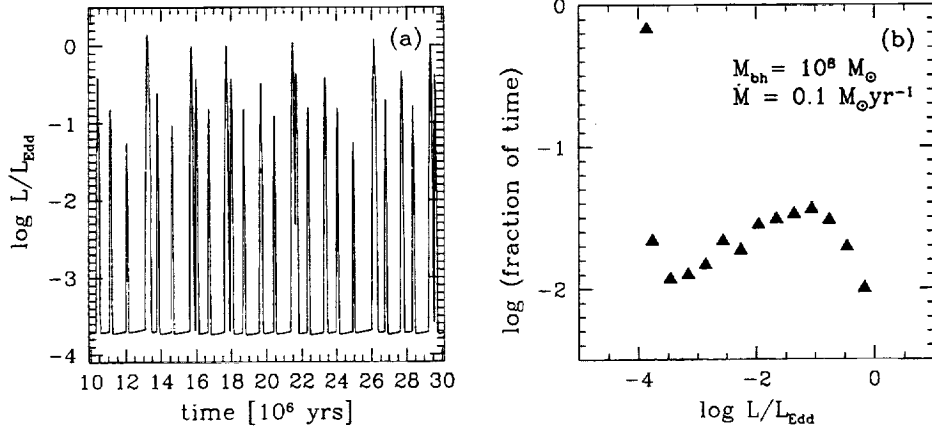


FIG. 1.—(a) Luminosity variations due to the disk instabilities around a black hole of $10^8 M_\odot$, when the accretion rate is $0.1 M_\odot \text{ yr}^{-1}$ and the viscosity parameter is different in the high and low states: $\alpha_{\text{hot}} = 0.1$ and $\alpha_{\text{cold}} = 0.025$. (b) Fraction of the time the source emits at a given luminosity for $10^8 M_\odot$ and $0.1 M_\odot \text{ yr}^{-1}$ accretion rate. The luminosity is given in the Eddington luminosity units.

However, since the characteristic timescales are roughly proportional to the central mass, the expected variability takes thousands to millions of years in AGNs. Since these timescales are not directly observable, these changes have been considered little more than a curiosity in AGNs.

Theoretically, accretion disks around the massive black holes in AGNs are expected to have a partial ionization zone, as in Galactic binaries, and therefore to be subject to the same instability (Lin & Shields 1986; Clarke 1989; SCK96).

Current models of the time evolution of accretion disks in AGNs have confirmed the presence of disk eruptions (Clarke & Shields 1989; Mineshige & Shields 1990; SCK96). SCK96 considered a geometrically thin Keplerian accretion disk around a supermassive black hole and assumed that the viscosity scales with the gas pressure ($\tau_{r\phi} = \alpha P_{\text{gas}}$). They found that, depending on the viscosity, the instability can either develop only in a narrow unstable zone, or can propagate over the entire disk resulting in large-amplitude optical/ultraviolet outbursts ($\sim 10^4$) (see Fig. 1a). The calculation of these light curves is at present computationally demanding (SCK96).

3. FROM LUMINOSITY VARIATIONS TO THE LUMINOSITY FUNCTION

3.1. A Single-Mass, Single-Accretion-Rate Population

The luminosity function of a population of quasars with the same mass and accretion rate is given simply by the product of a fraction of time one source spends in each luminosity bin and their space density. In Figure 1b we show the fraction of time a source emits at each luminosity, relative to the Eddington luminosity, for the light curve shown in Figure 1a. The luminosity range is between $10^{-4} L_{\text{Edd}}$ and L_{Edd} . The shape of the function reflects the fact that the amplitude of each outburst is not constant, and the variability is not precisely periodic. The details of each outburst and the overall variability characteristics depend on the physics of the accretion disk and the assumptions of the model. These details average over many outbursts (usually a few hundred over 10^8 – 10^9 years).

A single source will spend about $\sim 75\%$ of its life in quiescence ($L < 0.001 L_{\text{Edd}}$) and about $\sim 25\%$ in an active state, with $\sim 10\%$ in a high state ($L > 0.1 L_{\text{Edd}}$). Likewise, in a population $\sim 10\%$ of sources will be in the high state, $\sim 25\%$ will be active and $\sim 75\%$ will be in quiescence at any given time.

There are two characteristic transition points in the function shown in Figure 1b: a broad maximum at $\sim 0.1 L_{\text{Edd}}$ and a minimum at $\sim 0.001 L_{\text{Edd}}$. When we construct a luminosity function for a realistic population, these features will be modified by the distribution of accretion rates and masses. A range of accretion rates affects the low luminosity part of the curve by smoothing at the minimum. The maximum at $\sim 0.1 L_{\text{Edd}}$ is caused by the fraction of outburst amplitudes reaching close to the Eddington luminosities. The maximum is thus smoothed by the distribution of black hole masses.

3.2. Fit to the Observed Luminosity Function

The luminosity in Figure 1b is expressed in terms of the Eddington luminosity, in order to make the function independent of the central mass (see the “single-mass” luminosity function in Fig. 2a). Thus, for a given distribution of black hole masses, we can calculate the quasar luminosity function. The luminosity function is defined as:

$$\Phi(L, z) = \int \Phi(L, z, M) N(M, z) dM, \quad (1)$$

where $\Phi(L, z, M)$ describes which central mass contributes to a given luminosity bin at a given redshift, and $N(M, z)$ represents a number of sources with a given central mass at a given redshift. The mass density function $[N(M, z)M]$ can be derived, with assumptions, from cosmological models and theoretical models on the formation of structures in the universe (Heahnel & Rees 1993; Small & Blandford 1992). Here we do not consider any particular model for the formation of the black holes, galaxies, and quasars. Instead we assume, arbitrarily, that $N(M, z)$ can be represented by a simple parabola. We then fitted the observed luminosity function from Boyle et al. (1991) at different epochs varying the peak, position, and width of the parabola. The mass function is convolved with the single-mass luminosity function (Fig. 1b). We held \dot{M} constant and so did not change the minimum in Figure 1b. However, this minimum is not within the range covered by the Boyle et al. (1991) data.

We were able to obtain good fits (Table 1) to the luminosity function at three of four redshifts, as shown in Figure 2a. The black hole mass density function required by the fit is plotted in Figure 2b, and the parameters of the fit are given in the

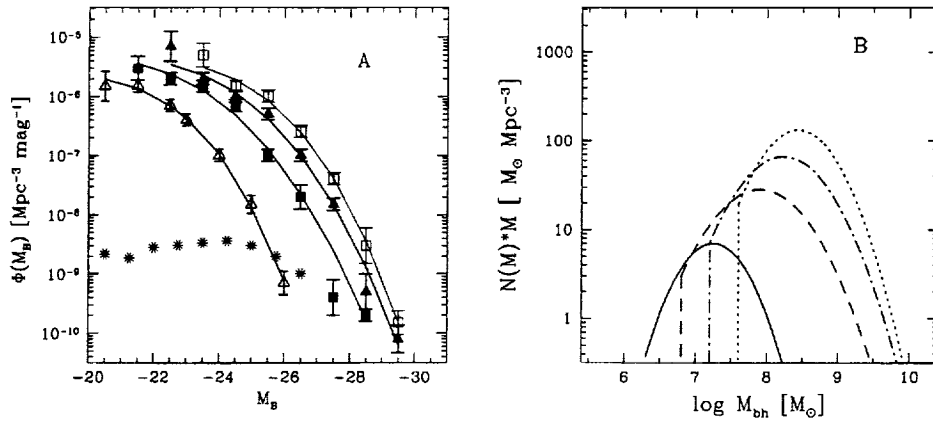


FIG. 2.—(a) Observed luminosity function (Boyle et al. 1991) at four redshifts indicated by points with error bars: $0.25 < z < 0.75$ (open triangles), $0.75 < z < 1.25$ (filled squares), $1.25 < z < 2.00$ (filled triangles), $2.00 < z < 2.90$ (open squares). The predicted single-mass luminosity function is indicated with the stars. The model luminosity function is plotted with the solid line. (b) The predicted black hole mass density function at each epoch obtained from the fit to the observed luminosity function: $0.25 < z < 0.75$ (solid line); $0.75 < z < 1.25$ (dashed line); $1.25 < z < 2.00$ (dash-dotted line); $2.00 < z < 2.90$ (dotted line). The truncation at the mass required by the lowest luminosity data point is indicated by the straight lines at the lowest mass point for each parabola.

Table 1. The poor fit at redshift ~ 1 is due to the highest luminosity point, which seems to require a kink in the luminosity function. We fitted the data excluding this point and obtain a good fit (Table 1). The mass density peaks at lower mass in this case, since the luminosity function ends at lower luminosity.

Only active sources contribute to the black hole mass density function. The maximum indicates which central black hole mass dominates the population at each redshift. This peak mass declines from $\sim 2 \times 10^7 M_\odot$ at $z \sim 2.5$, to $\sim 2 \times 10^6 M_\odot$ at $z \sim 0.5$ with most of the change occurring between $z \sim 1.75$ and $z \sim 1$ (Table 1). The mass density of high-mass sources gets smaller rapidly (e.g., a factor ~ 100 at $M = 10^9 M_\odot$) with lower redshift, while the peak mass density declines by less than a factor 2. The relative constancy of this peak implies that the number of sources at the peak remains constant between $z = 2.5$ and $z = 1$, and then decreases by a factor of ~ 2 between redshift $z = 1$ and $z = 0.5$. The low-mass end of the distribution is not constrained by the data, so we truncate the functions at the mass where the Eddington limit gives the lowest observed luminosity. This lowest luminosity point of the observed luminosity function at $z = 2.5$ ($L_{\text{Edd}} \sim 8 \times 10^{44} \text{ ergs s}^{-1}$) gives the limit of $6.3 \times 10^7 M_\odot$. Even if less massive sources are present in the population, we cannot see them.

4. DISCUSSION

We have shown that the thermal-viscous instability provides a natural mechanism to generate the quasar luminosity func-

tion. We were able to fit the observed luminosity function and estimate the parameters of the mass density function, independent of cosmological models.

The overall shape of the mass density function and the evolution of the peak of the mass distribution toward lower masses with lower redshift are similar to the results obtained by previous studies (Haehnelt & Rees 1993; Small & Blandford 1992). The 30% ON fraction in these models is also comparable with the fraction of active time input light curve (Fig. 1b). This is not too surprising, because the same observational luminosity function was used in all the studies.

The problem of whether the low-mass sources are present at high redshift or are born subsequently remains unsolved. In our scenario this question could be answered by extending the observed luminosity function at $z \gtrsim 1$ fainter by $\Delta m \sim 3$. If the fitted mass functions match the low z mass density functions, this would suggest that all quasars are born at the same time and that the high-mass ones “burn out” much more quickly. This scenario, in which single mass density function declines more rapidly at high luminosities, is strikingly different from the conventional “pure luminosity evolution” that is used to describe the apparent fading of the whole observed luminosity function to lower z . It reminds us of the warning by Green (1985) against interpreting phenomenological descriptions as physically meaningful.

Looking at the sources in the present epoch should provide the information on the lowest luminosity end of the distribution together with the contribution of the massive sources. However, the luminosity of the host galaxy becomes comparable to the nuclear luminosity for a low-mass black hole, and it is hard to observe the nucleus of a normal galaxy even if it contains an accretion disk in the active state ($L \sim L_{\text{Edd}}$). On the other hand, Seyfert nuclei are found in $\sim 10\%$ of galaxies, consistent with the high state fraction from SCK96. The problem is how can we see low-mass sources in quiescence.

The high-luminosity end of the luminosity function accounts for all the high-mass sources which are active at each epoch. The number of these sources gets smaller with redshift. This decrease is often supposed to relate to the limited fuel supply and the mechanisms of transfer of the matter into the disk. We note, though, that the location and the size of the ionization zone depends on the accretion rate onto the outer edge of the

TABLE 1
RESULTS OF THE MODELING

| Redshift (z) | $\log M_{\text{peak}}$ | $\log N(M_{\text{peak}})$ | χ^2 |
|---------------------|------------------------|---------------------------|-------------------|
| 2.0–2.9 | 8.1 | –5.30 | 2.78 |
| 1.25–2.0 | 7.7 | –5.33 | 4.98 |
| 0.7–1.25 | 7.3 | –5.34 | 12.79 |
| 0.3–0.7 | 6.9 | –5.38 | 3.48 ^a |
| 0.3–0.7 | 6.9 | –5.52 | 1.18 |

^a Excluding the highest luminosity data point at redshifts $0.7 < z < 1.25$.

disk (SCK96; Clarke & Shields 1989). For high accretion rates, this zone moves toward the outer regions of the accretion disk. In the case of the high-mass black holes, the ionization zone can be pushed out to the self-gravitating regions of the disk, and the instability will not develop. The source then remains in the active state until its fuel supply is exhausted and then dies.

Another consideration that could lead to the more rapid demise of high-mass quasars is that massive sources require more fuel than low-mass sources to emit at a given L/L_{Edd} . Only $\sim 0.0027 M_{\odot} \text{ yr}^{-1}$ is needed to power a $10^6 M_{\odot}$ black hole at $0.1 M_{\text{Edd}}$, while a $10^9 M_{\odot}$ black hole requires accretion rates of order $2.7 M_{\odot} \text{ yr}^{-1}$. Recent studies of quasar host galaxies (at $z < 0.3$) show that the most luminous quasars reside in the most massive galaxies, while lower luminosity quasars can be found in any type of a galaxy (McLeod & Rieke 1995a, 1995b; Bahcall et al. 1997). Based on the *HST* observations of 61 elliptical galaxies, Faber et al. (1996) conclude that about $\sim 1\%$ of the galaxy mass is contained within a central core of few parsecs. This means that for a typical $\sim 10^{11}$ – $10^{12} M_{\odot}$ galaxy, there is about 10^9 – $10^{10} M_{\odot}$ available to feed a black hole. While at $10^6 M_{\odot}$ it would last for 10^{11} – 10^{12} years, at $10^9 M_{\odot}$ it would last for 10^9 years at $0.1 M_{\text{Edd}}$.

A third possibility is that the (unknown) mechanism responsible for transferring the matter toward the central potential well and into the outer parts of accretion disks becomes rapidly less efficient in massive systems, so they would systematically die young.

Recently Yi (1996) considered the cosmological evolution of quasars, assuming that advection becomes important for accretion rates below a $0.01 L_{\text{Edd}}$ accretion rate. The theoretical and observational studies of the X-ray transients suggest that advection is important in quiescence below a critical accretion rate (Narayan & Yi 1994; Narayan, McClintock, &

Yi 1996). Advection has not been included in our accretion-disk model. It will modify the low-luminosity part of the light curve in Figure 1a and influence the quasar evolution. We shall include the advection in our further studies, since the quasar remains in quiescence for $\sim 75\%$ of its life.

In previous studies the sources making up the luminosity function were assumed to begin by emitting at their Eddington luminosities and steadily become fainter with time. This does not apply in our model. The stationary accretion rate onto the outer edge of the disk can be much lower than the Eddington limit. This prevents accumulation of a large mass in the center and removes the problem of creating overly massive quasar remnants.

Small & Blandford (1992) suggested two phases of the quasar activity, which are related to the accretion rate. Just after a black hole is born the matter is supplied at super-Eddington rates, but the actual accretion onto the black hole is limited by the radiation pressure. The black hole accretes continuously at the Eddington rate until the fuel supply gets lower, and then the accretion becomes intermittent. The intermittent activity can be related to the active state of the disk in our scenario.

The model we use to produce the quasar luminosity function works for the optical/ultraviolet bands. The radio and X-ray luminosity function show similar form and evolution (Maccararo et al. 1992; Della Ceca et al. 1994). Physically the radio and X-ray luminosities must then be a result of the accretion-disk state.

We thank Bożena Czerny, Andrzej Soltan, Tom Aldcroft, Kim McLeod, Pepi Fabbiano, and Avi Loeb for valuable discussions. We also thank the anonymous referee for useful comments. This work was supported by NASA Contract NAS8-39073 (ASC) and NASA grant NAG5-3066 (ADP).

REFERENCES

- Bahcall, J. N., Kirhakos, S., Saxe, D. H., & Schneider, D. P. 1997, *ApJ*, 479, 642
 Boyle, B. J., et al. 1991, in *ASP Conf. Ser. 21, The Space Distribution of Quasars*, ed. D. Crampton (San Francisco: ASP), 191
 Caditz, D. M., Petrosian, V., & Wandel, A. 1991, *ApJ*, 372, L63
 Cannizzo, J. K. 1993, in *Accretion Disks in Compact Stellar Systems*, ed. J. C. Wheeler (Singapore: World Scientific), 6
 Cavaliere, A., Giallongo, E., Messina, A., & Vagnetti, F. 1983, *ApJ*, 269, 57
 Cavaliere, A., & Padovani, P. 1988, *ApJ*, 333, L33
 ———. 1989, *ApJ*, 340, L5
 Cavaliere, A., & Szalay, A. S. 1986, *ApJ*, 311, 589
 Clarke, C. J. 1989, *MNRAS*, 235, 881
 Clarke, C. J., & Shields, G. A. 1989, *ApJ*, 338, 32
 Della Ceca, R., Zamorani, G., Maccararo, T., Wolter, A., Griffiths, R., Stocke, J. T., & Setti, G. 1994, *ApJ*, 430, 533
 Faber, S. M., et al. 1996, *AJ*, submitted
 Fiore, F., & Elvis, M. 1997, *Adv. Space Res.*, 12(1), 85
 Green, R. F. 1986, in *IAU Symp. 119, Quasars*, ed. G. Swarup & V. K. Kapahi (Dordrecht: Reidel), 429
 Haehnelt, M. G., & Rees, M. J. 1993, *MNRAS*, 263, 168
 Lin, D. N. C., & Shields, G. A. 1986, *ApJ*, 305, 28
 Lynden-Bell, D. 1969, *Nature*, 223, 690
 Maccararo, T., Della Ceca, R., Gioia, I. M., Stocke, J. T., & Wolter, A. 1992, in *X-ray Emission from AGN and Cosmic X-ray Background*, ed. W. Brinkmann & J. Trümper (Garching: MPI), 291
 McLeod, K. K., & Rieke, G. H. 1995a, *ApJ*, 454, L77
 ———. 1995b, *ApJ*, 441, 96
 Meyer, F., & Meyer-Hoffmeister, E. 1982, *A&A*, 106, 34
 Mineshige, S., & Shields, G. A. 1990, *ApJ*, 351, 47
 Narayan, R., McClintock, J. E., & Yi, I. 1996, *ApJ*, 457, 821
 Narayan, R., & Yi, I. 1994, *ApJ*, 428, L13
 Press, W. H., & Schechter, P. L. 1974, *ApJ*, 187, 425
 Rees, M. Y. 1984, *ARA&A*, 22, 471
 Shakura, N. I., & Sunyaev, R. A. 1973, *A&A*, 24, 337
 Siemiginowska, A., Czerny, B., & Kostyunin, V. 1996, *ApJ*, 458, 491 (SCK96)
 Smak, J. I. 1982, *Acta Astron.*, 32, 199
 Small, T. A., & Blandford, R. D. 1992, *MNRAS*, 259, 725
 Tanaka, Y., & Lewin, W. H. G. 1995, in *X-ray Binaries*, ed. W. H. G. Lewin, J. van Paradijs, & E. P. J. van den Heuvel (Cambridge: Cambridge Univ. Press), 126
 Yi, I. 1996, *ApJ*, 473, 645

X-RAY CONSTRAINTS ON THE INTERGALACTIC MEDIUM

THOMAS ALDCROFT, MARTIN ELVIS, JONATHAN McDOWELL, AND FABRIZIO FIORE¹

Harvard-Smithsonian Center for Astrophysics, 60 Garden Street, Cambridge, MA 02138

Received 1994 April 5; accepted 1994 June 23

ABSTRACT

We use *ROSAT* PSPC spectra of $z \approx 3$ quasars to constrain the density and temperature of the intergalactic medium (IGM). Strong low-energy cutoffs in PSPC spectra of high-redshift quasars are common. However, the absence of absorption toward some high-redshift quasars can be used to put limits on the possible cosmological density, Ω_G , of a hot diffuse IGM, via an X-ray “Gunn-Peterson” test using edge and line opacity in the soft X-rays. The K-edges of oxygen, neon, and carbon and the L-edge of iron produce most of the absorption which is spread out by the redshift of the source. We assume an isotropic, isothermal, non-evolving model of the IGM and calculate the optical depth of this absorption. We find that this test can constrain an enriched IGM at temperatures near 10^5 – 10^6 K, intermediate between the hot IGM ruled out by *COBE*, and the cold IGM ruled out by the traditional Ly α Gunn-Peterson test. Photoionization of the IGM by the ultraviolet and X-ray background has a large effect. We give results for three $z \approx 3$ quasars and discuss how the various trade-offs among temperature, abundance, and background radiation strength affect the limits on Ω_G . In addition to the high-redshift case, we discuss techniques for constraining the IGM using X-ray spectra of low-redshift quasars ($z \approx 0.1$ – 0.3). Currently available X-ray spectral data have insufficient energy resolution to constrain the IGM unambiguously, and so expected detection limits for future high-resolution spectrometers are presented. We find that with a large effective area (~ 2000 cm²), it is possible to substantially constrain or detect the IGM at the densities which are typically predicted.

Subject headings: intergalactic medium — quasars: absorption lines — quasars: general — X-rays: galaxies

1. INTRODUCTION

For some time there has been indirect evidence which indicates the existence of a diffuse intergalactic medium (IGM). The most compelling pieces of observational evidence are the detection of X-ray-emitting gas in galaxy clusters, and the Ly α forest clouds which are seen in the spectra of high-redshift QSOs. Both of these are a direct demonstration that a significant amount of matter exists in the universe which is not condensed into galaxies. In both cases as well, plausible models explaining the phenomena would point to the existence of an IGM. In the case of the cluster gas, it is found that the gas is highly enriched, and one possible mechanism explaining this is the ejection of processed gas by supernova explosions (e.g., Sarazin 1988). The same process could take place in noncluster galaxies, which would return the enriched gas to the IGM. In fact, recent numerical simulations of CDM cosmological models find that feedback of energy due to supernovae in forming galaxies can successfully reionize the IGM (Cen & Ostriker 1993, hereafter CO93; Shapiro, Giroux, & Bubul 1994, hereafter SGB). CO93 find that this energy in the form of galactic superwinds can produce a “warm” IGM by heating over 30% of the intergalactic material to temperatures of 10^5 – 10^6 K. In the case of the Ly α forest clouds, one of the most natural models which explains their stability relies on pressure confinement from a hot diffuse IGM (Sargent 1988 and references therein).

Other theoretical evidence for the IGM comes from studies of galaxy formation, which generally predict that a significant fraction of the baryonic mass in the universe should remain in

the form of a diffuse IGM (Ikeuchi & Ostriker 1986; Shapiro 1989; CO93; SGB). For example, the numerical simulations of SGB reveal that at the very least 20% of the initial baryonic mass is left in the IGM after the epoch of galaxy formation, and for reasonable reionization schemes the fraction is 50%–90%. The simulations of SGB and CO93 both imply an IGM density in the neighborhood of $\Omega_G \approx 0.02$ and temperature $T \approx 10^5$ – 10^7 K.

Despite the evidence that a diffuse IGM should exist, there still has been no direct detection, nor have the basic properties of the medium such as temperature, density, and chemical composition been strongly constrained. Early efforts to detect the IGM or constrain its properties are summarized in Shapiro & Bahcall (1982, hereafter SB). The most sensitive tests to date are the high-temperature limit based on the distortion of the cosmic microwave background spectrum (the Compton y -parameter) as measured by the *COBE* satellite (Mather et al. 1994), and the low-temperature limit based on the Ly α Gunn-Peterson test (Giallongo, Cristiani, & Trevese 1992 & Peterson 1965). The latter test is based on the fact that neutral hydrogen in the IGM can cause absorption in the spectrum of a QSO blueward of the Ly α emission line. The limit on absorption optical depth is converted into a constraint on the temperature and density of the IGM by determining the neutral hydrogen fraction, assuming ionization equilibrium. The *COBE* and Ly α Gunn-Peterson limits are shown in Figure 1. We also show for comparison the limit on density based on the standard model of big bang nucleosynthesis $\Omega_b < 0.026 h_{100}^{-2}$ (Kolb & Turner 1990), and well as the predicted temperature and density of the IGM based on the simulation of CO93. Finally, we show the best-fit values for the IGM if the X-ray background were entirely due to thermal free-free emission in a hot IGM (Field & Perrenod 1977). These values are excluded by the *COBE*

¹ Present address: Osservatorio Astronomico di Roma, via dell'Osservatorio, 5, Monteporzio-Catone (Rm), I-00040 Italy.

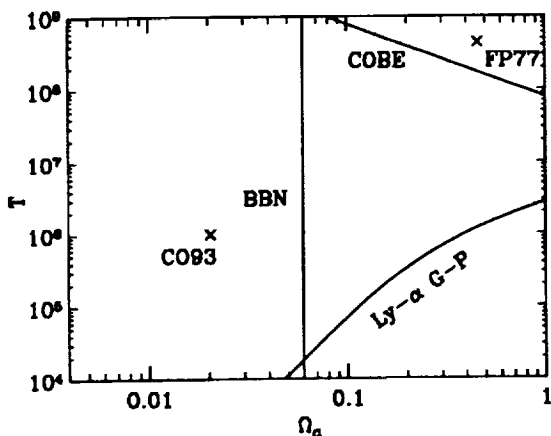


FIG. 1.—Current observational limits on the density and temperature of the IGM. The BBN line is the upper limit for baryonic mass based on standard big bang nucleosynthesis and $H_0 = 75 \text{ km s}^{-1} \text{ Mpc}^{-1}$. The temperature and density of the IGM calculated by CO93 and Field & Perrenod (1977; FP77) are marked.

limit. We see that there is a large range of temperature and density which is unconstrained by the current tests. In particular, the interesting region with $T \approx 10^5\text{--}10^6 \text{ K}$ and IGM density $\Omega_g \approx 0.01\text{--}0.1$ has not been probed.

It was realized when quasars were detected in the X-ray band that a Gunn-Peterson test using the X-ray transitions in heavy elements might constrain the IGM at higher temperatures than the original Ly α Gunn-Peterson test (SB; Sherman & Silk 1979; Sherman 1979). These transitions occur even in the highly ionized species which dominate in plasmas at temperatures between 10^4 to 10^8 K . SB calculated the total absorption optical depth to X-rays due to line and edge transitions and found substantial absorption for high-redshift sources over a wide range of interesting temperatures and densities. However, their calculations did not include the effect of the ionizing background radiation which is now known to exist. We find that this radiation strongly affects the ionization equilibrium and can significantly lower the X-ray opacity of the IGM.

In addition to theoretical advances, the quasar X-ray spectra which were available at the time of SB were inadequate to usefully apply their calculations, both because there were too few counts and the energy resolution was too low. The *ROSAT* mission (Trümper 1983) now provides an opportunity to set limits on the IGM because its high sensitivity in the soft X-ray range allows high-redshift quasars to be detected down to $\sim 0.1 \text{ keV}$ (observed frame). Moreover, the Position Sensitive Proportional Counter (PSPC; Pfefferman et al. 1987) has sufficient spectral resolution to allow several parameter fits for spectra containing a few hundred counts (see, e.g., Fiore et al. 1993). High signal-to-noise ratio observations of high-redshift quasars with the *ROSAT* PSPC have revealed that some of these quasars can be well fitted in the soft X-ray band with only a single power law and Galactic absorption. This lack of observed X-ray absorption in the IGM can be used to constrain the temperature, density, and heavy-element abundance of the IGM.

In this paper we explore the limits which can be placed on the IGM using the X-ray Gunn-Peterson test at high redshift ($z \approx 3$) and at low redshift ($z \lesssim 0.4$). In § 2 we explain the calculational details and assumptions used for determining the

X-ray optical depth due to the IGM out to a certain redshift, at a particular temperature and density. In § 3, we use *ROSAT* PSPC spectra of three high-redshift quasars to set observational constraints on the IGM. Section 4 discusses detection limits for the IGM using high-energy resolution ($E/\Delta E \gtrsim 100$) observations of low-redshift quasars.

2. X-RAY OPACITY OF IGM

The total absorption optical depth due to a column of intergalactic material out to a quasar redshift z_q is calculated by summing the optical depth of each small pathlength to the quasar. Since the contribution from each pathlength is effectively redshifted (because the transmitted photons are redshifted), summing the parts amounts to smearing the rest-frame optical depth over frequency. The equation describing this is

$$\tau_\nu = \int_0^{z_q} \kappa_\nu(z) |v(1+z)| \frac{dl}{dz} dz, \quad (1)$$

where $\kappa_\nu(z)$ is the gas opacity of material at redshift z , evaluated at the frequency $\nu(1+z)$, and $dl/dz = cH_0^{-1}(1+z)^{-2}(1+\Omega_0 z)^{-1/2}$ for the standard Friedmann cosmology. The opacity $\kappa_\nu(z)$ is a function of the gas density, the element abundances, and the ionization state of the elements at each redshift. If we make the assumption that ionization equilibrium holds (discussed in § 2.5), then the ionization state is determined by the element abundances, the gas temperature and density, and the ionizing background radiation.

We now discuss in §§ 2.1–2.5 the assumptions and calculational details which enter into evaluating equation (1).

2.1. Physical Model of IGM

Because very little is known about the physical conditions of the IGM, in our calculations we adopt a model with the simplest possible assumptions: the IGM is isotropic, with density $n(z) = n_0(1+z)^3$; and the heavy element abundances $A(Z)$ (relative to hydrogen, for atomic element Z) and temperature T are independent of redshift. These conditions correspond to isothermal, no-evolution expansion of the IGM. The approximation that the IGM expands isothermally is more accurate than one might initially suppose, according to the simulations of CO93. They find that the energy input from supernova superwinds keeps the IGM temperature in the range $10^5\text{--}10^6 \text{ K}$ after $z \approx 4$. For the heavy element abundances $A(Z)$ we consider only two possibilities, that of uniform depletion from the “cosmic” abundances of Cameron (1973), and that of a primordial composition with negligible heavy elements. In subsequent discussion, we denote the heavy element abundance by m , where m is the numerical value of the depletion. In the case of primordial abundances, we use $m = 0$. Note that all of the calculations are done for two values of the total mass density, $\Omega_0 = 0.2$ and $\Omega_0 = 1$, with Hubble constant $H_0 = 75 \text{ km s}^{-1} \text{ Mpc}^{-1}$ (or $h_{100} = 0.75$) throughout.

2.2. Background Radiation

Because of the very low particle densities ($n \approx 10^{-6} \text{ cm}^{-3}$ for $\Omega_g = 1$) in models of the IGM, the ionizing background radiation can be an important factor in determining the ionization equilibrium. Since we are interested in the equilibrium of highly ionized heavy elements, we need an estimate of the

background radiation spectrum covering the UV-to-soft X-ray energy band.

The UV background radiation is best measured by means of the Ly α proximity effect, which is the observed decrease in the density of Ly α forest clouds near the QSO redshift (Bechtold 1994; Fall & Pei 1993; Bajtlik, Duncan, & Ostriker 1988; Bechtold et al. 1988; Murdoch et al. 1986). The UV background radiation determined by this method is generally taken to have the power-law form

$$J_\nu(z) = 10^{-21} J_{21} \left(\frac{1+z}{1+z_q} \right)^\beta \left(\frac{\nu}{\nu_{LL}} \right)^{-\alpha} \text{ ergs s}^{-1} \text{ cm}^{-2} \text{ Hz}^{-1} \text{ sr}^{-1}. \quad (2)$$

Here J_{21} is the dimensionless strength, z_q is the redshift at which the proximity effect is observed, ν_{LL} is the frequency at the hydrogen Lyman limit, and β characterizes the redshift evolution. Based on the range of parameter values found in the literature (which are generally in rough agreement but often formally inconsistent), we use the values $\beta = 4$, $\alpha = 1.5$, and $z_q = 2.5$. The strength J_{21} of the background radiation is uncertain by about a factor of 10, so we do all calculations for two values, $J_{21} = 1.0$ and $J_{21} = 0.1$. An evolution of the background in which $\beta = 3-5$ for $z < 2$ (Stanek 1992; Ikeuchi & Turner 1991) and $J_\nu(z)$ is constant for $z > 2$ is probably more realistic; however, in these scenarios the radiation strength differs from the value we have used by less than about a factor of 5. This is comparable to the uncertainty in the radiation strength itself, and so our conclusions would be unchanged if we used this evolution.

The soft X-ray background radiation has been directly measured in the range 0.5–3.5 keV by Wu et al. (1991) using the *Einstein Observatory* IPC, and in the range 0.1–2.4 keV by Hasinger, Schmidt, & Trumper (1991) with the *ROSAT* PSPC. These measurements are at zero redshift, so in our calculations we have assumed the same redshift evolution as the UV background, namely $J_\nu(z) \propto (1+z)^4$. Connecting the UV and soft X-ray components together by power-law extrapolation gives the ionizing background which we use calculating the ionization equilibrium. Note that the relative normalization of the components of the background spectrum is determined for $J_{21} = 1.0$, and stays fixed for different values of J_{21} . This means the entire spectrum is scaled, not just the UV component.

2.3. Contributions to Opacity

The dominant processes contributing to the opacity k_ν in equation (1) are atomic line transitions, bound-free (continuum) transitions, and electron Compton scattering. For our purposes the latter process can be ignored because for photon energies much less than 500 keV the cross section is independent of energy. This means the absorption is not detectable without a priori knowledge of the intrinsic quasar luminosity.

Following the discussion in SB, the opacity due to an atomic line transition in a particular ion of an element can be written

$$\kappa_\nu^{\text{line}} = n_{\text{abs}} \frac{\pi e^2}{m_e c} f_{12} \delta(\nu - \nu_a),$$

where n_{abs} is the density of the ion, f_{12} is the oscillator strength of the transition, ν_a is the transition frequency, and $\delta(x)$ is the

Dirac delta function with $\int \delta(x) dx = 1$. If we insert this formula into equation (1) we get the result

$$\begin{aligned} \tau_\nu^{\text{line}} &= 0.94 \left(\frac{1 \text{ keV}}{E_a} \right) f_{12} \Omega_G \left[\frac{A(Z)}{10^{-4}} \right] y(Z, \xi) \left(\frac{\nu_a}{\nu} \right)^2 \\ &\times \left(1 - \Omega_0 + \Omega_0 \frac{\nu_a}{\nu} \right)^{-1/2} \text{ for } \nu_a(1+z)^{-1} \leq \nu \leq \nu_a \\ &= 0 \text{ for } \nu < \nu_a(1+z)^{-1} \text{ or } \nu > \nu_a, \end{aligned} \quad (3)$$

where E_a is the line energy, Ω_G is the fraction of the critical density in the IGM, and $y(Z, \xi)$ is the normalized population of the ionic level ξ . To calculate the total optical depth due to lines, we use equation (3), with the ion populations $y(Z, \xi)$ determined by the CLOUDY (Version 84.09) program (Ferland 1993) and the oscillator strengths and line energies as given in Kato (1976).

The continuum or edge opacity due to photoionization can be approximated by

$$\begin{aligned} \kappa_\nu^{\text{edge}} &= n_{\text{abs}} \sigma_{\text{th}} (\nu_{\text{th}}/\nu)^3 \quad (\nu \geq \nu_{\text{th}}) \\ &= 0 \quad (\nu < \nu_{\text{th}}), \end{aligned} \quad (4)$$

where ν_{th} is the frequency of the photoionization threshold and σ_{th} is the cross section at the threshold. In theory we can sum the opacity from equation (4) for all the elements and ions, but in practice this is done automatically by CLOUDY and we simply insert the total opacity returned by CLOUDY into equation (1).

2.4. CLOUDY

To evaluate the opacity and ionization equilibrium as a function of redshift equation (1), we use the CLOUDY program. The temperature of the gas is fixed, and no attempt is made to balance heating and cooling. Instead, the gas is assumed to be heated by some unspecified mechanism to the given temperature. One means for this heating could be shocks from supernova-driven superwinds (e.g., SGB; CO93). Note that the ionizing background radiation alone is insufficient to heat the gas to the temperatures we are considering (Miralda-Escudé & Rees 1994).

The parameters which we input to CLOUDY for calculating the opacity and ionization state are the density, temperature, abundances, and background radiation. We can reduce the total number of calculations required to constrain the IGM properties by taking advantage of the homology relation which applies for particle densities $n \lesssim 10^3 \text{ cm}^{-3}$,

$$\frac{\kappa_\nu(n_1, U)}{n_1} = \frac{\kappa_\nu(n_2, U)}{n_2},$$

where U is the ionization parameter. This gives

$$\begin{aligned} \kappa_\nu[n(z), J_\nu(z), T, m] \\ &= \kappa_\nu[\Omega_G Y n_c (1+z)^3, J_\nu(0)(1+z)^4, T, m] \\ &= \kappa_\nu \left[Y n_c, J_\nu(0) \frac{(1+z)}{\Omega_G}, T, m \right] \Omega_G (1+z)^3. \end{aligned}$$

Here $n_c = 3H_0^2/8\pi G m_p = 11.2 \times 10^{-6} h_{100}^2 \text{ cm}^{-3}$ is the critical baryon density. The hydrogen density is related to the baryon density by $n_0 = \Omega_G Y n_c$, where $Y = 0.76$ is the fraction of baryons in hydrogen. The above equation shows that the computationally difficult part of the opacity calculation depends

only on the two quantities $(1+z)\Omega_G^{-1}$ and T , not on all three variables z , Ω_G , and T . In addition to reducing computation time, use of the homology relation is in fact necessary because CLOUDY is numerically unable to do calculations at the very low densities of the IGM. The actual computations in CLOUDY are all done at a fixed density of 10^{-4} cm^{-3} .

2.5. Ionization Equilibrium

An important assumption which is implicit in our calculation is that ionization equilibrium is established at all epochs. At the very low densities characteristic of the IGM, this assumption requires careful evaluation, in particular for the ionized heavy elements which are responsible for the X-ray opacity. For hydrogen, it is well known that at typical IGM densities and temperatures, the H II recombination timescale can easily be greater than the Hubble time (e.g., Ikeuchi & Ostriker 1986). However, for our purposes this is not a problem because in calculating the ionization state of the heavy elements, we only need to know that the hydrogen is very nearly 100% ionized. Thus the assumption of ionization equilibrium for the heavy elements rest only on their recombination rate coefficients. The two most important processes are radiative recombination and dielectronic recombination. These two rates can be approximated over the temperature range 10^4 – $10^{7.5}$ K by the following formulae (Shull & Van Steenberg 1982):

$$\alpha_{\text{rad}}(T) = A_{\text{rad}}(T/10^4 \text{ K})^{-\chi_{\text{rad}}} \quad (5)$$

$$\alpha_{\text{di}}(T) = A_{\text{di}} T^{-3/2} \exp(-T_0/T)[1 + B_{\text{di}} \exp(-T_1/T)] \quad (6)$$

The coefficients A_{rad} , χ_{rad} , A_{di} , B_{di} , T_0 , and T_1 for each ionization level of the elements C, N, O, Ne, Mg, Si, S, Ar, Ca, Fe, and Ni have been tabulated by Shull & Van Steenberg, based on theoretical and experimental results.

Using equations (5) and (6) we can calculate the recombination timescale of each element and ionic level at redshift z and compare this to the age of the universe at that epoch. The main result of this calculation is that for the values of temperature and density for which there is significant X-ray optical depth (i.e., the parameter values where we can set constraints on the IGM, as given in §§ 3.2 and 3.3), the recombination

timescale is generally less than the age of the universe. As an example, in Figure 2 we plot lines which indicate the temperature and density at which the two timescales are equal, for the dominant ionization levels of oxygen and iron. In the region to the right of each line, ionization equilibrium is a reasonable approximation. Comparison of oxygen and iron illustrates a general trend that the heavier elements are in equilibrium over a larger region, primarily because the radiative recombination coefficient scales roughly as atomic number squared. It should be noted that at temperatures above $\sim 10^6$ K, the primary contribution to the X-ray optical depth comes from iron, and so the fact that oxygen and other lighter elements are not in equilibrium does not significantly alter our limits on the IGM.

3. HIGH-REDSHIFT REGIME ($z \approx 3$)

3.1. Optical Depth

Given the assumptions we have made, we can now calculate the optical depth due to the IGM as a function of six variables, $\tau_v = \tau_v(\Omega_G, T, m, J_{21}, \Omega_0, z)$. It is informative to show examples of the optical depths and also to illustrate their dependence on the various input parameters. In all cases, unless otherwise specified, we use the following reference values $z = 3$, $\Omega_0 = 1$, $\Omega_G = 0.1$, $J_{21} = 1.0$, $m = 0.1$, and $T = 10^6$ K.

The optical depth due to the IGM for the $z = 3$ ($J_{21} = 1.0$, $m = 0.1$, and $\Omega_0 = 1$) is shown in Figure 3. Here we have plotted the optical depth, multiplied by the value indicated in each plot, over a grid of values of Ω_G and T . This shows the general dependence of the optical depth on density and temperature.

The dependence of optical depth on J_{21} , the strength of the ionizing background radiation, is shown in Figure 4. Here we see more than a factor of 10 decrease in the optical depth between negligible radiation ($J_{21} = 10^{-3}$) and a realistic radiation strength ($J_{21} = 1$). This shows that any observational limits on IGM properties which do not account for the ionizing radiation must be viewed with caution, in particular the results of SB.

The importance of the ionizing radiation is also evident in Figure 5, where we show the scaling of the optical depth with

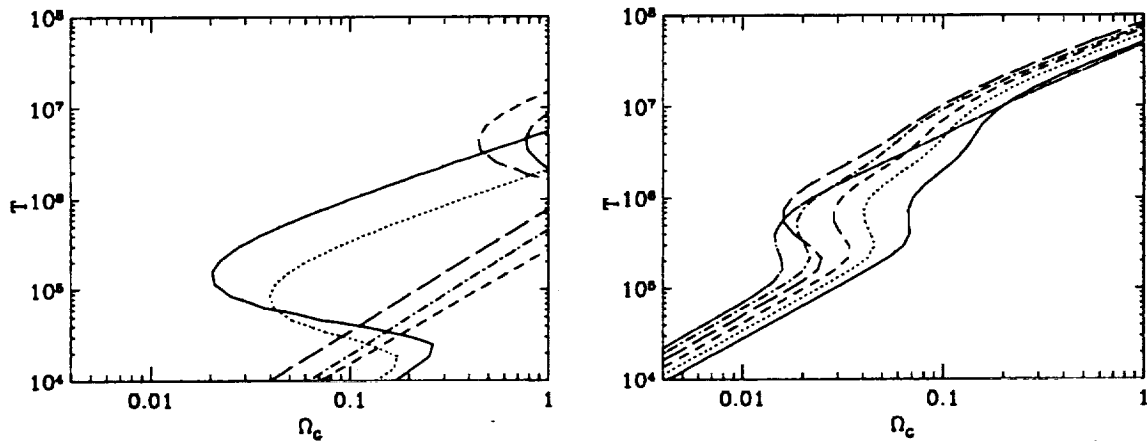


FIG. 2.—Comparison of the recombination timescale for (left) oxygen and (right) iron to the age of the universe at $z = 1$, for the dominant ionization levels in our modeling. The lines indicate the temperature and density at which the recombination timescale is equal to the age of the universe. In the region to the right of each line the species is in ionization equilibrium. On the left side are plotted lines for O IV (solid), O V (dotted), O VI (short dashed), O VII (long dashed), and O VIII (dot-dashed). On the right side are plotted lines for Fe XVII (solid), Fe XVIII (dotted), Fe XIX (short dashed), Fe XX (long dashed), Fe XXI (dot-short dashed), and Fe XXII (dot-long dashed).

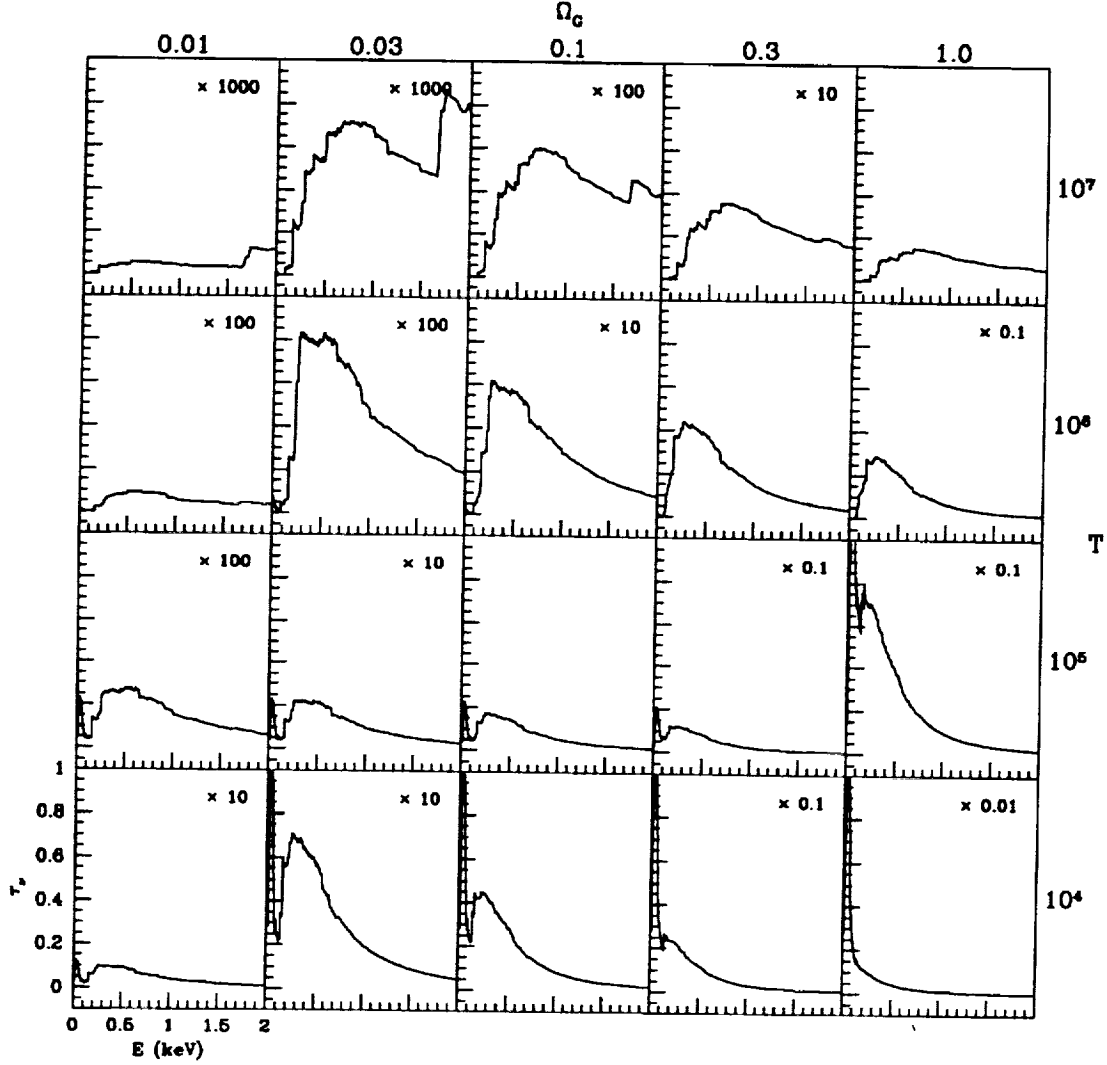


FIG. 3.—Optical depth for an array of Ω_G and T , for $z = 3$, $J_{21} = 1.0$, $m = 0.1$, and $\Omega_0 = 1$. Each of the subplots uses the same axis scaling as in the one marked on the lower left-hand corner. The optical depth in each subplot has been multiplied by the value indicated.

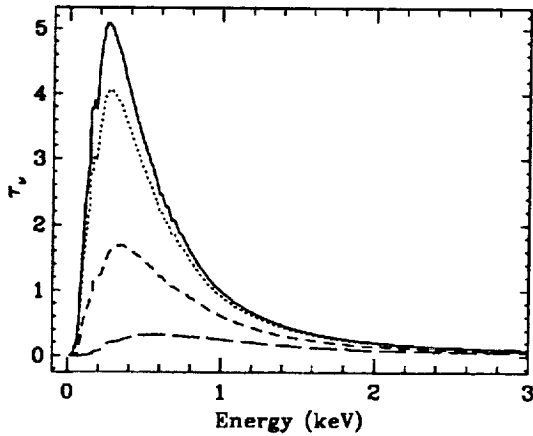


FIG. 4.—X-ray optical depth for values of the ionizing background normalization, $J_{21} = 10^{-3}$ (solid), 10^{-2} (dotted), 10^{-1} (short dashed), and 1 (long dashed). All curves are for $z = 3$, $\Omega_0 = 1$, $T = 10^6$ K, and $m = 0.1$.

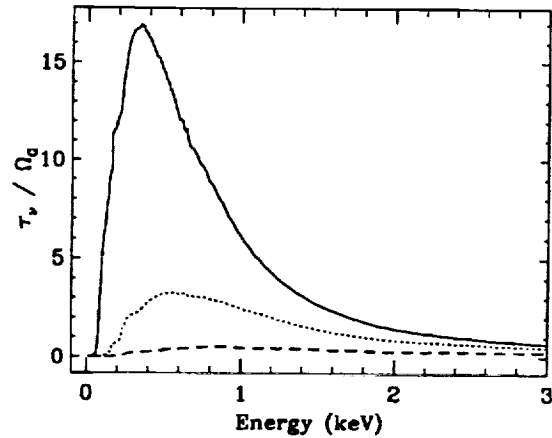


FIG. 5.—Scaling of optical depth with IGM density. We have plotted (τ_ν / Ω_G) , which would be independent of Ω_G if there were no background radiation field. In this case, with $J_{21} = 1$, a decrease by a factor of 10 in density results in a decrease in τ_ν of more than a factor of 50. All curves are for $z = 3$, $\Omega_0 = 1$, $J_{21} = 1$, $T = 10^6$ K, and $m = 0.1$.

IGM density Ω_G . Here we have plotted the quantity τ_v/Ω_G , which in the absence of a radiation field would be independent of Ω_G . We see, however, that there is a strong dependence, and a factor of 10 decrease in Ω_G results in about a factor of 50 decrease in τ_v . This is primarily due to the increase in the ionization parameter, although it should be noted that decreasing the density is not simply equivalent to increasing J_{21} , because of density dependent atomic processes such as collisional ionization in the equilibrium calculations.

In Figure 6 we show the temperature dependence of the optical depth for $T = 10^4$ – 10^8 K. The strong decline in τ_v reflects the trend that at higher temperatures the atoms are more highly ionized, and that the absorption cross section is lower for higher ionic levels. The peak at 0.1 keV is due to helium and can be seen to become unimportant at $T \gtrsim 10^6$ K, where almost all of the helium is fully ionized. We also see from Figure 5 that τ_v peaks at higher energies as temperature increases, because the K-edge energy increases at higher ionization level. A specific example of the absorption opacity for oxygen ions O v–O viii is given in Figure 7 and illustrates dependence of cross section and K-edge energy on ionization level.

The relative contribution of the important heavy elements in our calculation can be illustrated in two ways. First, in Figure 8 we plot the optical depth due to each element at the reference IGM parameter values. This shows that oxygen and iron are the most important elements, followed by carbon and neon. The relative strength of these elements is a strong function of temperature, as shown in Figure 9. Here we plot the peak optical depth due to oxygen and iron as a function of temperature. In oxygen, as the temperature increases above 10^6 K, a significant fraction of the atoms become fully ionized and lose their photoabsorptive opacity. This is not the case for iron, and hence the change in relative optical depth.

3.2. IGM Constraints

The X-ray spectra of high-redshift quasars are found in many cases to show strong low-energy cutoffs (Elvis et al. 1994). The origin of the cutoffs is not fully understood, although recent work indicates that at least in some cases the absorption is due to warm gas associated with the quasar (Fiore et al. 1993; Mathur et al. 1994). This absorption cannot,

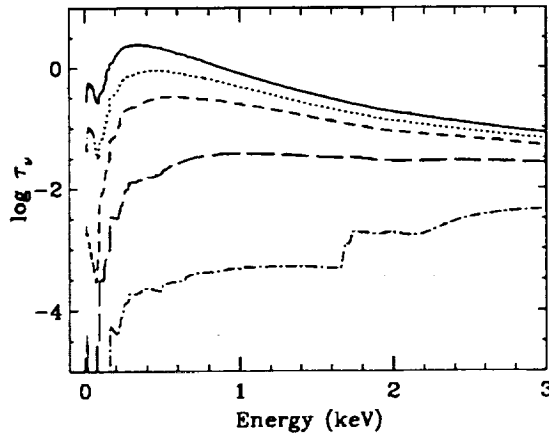


FIG. 6.—Log of the X-ray optical depth for values of the IGM temperature $T = 10^4$ K (solid), 10^5 K (dotted), 10^6 K (short dashed), 10^7 K (long dashed), and 10^8 K (dot dashed). All curves are for $z = 3$, $\Omega_0 = 1$, $\Omega_G = 0.1$, $J_{21} = 1$, and $m = 0.1$.

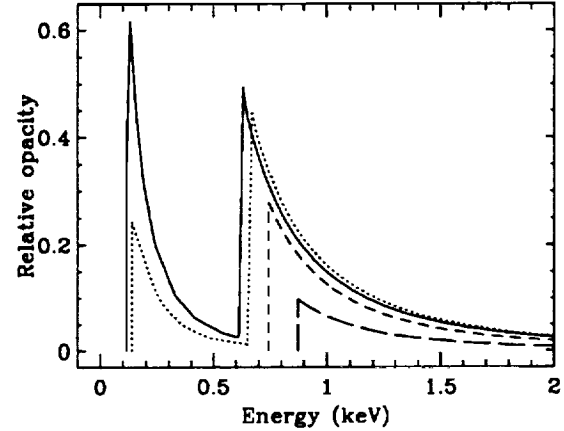


FIG. 7.—Relative opacity for oxygen ions O v (solid), O vi (dotted), O vii (short dashed), and O viii (long dashed).

however, arise in an isotropic IGM because there exist some high- z quasars whose X-ray spectra are well fit by a single power law with only Galactic absorption. The existence of these quasars implies that with the current data it is only meaningful to set limits on the conditions of the IGM. Currently, we know of three quasars which are at $z > 2$ and have an unabsorbed PSPC spectrum with at least 300 counts. PKS 0237–233 (297 counts), Q0420–388 (363 counts: Elvis et al. 1994), and Q1445+101 (OQ172; 656 counts).

For each quasar spectrum at an observed redshift z the optical depth can, given our assumptions, be calculated as a function of Ω_G , T , m , J_{21} , and Ω_0 . In order to compare our results with previous work constraining the nature of the IGM, it is convenient to calculate the optical depth over a grid of values for Ω_G and T , for specified reasonable values of m , J_{21} , and Ω_0 . For each value of Ω_G and T , we fit the observed quasar PSPC energy spectrum with an absorbed power-law of the form

$$f_v^G = CW_v(N_{H1})v^{-\alpha} \exp[-\tau_v(\Omega_G, T)], \quad (7)$$

where C is a normalization constant and $W_v(N_{H1})$ is the Wisconsin model of absorption due to Galactic gas (Morrison & McCammon 1983), with the neutral hydrogen column density fixed at the value derived from 21 cm observations. Only the parameters C and α are free to vary. We then calculate the statistic

$$\Delta\chi^2(\Omega_G, T) = \sum_{\text{quasars}} \chi^2(\Omega_G, T) - \chi^2(\Omega_G = 0).$$

The function $\Delta\chi^2(\Omega_G, T)$ is distributed as χ^2 with two degrees of freedom, which we use to define confidence intervals in which absorption due to an IGM can be excluded.

In Figure 10 we illustrate the effect of including the IGM X-ray absorption term in the model fitting of PKS 0237–233, for IGM parameters $T = 10^6$ K, $J_{21} = 1$, $m = 1.0$, and $\Omega_G = 0.05$ (left side) and $\Omega_G = 0.3$ (right side). In both plots the points are the “intrinsic” X-ray spectral data, in which the PSPC instrument response has been deconvolved, and the solid line is the best-fit power-law \times Galactic absorption \times IGM absorption model. For $\Omega_G = 0.05$ the IGM model is consistent with the observed data, whereas for $\Omega_G = 0.3$, the IGM opacity produces a broad absorption trough of width $\Delta E \approx 0.5$ keV and maximum optical depth $\tau \approx 1$. This results in a statistically

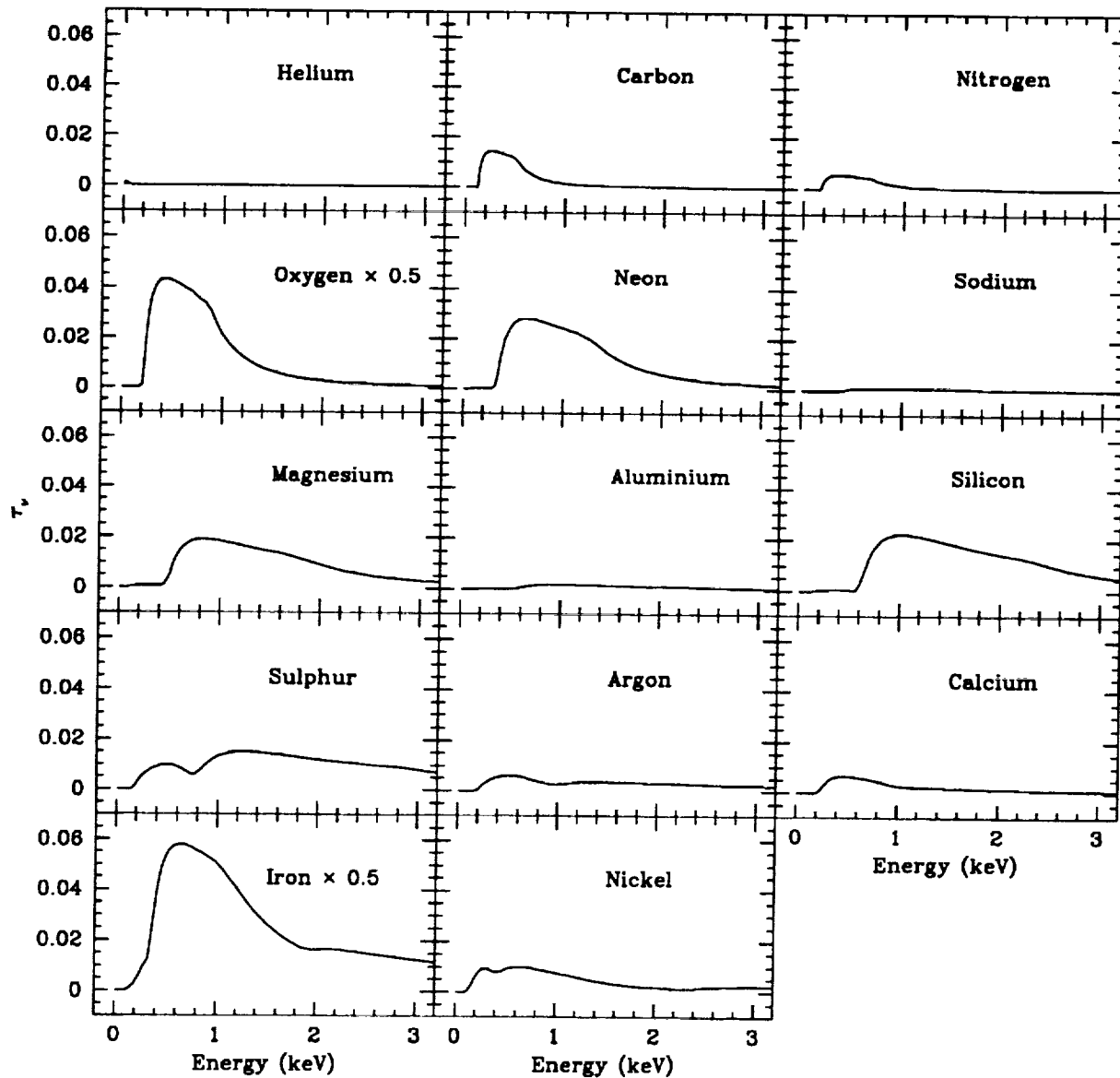


FIG. 8.—Contribution of individual elements to X-ray optical depth for $z = 3$, $\Omega_0 = 1$, $\Omega_G = 0.1$, $J_{21} = 1$, $T = 10^6$ K, and $m = 0.1$. At this temperature the optical depth is dominated by oxygen and iron.

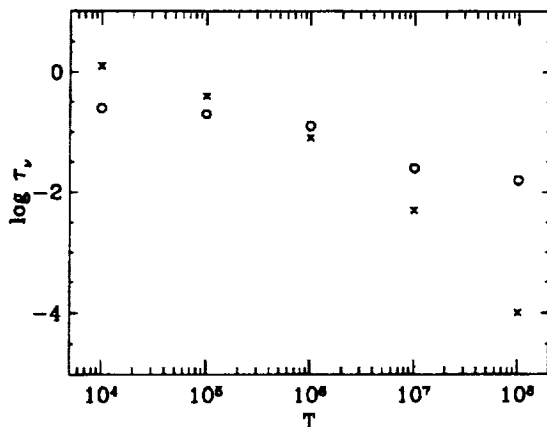


FIG. 9.—Maximum optical depth due to oxygen (crosses) and iron (circles) as a function of temperature.

unacceptable increase in the fit χ^2 , and we can rule out an IGM with the given parameters.

In Figure 11 we plot the 3σ contour lines of $\Delta\chi^2(\Omega_G, T)$ for the three quasars in our sample for various values of J_{21} , Ω_0 , and m . An IGM which is colder or denser than the limits shown is excluded by the observed lack of X-ray absorption. In the left-hand plots we show the results for $J_{21} = 1.0$, which is the most reasonable strength of the ionizing background radiation; in the right-hand plots we use $J_{21} = 0.1$, which is likely the smallest reasonable value. In the upper and lower plots we show the cases $\Omega_0 = 1$ and $\Omega_0 = 0.2$, respectively. In each we have drawn contours calculated for an IGM with heavy element abundances of $m = 1, 0.1, 0.01$, and primordial. The vertical dashed line shows for reference the limit on the IGM density imposed by the standard model of big bang nucleosynthesis, $\Omega_B < 0.026 h_{100}^{-2}$, for our adopted value $h_{100} = 0.75$. We also mark the density and temperature of the diffuse IGM predicted by CO93.

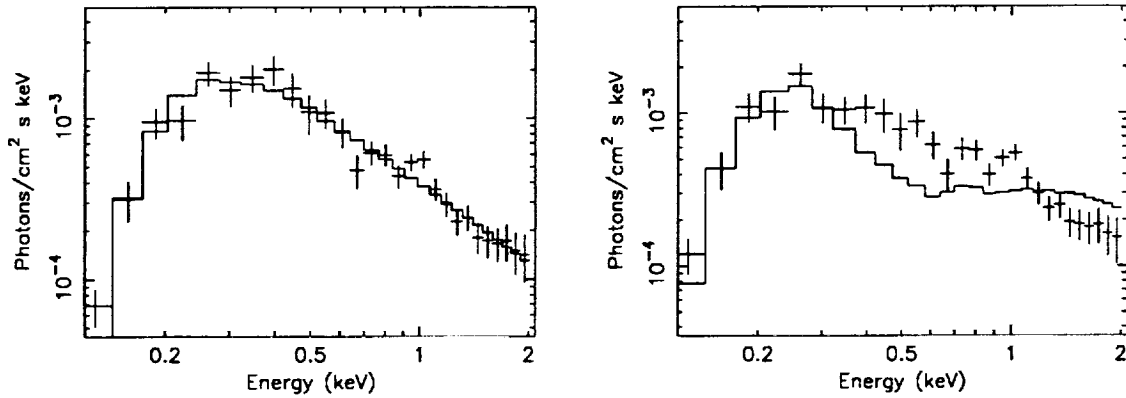


FIG. 10.—Illustration of the effect of the IGM X-ray absorption term for $T = 10^6$ K, $J_{21} = 1$, $m = 1.0$, and $\Omega_G = 0.05$ (left) and $\Omega_G = 0.3$ (right) in the model fitting of PKS 0237–233. The points are the intrinsic X-ray spectrum with the PSPC instrument response deconvolved, and the solid lines are the model fits. Clearly $\Omega_G = 0.05$ is consistent with the data while $\Omega_G = 0.3$ is not consistent.

3.3. Discussion

Comparison of the left and right sides of Figure 11 shows the strong dependence of the X-ray constraints on the assumed ionizing background. This is important to note because previous work which predicted strong constraints (SB; Rees & Sciama 1967) did not take the background into account. The effect of this radiation is to ionize more highly the heavy ele-

ments which contribute to the X-ray opacity, thereby reducing the overall absorption cross section.

Inspection of Figure 11 shows that for a primordial IGM, the X-ray Gunn-Peterson test we have calculated is not particularly sensitive. Referring back to Figure 8 we see that the absorption due to helium is relatively weak and more importantly it is confined to energies $h\nu \lesssim 0.3$ keV. Since Galactic absorption is significant at this energy, the quasar spectra have

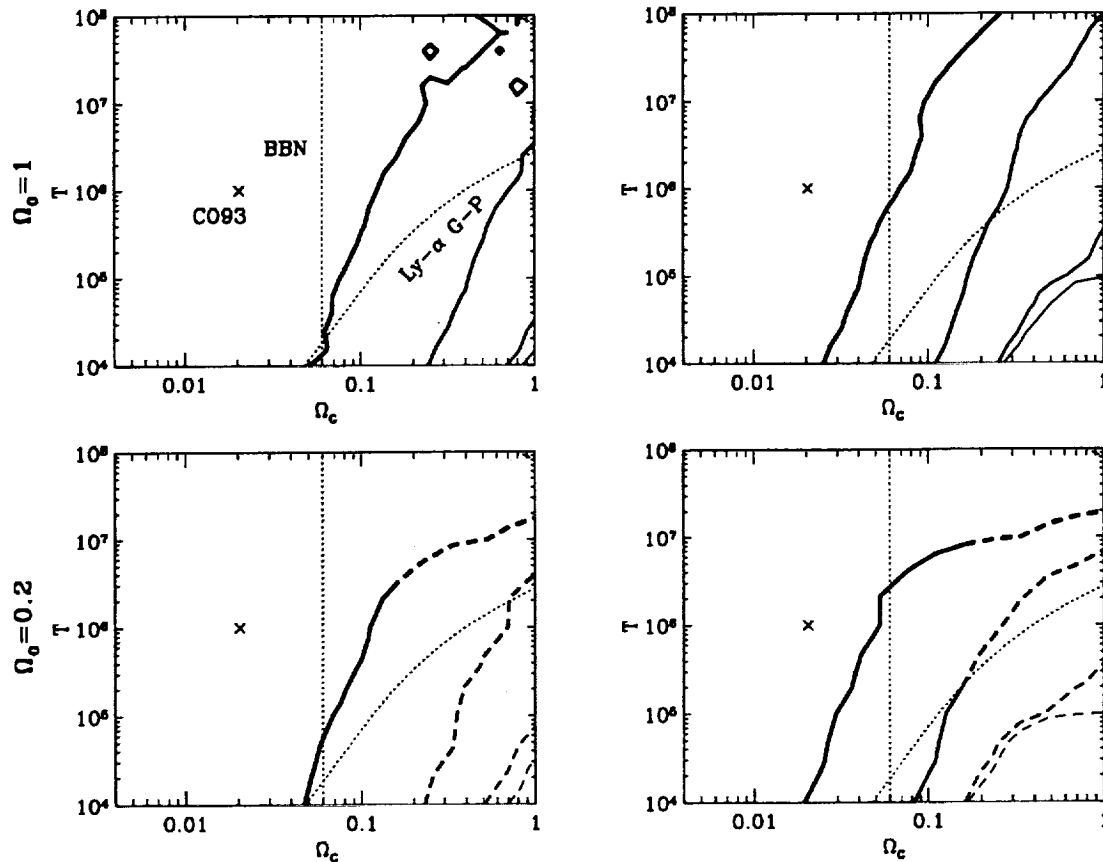


FIG. 11.—Limits at 3σ on temperature and density of IGM based on X-ray optical depth toward high-redshift quasars. The region to the right of and below the lines are excluded. The upper plots show limits for $\Omega_0 = 1$, and the lower plots are for $\Omega_0 = 0.2$. The right plots show limits for $J_{21} = 0.1$. In all plots there are four solid contour lines, which from boldest to thinnest correspond to heavy element abundances $m = 1, 0.1, 0.01$, and primordial ($m = 0$). In the lower two plots, the contour lines are dashed for the unphysical region $\Omega_G > \Omega_0$. We also show the limits due to big bang nucleosynthesis (BBN) and Ly α Gunn-Peterson, as well as the IGM temperature and density predicted by C093.

much lower signal-to-noise ratio in this region. It should be noted here that the He II (304 Å) line is expected to have a very large optical depth for reasonable IGM models. For instance, CO93 predict that at $z = 3$ optical depth is approximately 1000. This line has not been observed because in all currently known QSOs with $z > 3$ (which corresponds to rest-frame 304 Å for an observed-frame wavelength of 1215 Å), there is an intervening Lyman-limit system which blackens the spectrum in the relevant wavelength range. Some recent *HST* observations have come frustratingly close, for instance the $z = 2.72$ which has no optically thick Lyman-limit systems (Reimers et al. 1992). It is somewhat ironic to note that if the optical depth is as large as predicted, it will be difficult to usefully constrain the IGM properties, apart from proving the existence of the IGM.

For an enriched IGM the X-ray Gunn-Peterson test is much more sensitive than for a primordial IGM, since as we have seen in § 3.1, most of the X-ray opacity is due to heavy elements such as oxygen, iron, neon, and carbon. We can now examine Figure 11 to determine the lower bounds on IGM temperature for various values of J_{21} and abundance, at two interesting IGM densities, $\Omega_G = 0.06$ and $\Omega_G = 1.0$. In the former case the IGM makes up the bulk of baryonic matter predicted by standard big bang nucleosynthesis, while in the latter case the IGM contains the baryonic matter necessary to close the universe. With $\Omega_G = 1.0$, a nonstandard model for nucleosynthesis must be adopted in order not to conflict with the observed light element abundances. Despite the success of the standard model, one should not dismiss entirely the alternatives (e.g., Dimopoulos et al. 1988). From the figure we see that if the ionizing background radiation is as strong as $J_{21} = 1.0$, then our X-ray Gunn-Peterson test does not constrain the temperature (above 10^4 K) of an IGM with $\Omega_G = 0.06$, even with solar abundances. For an IGM with the closure density, we see from Figure 11 that we can significantly constrain the temperature, especially for the weak ionizing background case. However, it should be noted that in this case, with such a large amount of matter in the IGM, it is unlikely that any enrichment processes are efficient enough to produce a heavy element abundance above 0.01 solar. In all cases, comparison with the IGM temperature and density predicted by CO93 as shown in Figure 11 reveals that the X-ray opacity of a hot diffuse IGM is too small to test their prediction with the current data.

In order to investigate the ultimate utility of the X-ray Gunn-Peterson test using PSPC spectra, we have constructed simulated PSPC spectra with higher signal-to-noise ratio and carried out the procedure described in § 3.2. The simulated data were created using the best fit-power-law with Galactic absorption model for PKS 0237–233, with roughly 10,000 and 100,000 counts, respectively. We find that the factor of 100 in counts gives only a factor of 5 improvement in the density limit at constant temperature, for $J_{21} = 1.0$ and $m = 0.1$. On the other hand, at a given density the temperature limit scales almost linearly with number of counts. For solar abundance with $J_{21} = 1.0$, or 0.1 solar with $J_{21} = 0.1$, a quasar with 10^5 counts and no observed absorption would exclude a large range of temperatures and densities. However, even in these cases, the test would not be sensitive enough to test the predicted IGM properties from CO93.

4. LOW-REDSHIFT REGIME ($z \lesssim 0.4$)

The calculations of SB showed that the IGM optical depth at low redshift ($z \lesssim 0.4$) has a qualitatively different character

than at high redshift. In the low-redshift case the optical depth is dominated by narrow absorption “troughs,” with sharp edges and fractional width $\Delta E/E \approx z$. The peak optical depth due to the IGM is much smaller than at high redshift. However, it is possible to take advantage of the very distinctive absorption troughs, as well as the much higher signal-to-noise ratio possible in nearby low-redshift quasars, to compensate for the weakness of the absorption. We now consider the question of detecting or constraining the IGM using low-redshift quasars.

4.1. Optical Depth

The optical depth due to the IGM for the low-redshift case $z = 0.15$ ($J_{21} = 1.0$, $n = 0.1$, and $\Omega_0 = 1$) is shown in Figure 12. Here we have plotted the optical depth, multiplied by the value indicated in each plot, over a grid of values of Ω_G and T . The strong peaks and discontinuities in the optical depth reflect that, in contrast to the high-redshift case, the dominant contributor here is the opacity from atomic line transitions. From equation (3) we see that the absorption due to a line with rest frequency ν_a is “redshifted” over the frequency range $\nu_a(1+z)^{-1} \leq \nu \leq \nu_a$. At the edges of this range the optical depth due to the line drops discontinuously to zero. The discrete nature and well-defined wavelengths of the absorption troughs allow for easy identification of the species responsible for the opacity. For instance, for $\Omega_G = 1.0$ and $T = 10^6$ K, the dominant lines are C V, C VI, N VII, O VII, O VIII, Fe XIX, and Fe XX. The largest peak, starting at 0.5 keV, is a blend of O VII and O VIII. These two lines show the temperature dependence of the ionization equilibrium, most clearly at low densities. At $\Omega_G = 0.1$ and $T = 10^4$ K, O VII predominates, while at $T = 10^6$ K the dominant ion is O VIII. Figure 12 also shows that at high density and low temperature, there is significant continuum opacity due to helium.

4.2. IGM Detection Limits

We first consider detection of absorption due to the IGM using existing X-ray satellite data. The *ROSAT* PSPC has energy resolution $E/\Delta E \sim 4$, which is too low even to resolve the absorption trough and is hence unsuitable for this type of investigation. The *ASCA* SIS instrument has sufficient resolution, $E/\Delta E \sim 15$ at 1 keV, to begin resolving the trough for $z \gtrsim 0.15$, but it is inadequate to determine the trough shape. For both these instruments, if a quasar is found which is well fitted by the power-law and Galactic absorption model, then the same technique we described for high-redshift quasars can be applied to constrain the IGM properties. However, at very high signal-to-noise ratio one begins to see intrinsic deviations from a power law, possibly due to intervening cold or warm material in the line of sight to the X-ray source (Elvis et al. 1994; Mathur et al. 1994) or Compton reflection from an accretion disk (White, Lightman, & Zdziarski 1988; Lightman & White 1988). In addition, it is difficult to calibrate the energy response in X-ray mirrors and spectrometers to much better than a few percent, and in particular it is difficult to determine the exact depth of absorption edges due to material in the mirrors and other components. These two effects generally produce X-ray spectra that have structure beyond a simple power law, considerably weakening any conclusions about a possible IGM based on low- to moderate-resolution spectra. It is interesting to note that the power-law fit to one of the *ROSAT* PSPC spectra of 3C 273 (obtained from the *ROSAT* archive) is substantially improved by the addition of IGM

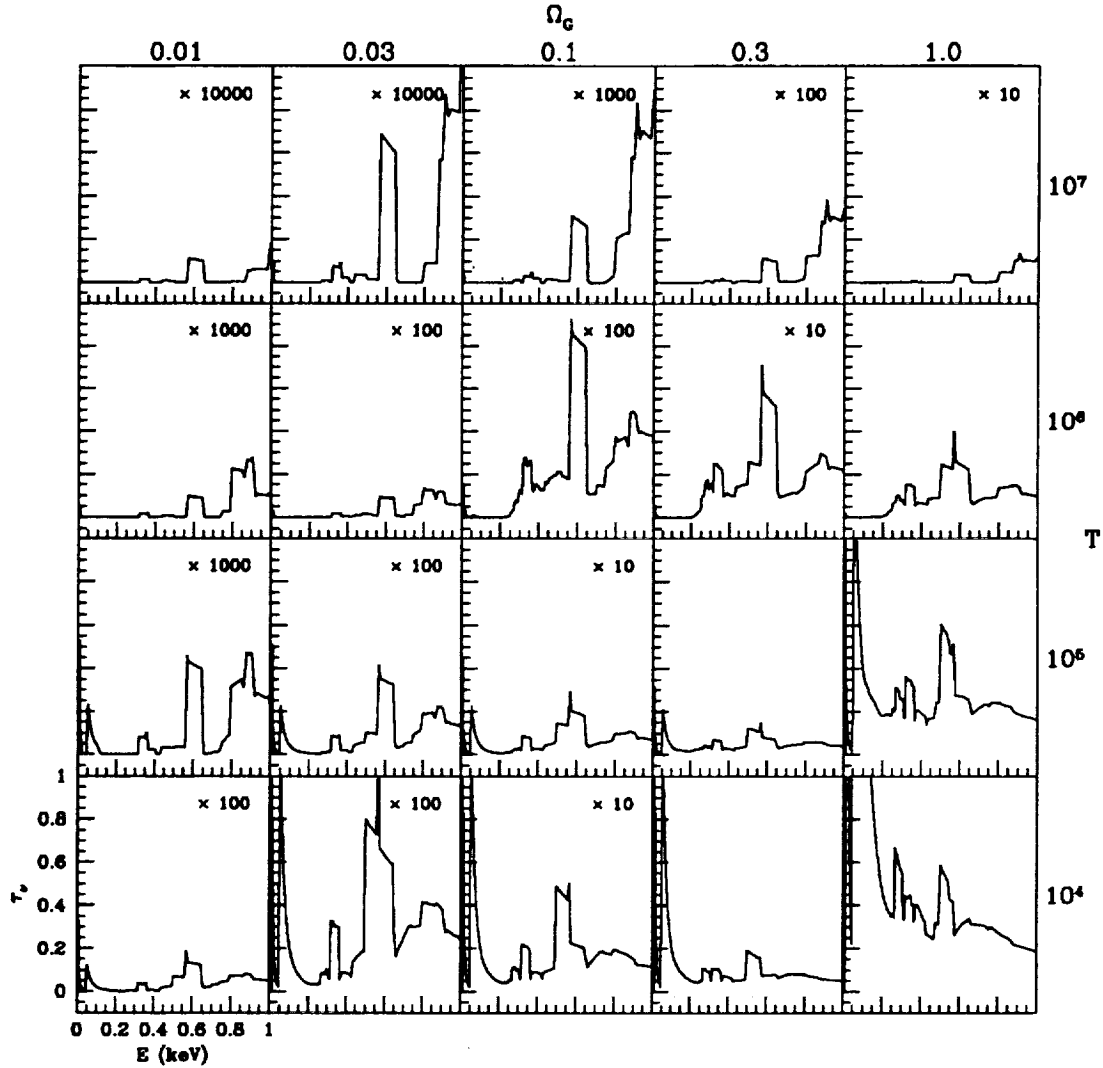


FIG. 12.—Optical depth for an array of Ω_G and T , for $z = 0.15$, $J_{21} = 1.0$, $m = 0.1$, and $\Omega_0 = 1$. Each of the subplots uses the same axis scalings as in the one marked on the lower left-hand corner. The optical depth in each subplot has been multiplied by the value indicated.

absorption with $\Omega_G = 1.0$, $T = 10^{5.3}$ K, $m = 0.1$, and $J_{21} = 1.0$. In this case the fit statistic changes from $\chi^2 = 70$ (25 DOF) to $\chi^2 = 39$ (23 DOF), which has an F -test probability of much less than 1%. However, such a cool, dense IGM is ruled out by the Ly α Gunn-Peterson test, hence illustrating the problems inherent in using low-resolution, high signal-to-noise ratio spectra to derive IGM properties.

However, if the spectral resolution is high enough ($E/\Delta E \gtrsim 100$ at 1 keV) then the absorption troughs can be used to identify or constrain IGM absorption with much greater confidence. Instead of focusing on the overall fit of a spectral model (power-law \times Galactic absorption \times IGM absorption) as in the high-redshift case, we determine a local continuum near the known position of strong lines. We then sum the spectrum over the extent of the absorption trough for the particular line, which then allows calculation of the trough optical depth. The two problems mentioned previously, uncertainty in both the quasar spectrum and detector energy calibration, can be avoided by carefully selecting energy bands (for the contin-

uum and absorption trough) which are free of any contaminating sharp edges or lines.

Since it is evident from Figure 12 that O VII (0.574 keV) and O VIII (0.654 keV) are the strongest lines over most of the range where the IGM has significant optical depth, we now look in detail at possible detection of these two lines. In Figure 13 we show a schematic diagram of a quasar spectrum at $z = 0.15$ which shows absorption due to N VI, O VII, and O VIII in the IGM, along with the edges and lines which can be potential sources of uncertainty in the spectrum. In this energy range, the important spectral features intrinsic to the quasar are possible absorption lines due to a warm absorber containing O VII or O VIII. Most evidence indicates that these absorbers are associated with the quasar and are due to either a previously unidentified component which also gives rise to UV absorption (Mathur et al. 1994; Mathur 1994) or broad emission line clouds (Shields, Ferland, & Peterson 1994). In both cases the velocity of the material with respect to the quasar will be less than about 5000 km s^{-1} , and hence the regions further than

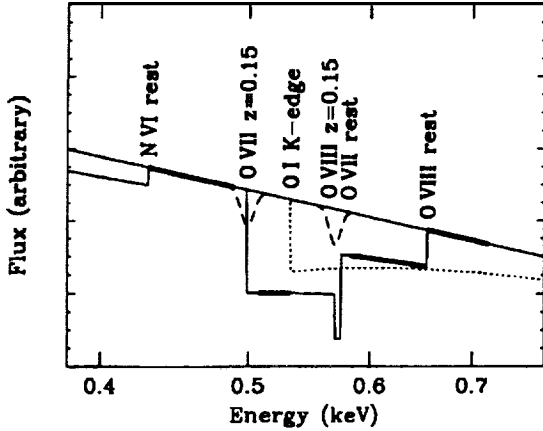


FIG. 13.—Schematic diagram of quasar power-law continuum, with O VII and O VIII IGM absorption, as well as with potential sources of uncertainty in spectrum arising from intrinsic absorption in quasar and imperfect knowledge of detector energy response. The spectral ranges drawn in bold are used for summing the continuum and absorption trough counts.

about 9 eV from the line energy will be unaffected. Note that these lines will be redshifted because they are associated with the quasar. The only strong spectral feature expected in the mirror and spectrometer energy response in this energy range is the O I K-edge (0.532 keV).

If we now make the conservative presumption that the strengths of the warm absorber lines and energy response edges are not well known, the energy ranges which can be used to search for IGM absorption are limited. Any region which contains a possible intrinsic line or crosses an edge boundary is excluded. It is particularly important to ensure that there be no edge between the regions used to determine the continuum and the IGM absorption. The regions which are free of contamination and can be used for determining the O VII and O VIII absorption trough optical depth are drawn in bold in Figure 13. From our discussion and Figure 13 it is apparent that in most cases the continuum can be determined only on one side of the absorption trough. In this case the local spectral slope is determined by the spectral model. In practice, this means using

the fit residuals instead of the raw spectrum for calculating the continuum and trough counts.

As a specific example of the previous discussion, we now consider the AXAF low-energy transmission grating spectrometer (LETGS), which will have an energy resolution of roughly 500 near 0.5 keV. This is sufficient to allow discrimination of the contaminating edges and lines. For a specified source flux and observation time, we can calculate the expected number of counts in the clean energy bands and thus determine the absorption trough optical depth which could be detected. We then compare this limit to the predicted optical depth of the troughs for given IGM parameters (Ω_G , T , m , J_{21} , Ω_0) and so determine the ranges over which the IGM could be constrained or detected. To estimate the expected number of counts, we assume a spectrum which is a power law with energy index -0.7 and with absorption due to a galactic neutral hydrogen column density $N_H = 2 \times 10^{20} \text{ cm}^{-2}$. The 3σ optical depth detection limit for this spectral shape, based on counting statistics and using $\tau \ll 1$, is

$$\tau < 0.1 \left(\frac{1 + \Delta E_c / \Delta E_a}{2} \right)^{1/2} \left(\frac{E}{0.5 \text{ keV}} \right)^{0.7} \times \left\{ C_p \left(\frac{\Delta E_c}{0.1 \text{ keV}} \right) \left[\frac{A(E)}{20 \text{ cm}^2} \right] \left(\frac{t}{10^5 \text{ s}} \right) \right\}^{-1/2} \quad (8)$$

Here ΔE_c and ΔE_a are energy widths over which the continuum and absorption trough counts are summed, respectively; E is the central energy of the trough; C_p is the ROSAT PSPC unfiltered count rate; $A(E)$ is the effective area of the X-ray spectrometer; and t is the duration of the observation. For reference, $C_p = 1$ corresponds to an energy flux $F = 1.1 \times 10^{-11} \text{ ergs s}^{-1} \text{ cm}^{-2}$ (0.1–2.4 keV) or $F = 1.5 \times 10^{-11} \text{ ergs s}^{-1} \text{ cm}^{-2}$ (2–10 keV).

In the left-hand plot of Figure 14 we show the 3σ detection limits for O VII and O VIII from equation (8) for a spectrum equivalent to a 100 ks observation of 3C 273 by the AXAF LETGS. This assumes an effective area $A(E) = 20 \text{ cm}^2$ and a PSPC count rate of $C_p = 6 \text{ counts s}^{-1}$, for $z = 0.15$. We use energy bands for the continuum and trough shown in Figure 13, which gives a 3σ detection limit of $\tau \approx 0.1$. In both of the

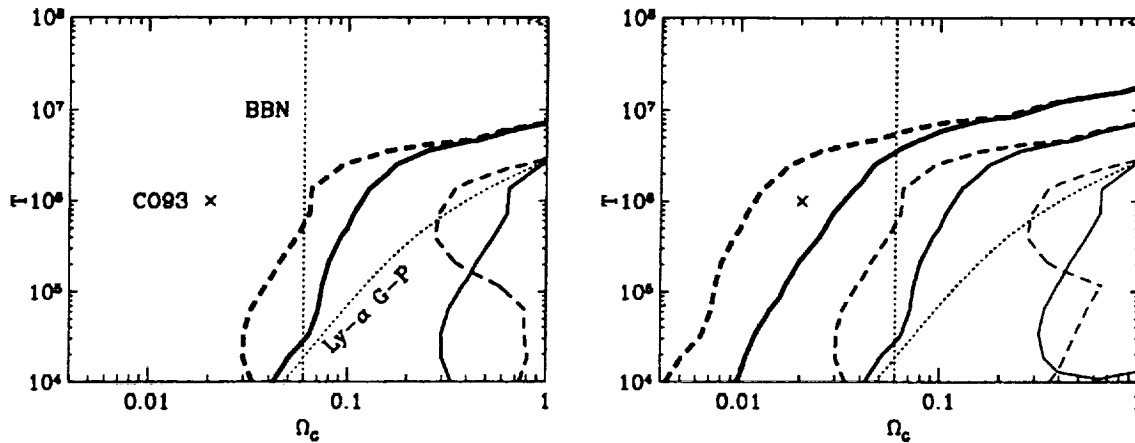


FIG. 14.—Detection limits at 3σ for a spectrum equivalent to a 100 ks observation of 3C 273 ($z = 0.15$) by a detector with effective area (left) $A = 20 \text{ cm}^2$ (AXAF LETGS) and (right) $A = 2000 \text{ cm}^2$. The solid and dashed lines correspond to $J_{21} = 1.0$ and $J_{21} = 0.1$, respectively. The thick, medium, and thin lines are for heavy element abundances $m = 1.0, 0.1$, and 0.01 , respectively. Also shown for reference are the big-bang nucleosynthesis limit (BBN), the Ly α Gunn-Peterson limit, and the IGM temperature and density predicted by CO93.

plots, the solid line and dashed line correspond to $J_{21} = 1.0$ and $J_{21} = 0.1$, respectively. The bold lines are for heavy element abundance $m = 1.0$ and the medium lines are for $m = 0.1$. For $m = 0.01$, the IGM optical depth is too low to detect the IGM in the range we have plotted. We also show for reference the big-bang nucleosynthesis limit (BBN), the Ly α Gunn-Peterson limit, and the IGM temperature and density predicted by CO93. The plot illustrates that in some cases the sensitivity increases at higher temperature, for a given density. This is simply a reflection of the temperature and density regime in which O VII and O VIII are the dominant oxygen species in the ionization equilibrium. The overall result shown in the plots is that only in the cases of nearly solar heavy element abundance ($m = 1.0$) or high density ($\Omega_G \approx 1$) will the X-ray spectra of low-redshift quasars be sensitive to absorption caused by the IGM. In no cases can the test detect an IGM at the temperature and density predicted by CO93.

Looking optimistically to future X-ray telescopes, we show in right-hand plot of Figure 14 the 3σ detection limits for a telescope effective area of 2000 cm², which is a factor of 100 increase over the *AXAF* LETGS. With this effective area the detection limit is $\tau \approx 0.01$, below which it will be very difficult indeed to make any convincing determination that an absorption trough is present. This plot shows that with such a large effective area the X-ray Gunn-Peterson test is sensitive to an IGM with $m = 1.0$ the temperature and density near that predicted by CO93. For $m = 0.1$, the test can detect the IGM for temperature $T \lesssim 10^6$ K for $J_{21} = 0.1$. For $m = 0.01$ the test is unable to detect the IGM outside the current Ly α Gunn-Peterson limits.

Although we have shown only the IGM detection limits for the case $z = 0.15$, we have also calculated these limits for several other redshifts, and we find that they are largely insensitive to z in the range $0.15 \lesssim z \lesssim 0.25$. Outside this range, the widths of the regions over which the continuum or the trough counts are summed become small, with a corresponding decrease in sensitivity.

5. SUMMARY

We have derived the constraints which can be placed on the density and temperature of the IGM based on *ROSAT* X-ray spectra of $z \approx 3$ quasars, as well as the expected detection limits based on high-resolution ($E/\Delta E \gtrsim 100$) spectra of $z \lesssim 0.4$ quasars. In order to calculate the X-ray optical depth due to the IGM, we made the following assumptions: the IGM is isotropic with no redshift evolution of density Ω_G and temperature; the heavy-element abundances are independent of redshift and are uniformly depleted from the "cosmic" abundances of Cameron (1973); the UV-to-soft X-ray background radiation spectrum scales with redshift as $(1+z)^4$; and ionization equilibrium can be assumed to hold for the heavy elements. Given these assumptions, we have shown how to calculate the optical depth due to the IGM as a function of redshift (z), total mass density (Ω_0), IGM density (Ω_G), temperature (T), heavy-element abundance (m), and background radiation strength (J_{21}). The calculation of ionization equilibrium is done entirely within the program CLOUDY.

We find the following about our model of the X-ray optical depth of the IGM out to high redshift. The ionizing background radiation, which was not included in previous calculations of this nature, strongly affects the optical depth.

Changing the background strength from $J_{21} = 10^{-3}$ to $J_{21} = 1$ decreases the peak optical depth by over a factor of 10. In addition, the background radiation causes the optical depth to be nonlinear in Ω_G , and for $J_{21} = 1$, a factor of 10 decrease in Ω_G results in a factor of over 50 decrease in optical depth. Our calculations reveal that at high redshift the X-ray optical depth is dominated by the heavy element edge transitions O-K, Fe-L, Ne-K, and C-K. Below about 10^6 K, oxygen is the most important, while for higher temperature iron is the largest contributor.

The constraints on IGM temperature and density were made by choosing representative values for the parameters Ω_0 , m , and J_{21} and calculating the optical depth for each quasar redshift z over an array of values of Ω_G and T . This optical depth was incorporated into the X-ray spectral fitting model for that quasar, and we determined the IGM parameter values for which the model produced an unacceptable fit. This was done for the three $z \approx 3$ quasars PKS 0237–233, Q0420–388, and OQ 172.

We find that if the IGM density is at the limit allowed by the standard theory of big bang nucleosynthesis ($\Omega_G \leq 0.026 h_{100}^2$), the X-ray Gunn-Peterson test with high-redshift *ROSAT* PSPC spectra can significantly constrain the temperature of the IGM only for nearly solar heavy element abundances ($m \approx 1$). For a temperature of 10^5 K and $m = 0.1$, this test limits the density to $\Omega_G \lesssim 0.3$. Near the IGM density and temperature predicted by CO93, the X-ray optical depth is negligible ($\tau, < 0.01$). Simulated PSPC spectra with up to 100,000 counts were created, and we found that even with such high signal-to-noise ratio, the test would not be sensitive to the predicted IGM. We conclude that with the energy resolution available in *ROSAT* data, the X-ray optical depth out to high redshift allows substantial constraint of the IGM only in the cases of nearly solar heavy element abundance or density near that required to close the universe.

For low-redshift quasars ($z \lesssim 0.4$) the IGM X-ray optical depth is generally less than unity and is dominated by sharp absorption troughs. Constraining or detecting the IGM in this regime therefore requires high signal-to-noise ratio, at which point intrinsic deviations from a power-law spectrum are usually apparent. We have presented a detection method which minimizes the effect of these uncertainties by avoiding contaminating edges and lines in the spectrum. Using this method and two assumed values of the X-ray spectrometer effective area (20 cm², equivalent to the *AXAF* LETGS, and 2000 cm²) we have derived the temperature and density ranges over which the IGM could be detected. At plausible densities, the IGM out to $z = 0.15$ could not be detected with an *AXAF* LETGS spectrum equivalent to a 100 ks observation of 3C 273. However, with the large area detector, the IGM could be detected over a substantial range of temperatures and densities.

The authors wish to thank Belinda Wilkes for supplying the PSPC spectrum of PKS 0237–233 in advance of publication, Gary Ferland for help with CLOUDY, Adam Dobrzycki and Smita Mathur for useful discussions, and Claude Canizares for initially suggesting we do this investigation. The work was supported by NASA grants NAGW-2201 (LTSARP) and NAG 5-1872 (*ROSAT*).

REFERENCES

- Bajtlik, S., Duncan, R. C., & Ostriker, J. P. 1988, *ApJ*, 327, 570
 Bechtold, J. 1994, *ApJS*, 91, 1
 Bechtold, J., Weymann, R. J., Lin, Z., & Malkan, M. 1987, *ApJ*, 315, 180
 Cameron, A. G. W. 1973, *Space Sci. Rev.*, 15, 121
 Cen, R., & Ostriker, J. P. 1993, *ApJ*, 417, 404 (CO93)
 Dimopoulos, S., Esmailzadeh, R., Hall, L. J., & Starkman, G. D. 1988, *ApJ*, 330, 545
 Elvis, M., Fiore, F., Wilkes, B., McDowell, J., & Bechtold, J. 1994, *ApJ*, 422, 60
 Fall, S. M., & Pei, Y. C. 1993, *ApJ*, 402, 479
 Ferland, G. J. 1993, University of Kentucky Department of Physics and Astronomy Internal Report
 Field, G. B., & Perrenod, S. C. 1977, *ApJ*, 215, 717
 Fiore, F., Elvis, M., Mathur, S., Wilkes, B. J., & McDowell, J. C. 1993, *ApJ*, 415, 129
 Giallongo, E., Cristiani, S., & Trevese, D. 1992, *ApJ*, 398, L9
 Gunn, J. E., & Peterson, B. A. 1965, *ApJ*, 142, 1633
 Hasinger, G., Schmidt, M., & Trümper, J. 1991, *A&A*, 246, L2
 Ikeuchi, S., & Ostriker, J. P. 1986, *ApJ*, 301, 522
 Ikeuchi, S., & Turner, E. L. 1991, *ApJ*, 381, L1
 Kato, T. 1976, *ApJS*, 30, 397
 Kolb, E. W., & Turner, M. S. 1990, *The Early Universe* (New York: Addison-Wesley)
 Lightman, A. P., & White, T. R. 1988, *ApJ*, 335, 57
 Mather, J. C., et al. 1994, *ApJ*, 420, 439
 Mathur, S. 1994, *ApJ*, 431, L75
 Mathur, S., Wilkes, B., Elvis, M., & Fiore, F. 1994, *ApJ*, 434, 493
 Miralda-Escudé, J., & Rees, M. J. 1994, *MNRAS*, 266, 343
 Morrison, R., & McCammon, D. A. 1983, *ApJ*, 270, 119
 Murdoch, H. S., Hunstead, R. W., Pettini, M., & Blades, J. C. 1986, *ApJ*, 309, 19
 Pfefferman, E., et al. 1987, *Proc. SPIE*, 733, 519
 Rees, M. J., & Sciama, D. W. 1967, *ApJ*, 147, 353
 Reimers, D., Vogel, S., Hagen, H.-J., Engels, D., Groote, D., Wamsteker, W., Clavel, J., & Rosa, M. P. 1992, *Nature* 360, 561
 Sarazin, C. L. 1988, *X-Ray Emission from Clusters of Galaxies* (Cambridge: Cambridge Univ. Press)
 Sargent, W. L. W. 1988, in *QSO Absorption Lines*, ed. J. C. Blades, D. A. Turnshek, & C. A. Norman (Cambridge: Cambridge Univ. Press), 1
 Shapiro, P. R. 1989, in *Fourteenth Symposium on Relativistic Astrophysics*, ed. E. J. Fenyves (Ann. NY Acad. Sci., 571), 128
 Shapiro, P. R., & Bahcall, J. N. 1980, *ApJ*, 241, 1 (SB)
 Shapiro, P. R., Giroux, M. L., & Bubul, A. 1994, *ApJ*, 427, 25 (SGB)
 Sherman, R. D. 1979, *ApJ*, 232, 1
 Sherman, R. D., & Silk, J. 1979, *ApJ*, 234, L9
 Shields, J. C., Ferland, G. J., & Peterson, B. M. 1994, *ApJ*, submitted
 Shull, J. M., & Van Steenberg, M. 1982, *ApJ*, 48, 95
 Stanek, K. Z. 1992, *MNRAS*, 259, 247
 Trümper, J. 1983, *Adv. Space Res.*, 2(4), 241
 Turner, M. S. 1988, *Phys. Rev. D*, 37, 304
 White, T. R., Lightman, A. P., & Zdziarski, A. A. 1988, *ApJ*, 331, 939
 Wu, X., Hamilton, T., Helfant, D. J., & Wang, Q. 1991, *ApJ*, 379, 564

Note added in proof.—P. Jakobsen et al. (*Nature*, 370, 35 [1994]) have found a strong absorption edge, very probably arising from diffuse He II ($\lambda 304$) in the IGM, in the spectrum of Q0302–003. If confirmed, this will be direct evidence for the existence of a diffuse IGM. Their optical depth limit ($\tau_{\text{He II}} > 1.7$) implies a lower bound on Ω_G of between 10^{-5} and 10^{-3} , depending on the ionizing background slope.

THE SPECTRAL ENERGY DISTRIBUTION OF THE $z = 3$ QUASAR: HS 1946+7658¹

O. KUHN,² J. BECHTOLD,³ R. CUTRI,³ M. ELVIS,² AND M. RIEKE³

Received 1994 March 21; accepted 1994 July 15

ABSTRACT

For the bright $z = 3.02$ radio-quiet quasar, HS 1946+7658, we have obtained radio to X-ray data within the past year: 5 GHz and 1415 MHz data from the VLA; IR photometry at J , H , K , L' ($3.4 \mu\text{m}$) and N ; IR spectroscopy; $UBVRI$ photometry; optical spectrophotometry and high-resolution spectra; and an X-ray spectrum from the *ROSAT* PSPC. The spectral energy distribution (SED) constructed from these data is compared to the mean SED for a set of low-redshift quasars, and while they appear generally similar, there are several differences. In relation to the low-redshift mean, the SED of HS 1946+7658 shows (1) only an upper limit at $10 \mu\text{m}$ (a rest wavelength of $2.5 \mu\text{m}$), indicating that HS 1946+7658 does not have a strong near-IR excess such as hot dust would produce; (2) relatively weak Fe II and Balmer continuum emission at $\sim 3000 \text{ \AA}$; and (3) a steeper turn-down shortward of Ly α , even after correction for the Ly α forest absorption lines.

Subject headings: quasars: individual (HS 1946+7658) — radio continuum: galaxies — X-rays: galaxies

1. INTRODUCTION

The recent discovery of the bright ($m_v = 16.2$) $z = 3.02$ quasar, HS 1946+7658 (Hagen et al. 1992) provides an opportunity to study the spectral energy distribution (SED) of a high-redshift quasar at many wavelengths. For samples at lower redshifts, $z < 1$, radio to X-ray SEDs have been compiled (Neugebauer et al. 1987; Elvis et al. 1994), and these are being used to investigate the nature of the quasar central engine (e.g., Czerny & Elvis 1987; Sun and Malkan 1989; Laor and Netzer 1989; Barvainis 1993). Since quasars evolve strongly with redshift (Boyle et al. 1991), a comparison between the SEDs of high- and low-redshift quasars should enable us to constrain physical models for their origin and energy source.

From 1992 September through 1993 November, we observed HS 1946+7658 at radio, infrared, optical, and X-ray wavelengths. In this paper we present the SED for HS 1946+7658 and compare it with the mean SED for a set of low-redshift, $z \sim 0.1$, quasars (Elvis et al. 1994). While their SEDs are generally similar, we find differences within specific spectral regions: in the near-infrared (IR); around the 3000 \AA “small bump”; and in the ultraviolet (UV). We assume a Friedmann cosmology with $H_0 = 75 \text{ km s}^{-1} \text{ Mpc}^{-1}$, $q_0 = 0.1$, except where otherwise noted.

2. OBSERVATIONS

The log of observations and the resulting fluxes are listed in Table 1. Below, we give details of the observations made in each band.

2.1. Radio

HS 1946+7658 was observed at 5 GHz and 1415 MHz with the NRAO⁴ VLA in the C-configuration on 1992 November

22. Two “snapshots” were taken at each frequency, and a nearby secondary calibrator was observed immediately before or after the quasar. Two primary flux calibrators, 3C 48 and 3C 286, were observed during the run. HS 1946+7658 was detected at 5 GHz, but not at 1415 MHz. The observed frame 20 cm ($\lambda_{\text{rest}} = 5 \text{ cm}$) to 6 cm ($\lambda_{\text{rest}} = 1.5 \text{ cm}$) spectral index, $\alpha_{6\text{cm}}^{20\text{cm}}$ is less than ~ 0.043 , [$\alpha_{6\text{cm}}^{20\text{cm}} \equiv -\log(F_{6\text{cm}}/F_{20\text{cm}})/\log(v_{6\text{cm}}/v_{20\text{cm}})$; $F_\nu \sim \nu^{-\alpha}$], and is less than the values of $\alpha_{6\text{cm}}^{20\text{cm}}$ for a subset of low-redshift, radio-quiet quasars and Seyfert galaxies which have notably flat radio spectra, possibly indicating an additional continuum component (Antonucci & Barvainis 1988; Edelson 1987). Radio observations shortward of 6 cm are needed to determine the behavior of the radio to far-infrared continuum of HS 1946+7658. The radio to optical flux ratio, $R \equiv \log F(v_{\text{obs}} = 5 \text{ GHz})/F(\lambda_{\text{rest}} = 1450 \text{ \AA})$ (Bechtold et al. 1994), is -0.1 , which categorizes HS 1946+7658 as radio-quiet.

2.2. IRAS Data

IRAS ADDSCAN processing was carried out at IPAC⁵ at the position of HS 1946+7658. The quasar is not detected in any of the bands, and 3σ upper limits are given in Table 1.

2.3. IR Photometry

HS 1946+7658 was observed in photometric conditions at J , H , K , and L ($3.4 \mu\text{m}$) at the MMT using the facility IR photometer (Rieke 1984), and at N ($10.2 \mu\text{m}$) using the facility bolometer (Keller, Sabol, & Rieke 1990). The photometer observations were made using a $5''$ aperture and a chopper spacing of $15''$. With each filter, a series of 10 s integrations, alternating on the source and the sky was made, yielding total integration times of approximately 1, 1, 3.5, and 16 minutes at J , H , K , and L , respectively. Photometric transformations and calibrations were made using the measurements of standard stars from Elias et al. (1982). Zero magnitude fluxes for J , H , and K were taken from Campins, Rieke, & Lebofsky (1984), and a zero magnitude flux at L was assumed to be 309.0 Jy based on a blackbody fit to the spectrum of Vega. Extinction

¹ Work reported here was based on observations obtained with the Multiple Mirror Telescope, a joint facility of the Smithsonian Institution and the University of Arizona.

² Harvard-Smithsonian Center for Astrophysics, 60 Garden Street, Cambridge, MA 02138.

³ Steward Observatory, University of Arizona, Tucson, AZ 85721.

⁴ The NRAO is operated by the Associated Universities Inc. under cooperative agreement with the NSF.

⁵ IPAC is funded by NASA as part of the Extended Mission Program, under contract to JPL.

TABLE 1
LOG OF OBSERVATIONS AND BROAD BAND FLUXES

| Wavelength Range | Telescope | F_ν (mJy) ^a | Date(s) |
|------------------------|-------------|----------------------------------|-----------------|
| 1415 MHz | VLA | < 0.94 | 1992 Nov 27 |
| 5 GHz | VLA | 0.89 ± 0.13 | 1992 Nov 27 |
| 100 μm | IRAS | < 378 | 1983 |
| 60 μm | IRAS | < 126 | 1983 |
| 25 μm | IRAS | < 80 | 1983 |
| 12 μm | IRAS | < 111 | 1983 |
| 10.2 μm | MMT | < 13.2 | 1992 Nov 7 |
| 3.4 μm | MMT | 3.23 ± 0.481 | 1993 Jun 3 |
| 2.2 μm | MMT | 2.80 ± 0.048 | 1993 Jun 3 |
| 1.95–2.4 μm | MMT | | 1993 Nov 26 |
| 1.65 μm | MMT | 2.67 ± 0.039 | 1993 Jun 3 |
| 1.25 μm | MMT | 2.35 ± 0.022 | 1993 Jun 3 |
| 0.9–1.35 μm | MMT | | 1992 Sep 15 |
| I (9000 Å) | FLWO 48" | 1.69 ± 0.017 | 1993 Oct 25, 26 |
| R (6350 Å) | FLWO 48" | 1.37 ± 0.026 | 1993 Oct 25, 26 |
| V (5400 Å) | FLWO 48" | 1.17 ± 0.024 | 1993 Oct 25, 26 |
| B (4400 Å) | FLWO 48" | 0.644 ± 0.029 | 1993 Oct 25, 26 |
| U (3600 Å) | FLWO 48" | 0.210 ± 0.058 | 1993 Oct 25, 26 |
| 3000–9000 Å | Steward 90" | | 1993 Sep 23 |
| 1.0 keV | ROSAT PSPC | $(2.67 \pm 0.03) \times 10^{-2}$ | 1993 Jun |

^a When the object was not detected with $S/N > 3$, then the F_ν listed is the 3σ upper limit.

corrections of 0.1 mag airmass⁻¹ at J , H , and K , and 0.2 mag airmass⁻¹ at L were assumed.

For the bolometer observations, a 5".4 aperture was used, and the beam spacing was set to 15". The procedures for observing with the IR bolometer were the same as for the photometer. For HS 1946+7685, we obtained a 20 minute integration. β Andromeda was observed several times during the night for calibration.

2.4. IR Spectroscopy

The IR spectrometers Fspec (Williams et al. 1993) and the Germanium Spectrometer (Rieke et al. 1987) were used at the MMT to obtain 1.95–2.4 μm and 0.9–1.35 μm spectra for HS 1946+7658. Fspec has a 1".2 \times 30" slit. The detector is a NICMOS 256 \times 256 HgCdTe array, and with the low-dispersion, 75 lines per mm, grating, we obtained a K band spectrum with a resolution of $\sim 35 \text{ \AA}$ over 2 pixels. A series of eight 2 minute integrations on HS 1946+7658 was made. During each integration, the telescope was dithered to place the object in four different positions along the slit. The differences between each of the object spectra and the average of the sky spectra which bracketed it (or the sky immediately after or before, if the object frame was the first or last in the sequence) were aligned and then summed to produce a two-dimensional object spectrum for each of the eight integrations. The final spectrum was extracted from the sum of these. The standard star HR 7654 (spectral type A3 V) was divided into the quasar spectrum to remove telluric absorption, and the artificial features produced by intrinsic absorption in the star ($\text{Br}\gamma$ at 2.165 μm and another feature at 2.201 μm) were removed. The spectral type and V magnitude of the standard star were used to correct the shape and flux calibrate the quasar spectrum. All the reductions were done within IRAF. The final spectrum shown in Figure 1a was smoothed using a box size of 2 pixels and grayshifted by +0.18 dex to match the K -band photometry. The $\text{H}\beta$ and $[\text{O III}]$ 5007 emission lines are predicted to fall at 1.954 μm and 2.013 μm , respectively, and it is probable that the

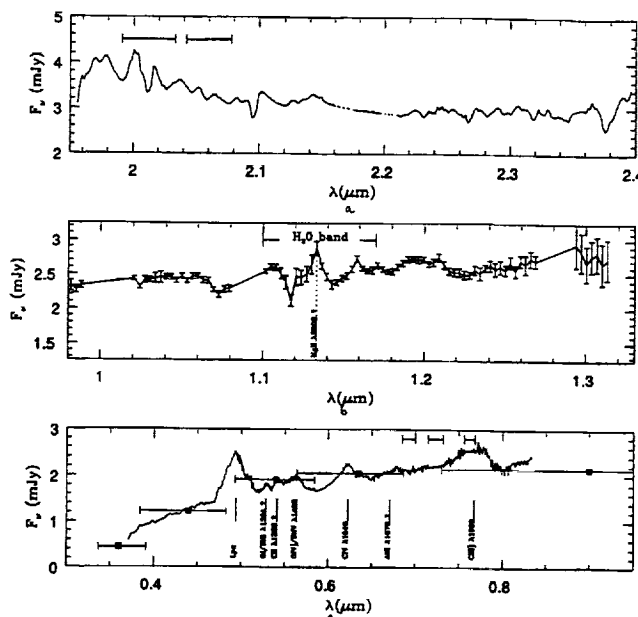


FIG. 1.—(a) The Fspec K -band spectrum for HS 1946+7658 with a grayshift of +0.18 dex (see text) applied. The horizontal segments mark the FWZI of the telluric CO_2 absorption bands, which were removed from the quasar spectrum. The regions from 2.160 to 2.175 μm and 2.197 to 2.209 μm were extrapolated over to remove effects of dividing by absorption features intrinsic to the spectral standard star. (b) The Germanium Spectrometer 0.9–1.35 μm spectrum for HS 1946+7658 with a grayshift of -0.15 dex (see text) applied. The dotted vertical line marks the feature which may be $\text{Mg II } \lambda 2800$, and the VWZI of the telluric H_2O band is also marked. (c) The optical spectrophotometry and $UBVR$ photometry for HS 1946+7658. A grayshift of -0.05 dex was applied to the spectrophotometry so that it matches the photometry. Both the IR and optical data were corrected for reddening by dust in the Galaxy and the line-of-sight damped $\text{Ly}\alpha$ system as discussed in § 4. The horizontal segments mark the positions of telluric H_2O absorption bands. The observed wavelengths, $\lambda_{\text{rest}}(1+z)$, for the emission lines are labeled where $z = 3.02$ for all except O I/S II and C II , in which cases we assume $z = 3.051$.

steep positive slope of the spectrum in $\log(\nu F_\nu)$ (see Figs. 3a and 4) is due to the red wing of $\text{H}\beta$.

The Germanium Spectrometer has two apertures, each 3" in diameter, separated by 22".4. Object and sky spectra were recorded, one on each half of a 32 \times 2 array of germanium diodes. A 150 lines per mm grating provided a resolution of 0.003 μm per pixel, and each grating setting covered $\sim 0.1 \mu\text{m}$. Therefore, to cover the 0.9–1.35 μm region, allowing for overlap, required eight grating settings. We observed in two groups of four settings each, with the quasar observations bracketed by those of the star HR 7611, which has an A3 spectrum and was used to flat-field and flux-calibrate the data. The synthetic stellar spectrum for an A0 star (R. Kurucz, private communication) has strong Paschen β (1.282 μm), γ (1.094 μm), and δ (1.005 μm) absorption, and we therefore disregard the spectral regions centered about and having widths equal to the FWZI of these lines. Integration times at each setting were ~ 25 minutes, and a total of about 3.5 hr was needed to obtain the 0.9–1.35 μm spectrum.

We detect a possible emission feature at $\lambda_{\text{obs}} = 1.13 \mu\text{m}$ (Fig. 1b), corresponding to 2810 \AA in the rest frame. It may be identified with the Mg II (2800 \AA) doublet. The feature has an observed FWHM $\approx 60 \text{ \AA}$, corresponding to $v \approx 2000 \text{ km s}^{-1}$, much smaller than the FWHM of the optical lines ($v \sim 10,000 \text{ km s}^{-1}$). The feature is present in one spectrum. On the two

overlapping spectra, it would cover only the 3–4 pixels at the edge, where the data are not very reliable. The fact that it lies within the atmospheric H_2O absorption band also reduces our confidence that it is real.

The Germanium Spectrometer data used in constructing the SED (Figs. 3 and 4) were smoothed by a running mean where the number of data points averaged was enough to give a signal-to-noise greater than 50, a criterion chosen to produce a spectrum which is smoother than the original data but does not deviate on the small scale. The data are truncated at the ends, where the noise rises and there was a sharp increase in the number of points to be binned in order to achieve the required signal-to-noise. The conditions for the J -band spectroscopic observations were nonphotometric, and so the spectrum ($\log \nu F_\nu$) was grayshifted by -0.15 dex (factor of 1.4 in F_ν) to match the J -band photometry.

2.5. Optical Photometry

UBVRI photometry was obtained using a 2048×2048 Ford CCD (Robinson et al. 1990) on the Whipple Observatory 48 inch (1.2 m) telescope on Mount Hopkins. The overscan region and residual bias level were subtracted from each image, and the data were flat-fielded using dome exposures, except at U where a median of the U data frames was needed since both dome and sky flats exhibited a strong gradient over the array. The data were reduced using the IRAF software package. Four standard star fields of Landolt (1992) were monitored for flux calibration. The quasar was observed on two different nights, and, although neither night was strictly photometric, the averaged magnitudes from each night (excluding one highly discrepant U magnitude from the second night) agree to within 0.025 mag, except at B where the difference is ~ 0.1 mag. The magnitudes from both nights were averaged together, and the resulting fluxes are plotted in Figure 1c. The fluxes were computed assuming zero magnitude fluxes appropriate for an $\alpha = 1$ power law ($F_\nu \sim \nu^{-\alpha}$) which is a good approximation to the shape of the quasar optical continuum. These are taken from Table 14 of Elvis et al. (1994) for all but the R band, where the transmission curve for the filter we have used peaks at a shorter wavelength than for the standard R filter used by Elvis et al. At R , we derive a zero point flux at 6350 Å equal to 3037 Jy. With a color correction of -0.03 at V , we obtain $m_V = 16.17 \pm 0.02$ for HS 1946+7658. This is close to the approximate V magnitude of 15.9 which Hagen et al. (1992) derive from their spectrophotometry.

2.6. Optical Spectrophotometry

Optical spectrophotometry for HS 1946+7658 was obtained at the Steward Observatory 90 inch (2.3 m) telescope using the Boller & Chivens spectrograph and a Loral 1200×800 CCD. The slit was 4.5 wide and was oriented perpendicular to the horizon. There were clouds at the start of the night; however, it seemed clear by the time HS 1946+7658 was observed. Both blue and red spectra were taken: the 3200–6500 Å spectrum was obtained with the 400 lines per mm grating which gave a resolution of 30 Å, and the 5500–9100 Å region was covered with the 300 lines per mm grating, giving 40 Å resolution. The spectra were extracted using the IRAF software package. The standard star, EG 129, was used for flux calibration, and the standard Kitt Peak extinction correction was assumed. The calibration error was roughly 10%, and it may result from uncertainties in the measurements and in the photometric transformations used to convert the EG 129

fluxes from the Palomar “AB69” to the Hayes-Latham system (P. Massey, private communication; Massey et al. 1988). The spectrophotometry was grayshifted by -0.05 dex (factor of 1.12 in F_ν) in order to match the photometry. Above ~ 8330 Å, interference in the CCD coating produced strong “fringing,” and the spectrum was truncated at this wavelength. The absorption lines produced by line-of-sight clouds at $z = 3.048$, $z = 2.841$ (a damped Ly α system), and $z = 1.738$ (Hagen et al. 1992) were removed; however the emission lines: Ly α /N v; O iv]/Si iv 1400 Å; C iv 1549 Å; and C iii] 1909 Å are left in the spectrum, and their measured FWHM values correspond to approximately $14,000 \text{ km s}^{-1}$, $10,000 \text{ km s}^{-1}$, 8000 km s^{-1} , and $16,000 \text{ km s}^{-1}$, respectively (see Fig. 1c). These are quite large compared to the FWHM of emission lines in low-redshift quasars (Wilkes 1986); however, N v affects the measured FWHM for Ly α , and the blue wing of C iii] may be enhanced by a λ 1858 Å emission. There is evidence in the spectrum for O i/Si ii 1304 Å and C ii 1335 Å, both at a redshift of 3.051 which is close to that of a line-of-sight absorber with C iv, Si iv, and Ly α (Hagen et al. 1992). Their redshift corresponds to a relative velocity of $\sim 500 \text{ km s}^{-1}$ between the high- and low-ionization emission lines, and this is consistent with previous measurements (Gaskell 1982; Wilkes 1984). The O i/Si ii and C ii, and a possible Al ii 1670 Å emission line, are too weak or contaminated by other features to measure their properties. As in the spectrum of the $z = 3.8$ quasar, Q1208+101 (Sargent et al. 1986), we do not find evidence for He ii 1640 Å.

2.7. X-Ray

In 1993 June, a 0.1–2.4 keV spectrum of HS 1946+7658 was obtained with the *ROSAT* PSPC. A detailed account of the observations and reductions is given in Bechtold et al. (1994). HS 1946+7658 is the only radio-quiet quasar from the high-redshift sample of Bechtold et al. (1994) with enough PSPC counts to enable the X-ray spectral index to be measured. Assuming only Galactic extinction, with N_{H} fixed at the Galactic value of $7.5 \times 10^{20} \text{ cm}^{-2}$, they determine the spectral index, $\alpha_E = 1.0 \pm 0.3$.

3. CORRECTION FOR THE Ly α FOREST

Ly α emission is observed in the spectrum of HS 1946+7658 at $\lambda_{\text{obs}} = 4888$ Å. Blueward of Ly α , absorption by neutral hydrogen in the host galaxy and in intervening Ly α forest clouds suppresses the continuum flux. To determine the true continuum level between the absorption lines, we used two high-resolution spectra ($\lambda/\delta\lambda \approx 10^4$; FWHM $\approx 80 \text{ km s}^{-1}$) that were obtained with the MMT Blue Channel (Dobrzycki & Bechtold 1994) and cover the 3200–5000 Å region. These data were necessarily taken using a narrow slit (1") and so some light was lost. To correct the overall flux level of the high-resolution spectrum, the data were binned to match the 2.74 Å bin size of the spectrophotometric data. The binned data were then divided into the spectrophotometric data and a polynomial fit to the ratio was taken to be the correction function. Only the data longward of 3650 Å were fitted. There was a difference in the wavelength calibrations for the two data sets, and before the ratio was computed, the spectrophotometry was shifted by $+4.5$ Å to match the wavelength scale for the high-resolution spectra. Finally, the continua determined from the high-resolution spectra were scaled by the correction function. This procedure is illustrated in Figure 2. The polynomial fits were not well-behaved near the endpoints of each spectrum, and therefore the corrected spectrum between 4060 Å and 4120

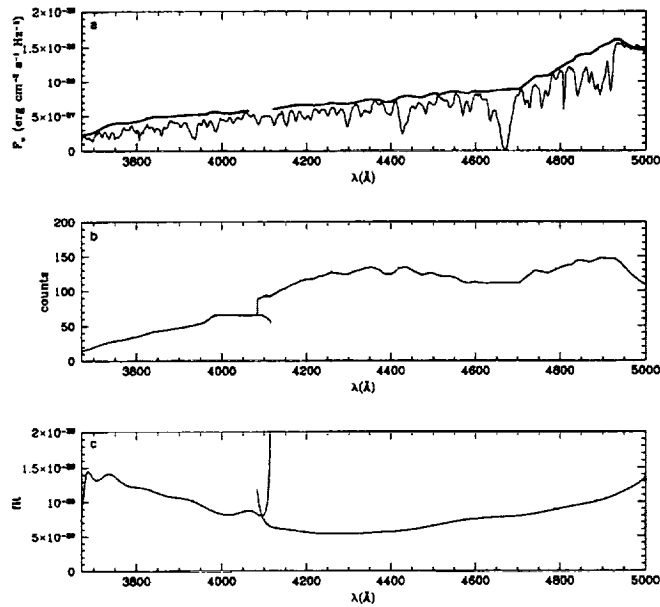


FIG. 2.—The fluxed continua determined from the high-resolution spectra (thick lines) are plotted with the low-resolution spectrophotometry (thin line). (b) The continuum derived from the original high-resolution spectra. (c) The polynomial fit to the ratio between the spectrophotometry and the binned high-resolution data. This fit corrects the high-resolution data for slit losses and detector response. The product of the fit in (c) and the continuum in (b) gives the corrected continuum shown in (a).

\AA is not plotted. The fluxed blue continuum is flatter than the original, showing that the fluxing procedure has corrected for the blue light lost when using the narrow slit. This procedure is limited in that it cannot correct for flux suppression by multiple, low column density clouds along the line of sight. A statistical treatment of these, such as that developed by Press & Rybicki (1993), may further enhance the UV flux.

4. DEREDDENING

The quasar continuum was corrected for extinction in the Galaxy and in a damped Ly α system at $z = 2.841$ (Hagen et al. 1992). Toward the quasar, the column density of Galactic H I, $N_{\text{H}}(\text{Gal}) = 7.5 \times 10^{20} \text{ cm}^{-2}$ (Stark et al. 1992), and the column density of H I in the damped Ly α system, as measured from the profile of the Ly α absorption line, is $1.5 \times 10^{20} \text{ cm}^{-2}$.

The Galactic extinction law used is a combination of that given by Savage & Mathis (1979) for the optical and UV and Rieke & Lebofsky (1985) for the IR. To correct for reddening due to the Ly α system, the extinction law for the Small Magellanic cloud (Bouchet et al. 1985; Prevot et al. 1984) is used, since the conditions (e.g., metallicity) in the SMC are likely to resemble those in damped Ly α clouds (Pei, Fall, & Bechtold 1991). Shortward of $\lambda = 1275 \text{ \AA}$, the SMC extinction is unknown and we have assumed both a simple extrapolation of the UV extinction curve and a turnover toward higher energies. Under these different assumptions, the resulting fluxes differ only by, at most, 2%, and therefore, throughout this paper we use only the extrapolated SMC extinction curve.

We assume the standard Galactic gas-to-dust ratio of $4.8 \times 10^{21} \text{ atoms cm}^{-2} \text{ mag}^{-1}$ (Savage & Mathis 1979), and that the dust-to-gas ratio in damped Ly α clouds may be 10 times smaller than the Galactic (Fall, Pei, & McMahon 1989; Pei et al. 1991). To cover a range of slopes and normalizations

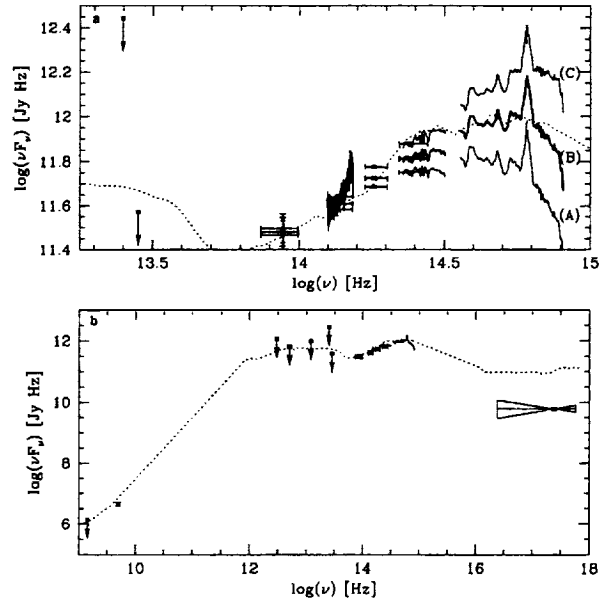


FIG. 3.—(a) The IR/optical observed frame SED: (A) not corrected for interstellar extinction; (B) dereddened by $N_{\text{H}}(\text{Gal}) = 7.5 \times 10^{20} \text{ cm}^{-2}$ and assuming the damped Ly α system has a column density, $N_{\text{H}} = 1.5 \times 10^{20} \text{ cm}^{-2}$ and a dust-to-gas ratio equal to 1/10 of the Galactic value; and (C) dereddened assuming the same parameters for the Galactic and damped Ly α system as (B), but assuming also an additional column intrinsic to the quasar, $N_{\text{H}} = 16 \times 10^{20} \text{ cm}^{-2}$. This is the column density required to bring the UV slope into agreement with the mean low redshift SED. (b) The radio to X-ray energy distribution. The data were dereddened using the same assumptions as in the spectrum labeled (B) above.

for the original quasar spectrum, we show, in Figure 3a, the observed-frame IR/optical continuum without any corrections for reddening (curve A) and corrected for extinction in both the Galaxy and the damped Ly α system, where the dust-to-gas ratio is assumed to be 0.1 times the Galactic (curve B). The third SED (curve C) represents how the continuum would appear if an additional intrinsic column (which will be discussed later) were present.

5. DISCUSSION

In Figure 3b, the radio to X-ray observed-frame continuum, dereddened assuming the dust-to-gas ratio of 0.1 times the Galactic for the Ly α cloud (bold line in Fig. 3a), is plotted together with the mean SED determined for a set of low-redshift, radio-quiet quasars from which the contribution from the host galaxy has been subtracted (Elvis et al. 1994; dotted line). The optical ($\lambda_{\text{rest}} = 6500 \text{ \AA}$) to UV ($\lambda_{\text{rest}} = 1250 \text{ \AA}$) slopes of these two SEDs are nearly identical, $\alpha_{\text{opt}} = 0.35$ ($F_{\nu} \sim \nu^{-\alpha}$), although the optical luminosity of HS 1946 + 7658 is nearly two orders of magnitude greater than the average luminosity of the sample of Elvis et al. The optical/UV continuum of HS 1946 + 7658 is also in good agreement with the composite QSO spectrum for a set of about 700 quasars and AGN from the Large Bright Quasar Survey (Foltz et al. 1987, 1989; Hewett et al. 1991) and for which the median optical ($\lambda_{\text{rest}} = 5050 \text{ \AA}$) to UV ($\lambda_{\text{rest}} = 1450 \text{ \AA}$) slope is 0.32 (Francis et al. 1991). This similarity in continuum shapes favors scenarios in which evolution of the quasar population is determined by successive generations of short-lived quasars ($\sim 10^{7-8} \text{ yr}$) rather than by a single generation of long-lived ($\sim 10^9 \text{ yr}$) quasars (Cavaliere et

al. 1989; Haehnalt & Rees 1993). In contrast, a correlation between α_{ou} and luminosity was reported by Zheng & Malkan (1993) who suggested that it was at least partly due to the contribution of starlight at 6500 Å. If no host galaxy subtraction were made for our low-redshift sample, α_{ou} would be ~ 0.5 , consistent with this interpretation. Further observations of high and intermediate, $z \sim 1$, redshift quasars are being made to test whether this result holds in general.

At a more detailed level, differences between the rest-frame SED for HS 1946+7658 and the mean low-redshift SED occur in three places: the near-IR; the 3000 Å “small bump” region; and the UV.

5.1. Near-IR

Our 10.2 μm limit, which corresponds to an emitted 2.5 μm luminosity, $L_{\nu} < 2.3 \times 10^{33} \text{ ergs s}^{-1} \text{ Hz}^{-1}$, lies a factor of 8 below the *IRAS* 12 μm limit and a factor of 1.2 below the mean low-redshift, radio-quiet SED. HS 1946+7658 shows no evidence for dust emission, which would be expected for high-redshift quasars if they are in the early stages of evolution from dusty IR luminous galaxies to optically selected quasars (Sanders et al. 1988). The rest-frame 2.5 μm fluxes relative to those at 1 μm , the IR inflection point, and in the optical, 2500 Å, are listed in Table 2 for HS 1946+7658, the mean radio-quiet SED and F10214+4724, a $z = 2.286$, IR luminous galaxy (Rowan-Robinson et al. 1993).

5.2. The 3000 Å “Small Bump” Region

In the rest-frame optical, there is little evidence of the 3000 Å “small bump” due to blended Fe II and Balmer continuum emission and commonly seen in the SEDs of low-redshift, radio-quiet quasars (Wills, Netzer, & Wills 1985). The continuum level for HS 1946+7658 lies a factor of ~ 1.5 times below the mean low-redshift, radio-quiet SED. The weak 3000 Å emission may imply that HS 1946+7658 has little UV Fe II, and even less optical Fe II emission, since optical Fe II around H β is typically 4–12 times weaker than the UV Fe II emission (Wills et al. 1985). Q0014+813 and Q0636+680 are two $z \geq 3$ radio-loud quasars in which optical Fe II has been detected (Elston, Thompson, & Hill 1994), and Hill, Thompson, & Elston (1993) have recently reported strong optical Fe II emission in four bright $z \sim 2.5$ quasars (two radio-quiet BALs, one radio-quiet, one radio-loud). We have recently obtained higher resolution and signal-to-noise *J* and *K*-band spectra of HS 1946+7658 which will enable us to search for individual Fe II

multiplets. Zheng & Malkan (1993) have suggested that the correlation between luminosity and UV slope is responsible for the Baldwin effect for C IV. Although they find that this effect is much weaker for low-ionization lines, a luminosity-dependent continuum shape might result in weaker Fe II emission and thus explain the lack of a significant 3000 Å bump in the continuum of HS 1946+7658.

5.3. UV

Shortward of Ly α , the spectral slope of HS 1946+7658 is steeper than that of the mean SED for low-redshift quasars, even after correcting for the Ly α forest and accounting for dust in the Galaxy and in the damped Ly α system (Fig. 3a, curve B). To bring this slope into agreement with the mean low-redshift SED would require an intrinsic absorption column of $N_{\text{H}} = 16 \times 10^{20} \text{ cm}^{-2}$. However, as the upper curve (C) in Figure 3a shows, dereddening by this additional column changes the 8000–5000 Å slope as well, making this quasar much bluer than the mean low-redshift quasar. Unless the UV turnover is produced by weak blended Ly α absorption lines for which we have not corrected, our data indicate that either HS 1946+7658 has an intrinsic turndown in the UV or it has strong optical/UV “big bump” plus extreme reddening.

Even after correction for the Ly α forest absorption, the continuum level blueward of Ly α lies below a simple linear extrapolation through the 5100–5200 Å and 6500–7400 Å regions. The Gunn-Peterson test for an ionized intergalactic medium (IGM) predicts such a drop. The optical depth implied is 0.095, as estimated from the ratio of observed (F_{obs}) to extrapolated flux (F_{ext}) at $\lambda_{\text{obs}} = 4700 \text{ Å}$, i.e., $\tau_{\text{GP}} = \ln(F_{\text{ext}}/F_{\text{obs}})$. This is marginally consistent (at 3σ) with the limit 0.013 ± 0.026 given by Giallongo, Cristiani, & Trevese (1993). However, the extrapolation of the continuum across Ly α is uncertain and depends on proper deblending of the lines between Ly α /N V and O IV]/Si IV 1400 Å. A 20% lower continuum flux between Ly α /N V and O IV]/Si IV would result in a Gunn-Peterson optical depth of zero.

5.4. Comparison with Models

At low redshifts accretion disk models are commonly fitted to the optical/UV continua of quasars. The turndown shortward of Ly α , if intrinsic, imposes stringent constraints on disk models for HS 1946+7658. We assume the disk emits a sum-of-blackbodies spectrum (Frank, King, & Raine 1992), the peak of which corresponds roughly to the temperature,

$$T = \left(\frac{3GM\dot{M}}{8\pi\sigma R^3} \right)^{1/4},$$

where M is the mass of the black hole, \dot{M} is the accretion rate and R is the inner radius of the disk. The paths of hard photons from the inner region of the disk are deflected by the central potential into the equatorial plane. As the viewing angle changes from face-on to edge-on, an increasing number of these photons are seen, and thus the peak wavelength of the model spectrum decreases (Cunningham 1975). For a given disk inclination, it is easy to show that the characteristic temperature, and thus also the peak wavelength, are proportional to f_L^2/L , where L is the total luminosity and f_L is the ratio of the total luminosity to the Eddington luminosity. Thus, if the luminosity of the quasar is increased, for example by assuming the largest plausible universe or intrinsic reddening, then, to maintain a fit to the continuum shape, either the value of f_L must be

TABLE 2
NEAR-IR PROPERTIES

| A. | | | |
|-----------------------|--|--|---|
| Quasar | $L(2500 \text{ Å})$ (ergs s $^{-1}$) | $\frac{L(2.5 \mu\text{m})}{L(2500 \text{ Å})}$ | $\frac{L(25 \mu\text{m})}{L(2500 \text{ Å})}$ |
| Mean low z , RQ SED | 3.5×10^{45} | 0.5 | 0.5 |
| HS 1946+7658 | 5.5×10^{47} | <0.5 | <1.5 |
| F10214+4724 | 3×10^{45} | <40 | 100 |
| B. | | | |
| Quasar | $L(1 \mu\text{m})$ (ergs s $^{-1}$) | $\frac{L(2.5 \mu\text{m})}{L(1 \mu\text{m})}$ | $\frac{L(25 \mu\text{m})}{L(1 \mu\text{m})}$ |
| Mean low z , RQ SED | 1×10^{45} | 1.6 | 1.5 |
| HS 1946+7658 | 2×10^{47} | <1.2 | <3.5 |
| F10214+4724 | 1×10^{46} | <18 | 50 |

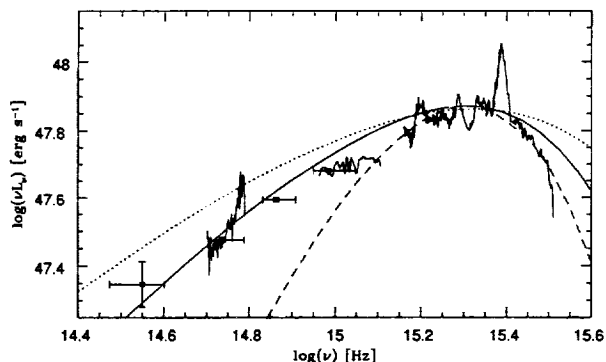


FIG. 4.—The rest-frame IR/optical/UV SED dereddened by $N_H(\text{Gal}) = 7.5 \times 10^{20} \text{ cm}^{-2}$ and assuming the damped Ly α system has $N_H = 1.5 \times 10^{20} \text{ cm}^{-2}$ and a dust-to-gas ratio 1/10 that in the Galaxy. We take H_0 ($\text{km s}^{-1} \text{ Mpc}^{-1}$) = 75 and $q_0 = 0.1$. The solid line represents the spectrum computed for a face-on Kerr disk model which assumes L (ergs s^{-1}) = 2.4×10^{48} and $L/L_{\text{Edd}} = 1$, corresponding to black hole mass and accretion rates equal to $1.7 \times 10^{10} M_\odot$ and $130 M_\odot \text{ yr}^{-1}$, respectively. Spectra emitted by free-free radiation from gas with $T = 10^5 \text{ K}$ (dotted line) and a single blackbody with $T = 25,000 \text{ K}$ (dashed line) are also plotted.

increased or the assumed angle between the equatorial plane and the line-of-sight decreased.

First, we assume no reddening intrinsic to the quasar. Figure 4 shows the rest-frame optical/UV continuum together with spectra for Kerr accretion disk (solid line), free-free (dotted line), and blackbody (dashed line) models. The best-fit disk models are for black hole masses and accretion rates of $1.7 \times 10^{10} M_\odot$ and $130 M_\odot \text{ yr}^{-1}$ ($7.5 \times 10^9 M_\odot$ and $30 M_\odot \text{ yr}^{-1}$ for $H_0 = 100 \text{ km s}^{-1} \text{ Mpc}^{-1}$, $q_0 = 0.5$). To produce a spectrum which peaks at sufficiently short wavelengths to fit the shape of the SED of HS 1946 + 7658 and also matches the high luminosity implied by the largest plausible universe (i.e., $H_0 = 50$, $q_0 = 0.0$) requires the assumption of super-Eddington accretion. Assuming the disk is viewed at an angle mitigates this, and an inclination of 40° ($\cos \theta = 0.75$) of the disk axis to the line of sight allows an Eddington-limited disk model to fit the data. However, this requires $M = 5 \times 10^{10} M_\odot$ and $\dot{M} = 415 M_\odot \text{ yr}^{-1}$ which are quite extreme. For three cosmologies (those which give the largest and smallest universes and an intermediate value) the parameters which give the best fits are summarized in Table 3.

If intrinsic reddening is assumed, then the UV slope is significantly flattened, and hotter disk models are required, thus exacerbating the problems with fitting the data for the largest universe with a Kerr disk. Furthermore, additional dereddening results in an optical continuum shape which rises too rapidly from 8000 to 5000 Å to be fitted well with the standard Kerr disk model.

Optically thin free-free radiation has also been fitted to quasar optical continua (Barvainis 1990, 1993). Figure 4 shows a free-free spectrum at $T = 10^5 \text{ K}$. A single blackbody at

TABLE 3
BEST-FITTING KERR DISK MODELS

| $(H_0, q_0)^a$ | $\cos \theta$ | M (M_\odot) | \dot{M} ($M_\odot \text{ yr}^{-1}$) | L (ergs s^{-1}) | L/L_{Edd} |
|-----------------|---------------|----------------------|--|---------------------------------|--------------------|
| (100, 0.5)..... | 1 | 7.5×10^9 | 30 | 5.5×10^{47} | 0.52 |
| (75, 0.1)..... | 1 | 1.7×10^{10} | 130 | 2.4×10^{48} | 1.0 |
| (50, 0.0)..... | 0.75 | 5.0×10^{10} | 415 | 7.5×10^{48} | 1.0 |

^a H_0 in $\text{km s}^{-1} \text{ Mpc}^{-1}$.

$T = 25,000 \text{ K}$ is plotted as well. The one-temperature, free-free model is too flat, while the single blackbody is too narrow to fit the data well.

6. CONCLUSIONS

The radio-X-ray SED for HS 1946 + 7658 is similar overall to those for low-redshift quasars with a few notable exceptions.

1. It has a steeper UV turnover even after correction for the Ly α forest absorption and interstellar extinction. Additional extinction by dust in the quasar seems unlikely; hence, an intrinsic turnover in the UV may have been found, although absorption by weak, blended Ly α forest lines for which we have not corrected may be partly responsible for this turnover.

2. In the continuum of HS 1946 + 7658, the 3000 Å region does not show any evidence of blended Fe II and BaC emission which is common in the spectra of low-redshift, radio-quiet quasars.

3. In the rest-frame near-IR, there are no detections, making the IR to optical flux for this quasar weak compared to the mean low-redshift quasar. A possible interpretation is that this quasar has a disproportionately small amount of hot dust.

In addition, a comparison between the models and the rest-frame optical/UV continuum illustrates that, for all but the largest plausible universe, sum of blackbodies Kerr accretion disk models can fit the data, except in the UV where they cannot account for the rapid turnover.

We thank the referee, M. Malkan, for his constructive suggestions on the interpretation of the data. We thank C. Fassnacht for reducing the VLA data, A. Siemiginowska for providing the free-free model, and B. Wilkes, J. McDowell, and S. Willner for valuable advice on data reduction and calibration. Also, we thank G. Rieke for his help with the Fspec observations and L. Shier, C. Engelbracht, and D. Williams whose software and IRAF scripts were used to reduce the Fspec data. This work was supported in part by a NASA Graduate Student Research Program grant, NGT-50802, NASA grants NAGW-2201 (Long Term Space Astrophysics Program) and NAG 5-1680 (ROSAT), and NSF grant AST-9058510.

REFERENCES

- Antonucci, R., & Barvainis, R. 1988, *ApJ*, 332, L13
 Barvainis, R. 1990, *ApJ*, 353, 419
 ———. 1993, *ApJ*, 412, 513
 Bechtold, J., et al. 1994, *AJ*, 108, 374
 Bouchet, P., Lequeux, J., Maurice, E., Prevot, L., & Prevot-Burnichon, M. L. 1985, *A&A*, 149, 330
 Boyle, B. J., Jones, L. R., Shanks, T., Marano, B., Zitelli, V., & Zamorani, G. 1991, in *The Space Distribution of Quasars*, ed. D. Crampton (ASP Conf. Ser., 21), 191
 Campins, H., Rieke, G. H., & Lebofsky, M. J. 1984, *AJ*, 90, 896
 Cavaliere, A., Giallongo, E., Padovani, P., & Vagnetti, F. 1988, in *Proc. Workshop on Optical Surveys for Quasars*, ASP Conf. Ser. Vol. 2, ed. P. Osmer, A. Porter, R. Green, & C. Foltz (San Francisco: ASP), 335
 Clavel, J., Wamsteker, W., & Glass, I. S. 1987, *ApJ*, 337, 236
 Cunningham, C. T. 1975, *ApJ*, 202, 788
 Czerny, B., & Elvis, M. 1987, *ApJ*, 321, 305
 Dobrzycki, A., & Bechtold, J. B. 1994, in preparation
 Edelson, R. A. 1987, *ApJ*, 313, 651
 Elias, J. H., Frogel, J. A., Matthews, K., & Neugebauer, G. 1982, *AJ*, 87, 1029
 Elston, R., Thompson, K. L., & Hill, G. J. 1994, *Nature*, 367, 250

- Elvis, M., et al. 1994, *ApJS*, 95, 1
- Fall, S. M., Pei, Y.-C., & McMahon, R. G. 1989, *ApJ*, 341, L5
- Foltz, C. B., Chaffee, F. H., Hewett, P. C., MacAlpine, G. M., Turnshek, D. A., Weymann, R. C., & Anderson, S. F. 1987, *AJ*, 94, 1423
- Foltz, C. B., Chaffee, F. H., Hewett, P. C., Weymann, R. C., Anderson, S. F., & MacAlpine, G. M. 1989, *AJ*, 98, 1959
- Francis, P. J., Hewett, P. J., Foltz, C. B., Chaffee, F. H., Weymann, R. J., & Morris, S. L. 1991, *ApJ*, 373, 465
- Frank, J., King, A., & Raine, D. 1992, *Accretion Power in Astrophysics* (Cambridge: Cambridge Univ. Press), 78
- Gaskell, C. M. 1982, *ApJ*, 263, 79
- Giallongo, E., Cristiani, S., & Trevese, D. 1992, *ApJ*, 398, L9
- Hachnelt, M. G., & Rees, M. J. 1993, *MNRAS*, 263, 168
- Hagen, H.-J. 1992, *A&A*, 253, L5
- Hewett, P. C., Foltz, C. B., Chaffee, F. H., Francis, P. J., Weymann, R. J., Morris, S. L., Anderson, S. F., & MacAlpine, G. M. 1991, *AJ*, 101, 1121
- Hill, G. J., Thompson, K. L., & Elston, R. 1993, *ApJ*, 414, L1
- Keller, L. D., Sabol, B. A., & Rieke, G. H. 1990, *Proc. SPIE*, 1235, 160
- Landolt, A. 1992, *AJ*, 104, 340
- Laor, A., & Netzer, H. 1989, *MNRAS*, 238, 897
- Massey, P., Strobel, K., Barnes, J., & Anderson, E. 1988, *ApJ*, 328, 315
- Neugebauer, G., Green, R. F., Matthews, K., Schmidt, M., Soifer, B. T., & Bennett, J. 1987, *ApJS*, 63, 615
- Pei, Y. C., Fall, S. M., & Bechtold, J. B. 1991, *ApJ*, 378, 6
- Prevot, M. L., Lequeux, J., Maurice, E., Prevot, L., & Rocca-Volmerange, B. 1984, *A&A*, 132, 389
- Press, W. H., & Rybicki, G. B. 1993, *ApJ*, 418, 585
- Rieke, G. H. 1984, in *MMTO Visiting Astronomer Information, Multiple Mirror Telescope Observatory Tech. Rep. No. 13*
- Rieke, G. H., & Lebofsky, M. J. 1985, *ApJ*, 288, 618
- Rieke, G. H., Elston, R. J., Lebofsky, M. J., & Walker, C. E. 1987, in *Infrared Astronomy with Arrays*, ed. C. G. Wynn-Williams & E. E. Becklin, (Honolulu: The University of Hawaii, Institute for Astronomy), 69
- Robinson, L. B., Brown, W. E., Gilmore, D. K., Stover, R. J., Wei, M.-Z., & Geary, J. C. 1990, *Proc. SPIE*, 1235, 315
- Rowan-Robinson, M., et al. 1993, *MNRAS*, 261, 513
- Sanders, D. B., Soifer, B. T., Elias, J. H., Madore, B. F., Matthews, K., Neugebauer, G., & Scoville, N. Z. 1988, *ApJ*, 325, 74
- Sargent, W. A., Fillipenko, A. V., Steidel, C. C., Hazard, C., & McMahon, R. G. 1986, *Nature*, 322, 40
- Savage, B. D., & Mathis, J. S. 1979, *ARA&A*, 17, 73
- Stark, A. A., Gammie, C. F., Wilson, R. F., Bally, J., Linke, R. A., Heiles, C., & Hurwitz, M. 1992, *ApJS*, 79, 77
- Sun, W.-H., & Malkan, M. A. 1989, *ApJ*, 346, 68
- Wilkes, B. J. 1984, *MNRAS*, 207, 73
- . 1986, *MNRAS*, 218, 331
- Williams, D. M., Thompson, C. L., Rieke, G. H., & Montgomery, E. F. 1993, *Proc. SPIE*, 1308, 482
- Wills, B. J., Netzer, H., & Wills, D. 1985, *ApJ*, 288, 94
- Zheng, W., & Malkan, M. A. 1993, *ApJ*, 415, 517

THE COMPLEX OPTICAL TO SOFT X-RAY SPECTRUM OF LOW-REDSHIFT RADIO-QUIET QUASARS.¹ II. COMPARISON WITH FREE-FREE AND ACCRETION DISK MODELS

FABRIZIO FIORE,² MARTIN ELVIS, ANETA SIEMIGINOWSKA, BELINDA J. WILKES,

JONATHAN C. MCDOWELL, AND SMITA MATHUR

Harvard-Smithsonian Center for Astrophysics, 60 Garden Street, Cambridge, MA 02138

Received 1994 March 31; accepted 1995 February 17

ABSTRACT

We compare the optical to soft X-ray spectral energy distributions (SEDs) of a sample of bright low-redshift ($0.048 < z < 0.155$), radio-quiet quasars, with a range of thermal models which have been proposed to explain the optical/UV/soft X-ray quasar emission: (1) optically thin emission from an ionized plasma, (2) optically thick emission from the innermost regions of an accretion disk in Schwarzschild and Kerr geometries. We presented *ROSAT* PSPC observations of these quasars in an earlier paper. Here our goals are to search for the signature of thermal emission in the quasar SEDs, and to investigate whether a single component is dominating at different frequencies.

We find that isothermal optically thin plasma models can explain the observed soft X-ray color and the mean optical-ultraviolet (OUV) color. However, they predict an ultraviolet (1325 Å) luminosity a factor of 3 to 10 times lower than observed. Pure disk models, even in a Kerr geometry, do not have the necessary flexibility to account for the observed OUV and soft X-ray luminosities. Additional components are needed both in the optical and in the soft X-rays (e.g., a hot corona can explain the soft X-ray color). The most constrained modification of pure disk models, is the assumption of an underlying power-law component extending from the infrared (3 μ m) to the X-ray. This can explain both the OUV and soft X-ray colors and luminosities and does not exceed the 3 μ m luminosity, where a contribution from hot dust is likely to be important. We also discuss the possibility that the observed soft X-ray color and luminosity are dominated by reflection from the ionized surface of the accretion disk.

While modifications of both optically thin plasma models and pure disk models might account for the observed SED, we do not find any strong evidence that the OUV bump and soft X-ray emission are one and the same component. Likewise, we do not find any strong argument which definitely argues in favor of thermal models.

Subject headings: quasars: general — X-rays: galaxies

1. INTRODUCTION

The most striking property of the continuum of unbeamed quasars (simply quasars hereafter) is the fact that it extends over at least seven decades in frequency, from 100 μ m to 100 keV, maintaining a similar luminosity per decade. The most prominent feature of a quasar's spectral energy distribution (SED) is the blue bump which dominates the optical/ultraviolet (OUV) emission and contains $\geq 50\%$ of the energy output. The blue bump could have a broad maximum in the 1300–1000 Å range, as suggested by Malkan (1988), or could extend into the so far unobserved extreme-UV region, if some intrinsic reddening is present. The observed soft X-ray flux is in most cases lower than that predicted by extrapolating the UV flux with the typical spectral indices measured at wavelengths longer than ~ 1000 Å. This requires a sharp drop in the extreme UV region. The soft X-ray flux (≤ 1 keV), however, is higher than the extrapolation of the higher energy (2–10 keV) power law. This low-energy X-ray turn-up, commonly known as the soft X-ray excess, is generally interpreted as the high-

energy tail of the blue bump. Although such a connection is suggestive given that both components increase into the unobservable extreme-UV, no direct evidence yet exists. However it is clear that the combination of OUV and soft X-ray data will provide invaluable constraints on models which seek to explain both components, such as thermal emission from an accretion disk (e.g., Shields 1978; Malkan & Sargent 1982; Czerny & Elvis 1987; Sun & Malkan 1989; and Laor 1990, on the OUV side; Turner & Pounds 1988 and Elvis et al. 1991, from the X-ray side), and optically thin free-free (see Barvainis 1993 for a review).

The soft X-ray excess was recognized as a distinct and common component below 1 keV of the X-ray spectra of Seyfert 1 galaxies and quasars in both *EXOSAT* and *Einstein* data (Turner & Pounds 1989; Wilkes & Elvis 1987; Masnou et al. 1992). However, the poor energy resolution of both instruments at these energies resulted in little or no information about the spectral form. The softer energy band and improved resolution of the *ROSAT* (Trümper 1983) PSPC (Pfeffermann et al. 1987) provides us with our first opportunity to study the spectrum of the soft excess and thus to realize its full potential as a constraint on models for the OUV/X-ray continuum.

We observed a sample of low-redshift, radio-quiet quasars selected to be the brightest with known soft excesses, to acquire high signal-to-noise ($> 100 \sigma$) spectra with the PSPC. The analysis of these X-ray observations is reported in a companion

¹ This paper is based in part on data obtained on the Multiple Mirror Telescope (MMT), a joint facility of the Smithsonian Institution and the University of Arizona.

² Postal address: Osservatorio Astronomico di Roma, via dell'Osservatorio 5, Monteporzio-Catone (RM), I00040 Italy; fiore@cfa.harvard.edu.

ion paper (Fiore et al. 1994, hereafter Paper I). The main results from this paper are the following:

1. The PSPC spectra span a broad range of slopes ($1.3 < \alpha_E < 2.3$, where $F_\nu \propto \nu^{-\alpha_E}$) and are steeper than at higher energies (typically 2–10 keV) by $\Delta\alpha_E = 0.5$ –1. They are dominated by the soft X-ray excess.

2. The deviations from a single power-law model in the 0.2–2 keV band are small but still significant. The “break point” between the hard and soft components is in all cases above 0.7 keV. The PSPC spectra exclude “narrow” models, such as a single line or a blackbody, for the soft X-ray component.

3. The strength of any line emission feature in the soft X-ray band is small (less than 10%–20% of the counts in each channel), unless the continuum is complicated.

Here we present the optical to soft X-ray SEDs of the quasars and compare them with the predictions of a wide range of thermal models which have been proposed to explain the OUV/soft X-ray quasar emission: (1) optically thin plasma emission, (2) optically thick thermal emission from the innermost regions of an accretion disk in Schwarzschild and Kerr geometries. Our aims are to search for the signature of thermal emission in the quasar SEDs and to investigate whether a single component is dominating at different frequencies or rather if the quasar SEDs are best reproduced by the superposition of different components.

2. THE SOFT X-RAY COMPONENT AND THE BIG BLUE BUMP

A longstanding question in quasar research is whether the soft X-ray emission and the OUV blue bump are one and the same component. The most direct way to verify this is to search for simultaneous/correlated variations in both the UV and soft X-ray emission. Unfortunately simultaneous UV and soft X-ray observations of longer than a few hours are difficult to schedule with *ROSAT* and *IUE* and have so far been performed only for a few, very bright objects like the BL Lacertae object PKS 2155–304 (Edelson et al. 1995).

A number of quasars have been observed nearly simultaneously by *IUE* and *ROSAT* during the *ROSAT* All-Sky Survey (Walter et al. 1995). These authors found that in six out of eight cases the shape of the UV to soft X-ray component is similar, while the relative strength of the UV emission compared to the hard X-ray power law varies by a factor of 10 over the sample.

A more indirect method is through the statistical properties of the UV and soft X-ray emission of a sample of quasars. Walter & Fink (1993) have reported a strong correlation between the soft X-ray (PSPC) spectral indices and the ratio between the flux at 1350 Å and that at 2 keV in a sample of about 50 quasars. Under the assumption that the PSPC spectral index is a good indicator of the strength of the soft excess, this was interpreted as evidence that the soft X-ray emission and OUV emission are part of the same component: a O-UV-X-ray bump. There are some concerns about this analysis. We note that: (1) the Walter and Fink sample is soft X-ray selected, since it includes only the brightest quasars in the *ROSAT* All-Sky Survey. Then, the PSPC spectral index and the 2 keV flux are strongly correlated quantities, since 2 keV is the upper end of the PSPC band: in a flux-limited soft X-ray survey a source with a low 2 keV flux is likely to have also a steep PSPC spectral index. (2) The Walter and Fink sample is very heterogeneous. It contains: low-luminosity Seyfert galaxies and high-luminosity, high-redshift quasars, sources with strong and

faint blue bumps; radio-loud and radio-quiet objects; strongly absorbed and unabsorbed sources. The correlations between these properties and the luminosity in the optical, UV, and soft X-ray bands are all complicated and could drive, at least in part, the Walter and Fink correlation.

Laor et al. (1994) report a result similar to the Walter and Fink correlation. They found a significant correlation between the PSPC spectral index and the optical (3000 Å) to X-ray (2 keV) rest frame spectral index α_{OX} in a sample of 10 optically selected, $z < 0.4$ ($\langle z \rangle = 0.22$), $M_B < -23$ quasars (three of which are radio-loud). Being optically selected, this small sample does not suffer from the selection bias mentioned above.

As an example we plot in Figure 1 α_{OX} as a function of the PSPC best-fit single power-law energy index α_E .³ We include the Laor et al. (1994) radio quiet objects, the sample presented in Paper I (four objects are PG quasars, and the remaining two, NAB 0205+024 and Mrk 205 have a comparably strong blue bump), and all the radio-quiet PG quasars in the Walter and Fink sample which have small Galactic N_H and $z < 0.4$. The combined sample consists of 22 objects, all radio-quiet, with a strong blue bump, without significant intrinsic absorption and spanning a large range in optical luminosity ($-26 < M_B < -21$). We estimate that a spread in α_{OX} of ± 0.1 is introduced by the fact that the observations in OUV and X-ray are not simultaneous (from the data in Tables 1 and 2, see below). It is not clear whether or not the amplitude of the long-term UV variability is correlated with the luminosity. O’Brien et al. (1988) found some evidence for an inverse correlation, but their sample of high luminosity objects was small. For the sample presented in this paper there is no evidence for a correlation between the amplitude of the UV variability and luminosity. We therefore assume that the spread in α_{OX} is roughly similar at all luminosities. For the objects in the sample presented in this paper the optical luminosity has been corrected for the

$$^3 \alpha_{OX} = \frac{\log [L(2500 \text{ Å})/L(2 \text{ keV})]}{2.6057}.$$

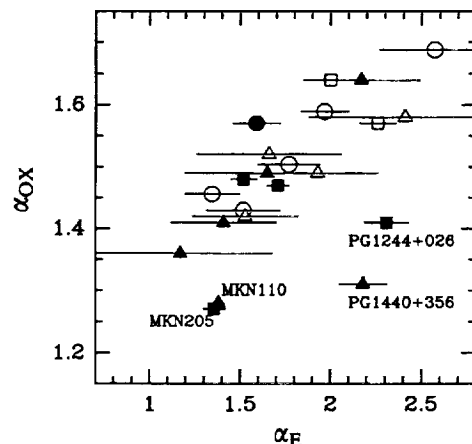


FIG. 1.—PSPC energy index plotted against the OUV to X-ray energy index α_{OX} for the quasars of the sample presented in this paper (squares), the radio-quiet quasars in the Laor et al. (1994) sample (circles), and the PG objects in the sample of Walter & Fink (1993) with $z < 0.4$ (triangles). Open symbols identify high-luminosity quasars ($M_B < -23.5$), filled symbols identify low-luminosity quasars ($M_B > -23.5$).

contribution from the host galaxy, while the objects in the Laor et al. and Walter and Fink samples were not so corrected. We note however that the contribution of the host galaxy should be small even in low-luminosity objects at 3000 Å (see the galaxy template in Elvis et al. 1994a), thus affecting α_{OX} only slightly.

The correlation between α_E and α_{OX} is quite good for the high optical luminosity objects (11 objects with $M_B < -23.5$, linear correlation coefficient equal to 0.855 corresponding to a probability of 99.95%). The linear correlation coefficient for the whole sample is lower ($r = 0.60$, corresponding to a probability of 99.6%). In fact, the four points which deviate most from the correlation are all lower optical luminosity sources. Two of these sources, PG 1440+356 (Mrk 478) and PG 1244+026 have a very steep PSC slope but their soft X-ray luminosity is comparable or even higher than their UV luminosity, unlike all the other sources in the sample. PG 1440+356 is one of the few quasars detected at ~ 0.1 keV by the *ROSAT* Wide Field Camera (Pounds et al. 1993). Another Wide Field Camera source (RE 1034+398) has a very steep PSC spectrum (Puchnarewicz et al. 1995), flat α_{OX} and soft X-ray luminosity higher than the UV luminosity. Pounds (1994) and Fiore & Elvis (1995) suggested that these sources could belong to a separate class of quasars, sources that emit the most of the power in soft X-rays, unlike the majority of optically selected quasars. Fiore & Elvis (1995) suggested that these source could resemble Galactic black hole candidates in the high (and soft) state.

Assuming that the PSC spectrum of radio-quiet, strong blue bump sources, is made up of two distinct components, a steep one dominating below ~ 1 –2 keV and a hard one dominating at higher energies, the correlation in Figure 1 can be interpreted in two ways. Either (1) the intensity of the soft component is more or less the same in all sources while that of the hard one varies over a broad range, or (2) the intensity of the soft component varies over a broad range in these sources while that of the hard one is more or less the same. The significantly larger scatter in the 2 keV luminosity found by Laor et al. (1994) with respect to that in the 0.3 keV luminosity, argues

for the first case. This suggests that, in high optical luminosity sources at least, a correlation between the blue bump and the soft X-ray component, does indeed exist. However, this does not prove that the luminosity in different frequency bands arises from the same emission component. In the following sections we test the single component hypothesis by discussing the ability of various models to reproduce both X-ray and OUV data.

3. OBSERVATIONAL DATA

3.1. X-Ray Data

The numerical results of the spectral fitting from Paper I are given in Table 1. Table 1 lists the soft X-ray monochromatic luminosities νL_ν at 0.4 keV and 1 keV (soft component only), the soft component energy index ($F_\nu \propto \nu^{-\alpha_{ES}}$), and 2 keV monochromatic luminosity (soft plus hard components) for the quasars in our sample. They are from Paper I and were obtained by fitting to the PSC data a two power-law model, or a power law plus thermal bremsstrahlung model, with low energy absorption (N_H was limited to values greater than the Galactic column along the line of sight). The power law plus thermal bremsstrahlung model gives a fit of quality comparable to the two power-law model in all sources but PG 1426+015, where it produces a significantly worse χ^2 (see Paper I). Errors on the luminosities represent 1 σ confidence intervals for four interesting parameters.

In Paper I we compared the PSC results concerning the soft component intensity with those obtained with previous satellites, finding that they always agree within the errors. In spite of the low energy resolution of the *EXOSAT* LE and the *Einstein* IPC several authors estimated the shape of the soft X-ray component in a number of quasars. In particular, Comastri et al. (1992) fitted the *EXOSAT* ME/LE data with a two power-law model (with N_H fixed to the Galactic value) for a sample of six quasars, three of which are in common with our sample. They found a soft component energy index α_{ES} of $3.33^{+0.66}_{-0.42}$ in PG 1211+143, $3.32^{+1.20}_{-0.67}$ in TON 1542 (PG 1229+204), and $2.66^{+1.09}_{-0.49}$ in PG 1426+015. For each source the *EXOSAT* indices and PSC indices in Table 1 are consis-

TABLE 1
X-RAY OBSERVATIONS

| Name | νL_ν , (0.4 keV) ^{a,b} | νL_ν , (1 keV) ^{a,b} | α_{ES} ^{b,c} | νL_ν , (2 keV) ^{a,d} | νL_ν , (1325 Å) ^{a,b} |
|---------------------------------|--|--------------------------------------|------------------------------|--------------------------------------|---------------------------------------|
| NAB 0205+024 ^e | $8.07^{+1.79}_{-2.09}$ | $1.60^{+0.33}_{-0.63}$ | 2.8 ± 0.5 | $1.07^{+0.07}_{-0.12}$ | |
| <i>f</i> | $5.53^{+1.49}_{-0.60}$ | $0.78^{+0.30}_{-0.30}$ | | $1.18^{+0.09}_{-0.09}$ | 2.2 |
| PG 1211+143 ^e | $2.46^{+0.90}_{-0.65}$ | $0.74^{+0.33}_{-0.41}$ | $2.3^{+1.1}_{-0.3}$ | $0.56^{+0.10}_{-0.06}$ | |
| <i>f</i> | $1.64^{+0.74}_{-0.25}$ | $0.25^{+0.19}_{-0.10}$ | | $0.62^{+0.08}_{-0.07}$ | 0.6 |
| Mrk 205 ^e | $1.15^{+0.62}_{-0.20}$ | $0.31^{+0.35}_{-0.10}$ | $2.3^{+1.1}_{-0.7}$ | $0.92^{+0.05}_{-0.04}$ | |
| <i>f</i> | $0.77^{+0.34}_{-0.28}$ | $0.124^{+0.16}_{-0.065}$ | | $0.94^{+0.06}_{-0.06}$ | 0.3 |
| TON 1542 ^e | $0.71^{+0.43}_{-0.25}$ | $0.135^{+0.225}_{-0.076}$ | $2.4^{+1.6}_{-0.7}$ | $0.44^{+0.02}_{-0.02}$ | |
| <i>f</i> | $0.41^{+0.20}_{-0.07}$ | $0.005^{+0.009}_{-0.003}$ | | $0.45^{+0.07}_{-0.07}$ | 0.8 |
| PG 1244+026 ^e | $0.72^{+0.12}_{-0.09}$ | $0.22^{+0.013}_{-0.062}$ | $2.3^{+0.4}_{-0.6}$ | $0.088^{+0.012}_{-0.004}$ | |
| <i>f</i> | $0.49^{+0.16}_{-0.04}$ | $0.090^{+0.050}_{-0.032}$ | | $0.099^{+0.019}_{-0.015}$ | 0.2 |
| PG 1426+015 ^e | $3.21^{+0.49}_{-0.58}$ | $1.69^{+0.29}_{-0.66}$ | $1.8^{+0.4}_{-0.3}$ | $1.43^{+0.12}_{-0.09}$ | |
| <i>f</i> | $2.22^{+0.54}_{-0.25}$ | $0.144^{+0.115}_{-0.034}$ | | $1.56^{+0.14}_{-0.14}$ | 0.7 |

^a Units of 10^{44} ergs s⁻¹.

^b Soft X-ray component.

^c $F_\nu \propto \nu^{-\alpha_{ES}}$.

^d Total X-ray luminosity.

^e Two power-law fit.

^f Power-law + thermal bremsstrahlung fit.

tent with each other, within the rather large errors. However, the *EXOSAT* best fit spectral indices are in all cases steeper by $\Delta\alpha \sim 1$ than the PSPC best fit indices, and the break energy of ~ 0.6 keV estimated by Comastri et al. (1992) falls short than the typical break energy of 1 keV found in Paper I. There could therefore be a systematic offset between the *EXOSAT* and the PSPC measurements. We note that the Comastri et al. indices were obtained by fitting the data from two distinct experiments (the ME and the LE). Since the ME starts to be sensitive only above 1 keV, while the peak of the LE sensitivity is below this energy, the best-fit parameters could be largely affected by inaccuracies in the relative calibration of the two instruments. For example a soft component slope steeper than the actual one would be easily obtained if, given the same incident spectrum, the normalization in the LE were systematically higher than that in the ME (also see the discussions on the relative calibration of two instruments in Masnou et al. 1992, and in Paper I). On the other hand, the energy band and resolution of the PSPC allow a quite accurate determination of the shape of the soft component of bright quasars. In Paper I we showed that calibration uncertainties currently limit this ability and forced us to adopt very conservative errors on the parameters describing the soft X-ray component. We remark here that the offset between the *EXOSAT* and PSPC results is in all cases smaller than the statistical + systematic uncertainties.

Masnou et al. (1992) fitted the IPC/MPC data with a broken power-law model (with N_H fixed to the Galactic value) for a sample of seven quasars, two of which are in common with the present sample. For these two quasars they found a low-energy slope of $\alpha_{ES} = 2.6$ (NAB 0205 + 024) and $\alpha_{ES} = 1.47$ (Mrk 205). These slopes are consistent with the ones obtained from our analysis (see Table 1).

Saxton et al. (1993) fitted the *EXOSAT* ME/LE data of a sample of 12 quasars parameterized the soft excess as a thermal bremsstrahlung model with a fixed temperature of 0.2 keV, close to the best fit temperature obtained fitting this model to the composite spectrum of the six quasars in our sample in Paper I.

3.2. IR-Optical-UV Data

Table 2 gives the infrared (3 μm), optical (5500 Å), and UV (2500 and 1325 Å) monochromatic luminosities (νL_ν). When

more than one infrared, optical or UV observation is available we report the maximum and minimum observed luminosities including errors, the number of observations and their date span. As a reference we also give in Table 2 the average α_{ox} of these quasars. The mean α_{ox} in the sample is 1.47, slightly lower than the mean value of 1.525 found by Laor et al. (1994) for a complete sample of optically selected, low-redshift, radio-quiet quasars (a difference of 0.06 in α_{ox} corresponds to a 40% difference in the optical to X-ray luminosity ratio). When available, the infrared, optical, and UV luminosities were extracted from the "Atlas of Quasar Energy Distributions" (Elvis et al. 1994a). Additional optical spectrophotometric data were included for NAB 0205 + 024 and PG 1244 + 026 (see below). The data from TON 1542 include optical data from Neugebauer et al. (1987), IR data from Rudy, Levan, & Rodriguez-Espinosa (1982), and archival *IUE* spectra.

The *IUE* data were corrected for the reduction in the efficiency of the cameras with the time (Bohlin & Grillmar 1988). Following the procedures in Elvis et al. (1994a), the data were corrected for reddening, shifted to the rest frame and corrected for the contribution of the host galaxy using the galaxy template given in Table 16 of Elvis et al. (1994a). These authors showed that the contribution of the host galaxy can be important ($\geq 20\%$) for $M_V < -25$ [$\nu L_\nu(5500 \text{ Å}) < 2 \times 10^{45}$]. Direct measurements of the host galaxy were used in two cases (NAB 0205 + 024 and PG 1211 + 143). In two cases (Mrk 205 and PG 1426 + 015) we used the *H*-band luminosity of the host galaxy in the Elvis et al. sample [$\log L(H) = 44.6^{+0.3}_{-0.6}$, but note that in Mrk 205 we modified the upper error bar, so as not to overpredict the total *H*-band luminosity]. In the remaining two cases the observed *H*-band luminosity is lower than the mean host galaxy luminosity in Elvis et al. (1994a), and we assumed therefore that the host galaxy luminosity in these objects is a little lower than the observed *H* luminosity. In all cases we used highly conservative error bars on the host galaxy luminosity. Table 2 lists the host galaxy normalization in the *H* band for each quasar. Mrk 205 was quoted as a "weak bump quasar" by McDowell et al. (1989), showing a very steep optical to UV slope, but this slope turns out to be consistent with the quasar average slope ($f_\nu \sim -0.1$) if the contribution from the host galaxy is close to the mean value in Elvis et al. (1994a). The errors on the host galaxy luminosity have been

TABLE 2
INFRARED-ULTRAVIOLET OBSERVATIONS

| Name | Redshift | $\log \nu L(H)^a$ of Galaxy | $\nu L_\nu(3 \mu\text{m})$ (No.; Dates) | $\nu L_\nu(5500 \text{ Å})$ (No.; Dates) | $\nu L_\nu(2500 \text{ Å})$ (No.; Dates) | $\nu L_\nu(1325 \text{ Å})$ (No.; Dates) | α_{ox}^b |
|----------------------|----------|-----------------------------|--|---|---|---|-----------------|
| NAB 0205 + 024 | 0.155 | 44.19 ± 0.04 | $9.4^{+1.0}_{-0.9}$ 1; 85/9 | 8.1–11.5 3; 78/2–91/9 | 33 ± 1 1; 82/12 | 31 ± 4 1; 82/12 | 1.57 |
| PG 1211 + 143 | 0.085 | $43.36^{+0.04}_{-0.23}$ | 10.9–14.7 5; 81/5–88/4 | 9.7–16.6 6; 80/6–88/9 | 23.4–27.8 2; 85/12–87/2 | 19.1–31.3 2; 83/12–85/2 | 1.64 |
| Mrk 205 | 0.070 | $44.60^{+0.1}_{-0.6}$ | 1.7–4.2 3; 76/6–85/6 | $1.6^{+1.5}_{-0.6}$ 1; 72/5 | 1.8–7.3 2; 78/7–83/2 | 3.3–6.1 2; 78/7–83/2 | 1.27 |
| TON 1542 | 0.064 | $44.48^{+0.1}_{-0.6}$ | $3.17^{+0.63}_{-0.38}$ 1; 81/5 | $2.61^{+0.75}_{-0.31}$ 1; 80/11 | 7.5 ± 0.2 1; 82/5 | 10.2 ± 0.3 1; 82/5 | 1.47 |
| PG 1244 + 026 | 0.048 | $43.76^{+0.1}_{-0.6}$ | $0.39^{+0.07}_{-0.04}$ 1; 83/2 | 0.53–0.92 2; 7/80–5/91 | 1.06 ± 0.05 1; 83/2 | 1.06 ± 0.05 1; 83/2 | 1.41 |
| PG 1426 + 015 | 0.086 | $44.60^{+0.3}_{-0.6}$ | 5.9–12.1 5; 81/7–88/5 | 2.6–7.3 6; 80/7–88/9 | 22.3–28.4 2; 83/2–85/5 | 24.9–42.8 2; 83/2–85/5 | 1.48 |

^a Units of $10^{44} \text{ ergs s}^{-1}$.

^b $\alpha_{ox} = \frac{\log [L(2500 \text{ Å})/L(2 \text{ keV})]}{2.6057}$.

^c Galaxy subtraction for TON 1542 used the mean values given in Elvis et al. 1994: $L_H = 4^{+4}_{-3} \times 10^{44} \text{ ergs s}^{-1}$; $r_e = 10^{+3}_{-6} \text{ kpc}$.

^d Galaxy normalization chosen to match the rest frame *H* luminosity.

propagated to find the uncertainties on the luminosity at optical and UV frequencies

Optical spectrophotometry was obtained for two of the quasars: NAB 0205+024 and PG 1244+026; on the Multiple Mirror Telescope (MMT) using the MMT spectrograph and the red channel on 1991 September 15 and 1991 May 17, respectively (the PSPC observations of these quasars were performed in 1992 January and 1991 December, respectively). On both dates conditions were photometric. Two spectra were obtained, the first through a wide slit ($5'' \times 180''$) to ensure photometric accuracy and the second through a narrow slit ($1.5'' \times 180''$) for improved spectral-resolution (~ 20 Å) and signal-to-noise. The 150 lines mm^{-1} grating was used yielding a wavelength range of ~ 3800 – 7600 Å. The spectra were reduced in the standard manner using IRAF. The wide-slit observation was flux calibrated with reference to a nearby standard star observed sequentially with the quasar. The continuum shape and level of the narrow-slit spectrum were then normalized to agree with this flux calibrated spectrum. Continuum fluxes at 5500 Å measured from these spectra are presented in Table 2. The spectra will be presented in a later paper.

The errors contain the evaluated uncertainty on all the above corrections, in addition to the statistical uncertainty. In the case of the *IUE* data a further 3% systematic uncertainty is folded into the errors (Bohlin 1980). The data in different bands are not simultaneous. Variations of a factor of ~ 2 were recorded for these quasars in optical and UV and of a factor of 5 in X-ray. The uncertainty due to source variability is generally larger than the quoted (statistical + systematic) errors.

4. MODELING THE INFRARED TO SOFT X-RAY SPECTRAL ENERGY DISTRIBUTIONS OF QUASARS

4.1. Optically Thin Plasma Models

4.1.1. The Model

Thermal bremsstrahlung at temperatures of 10^5 – 10^7 K emitted by an optically thin gas cloud is a candidate mechanism to produce the OUV/soft X-ray bump in quasar spectra (Barvainis 1993). We calculate the free-free contribution for a spherical and isothermal cloud assuming that the cloud has radius (R) and density (n_e) consistent with an optical depth less than 1 ($\tau_{\text{eff}} = [\tau_{\text{ff}} + \tau_{\text{es}}]^{1/2} < 1$; where τ_{ff} are the free-free and τ_{es} the electron scattering optical depths). The bremsstrahlung luminosity is calculated using (Rybicki & Lightman 1979):

$$L_{\nu} = 9.5 \times 10^{-38} \left(\frac{4}{3} \pi R^3 \right) n_e^2 T^{-1/2} \times \exp \left(-\frac{h\nu}{kT} \right) g_{\text{ff}} \text{ ergs s}^{-1} \text{ Hz}^{-1},$$

where g_{ff} is the Gaunt factor calculated using an approximation given by Gronenschild & Mewe (1978).

In the soft X-ray band the free-free emission from the ionized plasma represents only part of the total emission, since recombination, 2-photon, and line emission from the same plasma can also be important, depending on the temperature (Raymond & Smith 1977). We calculated the 2-photon and recombination continua as in Raymond & Smith (1977). We do not include line emission in our modeling but we discuss in the next sections how it can effect the spectral shape and intensity.

4.1.2. Comparison with the Data

We plot in Figure 2 the $3 \mu\text{m}$ – 2 keV SEDs of the six quasars, galaxy subtracted and including only the soft X-ray com-

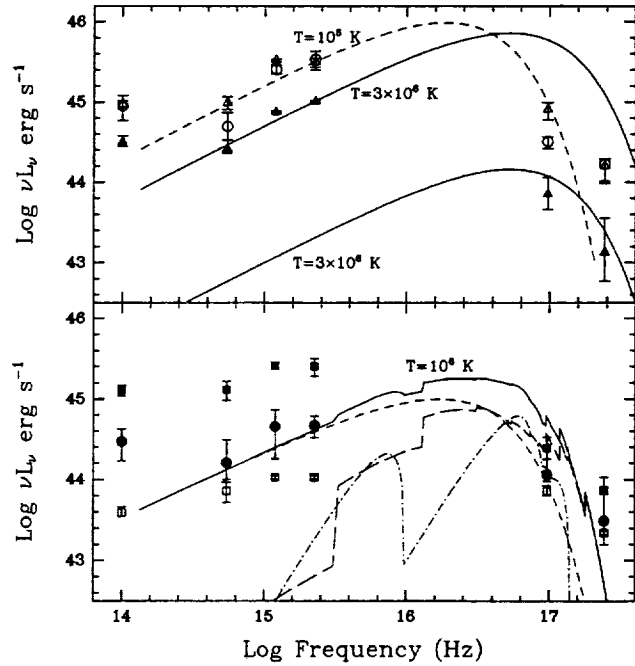


FIG. 2.—IR to soft X-ray SEDs of the six quasars (after the subtraction of the galaxy contribution and of the high-energy X-ray power law): NAB 0205+024: open triangles; PG 1211+143: filled squares; Mrk 205: filled circles; TON 1542: filled triangles; PG 1244+026: open squares; PG 1426+015: open circles. Upper panel: the solid lines represent the free-free continuum for $T = 3 \times 10^6$ K and two normalizations; the dashed line represents the free-free continuum for $T = 10^6$ K. Lower panel: the solid line represents the sum of the continua from an optically thin plasma with $T = 10^6$ K; the short-dashed line is the free-free continuum; the long-dashed line is the recombination continuum; the dot-dashed line is the two-photon continuum.

ponent. On the upper panel we also plot free-free models, for $T = 10^6$ and $T = 3 \times 10^6$, that roughly encompass the observed SED. On the lower panel we plot the free-free, 2-photon and recombination continua, as well as the sum of these continua, for $T = 10^6$ K. At this temperature free-free emission dominates the OUV part of the spectrum but the harder recombination continuum dominates the soft X-ray part of the spectrum. Note the numerous, rather deep edges present in the total continuum.

Rather than attempt a formal fit of these models to the data, we make use of color diagrams to evaluate their flexibility and to evaluate the range of the parameters for which they are able to reproduce the data (also see Siemiginowska et al. 1995).

In Figure 3 we plot the soft X-ray color $[\nu L_{\nu}(1 \text{ keV})/\nu L_{\nu}(0.4 \text{ keV})]$, soft component only, against the OUV color $[\nu L_{\nu}(1325 \text{ Å})/\nu L_{\nu}(5500 \text{ Å})]$ for the six quasars. The soft X-ray color is calculated using the X-ray monochromatic luminosities in Table 2. The dotted line with open squares shows the predictions of pure bremsstrahlung models with temperatures in the range 10^6 – 10^7 K. The additional contribution of recombination and 2-photon continua would increase by a factor of 6 the continuum at 0.4 keV and by a factor of 30 the continuum at 1 keV for $T = 10^6$ K thus increasing the soft X-ray color by a factor of 5. For $T = 10^7$ K the contribution of recombination and 2-photon continua would increase the flux at 0.4 keV by a factor of 1.2 and the flux at 1 keV by a factor of 1.4, thus increasing the X-ray color by 9%. Filled squares show soft X-ray color predicted in these two cases.

The bremsstrahlung model can reproduce the observed soft X-ray color for temperatures in the range 2 – 5×10^6 K (0.15 –

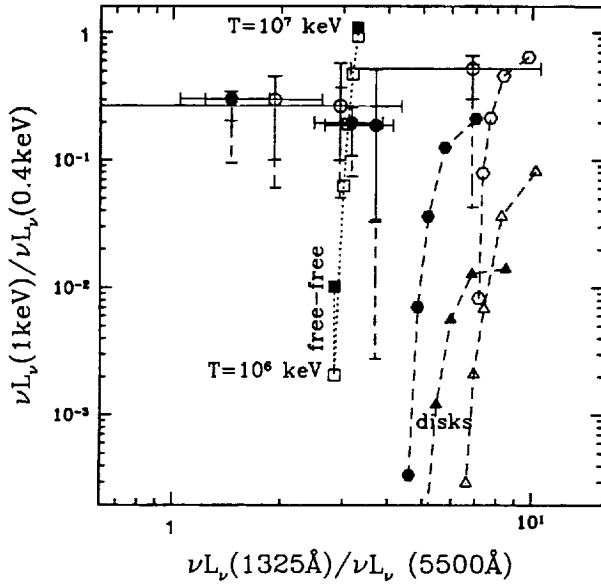


FIG. 3.—Soft X-ray color [$\nu L_\nu(1 \text{ keV})/\nu L_\nu(0.4 \text{ keV})$, soft component only], plotted against the OUV color [$\nu L_\nu(1325 \text{ \AA})/\nu L_\nu(5500 \text{ \AA})$]. Filled and open circles with error bars identify the six quasars, the dashed error bars indicate the error resulting from a power law plus free-free fit (Paper I). In these cases (open circles) (PG 1211+143, Mrk 205, and PG 1426+015) the quasars have been observed by *IUE* more than once and we plot the OUV color obtained using both the maximum and minimum optical and UV flux. The dotted line identifies the prediction of a pure free-free model as a function of temperature with open boxes indicating: 1, 2, 3, 5, $10 \times 10^6 \text{ K}$ (soft X-ray color increases with temperature). The filled boxes indicate the soft X-ray color predicted including the contribution of 2-photon and recombination continua for $T = 10^6$ and $T = 10^7 \text{ K}$. Dashed lines identify accretion disk models in a Kerr geometry. Filled hexagons and triangles indicate five disk inclinations, $\mu = \cos \theta = 1, 0.75, 0.5, 0.2, 0.1$ (soft X-ray color increases with inclination) with $M = 10^8 M_\odot$ and accretion rates $0.3L_{\text{Edd}}$ and $0.8L_{\text{Edd}}$. Open hexagons and triangles identify disk models with $M = 10^7 M_\odot$ for the same inclinations and accretion rates.

0.4 keV). Including the contribution of 2-photon and recombination continua yields a lower limit of $\sim 1.5 \times 10^6 \text{ K}$ on the temperature. These models can also reproduce the observed OUV color.

In Table 1 we also list the upper limits on the 1325 Å predicted luminosity calculated by extrapolating the best X-ray fit (for the power-law plus thermal bremsstrahlung model) into the UV. Because of the large extrapolation and the uncertainty on the contribution of the recombination and 2-photon continua in the X-ray band (which would lower the best fit temperature and raise the normalization, and hence produce higher UV luminosity), we assumed as upper limit on the predicted UV luminosity twice the best fit value. In Figure 4 we plot the observed 1325 Å luminosities versus the predicted ones. When more than one *IUE* observation is available we used the smallest observed 1325 Å luminosity. Figure 4 shows that the model underpredicts the 1325 Å luminosity by a factor 3 to 10.

4.1.3. Discussion

Optically thin plasma models can reproduce the observed soft X-ray color for temperatures in the range $1.5\text{--}5 \times 10^6 \text{ K}$ (0.13–0.4 keV). At these temperatures line emission can also be important in the X-ray band. The main emission lines, assuming collisional equilibrium, for temperatures $10^6 < T < 5 \times 10^6 \text{ K}$, are the iron *L* complex at about 0.9 keV and the O VII and O VIII *K α* lines at 0.57 and 0.65 keV. However, the ionization state of the soft X-ray emitting gas in quasar nuclei

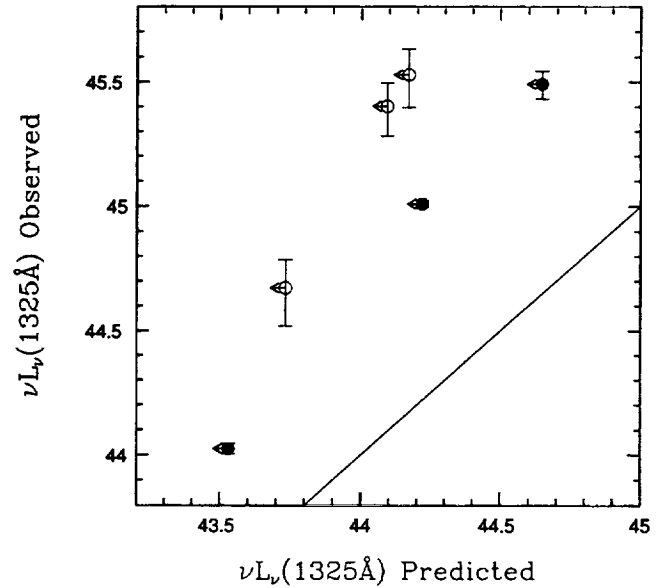


FIG. 4.—Observed 1325 Å luminosity plotted against that predicted by the best-fit power-law plus thermal bremsstrahlung model for the X-ray spectrum of the six quasars. The predicted luminosity upper limits are twice the best-fit luminosity from X-ray spectral fitting.

is unlikely to be controlled by collisions only, and photoionization is likely to be important, especially in the innermost regions close to the hard X-ray source. This strong radiation field could reduce the line emission intensities. Recent calculations by Kriss (1994) show that in the case of plasma in photoionization equilibrium the O VII and O VIII *K α* lines are still very strong. Paper I limits the amount of line emission in the six quasars in the 0.5–1 keV energy range (in most cases there is a deficit of counts with respect to a power-law model rather than an excess, see Figs. 1 and 3 in Paper I). It should be said however that emission features have been seen in the *Einstein* SSS spectra of some other quasars (Turner et al. 1992). In particular features, interpreted as oxygen lines in the framework of an ionized absorber model, have been recently seen in the X-ray spectrum of the Seyfert galaxy NGC 3783 (George, Turner, & Netzer 1995). The lack of strong emission in the quasars discussed in this paper argues against emission from isothermal optically thin ionized gas as the main contributor to the soft X-ray spectrum of these sources (see Paper I, §§ 3.5 and 3.6), unless the soft X-ray emission lines are optically thick while the continuum is optically thin. Since at temperatures of interest ($T < 10^7 \text{ K}$) most of the cooling is in the emission lines, this requires high plasma densities. In some free-free models the assumed gas density is very high ($\sim 10^{15} \text{ cm}^{-3}$, case 2 in Barvainis 1993). Whether such a density is high enough to suppress line emission efficiently should be investigated in detail.

Optically thin plasma models predict OUV colors consistent with the observed ones (taking into account the large uncertainties due to source variability and the fact that the observations were not simultaneous). This color, however, is not very sensitive to temperature for $T \gtrsim 5 \times 10^5 \text{ K}$, i.e., in the range for which the models can explain the soft X-ray color ($\sim 15\%$ change in the OUV color). Therefore, these models would not be able to produce the soft X-ray color higher than ~ 0.001 and at the same time give a spread in the OUV color. Detecting, through *simultaneous* observations in optical and UV, a

large spread in the OUV color in a sample of quasars with strong soft excesses and soft X-ray color higher than ~ 0.001 would therefore be a critical test for the single-temperature free-free models.

The best-fit power-law plus free-free models to the PSPC data underpredicts the UV luminosity of the six quasars. The reason is that the fit forces a high temperature, locating the maximum of the emission in the soft X-ray, while the highest luminosities are actually observed in the UV band. Fitting the X-ray data with the power-law plus free-free model while requiring that the predicted 1325 Å luminosity matches the observed value, yields χ^2 much worse than in the previous cases (by $\Delta\chi^2 = 20$ to 100) and temperatures between 0.05 and 0.13 keV (the best fit temperature in the fits with free thermal component normalization is between 0.15 and 0.3 keV in all cases). As mentioned before, for $T < 10^7$ K the contribution of the recombination continuum would significantly harden the spectrum, but still not enough to explain the soft X-ray color for the temperatures which would fit the OUV part of the spectrum.

In summary, the single temperature optically thin plasma models are probably too simple to explain both the OUV and soft X-ray component of these quasars *simultaneously*. The strong constraints posed by the present data could be relaxed by dropping the hypothesis that the OUV and soft X-ray emission are dominated by a single component. Optically thin plasma at increasing temperatures could dominate the optical to soft X-ray quasar SED. This conclusion is somewhat ironic, since one of the most celebrated results of optically thin plasma models for the quasar blue bump (see, e.g., Barvainis 1993) is the natural explanation of the simultaneous variations at different wavelength, observed in a few, typically low-luminosity ($L_{\text{bol}} < 10^{45}$ ergs s $^{-1}$) quasars, due to a single physical component dominating the OUV emission.

Different frequencies dominated by components at different temperature is the distinguishing feature of another large class of models: the accretion disk models, which we discuss in turn.

4.2. Accretion Disk Models

4.2.1. The Models

We consider emission from a geometrically thin accretion disk (outer radius of 1000 Schwarzschild radii) around a super-massive (10^6 – $10^8 M_\odot$) black hole with accretion rates (\dot{m}) corresponding to 0.01–0.08 L_{Edd} (the Eddington luminosity), assuming that the locally generated flux is emitted in the vertical direction only. Laor & Netzer (1989) pointed out that this assumption could be unsafe for $\dot{m} > 0.3$. In fact, for such high accretion rates disks become slim (Abramowicz et al. 1988), and additional cooling processes should be included (advective transport of energy in the radial direction. However, Szuszkiewicz et al. (1995) show that the spectra of thin and slim accretion disks differ significantly only when accretion rates are much higher than the critical one. We limited ourselves to the sub-Eddington regime only. The error introduced using our approach instead of the above more detailed calculations for $\dot{m} > 0.3$ should be smaller than all other uncertainties present in the analysis.

The efficiency of converting the potential energy into radiation is assumed to be equal to 0.08 for a nonrotating (Schwarzschild) and to 0.324 (Laor & Netzer 1989) for a maximally rotating (Kerr) black hole. Equations for the disk structure are taken from Novikov & Thorne (1973) and Page & Thorne (1974). We calculated the spectrum using the method

described by Czerny & Elvis (1987, taking into account comments of Maraschi & Molendi 1988; see also Czerny 1993) which includes electron scattering and Comptonization. For disk temperatures less than 10^6 K free-bound transitions are important and the electron scattering and Compton effects are correspondingly less significant. It is difficult to estimate this contribution, since free-bound opacities depend on the ionization state of matter and on a large number of transitions of many different ions. Ross et al. (1992) calculated spectra emitted by a radiation-dominated disk (in the Schwarzschild geometry) including free-bound processes from hydrogen and helium. However, at high frequencies, free-bound opacities from metals may be more important and may influence the final spectra strongly and should be taken into account. This has not been accomplished yet. Since we are interested in the general shape of the soft X-ray spectra we use the free-bound approximation of Maraschi & Molendi (1988). For rotating black holes we use the general relativistic transfer function of Laor, Netzer, & Piran (1990).

Pure accretion disk models in a Schwarzschild geometry systematically underpredict the soft X-ray emission for any choice of parameters that reproduces the OUV observed luminosity so we will no longer consider these models.

We consider also two modifications of the pure accretion disk model, namely inclusion of an underlying power law, and inclusion of a hot corona above the disk (Czerny & Elvis 1987).

4.2.1.1. An IR-to-X-Ray Underlying Power Law

It is well known that accretion disk models are falling too steeply to long wavelengths in the optical region. Many previous modeling attempts (Malkan & Sargent 1982; Sun & Malkan 1989; Laor 1990) have invoked an additional component in the form of an “underlying power law” that props up the disk flux in the optical and extends into the IR beneath the lumps clearly due to thermal dust emission (Clavel, Wamsteker, & Glass 1989; Barvainis 1992). The normalization of this power law would be such that it extrapolates quite well into the X-ray region (Carleton et al. 1987; Elvis et al. 1986).

Independent evidence for such a power law is weak and even contradictory (see McAlary & Rieke 1988; Green, Anderson, & Ward 1992) and in at least one quasar (NGC 4051, Done et al. 1990) there is a strong evidence *against* a power-law component representing the majority of the emission in IR and X-rays (even if the IR-to-X-ray SED of NGC 4051 actually resembles a power law, see Fig. 6 in Done et al. 1990). Nevertheless, since we need additional flux in both the optical and the soft X-ray bands, the minimal assumption is to add the same component to each, and the simplest form to assume is a power law. This adds two additional parameters (slope and normalization of the power-law), but because the model cannot overpredict either the 3 μm or hard X-ray luminosities it is also more constrained than a simple disk model, and so has predictive power.

4.2.1.2. Comptonization in a Corona above the Disk

A hot corona above a relatively cool accretion disk has been discussed by many authors (e.g., Liang & Price 1977; Begelman, McKee, & Shields 1983; Begelman & McKee 1983; White & Lightman 1989). The vertical thickness of the corona is small compared to its horizontal dimension. The corona is optically thin ($\tau_{\text{es}} < 0.8$) and has a high temperature (T_{cor} , 10–50 keV) compared to that of the photons emitted by the disk. These photons are upscattered by the hot electrons, and the primary disk emission is modified in that a power law is produced at frequencies $\nu_0 \ll \nu < kT_{\text{cor}}/h$ (with an exponential

tail $\sim \nu^3 \exp(-h\nu/kT_{\text{cor}})$ for $\nu > kT_{\text{cor}}/h$; Sunyaev & Titarchuk 1985; Górecki & Wilczewski 1984; Zdziarski 1985). In the above expression ν_0 is the typical frequency of the soft photons. We follow the simplified description of the process given by Sikora & Zbyszewska (1986) (see also Czerny & Zbyszewska 1991) in the Schwarzschild geometry to find the modified OUV-to-soft-X-ray disk spectrum.

The energy index of the power law of the Comptonized spectrum depends on the optical depth, temperature and geometry of the corona (Sunyaev & Titarchuk 1985). In Figure 5 we plot the energy index of the power law of the Comptonized spectrum as a function of the corona temperature for three values of τ_{es} . The temperature dependence is rapid: for $kT_{\text{cor}} = 50$ keV $\tau_{\text{es}} = 0.25$ and 0.5 the power-law energy index is 2.0 and 1.5, respectively. When $kT_{\text{cor}} = 10$ keV and $\tau_{\text{es}} = 0.5$ the power-law energy index is about 5. Corona models with low τ_{es} and $kT_{\text{cor}} < 50$ keV cannot explain the hard (2–10 keV) spectrum of quasars, but only that below ≈ 2 keV. The hard X-ray spectrum requires high τ_{es} and high temperatures.

4.2.2. Comparison with the Data

Disk models in a Kerr geometry for two choices of black hole masses ($10^7 M_\odot$ and $10^8 M_\odot$), accretion rates (Fig. 6a; $\dot{m} = 0.1, 0.8$) and inclination angles (Fig. 6b; $\mu = \cos \theta = 0.25, 1$) are compared with the six quasar SED in Figure 6. The models roughly encompass the observed SED.

In Figure 3 we plot the predicted soft X-ray and OUV colors for four families of the Kerr disk models spanning a typical range of parameters. Pure Kerr disk models cannot reproduce OUV color for the range of parameters for which they can match the observed soft X-ray color (with the exception of PG 1426+015): they are too “blue.” Only high inclination ($\mu = 0.25$), high accretion rate ($\dot{m} = 0.8$) models can reproduce the observed soft X-ray color.

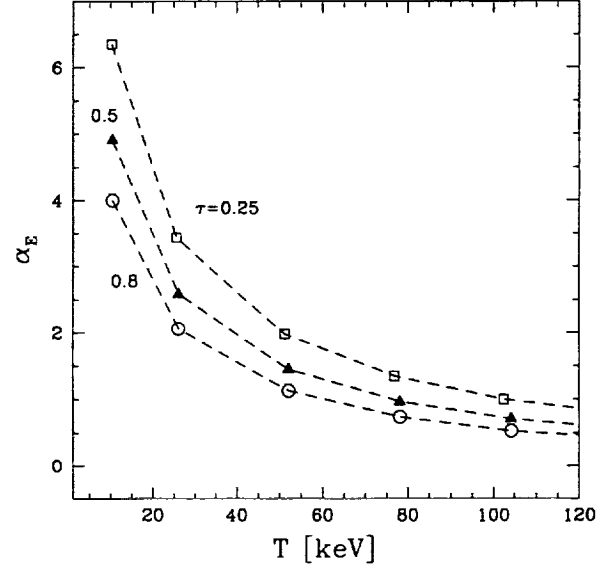


FIG. 5.—Spectral energy index of Comptonized spectrum in the corona model as a function of the temperature for three values of the optical depth.

In Figure 7 we plot the 0.4 keV soft X-ray component luminosity as a function of the 1325 Å luminosity for pure Kerr disk models. The $M = 10^7 M_\odot$ models underpredict the 1325 Å luminosity. The $M = 10^8 M_\odot$ models that could account for the soft X-ray color tend to overpredict the soft X-ray luminosity.

We study the effects of the inclusion of an underlying power law from IR to X-rays by using again the soft X-ray and the OUV colors. Figure 8 shows these colors with a set of models

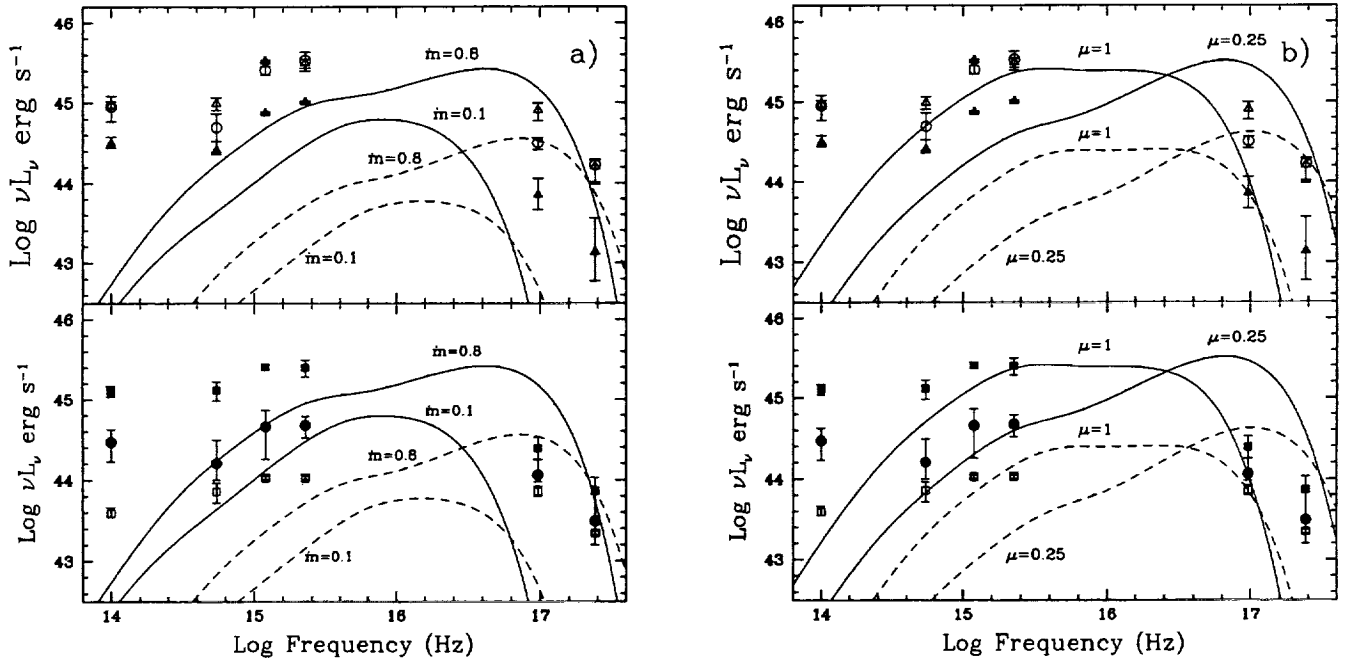


FIG. 6.—IR to soft X-ray SEDs of the six quasars (after the subtraction of the galaxy contribution and of the high-energy X-ray power law): NAB 0205+024: open triangles; PG 1211+143: filled squares; Mrk 205: filled circles; TON 1542: filled triangles; PG 1244+026: open squares; PG 1426+015: open circles. Solid lines in (a) represent accretion disk models in a Kerr geometry with $M = 10^8 M_\odot$, inclination $\mu = 0.5$, and two accretion rates ($\dot{m} = 0.1, 0.8$). Dashed lines identify Kerr disk models with $M = 10^7 M_\odot$ for the same accretion rates and inclinations. Solid lines in (b) represent Kerr disk models with $M = 10^8 M_\odot$, accretion rate 0.8 the critical one and three disk inclinations, $\mu = 1, 0.5, 0.2$. Dashed lines identify disk models with $M = 10^7 M_\odot$ for the same accretion rates and inclinations.

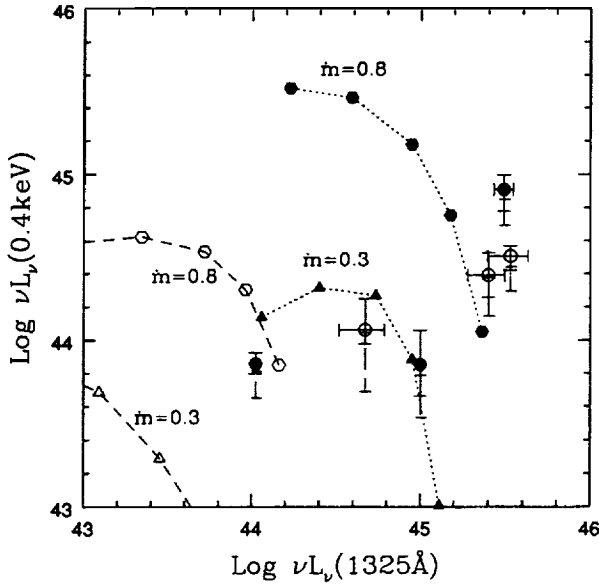


FIG. 7.—0.4 keV luminosity plotted against the 1325 Å luminosity. Filled hexagons and triangles identify accretion disk models in a Kerr geometry with $M = 10^8 M_\odot$, $\dot{m} = 0.3, 0.8$, and five disk inclinations from $\mu = 1$ to $\mu = 0.1$. Open hexagons and triangles identify disk models with $M = 10^7 M_\odot$ for the same accretion rates and inclinations.

for two black hole masses ($10^7 M_\odot$ and $10^8 M_\odot$), $\dot{m} = 0.3$ and $\mu = 0.5$, $\alpha_{\text{IRX}} = 1.25$ and three normalizations of the power-law component. The model can reproduce both the soft X-ray and the OUV colors with typical disk parameters. The $3 \mu\text{m}$ luminosity predicted by the above models is within the observed range (Fig. 9). Finally in Figure 10 we plot the 0.4 keV soft X-ray component luminosity as a function of the 1325 Å luminosity. Also here in most cases the predicted luminosity match

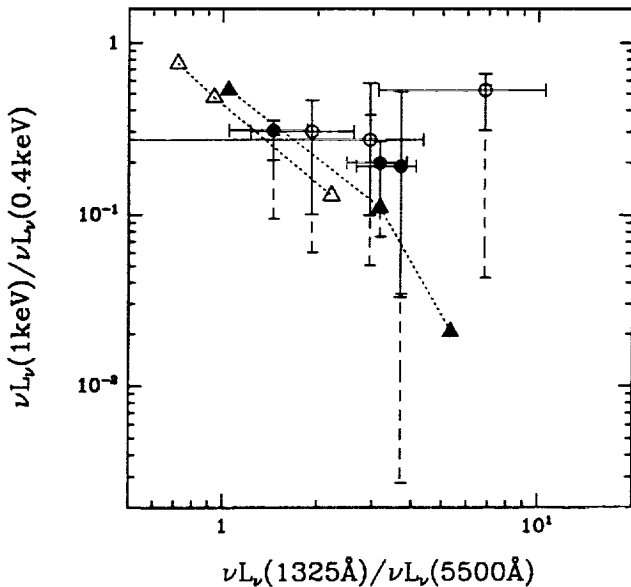


FIG. 8.—Soft X-ray color plotted against the OUV color as in Fig. 3. Filled triangles identify disk plus power-law models with $M = 10^8 M_\odot$, $\dot{m} = 0.3$, disk inclination $\mu = 0.5$, and three values of the power-law normalization. The power-law spectral index is fixed at 1.25. Open triangles identify disk models with $M = 10^7 M_\odot$ for the same accretion rate, inclination, power-law spectral index and normalizations as in the previous case.

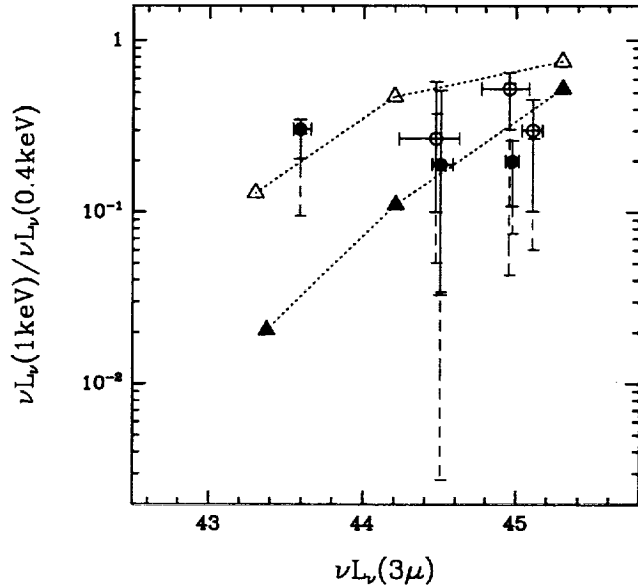


FIG. 9.—Soft X-ray color plotted against the $3 \mu\text{m}$ luminosity. Filled triangles identify disk plus power-law models with $M = 10^8 M_\odot$, $\dot{m} = 0.3$, disk inclination $\mu = 0.5$, and three values of the power law normalization. The power-law energy index is fixed at 1.25. Open triangles identify disk models with $M = 10^7 M_\odot$ for the same accretion rate, inclination, and power-law slope and normalizations as in the previous case.

that observed. We stress again that these models make use of a fixed accretion rate and a fixed inclination.

To study the effects of the inclusion of a hot corona we use the soft X-ray and OUV colors. These are plotted in Figure 11 along with the expectation of accretion disk plus corona models for two black hole masses, three accretion rates, 0.1, 0.3, and $0.8\dot{m}$, $T_{\text{cor}} = 10\text{--}50 \text{ keV}$ and $\tau_{\text{es}} = 0.25\text{--}0.5$. These models are able to reproduce the observed soft X-ray and

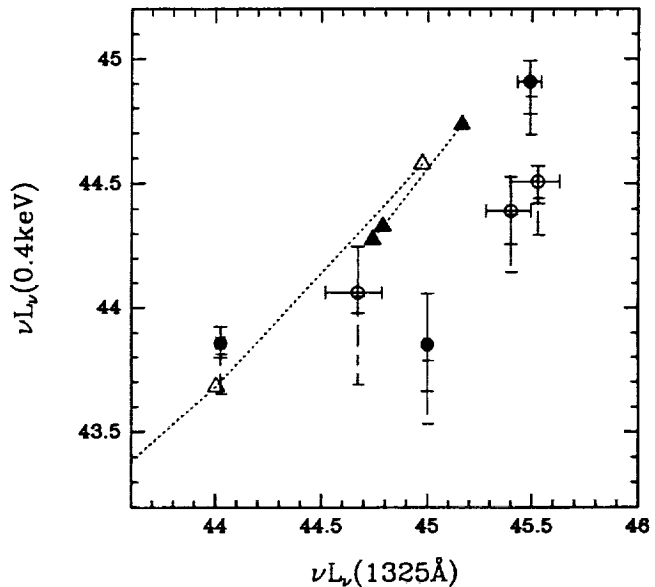


FIG. 10.—0.4 keV luminosity plotted against the 1325 Å luminosity. Filled triangles identify disk plus power-law models with $M = 10^8 M_\odot$, $\dot{m} = 0.3$, disk inclination $\mu = 0.5$, and three values of the power-law normalization. The power-law slope is fixed at 1.25. Open triangles identify disk models with $M = 10^7 M_\odot$ for the same accretion rate, inclination, and power law slope and normalizations as in the previous case.

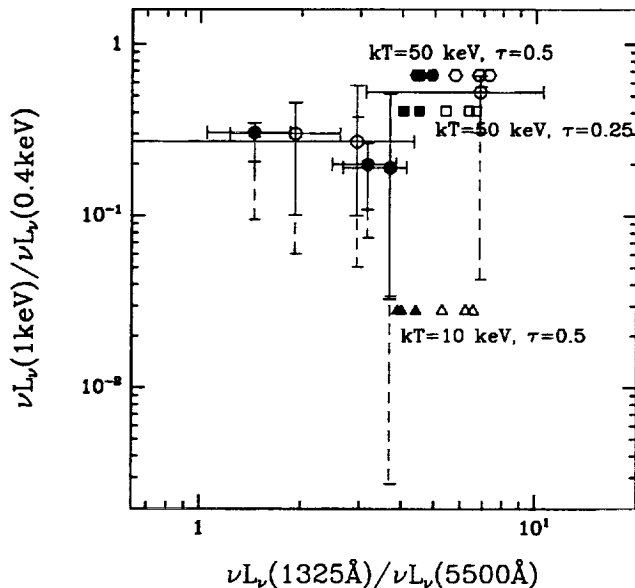


FIG. 11.—Soft X-ray color plotted against the OUV color as in Fig. 3. Filled hexagons identify accretion disk models in a Schwarzschild geometry with a hot corona with parameters: $M = 10^8 M_\odot$, $\dot{m} = 0.1, 0.3, 0.8$, $kT = 50$ keV, and $\tau = 0.5$. Filled squares identify models with $kT = 50$ keV and $\tau = 0.25$ and filled triangles models with $kT = 10$ keV and $\tau = 0.5$. Open symbols identify the same models but with $M = 10^7 M_\odot$. Higher accretion rates result in a higher UV to optical color.

OUV colors but they introduce two additional parameters with respect to the pure disk models.

4.2.3. Discussion

Accretion disk models have been widely used in the past to model the quasar blue bump. In spite of their popularity a clear proof that the majority of the OUV emission in the blue bump actually originates from a disk is still lacking. On the one hand there is both theoretical (e.g., Czerny 1993) and observational (e.g., double-peaked H α lines in radio-galaxies, Eracleous & Halpern 1994; the broad iron K α lines reportedly seen by ASCA in a number of Seyfert 1 galaxies, Mushotzky et al. 1995; especially the double-peaked iron K α line in MCG +5-23-16 reported by Weaver 1995) support to the idea that disks do exist in the innermost regions of quasars. On the other hand the UV spectra of quasars do not show characteristic signatures predicted by simple accretion disk models (e.g., the review of Kinney 1994).

We find that pure accretion disk models are not able to reproduce the observed optical-to-soft-X-ray SED for the blue bump and soft X-ray component simultaneously. Even to fit just three points (the luminosity at 1325 Å 0.4 and 1 keV), some fine tuning seems unavoidable. Furthermore the range of parameters which give reasonable predictions is particularly narrow and extreme: high inclination, high accretion rate, and a black hole mass $\sim 10^8 M_\odot$. The reason for this apparent lack of flexibility of Kerr disk models is that to account for the strength and shape of the soft X-ray component the luminosity of the spectrum must peak in the soft X-ray region rather than a decade lower $\sim 10^{16}$ Hz as the data suggest. On the other hand, pure accretion disk models capable of reproducing the observed quasar UV luminosity are steeper in the soft X-ray region than the observed spectra.

Adding an IR-to-X-ray power law to the disk models readily produces colors and luminosities in the observed range of

soft-X-ray and OUV simultaneously. Furthermore this combination does not violate the 3 μm or hard X-ray constraints. This success certainly does not prove the existence of an underlying power law, but does raise the possibility of its existence again.

A more physically based additional component is a hot corona above the disk. The inclusion of this component, not surprisingly, help in hardening the spectra and in reproducing the soft X-ray color and luminosity.

Recently, Haardt & Maraschi (1993) presented a model for the X-ray spectrum of quasars based on Comptonization of soft photons by a population of thermal electrons in a hot corona above a layer of cold reflecting matter. Their models reproduce well the 2–10 keV spectrum of radio-quiet quasars, as well as the sharp steepening above ~ 50 –100 keV found by SIGMA, OSSE, and ASCA in the spectra of a number of quasars (Jourdain et al. 1992; Maisack et al. 1993; Cameron et al. 1993; Elvis et al. 1994b). The soft X-ray spectrum, as inferred from Figures 4 and 5 in Haardt & Maraschi (1993), breaks sharply around a characteristic energy that depends mainly on the temperature of the cold reflecting layer, which in turn depends on the physical parameters of the system (the mass of the central object, the size of the emitting region, and the luminosity in units of L_{Edd}). For a black hole mass of $10^6 M_\odot$, $L = L_{\text{Edd}}$, and a size for the X-ray emitting region of $7R_s$, the temperature is ~ 50 eV and the break energy is around 1 keV. The slopes below and above the break energy depend on the temperature of the corona, its optical depth and the inclination of the system to the line of sight. For low optical depth ($\tau = 0.01$) the $\Delta\alpha_E$ between the soft and hard slopes is very large for any inclination: it is large (5–6) for face on systems and reduces to zero in the case of $\tau = 0.2$ and nearly edge-on systems. Our analysis (see Paper I) suggests a break energy at 1 keV and a $\Delta\alpha_E = 0.5$ –1. To reproduce our observations the Haardt and Maraschi models would then require a small black hole mass and a peculiar inclination. It appears therefore that these models suffer from problems similar to those of pure disk models.

Another possible mechanism for hardening the soft X-ray spectrum from an accretion disk is via irradiation of its surface by an external X-ray source. Irradiation of the disk not only modifies the ionization state of the disk surface and produces an additional soft X-ray component (Ross & Fabian 1993; Matt, Fabian, & Ross 1993; Życki et al. 1994), but also affects the vertical structure of the disk. In addition, the outer parts of the disk will also be influenced by external irradiation (by the X-rays and by the UV spectrum generated at small radii, if the fractional disk thickness increases outward and/or if relativistic deflection of the light is important, as in disks around a rotating black hole (Cunningham 1976). This may modify the OUV slope (Malkan 1991), and irradiation may be the cause for the flattening of the spectrum in the OUV band with respect to pure disk models and of the wide range of observed OUV slopes.

Ross & Fabian calculated the reflection spectrum from a slab of gas at $R = 7R_s$ under the assumption that the illuminating hard X-ray flux is equal to the soft flux locally produced in the slab. They found that the ionization parameter of the gas determines the emerging X-ray spectrum. In their model the ionization parameter ξ is directly linked to the accretion rate ($\xi \propto \dot{m}^3$). Most recently Matt et al. (1993) generalized this approach calculating the UV and X-ray spectrum from an accretion disk illuminated by a central X-ray source. In the models of Ross & Fabian the spectrum flattens by about

$\Delta\alpha_E \approx 0.4$ from the 0.3–2 keV region to the 2–20 keV region, for $0.15 < f < 0.3$ and for a black hole mass of 10^8 – $10^9 M_\odot$. A similar result is inferred from Figures 4 and 12 in Matt et al. (1993) for an illuminated accretion disk in a Schwarzschild geometry with a black hole mass of $10^9 M_\odot$ and $\dot{m} \lesssim 0.4$.

The average PSPC spectral index of low optical luminosity ($M_B > -23$), radio-quiet quasars without strong absorption (28 objects in the Walter & Fink 1993 sample) is 1.44, which implies a $\Delta\alpha_E$ with respect to the 2–10 keV spectrum similar to that predicted by Ross and Fabian. On the other hand in the same sample the average spectral index of the radio-quiet quasars with $M_B < -23$ (17 objects) is 1.64 (similar to the average slope of the radio-quiet quasars in Laor et al. 1994), steeper than in lower optical luminosity sources. Furthermore, in 30% of these objects and in half of the sources of the sample presented in this paper $\alpha_E > 2$ (e.g., NAB 0205+025, PG 1211+143, PG 1244+026, see Paper I). If the 2–10 keV spectrum of these quasars has a slope close to the mean *Ginga* slope in Williams et al. (1992), then a $\Delta\alpha_E \sim 1$ is implied, significantly larger than predicted by reflection. The reason is that the integrated intensity of the reflected spectrum in the soft X-ray band cannot be much greater than the intensity of the ionizing X-ray continuum at the same energies (unless the X-ray source is obscured in part, or strongly beamed toward the disk). Reflection might account for the soft component of low optical luminosity quasar, but probably it does not dominate the soft component of the high optical luminosity quasars in the sample presented in this paper. The luminosity locally generated (not reprocessed) is likely to be a non-negligible part of the total soft X-ray luminosity in these sources. PSPC calibration uncertainties presently limit the strength of this result.

5. CONCLUSIONS

We have compared the observed OUV to soft X-ray SED, of six, radio-quiet, low-redshift quasars with the predictions of several competing models. Our main results are as follows:

1. Isothermal optically thin continuum emission from an ionized plasma cannot explain simultaneously the soft X-ray color and the luminosity in the optical and UV of the six quasars. A distribution of temperatures would help in relaxing the strong constraints posed by the present data. While this is not inconceivable, this assumption is not justified by the model itself but represents an “a posteriori” tuning.

2. On the other hand, accretion disk models naturally predict that components at different temperature dominate dif-

ferent frequencies. However, we find that pure disk models, even in a Kerr geometry, cannot account for the observed OUV and soft X-ray colors and luminosities. The rather flat soft X-ray component slope found by the PSPC requires high inclinations and high accretion rates, which in turn overestimate the soft X-ray luminosity, when producing the correct UV luminosity.

3. The soft X-ray color can be explained if the soft X-ray emission is dominated by an additional component. The assumption of an underlying power law component extending from the infrared (3 μm) to the X-ray, can explain both the OUV and, soft X-ray colors and luminosities, while it does not overpredict the observed 3 μm luminosity. The presence of an optically thin hot ($T \lesssim 50$ keV) corona around the accretion disk can explain the soft X-ray color and luminosity.

4. A promising physical model is one involving reflection from an ionized accretion disk. This might explain the observed soft X-ray spectrum and luminosity of quasars with a soft X-ray component not much stronger than the primary component. However, it cannot readily explain the large soft excesses found in at least half of the quasars in this sample.

The present analysis, and the absence of strong line features in the PSPC spectra noted in Paper I, argue against single-temperature, solar metal abundance, optically thin emission as the only contributor to the OUV-to-soft-X-ray SED of the quasars in the sample presented in this paper. Pure disk models also fail to describe the quasar SED. While modifications of both optically thin plasma models and pure disk models might account for the observed SED, we do not find any strong evidence that the OUV bump and the soft X-ray emission are one and the same component, and that this component is thermal in origin. The observed SED could be produced by different components dominating different wavelengths, or by nonthermal emission mechanisms.

We thank Ari Laor for kindly providing us with the transfer function code for the Kerr geometry and for many useful discussions, Bożena Czerny, Magda Zbyszewska, and Giorgio Matt for discussions about Comptonization, disk emission and reflection. We also thank the referee, Richard Barvainis, for his comments that contributed to improve the paper. This work was supported by NASA grants NAGW-2201 (LTSARP), NAG5-1872, NAG5-1883 and NAG5-1536 (ROSAT), and NASA contracts NAS5-30934 (RSDC), NAS5-30751 (HEAO-2) and NAS8-39073 (ASC).

REFERENCES

- Abramowicz, M. A., Czerny, B., Lasota, J. P., & Szuszkiewicz, E. 1988, *ApJ*, 332, 646
 Barvainis, R. 1992, in *AIP Conf. Proc.* 254, Testing the AGN Paradigm, ed. S. S. Holt, S. G. Neff, & C. M. Urry (New York: AIP), 129
 ———. 1993, *ApJ*, 412, 513
 Begelman, M. C., & McKee, C. F. 1983, *ApJ*, 271, 89
 Begelman, M. C., McKee, C. F., & Shields, G. A. 1983, *ApJ*, 271, 70
 Bohlin, R. C. 1980, *A&A* 85, 1
 Bohlin, R. C., & Grillmar, C. J. 1988, *ApJS*, 68, 5487
 Cameron, R. A., et al. 1993, in *AIP Conf. Proc.* 280, Compton Gamma-Ray Observatory, ed. M. Friedlander, N. Gehrels, & D. J. Macomb (New York: AIP), 478
 Carleton, N. P., Elvis, M., Fabbiano, G., Willner, S. P., Lawrence, A., & Ward, M. 1987, *ApJ*, 318, 595
 Clavel, J., Wamsteker, W., & Glass, I. S. 1989, *ApJ*, 337, 236
 Comastri, A., Setti, G., Zamorani, G., Elvis, M., Giommi, P., Wilkes, B. J., & McDowell, J. C. M. 1992, *ApJ*, 384, 62
 Cunningham, C. T. 1976, *ApJ*, 208, 534
 Czerny, B. 1993, in *IAU Symp.* 159, Multi-wavelength Continuum Emission of AGN, ed. T. J. L. Courvoisier & A. Blecha (Dordrecht: Kluwer), 261
 Czerny, B., & Elvis, M. 1987, *ApJ*, 321, 305
 Czerny, B., Jaroszyński, M., & Czerny, M. 1994, *MNRAS*, 268, 135
 Czerny, B., & Zbyszewska, M. 1991, *MNRAS*, 249, 634
 Done, C., et al. 1990, *MNRAS*, 243, 713
 Elvis, M., Giommi, P., Wilkes, B. J., & McDowell, J. C. 1991, *ApJ*, 378, 537
 Elvis, M., Green, R. F., Bechtold, J., Schmidt, M., Neugebauer, B. T., Soifer, B. T., Matthews, K., & Fabbiano, G. 1986, *ApJ*, 310, 291
 Elvis, M., Matsuoka, M., Siemiginowska, A., Fiore, F., Mihara, T., & Brinkmann, W. 1994b, *ApJ*, 436, L55
 Elvis, M., Wilkes, B. J., McDowell, J. C., Green, R. F., Bechtold, J., Willner, S. P., Polonski, E., & Cutri, R. 1994a, *ApJS*, 95, 1
 Edelson, R., et al. 1995, *ApJ*, 438, 120
 Eracleous, M., & Halpern, J. P. 1994, *ApJS*, 90, 1
 Fiore, F., & Elvis, M. 1995, in *High Energy Radiation from Galactic and Extra-galactic Black Holes*, in press
 Fiore, F., Elvis, M., McDowell, J. C., Siemiginowska, A., & Wilkes, B. J. 1994, *ApJ*, 431, 515 (Paper I)
 George, I., Turner, T. J., & Netzer, H. 1995, *ApJ*, 438, L37
 Górecki, A., & Wilczewski, W. 1984, *Acta Astron.*, 34, 141
 Green, P. J., Anderson, S. F., & Ward, M. J. 1992, *MNRAS*, 254, 30

- Haardt, F., & Maraschi, L. 1993, *ApJ*, 413, 507
- Jourdain, E., et al. 1992, *A&A*, 256, L38
- Kinney, A. L. 1994, in *ASP Conf. Ser. 54, The Physics of Active Galaxies*, ed. G. V. Bicknell, M. A. Dopita, & P. J. Quinn (San Francisco: ASP), 61
- Kriss, G. A. 1994, *BAAS*, 26, No. 2, 879
- Laor, A. 1990, *MNRAS*, 246, 396
- Laor, A., Fiore, F., Elvis, E., Wilkes, B. J., & McDowell, J. C. 1994, *ApJ*, 435, 611
- Laor, A., & Netzer, H. 1989, *MNRAS*, 238, 897
- Laor, A., Netzer, H., & Piran, T. 1990, *MNRAS*, 242, 560
- Liang, E. P. T., & Price, R. H. 1977, *ApJ*, 218, 249
- Maisack, M., et al. 1993, *ApJ*, 407, L61
- Malkan, M. A. 1988, *Adv. Space Res.*, 8, No. 2-3, (2)49
- . 1991, in *Structure and Emission Properties of Accretion Disks*, ed. C. Bertout et al. (Gif-sur-Yvette: Éditions Frontières), 165
- Malkan, M. A., & Sargent, W. L. W. 1982, *ApJ*, 254, 22
- Maraschi, L., & Molendi, S. 1988, *ApJ*, 353, 452
- Masnou, J.-L., Wilkes, B. J., Elvis, M., McDowell, J. C., & Arnaud, K. A. 1992, *A&A*, 253, 35
- Matt, G., Fabian, A. C., & Ross, R. R. 1993, *MNRAS*, 264, 839
- McAlary, C. W., & Rieke, G. H. 1988, *ApJ*, 333, 1
- McDowell, J. C., Elvis, M., Wilkes, B. J., Willner, S. P., Oey, M. S., Polomski, E., Bechtold, J., & Green, R. F. 1989, *ApJ*, 345, L13
- Mushotzky, R., et al. 1995, *MNRAS*, 272, L9
- Neugebauer, G., Green, R. F., Matthews, K., Schmidt, B. T., Soifer, B. T., & Bennet, J. 1987, *ApJS*, 63, 615
- Novikov, I. D., & Thorne, K. S. 1973, in *Black Holes*, ed. C. De Witt & B. De Witt (New York: Gordon & Breach), 347
- O'Brien, P. T., Gondhalekar, P. M., & Wilson, R. 1988, *MNRAS*, 233, 845
- Page, D. N., & Thorne, K. S. 1974, *ApJ*, 191, 499
- Pfeiffer, E., et al. 1987, *Proc. SPIE*, 733, 519
- Pounds, K. A. 1994, in *New Horizon of X-Ray Astronomy*, ed. F. Makino & T. Ohashi (Tokyo: Universal Academic Press)
- Pounds, K. A., et al. 1993, *MNRAS*, 260, 77
- Puchnarewicz, E. M., Mason, K. O., Siemiginowska, A., & Pounds, K. A. 1995, *MNRAS*, in press
- Raymond, J. C., & Smith, B. W. 1977, *ApJS*, 35, 419
- Ross, R. R., & Fabian, A. C. 1993, *MNRAS*, 261, 74
- Ross, R. R., Fabian, A. C., & Mineshige, S. 1992, *MNRAS*, 258, 189
- Rudy, R. J., LeVan, P. D., & Rodriguez-Espinoza, J. M. 1982, *AJ*, 87, 598
- Rybicki, G. B., & Lightman, A. P. 1979, *Radiative Processes in Astrophysics* (New York: Wiley)
- Saxton, R. D., Turner, M. J. L., Williams, O. R., Stewart, G. C., Ohashi, T., & Kii, T. 1993, *MNRAS*, 262, 63
- Shields, G. A. 1978, *Nat*, 272, 706
- Siemiginowska, A., Kuhn, O., Elvis, M., Fiore, F., McDowell, J. C., & Wilkes, B. J. 1995, *ApJ*, submitted
- Sikora, M., & Zbyszewska, M. 1986, *Acta Astron.*, 36, 255
- Sun, W.-H., & Malkan, M. A. 1989, *ApJ*, 346, 68
- Sunyaev, R. A., & Titarchuk, L. G. 1985, *A&A*, 143, 374
- Szuskiewicz, E., et al. 1995, in preparation
- Trümper, J. 1983, *Adv. Space Res.*, 2, No. 4, 241
- Turner, T. J., & Pounds, K. A. 1988, *MNRAS*, 232, 463
- . 1989, *MNRAS*, 240, 833
- Turner, T. J., Weaver, K. A., Mushotzky, R. F., Holt, S. S., & Madejsky, G. M. 1991, *ApJ*, 381, 85
- Walter, R., & Fink, H. H. 1993, *A&A*, 274, 105
- Walter, R., Orr, A., Courvoisier, T. J.-L., Fink, H. H., Makino, F., Otani, C., & Wamsteker, W. 1995, *A&A*, in press
- Weaver, K. 1994, *BAAS*, 26, No. 4, 1500
- White, T. R., & Lightman, A. P. 1989, *ApJ*, 340, 1024
- Wilkes, B. J., & Elvis, M. 1987, *ApJ*, 323, 243
- Williams, O. R., et al. 1992, *ApJ*, 389, 157
- Zdziarski, A. A. 1985, *ApJ*, 289, 514
- Zycki, P. T., Krolik, J. H., Zdziarski, A. A., & Kallman, T. R. 1994, *ApJ*, 437, 597

THE X-RAY AND ULTRAVIOLET ABSORBING OUTFLOW IN 3C 351

SMITA MATHUR,¹ BELINDA WILKES, MARTIN ELVIS, AND FABRIZIO FIORE

Harvard-Smithsonian Center for Astrophysics, 60 Garden Street, Cambridge, MA 02138

Received 1994 January 3; accepted 1994 April 27

ABSTRACT

3C 351 ($z = 0.371$), an X-ray-“quiet” quasar, is one of the few quasars showing signs of a “warm absorber” in its X-ray spectrum; i.e., partially ionized absorbing material in the line of sight whose opacity depends on its ionization structure. The main feature in the X-ray spectrum is a K-edge due to O VII or O VIII. 3C 351 also shows unusually strong, blueshifted, associated, absorption lines in the ultraviolet (Bahcall et al. 1993) including O VI ($\lambda\lambda 1031, 1037$). This high ionization state strongly suggests an identification with the X-ray absorber and a site within the active nucleus.

In this paper we demonstrate that the X-ray and UV absorption is due to the same material. This is the first confirmed UV/X-ray absorber. Physical conditions of the absorber are determined through the combination of constraints derived from both the X-ray and UV analysis. This highly ionized, outflowing, low-density, high-column density absorber situated outside the broad emission line region (BELR) is a previously unknown component of nuclear material.

We rule out the identification of the absorber with a BELR cloud as the physical conditions in the two regions are inconsistent with one another. The effect of the X-ray quietness and IR upturn in the 3C 351 continuum on the BELR is also investigated. The strengths of the high-ionization lines of C IV $\lambda 1549$ and O VI $\lambda 1034$ with respect to Ly α are systematically lower (up to a factor of 10) in the material ionized by the 3C 351 continuum as compared to those produced by the “standard” quasar continuum, the strongest effect being on the strength of O VI $\lambda 1034$. We find that for a 3C 351-like continuum, C III] $\lambda 1909$ ceases to be a density indicator.

Subject headings: quasars: absorption lines — quasars: individual (3C 351) — ultraviolet: galaxies — X-rays: galaxies

1. INTRODUCTION

A minority of AGNs show optical and ultraviolet absorption lines within the profiles of their broad emission lines (Ulrich 1988). While this ionized absorbing material must be associated with the active nucleus, there is no accepted model for it (see, e.g., Kolman et al. 1993). Similarly, many AGNs, mostly Seyfert galaxies exhibit strong low-energy X-ray cutoffs (e.g., Turner & Pounds 1989) due to “cold” material in their nuclei, also with no accepted identification. The possibility of linking these two types of absorbers has not seemed promising to date (Ulrich 1988). However, recent observations of X-ray ionized (“warm”) absorbers promise to change this situation, 3C 351 provides a particularly good opportunity.

3C 351 ($z = 0.371$) is one of the few quasars showing signs of a warm absorber in its X-ray spectrum; i.e., a partially ionized absorbing material in the line of sight whose opacity depends on its ionization structure (Fiore et al. 1993, hereafter Paper I). The main feature in the X-ray spectrum is a K-edge due to O VII or O VIII. 3C 351 also shows unusually strong, associated, absorption lines in the ultraviolet (Bahcall et al. 1993) including O VI ($\lambda\lambda 1031, 1037$), strongly suggesting an identification with the X-ray absorber, and a site within the active nucleus.

In this paper we search for, and find, a model for the absorber which is consistent with both the X-ray and UV data. We reanalyze the X-ray and UV data with this aim in mind (§ 2). In order to produce self-consistent models, we find that use of the observed (ionizing) continuum of 3C 351, rather than a generic quasar continuum is critical (§ 4). We find that the

UV absorption-line clouds (§ 3), but not the broad emission line region (BELR) clouds (§ 4), can cause the X-ray absorption. We derive the physical characteristics of this outflowing material (§ 3) and consider why a previous similar attempt to identify an X-ray absorber with a strong UV absorber in a different AGN was not successful (§ 5).

2. X-RAY, ULTRAVIOLET, AND OPTICAL DATA

2.1. X-Ray Spectrum

The details of the X-ray observations, extraction of the source pulse height spectrum, and its analysis are presented in Paper I. This analysis concludes that an ionized (“warm”) absorber is present, whose dominant feature is a strong O VII/O VIII absorption edge. The inferred parameters of the best-fit X-ray spectrum (the total column density N_H and the ionization parameter U , defined as the dimensionless ratio of ionizing photon to baryon density) depend critically on the assumed ionizing continuum which in Paper I was assumed to be a simple power law between 10 μm and 5 MeV. To investigate the extent of this dependence, we refitted the X-ray spectrum using the observed 3C 351 continuum (§ 2.3) to ionize the absorber. Since the shape of the continuum in the extreme ultraviolet is unknown, a broken power-law model was used with the break energy varied from the unobserved EUV range to well within the PSPC range: 0.07 keV, 0.37 keV, and 0.7 keV. The slope ($f, \propto \nu^{-\alpha}$) in the soft energy range (α_1) was fixed by the observed flux in the UV at one end and the break energy at the other. The slope, α_2 , above the break energy was fixed at 1, typical for lobe-dominated, radio-loud quasars (Shastri et al. 1993). The resulting parameters are given in Table 1. The best-fit spectrum, folded through the instrument response and com-

¹ Internet: smita@cfa.harvard.edu.

TABLE 1
ROSAT TWO-POWER-LAW SPECTRAL FITS

| Break Energy (keV) (Fixed) | α_1 (Fixed) | α_2 (Fixed) | χ^2_a | N_H^b (10^{22} cm^{-2}) | $\log U^b$ |
|-------------------------------|-----------------------|-----------------------|------------|--|------------------------|
| 0.07..... | 4.7 | 1 | 24.73 | $1.8^{+0.4}_{-0.3}$ | $1.08^{+0.12}_{-0.08}$ |
| 0.37..... | 2.45 | 1 | 29.82 | 1.4 ± 0.3 | $0.83^{+0.13}_{-0.09}$ |
| 0.7..... | 2.16 | 1 | 31.66 | $1.0^{+0.4}_{-0.2}$ | $0.04^{+0}_{-0.35}$ |

^a For 21 degrees of freedom.

^b Errors are 1σ for 2 degrees of freedom.

pared with the data, is shown in Figure 1. The fits gave $\chi^2 = 24.7, 29.8$, and 31.7 , respectively, for the three models for 27 degrees of freedom. A χ^2 of 31.7 is unacceptably large (probability of 25%) so a break at a lower energy (0.37 keV or less) is preferred. The difference in the break energy in the two acceptable models results in a factor of two differences in the best fit values of the absorbing column density ($N_H = 1\text{--}2 \times 10^{22} \text{ atoms cm}^{-2}$), and in the ionization parameter U of the warm absorber ($\log U = 0.78\text{--}1.08$). The best-fit ionization parameter differs by a factor of ~ 30 from that for a single power law ($\log U = -1$ to -0.7), while the column density is similar ($N_H = 1\text{--}4 \times 10^{22} \text{ atoms cm}^{-2}$) (Paper I).

2.2. Ultraviolet and Optical Spectra

3C 351 was also observed by *HST* as a part of the Quasar Absorption Lines Key Project (Bahcall et al. 1993). By a fortunate coincidence, the *HST* ultraviolet observations were quasi-

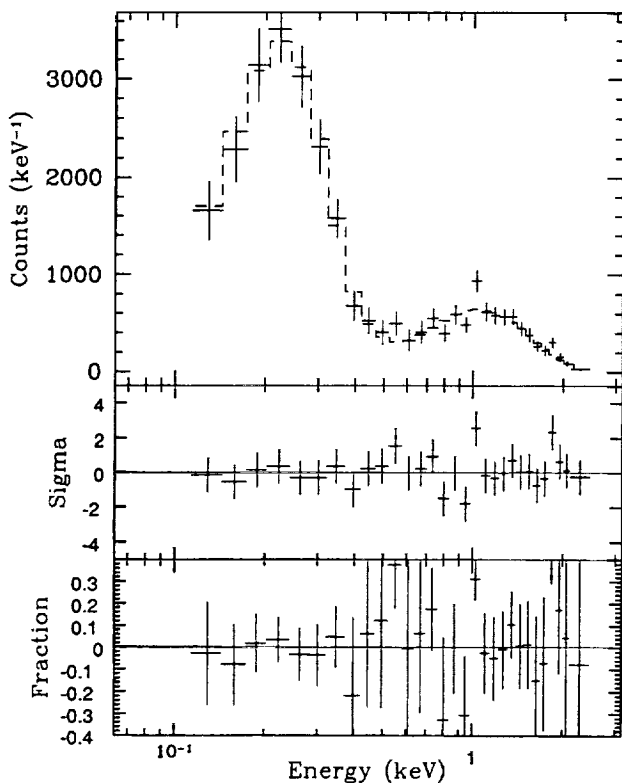


FIG. 1.—The best-fit X-ray spectrum. The data plus the folded model ($E_{\text{break}} = 0.37 \text{ keV}$, $N_H = 1.4 \times 10^{22} \text{ cm}^{-2}$, $U = 6.7$) are shown in the top panel; residuals after subtracting the best-fit model are shown in the lower two panels.

simultaneous with the X-ray observations (*ROSAT*: 1991 October 28–30; *HST*: 1991 October 22). The spectra were obtained from the *HST* archive and analyzed using IRAF. An unusually strong metal line absorption system (Figs. 2a–2d) is observed at $z = 0.3646$ (Bahcall et al. 1993) and contains the high ionization doublets of O vi, N v, and C iv and the Lyman series Ly α , Ly β , Ly γ (blended with another Ly α line at $z = 0.092$), and Ly δ . Bahcall et al. (1993) suggested that an associated cluster of galaxies is responsible for the UV absorber. However, a deep image of this field (Ellingson et al. 1994) shows that there are no associated galaxies. We conclude that the UV absorber is associated with the quasar itself.

Table 2 lists the equivalent widths (EW), and full width at half-maximum (FWHM), of the absorption lines in the $z = 0.3646$ system given by Bahcall et al. with the exception of C iv and N v which we remeasured. The automatic algorithm used by Bahcall et al. to identify the absorption lines finds a weak C iv doublet at 2112.8 and 2116.6 Å (EW = 0.26 Å and 0.12 Å, respectively) but leaves the strong (EW = 3.09 Å), broad (FWHM = 8.58 Å) line at 2114.5 Å unidentified. Inspection of the spectrum (Fig. 2c) shows that the C iv absorption doublet is not clearly resolved, which is not surprising given the typical FWHM (3–4 Å) of the absorption lines in this system. If we assume that the whole absorption for this broad system (FWHM = 8.58 Å) at 2114 Å is due to an unresolved C iv blend (1549.1 Å), the redshift is then 0.3646, in agreement with the rest of the system. We use this larger EW in our modeling.

Measurements of absorption lines embedded in a quasar's strong emission lines are prone to large uncertainties since their "continuum" is actually the unknown profile of an emission line. This can be seen in Figure 2 where the associated absorber covers most of the blue wing of both O vi and C iv emission lines. For the N v absorption doublet, situated in the blue wing of N v and red wing of Ly α , the problem is even greater. The published values of the N v ($\lambda\lambda 1238, 1242$) absorption line EWs are 1.60 Å and 1.63 Å using a continuum defined by a cubic spline fit to a number of discrete continuum points (Schneider et al. 1993). As can be seen in Figure 2, the resulting Ly α emission line profile is symmetric allowing for little or no N v emission. We measured the N v absorption using several plausible continuum levels and conclude $\sim 40\%$

TABLE 2
UV EMISSION AND $z = 0.3646$ ABSORPTION-LINE PARAMETERS

| Line Identification | λ_{obs} (Å) | EW _{obs} ^b (Å) | FWHM (Å) |
|--|-------------------------------|---------------------------------------|-------------|
| A. Absorption ^a | | | |
| C iv $\lambda 1549$ | 2113 | 3.09 | 8.58 |
| N v $\lambda 1238$ | 1690.74 | 1.60 ^c | 3.22 |
| N v $\lambda 1242$ | 1695.67 | 1.63 ^c | 3.44 |
| Ly α | 1658.92 | 3.54 ^c | 4.46 |
| O vi $\lambda 1031$ | 1408.34 | 2.73 | 3.09 |
| O vi $\lambda 1037$ | 1416.39 | 1.99 | 2.85 |
| B. Emission | | | |
| C iii] $\lambda 1909$ | 2614.6 | 18.5 | 25.0 |
| C iv $\lambda 1549$ | 2121.98 | 68.2 | 32.2 |
| Ly α /N v | 1664.11 | 60.5 | 31.6 |
| O vi $\lambda\lambda 1031, 1037$ | 1426.14 | 6.8 | 23.0 |

^a From Bahcall et al. 1993 except for the uncertainties in EWs.

^b Uncertainties are $\sim 10\%$ except where noted.

^c Uncertainties are estimated to be $\sim 40\%$.

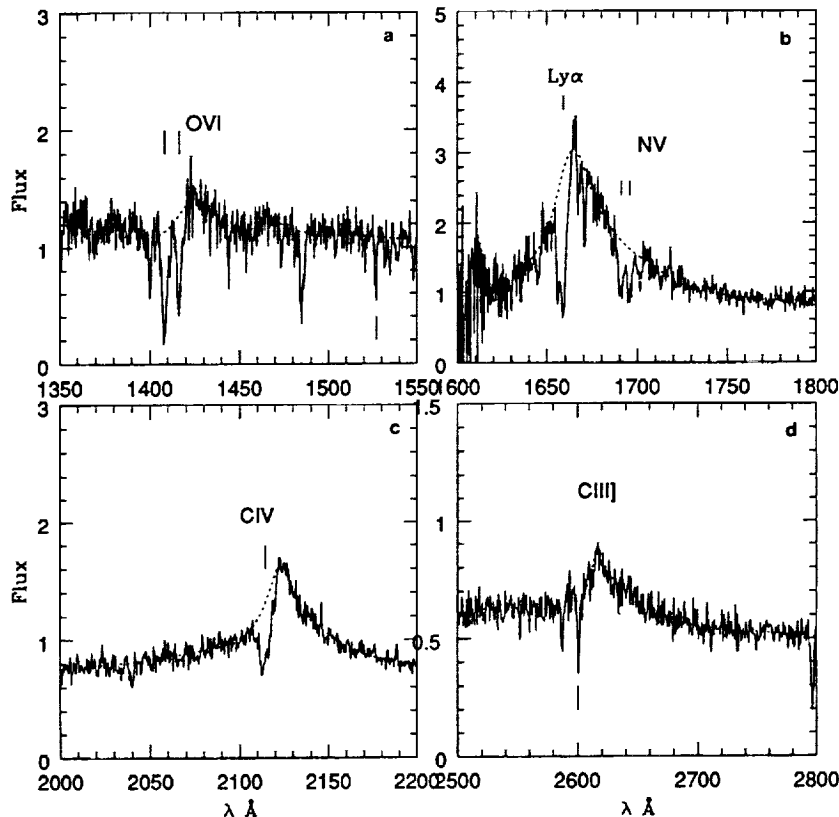


FIG. 2.—The *HST* UV spectrum: (a) O VI, (b) Ly α /NV, (c) C IV, (d) C III]. Flux is in the units of 10^{-14} ergs s^{-1} cm^{-2} \AA^{-1} . The dotted line is the continuum defined in Bahcall et al. (1993). The prominent emission lines are labeled. The absorption lines in $z = 0.3646$ system are marked above the spectrum, and the Galactic absorption lines are marked below the spectrum.

uncertainties which we take into account in our modeling. A similar level of uncertainty was deduced for the Ly α absorption line ($z = 0.3646$) due to blending with another Ly α absorption line ($z = 0.3621$) and the highly uncertain blue wing of the Ly α profile.

The FWHM of these absorption lines in the $z = 0.3646$ system ranges from 2.08 \AA to 6.26 \AA (rest frame). This implies a maximum value of the velocity spread parameter “ b ” to be $< 600\text{--}1200$ km s^{-1} (see § 4 for further details).

No lines from the low-ionization ions of C II, N I, N II, O I, Si II, Al II, and Fe II are present (equivalent widths $\lesssim 0.4$ \AA) (Bahcall et al. 1993). Also, ground-based observations by Boissé et al. (1992) show no $z = 0.3646$ Mg II absorption doublet, giving an upper limit of 0.1 \AA to its equivalent width.

Bahcall et al. (1993) do not report emission-line strengths. In order to see whether the high-ionization emission-line clouds could produce the X-ray absorption, equivalent widths and fluxes were measured for lines of Lyman- α , C IV $\lambda 1549$, C III] $\lambda 1909$, and O VI $\lambda 1034$ using local continuum estimates, and the results are given in Table 2. As discussed above, the spectral lines show strong absorption features. Lyman- α is also blended with emission lines of Si II $\lambda 1260$ and N V $\lambda 1240$, and the Si II $\lambda 1537$, Ne V $\lambda 1575$ features cannot be separated from the C IV $\lambda 1549$ emission line. Apart from N V $\lambda 1240$, which is a strong contaminant, these lines are weak and are not expected to exceed $\sim 10\%$ of the line. In all cases the weaker lines were included in the line strengths predicted by photoionization models so that a proper comparison with observed lines could

be made. The emission line fluxes were corrected for the absorption-line systems using the EWs in Table 2.

3C 351 was also observed in the ultraviolet by *IUE*. Kinney et al. (1991) have published an optimally extracted, “co-added” spectrum of 3C 351. As a consistency check, the co-added spectrum of 3C 351 was obtained from the *IUE* archive and analyzed to measure the strengths of the emission lines. The equivalent widths of the lines were found to be consistent with those measured from the *HST* spectra.

2.3. Observed Energy Distribution of 3C 351

The thermal and ionization structure of a photoionized gas cloud is dependent on the strength and shape of the complete millimeter–X-ray incident continuum. Most photoionization studies to date have used a standard continuum shape (e.g., Mathews & Ferland 1987), neglecting this as a variable, due to the general lack of good continuum observations. However, 3C 351 has a well-observed radio–X-ray continuum which is significantly different from the standard continuum, allowing us to carry out more realistic modeling of photoionized gas in its vicinity.

Figure 3 shows the observed continuum of 3C 351 (solid line; data from Elvis et al. 1994). The X-ray slope α ($f_\nu \propto \nu^{-\alpha}$) is not well constrained due to the presence of the ionized absorber. We use two extreme values of α for radio loud quasars (0.0, 1.0) (Wilkes & Elvis 1987) to investigate its effect on the resulting emission line strengths (Fig. 3). We have extrapolated our best-fit spectrum into the submillimeter region with $\alpha = -5/2$

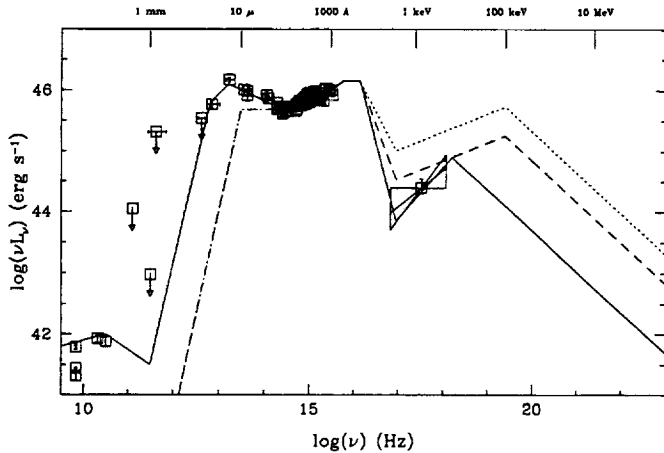


FIG. 3.—The 3C 351 (PG 1704+608) continuum. Solid line: the best-fit continuum; dashed line: “standard” continuum; and dotted line: average X-ray continuum for radio-loud quasars. The bow shows our adopted limits to the X-ray slope α (see text).

(appropriate for synchrotron self-absorption) and the core radio component is smoothly joined onto it. The exact point when the two components join is not well defined but small differences here do not change our results significantly. The short dashed line is the AGN continuum defined in CLOUDY (Ferland 1991) which we shall call the “standard continuum.” This standard continuum is similar to that used by Mathews & Ferland (1987) with the exception that the spectral index is changed from -1 to $-5/2$ for frequencies below the millimeter break. The dotted line shows the average X-ray continuum for the radio-loud quasars. All the continua are normalized to match the observations in the optical/UV.

The observed 3C 351 continuum and the standard continuum differ significantly in the X-ray, IR, and radio regions (Fig. 3). 3C 351 is X-ray-“quiet,” i.e. it has a factor of ~ 5 lower X-ray flux than the average radio-loud quasar: the effective optical-to-X-ray slope α_{OX} for 3C 351 is 1.6, as compared to $\alpha_{OX} = 1.3$ for an average radio-loud quasar (Wilkes et al. 1994). The weak flux in the X-ray is not due to X-ray variability or to the effect of the ionized absorber (Paper I). 3C 351 also shows a clear upturn in the IR at $\sim 1 \mu\text{m}$, turning over again at $\sim 25 \mu\text{m}$. IR and radio emission can produce large amounts of free-free heating which can influence the relative strength of emission lines (Ferland & Persson 1989). The 1.3 mm observations by Antonucci & Barvainis (1993) are critical to the thermal balance since they strongly limit the extrapolation of the IR continuum. If the IR points are smoothly joined onto the radio, then the resulting continuum produces a large amount of free-free heating and unacceptably strong C IV $\lambda 1549$ emission relative to Ly α . If, instead, the 1.3 mm observations are

used, the slope in the submillimeter region is constrained to $-5/2$, similar to that of radio-quiet quasars (Chini, Kreysa, & Biermann 1989). This provides another argument in favor of the Antonucci & Barvainis (1993) hypothesis that the IR and radio emission comes from two distinct components and must arise at different locations. In § 4 we investigate the effect of using the 3C 351 continuum on the physical conditions in photoionized gas clouds and so on the resulting emission line strengths.

3. THE X-RAY ABSORBER AS THE UV ABSORBER

Table 2A gives the EW and FWHM of the absorption lines in the $z = 0.3646$ system. The existence of highly ionized O VI lines is particularly intriguing given the O VII absorption edge seen in soft X-rays (§ 2). If the two absorbers are identical, then the X-ray and UV constraints would allow us to solve for a consistent model for both the UV lines and the X-ray absorber.

In the context of photoionization models, we look for a consistent solution for the ionization state of an absorbing gas cloud satisfying both the X-ray and UV constraints. All the photoionization calculations were made using G. Ferland’s CLOUDY software (Ferland 1991). Photoionization models predict f_{ion} given the input continuum, column density, number density (n_H), and the ionization parameter (U) of the gas, where f_{ion} is the fractional abundance of an element in a given ionization state. For the best-fit parameters of the X-ray absorber (see § 2.1, Table 1), f_{ion} was calculated for the ions O VI, N V, C IV, and H I. Assuming a solar abundance of elements relative to hydrogen and using the total N_H from the X-ray analysis, the column density of each ion, N_{ion} , was then derived. For example, f_{OVI} , the fraction of oxygen in the O VI state of ionization, is 0.03 for the continuum model with break energy at 0.37 keV (§ 2.1). Given a solar abundance of oxygen relative to hydrogen (8.51×10^{-4} ; Grevesse & Anders 1989) and using the total N_H ($1.4 \times 10^{22} \text{ cm}^{-2}$), the column density of O VI is $N_{OVI} = 3 \times 10^{17} \text{ cm}^{-2}$. N_{ion} for the other ions has been derived similarly. These model values are listed in Table 3.

A measured column density for each ion of the UV absorber was derived from the line EW with a standard curve-of-growth analysis (e.g., Spitzer 1978). Figure 4 shows curves of growth for “ b ” values ranging from 80 to 130 km s^{-1} , where “ b ” is the velocity spread parameter. Abscissa is $\log(N\lambda f)$, where N is the column density of an ion and $N\lambda$ has the dimension cm^{-1} . f is the oscillator strength of the transition. Values of f are taken from Wiese, Smith, & Glennon (1966). The lower limit to the column density of an ion is obtained from the linear part of the curve of growth, e.g., for the O VI doublet transition $N_{OVI} > 1.7 \times 10^{15} \text{ cm}^{-2}$. Small values of “ b ” imply unacceptably large column densities (“ b ” = 4 km s^{-1} gives $N_{OVI} \sim 10^{27} \text{ cm}^{-2}$), making the absorbing material optically thick to Thompson scattering. The maximum value of b is ~ 600 –1200

TABLE 3
COMPARISON OF COLUMN DENSITIES IN MODEL AND DATA

| ION | $\log N_{ion}$ (Measured) ^a | $\log N_{ion}$ (Model) | | |
|-------------------------|--|---------------------------------------|---------------------------------------|--------------------------------------|
| | | $E_{\text{Break}} = 0.07 \text{ keV}$ | $E_{\text{Break}} = 0.37 \text{ keV}$ | $E_{\text{Break}} = 0.7 \text{ keV}$ |
| O VI | 17.5–18.0 | 17.5 | 17.5 | 18.3 |
| N V | 15.3–15.8 | 15.7 | 15.8 | 16.8 |
| C IV | 15.9–16.1 | 15.9 | 15.9 | 17.3 |
| H I(Ly α) | 15.4–17.4 | 15.3 | 15.6 | 16.5 |

^a Assuming $b = 110 \text{ km s}^{-1}$.

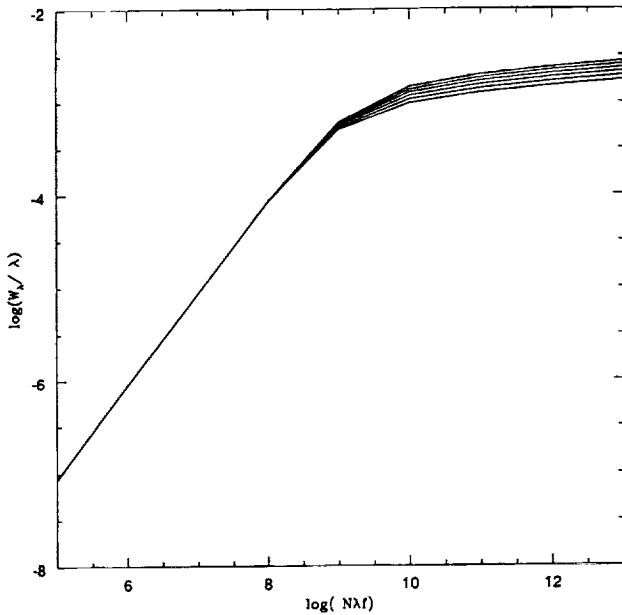


FIG. 4a

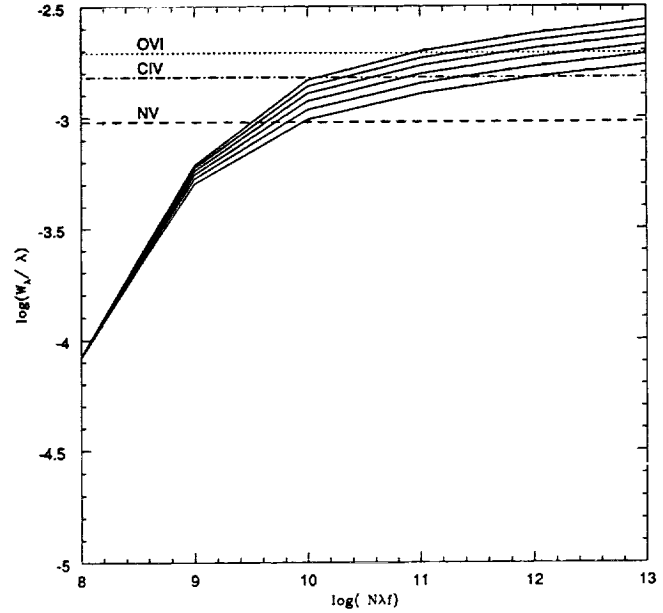


FIG. 4b

FIG. 4.—(a) The curve of growth for “ b ” values ranging from 80 to 130 km s⁻¹ in steps of 10. f is the oscillator strength of the transition and $N\lambda$ has the dimension cm⁻¹. (b) A part of (a) expanded. Observed values of W_λ/λ for O VI λ 1031, C IV λ 1549, and N V λ 1242 are marked by the horizontal lines.

km s⁻¹ given by the observed line widths (see § 2.2). Higher resolution data are needed to allow b to be directly measured and then b and N_{ion} to be fitted independently. Given the observational limits, we find that a value of $b \sim 105$ –115 km s⁻¹ gives consistent solutions to the X-ray and UV line constraints (Table 3), a value $b = 110$ km s⁻¹ was adopted. The measured column density of O VI is then $N_{\text{O VI}} = 3 \times 10^{17}$ cm⁻² consistent with that derived from photoionization model.

Table 3 compares the column densities of each ion derived from the UV line analysis to those predicted by the photoionization models for different values of X-ray spectral break energy. A consistent solution was obtained for all the UV lines: O VI, C IV, N V, and Ly α (Fig. 4b). The range in the measured values of column density is due to the uncertainty in the equivalent width measurements. For X-ray continua with break energies at 0.07 and 0.37 keV, the match provided by the models is good to better than 5% for C IV and O VI and consistent for N V and Ly α . As noted in § 2.2, the heavy blending of Ly α and N V results in a large uncertainty in the continuum level and so in the resulting equivalent width of N V. Thus the inferred range of $N_{\text{N V}}$ is large (15.3–15.8). Similarly, the uncertainty in $N_{\text{H I}}$ is large (15.4–17.4) due to the large uncertainty in the measurement of equivalent width of Ly α absorption line (§ 2.2).

In a highly ionized system such as this, magnesium is highly ionized (Mg VI and higher) leaving no magnesium in the Mg II state ($\log f_{\text{Mg II}} < -30$), and thus Mg II absorption should not occur. The same is also true for the low ionization ions of C II, N I, N II, O I, Si II, Al II, and Fe II. This is consistent with the observations (see § 2.2).

For the X-ray model with break energy at 0.7 keV, the inferred parameters for the UV absorber are inconsistent with the parameters of the X-ray absorber (Table 3). If the X-ray absorber is indeed the UV absorber, for which the above evidence is compelling, then the break in the X-ray power law must be at lower energies. We note that this model also has the

highest χ^2 (31.66 for 27 dof) among all the three models (§ 2) and the X-ray fit is unacceptable (Table 1). A break at lower energies (~ 0.37 keV or less) is thus preferred by both X-ray and UV data.

We conclude that in 3C 351 the X-ray and UV absorbers are one and the same.

3.1. The Physical Characteristics of the Absorber

Since the X-ray absorber is strongly identified with the UV absorber, constraints from both UV and X-ray data can be combined to derive its physical properties. These properties describe a component of nuclear material not previously recognized. We have already shown that the absorber has high N_{H} (1 – 1.8×10^{22} cm⁻²), and high U ($\log U = 0.78$ – 1.08). We tested a range of density from 10^3 to 10^{11} cm⁻³ in the photoionization models and found that there is no significant change in the values of fractional ionization, so the density is not constrained directly.

The absorption lines are blueshifted with respect to the high ionization emission lines by ~ 2000 km s⁻¹. The high ionization lines themselves generally show blueshifts of 1000–2000 km s⁻¹ (Espey et al. 1989) relative to the Balmer lines. An MMT spectrum taken in 1991 September shows that the high-ionization emission lines of 3C 351 are blueshifted by ~ 1050 km s⁻¹ relative to [O III] λ 4959, implying an outflow velocity for the absorber of ~ 3050 km s⁻¹ in the quasar rest frame.

The UV absorption troughs extend through the emission lines down below the continuum level (Fig. 2) requiring that both the continuum-emitting region and the BELR are at least partially covered by the absorber. This places the absorber outside the BELR. Scaling from the BELR size deduced from the reverberation mapping of NGC 5548 (Clavel et al. 1991) by the square root of 3C 351 luminosity ($L_{3\text{C } 351} = 2 \times 10^3 L_{\text{N5548}}$, $r_{5548} = 10$ lt-days) yields a distance of the BELR from the central continuum of $\sim \frac{1}{3}$ pc. So the distance of the absorber is $r_{\text{abs}} \gtrsim \frac{1}{3}$ pc. The larger ionization parameter and

larger radial distance compared to the BELR imply a lower density for the absorber. The radial distance of the ionized absorber is given by $r_{\text{abs}} = (Q/4\pi n_{\text{H}} c)^{1/2}$, where Q is the number of ionizing photons. For the best-fit parameters of the warm absorber this gives $r_{\text{abs}} = 5 \times 10^{19} n_5^{-1/2}$ cm, where n_5 is the number density in units of 10^5 cm^{-3} . Hence the density of the absorber must be $\lesssim 5 \times 10^7 \text{ cm}^{-3}$. This low density in combination with the large column density ($1\text{--}2 \times 10^{22} \text{ cm}^{-2}$), implies a depth for the absorber, $\gtrsim 2 \times 10^{14}$ cm. Given the above density and physical depth, this leads to a mass for the absorber of $\gtrsim 10^3 M_{\odot}$ for a covering factor of unity.

The depth of the Ly α absorption line ($2.06 \times 10^{-14} \text{ ergs}^{-1} \text{ cm}^{-2} \text{ \AA}^{-1}$) exceeds the continuum level ($0.77 \times 10^{-14} \text{ ergs}^{-1} \text{ cm}^{-2} \text{ \AA}^{-1}$) (Fig. 2b) implying that the absorber covers most ($\gtrsim 60\%$) of the BELR. However we note that the different lines indicate different percentages of the emission lines being covered, e.g., assuming that 100% continuum source is covered, the depth of the O VI line implies that the BELR may not be covered.

Further constraints come from the fact that a cloud with these physical properties exposed to the quasar continuum radiation would necessarily emit line radiation. If the covering factor of the absorption-line clouds is not small, the line ratios to Ly α would be much larger than the observed ones, as discussed in § 4.2. The contribution of the absorbing clouds to the total emission line flux should be $< 10\%$ to be consistent with the observed line ratios. The covering factor of such clouds must then be low (< 0.01).

The radiation pressure experienced by the warm absorber is easily sufficient to accelerate it to outflow velocities of a few thousand km s^{-1} , as shown by Turner et al. (1993). The effective Eddington limit for the warm absorber gas is given by $L_{\text{Edd}}^{\text{eff}} = L_{\text{Edd}} \times \sigma_{\text{T}}/\sigma_{\text{eff}}$, where σ_{T} is the Thomson cross section and σ_{eff} is the effective cross section including photoelectric absorption. σ_{eff} is defined such that

$$e^{-\sigma_{\text{eff}} N_{\text{H}}} \int_E f(E) dE = \int_E f(E) e^{-\sigma(E) N_{\text{H}}} dE,$$

where $f(E)$ is the transmitted flux at energy E and $\sigma(E)$, the absorption cross section at energy E , is $\sum_{\text{ion}} \sigma_{\text{ion}}(E) f_{\text{ion}} A(\text{atom}/\text{H})$. σ_{eff} is $\sim 1.4 \times 10^{-23}$ for a break energy of 0.37 keV. Thus $L_{\text{Edd}}^{\text{eff}} = 4.7 \times 10^{-2} L_{\text{Edd}}$. A quasar (or a Seyfert galaxy) emitting not too far below its Eddington luminosity must necessarily accelerate a warm absorber outward due to its radiation pressure. This is consistent with the blueshift seen in the UV absorber. Turner et al. (1993) reached a similar conclusion for the ionized absorber in NGC 3783.

The corresponding mass-loss rate is $0.05 < \dot{M} < 5 M_{\odot} \text{ yr}^{-1}$ for covering factors between 1% and unity. This is comparable to the accretion rate needed to power the central continuum source, $\dot{M}_{\text{accretion}} = 2 M_{\odot} \text{ yr}^{-1}$ for an efficiency of 0.1. Thus the net amount of inflowing matter must be at least a factor of 2 larger than the accretion rate. The outflow implies a kinetic luminosity of $(0.06\text{--}6) \times 10^{42} \text{ ergs s}^{-1}$, which is only 10^{-5} to 10^{-3} of the radiative luminosity of the quasar, i.e., outflow velocities as high as 4000 km s^{-1} are consistent with the energy balance. This is in contrast with the upper limit on velocity ($v < 1000 \text{ km s}^{-1}$) by Turner et al. (1993) for NGC 3783, which depended on their assumption of a covering factor of unity. This is unlikely to be applicable to 3C 351 where the covering factor is $\sim 1\%$ (see above). Even for NGC 3783, a covering factor of $\sim 1\%$ would allow for outflow velocities of 3000–4000

km s^{-1} since their limit was based on energy balance requirement that $L_{\text{kinetic}} < L_{\text{radiative}}$.

Variations in the continuum will change the ionization state of the absorbing gas resulting in corresponding changes in the column densities of individual lines. However, the absorption lines lie on the flat portion of the curve of growth, so a large change in column density would result in a small change in the equivalent widths of the lines. Thus the model predicts no significant correlation between variations in the continuum and the EW of the UV absorption lines. However, a continuum change will result in a change in X-ray opacity and thus in the effective value of U . The signature at the oxygen absorption edge in the X-ray spectrum is predicted to correlate with changes in continuum luminosity.

4. A HIGH-IONIZATION BELR AS THE ABSORBER?

It appears unlikely, based on the results of the previous section, that the absorber can be associated with a BELR cloud. However, given the ambiguity of the BELR covering result and the need for a new population of clouds, we wish to be certain that the BELR is not responsible. Thus we investigate whether the physical characteristics of a BELR cloud are similar to those of the UV/X-ray absorber. Until recently models for the BELR had typical values of the ionization parameter in the line-emitting clouds of $\sim \log U = -2$ (Davidson & Netzer 1978). The value of U for the ionized X-ray absorber in 3C 351 is 100–1000 times larger (Table 1). The line ratio C III] $\lambda 1909$ /C IV $\lambda 1549$ is a sensitive function of U , and such large values would produce unusually low values for C III]/C IV ($\ll 0.3$), and thus it appeared unlikely that a BELR cloud was responsible for the X-ray absorption.

However, in the last few years reverberation studies of a few low-luminosity Seyfert 1 galaxies have revealed that BELR clouds, at least those emitting the high-ionization lines, are closer to the continuum source (lt-days–lt-weeks) and so are exposed to a far more intense radiation field than previously thought (Peterson 1993) with an ionization parameter of $\sim \log U = -0.5$. This result, in combination with the fact that 3C 351 is X-ray-quiet, raises the possibility that BELR clouds could be responsible for the X-ray absorption. These studies have also shown that the C III] $\lambda 1909$ line, previously used to deduce $n_e \gtrsim 10^9 \text{ cm}^{-3}$, is formed at a larger distance than the permitted lines (C IV, N V, etc.), $\sim 3\text{--}4$ lt-weeks (Clavel et al. 1991) and so is produced in different clouds. Thus, there is no clear density indicator for the Lyman α –C IV region. Several implications of this intense radiation at the BELR inner radius are discussed in detail by Ferland & Persson (1980). Of particular relevance to the present study are the following:

1. Free-free heating is more important for higher fluxes or ionization parameters.
2. The strongest effect of the continuum shape is upon the higher ionization lines which are formed near the illuminated face of a cloud.
3. The ratio of C IV $\lambda 1549$ to Ly α is an increasing function of density because of both the increased free-free heating and the decreased efficiency of Ly α emission.
4. The O VI $\lambda 1034$ line increases in strength with increasing ionization parameter.

Since the importance of free-free heating increases with the intensity of the incident radiation field, a knowledge of the complete IR–X-ray spectral energy distribution (SED) is needed to understand and model the high ionization emission

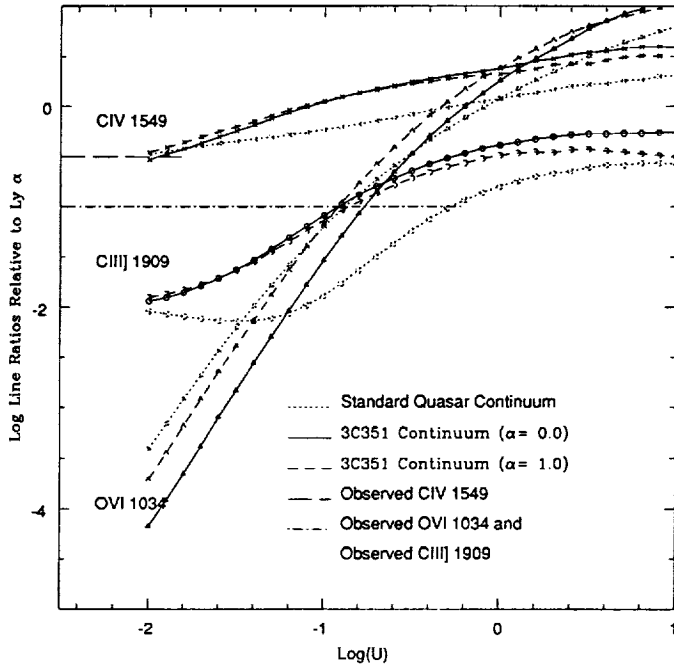


FIG. 5a

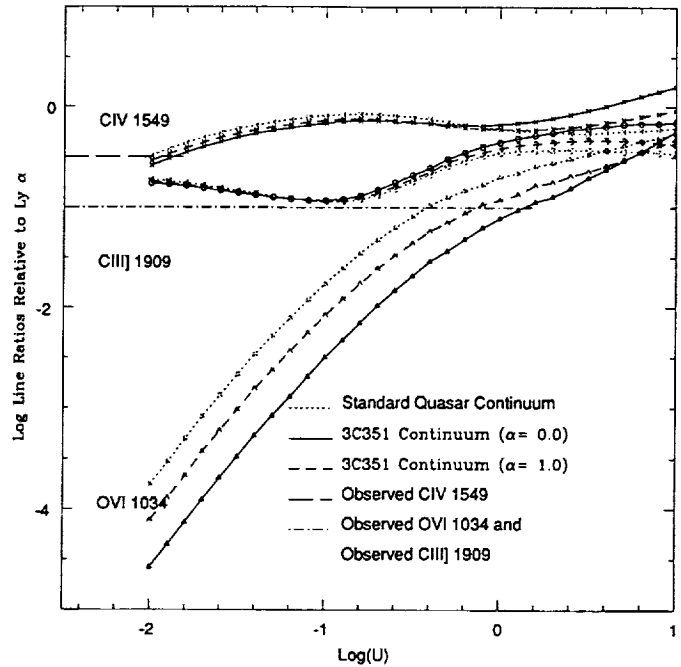


FIG. 5b

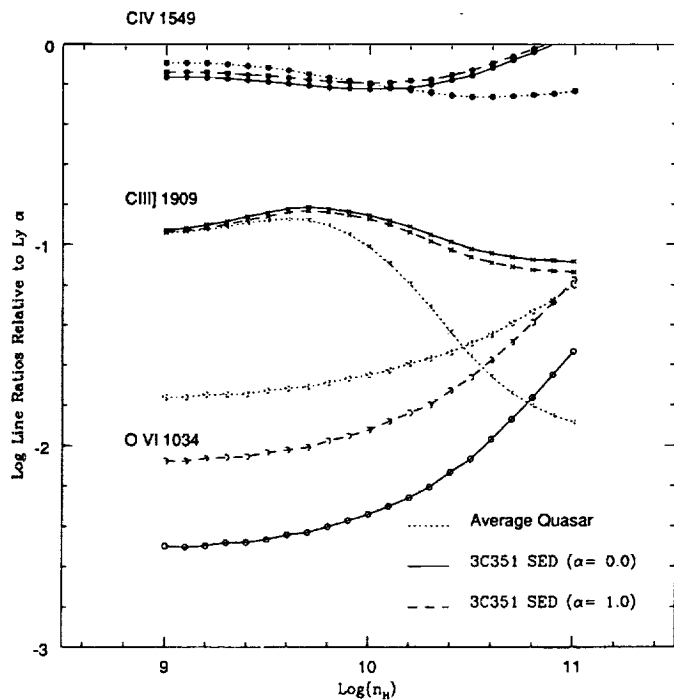


FIG. 5c

FIG. 5.—Line strengths relative to Ly α as a function of (a) U for $n_H = 10^{11} \text{ cm}^{-3}$, (b) for $n_H = 10^9 \text{ cm}^{-3}$, (c) as a function of n_H for $\log U = -1.0$ as predicted by photoionization models using the complete observed 3C 351 continuum. Observed values of the line strengths are shown by horizontal lines.

lines. We compared the observed O VI, C IV, and Ly α /N V emission-line EWs with photoionization models to derive the parameters of the emission-line clouds and compared them with the physical parameters of the X-ray/UV absorber. The input spectrum, ionization parameter, hydrogen density, and the column density of a cloud are the physical parameters which uniquely determine the strengths of the emission lines. We have explored a wide range of this parameter space: the hydrogen density was varied between 10^8 and 10^{11} cm^{-3} ; Lyman-continuum optical depth: 10^4 – 10^6 ; and the ionization parameter $\log U$: -2 to 1 ; in each case both a standard quasar continuum (Ferland 1991) and the 3C 351 observed continuum were used as input. In the following section we discuss the results.

4.1. The Effect of the Continuum on the Emission Lines

The dependence of the emission line strengths measured relative to Lyman- α on the ionization parameter (U) and number density (n_H) is shown in Figures 4 and 5 for all three continua. The effect of the Lyman-continuum optical depth on the line ratios was small ($<10\%$) for optical depths between 10^4 and 10^6 . The strongest effect is that using the observed continuum of 3C 351 instead of the standard continuum results in significant changes in the relative emission line strengths (up to a factor of 10).

4.1.1. The Relation between the Continuum and the Ionization Parameter

The two extreme wavelength intervals in the 3C 351 continuum, the X-ray and IR-radio, act competitively with opposite effects on the strengths of the emission lines of interest. In Figure 5a, C IV, C III], and O VI line strengths relative to Ly α are plotted as a function of U for $n_H = 10^{11} \text{ cm}^{-3}$. The larger IR-radio flux in the 3C 351 continuum increases the line ratios due to increased free-free heating. Conversely, the smaller X-ray flux produces lower numbers of ions and decreases the

line ratios. For lower values of U , the low X-ray flux level in the 3C 351 continuum dominates and the line ratios are systematically lower than those produced by the standard continuum. Above some U_{critical} the effect of free-free heating dominates (Fig. 5a). The value of U_{critical} is higher for ions with higher ionization potentials and increases with decreasing n_H ; for example U_{critical} for C iv at $n_H = 10^{11} \text{ cm}^{-3}$ is ~ 0.25 , whereas for $n_H = 10^9 \text{ cm}^{-3}$ is ~ 0.63 . For low $n_H (= 10^9 \text{ cm}^{-3})$, U_{critical} for O vi is sufficiently high that the effect of free-free heating is negligible for almost the entire range of U (Fig. 5b).

The strongest effect of the low X-ray flux in 3C 351 is on the strength of the O vi line. This is not surprising since the ionization potential of O v is 0.11 keV. The strength of the O vi line is lower by a factor of ~ 10 with an input spectrum which is X-ray-quiet ($\alpha_{\text{OX}} = 1.6$) (Fig. 5a). In addition, the low X-ray flux leads to a value of the ionization parameter higher by a factor of 2.5 than that using the standard continuum (Fig. 5a). The IR upturn and radio loudness have the opposite effect, but this is significant only when both U and n_H are high ($\log U \gtrsim -1$, $n_H \sim 10^{11} \text{ cm}^{-3}$).

4.1.2. The Relation between the Continuum and the Density

When U is low, the shape of the input continuum makes no significant difference to the dependence of emission-line strengths of the C iv and C iii] on density, but it always has a significant effect on the dependence of O vi on density. For the standard continuum, the strength of C iii] $\lambda 1909$ drops rapidly for densities higher than the critical density for collisional deexcitation (10^9 cm^{-3}) (Fig. 5c), and so C iii] is normally used to put an upper limit on the BELR cloud densities. This effect vanishes using the 3C 351 continuum for high values of U ($\log U > -1$) due to increased free-free heating, which produces heating without ionization. Thus, for a 3C 351-like continuum, i.e., with strong IR emission, C iii] $\lambda 1909$ ceases to be a density indicator for $\log U > 0.1$.

Kwan (1984) pointed out that uncertainty in the dielectronic recombination rates and the strong dependence of C iii] $\lambda 1909$ /C iv $\lambda 1549$ on U compromised its role as a density indicator. Our results show a second reason to discount the value of C iii] as a density diagnostic. We conclude that, even without variability information to confirm C iii]'s origin in different gas, it is not a good indicator of density in the high-ionization Ly α -C iv-emitting region.

4.2. Comparison with Observations

To investigate whether the physical parameters of BELR clouds are the same as those of the warm absorber, we compared the photoionization model calculations described above with the observed emission lines C iii], C iv, O vi, and Ly α . The observed strength of C iii] $\lambda 1909$ relative to Ly α ($= 0.1$) is used only as an upper limit in this comparison because, as discussed earlier, it is believed to originate in a separate, larger region than the C iv-O vi-producing clouds. As shown in Figure 5b, this constraint is not satisfied for low densities ($n_H = 10^9 \text{ cm}^{-3}$) for the entire range of U . Even for higher densities (Fig. 5a, $n_H = 10^{11} \text{ cm}^{-3}$), the constraint is satisfied only for $\log U < -1.2$, lower than that required for O vi production, i.e., no consistent result can be found.

The large predicted strength of C iii] results from the large amount of free-free heating due mainly to the IR upturn in the 3C 351 continuum. If this IR is produced by thermal emission from dust at larger distances from the nucleus, instead of in the central region, the BELR clouds will see much weaker IR flux,

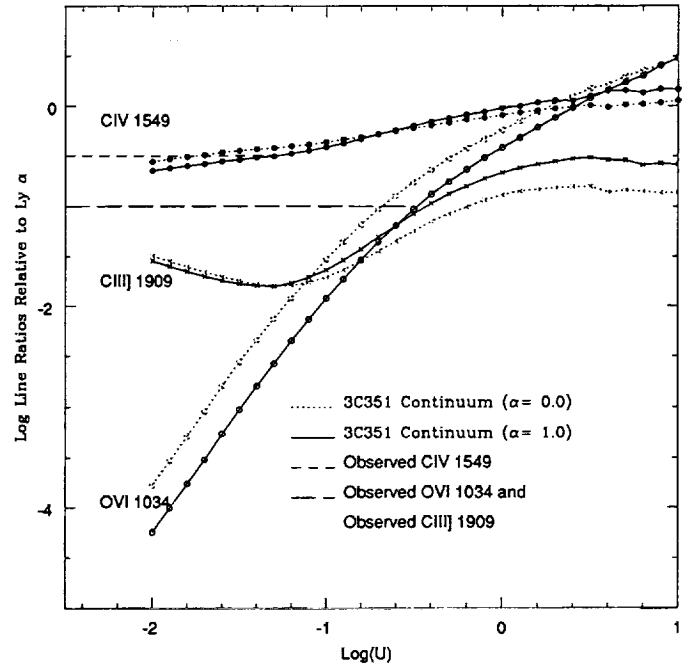


FIG. 6.—Line strengths relative to Ly α + N v as a function of U for $n_H = 10^{11} \text{ cm}^{-3}$. The 3C 351 continuum here is that without either the IR upturn or radio (see § 4.2). Observed values of the emission lines are shown by horizontal lines.

reducing the free-free heating. In this scenario, we compared the observed line ratios of C iv/Ly α and O vi/Ly α with those predicted by the 3C 351 continuum without the IR upturn (Fig. 6). The C iii] line constraint is now satisfied for the range of U relevant for the C iv-O vi producing clouds (up to $\log U \sim -0.2$, for $n_H = 10^{11} \text{ cm}^{-3}$). If C iii] is produced predominantly at a distance larger than the C iv-Ly α clouds, then the IR upturn is necessarily produced beyond the BELR clouds arguing in favor of a dust model for the IR emission (Sanders et al. 1989; Barvainis 1993).

The observed C iv/Ly α ratio give a value of the ionization parameter for C iv-Ly α -producing clouds of $\log U = -1.5 \pm 0.2$ for $n_H = 10^{11} \text{ cm}^{-3}$ (Fig. 6). The inferred value for O vi $\lambda 1034$ is much larger, $\log U = -0.6 \pm 0.1$, implying that O vi is produced closer to the ionizing continuum than the C iv-Ly α clouds. Even though this U is much larger than the standard value ($\log U = -0.5$ as compared to -2) (Fig. 6), it is still much lower than that required for the X-ray absorber ($\log U = 0.78-1.08$). Thus, we rule out the possibility of identifying the X-ray absorber as a BELR cloud.

It is still possible that the BELR clouds provide the parent population for the outflowing absorption line clouds. We discuss this possibility further in section 5.2.

5. ARE THERE OTHER UV/X-RAY ABSORBERS?

5.1. Previous Studies

Strong, associated metal line absorption has been observed before in AGNs with soft X-ray absorption. However, in no case was the UV absorber identified with the X-ray absorber as the physical parameters of the two were deduced to be very different. Our results for 3C 351 show that there are five reasons for these apparently discrepant conditions:

1. The Mg ii ion is not produced in enough abundance until

column densities are high (Kwan & Krolik 1981), so the absence of Mg II absorption in a high-ionization absorption system was interpreted as due to a low ($N_H < 10^{20.5}$) column density. However, the column densities inferred from the X-ray data were some two orders of magnitude higher ($N_H \sim 10^{22}-10^{23}$) and thus completely inconsistent. Our analysis shows that the reason for the lack of Mg II absorption may instead be that the material is highly ionized. In this case large column densities are allowed despite the absence of Mg II absorption as magnesium is predominantly in high-ionization states.

2. A second consequence of the assumed low column densities for the UV absorbers is that the absorbing gas would be fully ionized (Shull & Sachs 1993) in hydrogen. In our analysis the column densities are large enough to allow partial ionization and hence the Ly α absorption.

3. The key high-ionization line O VI $\lambda 1034$ is not easily observed in AGNs with *IUE*. It can only be seen for $z \gtrsim 0.2$, and few AGNs at such redshift are bright enough to be studied with *IUE*. C IV was thus the most commonly observed high-ionization absorption line. For optically thin, AGN-photoionized gas, C IV is the dominant carbon ionization state when $\log U \sim -2.3$ (Donahue & Shull 1991). Since strong C IV absorption was observed, such values were assumed to be appropriate for the UV absorber. This is much lower than that required for a warm absorber. However the combination of C IV and O VI absorption in 3C 351 demonstrates that this assumption does not apply. In the present model the ionization parameter of the absorber is high ($\log U \sim 0.78$), and C VI rather than C IV is the dominant state of ionization.

4. Early X-ray observations constrained only the total absorbing column density along the line of sight due to either a lack of sensitivity below the 0.6 keV oxygen edge, or of resolution to detect the edge. Absorption as seen in the X-rays was assumed to be due to neutral, "cold" gas because "hot" gas would be transparent to X-rays. There was no observational constraint on the actual ionization structure of the absorber. The higher spectral resolution of *ROSAT* allows detection of absorption edges, thus constraining the ionization state of the absorber and providing clear evidence for partially ionized gas.

5. The physical conditions of the absorbing gas are poorly determined from absorption line studies in the UV alone (Lanzetta et al. 1991) because only a few lines are measured (N V $\lambda 1240$, C IV $\lambda 1549$, and possibly Mg II $\lambda 2798$ or O VI $\lambda 1034$) yielding column density estimates of a few ions but no information on the ionization state. Since the X-ray absorption cross section is relatively insensitive to ionization and depletion (Morrison & McCammon 1983), X-ray measurements give a total column density.

We have now demonstrated that the combination of UV and X-ray provides information on the ionization state of the gas and hence the physical conditions.

The case of the Seyfert galaxy NGC 3516 ($z = 0.009$) is instructive. Kolman et al. (1993) present simultaneous X-ray and UV observations of NGC 3516 with absorption features seen in the UV spectrum and the signature of a warm absorber in the X-ray spectrum. The authors rule out a common origin of the UV and X-ray absorption.

The X-ray observations were made with *Ginga* which has its response at higher energies (1–20 keV) than *ROSAT* (0.1–2 keV). The warm absorber in NGC 3516 has an absorption edge in the range 7.4–8.3 keV, which includes ionization stages from

Fe $^{+12}$ to Fe $^{+21}$. A simple warm absorber model was constructed by introducing an additional absorption edge in to the model; a physical warm absorber was not constructed, and thus U could not be constrained. The UV spectrum from *IUE* contains absorption lines of C IV, N V, and Si IV and the low-ionization line Mg II. U was deduced by assuming that the fractional abundance of C IV is a maximum yielding a low value of U ($\log U = -2.18$ to -0.83 for $\log N_H = 20-22$). In the warm absorber, iron is at least 12 times ionized, which is consistent with C $^{+5}$ and higher stages of ionization. Therefore, such matter is probably too highly ionized to produce the observed UV absorption lines, especially Mg II; hence their conclusion that the absorbers were distinct. However, we note that the evidence for Mg II absorption in NGC 3516 is rather weak (Kolman et al. 1993) due to blending with a Galactic absorption line. If this line is not confirmed (e.g., in an *HST* spectrum), then highly ionized matter similar to that in 3C 351 is a possibility. It may then be possible to reconcile the ionization states of the UV and X-ray absorbers in NGC 3516.

5.2. Implications

The identification of the UV and X-ray absorbers in 3C 351 with the same absorbing gas opens up many possibilities. We note, for example, that if the clouds are expanding laterally at their sound speeds, then the ionization parameter of the clouds would change as they flow out with $U \propto R(v_{\text{sound}}/v_{\text{outflow}})^3$. Projecting the cloud density and U back to the radius of the BLR gives values consistent within a factor of 2 with those for the BELR clouds, so that the outflow may be built from outflowing BELR material. These clouds could attain velocities an order of magnitude larger without disrupting the energy balance (see § 3.2), which would then give them properties closely similar to the BAL outflows (Turnshek 1988). BALQSOs typically have $N_H \sim 10^{21-22} \text{ cm}^{-2}$, are highly ionized and have a complex velocity structure. Initial results from *ROSAT* (Kopko, Turnshek, & Espey 1993) imply that they are relatively faint in soft X-rays, suggestive of strong absorption and another UV/X-ray absorber connection. Cold, yet variable, absorbers are quite common in the X-rays (Turner & Pounds 1989; Warwick et al. 1993). If we assume that these absorbers are related to the UV/X-ray ionized absorbers only denser, or more distant so that they have lower U , then we can begin to make progress in understanding them. This is shown to be the case in 3C 212 which was originally thought to be a cold absorber (Mathur 1994). Presently these absorbers are usually associated with the "obscuring tori" indicated in unified schemes (e.g., Antonucci & Miller 1985). Identification with the kind of outflow seen here suggests a more dynamic "expanding shell" picture (see also Lawrence 1991). Once again the combination of UV and X-ray data would result in strong constraints on the physical conditions of the absorber.

6. CONCLUSIONS

In this paper we have shown that the X-ray and UV absorbers in 3C 351 are highly likely to be one and the same. The physical conditions of the absorber are determined through the combination of constraints derived from both the X-ray and UV analysis. The absorber is found to be highly ionized ($\log U = 0.78-1.08$), outflowing with a velocity $\sim 3050 \text{ km s}^{-1}$, having high column density ($N_H = 1-2 \times 10^{22} \text{ cm}^{-2}$), low density ($n \lesssim 10^7 \text{ cm}^{-3}$); probably a low covering factor ($\sim 1\%$) and situated outside the BELR. These properties

describe a component of the active nucleus not previously recognized.

This is the first confirmed X-ray/UV absorber. We have shown that the previous attempts to identify an UV absorber with a X-ray absorber were unsuccessful because of the lack of high-quality data which forced overly constraining assumptions to be made in photoionization modeling. These led to incompatible conditions being derived for the UV and X-ray absorbers. The identification of the UV and X-ray absorbers in 3C 351 with the same absorbing gas opens up new possibilities for studying the physical conditions in other UV and X-ray absorbers, e.g., BALQSOs. We have demonstrated the great advantage in determining the properties of the absorber that is afforded by the combination of UV and X-ray data.

We have also investigated the effect of the 3C 351 continuum on emission-line strengths. The 3C 351 continuum differs significantly from the standard continuum in that it is X-ray-quiet, radio-loud, and has an upturn in the IR. We demonstrate that it is important to use observed continuum, rather than a standard one, to derive the physical parameters in the BELR self-consistently. The strongest effect of the low X-ray flux is on the strength of O VI $\lambda 1034$. The strengths of the high-ionization lines of C IV $\lambda 1549$ and O VI $\lambda 1034$ with respect to Ly α are systematically lower (up to a factor of 10) with the 3C 351 continuum as compared to those produced by the standard continuum for $U < U_{\text{critical}}$. This is mainly due to the weak X-ray flux. Free-free heating was found to be impor-

tant for large values of the ionization parameter ($\log U > -1$) and higher densities ($n \sim 10^{11} \text{ cm}^{-3}$). We find that for a 3C 351-like (IR-strong) continuum, C III] $\lambda 1909$ ceases to be a density indicator if the BELR gas sees the same continuum. We rule out the identification of the absorber with a BELR cloud as the physical conditions in the two regions are inconsistent with one another. It is possible that the BELR clouds provide the parent population for the outflowing absorption-line clouds.

3C 351 was observed by us with ROSAT because it was known to be X-ray-quiet, as a part of our program to observe quasars with extreme continuum properties. Our expectation was that they would produce new insights into the underlying physical processes. This strategy indeed seems to be fruitful.

We thank the Quasar Absorption Line Key Project team for making the *Hubble Space Telescope* observations available. We acknowledge the Data Management Facility/Data Archiving and Distributing System (DMF/DADS) at STScI for making the archived *IUE* Quasar Atlas available. We thank T. Kallman, H. Netzer, A. Dobrzycki, and J. McDowell for useful discussions; B. Jannuzi for help with the *HST* spectra; and G. Ferland for providing us with the photoionization code CLOUDY.

This work was supported by NASA grants NAGW-2201 (LTSA), NASA 5-30934 (RSDC), and NAG 5-1883 (ROSAT).

REFERENCES

- Antonucci, R. R. J., & Barvainis, R. 1988, *ApJ*, 325, L21
 Antonucci, R. R. J., & Miller, J. S. 1985, *ApJ*, 297, 621
 Bahcall, J. N., et al. 1993, *ApJS*, 87, 1
 Barvainis, R. 1993, *ApJ*, 412, 513
 Boissé, O., Boule, D., Kunth, D., Tytler, D., & Vigroux, L. 1992, *A&A*, 262, 401
 Chini, R., Kreysa, E., & Biermann, P. L. 1989, *A&A*, 219, 87
 Clavel, J., et al. 1991, *ApJ*, 366, 64
 Davidson, K., & Netzer, H. 1979, *Rev. Mod. Phys.*, 51, 715
 Donahue, M., & Shull, J. M. 1991, *ApJ*, 383, 511
 Ellingson, E., Yee, H. K. C., Bechtold, J., & Dobrzycki, A. 1994, *ApJ*, submitted
 Elvis, M., et al. 1994, *ApJS*, in press
 Espey, B. R., Carswell, R. F., Bailey, J. A., Smith, M. G., & Ward, M. J. 1989, *ApJ*, 342, 666
 Ferland, G. F. 1991, "HAZY" (OSU Astronomy Department Internal Report)
 Ferland, G. F., & Persson, S. E. 1989, *ApJ*, 347, 656
 Fiore, F., Elvis, M., Mathur, S., Wilkes, B., & McDowell, J. 1993, *ApJ*, 415, 129 (Paper I)
 Grevesse, N., & Anders, E. 1989, in *Abundances of Matter*, ed. C. J. Waddington (New York: AIP)
 Kinney, A. L., Bohlin, R. C., Blades, J. C., & York, D. G. 1991, *ApJS*, 75, 645
 Kolman, M., Halpern, J. P., Martin, C., Awaki, H., & Koyama, K. 1993, *ApJ*, 403, 592
 Kopko, M., Turnshek, D. A., & Espey, B. 1993, in *IAU Symp. 159, Quasars Across Electromagnetic Spectrum*, ed. T. J.-L. Courvoisier & A. Blecha (Dordrecht: Kluwer), 450
 Kwan, J. 1984, *ApJ*, 283, 70
 Kwan, J., & Krolik, J. H. 1981, *ApJ*, 250, 478
 Lanzetta, K. M., Wolfe, A. M., Turnshek, D. A., Lu, L., McMahon, R. G., & Hazard, C. 1991, *ApJS*, 77, 1
 Lawrence, A. 1991, *MNRAS*, 252, 586
 Mathews, W. G., & Ferland, G. J. 1987, *ApJ*, 323, 456
 Mathur, S. 1994, *ApJ*, 431, L75
 Morrison, R., & McCammon, D. 1983, *ApJ*, 270, 119
 Peterson, B. M. 1993, *PASP*, 105, 247
 Sanders, D., Phinney, E. S., Neugebauer, G., Soifer, B. T., & Mathews, K. 1989, *ApJ*, 347, 29
 Schneider, D. P., et al. 1993, *ApJS*, 87, 45
 Shastri, P., Wilkes, B. J., Elvis, M., & McDowell, J. C. 1993, *ApJ*, 410, 29
 Shull, J. M., & Sachs, E. R. 1993, *ApJ*, 416, 536
 Spitzer, L. 1978, *Physical Processes in the Interstellar Medium* (New York: Wiley-Interscience)
 Turner, T. J., Nandra, K., George, I. M., Fabian, A., & Pounds, K. A. 1993, *ApJ*, 419, 127
 Turner, T. J., & Pounds, K. A. 1988, *MNRAS*, 232, 463
 ———, 1989, *MNRAS*, 240, 833
 Turnshek, D. A. 1988, in *QSO Absorption Lines: Probing the Universe*, ed. J. C. Blades, D. Turnshek, & C. A. Norman (Cambridge: Cambridge Univ. Press), 17
 Ulrich, M. H. 1988, *MNRAS*, 230, 121
 Warwick, R., Sembay, S., Yaqoob, T., Makishima, K., Ohashi, T., Tashiro, M., & Kohmura, Y. 1993, *MNRAS*, 265, 412
 Wiese, W. L., Smith, M. W., & Glennon, B. M. 1966, *Atomic Transition Probabilities* (Washington: US Government Printing Office)
 Wilkes, B. J., & Elvis, M. 1987, *ApJ*, 323, 243
 Wilkes, B. J., Tananbaum, H., Worall, D. M., Avani, Y., Oey, M. S., & Flanagan, J. 1994, *ApJS*, in press

TESTING UNIFIED X-RAY/ULTRAVIOLET ABSORBER MODELS WITH NGC 5548

SMITA MATHUR, MARTIN ELVIS, AND BELINDA WILKES

Harvard-Smithsonian Center for Astrophysics, 60 Garden Street, Cambridge, MA 02138; smita@cfa.harvard.edu

Received 1995 February 21; accepted 1995 April 21

ABSTRACT

The bright Seyfert galaxy NGC 5548 shows absorption features in its X-ray and UV spectra. The large amount of optical/UV and X-ray monitoring data available for this object makes it an ideal candidate to test our model of a common X-ray/UV absorber. We show that the X-ray/UV absorption is caused by a highly ionized ($2.2 < U < 2.8$), high column density ($N_H = 3.8 \times 10^{21} \text{ cm}^{-2}$) gas situated outside the C IV emitting region ($2 \times 10^{16} \text{ cm} < r_{\text{abs}} < 2 \times 10^{18} \text{ cm}$). The gas is outflowing with a mean velocity of $1200 \pm 260 \text{ km s}^{-1}$ and corresponding kinetic luminosity of $\sim 10^{43} \text{ ergs s}^{-1}$. The gas is more highly ionized and has a much larger column density than earlier estimates based on UV data alone. This third example of an X-ray/UV absorber reinforces our earlier conclusion that outflowing, highly ionized gas is common in the inner regions of quasars.

Subject headings: galaxies: individual (NGC 5548) — galaxies: active — galaxies: Seyfert — ultraviolet: galaxies — X-rays: galaxies

1. INTRODUCTION

Recently we found that the ionized (“warm”) X-ray absorbers and the associated UV absorbers were due to the same material in two radio-loud quasars: an X-ray-quiet quasar, 3C 351 (Mathur et al. 1994), and a red quasar, 3C 212 (Mathur 1994). In both cases the absorber is situated outside the broad emission line region (BELR), is outflowing, and is highly ionized. While this result delineates a new nuclear component in lobe-dominated radio-loud quasars, it would clearly be much more interesting if the same component were present in all quasars and active galactic nuclei (AGNs) with both X-ray and UV absorption (Ulrich 1988). In this paper we test this generalization by applying the same model to the best studied of all AGNs, NGC 5548.

NGC 5548, a radio-quiet Seyfert 1 galaxy, provides the best test case for the equivalence of the X-ray and UV absorbers and will yield a highly constrained determination of the physical properties of the absorber. This is because NGC 5548 has been extensively studied in reverberation mapping experiments in the optical and UV (Peterson et al. 1992; Clavel et al. 1991; Korista et al. 1995). These have led to the accurate determination of the physical size of the BELR. NGC 5548 has both an X-ray-ionized absorber (Nandra et al. 1991; Fabian et al. 1994a) and an UV absorber (Shull & Sachs 1993), and the reverberation observations place limits on the response time of the UV absorbers to changes in the UV continuum. Note that this response time is due to the physical conditions of the absorber only, since there is no light-travel time delay along the line of sight.

We apply the photoionization modeling method of Mathur et al. (1994) to the X-ray and UV absorbers in NGC 5548 to determine whether consistent values for abundances of all the observed ions can be obtained. In NGC 5548 the model must meet two extra requirements: it must not lead to a density for the absorber in conflict with its recombination time; and the distance of the absorber from the continuum source must not conflict with the well-determined BELR size.

2. DATA

2.1. X-Ray Data

X-ray observations of NGC 5548 have revealed a complex spectrum. *EXOSAT* showed that the source has a strong soft excess (Branduardi-Raymont 1986, 1989). *Ginga* showed, moreover, that the X-ray spectrum and flux were variable (Nandra et al. 1991) and that the X-ray variability was correlated with the ultraviolet variability (Clavel et al. 1992). In addition, complex absorption was observed by *Ginga* with a possible Fe K edge at $\sim 8 \text{ keV}$, corresponding to an intermediate ionization stage of iron ($\sim \text{Fe XX}$) with $\tau_{\text{Fe K}} \sim 0.03$ and variable soft X-ray absorption. *ROSAT* observations of NGC 5548 (1990 July 16–21) showed an absorption feature in its X-ray spectrum arising from highly ionized oxygen, demonstrating the presence of an ionized absorber; $E = 0.81 \pm 0.06 \text{ keV}$, $\tau = 0.35 \pm 0.13$ (Nandra et al. 1993).

Recent observations with *ASCA* (1993 July 28) confirmed the presence of an ionized absorber (Fabian et al. 1994a). O VII and O VIII absorption edges observed at 0.72 keV and 0.86 keV, respectively, were resolved in the *ASCA* spectrum. The optical depths of the edges were $\tau_{\text{O VII}} = 0.26^{+0.04}_{-0.08}$ and $\tau_{\text{O VIII}} = 0.12^{+0.07}_{-0.03}$. The combined O VII and O VIII opacity from *ASCA* agrees well with that observed with *ROSAT*. An equivalent hydrogen column density was $N_H = 3.8 \times 10^{21} \text{ cm}^{-2}$. However, the presence of an Fe K edge is not confirmed ($\tau_{\text{Fe K}} \leq 0.1$).

The absorption cross sections of O VII and O VIII are $0.28 \times 10^{-18} \text{ cm}^2$ and $0.098 \times 10^{-18} \text{ cm}^2$, respectively (CLOUDY version 80.06; Ferland 1991). The column densities in the two ions are thus $N_{\text{O VII}} = 0.93^{+0.14}_{-0.29} \times 10^{18} \text{ cm}^{-2}$ and $N_{\text{O VIII}} = 1.22^{+0.72}_{-0.30} \times 10^{18} \text{ cm}^{-2}$. Given the total hydrogen column density and the solar abundance of oxygen relative to hydrogen ($= 8.51 \times 10^{-4}$; Grevesse & Andres 1989) the fraction of oxygen in the two stages of ionization is calculated; $f_{\text{O VII}} = 0.29^{+0.04}_{-0.09}$ and $f_{\text{O VIII}} = 0.38^{+0.22}_{-0.10}$. The absorber must thus be highly ionized to have two-thirds of the oxygen in hydrogen-like and helium-like states.

2.2. Ultraviolet Data: *IUE*

NGC 5548 has been studied extensively in the ultraviolet (Clavel et al. 1991; Korista et al. 1995). The UV spectrum shows absorption lines of C iv and N v within the profiles of their broad emission lines (Shull & Sachs 1993, hereafter SS). The source was found to be highly variable in its continuum flux and also in the strengths of its emission and absorption lines. The UV continuum was found to vary by a factor of ~ 3 , while the C iv absorption line equivalent width (EW) varied by a factor of ~ 2 over a period of about 10 days. There is no observed lag between the variations in the continuum and the EW of the C iv absorption line ($\Delta t \leq 4$ days; SS). Note that any delay between the continuum and absorption-line variability is *not* due to light-travel time (reverberation) effects, which are not operative along the line of sight. It is instead due to physical conditions within the absorber, specifically, the recombination time (see § 3.4). SS also infer a blueshift of $1200 \pm 260 \text{ km s}^{-1}$ with respect to the systemic velocity of NGC 5548. We note that the earliest *IUE* spectra of NGC 5548 are also suggestive of an absorption feature at this position (Wu, Boggess, & Gull 1981; Ulrich & Boisson 1983). We reanalyzed the 1979 *IUE* data (SWP05500, SWP05687, SWP05688, SWP05689, SWP07345, SWP073930), including those reported by Wu et al. (1981) using current extraction techniques. The C iv absorption line is present at similar velocity and is of comparable strength to the later data (SS).

No associated Ly α absorption has been reported in the large literature on NGC 5548. Observationally it is difficult because the Ly α emission line of this low-redshift source lies very close to geocoronal Ly α . Theoretically, Ly α absorption was not expected (SS), since the absorbing gas was considered “fully ionized” in hydrogen. As a result, all the published spectra cut off the blue wing of Ly α in the AGN emission line in order to remove geocoronal Ly α from the spectrum, cutting out also part of the Ly α absorption line.

Because our models predict significant Ly α absorption, we retrieved and reanalyzed a set of *IUE* spectra, taking care to go to shorter wavelengths. In Figure 1 we present an *IUE* spectrum of NGC 5548, without removing the geocoronal Ly α . This clearly shows the presence of a Ly α absorption line at a redshift consistent with that of the other absorption lines.

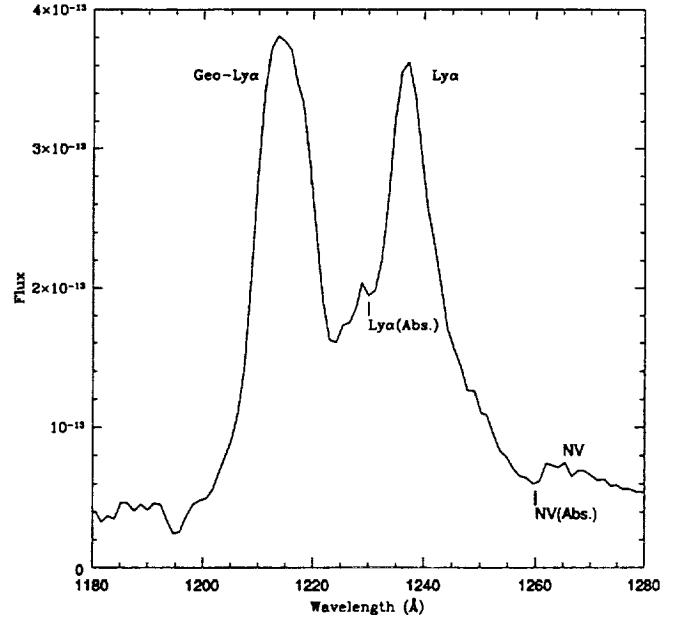


FIG. 1.—*IUE* spectrum of NGC 5548 (an average of SWP35029, SWP35284, SWP35461, SWP35636, SWP35849, SWP36018, SWP36369, SWP36567, and SWP36715) showing the presence of Ly α absorption line.

2.3. Ultraviolet Data: *Hubble Space Telescope*

NGC 5548 was observed daily for a total of 39 times by *HST* in 1993 April/May to monitor the variability of the source in the ultraviolet ($1140 \text{ Å} < \lambda < 2312 \text{ Å}$; Korista et al. 1995). *HST* Faint Object Spectrograph (FOS) resolution is $\sim 1 \text{ Å}$ over this wavelength range (cf. $\sim 6 \text{ Å}$ with *IUE*). Figures 2a and 2b show the emission- and absorption-line profiles of Ly α and C iv, respectively, for the mean FOS spectrum. This spectrum was constructed by joining the combined G130H and G190H spectra; no scale factors were applied (see Korista et al. 1995, § 2.4). We measured the EWs of the absorption lines both in the individual *HST* spectra and in the mean. The C iv doublet $\lambda\lambda 1548, 1551$ is resolved with $\text{EW} = 0.32 \pm 0.1$ and $0.08 \pm 0.03 \text{ Å}$, respectively, in the mean FOS spectrum (Table

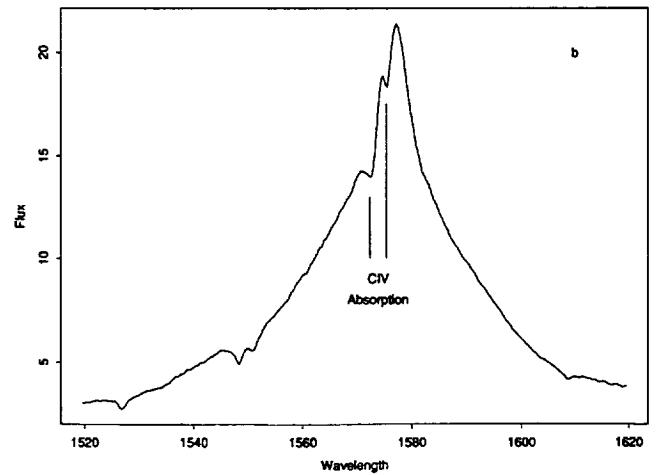
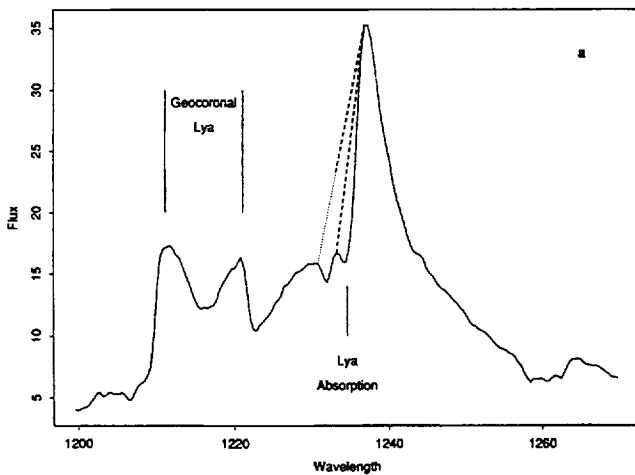


FIG. 2.—*HST* mean FOS spectrum of NGC 5548 showing (a) Ly α , N v and (b) C iv absorption troughs. In (a) we also indicate our maximal and minimal estimates of the absorption-line strength (dashed line). The dotted line indicates the extrapolation to the observed line profile.

TABLE 1
ABSORPTION-LINE PARAMETERS

| LINE | λ_{obs} (Å) | EW (Å) | |
|-----------------------------|-------------------------------|-------------------------|-----------------|
| | | <i>HST</i> ^a | <i>IUE</i> |
| C iv $\lambda 1548.2$ | 1572.4 | 0.30 ± 0.10 | 1.6 ± 0.3^b |
| C iv $\lambda 1550.8$ | 1575.4 | 0.08 ± 0.03 | |
| N v $\lambda 1238.8$ | 1260.7 | 0.04 ± 0.01 | ... |
| N v $\lambda 1242.8$ | 1262.5 | 0.10 ± 0.03 | |
| Ly α | 1234.1 | 0.5 ± 0.3 | ... |

^a In mean spectrum.

^b SS mean value scaled by our correction factor, 0.6 (see text).

1). The measurement of absorption lines situated within a broad emission line profile is notoriously difficult, since the real shape of the emission line is unknown. We estimated the magnitude of our errors by making maximal, minimal, and optimal measurements in each case (see, e.g., Fig. 2a). This yielded a typical error of about a factor of 2 in individual spectra and about 30% error in the mean FOS spectrum. The N v doublet is also resolved in the *HST* data with EW = 0.1 and 0.04 Å ($\pm 30\%$) in the mean spectrum.

An associated Ly α absorption line, at the same relative blueshift ($\Delta z = 0.002$) as the C iv–N v absorption system, is clearly seen with EW 0.5 ± 0.3 Å; a minimum H I column density is thus $N_{\text{H I}} \geq 4 \times 10^{13} \text{ cm}^{-2}$. There is another absorption feature immediately shortward ($\lambda_{\text{obs}} = 1231.9$ Å, $\Delta z = 0.004$, EW ~ 0.6 Å). There are no corresponding C iv or N v absorption features at a similar relative blueshift, and the line appears to be unrelated to the associated absorption system we discuss here. The uncertainty in the Ly α EW is large owing to its proximity both to this nearby absorption feature and to the peak of the emission-line profile.

Note that the C iv EW in the mean *HST* spectrum is significantly lower than those reported for the *IUE* spectra (2 or 8 Å; SS) in 1989. The larger of the two SS EW values was derived by assuming that much of the emission-line peak was absorbed. This is clearly not the case in the higher resolution *HST* data. The *HST* spectra also show that the absorption feature covers a smaller range in wavelength than was apparent from the *IUE* data. We remeasured nine *IUE* spectra around JD 2,447,580, the time of the maximum continuum change, using $\Delta\lambda \sim 10$ Å, rather than the 16 Å used by SS. The exact wavelengths varied due to the inherent uncertainty in the wavelength calibration for spectra observed with the large *IUE* aperture. Our EW values are systematically smaller than SS's small values for the same spectra by a factor of 0.6. We used our revised measurements for the remainder of this paper. We note that the 1989 *IUE* C iv EWs are still larger than the *HST* values. This may be due to the measurement difficulties in the low-resolution *IUE* spectra.

3. MODELS

In the context of photoionization models we look for an ionized absorber that satisfies the X-ray constraints. Photoionization models predict the fraction of atoms in each ionization state, f_{ion} , given the column density (N_{H}), density (n), and ionization parameter U [$U = (Q/4\pi r^2 n_{\text{H}} c)$, where Q is the number of ionizing photons] of a cloud of gas exposed to a continuum source with a defined continuum shape. All the photoioniza-

tion calculations in this paper were performed using CLOUDY (Ferland 1991).

Mathur et al. (1994) have shown that the particular spectral energy distribution (SED) of each AGN should be used, rather than a "typical" quasar SED, since this might lead to incompatible physical conditions in a photoionized cloud. The observed radio to X-ray continuum of NGC 5548 is shown in Figure 3 (data from Ward et al. 1987; SS; Korista et al. 1995; Nandra et al. 1991). The continuum is corrected for Galactic reddening by $E(B-V) = 0.033$, assuming a fixed conversion of $N_{\text{H}}/E(B-V) = 5.0 \times 10^{21} \text{ cm}^{-2} \text{ mag}^{-1}$ and N_{H} ($1.65 \times 10^{20} \text{ cm}^{-2}$; Nandra et al. 1993). The shape of the IR/optical continuum is similar to a typical AGN (Elvis et al. 1994) with the IR break shifted shortward to 100 μm . The standard radio-quiet AGN continuum used by Mathews & Ferland (1987) is shown for comparison as a dashed line. NGC 5548 is much brighter in X-rays than a typical AGN, but has a normal X-ray spectral slope, $\alpha_{\text{E}} = 0.8 \pm 0.2$ in the 2–10 keV range (Nandra et al. 1991). In addition, it has a soft X-ray excess which can be approximated by a blackbody spectrum of temperature 150,000 K (Fig. 3, dotted line). The heavy solid line in Figure 3 shows the adopted input continuum. The X-ray column density N_{H} was fixed at the observed *ASCA* value of $3.8 \times 10^{21} \text{ cm}^{-2}$ (Fabian et al. 1994a).

3.1. The X-Ray Absorber

Figure 4 shows the ionization fractions of O VII and O VIII as a function of U , using the dereddened continuum for NGC 5548 and assuming solar abundances (Grevesse & Andres 1989). The number of ionizing photons Q is equal to $2.5 h_{50}^2 \times 10^{54} \text{ s}^{-1}$, where h_{50} is the Hubble constant in units of 50 km $\text{s}^{-1} \text{ Mpc}^{-1}$. Note that this value of Q is in fact smaller than that used by Ferland et al. (1992), $Q = 4 h^{-2} \times 10^{54} \text{ s}^{-1}$, which is based on a scaled version of the standard continuum. This is because most of the ionizing photons come from the energy range 1–20 rydbergs, where the standard continuum is brighter (Fig. 3). The observed values are highlighted with heavy lines. Using the constraints on the fractional ionization of O VII and O VIII from the *ASCA* data ($\tau_{\text{O VII}} = 0.29^{+0.04}_{-0.09}$, $\tau_{\text{O VIII}} = 0.38^{+0.22}_{-0.09}$; Fabian et al. 1994a; see § 2.1 above), the allowed

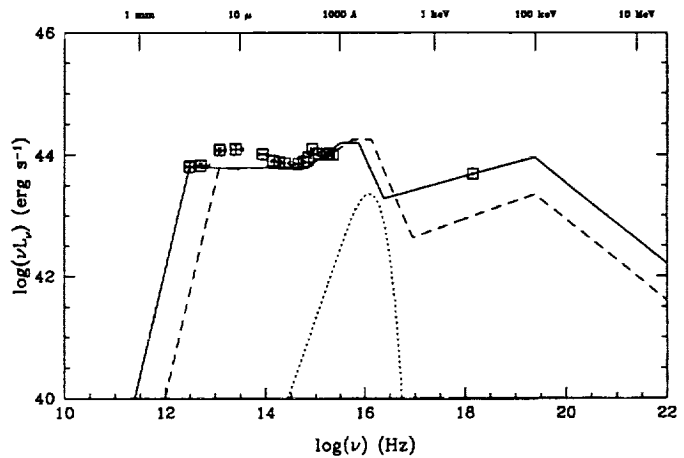


FIG. 3.—Spectral energy distribution of NGC 5548: the data are from Ward et al. (1987), SS, and Nandra et al. (1991). The solid line represents our adopted SED. The dotted line is a 150,000 K blackbody spectrum. The dashed line is a "standard" AGN continuum shown for comparison (see text).

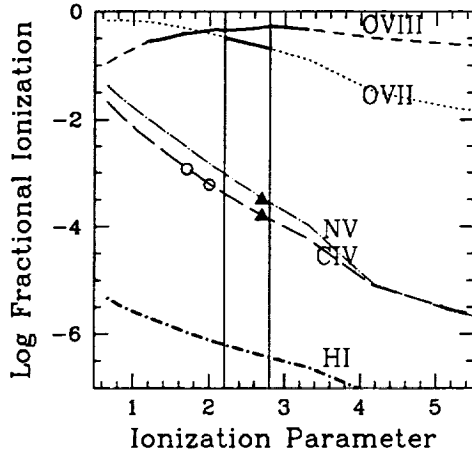


FIG. 4.—Ionization fractions of O VII, O VIII, C IV, N V, and H I as a function of U . The heavy lines mark the observed ranges for O VII and O VIII (ASCA). Triangles HST values for C IV and N V; circles IUE range. The HST range for H I is large (see text), represented by the heavy curve. The vertical lines define the best-fit model parameter: $2.2 < U < 2.8$.

range of the ionization parameter is narrow, $2.2 < U < 2.8$. (Note that this is a linear scale.) If instead the observed continuum is used, i.e., with no reddening correction, the inferred range changes to $1.2 < U < 1.3$ and the dependence of $\log f_{\text{ion}}$ on U remains qualitatively the same. In the rest of the paper we quote all the parameters only for the reddening-corrected SED. The values of the ionization fraction are independent of the gas density, so the density n is not constrained by photoionization models alone (see § 3.4). The value $n = 10^7$ atoms cm^{-3} was used in the input to CLOUDY.

We investigated whether the lack of an Fe K absorption feature observed by ASCA (§ 2.1) is consistent with our model. The ~ 8 keV Fe K absorption edge would most likely be due to an intermediate ionization stage of iron around Fe XX (Nandra et al. 1991), most likely Fe XVII, since it dominates over a wider range of U than other ionization states because it is neon-like and so more stable than other iron ions.

We find that, for the best-fit models for the oxygen edges, the dominant stage of iron is indeed Fe XVII, $\log f_{\text{Fe XVII}} = -0.77$, implying $N_{\text{Fe XVII}} < 2.2 \times 10^{18} \text{ cm}^{-2}$. The ASCA upper limit to an Fe K edge is $\tau < 0.1$ (§ 2.1), so $N_{\text{Fe XVII}} = 3 \times 10^{16} \text{ cm}^{-2}$, assuming solar abundance of iron (4.68×10^{-5} ; Grevesse & Andres 1989). This is consistent with the absence of any Fe K X-ray absorption edges. This absorption system, however, falls short by a factor of ~ 25 of producing the large observed EW of the Fe K emission line even for a uniform spherical shell (model EW ~ 7 eV, observed EW = 180 ± 60 eV), consistent with the conclusion of Nandra et al. (1991).

3.2. Combined X-Ray and Ultraviolet Constraints

We follow the technique developed in Mathur et al. (1994) to look for an absorption system that satisfies both X-ray and UV constraints. The X-ray constraints require $2.2 < U < 2.8$, as discussed above. Thus, if the X-ray and UV absorbers are one and the same (as was found to be the case in 3C 351 and 3C 212) in NGC 5548, then it can be seen from Figure 4 that the ionization fraction of C IV is constrained to be $f_{\text{C IV}} = 2.0^{+0.5}_{-0.4} \times 10^{-4}$ ($\log f_{\text{C IV}} = -3.7^{+0.3}_{-0.3}$).

In the mean HST spectrum, the C IV doublet ratio is 3.8 ± 0.2 ; thus the C IV absorption lines lie off the linear portion of the curve of growth (see, e.g., Spitzer 1978; Wiese et

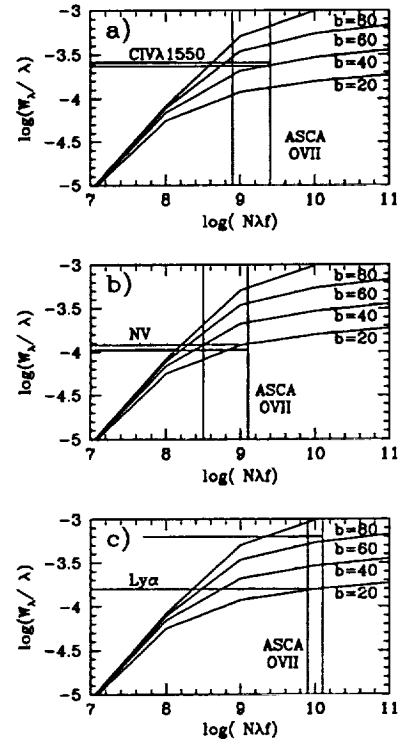


FIG. 5.—Curve of growth for b -values from 20 to 80 km s^{-1} in steps of 20 km s^{-1} . Horizontal lines are for the observed values of absorption lines in the mean HST spectrum. (a) C IV; (b) N V; and (c) Ly α .

al. 1966). In Figures 5a–5c the curves of growth for velocity spread parameters $b = 20, 40, 60$, and 80 km s^{-1} are shown. Figure 5a shows the observed equivalent width for C IV (Table 2) and the constraint on $\log(N\lambda f)$ derived from the X-ray constraint on $f_{\text{C IV}}$ (see above) assuming a solar abundance for carbon (3.63×10^{-4} ; Grevesse & Andres 1989) and oscillator strength $f = 0.285$ (Allen 1973). Similar plots (Figs. 5b and 5c) for N V (at solar abundance, 3.63×10^{-4} ; Grevesse & Andres 1989) and Ly α (using oscillator strengths of 0.235 and 0.4162 for N V and Ly α , respectively; Allen 1973) lead to the allowed b -values given in Table 2. A consistent solution for all three ions is obtained for $b = 40 \text{ km s}^{-1}$, with a small tolerance for both UV and X-ray constraints to be met.

The measured line widths for the C IV doublet are $\sim 350 \text{ km s}^{-1}$ (FWHM), broader than the nominal spectral resolution for this observation and thus possibly resolved. This would imply that the absorber is dispersed in velocity space (see also SS). However, we note that the resolution of the FOS using the 4"3 slit (as in the case) is not well defined. In particular, $\sim 50\%$ of the light is in very broad wings (K. Korista 1995, private communication), and thus we cannot be certain that the line is

TABLE 2
UV AND X-RAY CONSTRAINTS ON b^a

| Ion | $\log(W_\lambda/\lambda)$ (from UV) | $\log(N\lambda f)$ (from X-Ray) | b (km s^{-1}) |
|------------|--|------------------------------------|-------------------------------|
| C IV | -3.61 ± 0.02 | 8.9–9.4 | 40–50 |
| N V | -3.92 ± 0.03 | 8.5–9.1 | 18–40 |
| H I | $-3.8^{+0.3}_{-0.2}$ | 9.9–10.1 | 20–60 |

^a Ranges are $\pm 1\sigma$.

resolved from these data. As discussed in § 2.3, the uncertainty in the Ly α EW is large, leading to a large uncertainty in the H I column density: $13 < \log N_{\text{H I}} < 18$, while the model value ranges from 15.2 to 15.4 (Table 2). An actual H I column density in the higher end of the observed range would imply that the heavy-element abundance in the X-ray/UV absorber is depleted. Conversely, if it is in the lower end of the range, enhanced metal abundance is implied. A Lyman edge absorption would be observed if $N_{\text{H I}}$ is large ($\log N_{\text{H I}} > 16.3$). The recent HUT observations (1995 spring) will be able to detect such a Lyman edge.

The *ASCA* observations were made on 1993 July 28, while the *HST* observations were made between 1993 April and 1993 May. The close agreement of U from the *ASCA* and *HST* data requires that the UV continuum flux be similar in both observations. The optical light curve of NGC 5548 (Korista et al. 1995) shows that the mean continuum level during the *HST* observations [$f_{\lambda}(5100 \text{ \AA}) = 9.14 \times 10^{-15} \text{ ergs s}^{-1} \text{ cm}^{-2} \text{ \AA}^{-1}$] was indeed only 4% below the continuum at the time of the *ASCA* observations ($\sim 9.4 \times 10^{-15} \text{ ergs s}^{-1} \text{ cm}^{-2} \text{ \AA}^{-1}$).

One additional consistency check is possible. In a highly ionized system such as this, magnesium is highly ionized (Mg VI and higher), leaving no magnesium in the Mg II state ($\log f_{\text{Mg II}} < -30$), and thus Mg II absorption should not occur. This is consistent with the observations (§ 2.2).

Thus we have a single consistent model that simultaneously, correctly predicts the fractional ionization of O VII, O VIII, N V, C IV, H I, and Fe XVII and the lack of presence of Mg II and other low-ionization species. We conclude that the UV and X-ray absorbers in NGC 5548 are one and the same.

3.3. Variability

Our photoionization model of the UV absorber in NGC 5548 must explain the observed variability of the C IV absorption line (SS), assuming that their relative measurements are correct (see § 2.3). As can be seen from Figure 5, the absorption line lies slightly off the linear part of the curve of growth. The slope of the curve of growth in that region is about 0.5. Since this is a log-log plot, a factor of 2 change in the column density of the C IV ion would result in a factor of 1.4 change in the EW of the line. In our model, the variations in N_{ion} are caused by variations in the ionization parameter of the absorber (Fig. 4), which is directly proportional to the variations in the ionizing flux. An increase in U results in a decrease in $N_{\text{C IV}}$ (Fig. 4). Our measurements of the *IUE* data show the continuum at 1500 Å varying from 2.0×10^{-14} to $4.7 \times 10^{-14} \text{ ergs cm}^{-2} \text{ s}^{-1} \text{ \AA}^{-1}$, a factor of 2.4, while the C IV absorption-line EW changes from 1.9 ± 0.3 to $1.4 \pm 0.4 \text{ \AA}$, consistent with the model prediction of a factor of 1.5.

During the *HST* observations the maximum continuum variations were only a factor of ~ 1.5 (Fig. 6). There is no obvious variability observed in the C IV absorption line EW. Unfortunately, the errors in the C IV EW are large, owing to the inherent measurement difficulty discussed earlier (§ 2.3). The two solid lines indicate the variability predicted by our model based on the observed continuum variations and both zero time lag and a time lag of 2 days. The data are certainly consistent with the model ($\chi^2 = 6.05$ for 35 degrees of freedom); however, no strong conclusions can be drawn.

3.4. Physical Properties of the Absorber

The X-ray/UV absorber in NGC 5548 shows absorption features due to Ly α , N V, C IV, O VII, O VIII, and Fe XVII. The

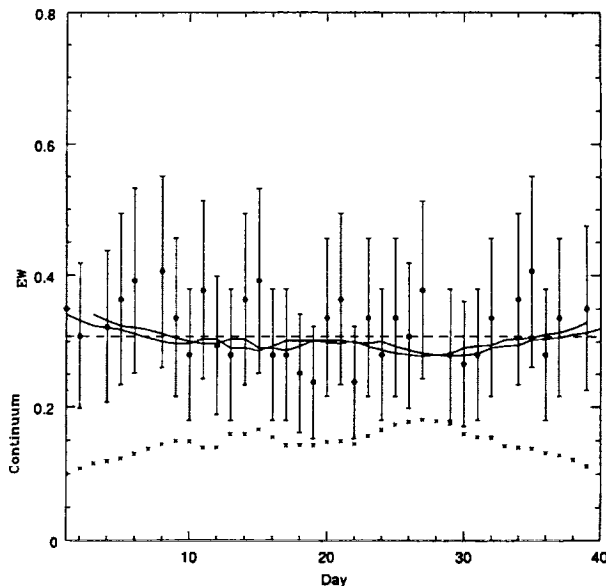


FIG. 6.—Variability in the continuum and C IV absorption-line EW during *HST* observations. The continuum is in arbitrary units. The dashed horizontal line is the mean EW. The two solid lines represent the predicted variability for no time lag and for a time lag of 2 days.

X-ray and UV constraints can now be combined to derive the physical properties of the absorber. It is highly ionized ($2.2 < U < 2.8$) and has a large column density ($N_{\text{H}} = 3.8 \times 10^{21} \text{ cm}^{-2}$). The C IV recombination time must be shorter than the variability response timescale of ≤ 4 days (SS), which sets a lower limit to the density of the absorber; $n \gtrsim 5 \times 10^5 t_4^{-1} \text{ cm}^{-3}$, where t_4 is the lag between the continuum and absorption-line variation in units of 4 days. The thickness of the absorbing slab is then $\Delta r \lesssim 8 \times 10^{15} \text{ cm}$. It is outflowing with a mean velocity of $v_{\text{out}} = 1200 \pm 260 \text{ km s}^{-1}$, as inferred by its blueshift with respect to the systemic velocity of the galaxy (SS) and possibly dispersed in velocity (FWHM $\sim 300 \text{ km s}^{-1}$).

The radial distance of the absorber, $r_{\text{abs}} = (Q/4\pi n_{\text{H}} c)^{1/2}$, is $\lesssim 0.7\text{--}0.8 t_4^{1/2} \text{ pc}$, given the above density constraint. The maximum depth of the C IV absorption line during the *IUE* observations is greater than the continuum level (SS). This implies that the absorber at least partially covers the C IV emitting region, whose size has been accurately determined for NGC 5548 as $7.5 \pm 0.5 \text{ lt-days}$. Combining these two limits gives $8 \text{ lt-days} < r_{\text{abs}} < 0.8 \text{ pc}$, i.e., $2 \times 10^{16} < r_{\text{abs}} < 2 \times 10^{18} \text{ cm}$.

The lower limit on r_{abs} limits the density to $n < 5 \times 10^9 \text{ cm}^{-3}$. The density is thus constrained to be $5 \times 10^5 t_4^{-1} < n < 5 \times 10^9 \text{ cm}^{-3}$. The radial distance and density are not strongly constrained, nor are the model constraints in conflict with those from the variability data.

Associated absorption has been observed in $\sim 10\%$ of Seyfert 1 galaxies (Ulrich 1988), which implies a $\sim 10\%$ covering factor of the absorber in all Seyfert 1 galaxies. If we assume that this covering factor, $f_{0.1}$, applies to NGC 5548, then the mass of the absorber is $M_{\text{abs}} \sim 20 f_{0.1} M_{\odot}$. The mass outflow rate can be calculated, by assuming uniform density: $\dot{M}_{\text{out}} = M_{\text{abs}} v_{\text{out}} \Delta r^{-1} f_{0.1} = 10 f_{0.1} M_{\odot} \text{ yr}^{-1}$. This is an upper limit in that the absorber is much thinner than its radius from the

TABLE 3
PHYSICAL CONDITIONS OF X-RAY/UV ABSORBER

| Parameter | Constraint | Derived from: |
|---|--|---|
| Neutral hydrogen column density N_H | $N_H \sim 3.8 \times 10^{21} \text{ cm}^{-2}$ | X-ray (Fabian et al. 1994a) |
| Ionization parameter U | $2.2 < U < 2.8$ | $\tau(\text{O VII}, \text{O VIII})$, X-ray (Fabian et al. 1994a; Nandra et al. 1993) |
| Radial distance r_{abs} | $2 \times 10^{16} \text{ cm} < r_{\text{abs}} < 2 \times 10^{18} \text{ cm}$ | LL: BELR covered (Peterson et al. 1992); UL: n , U |
| Density n | $5 \times 10^5 \text{ cm}^{-3} \lesssim n < 5 \times 10^9 \text{ cm}^{-3}$ | LL: recombination time < 4 days (SS); UL: r_{abs} , U |
| Outflow velocity v | $1200 \pm 260 \text{ km s}^{-1}$ | Line redshift (SS) |
| Thickness Δr | $\lesssim 8 \times 10^{15} \text{ cm}$ | N_H , n |
| Mass..... | $\sim 20 f_{0.1} M_\odot$ | n , r_{abs} , Δr (covering factor $f_{0.1} = 0.1$) |

center, so that the time-averaged \dot{M}_{out} is likely to be much smaller. The same rate is a lower limit in that we measure only the velocity component in our line of sight (see § 4.4). This mass outflow rate is quite a bit larger than the accretion rate of $0.08 M_\odot \text{ yr}^{-1}$ needed to power the $L_{\text{bol}} = 5 \times 10^{44} \text{ ergs s}^{-1}$ continuum source at 10% efficiency. The outflow would carry a kinetic luminosity of $\dot{M}_{\text{out}}^2 v_{\text{out}}^2 / 2 = \sim 10^{43} \text{ ergs s}^{-1}$ about 50 times lower than the radiative luminosity of NGC 5548. A summary of the properties of the absorber is given in Table 3.

4. DISCUSSION

4.1. Comparison with Previous Models

The combination of X-ray and improved UV constraints from *HST* have led to derived conditions very different from those reported earlier by SS based on the *IUE* data alone. SS necessarily assumed C IV to be the dominant state of ionization ($f_{\text{C IV}} = 0.1$), leading to $U \sim 10^{-3}$. Combining this with the lack of Mg II absorption led to $N_H < 10^{20.5} \text{ cm}^{-2}$. However, in our model these parameters are constrained: $2.2 < U < 2.6$, $-3.4 < f_{\text{C IV}} < -3.9$. We are thus led to conclude that the absorber is highly ionized and has a large column density ($N_H = 3.8 \times 10^{21} \text{ cm}^{-2}$; Fabian et al. 1994a).

4.2. Generalizing X-Ray/Ultraviolet Absorbing Outflows

The physical properties of the long-known UV absorber in NGC 5548 are now well constrained with the identification of an X-ray/UV absorber. We can therefore generalize our unification of X-ray and UV absorbing outflows for lobe-dominated radio-loud quasars to include radio-quiet Seyfert galaxies, and most likely to include all associated absorbers in AGNs.

A strong correlation has been observed between the radio properties and associated absorption-line properties of AGNs: all broad absorption line quasars (BALQSOs) are radio-quiet (Stoche et al. 1992), and all Mg II associated absorption-line quasars are lobe-dominated and radio-loud (Aldcroft, Elvis, & Bechtold 1995). Associated C IV absorbers are a mixture of lobe- and core-dominated radio-loud quasars, and radio-quiet quasars. It is of interest to note that even though NGC 5548 is radio-quiet, it is unusual in that its radio luminosity is dominated by the extended radio flux, which has a larger physical size than in any other radio-quiet Seyfert galaxy (Wilson & Ulvestad 1982). In this respect it is similar to a lobe-dominated quasar, providing a link between lobe-dominated, radio-loud AGNs with associated absorption and radio-quiet AGNs, perhaps also the BALQSOs. It further suggests that AGNs with X-ray/UV absorbers are edge-on. To have an inclination indicator in radio-quiet AGNs would be most valuable, and this possibility should be studied further.

4.3. Comments on Variability in NGC 3227 and MCG -6-30-15

Variable X-ray spectra and the existence of ionized absorbers have been observed with *ASCA* in two more AGNs: NGC 3227 (Ptak et al. 1994) and MCG -6-30-15 (Fabian et al. 1994b). In both cases the variations in the properties of the ionized absorbers were deduced to be incompatible with the variations seen in the continuum.

In NGC 3227 (Ptak et al. 1994) rapid flux variations were observed with a timescale of $\sim 10^4$ s. An O VI absorption edge was detected with opacity $\tau \sim 0.75$. The model fits to the spectra in high- and low-flux states showed that (1) for the same value of photon index Γ in both high and low states, N_H and U decrease when the luminosity increases; (2) for different values of Γ , the same N_H and U can be fitted in both high and low states. Both of these models seem unphysical, and hence the authors suggested that a warm absorber model may be too simple.

This however, may not be the case, since it does not allow for delays due to the recombination time of the absorber. The best-fit τ in NGC 3227 is remarkably similar in both high and low states, implying that the ionization structure of the absorber has not changed even though the luminosity has changed. This implies a recombination time of O VI $> 10^4$ s. For O VI the recombination time is $T = 4.3 \times 10^4 n_6^{-1} \text{ s}$ (Shull & Van Steenberg 1982), where n_6 is the density in the units of 10^6 cm^{-3} . This implies a density of the warm absorber, $n < 10^6 \text{ cm}^{-3}$. With the model value of U is of order 0.05, this places the absorber at $r = 10^{19} \text{ cm}$, well outside the BELR (which would have a radius of $7 \times 10^{15} \text{ cm}$, assuming an $L^{1/2}$ scaling from NGC 5548).

It should be noted that the physical parameter which responds to continuum variations is τ rather than U . Indeed, if τ remains the same while the luminosity increases, the fitted value of U , which assumes the system is in equilibrium, would necessarily decrease.

A similar apparent discrepancy was observed in MCG -6-30-15 (Fabian et al. 1994b) which has an O VII absorption edge. In this case τ decreased significantly over 23 days. The luminosity also decreased over this period, while the fitted value of the ionization parameter increased. Whether the change in τ correlates or anticorrelates with the change in luminosity depends upon U (see Fig. 4). The recombination time of O VII is $\sim 0.28 n_6^{-1} \text{ days}$ (Shull & Van Steenberg 1982). The data imply that $t \leq 23$ days and so $n \geq 10^4 \text{ cm}^{-3}$, a very reasonable constraint.

We argue that the warm absorber models in NGC 3227 and MCG -6-30-15 are not unphysical and that the data do not require more complex models. The information provided by the variability not only helps us understand this fact but also

provides an important constraint on the density of the absorber.

The low value of U for NGC 3227 (cf. $U = 2.6$ for NGC 5548) implies a wide range of ionization states from object to object for the associated absorbers in radio-quiet AGNs as in radio-loud.

4.4. Implications for the Nature of the Outflowing Material

Now that we understand the physical properties of the absorber, we can begin to ask astrophysical questions.

The lack of differential time delays between the red and blue wings of the broad-line profiles shows that the BELR motions are not primarily radial (Korista et al. 1995). Yet the absorbing material outside the BELR shows large outflows, both in NGC 5548 and in the other UV absorbers (Ulrich 1988). How is the orbital or random motion at BELR radii converted to an organized flow? What is the driving force? The continuum radiation pressure acting on the partially ionized gas (Mathur et al. 1994; Turner et al. 1994) may play an important role. In a more specific scenario, Glenn, Schmidt, & Foltz (1994) and Aldcroft et al. (1995) have independently suggested that in BALQSOs and radio-loud quasars, respectively, we are looking almost edge-on at material blown off a dusty disk (which itself may be the BELR) by radiation pressure. Since there is some evidence that NGC 5548 too is edge-on, the same picture may apply there.

Material escaping vertically from an edge-on disk would then follow a path that is not purely radial, since it is accelerated by the continuum radiation pressure. If the material originates at only a restricted range of radii in the disk, this could explain a number of otherwise puzzling features. In particular, the limited thickness of the absorber in NGC 5548 cannot be understood in any continuous radial wind model. The X-ray column density directly rules out significant additional accelerated or decelerated material, unless it is fully stripped through iron (Nandra et al. 1991). Only by making the wind intermittent, or by allowing for a velocity component in the plane of the sky (so moving the rest of the flow out of our line of sight), can we keep the thickness small.

Another consistency check is to confirm that the persistence of the absorber is consistent with the large observed outflow velocity ($1200 \pm 200 \text{ km s}^{-1}$). In the 3 years separating the *ROSAT* and *ASCA* observations, no significant change in the O VII/O VIII opacity was detected. (*ROSAT* $\tau = 0.35 \pm 0.13$ [Nandra et al. 1993]; *ASCA* $\tau = 0.38^{+0.08}_{-0.09}$ [Fabian et al. 1994a]). A formal 3σ upper limit for a change in τ is 0.27 (i.e., $\sim 80\%$). The distance traveled by the absorber in 3 yr is $1.2 \times 10^{16} \text{ cm}$. In order to limit a change in U to less than 80%, this must represent less than a 34% change in distance from the ionizing continuum (assuming a constant-density system). This leads to $r_{\text{abs}} \geq 3.5 \times 10^{16} \text{ cm}$, slightly larger than the minimum distance determined from the size of the BELR ($2 \times 10^{16} \text{ cm}$; § 3.4) and so consistent with our earlier derived parameters for the absorber.

The first *IUE* observations, some 15 years ago, also showed a C IV absorber at a similar velocity and depth (§ 2.2). These observations provide more constraints. The outflow cannot be intermittent if it has persisted for 15 yr. Assuming a constant mean velocity for the absorber leads to a present minimum distance $r_{\text{abs}} > 5 \times 10^{16} \text{ cm}$, and a corresponding maximum density $n < 8 \times 10^8 \text{ cm}^{-3}$. These are both consistent with the derived absorber parameters (§ 3.4). However, if the apparent width of the absorption line in the *HST* data is real ($\sim 300 \text{ km s}^{-1}$) and represents the internal velocity dispersion of the gas

over the past 15 yr, then it will have led to a thickening by $\sim 10^{16} \text{ cm}$ over 15 yr, comparable to our estimate of the present absorber thickness (less than $8 \times 10^{15} \text{ cm}$; § 3.4). In this case the absorber would have had zero depth when *IUE* first observed it, which is unlikely, since otherwise it has not changed significantly. This difficulty disappears if we are looking through a flow with a component in the plane of the sky, since then we are seeing a steady state flow crossing our path. This dynamical picture, derived from observations, is similar to the model of broad absorption line quasars (BALQSOs) by Murray et al. (1995).

Testing the model further in NGC 5548 could be achieved by measuring the recombination time, and hence the absorber density. This implies a small sampling interval (less than 1 day) accompanied by continuum changes by at least a factor of 2. Monitoring the ionization parameter at a given continuum flux over a number of years to search for density changes would also test the model. High spectral resolution observations (e.g., with the *HST* Goddard High-Resolution Spectrograph) could examine the velocity structure of the absorber, and perhaps measure b -values of any components. Tests for the edge-on nature of AGNs with X-ray/UV absorbers also need to be pursued.

5. CONCLUSIONS

In this paper we have shown that the X-ray and UV absorption in NGC 5548 can be explained quantitatively by having the same material produce the absorption features due to O VII, O VIII (in X-rays), C IV, N V, and H I (in the UV), and not produce observable features due to Fe XVII and Mg II and other low-ionization lines. This simple model passes further tests by not violating the size and density limits imposed by the reverberation mapping data. We conclude that the X-ray and the UV absorption do indeed arise from the same material.

Combining the improved X-ray and UV constraints from *ASCA* and *HST*, together with the reverberation mapping variability constraints, leads us to understand the physical properties of the absorber. The absorber is highly ionized ($2.2 < U < 2.8$), has high column density ($N_{\text{H}} = 3.8 \times 10^{21} \text{ cm}^{-2}$), low density ($5 \times 10^5 \text{ cm}^{-3} < n < 5 \times 10^9 \text{ cm}^{-3}$), and is situated outside the C IV emitting region ($2 \times 10^{16} < r_{\text{abs}} < 2 \times 10^{18} \text{ cm}$). The gas is outflowing with a mean velocity of $1200 \pm 200 \text{ km s}^{-1}$ and has a corresponding kinetic luminosity of $\sim 10^{43} \text{ ergs s}^{-1}$.

We can now generalize our unification of UV and X-ray absorbing outflows from the lobe-dominated radio-loud quasars to include radio-quiet Seyfert galaxies. This may also provide a link to the radio-quiet BALQSOs. This analogy suggests that the X-ray/UV absorbers in radio-quiet AGNs may be viewed close to edge-on, which would be a valuable known parameter if it can be independently supported. Now that we understand the physical properties of the absorber, we can begin to ask astrophysical questions about the dynamics of the outflow and its role in the circumnuclear region of AGNs. A scenario in which the absorbing material comes off a disk and is accelerated by the radiation pressure of the continuum source may explain the persistence of the absorber in spite of its large velocity and thin shell-like geometry.

We thank Brad Peterson and Kirk Korista for valuable discussions and for early access to the *HST* spectra. We also thank Jonathan McDowell for his TIGER software. This work was supported in part by NASA grant NAGW5-2201 (LTSA), and NASA contracts NAS8-39073 (ASC), NAS5-30934 (RSDC).

REFERENCES

- Aldcroft, T., Elvis, M., & Bechtold, J. 1995, MNRAS, submitted
- Allen, C. W. 1973, *Astrophysical Quantities* (London: Athlone)
- Branduardi-Raymont, G. 1986, in *The Physics of Accretion onto Compact Objects*, ed. K. O. Mason, M. G. Watson, & N. E. White (Berlin: Springer), 407
- . 1989, in *Active Galactic Nuclei*, ed. D. E. Osterbrock & J. S. Miller (Dordrecht: Kluwer), 177
- Clavel, J., et al. 1991, *ApJ*, 366, 64
- . 1992, *ApJ*, 393, 113
- Elvis, M., et al. 1994, *ApJS*, 95, 1
- Fabian, A., Nandra, K., Brandt, W., Hayashida, K., Makino, F., & Yamauchi, M. 1994a, in *New Horizons in X-Ray Astronomy*, ed. F. Makino & T. Ohashi (Tokyo: Universal Academy Press), 573
- Fabian, A., et al. 1994b, *PASJ*, 46, L59
- Ferland, G. F. 1991, "HAZY": OSU Astronomy Dept. Internal Rep.
- Ferland, G. F., Peterson, B., Horne, K., Welsh, W. F., & Nahar, S. N. 1992, *ApJ*, 387, 95
- Glenn, J., Schmidt, G., & Foltz, C. 1994, *ApJ*, 434, L47
- Grevesse, N., & Andres, E. 1989, in *AIP Conf. Proc. 183, Cosmic Abundances of Matter*, ed. C. J. Waddington (New York: AIP)
- Korista, K., et al. 1995, *ApJS*, 97, 285
- Mathews, W. G., & Ferland, G. J. 1987, *ApJ*, 323, 456
- Mathur, S. 1994, *ApJ*, 431, L75
- Mathur, S., Wilkes, B., Elvis, M., & Fiore, F. 1994, *ApJ*, 434, 493
- Murray, N., Chiang, J., Grossman, S. A., & Voit, G. M. 1995, *ApJ*, in press
- Nandra, K., et al. 1991, MNRAS, 248, 760
- . 1993, MNRAS, 260, 504
- Peterson, B. M., et al. 1992, *ApJ*, 392, 470
- Ptak, A., Yaqoob, T., Serlemitsos, P. J., Mushotzky, R., & Otani, C. 1994, *ApJ*, 436, 31
- Shull, M. J., & Sachs, E. R. 1993, *ApJ*, 416, 536 (SS)
- Shull, M. J., & Van Steenberg, M. E. 1982, *ApJS*, 48, 95
- Spitzer, L. 1978, *Physical Processes in the Interstellar Medium* (New York: Wiley-Interscience), 46
- Stoeck, J. T., Morris, S. L., Weymann, R. J., & Foltz, C. B. 1992, *ApJ*, 396, 487
- Turner, T. J., Nandra, K., George, I. M., Fabian, A., & Pounds, K. A. 1994, *ApJ*, 419, 127
- Ulrich, M. H. 1988, MNRAS, 230, 121
- Ulrich, M. H., & Boisson, C. 1983, *ApJ*, 267, 515
- Ward, M., Elvis, M., Fabbiano, G., Carleton, N. P., Willner, S. P., & Lawrence, A. 1987, *ApJ*, 315, 74
- Wiese, W. L., Smith, M. W., & Glennon, B. M. 1966, *Atomic Transition Probabilities* (Washington, DC: GPO)
- Wilson, A., & Ulvestad, J. 1982, *ApJ*, 263, 576
- Wu, C., Boggess, A., & Gull, T. 1981, *ApJ*, 247, 449

STRONG X-RAY ABSORPTION IN A BROAD ABSORPTION LINE QUASAR: PHL 5200

SMITA MATHUR¹ AND MARTIN ELVIS

Harvard-Smithsonian Center for Astrophysics, 60 Garden Street, Cambridge, MA 02138

AND

K. P. SINGH²

Laboratory for High Energy Astrophysics, Code 668, NASA/GSFC, Greenbelt, MD 20771

Received 1995 September 5; accepted 1995 September 26

ABSTRACT

We present *ASCA* observations of the $z = 1.98$ prototype broad absorption line quasar (BALQSO): PHL 5200. The source was detected in both SIS and GIS. A power-law spectrum ($\alpha_E = 0.6^{+0.9}_{-0.6}$) with large intrinsic absorption ($N_H = 1.3^{+2.3}_{-1.1} \times 10^{23} \text{ cm}^{-2}$) best describes the spectrum. Excess column density over the local Galactic value is required at the 99% confidence level. This detection suggests that, although BALQSOs are X-ray-quiet, it is strong absorption in the BAL region that makes them appear faint to low-energy X-ray experiments. The required intrinsic absorbing column density is 2–3 orders of magnitude larger than earlier estimates of column densities in BALQSOs. This implies that the BAL systems are much more highly ionized than was previously thought.

Subject headings: quasars: absorption lines — quasars: individual (PHL 5200) — X-rays: galaxies

1. INTRODUCTION

Associated absorption is common in the optical and ultraviolet spectra of quasars (Ulrich 1988). A subset of these have very broad absorption line profiles extending up to $\Delta v = 0.1c$ – $0.2c$ redward with respect to the quasar rest frame (see, e.g., Turnshek 1988). These broad absorption line quasars (BALQSOs) show absorption features due to high-ionization lines of C^{+3} , Si^{+3} , and other ions. Low-ionization BALQSOs have also been observed which show Mg^{+1} and/or Al^{+2} absorption troughs. BALQSOs have been estimated to have column densities $N_H \sim 10^{20}$ – 10^{21} cm^{-2} (Turnshek 1984; Hamann, Korista, & Morris 1993). As a class, BALQSOs share some common properties: they are always radio-quiet (Stocke et al. 1992), may have abundances 10–100 times solar (in their emission lines; Turnshek 1988, Hamann & Ferland 1993), and are X-ray-quiet (Green et al. 1995). Recent work suggests that BALQSOs are normal radio-quiet quasars seen from an unusual direction (Weymann et al. 1991; Hamann et al. 1993). In this case all radio-quiet quasars have collimated BAL outflows, which, however, are pointed out of our line of sight in some 90% of cases. Thus BALQSOs, far from being exotic objects, give us a special probe into the gasdynamics around the typical quasar.

However, physical conditions in the absorbing gas in the BALQSOs are poorly determined from optical/UV absorption-line studies (Lanzetta et al. 1991). This is because only a few, usually saturated, lines are measured, yielding lower limits to column densities for a few ions but little information on the ionization state. If, as in the narrow-line-associated absorbers, there is X-ray absorption as well as optical and UV, then the combined X-ray and UV analysis would allow us to derive the physical conditions in BALQSO absorption systems (Mathur et al. 1994; Mathur 1994; Mathur, Elvis, & Wilkes 1995). This, however, has been difficult, since BALQSOs are elusive X-ray

sources and so are otherwise essentially unconstrained in their X-ray properties. In a soft X-ray study of quasars with *Einstein*, only four out of nine BALQSOs were detected (Zamorani et al. 1981). Initial results from *ROSAT* are mainly upper limits (Kopko, Turnshek, & Espey 1993; Green et al. 1995), implying that they are relatively faint in soft X-rays (i.e., have steep α_{ox}). Our understanding of BALQSOs is incomplete without a knowledge of their X-ray properties. In fact, lack of knowledge of the underlying ionizing continuum is one of the major uncertainties in the models of BALQSOs: Are they intrinsically X-ray-quiet (i.e., large α_{ox})? Or is it strong absorption that makes them look faint?

PHL 5200, a prototype BALQSO at $z = 1.98$ (Burbidge 1968), was detected in hard X-rays by the *EXOSAT* medium-energy (ME) experiment but not by the low-energy (LE) experiment (Singh, Westergaard, & Schnopper 1987). To obtain consistency between the *EXOSAT* ME and LE requires a column density of $\geq 10^{22} \text{ atoms cm}^{-2}$, making it an excellent candidate for examining the BAL region. We observed PHL 5200 with *ASCA* with this aim in mind. *Einstein* did not detect (Zamorani et al. 1981) and *ROSAT* has not observed PHL 5200.

2. ASCA OBSERVATIONS AND DATA ANALYSIS

ASCA (Tanaka et al. 1994) observed PHL 5200 on 1994 June 21 for a net exposure time of 17.7 ks (Table 1). *ASCA* has two solid-state imaging spectrometers (SIS0 and SIS1; Loewenstein & Isobe 1992) and two gas imaging spectrometers (GIS3 and GIS4; Ohashi et al. 1991). The SISs were operated in 2 CCD mode (see Fig. 1). The source was faint but was clearly detected in SIS0 and GIS3 (Fig. 1). The X-ray position from SIS0 is (J2000) $22^h28^m26^s$, $-5^{\circ}18'54''$, 1.1' from the optical position (Schneider et al. 1992), consistent with the current satellite pointing uncertainties (Tanaka et al. 1994). The source was off-axis in SIS1 (where it lay close to the gap between two chips) and GIS2 and was not detected in either. This is consistent with the fact that the optical axes of

¹ smita@cfa.harvard.edu.

² NRC Senior Research Associate, on leave from Tata Institute of Fundamental Research, Bombay, India.

TABLE 1
ASCA OBSERVATIONS OF PHL 5200

| Instrument | Total Counts | Exposure (s) | Net Count Rate (s^{-1}) |
|------------|--------------|--------------|-----------------------------|
| SIS0 | 513 | 16,587 | 0.01 ± 0.001 |
| GIS3 | 505 | 16,788 | 0.006 ± 0.001 |

telescopes containing SIS0 and GIS3 are much closer to each other than the others. No other sources were seen in any of the instruments to a level similar to the count rates of PHL 5200.

Data were extracted in a standard way using the *FTOOLS* and *XSELECT* software.³ Standard screening criteria were used as recommended in the *ASCA* ABC guide: a greater than 10° bright Earth angle, and a cutoff rigidity greater than 6 GeV/c. Hot and flickering pixels were removed from the SIS data using *XSELECT*. All SIS events of grade 0, 2, 3, and 4 were accepted. Data of both faint and bright modes with high, medium, and low telemetry rates were combined. These data can be combined without any calibration compromises. The *ASCA* X-ray telescope has a broad point-spread function, and jittering of the spacecraft can appear on arcminute scales. To take this into account, source counts were extracted from a circular region of $6'$ radius for GIS3 and from a $4'$ radius for SIS0. The source was pointed at the center of chip 1 of SIS0, putting the bulk of its photons into just one chip. Detectors SIS0 and GIS3 yielded ~ 500 total counts each. Data from these detectors cannot be combined, since the detectors have different properties. The background was estimated using the same spatial filter on the deep field background images (*ASCA* ABC guide). A background-subtracted count rate of $(1.04 \pm 0.15) \times 10^{-2}$ was observed by SIS0, and $(6.26 \pm 1.47) \times 10^{-3}$ by GIS3. The data were grouped to contain at least 10 counts (background-subtracted) per pulse-height analysis (PHA) channel to allow the use of the Gaussian statistic. The data have modest signal-to-noise ratio; however, it can be clearly seen that there are essentially no counts below ~ 1 keV (~ 3 keV in the rest frame) (see Fig. 2). The highest rest energy

³ *FTOOLS* is a collection of utility programs to create, examine, or modify data files in FITS format. *XSELECT* is a command-line interface to the *FTOOLS*, for X-ray astrophysical analysis. The software is distributed by the *ASCA* Guest Observer Facility.

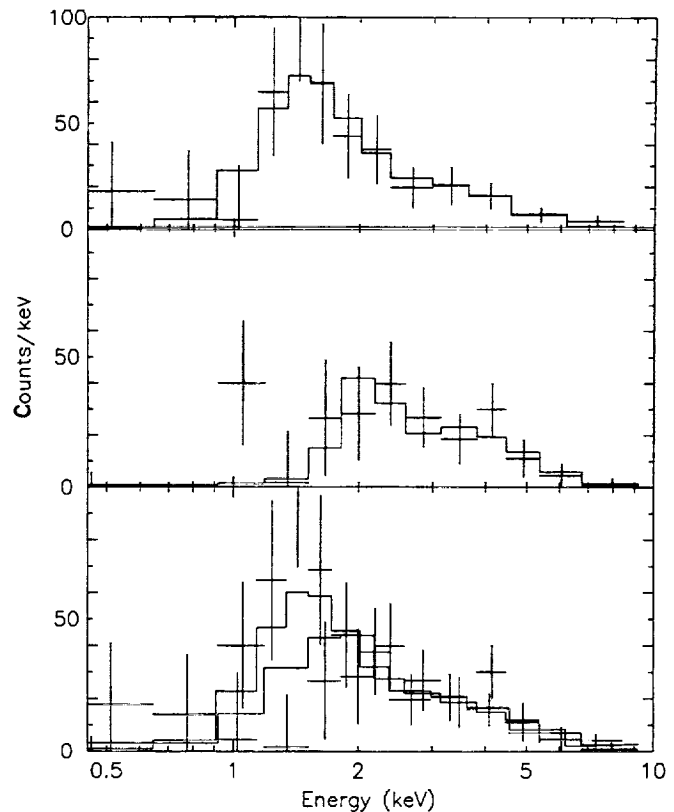


FIG. 2.—*ASCA* spectral data (crosses) with best-fit power law with fixed Galactic and intrinsic absorption models. Top: SIS; middle: GIS; bottom: both SIS and GIS.

detected for PHL 5200 is 12 keV at 3σ for 0.5 keV wide bins. Figure 2 shows the SIS and GIS spectra of PHL 5200.

The SIS and GIS spectra extracted in this way were then analyzed using *XSPEC*. The 1995 March release of the response matrices was used for the GIS data, and the 1994 November release for the SIS data. A power-law spectrum with fixed Galactic absorption (4.8×10^{20} atoms cm^{-2} ; Stark

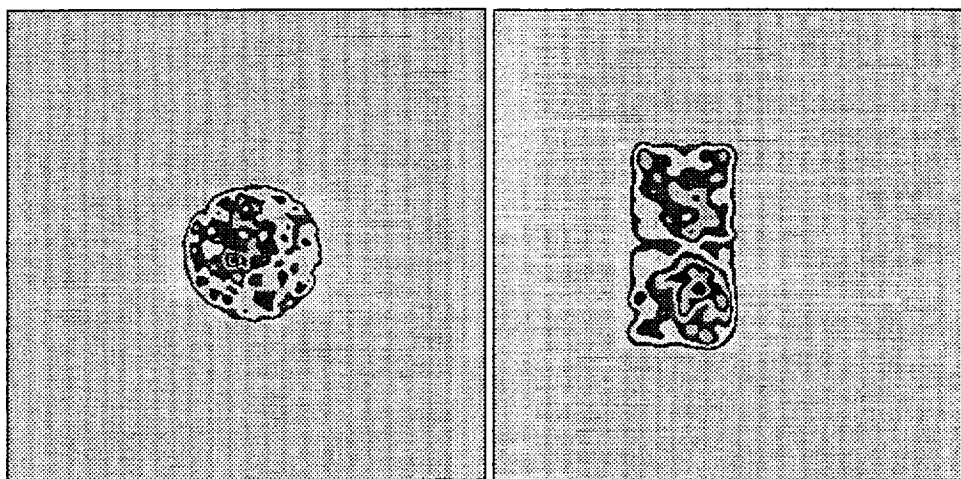


FIG. 1.—*ASCA* GIS3 (left) and SIS0 (right) gray-scale images around PHL 5200. North is 66.7° clockwise from the top. The GIS field of view is $50'$ in diameter, and each SIS chip is $11.1'$ on a side (*ASCA* Technical Description 1993).

TABLE 2
SPECTRAL FITS TO *ASCA* DATA OF PHL 5200

| Model | α_E | N_H (free) ^a | Normalization ^b | $\chi^2(\text{dof})^c$ |
|-------------------------------------|----------------------|------------------------------|----------------------------|------------------------|
| SIS | | | | |
| Power law: | | | | |
| + N_H | $0.9^{+1.3}_{-1.0}$ | $0.9^{+1.2}_{-0.8}$ | $1.3^{+4.8}_{-0.3}$ | 5.2 (12) |
| + $N_H(\text{Galactic})$ fixed..... | $-0.1^{+0.4}_{-0.4}$ | ... | $0.3^{+0.1}_{-0.2}$ | 8.4 (13) |
| + $N_H(z = 1.98)$ | $0.8^{+1.1}_{-0.9}$ | $14.0^{+19.7}_{-12.4}$ | $1.2^{+3.4}_{-0.4}$ | 4.8 (12) |
| GIS | | | | |
| Power law: | | | | |
| + N_H | $2.0^{+3.1}_{-1.8}$ | $4.5^{+0.0}_{-3.8}$ | $9.6^{+8.5}_{-0.5}$ | 5.4 (9) |
| + $N_H(\text{Galactic})$ fixed..... | $-0.1^{+0.5}_{-0.6}$ | ... | $0.3^{+0.2}_{-0.1}$ | 9.8 (10) |
| + $N_H(z = 1.98)$ | $2.8^{+6.2}_{-2.6}$ | 130^{+0}_{-118} | $47^{+170}_{-0.5}$ | 5.7 (9) |
| SIS + GIS | | | | |
| Power law: | | | | |
| + N_H | $0.6^{+0.0}_{-0.7}$ | $0.9^{+1.4}_{-0.7}$ | $1.0^{+2.9}_{-0.4}$ | 14.1 (24) |
| + $N_H(\text{Galactic})$ fixed..... | $-0.1^{+0.3}_{-0.3}$ | ... | $0.3^{+0.1}_{-0.2}$ | 18.4 (25) |
| + $N_H(z = 1.98)$ | $0.6^{+0.9}_{-0.6}$ | $13.1^{+23.2}_{-11.1}$ | $0.9^{+3.0}_{-0.4}$ | 14.2 (24) |

^a Times 10^{22} cm^{-2} .

^b In units of $10^{-4} \text{ photons keV}^{-1} \text{ cm}^{-2} \text{ s}^{-1}$ at 1 keV.

^c Degrees of freedom in parentheses.

et al. 1992) provides an acceptable fit to the SIS0 data (Table 2). However, if absorption is allowed to be a free parameter, then the fit is improved with greater than 98% confidence (*F*-test; Table 2). The fitted value [$N_H(z = 0) = 9 \times 10^{21} \text{ atoms cm}^{-2}$; solar abundance] is much larger than the Galactic column density toward PHL 5200, indicating excess absorption along the line of sight. This is also much larger than the uncertainties in the SIS low-energy response, which may overestimate the column density by up to $2 \times 10^{20} \text{ cm}^{-2}$ (C. S. R. Day, Calibration Uncertainties [1995], *ASCA* GOF WWW page [URL: http://heasarc.gsfc.nasa.gov/docs/asca/cal_probs.html]). We then fitted a power-law spectrum with Galactic column and an additional column of absorber allowing its redshift to be free. We found no preferred redshift for the additional absorber. Fixing the absorber at the source gives a column density of $1.4^{+2.0}_{-1.2} \times 10^{23} \text{ cm}^{-2}$ (90% confidence for one parameter; solar abundance). The power-law energy index is $\alpha_E = 0.8^{+1.1}_{-0.9}$.

For the GIS data, a similar fit of a power-law spectrum with fixed Galactic and additional $z = 1.98$ absorption is acceptable but does not constrain the parameters well because the data have large errors (Table 2).

A combined SIS and GIS analysis does constrain the parameters of the model slightly better (Fig. 3; Table 2). The column density at the source is $1.3^{+2.3}_{-1.1} \times 10^{23} \text{ cm}^{-2}$, and $\alpha_E = 0.6^{+0.9}_{-0.6}$. This excess absorption, above Galactic N_H , is required at 99% confidence (*F*-test).

The 2–10 keV (observed frame) flux is $2.9^{+1.39}_{-1.3} \times 10^{-13} \text{ ergs s}^{-1} \text{ cm}^{-2}$ (corrected for best-fit absorption), and a 2–10 keV (rest frame) luminosity is $9.3 \times 10^{45} \text{ ergs s}^{-1}$ ($H_0 = 50, q_0 = 0$). The flux in the *EXOSAT* ME band (2–6 keV observed) is $2^{+6}_{-1} \times 10^{-13} \text{ ergs s}^{-1} \text{ cm}^{-2}$. This is smaller than the *EXOSAT* flux ($\sim 2 \times 10^{-12} \text{ ergs s}^{-1} \text{ cm}^{-2}$; Singh et al. 1987) by at least a factor of 2.5. The optical continuum of PHL 5200 does not

vary by such a large amount (Barbieri, Romano, & Zambon 1978). It is possible that it is variable absorption rather than intrinsic source variability that might be responsible for the difference in the *ASCA* and *EXOSAT* ME fluxes. The *ASCA* flux is consistent with the upper limits observed by the *Einstein* IPC (less than $4.5 \times 10^{-13} \text{ ergs s}^{-1} \text{ cm}^{-2}$) and the *EXOSAT* CMA (less than $5 \times 10^{-13} \text{ ergs s}^{-1} \text{ cm}^{-2}$).

The *ASCA*-derived monochromatic luminosity at 2 keV

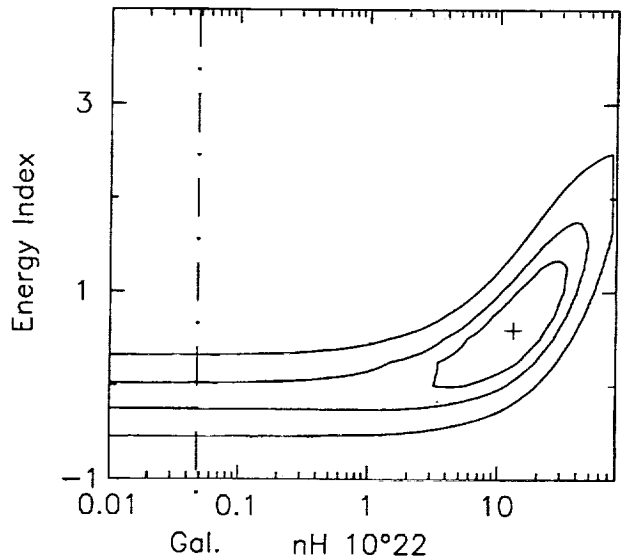


FIG. 3.—Confidence contours for the combined SIS and GIS spectrum. Contours of 68%, 90%, and 99% confidence regions are shown. The Galactic column density is shown as a dot-dashed line.

(rest frame) is 1.3×10^{28} ergs s⁻¹ Hz⁻¹, and at 2500 Å (rest frame) it is 1.2×10^{32} ergs s⁻¹ Hz⁻¹ (Zamorani et al. 1981), giving $\alpha_{\text{ox}} = 1.5$.

An Fe K absorption edge is not detected ($\tau < 0.9$; 90% confidence for one interesting parameter). The opacity of an Fe edge corresponding to $N_{\text{H}} = 10^{23}$ cm⁻² is $\tau = 0.1 f_{\text{ion}}$, where f_{ion} is the ionization fraction of iron in hydrogen-like state. Our data are not sensitive enough to detect such an edge.

The Fe K emission line (Ross & Fabian 1993) is also not detected (see Fig. 2). We place a 0.5 keV upper limit (90% confidence for one interesting parameter) to the rest-frame equivalent width of a narrow ($\sigma < 10$ eV) line between 2.1 and 2.4 keV (6.3–7.1 keV rest frame). This can be used to place an upper limit on the covering factor of the absorber. If the absorber is a uniform spherical shell surrounding the X-ray continuum source, then the Fe K α line flux through recombination after photoionization of helium-like iron is given by $I_{\text{line}} = [N_{\text{H}} A(\text{Fe}) / 10^{19.8}] (\Omega / 4\pi) I_{\text{abs}} \eta$ (Basko 1980), where η is the fluorescent yield, the efficiency with which the flux above 7.1 keV (I_{abs}) is reemitted as an Fe K line. Assuming solar abundance of iron [$A(\text{Fe}) = 3.3 \times 10^{-5}$; Grevesse & Andres 1989] and $\eta = 0.5$ (Krolik & Kallman, 1987), we estimate the covering factor of the line emitting region, $\Omega / 4\pi < 4 f_{\text{ion}}^{-1}$, which is not an interesting limit. If, however, the heavy-element abundance is 10 times solar (Hamann & Ferland 1993), then $\Omega / 4\pi < 0.4 f_{\text{ion}}^{-1}$, consistent with Hamann et al. (1993).

3. DISCUSSION

The *ASCA* spectrum of PHL 5200 shows excess absorption at 99% confidence. A column density of $(0.2\text{--}4) \times 10^{23}$ (Z_⊙/Z) cm⁻² is obtained if the absorber is at the source. A power law was a good fit to the data with the spectral slope ($\alpha_E = 0.6^{+0.9}_{-0.6}$) in the normal range (Wilkes et al. 1994). The PHL 5200 value of $\alpha_{\text{ox}} = 1.5$ is also normal for a radio-quiet quasar (Wilkes et al. 1994).

The inferred absorbing column density for PHL 5200 is 2–3 orders of magnitude larger than the earlier estimates of column density in BALQSOs (Hamann et al. 1993; Turnshek 1984). This implies that the BAL clouds may be more highly ionized ($N_{\text{H}}/N_{\text{H}} \sim 10^{-8}$) than previously thought ($N_{\text{H}}/N_{\text{H}} \sim 10^{-5}$; Hamann et al. 1993), as was true with narrow associated absorbers (Mathur et al. 1994, 1995). The estimates from

the saturated UV lines appear to have been misleading. Recent models of BALQSOs (Murray et al. 1995), however, do consider column densities as large as we find in PHL 5200. If, on the other hand, the abundances are 100–1000 times solar, then the hydrogen column density would be smaller ($N_{\text{H}} \sim 10^{20}$ cm⁻²). However, the ionization state would still be high, since the comparison is between metal line absorption in the UV and absorption in X-rays. The column density in PHL 5200 is also about an order of magnitude larger than other, narrow, associated absorption systems (Fiore et al. 1993; Turner et al. 1994). In this respect, as in velocity width, the BALQSOs may be extreme examples of other associated absorbers.

This is consistent with our earlier conjecture that all associated absorbers may form a continuum of properties with column density, outflow velocity, and the distance from the central continuum (Mathur et al. 1994). Are BALQSOs also similar to these in being “XUV absorbers,” i.e., are the broad absorption lines observed in the UV caused by the same matter producing X-ray absorption? This can be investigated by combined analysis of X-ray and UV spectra (Mathur et al. 1994, 1995) of PHL 5200 but is beyond the scope of this paper. If they are indeed the same, it would allow us to further constrain the physical properties of the absorber and so of the outflowing circumnuclear matter (Mathur et al. 1995).

The present study implies that BALQSOs are not intrinsically X-ray quiet; it is the extreme absorption that makes them appear faint to low-energy experiments. Since the absorption is significant only in soft X-rays, hard X-ray observations, above a few keV, would reveal their presence as X-ray sources. This can be done with missions like *ASCA*, *XTE*, *SAX*, and *AXAF*. We have been awarded *XTE* time to observe BALQSOs with this aim.

This research has made use of the NASA/IPAC Extragalactic Database (NED), which is operated by the Jet Propulsion Laboratory, Caltech, under contract with the National Aeronautics and Space Administration. This work was supported by NASA grants NAGW-2201 (LTSA), NAG5-2563 (*ASCA*), NAGW-4490 (LTSA), and NASA contract NAS8-39073 (*ASC*).

REFERENCES

- Barbieri, C., Romano, G., & Zambon, M. 1978, *A&AS*, 31, 401
 Basko, M. M. 1980, *A&A*, 87, 330
 Burbidge, E. M. 1968, *ApJ*, 152, 111
 Fiore, F., Elvis, M., Mathur, S., & Wilkes, B. 1993, *ApJ*, 415, 129
 Green, P. J., et al. 1995, *ApJ*, 450, 51
 Grevesse, N., & Andres, E. 1989, in *AIP Conf. Proc.* 183, *Cosmic Abundances of Matter*, ed. C. J. Waddington (New York: AIP), 1
 Hamann, F., & Ferland, G. 1993, *ApJ*, 418, 11
 Hamann, F., Korista, K., & Morris, S. L. 1993, *ApJ*, 415, 541
 Kopko, M., Turnshek, D. A., & Espey, B. 1993, in *IAU Symp.* 159, *Quasars across the Electromagnetic Spectrum* ed. T. J.-L. Courvoisier & A. Blench (Dordrecht: Kluwer), 450
 Krolik, J. H., & Kallman, T. R. 1987, *ApJ*, 320, L5
 Lanzetta, K. M., Wolfe, A. M., Turnshek, D. A., Lu, L., McMahon, R. G., & Hazard, C. 1991, *ApJS*, 77, 1
 Loewenstein, T., & Isobe, T. 1992, translation of *ASCA Interim Rep.*, ISAS
 Mathur, S. 1994, *ApJ*, 431, L75
 Mathur, S., Elvis, M., & Wilkes, B. 1995, *ApJ*, 452, 230
 Mathur, S., Wilkes, B., Elvis, M., & Fiore, F. 1994, *ApJ*, 434, 493
 Murray, N., Chiang, J., Grossman, S. A., & Voit, G. M. 1995, *ApJ*, 451, 498
 Ohashi, T., et al. 1991, *Proc. SPIE*, 1549, 9
 Ross, R. R., & Fabian, A. C. 1989, *MNRAS*, 261, 74
 Schneider, D. P., et al. 1992, *PASP*, 104, 678
 Singh, K. P., Westergaard, N. J., & Schnopper, H. W. 1987, *A&A*, 172, L11
 Stark, A. A., Gammie, C. F., Wilson, R. W., Bally, J., Linke, R., Heiles, C., & Hurwitz, M. 1992, *ApJS*, 79, 77
 Stocke, J. T., Morris, S. L., Weymann, R. J., & Foltz, C. B. 1992, *ApJ*, 396, 487
 Tanaka, Y., Holt, S. S., & Inoue, H. 1994, *PASJ*, 46, L37
 Turner, T. J., Nandra, K., George, I. M., Fabian, A., & Pounds, K. A. 1994, *ApJ*, 419, 127
 Turnshek, D. A. 1984, *ApJ*, 280, 51
 ———, 1988, in *OSO Absorption Lines: Probing the Universe*, ed. J. C. Blades, D. Turnshek, & C. Norman (Cambridge: Cambridge Univ. Press), 17
 Ulrich, M. H. 1988, *MNRAS*, 230, 121
 Weymann, R., Morris, S. L., Foltz, C. B., & Hewett, P. C. 1991, *ApJ*, 373, 23
 Wilkes, B. J., Tananbaum, H., Worrall, D. M., Avni, Y., Oey, M. S., & Flanagan, J. 1994, *ApJS*, 92, 53
 Zamorani, G., et al. 1981, *ApJ*, 245, 357

X-RAY CONTINUUM AND IRON K EMISSION LINE FROM THE RADIO GALAXY 3C 390.3

M. INDA,¹ K. MAKISHIMA,¹ Y. KOHMURA,¹ M. TASHIRO,¹ T. OHASHI,² P. BARR,³ K. HAYASHIDA,⁴
 G. G. C. PALUMBO,⁵ G. TRINCHIERI,⁶ M. ELVIS,⁷ AND G. FABBIANO⁷

Received 1993 February 8; accepted 1993 July 8

ABSTRACT

X-ray properties of the radio galaxy 3C 390.3 were investigated using the *EXOSAT* and *Ginga* satellites. Long-term, large-amplitude X-ray intensity changes were detected over a period extending from 1984 through 1991, and high-quality X-ray spectra were obtained especially with *Ginga*. The X-ray continuum spectra were described with power-law model with photon slope in the range 1.5–1.8, and the slope flattened as the 2–20 keV luminosity decreased by 40%. There was a first detection of the iron emission line from this source at the 90% confidence level. An upper limit was derived on the thermal X-ray component. X-ray emission mechanisms and possible origins of the long-term variation are discussed.

Subject headings: galaxies: individual (3C 390.3) — galaxies: active — X-rays: galaxies

1. INTRODUCTION

Radio galaxies occupy an important position as a possible parent population for quasars (QSOs) and BL Lac objects (Brown & Murphy 1987; Barthel 1989). In fact, certain models (called “Unified Scheme”; see Orr & Brown 1982) claim that a group of radio galaxies that are seen nearly end-on to their radio jets should become a highly relativistically beamed luminous class of active galactic nuclei (AGNs). In order to test the Unified Scheme, it is important to better understand the X-ray characteristics of radio galaxies and compare them with those of other types of AGN, because X-ray emission is thought to be directly related to the emission mechanism of the central engine of the AGN.

3C 390.3 is a broad-line radio galaxy at $z = 0.057$. In the radio, it is classified as F-R II (lobes with leading edge hot spots; Fanaroff & Riley 1974), and has a prominent double-lobed morphology, together with a compact nucleus which shows evidence of superluminal motion (Alef et al. 1988). The optical spectrum, which classifies it as an N galaxy (Burbidge & Burbidge 1971; Penston & Penston 1973), shows broad H α and H β lines whose double-peaked structure provides evidence for an accretion disk (Perez et al. 1988). Since its first X-ray detection by *Uhuru* (Giacconi & Gursky 1974; Forman et al. 1978), 3C 390.3 has also been known to have an X-ray luminosity as large as $L_x \sim 10^{44}$ ergs s⁻¹. The galaxy has been subsequently monitored in X-rays by several satellites, up to the most recent observations with *EXOSAT* (Shafer, Ward, & Barr 1985, hereafter SWB85), and the new results from *Ginga* that we are presenting here. The *HEAO 1* data indicate X-ray

spectra of power-law form with photon index $\Gamma = 1.65 (+0.50, -0.25)$ in 2–50 keV (error is 90% confidence level) and $\Gamma = 1.40 \pm 0.37$ in 12–165 keV (error is 1 σ uncertainty) (Rothschild et al. 1983; Mushotzky 1984), which are typical of an AGN, and has a 2–10 keV luminosity of $L_x = 10^{43.8}$ ergs s⁻¹. A continuous decline of 3C 390.3 has been observed over a period of ~ 15 yr up to ~ 1984 , in the optical blue continuum (from 14.8 to 16.6 mag; Barr et al. 1980; Lloyd 1984; SWB85), in the optical broad-line components (Oke 1986), in ultraviolet lines (Clavel & Wamsteker 1987), and in X-rays (SWB85).

Here we report on the X-ray observations of 3C 390.3 made with the *EXOSAT* and *Ginga* satellites, and present high-quality X-ray spectra obtained with *Ginga*. In § 2 and § 3 we describe our observations and results respectively, followed by the discussion in § 4.

2. OBSERVATIONS

2.1. EXOSAT Observations

A total of six *EXOSAT* observations of 3C 390.3 were performed between 1984 and 1986. Data from the first two observations have already been reported (SWB85); processed data from all six observations are publicly available in the *EXOSAT* data base. However, for a weak source like 3C 390.3, where the hard X-ray data are background-noise dominated, it is often possible to obtain significantly better reduced data than available in the archive by interactive reanalysis of the raw data. Therefore, we have systematically reanalyzed all data from the Medium Energy proportional counter array (ME; Turner, Smith, & Zimmerman 1981) to obtain a uniform sample of X-ray spectra.

Observations were performed on 1984 day 153, day 259; 1985 day 33, day 311; and 1986 day 76, day 77. Both observations in 1984 were affected by solar activity; on day 153, 63 minutes of data were not used due to background variations, while on day 259 the ME data were completely unusable due to solar flaring. We therefore exclude 1984 day 259 data from the present analysis. The useful data on 1985 day 33 were truncated by 3 hours due to spacecraft pointing problems. Only 54 minutes of useful data were obtained on 1985 day 311 due to background variations.

The ME was usually operated with one-half of the detector array pointed at the source and the other offset at a blank

¹ Department of Physics, University of Tokyo, 7-3-1 Hongo, Bunkyo-ku, Tokyo, Japan 113.

² Department of Physics, Tokyo Metropolitan University, 1-1 Minami-Osawa, Hachioji, Tokyo, Japan 192-03.

³ *EXOSAT* Observatory, Astrophysics Divisions, Space Science Department, ESTEC, NL-2200 AG Noordwijk, The Netherlands.

⁴ Department of Earth and Space Science, Osaka University, 1-1 Machikaneyama, Toyonaka, Osaka, Japan 560.

⁵ Dipartimento di Astronomia, Università di Bologna, Via Zamboni 33, 40126 Bologna, Italy.

⁶ Osservatorio Astrofisico di Arcetri, Largo Enrico Fermi 5, 50125 Firenze, Italy.

⁷ Harvard-Smithsonian Center for Astrophysics, 60 Garden Street, Cambridge, MA 02138.

region of the sky, to measure the detector background, the two halves being exchanged at mid-observation. However, for the 1984 day 153 and 1985 day 311 observations, significantly better background subtraction was obtained using data from the slews onto and off the target.

2.2. *Ginga* Observations

We observed 3C 390.3 with the *Ginga* LAC (Large area Proportional Counter; Turner et al. 1989) in the pointing mode on two occasions; 1988 November 12 (=day 316) 2:02–22:53 UT and November 13 (=day 317) 0:14–17:14 UT, and 1991 February 14 (=day 45) 9:10–23:08 UT. We accumulated $\sim 3 \times 10^4$ s and 1.5×10^4 s of net on-source exposure, for the 1988 and 1990 observations, respectively. The background data were obtained on 1988 November 11 at $(\alpha^{1950}, \delta^{1950}) = (18^h30^m8, 81^\circ28'8)$, $1^\circ9$ off 3C 390.3, and on 1991 February 13 at $(16^h23^m1, 76^\circ15'6)$, $8^\circ0$ off. We performed no scanning observations which are sometimes done to obtain estimates of contamination from nearby sources, since, upon examination of the *Einstein* Extended Medium Sensitivity Survey (Gioia et al. 1991), we expect negligible contribution from other sources in the same field of view. During these observations events from each of the LAC detectors were pulse-height analyzed and accumulated on board into 48 spectral channels covering an

energy range of 1–36 keV, with time resolution of either 4 or 16 s (MPC-1 mode).

Significant source flux was detected in both observations. The background-subtracted and aspect-corrected 2–20 keV signal counting rate was ~ 24 counts s^{-1} and ~ 13 counts s^{-1} in the first and second observation, respectively. Note that a 1 mCrab flux corresponds to ~ 10 counts s^{-1} (2–20 keV) in the *Ginga* LAC. These values are subject to a statistical error of ~ 0.05 counts s^{-1} for a 1 day long observation, and a systematic source confusion noise of 1.4 counts s^{-1} (both 2–20 keV, at the 90% confidence; Hayashida et al. 1989). Figure 1 shows the background-subtracted light curve, binned at 128 s. The LAC counting rates remained constant within $\sim 5\%$ within each day of observation, but the average X-ray intensity decreased from 26 counts s^{-1} to 23 counts s^{-1} by 3 ± 1 counts s^{-1} between the 2 days in 1988. This decrease is significant compared with the statistical errors, as well as the background and aspect uncertainties.

Toward the end of the second *Ginga* observation, namely at 22:29 UT on 1991 February 14, a prominent flare event was detected. During the flare, which lasted for ~ 30 minutes until the end of the observation, the LAC counting rate increased by a factor of 10 (Fig. 1c). We describe this event in detail in § 3.3, where we argue that the flare is due to a dMe star in the same field of view and that “quiescent” emission from the flare

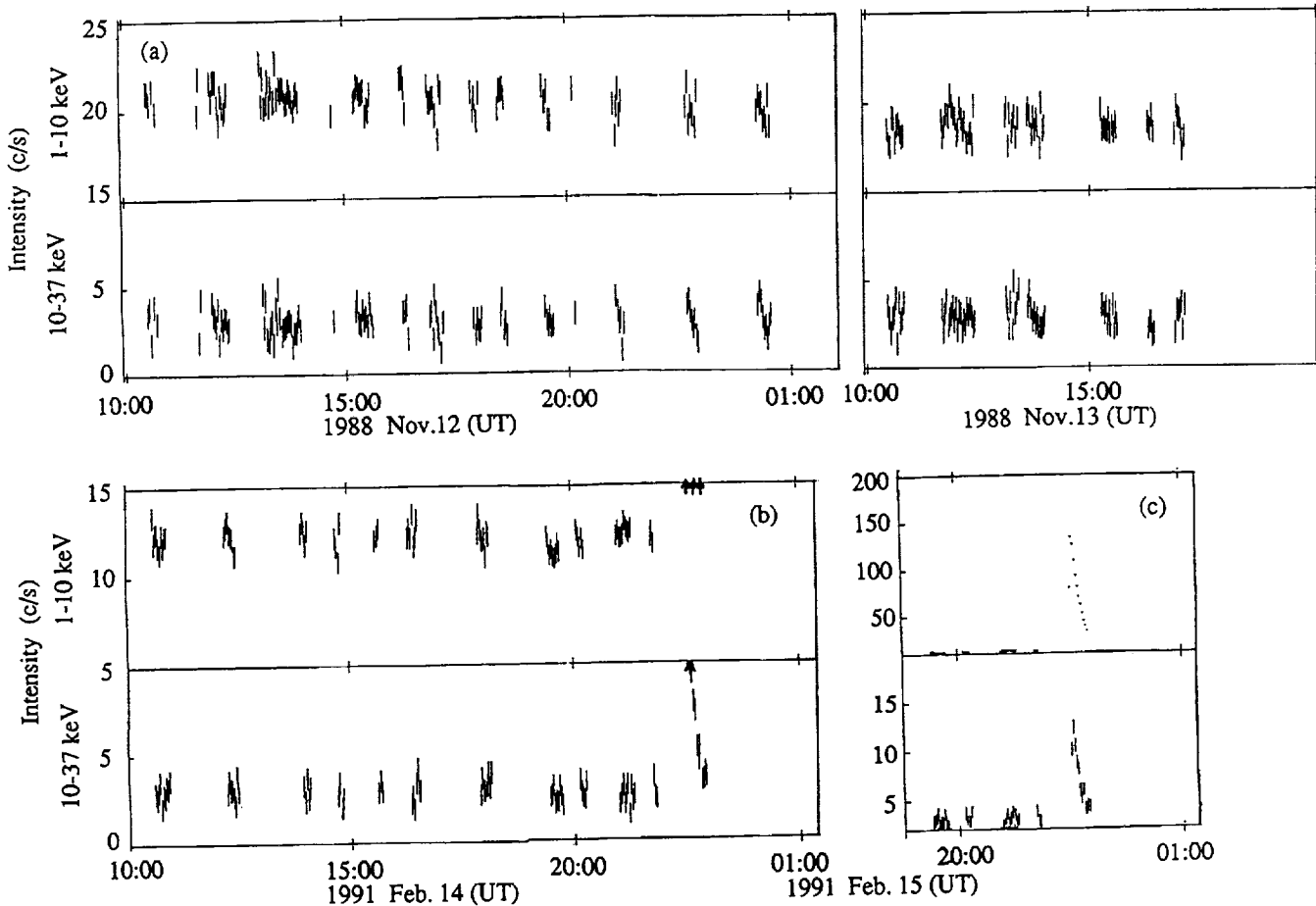


FIG. 1.—The two-color X-ray light curves of 3C 390.3 obtained by *Ginga*. (a) 1988 November observation. (b) 1991 February observation; as discussed in the text, a large flare-like event occurred at about 22:29 UT on February 14. The flare position is replotted in (c) with compressed flux scales.

TABLE 1
X-RAY FLUXES AND LUMINOSITIES OF 3C 390.3 OBSERVED WITH EXOSAT AND Ginga^a

| SATELLITE | YEAR/DAY | Γ^b | 2–6 keV FLUX ^c | LUMINOSITY ^d | |
|--------------|----------|-----------------|---------------------------|-------------------------|-----------------|
| | | | | 2–6 keV | 2–20 keV |
| EXOSAT | 1984/153 | (1.7) | 0.28 ± 0.03 | 0.10 ± 0.01 | 0.25 ± 0.03 |
| EXOSAT | 1985/033 | (1.7) | 1.75 ± 0.05 | 0.61 ± 0.02 | 1.56 ± 0.04 |
| EXOSAT | 1985/311 | (1.7) | 1.44 ± 0.07 | 0.50 ± 0.02 | 1.28 ± 0.06 |
| EXOSAT | 1986/076 | (1.7) | 1.26 ± 0.03 | 0.44 ± 0.01 | 1.12 ± 0.03 |
| EXOSAT | 1986/077 | (1.7) | 1.27 ± 0.04 | 0.44 ± 0.01 | 1.13 ± 0.03 |
| Ginga | 1988/316 | 1.79 ± 0.02 | 3.11 ± 0.08 | 1.09 ± 0.03 | 2.60 ± 0.06 |
| Ginga | 1988/317 | 1.76 ± 0.02 | 2.84 ± 0.08 | 0.99 ± 0.03 | 2.43 ± 0.07 |
| Ginga | 1991/045 | 1.54 ± 0.02 | 1.62 ± 0.05 | 0.57 ± 0.02 | 1.62 ± 0.05 |

^a All the errors are 90% confidence limits.

^b Photon index of the power-law spectrum. It was fixed at 1.7 for the EXOSAT data.

^c Calculated using the power-law fits and expressed in units of 10^{-11} ergs cm^{-2} s^{-1} .

^d In units of 10^{44} h^{-2} ergs s^{-1} .

source is negligible. Therefore, the analysis of the *Ginga* data will not cover the flare period.

3. RESULTS

3.1. X-Ray Intensity

The X-ray fluxes observed with EXOSAT and *Ginga* are shown in Table 1, together with the luminosities calculated for a distance of $D = 171 h^{-1}$ Mpc (for $H_0 = 100h$ km s^{-1} Mpc $^{-1}$). Here 2–6 keV fluxes of the EXOSAT observations were calculated from the observed 2–10 keV ME spectrum, in which the photon index Γ was fixed at 1.7. Leaving Γ to vary freely resulted in consistent flux values within errors (see § 3.2). The photoelectric absorption was assumed to be negligible, because for all the EXOSAT spectrum it is consistent with zero (see § 3.2) and did not affect the calculation in the 2–6 keV flux.

In Figure 2, we compare these 2–6 keV intensity measure-

ments with previous X-ray observations of 3C 390.3. The figure clearly reveals a large amplitude (more than an order of magnitude even excluding the single Copernicus point which is rather uncertain) X-ray variation on a time scale of $10 \sim 20$ yr; following the long-term decline over 1973–1984 (Barr et al. 1980; SWM85), the X-ray intensity has been increasing in the years 1984–1989. The X-ray flux also exhibits a factor ~ 3 random variability on somewhat shorter time scales (a few years). It is thus not obvious whether the flux decrease from 1988 to 1991 signals the start of another long-term source decline, or just a short-term fluctuation.

3.2. EXOSAT Spectra

A series of trial power-law spectra were folded through the detector response and fitted to the ME data at each epoch. Results are given in Table 2. The photoelectric absorption is included as a free parameter in the fits to the EXOSAT data. In all cases it is consistent with zero. For the 1984 day 153 observations, SWB85 reported a flat X-ray power law with little or no absorption. In our reanalysis, the derived *best-fit* spectrum is steep. However, the uncertainty in the spectral index is quite large. In fact, there is no evidence that the spectral index measured by EXOSAT is variable. The hypothesis of constant spectral index yields a reduced χ^2 of 0.84 for four d.o.f. The (weighted) mean 2–10 keV spectral index measured by EXOSAT is 1.66, typical of hard X-ray power laws for AGNs (Turner & Pounds 1989).

Addition of a Gaussian emission feature near 6.4 keV yields no significant decrease in χ^2 ; however, the upper limits to the strength of any iron line are uninteresting, 3σ limits to the equivalent width in all observations being in excess of 600 eV.

3.3. Ginga Spectra

3.3.1. Continuum Characteristics

The two *Ginga* observations yielded high-quality X-ray spectra in the 2–36 keV range, as shown in Figure 3. The data have been background subtracted (using the standard method by Hayashida et al. 1989) and aspect corrected, but the detector response has not been removed. The 1991 spectrum (Fig. 3b) excludes the period of the flare event (§ 2.2).

We fitted the spectra with power-law and thermal bremsstrahlung models with three free parameters; normalization factor, photon index Γ or temperature kT , and absorption by cold matter of cosmic abundance with a column density N_H .

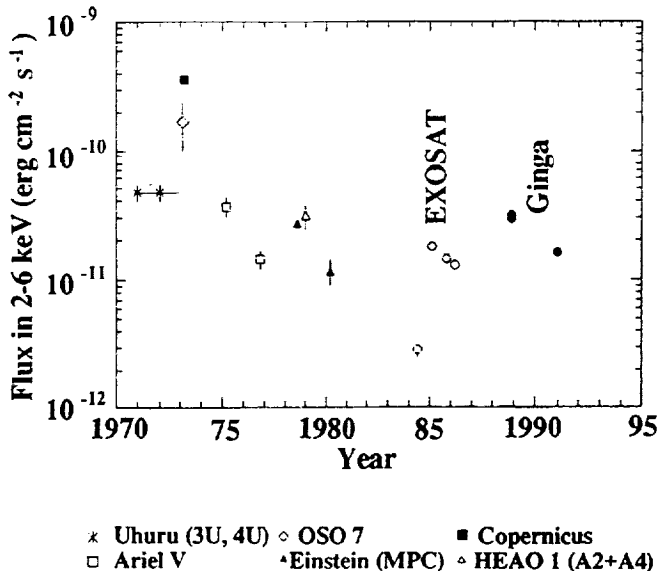


FIG. 2.—The long-term 2–6 keV X-ray light curve of 3C 390.3. Previous X-ray observations refer to; 3U catalog, Giacconi & Gursky (1974) (recalculated for position); 4U catalog, Forman et al. (1978); OSO 7, Mushotzky et al. (1977); Copernicus, Charles et al. (1975); Ariel 5, Barr et al. (1980); HEAO 1, Marshall et al. (1978), Rothschild et al. (1983), and Wood et al. (1984); Einstein, Halpern (1982). The OSO 7 flux was calculated assuming a power-law model with photon index $\Gamma = 1.7$.

TABLE 2
RESULTS OF MODEL FITS TO THE 3C 390.3 SPECTRA^a

| Year/Day | Model | N_0^b | Γ^c or kT^d | $E_c(1+z)^e$ | EW ^f | $\chi^2/\text{d.o.f.}^g$ |
|-------------------|------------------|-------------------|----------------------|-----------------|-----------------|--------------------------|
| 1984/153 | Power law | $2.9(+3.3, -1.4)$ | 2.5 ± 0.7 | ... | ... | 27/18 |
| 1985/033 | Power law | 5.1 ± 1.5 | 1.75 ± 0.2 | ... | ... | 37/35 |
| 1985/311 | Power law | 5.7 ± 1.2 | 1.7 ± 0.2 | ... | ... | 26/32 |
| 1986/076 | Power law | 4.4 ± 0.1 | 1.6 ± 0.1 | ... | ... | 27/32 |
| 1986/077 | Power law | 4.3 ± 0.5 | 1.57 ± 0.08 | ... | ... | 21/36 |
| 1988 ^b | Power law | 12.9 ± 0.27 | 1.77 ± 0.01 | ... | ... | 40.1/37 |
| | Thin-thermal | 17.3 ± 0.17 | 14.2 ± 0.4 | ... | ... | 333/37 |
| | Power law + line | 12.9 ± 0.28 | 1.77 ± 0.01 | 6.60 ± 0.35 | 70 ± 36 | 30.9/35 |
| 1991/045 | Power-law | 5.13 ± 0.16 | 1.54 ± 0.02 | ... | ... | 45.0/35 |
| | Thin thermal | 9.28 ± 0.09 | 27.2 ± 2.0 | ... | ... | 55.7/35 |
| | Power law + line | 5.13 ± 0.16 | 1.54 ± 0.02 | 6.49 ± 0.37 | 96 ± 56 | 36.2/35 |

^a Errors represent single-parameter 90% confidence levels.

^b Normalization (10^{-3} counts $\text{s}^{-1} \text{keV}^{-1} \text{cm}^{-2}$).

^c Photon index.

^d Thermal bremsstrahlung temperature (keV).

^e Line center energy (keV) with redshift correction assuming $z = 0.057$.

^f Line equivalent width (eV).

^g Degree of Freedom.

^b The 2 day long *Ginga* data were combined together.

Results of the fitting in Table 2 show that the power-law model is clearly more favored than the thermal model for the 1988 data, although in the 1991 data the distinction between the two models is less clear and even the power-law fit gives somewhat large chi-squared. As shown in Figure 4a, we obtained only upper limits to N_H which are consistent with the line-of-sight

absorbing column within our galaxy, in this direction of the sky ($3 \times 10^{20} \text{ cm}^{-2}$; Heiles & Habing 1974).

One intriguing result is the detection of a significant change, by ~ 0.23 , in the photon index Γ between the two *Ginga* observations (see Table 2). As shown by the contour map of Figure 4a, this spectral difference is statistically significant. The differ-

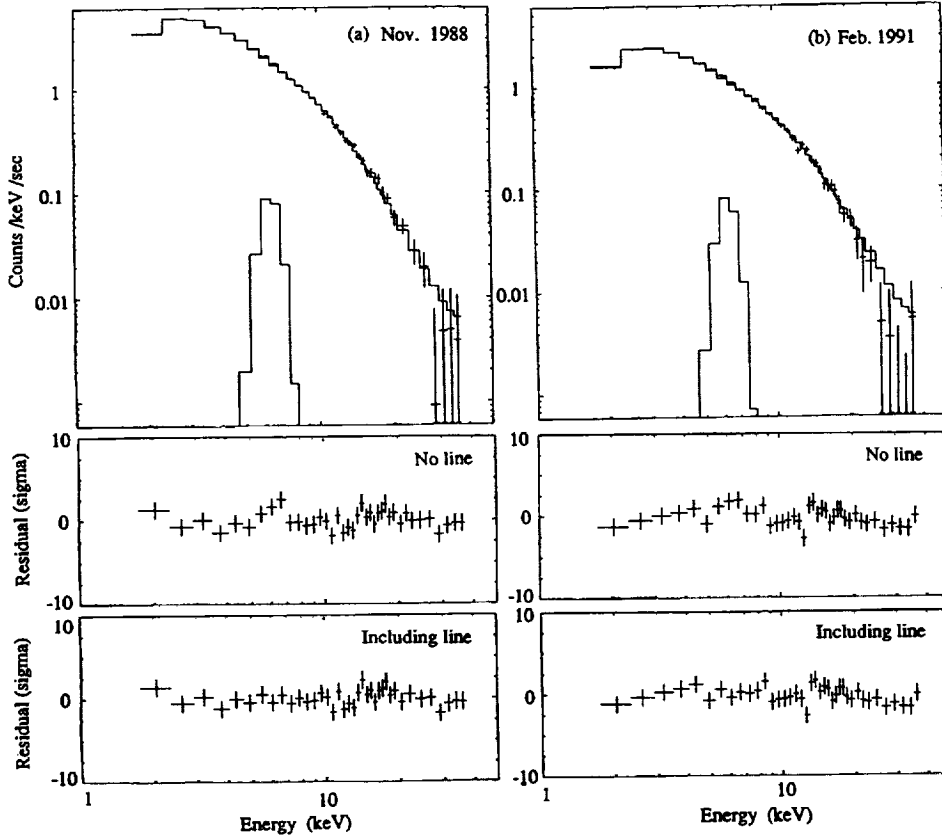


FIG. 3.—X-ray spectra of 3C 390.3 obtained in the first (a) (total $23.5 \text{ counts s}^{-1}$) and the second (b) (total $13.4 \text{ counts s}^{-1}$) *Ginga* observations. Top panels display X-ray pulse-height spectra (cross) without removing instrumental response, in comparison with the best-fitting power-law plus iron emission line models (solid line). Middle panels are residuals from the single power-law fits, while bottom panels show those from the power-law plus iron emission line models. The best-fit model parameters are summarized in Table 2.

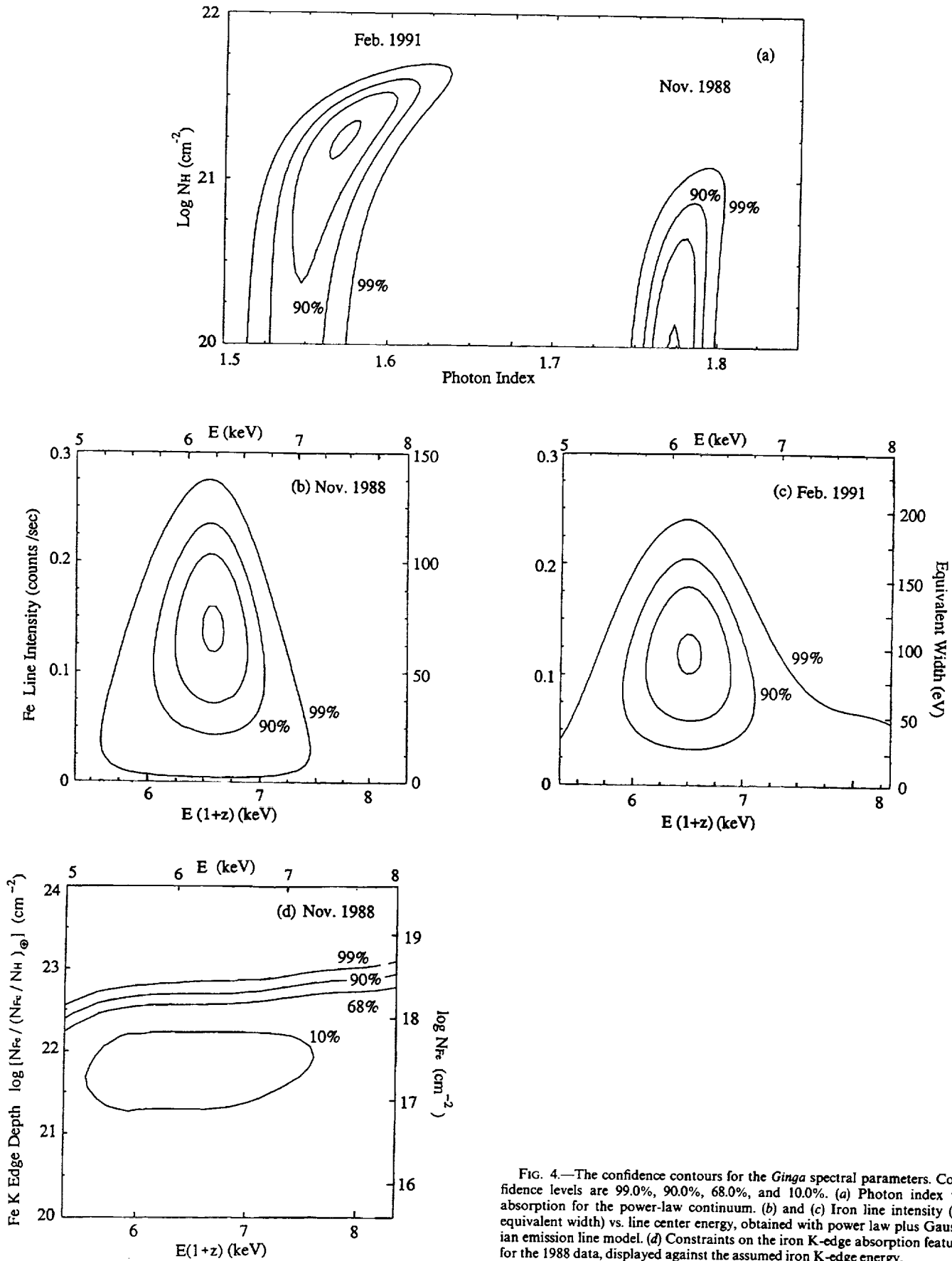


FIG. 4.—The confidence contours for the *Ginga* spectral parameters. Confidence levels are 99.0%, 90.0%, 68.0%, and 10.0%. (a) Photon index vs. absorption for the power-law continuum. (b) and (c) Iron line intensity (or equivalent width) vs. line center energy, obtained with power law plus Gaussian emission line model. (d) Constraints on the iron K-edge absorption feature for the 1988 data, displayed against the assumed iron K-edge energy.

ence is also much larger than the systematic errors (mainly due to background uncertainties) in Γ , which is no larger than ± 0.05 in the present case. We further searched the *Ginga* data for fast spectral changes on time scales of minutes to days, but none was found. In particular, the first and second day of the 1988 observation yielded the same value of Γ within errors of ± 0.03 .

3.3.2. Iron K-Emission Line and Iron K-Edge Feature

The single power-law fits to the *Ginga* spectra exhibit a hint of positive residual around 6 keV (Fig. 3, middle panels). This suggests the existence of a redshifted iron K-emission line. We accordingly added to the power-law model a narrow (0.1 keV FWHM) Gaussian component, leaving its intensity and center energy free to vary. This significantly improved the χ^2 of the fit (Table 2 and the bottom panels of Fig. 3). Confidence contour maps for the Gaussian parameters, Figure 4b and 4c, show evidence of line emission in both spectra. Also, F-tests confirm the line significance at a 99.9% confidence level for the 1988 observation and at a 99.0% confidence level for the 1991 observation. The derived line-center energies, after correction for $z = 0.057$, are consistent with those of iron K-lines (6.4–6.93 keV in the rest frame). We therefore conclude that the *Ginga* spectra provide the first significant evidence of the iron K-line emission from 3C 390.3, with equivalent width (EW) of ~ 100 eV. In a later discussion (§ 3.3.3) we show that the iron line is unlikely to originate in the contaminating flare source. We cannot, however, constrain the line energy enough to determine, within the 90% confidence levels, whether the inferred iron line is of fluorescent origin (expected at 6.4 keV in the rest frame) or of thermal origin (expected at 6.7–6.9 keV in the rest frame). Also, we cannot discriminate between the line flux or the line EW being the same between the two observations.

Motivated by a series of *Ginga* detections of iron K-edge features from many Seyfert galaxies (e.g., Pounds et al. 1990; Matsuoka et al. 1990), we examined the 3C 390.3 spectra for similar iron K-edge absorption features. We multiplied the power-law model by the K-edge absorption factor and varied both the edge energy and depth in comparison with the data. However, no edge feature was detected from either spectrum of 3C 390.3, and the derived upper limits on the iron column density are of order $4 \times 10^{18} \text{ cm}^{-2}$ as shown in Figure 4d, corresponding to an equivalent hydrogen column of $1 \times 10^{23} \text{ cm}^{-2}$ assuming cosmic abundance.

3.3.3. Origin of the X-Ray Flare and Its Effects on the *Ginga* Data

In this subsection we will discuss the flare in the second *Ginga* observation and justify the exclusion of these data from the analysis. The flare is due to valid aperture X-rays, because background monitor counts (Hayashida et al. 1989) did not increase. The flare exhibited a rapid (5 minutes) tenfold flux rise followed by a ~ 30 minutes decay, although the observation ended before the flux recovery to the preflare level. We derived X-ray spectra of the flare component, in time series, by subtracting preflare data including both background and the 3C 390.3 signal. These flare spectra are well fitted with thermal bremsstrahlung continuum, plus an iron emission line with a center energy of 6.7 ± 0.1 keV and an EW in the range 600–1400 eV. Fitting with the Raymond-Smiths (1977) model resulted in consistent parameter values. The continuum temperature gradually decreased from $kT = 10$ keV (flare peak) to 4 keV.

The flare spectra cannot be fitted with power law plus line model.

From the spectral analysis, it is most likely that the flare X-rays are emission from optically thin hot plasma, whose size is at most 10^{13} cm corresponding to the flare rise time. Any detectable thin-thermal emission associated with the radio galaxy would not exhibit such a rapid variation (Elvis et al. 1991). We can also exclude a solar origin, since, during the flare, the LAC field of view was clear from direct solar illumination and terrestrial scattering of solar X-rays. On the other hand, this event is very reminiscent of solar and late-type stellar X-ray flares (e.g., Haish 1983; Tsuru et al. 1989; Pallavicini, Tagliaferri, & Stella 1990). We therefore suggest that a dMe star EQ 1839.6+8002 (Caillaut et al. 1986), only $0^\circ.4$ away from 3C 390.3, to be the flare source. The estimated distance of $D = (11\text{--}40)$ pc to this star implies a 2–10 keV flare peak luminosity of $1.3 \times 10^{30} (D/10 \text{ pc})^2 \text{ ergs s}^{-1}$. This value is consistent with those of dMe flares. Further details of this event will be reported elsewhere.

The flare source was in the LAC field of view throughout both observations, and we must estimate its contribution during its quiescent state for possible contamination. Because the X-rays from 3C 390.3 are of nonthermal nature (§3.3.1), the amount of thermal component allowed by the *Ginga* spectra is expected to set an upper limit on the contamination. We accordingly fit the 3C 390.3 spectra (Fig. 3) with a model consisting of power-law and thermal bremsstrahlung continua (both without absorption), leaving all the continuum parameters free while masking out the iron line region (5.8–7.0 keV). The upper limit on the thermal flux thus constrained is shown in Figure 5a as a function of the assumed bremsstrahlung temperature. The result indicates that thermal flux is at most $\sim 8\%$ of the total flux in both spectra, or less than $(3.9\text{--}5.8) \times 10^{-12} \text{ ergs cm}^{-2} \text{ s}^{-1}$, for coronal temperatures below ~ 4 keV (assuming that the coronal temperature is lower in quiescence than during flares). This is consistent with the IPC flux of EQ 1839.6+8002, which is $7.8 \times 10^{-13} \text{ ergs cm}^{-2} \text{ s}^{-1}$ in 0.15–4 keV (Caillaut et al. 1986). The above results imply that the flare peak luminosity is at least 10^3 times larger than the quiescent X-ray luminosity of the flare source. This is not unusual for late-type flare stars. From these arguments, we conclude that the contamination to the continuum emission by the quiescent stellar emission is negligible.

To examine whether the iron line emission comes from the flare star or from the radio galaxy, we have calculated the maximum iron line EW (relative to the observed total continuum) attributable to the quiescent stellar emission, by utilizing the upper limit on the thermal continuum (Fig. 5a) and the iron line EW (relative to the calculated thermal continuum) expected for a plasma of solar abundance (Rothenflug & Arnaud 1985). The result, shown in Figure 5b, indicates that the estimated upper limits on the stellar line EW are comparable to those actually observed in the 3C 390.3 spectra. However, the redshift-uncorrected line energies for the 3C 390.3 spectra, 6.24 ± 0.33 keV (in 1988) and 6.14 ± 0.35 keV (in 1991), are inconsistent with the energy of ~ 6.7 keV expected for stellar coronae of temperature $kT = 2\text{--}10$ keV, which has actually been observed in the flare X-rays. (Note that the line energies observed from 3C 390.3 become consistent with either 6.7 or 6.4 keV after the redshift correction.) We therefore conclude that the quiescent stellar emission cannot be a main source of the detected iron K-line photons.

3.3.4. Upper Limits on the Thermal Component

X-ray bright elliptical galaxies are surrounded by hot ($kT \sim 1$ keV) gaseous halos which emit thermal X-rays with luminosities in the range 10^{41} – 10^{42} ergs s^{-1} (Forman, Jones, & Tucker 1985; Canizares, Fabbiano, & Trinchieri 1987; Fabbiano, Kim, & Trinchieri 1992). In radio galaxies, hydrostatic pressure of such a hot halo may significantly contribute to the confinement of the radio lobes. The analysis conducted in the preceding subsection is particularly useful in setting upper limits on possible thermal X-ray emission from such an extended gaseous halo in the 3C 390.3 system. Assuming that thermal flux should not vary and therefore combining the two results in Figure 5a, 2–20 keV thermal flux from 3C 390.3 itself can be constrained to less than 4×10^{-12} ergs s^{-1} cm^{-2} for $kT < 10$ keV, corresponding to a 2–20 keV luminosity of less

than $1h^{-2} \times 10^{43}$ ergs s^{-1} ($< 5\%$ of the total luminosity seen in *Ginga*). The upper limit is further reduced for lower temperatures, e.g., less than $2h^{-2} \times 10^{42}$ and less than $1h^{-2} \times 10^{42}$ ergs s^{-1} for $kT = 3$ and 2 keV, respectively.

4. DISCUSSION

4.1. Long-Term Variability

Over the period of ~ 1970 to mid 1980s, 3C 390.3 exhibited a long-term decline in its optical blue continuum, optical broad-line components, and X-rays (Barr et al. 1980; van Breugel & Jagers 1982; Lloyd 1984; Laing, Riley, & Longair 1983; SWB85). The X-ray observations from *EXOSAT* and *Ginga* have shown an increase, from the minimum in 1984 May to a peak in 1988 November, by almost an order of magnitude. This is one of the largest amplitude variations in X-rays observed in AGNs (see Grandi et al. 1992). The *IUE* observations made in 1989 March (Wamsteker & Clavel 1989) also reported a marked increase in the ultraviolet continuum and lines of 3C 390.3 (doubling of the continuum, a 70% and a 160% increase in the Ly α and C iv line, respectively) with respect to the observation in early 1988.

These results immediately indicate that thermal or inverse-Compton X-ray emission from large extended regions, including the radio lobes, and hot plasmas which might be necessary to confine the radio lobes, is at most $3h^{-2} \times 10^{43}$ ergs s^{-1} in 2–20 keV corresponding to the minimum intensity observed on 1984 day 153. All the variable X-ray flux, with luminosities reaching $\sim 2.5h^{-2} \times 10^{44}$ ergs s^{-1} , must originate in the compact nucleus. This conclusion is quite consistent with the fact that the *Ginga* spectra are clearly of a nonthermal nature with characteristics very similar to those of other AGNs, and that the allowed thermal X-ray luminosity is less than $1h^{-2} \times 10^{43}$ ergs s^{-1} (Fig. 5a) for a rather wide range of assumed temperature ($kT = 2$ –10 keV).

There are several alternative interpretations for the cause of the observed X-ray variability. One obvious possibility is a real change in the intrinsic luminosity of the nucleus. Changes in the nuclear obscuration by cold matter can also cause apparent X-ray intensity changes, and this is actually suggested by the reduced optical broad lines during the low flux period. Also evidence was reported previously for occasional variation in the X-ray absorption (Charles, Longair, & Sanford 1975). However, a tenfold intensity reduction in the *EXOSAT* ME range by increased absorption would have required an equivalent hydrogen column density in excess of 3×10^{23} cm^{-2} , which would have caused a serious change in the ME spectrum. Since such a drastic spectral change was not observed the increased absorption alone seems difficult to explain the variation. A third alternative is changes in the X-ray beaming direction, as suggested by the evidence of the superluminal motion (Alef et al. 1988). This alternative is, however, doubtful, because the radio lobes indicate a jet that is fairly stable on time scales of millions of years and is not pointing toward us. We therefore presume that the long-term variability of 3C 390.3 is mainly due to intrinsic luminosity changes in the nonthermal radiation from the nucleus, possibly accompanied by an increase in the circumnuclear absorption as a secondary effect (e.g., through reduced photoionization flux).

Compared to the long-term variations, short-term variability seems to be a less clear phenomenon for this galaxy. This characteristic is rather commonly seen in other high-luminosity AGNs (e.g., Barr & Giommi 1992; Grandi et al. 1992; Williams et al. 1992; Ohashi et al. 1992). It is interesting

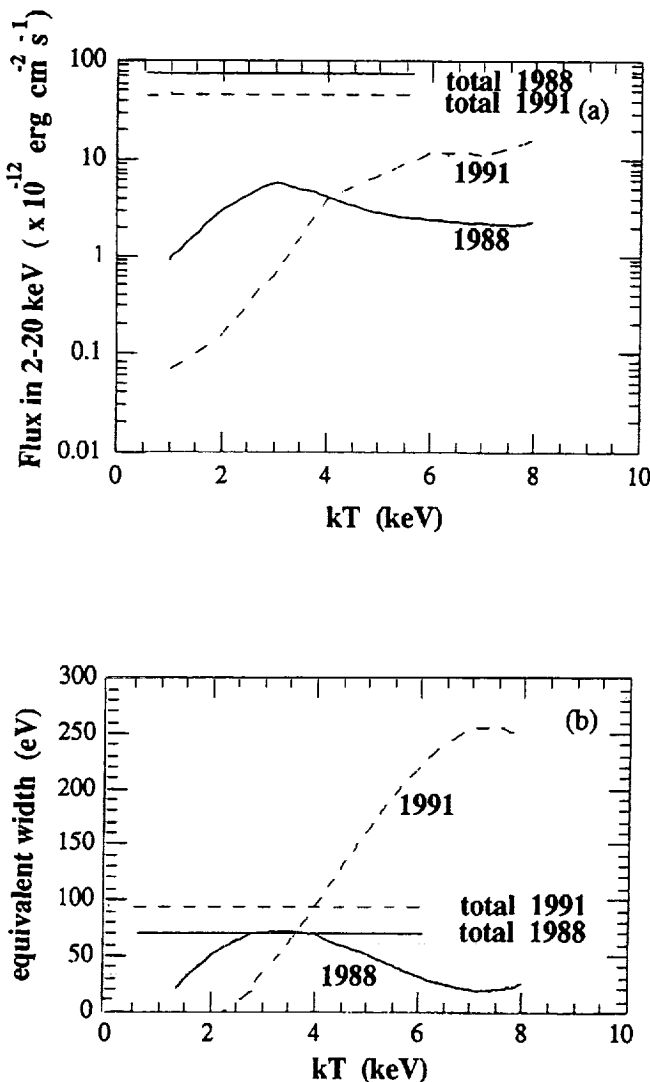


FIG. 5.—(a) Upper limits (90% confidence level) on the 2–20 keV thermal continuum flux allowed by the *Ginga* spectra of 3C 390.3. The total 2–20 keV *Ginga* fluxes are also shown. (b) Upper limits (90% confidence level) on thermal iron K-emission line equivalent width (with respect to the observed total continuum) expected for a solar-abundance plasma in ionization equilibrium whose continuum flux is constrained by (a). The straight lines indicate actually observed equivalent widths.

to consider here Centaurus A, which is also a double-lobed radio galaxy (at a $D \sim 5$ Mpc distance) but is two orders of magnitude less luminous than 3C 390.3. In fact, Cen A not only shows long-term large amplitude changes up to a factor of 30 or so (Morini, Anselmo, & Moltini 1989), but also a rapid intensity decrease by a factor of three within 5 minutes (Wang et al. 1986). Cen A is further distinguished from 3C 390.3 in that it exhibits a large X-ray absorption ($N_H \sim 10^{23}$ H atoms cm^{-2}) as well as much stronger iron fluorescence lines and is not an OVV. These differences between Cen A and 3C 390.3 are most naturally attributed to the difference in the intrinsic luminosity.

4.2. Continuum Spectra and X-Ray Emission Mechanism

The continuum X-ray spectra of 3C 390.3 obtained with *Ginga* are dominated by a nonthermal component, with rather tight upper limits on contribution from thermal emission ($<5\%$ of the total luminosity seen in *Ginga*). The photon indices Γ from the two *Ginga* observations are 1.77 ± 0.01 (average of the 2 days) and 1.54 ± 0.02 , while all the measured *EXOSAT* spectra are consistent with Γ of 1.6–1.8. Spectral indices determined by earlier satellites (Halpern 1982; Rothschild et al. 1983; Barr et al. 1980; Mushotzky, Baity, & Peterson 1977) are generally consistent with these values, although subject to larger errors. Thus the X-ray spectra of 3C 390.3 are similar to those of other AGNs, including Seyfert galaxies, QSOs, and some BL Lac objects with flat-X-ray spectra.

EXOSAT measurements of the spectral index are subject to too large error bars to search for any correlation between flux and spectral index. On the other hand, between the two *Ginga* observations separated by ~ 2 years, the X-ray spectrum of 3C 390.3 flattened as its 2–20 keV luminosity decreased from $(2.57 \pm 0.06)h^{-2}$ to $(1.62 \pm 0.05)h^{-2} \times 10^{44}$ ergs s^{-1} . This luminosity-spectrum correlation is reminiscent of the behavior of Seyfert galaxies, in which X-ray flux decrease is often, if not always, accompanied by spectral flattening (e.g., Pound et al. 1990; Matsuoka et al. 1990; Grandi et al. 1992). In QSOs and BL Lac objects, the X-ray spectrum on the contrary tends to become steeper as the source gets fainter (e.g., Makino et al. 1989; Sembay et al. 1992). In most other respects, however, 3C 390.3 does not resemble Seyfert galaxies. For example, the iron K-edge absorption feature and low-energy absorption, both quite common to the X-ray spectra of Seyfert galaxies, have not been detected in the 3C 390.3 spectra. In addition, the intense radio emission from the nucleus and from the lobes of 3C 390.3 provides the most outstanding difference of this object from Seyfert galaxies.

When 3C 390.3 is X-ray bright, its X-ray flux lies above the smooth extrapolation of radio-IR wide band spectrum (Fig. 6), thus bearing close similarity to radio-loud QSOs (e.g., Ohashi et al. 1992). It is therefore likely that a major fraction of X-rays from 3C 390.3 is emitted through the same mechanism as those from radio-loud QSOs. A favorite model in this case is synchrotron-self-Compton (SSC) mechanism; low-energy “seed” photons produced via synchrotron radiation by relativistic particles are Compton up-scattered into the X-ray region by the same electron population. The relatively slow X-ray variation observed from 3C 390.3 supports this picture, because the synchrotron cooling time of the electrons which emit soft seed photons (typically in the radio frequency) is expected to be quite long. Assuming that the electron spectrum is kept constant, we further expect that the spectral slope of the synchrotron component, hence of the self-Compton com-

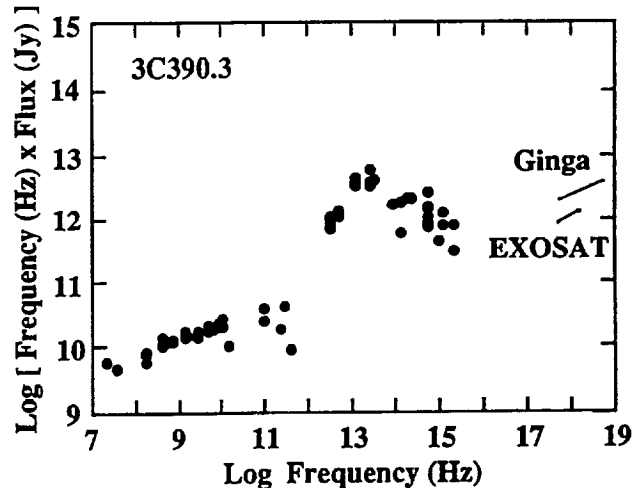


FIG. 6.—Wide-band spectrum of 3C 390.3. Radio and IR observations refer to Poggiali (1991), which are not simultaneous ones. Present *EXOSAT* (1984 day 153) and *Ginga* (1988 day 316–317) observations are also shown in the figure.

ponent too, depends on the change of the electron injection rate rather than the injection rate itself; when the injection rate increases, the spectrum flattens temporarily on time scales shorter than the relevant synchrotron cooling time. In other words, we should not expect unique relation between instantaneous X-ray intensity and spectral slope in the SSC scheme. The apparent spectral flattening observed in the fainter *Ginga* data may be manifestation of such a complex hysteresis between flux and spectrum.

4.3. Iron Line Emission

We have obtained a firm evidence of iron K-line emission from 3C 390.3, with EW of order 100 eV, although we could not constrain the ionization state of iron. Previous iron line detections from high-luminosity AGNs have been limited to a few cases, including the radio-loud QSO 3C 273 (EW ~ 50 eV; Turner et al. 1990), the radio-quiet QSO 1821+643 (EW ~ 150 eV; Kii et al. 1991), and the broad-line radio galaxy 3C 382 (EW ~ 280 eV; Kaastra, Kuniera & Awaki 1991) whose luminosity was about one-fourth of the 1988 luminosity of 3C 390.3. Williams et al. (1992) obtained upper limits of order 100 eV on the iron line EW for about a dozen QSOs observed with *Ginga*. From Seyfert galaxies, iron lines have been observed much more commonly, with EW reaching 200 eV or more (Pounds et al. 1990; Matsuoka et al. 1990). These lines have been interpreted as due to fluorescence from cool and warm materials around the central continuum source. On the other hand, iron lines have not been observed from BL Lac objects and OVV quasars, and the obtained upper limits are sometimes as stringent as ~ 20 eV (Makino et al. 1989).

These results altogether suggest that iron line EW from these sources is inversely correlated to the continuum luminosity. This tendency has been investigated by Iwasawa & Taniguchi (1993), who call it “X-ray Baldwin effect.” Although the interpretation is complex, for QSOs and radio galaxies the inverse correlation is likely to include the effect of continuum enhancement due to beamed emission. In this sense, the detection of iron line from 3C 390.3 with a moderate EW is reasonable, since the radio jets and the evidence of superluminal motion clearly indicate beamed emission for 3C 390.3 but the promi-

ment radio lobes indicate that the beam is not directly pointing toward us.

4.4. Radio Lobe Confinement

The *Ginga* observations have constrained the thermal X-ray luminosity of 3C 390.3 to be less than $1h^{-2} \times 10^{43} \text{ ergs s}^{-1}$ in 2–20 keV, for thermal temperature of $kT < 10 \text{ keV}$ or $T < 1.2 \times 10^8 \text{ K}$. This implies that any spherical and uniform hot gaseous halo around 3C 390.3, of an assumed radius $R_{100} \times 100 \text{ kpc}$ and temperature $T_7 \times 10^7 \text{ K}$ must have electron density less than $2.8 \times 10R_{100}^{-3/2}T_7^{-1/4}h^{-1} \text{ cm}^{-3}$. Here we use a relation that bolometric bremsstrahlung luminosity of a fully ionized hydrogen plasma with volume $V \text{ (cm}^3\text{)}$, temperature $T \text{ (K)}$, and uniform electron density $n_e \text{ (cm}^{-3}\text{)}$ is given as $10^{-26.6}n_e^2VT^{1/2} \text{ ergs s}^{-1}$ for $T \geq 10^7 \text{ K}$. This constrains the thermal pressure of the halo to be less than $4 \times 10^{-11}R_{100}^{-3/2}T_7^{3/4}h^{-1} \text{ ergs cm}^{-3}$.

This limit is comparable to the hydrostatic pressure required to confine the radio lobes of 3C 390.3 calculated by Hargrave & McEllin (1975) based on the radio results, namely $(2\text{--}6) \times 10^{-10}$ and $2.4 \times 10^{-11} \text{ ergs cm}^{-3}$ for the south and north heads of the radio lobe, respectively. Thus we cannot make definite statement, either affirmative or negative, as to the case of hydrostatic confinement of the radio lobes by hot halo. However, Figure 5a gives an order of magnitude tighter limit on the thermal luminosity, if the hypothesized hot halo is cooler than $kT = 2 \text{ keV}$ as is usually the case for individual elliptical galaxies and poor clusters of galaxies. It therefore seems likely that some other mechanism, e.g., magnetic confinement, is operating in the radio lobes of 3C 390.3.

5. CONCLUSIONS

The radio galaxy 3C 390.3 was observed in X-rays by the *EXOSAT* and *Ginga* satellites over the period 1984–1991. The

main results of these observations are as follows:

1. In the 2–20 keV energy band the source luminosity was found to be $L_X \sim 10^{44} \text{ ergs s}^{-1}$. Long-term X-ray time variability with a large amplitude (more than an order of magnitude) on a time scale of years was confirmed.
2. High-quality X-ray spectra were obtained, especially with *Ginga*. The continuum X-ray spectra obtained with *EXOSAT* and *Ginga* are well described with unabsorbed power-law model with the photon slope in the range 1.5–1.8. There was a change of slope between the two *Ginga* observations within an interval of ~ 2 years; it flattened by ~ 0.2 as its 2–20 keV luminosity decreased by $\sim 40\%$.
3. Iron K-emission line was for the first time detected from this source with the *Ginga* observations. The line EW was of order $\sim 100 \text{ eV}$. We could not determine the line origin within the error bars. Iron K-edge feature was not detected.
4. We derived upper limits on the thermal component from 3C 390.3 of less than $1h^{-2} \times 10^{43} \text{ ergs s}^{-1}$ in 2–20 keV for thermal temperature of $kT < 10 \text{ keV}$. This upper limit is not yet tight enough to completely exclude the confinement of the radio lobes by thermal pressure of extended hot gas.

We are grateful to the *Ginga* team members for continuous support. M. I. thanks R. Stern for his help in the search for the flare star candidate. G. G. C. P. acknowledges financial support from the Italian MURST and the Italian Space Agency (ASI) and Japan SPS for a travel grant. G. T. acknowledges financial support from ASI. This work was supported in part by NASA Contract NAS 8-39073 (ASC) and NASA grants NAGW-2681 (LTSA), NAGW-2681 (LTSA) and NAG 8-801 (*Ginga*).

REFERENCES

- Alef, W., Gotz, M. M. A., Preuss, E., & Kellermann, K. I. 1988, *A&A*, 192, 53
 Barr, P., & Giommi, P. 1992, *MNRAS*, 225, 495
 Barr, P., et al. 1980, *MNRAS*, 193, 549
 Barthel, P. D. 1989, *ApJ*, 336, 606
 Brown, I. W. A., & Murphy, D. W. 1987, *MNRAS*, 226, 601
 Burbidge, E. M., & Burbidge, G. R. 1971, *ApJ*, 163, L21
 Caillaut, J.-P., Helfand, D. J., Nousek, J. A., & Takalo, L. O. 1986, *ApJ*, 304, 318
 Canizares, C. R., Fabbiano, G., & Trichieri, G. 1987, *ApJ*, 312, 503
 Charles, P. A., Longair, M. S., & Sanford, P. W. 1975, *MNRAS*, 170, 17
 Clavel, J., & Wamsteker, W. 1987, *ApJ*, 320, L9
 Elvis, M., Giommi, P., Wilkes, B. J., & McDowell, J. 1991, *ApJ*, 378, 537
 Fabbiano, G., Kim, D. W., & Trinchieri, G. 1992, *ApJS*, 80, 531
 Fanaroff, B. L., & Riley, J. M. 1974, *MNRAS*, 167, 31
 Forman, W., Jones, C., Cominsky, L., Julien, P., Murray, S., Peters, G., Tananbaum, H., & Giacconi, R. 1978, *ApJS*, 38, 357
 Forman, W., Jones, C., & Tuchker, W. 1985, *ApJ*, 293, 102
 Giacconi, R., & Gursky, H. 1974, in *X-Ray Astronomy*, ed. R. Giacconi & H. Gursky (Dordrecht: Reidel), 397
 Gioia, I. M., Maccacaro, T., Shild, R. E., Wolter, A., Stocke, J. T., Morris, S. L., & Henry, J. P. 1990, *ApJ*, 72, 567
 Grandi, P., Tagliaferri, G., Giommi, P., Barr, P., & Palumbo, G. G. C. 1992, *ApJS*, 82, 93
 Haish, B. M. 1983, in *Activity in Red-Dwarf Stars*, ed. P. B. Byrne & M. Rodono (Dordrecht: Reidel), 255
 Halpern, J. P. 1982, Ph.D. thesis, Harvard University
 Hargrave, P. F., & McEllin, M. 1975, *MNRAS*, 173, 37
 Hayashida, K., et al. 1989, *PASJ*, 41, 373
 Heiles, C., & Habing, H. J. 1974, *A&AS*, 14, 1
 Iwasawa, K., & Taniguchi, Y. 1993, *ApJL*, in press
 Kaastra, J. S., Kunieda, H., & Awaki, H. 1991, *A&A*, 242, 27
 Kii, T., et al. 1991, *ApJ*, 367, 455
 Laing, R. A., Riley, J. M., & Longair, M. S. 1983, *MNRAS*, 204, 151
 Lloyd, C. 1984, *MNRAS*, 209, 697
 Makino, F., et al. 1989, *ApJ*, 347, L9
 Marshall, F. E., Mushotzky, R. F., Boldt, E. A., Holt, S. S., Rothschild, R. E., & Serlemitsos, P. J. 1978, *Nature*, 275, 624
 Matsuoka, M., Piro, L., Yamauchi, M., & Murakami, T. 1990, *ApJ*, 362, 440
 Morini, M., Anselmo, F., & Molteni, D. 1989, *ApJ*, 347, 750
 Mushotzky, R. F. 1984, *Adv. Space Res.*, Vol. 3, Nos. 10–12, 157
 Mushotzky, R. F., Baity, W. A., & Peterson, L. E. 1977, *ApJ*, 212, 22
 Ohashi, T., Tashiro, M., Makishima, K., Kii, T., Makino, F., Turner, M. J. L., & Williams, O. R. 1992, *ApJ*, 398, 87
 Oke, J. B. 1986, in *Superluminal Radio Sources*, ed. J. A. Zensus & T. J. Pearson (Cambridge Univ. Press), 267
 Orr, M. J. L., & Brown, I. W. A. 1982, *MNRAS*, 200, 1067
 Pallavicini, R., Tagliaferri, G., & Stella, L. 1990, *A&A*, 228, 403
 Penston, M. V., & Penston, M. J. 1973, *MNRAS*, 162, 109
 Perez, E., Penston, M. W., Tadhunter, C., Mediavilla, E., & Moles, M. 1988, *MNRAS*, 230, 353
 Poggioni, M. 1991, M.A. in Astronomy, University of Bologna
 Pounds, K. A., Nandra, K., Stewart, G. C., George, I. M., & Fabian, A. C. 1990, *Nature*, 344, 132
 Raymond, J. C., & Smith, B. W. 1977, *ApJS*, 35, 419
 Rothenflug, R., & Arnaud, M. 1985, *A&A*, 144, 431
 Rothschild, R. E., Mushotzky, R. F., Baity, W. A., Gruber, D. E., Matteson, J. L., & Peterson, L. E. 1983, *ApJ*, 269, 423
 Sembay, S., et al. 1993, *ApJ*, 404, 112
 Shafer, R., Ward, M., & Barr, P. 1985, *Space Sci. Rev.*, 40, 637 (SWB85)
 Tsuru, T., et al. 1989, *PASJ*, 41, 679
 Turner, M. J. L., et al. 1989, *PASJ*, 41, 345
 ———. 1990, *MNRAS*, 244, 310
 Turner, M. J. L., Smith, A., & Zimmerman, H. U. 1981, *Space Sci. Rev.*, 30, 513
 Turner, T. J., & Pounds, K. A. 1989, *MNRAS*, 240, 833
 van Breugel, W., & Jagers, W. 1982, *A&AS*, 49, 529
 Wamsteker, W., & Clavel, J. 1989, *IAU Circ.*, No. 4763
 Wang, B., Inoue, H., Koyama, K., Tanaka, Y., Hirano, T., & Nagase, F. 1986, *PASJ*, 38, 685
 Williams, O. R., et al. 1992, *ApJ*, 389, 157
 Wood, K. S., et al. 1984, *ApJS*, 56, 507

The interstellar medium in the Seyfert galaxy NGC 7172

G. C. Anupama,¹ A. K. Kembhavi,¹ M. Elvis² and R. Edelson³

¹ Inter-University Centre for Astronomy and Astrophysics, Post Bag 4, Ganeshkhind, Pune 411007, India

² Harvard-Smithsonian Center for Astrophysics, 60 Garden Street, Cambridge, MA 02138, USA

³ Department of Physics and Astronomy, University of Iowa, 203 Van Allen Hall, Iowa City, IA 52242, USA

Accepted 1995 March 17. Received 1995 March 15; in original form 1994 December 7

ABSTRACT

We present aperture and surface photometry of the Seyfert galaxy NGC 7172, which is a member of the compact group HCG 90, and has a prominent equatorial dust lane. We use the observed colour excess in the dust lane, obtained from broad-band *B* and *V* images, to estimate the neutral hydrogen content as $M_{\text{H I}}^{\text{tot}} = 2.6 \times 10^8 M_{\odot}$ and $\log(M_{\text{H I}}/L_B) = -1.8$. We analyse the flux from NGC 7172 at various wavelengths and discuss the properties of the interstellar medium in the galaxy. Based on the results from surface photometry, and the properties of the interstellar medium, we conclude that the morphology of NGC 7172 is of type S0–Sa.

Key words: galaxies: active – galaxies: individual: NGC 7172 – galaxies: ISM – galaxies: photometry – galaxies: Seyfert – galaxies: structure.

1 INTRODUCTION

Studies of the morphology and stellar content of the host galaxies of Seyfert nuclei (Adams 1977; Simkin, Su & Schwarz 1980; Yee 1983; MacKenty 1990) have shown that almost all Seyferts occur in early-type normal or barred spirals. The disc parameters of the host galaxies are similar to those of normal spirals (Yee 1983; MacKenty 1990; Kotilainen & Ward 1994), while the colours are redder than in the normal galaxies, which is explained as being due to dust extinction in the optical and reradiation from this dust in the infrared (Kotilainen & Ward 1994).

Nuclear activity can influence the interstellar medium in the host galaxy, as evidenced by the detection of extended line-emitting regions on kiloparsec scales in many Seyferts (Unger et al. 1987; Baum & Heckman 1989; Wilson 1992), and theoretical studies of the effect of continuum radiation on the interstellar medium (Begelman 1985; Shanbhag & Kembhavi 1988; Storchi-Bergmann, Mulchaey & Wilson 1992). The interstellar medium is an indicator of star formation activity in galaxies, and an important tool in the study of their structure, dynamics and evolution.

In this paper we report observations of the Seyfert NGC 7172, an Sa(pec)-type spiral galaxy (de Vaucouleurs, de Vaucouleurs & Corwin 1976) with a strong equatorial dust lane. Using colour differences between the dust lane and the body of the galaxy, we obtain an estimate of the total neutral hydrogen content in the dust lane. We further use published far-infrared (FIR) and CO fluxes to study the dust properties in the galaxy.

NGC 7172 belongs to a compact group (HCG 90) including NGC 7173 (E2), NGC 7174 (Sb pec) and NGC 7176 (E0) (Hickson 1982). Sharples et al. (1984) discovered the active nucleus based on a search of galaxies in HEAO-A2 X-ray source error boxes (Piccinotti et al. 1982). They classified the nucleus as Seyfert 2 on the basis of narrow widths of its emission lines. The nucleus is heavily obscured by the dust lane. The Balmer decrement $H\alpha/H\beta > 6.5$ (Sharples et al. 1984) and polarization studies (Brindle et al. 1990) indicate strong reddening. Assuming case B recombination, the Balmer decrement implies $E(B-V) = 0.77$ mag. For standard Milky Way dust and dust-to-gas ratios this is equivalent to a neutral hydrogen column density $\approx 4 \times 10^{21}$ atom cm^{-2} .

Results from surface photometry of this object in the near-infrared (NIR) and optical wavelengths have been presented in a series of papers by Kotilainen et al. (1992a, b) and Kotilainen, Ward & Williger (1993, hereafter KWW). These studies were, however, restricted to the inner 30-arcsec radius, which is too small to define the disc structure. We present results of surface photometry based on broad-band optical CCD images reaching out to radii of 70 arcsec.

2 OBSERVATIONS AND DATA REDUCTION

BVR CCD images of NGC 7172 were obtained at the prime focus of the CTIO 4-m telescope in 1983 August 17, as a part of a programme (KWW) to study Seyfert galaxies in the Piccinotti sample of hard X-ray-flux-limited AGN (Piccinotti

et al. 1982). The seeing was ~ 1.5 arcsec. The images were bias-subtracted and flat-field-corrected, following the standard procedure. The sky background was subtracted by taking the mean sky value from regions clearly unaffected by the galaxy ($r \geq 100$ arcsec) and stars. The R frame was found to be out of focus, and so the image was not used in surface photometry. The aperture photometry is not as seriously affected, since we obtain the average values over apertures of size larger than the defocused point spread function (PSF) value.

Transformation coefficients to the standard BVR system were derived from observations of six standard stars in the E-region standards list (Graham 1982). The transformation equations relating the instrumental magnitudes to the standard system are

$$B - V = 1.348(b - v) - 0.230,$$

$$V - R = 0.677(v - r) + 0.046,$$

$$V = v - 1.447 - 0.235(B - V),$$

where b , v and r are the instrumental magnitudes. No atmospheric extinction correction has been applied to the data since the observations were made close to the meridian, at airmass < 1.5 . All reductions were performed using IRAF and other associated packages.

2.1 Colour map

The V and R frames were aligned to the B frame using stars in the frames and applying a shift + rotation transformation. $B - V$ and $V - R$ colour maps were then obtained. Fig. 1(a) shows the $B - V$ colour map of the galaxy. The $B - V$ and $V - R$ colours of the galaxy are approximately constant outside the dust lane, with mean colours $\langle B - V \rangle = 0.90 \pm 0.03$ and $\langle V - R \rangle = 0.88 \pm 0.05$. The bad focus in the R frame would increase the systematic error in the $V - R$ colour about the estimated mean, but not the constancy of the value. We do not, however, use the $V - R$ colour map in further analysis.

Fig. 1(b) shows a plot of the $B - V$ colour across the dust lane. Along the dust lane, the colours indicate an increase in reddening towards the centre (Fig. 1a). There is an extremely blue region of size ≈ 13 arcsec, about ≈ 45 arcsec east of the nucleus. The colour of this region, corrected for an $E(B - V) = 0.77$ (Sharples et al. 1984), is $B - V = -0.25 \pm 0.05$. This value compares well with the colours of giant extragalactic H II regions with massive stars (Mayya 1993).

2.2 Aperture photometry

BVR magnitudes of the galaxy were obtained using circular apertures of sizes 3, 6, 9, 12, 18 and 24 arcsec diameter on the images, with the origin on the central pixel of the galaxy. The magnitudes, zero-point-calibrated with respect to the estimates of Hamuy & Maza (1987), are listed in Table 1; also tabulated are the magnitudes from these authors and KWW. The magnitudes estimated by us are in agreement with the other estimates, within errors.

2.3 Surface photometry

Elliptical isophotes were fitted to the galaxy using the ellipse-fitting routine in the STSDAS software package, which is based on the method outlined by Jedrzejewski (1987). The foreground stars in the galaxy region were masked and excluded from the isophotal analysis. Ellipses of mean intensity were iteratively fitted to isophotal contours for different lengths of the semimajor axis, starting with trial values of ellipticity, position angle and ellipse centre. The fitting program estimates the first two harmonics of the Fourier series representing the deviations from the trial ellipse, and minimizes these to obtain the best-fitting ellipse. Parameters of this ellipse, such as mean intensity along the isophote, ellipticity and position angle are then estimated. The third and fourth harmonics of the residual intensity from the best-fitting ellipse are then evaluated using the method of least squares.

The fitting was started from the 6-arcsec isophote, which is unaffected by the seeing PSF of 1.5-arcsec FWHM. Ellipses were fitted outwards up to 70-arcsec radius along the major axis, and inwards up to the centre. The semimajor axis length for each successive ellipse was increased (or decreased) by 10 per cent. The ellipse centre was held fixed during the fitting. In Fig. 2, we show the isophotal contours with the fitted ellipses. The latter are seen to fit well to the contours outside the dust lane.

3 ANALYSIS AND RESULTS

3.1 Estimation of neutral hydrogen

H I 21-cm line studies by Bottinelli, Gouguenheim & Paturel (1980) give an upper limit to the total neutral hydrogen content as $M_{\text{H I}} < 7.4 \times 10^8 M_{\odot}$. X-ray observations imply a high absorbing column $N_{\text{H}} = 9^{+10}_{-9} \times 10^{22} \text{ cm}^{-2}$, an order of magnitude greater than that implied by the IR and optical extinction, and also 21-cm line measurements (Turner & Pounds 1989; Warwick et al. 1993). The Galactic foreground reddening to NGC 7172 is small, $N_{\text{H}}(21 \text{ cm}) = 1.65 \times 10^{20} \text{ atom cm}^{-2}$ (Elvis, Lockman & Wilkes 1989).

Table 1. Aperture photometry.

| Filter | Aperture Size (arcsec) | This Work | K et al ¹ | HM ² |
|----------|---------------------------|-----------|----------------------|-----------------|
| <i>B</i> | 3.0 | 17.82 | 17.47 | |
| | 6.0 | 16.63 | 16.38 | |
| | 9.0 | 16.02 | 15.84 | |
| | 12.0 | 15.60 | 15.47 | |
| | 18.0 | 15.04 | | 15.10 |
| | 24.0 | 14.67 | | 14.61 |
| <i>V</i> | 3.0 | 16.48 | 16.33 | |
| | 6.0 | 15.35 | 15.22 | |
| | 9.0 | 14.80 | 14.70 | |
| | 12.0 | 14.41 | 14.34 | |
| | 18.0 | 13.91 | | 13.97 |
| | 24.0 | 13.58 | | 13.51 |
| <i>R</i> | 3.0 | 15.95 | 15.50 | |
| | 6.0 | 14.73 | 14.47 | |
| | 9.0 | 14.12 | 13.96 | |
| | 12.0 | 13.71 | 13.59 | |
| | 18.0 | 13.18 | | 13.22 |
| | 24.0 | 12.83 | | 12.78 |

¹KWW.

²Hamuy & Maza (1987).

We estimate here the neutral hydrogen content using the optical extinction due to dust measured from the $B-V$ image. The extinction $E(B-V)$ in the dust lane is estimated as

$$E(B-V) = (B-V)_{\text{dust}} - (B-V)_{\text{gal}}.$$

3.1.1 Effective optical depth

If we assume very little or no extinction in the galaxy outside the dust lane, then an estimate of the unobscured galaxy intensity along the dust lane may be obtained from a smooth

model of the galaxy generated using parameters of the fitted ellipses. The task `BMODEL` in `STSDAS` has been used to construct such a smooth galaxy model, linearly interpolating the intensity values between the ellipses. The observed intensities when divided by the model galaxy give an estimate of the optical depth A_λ across the dust lane.

We have obtained the optical depth in both B and V bands in this manner, and find the values to be close to unity except in the dust obscured regions. Using a 3×9 arcsec² aperture along the dust lane, we estimate the ratio A_B/A_V and find it to be nearly constant, with mean value $\langle A_B/A_V \rangle = 1.27 \pm 0.2$. This value is similar to that determined for the interstellar

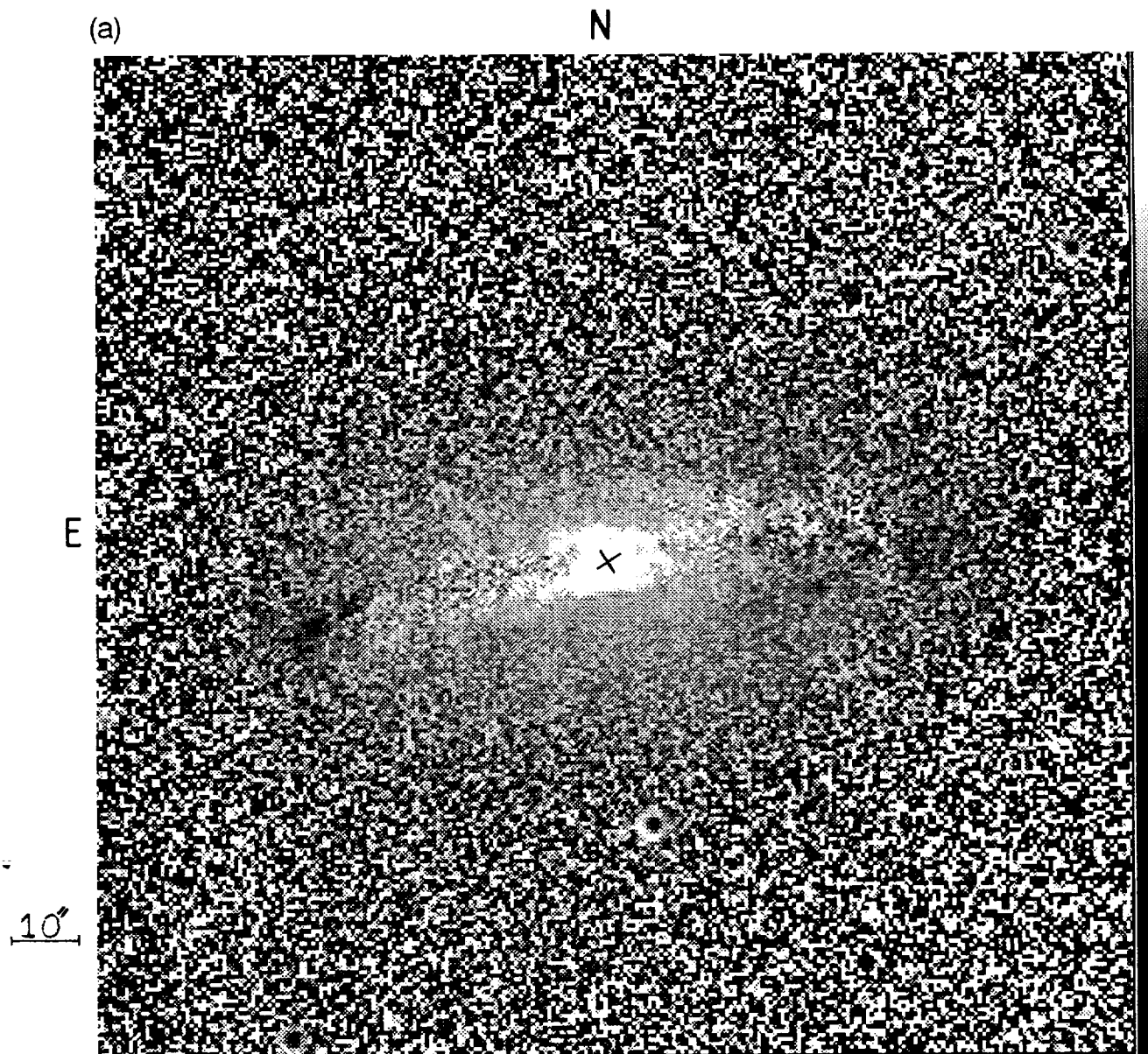


Figure 1. (a) $B-V$ colour map of NGC 7172. Lighter regions correspond to redder colours. Range in $B-V$ is between 2.5 and 0.52 mag. X denotes the centre. (b) $B-V$ across the galaxy, averaged over 10 pixels about the centre, showing the increase in reddening due to the dust lane. Scale: 1 pixel = 0.6 arcsec. Pixel 122 corresponds to the centre of the galaxy.

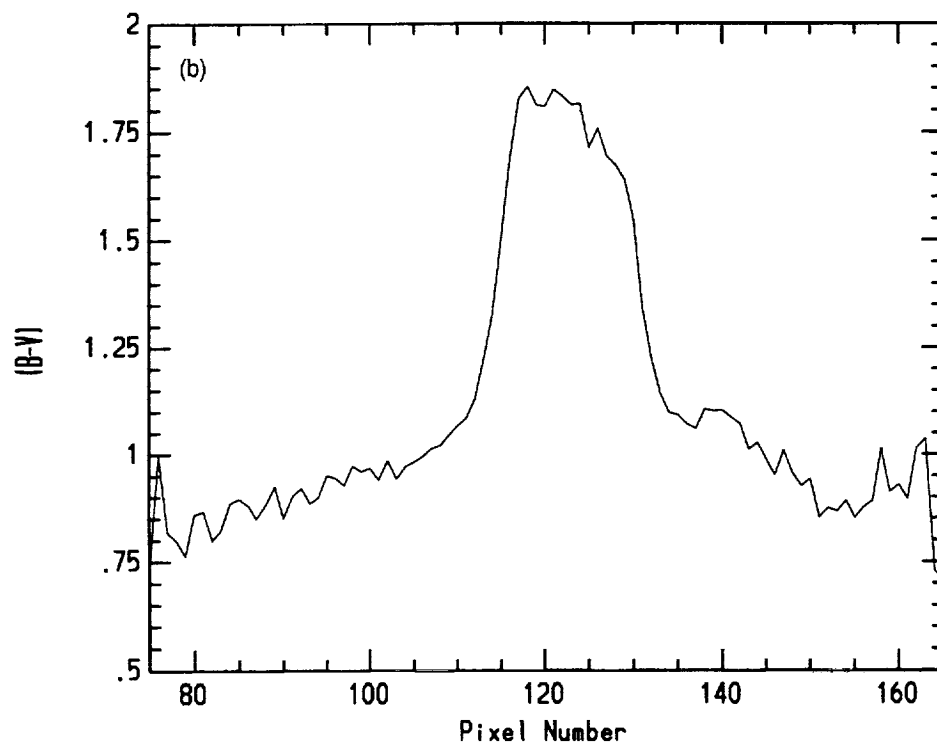


Figure 1 - continued

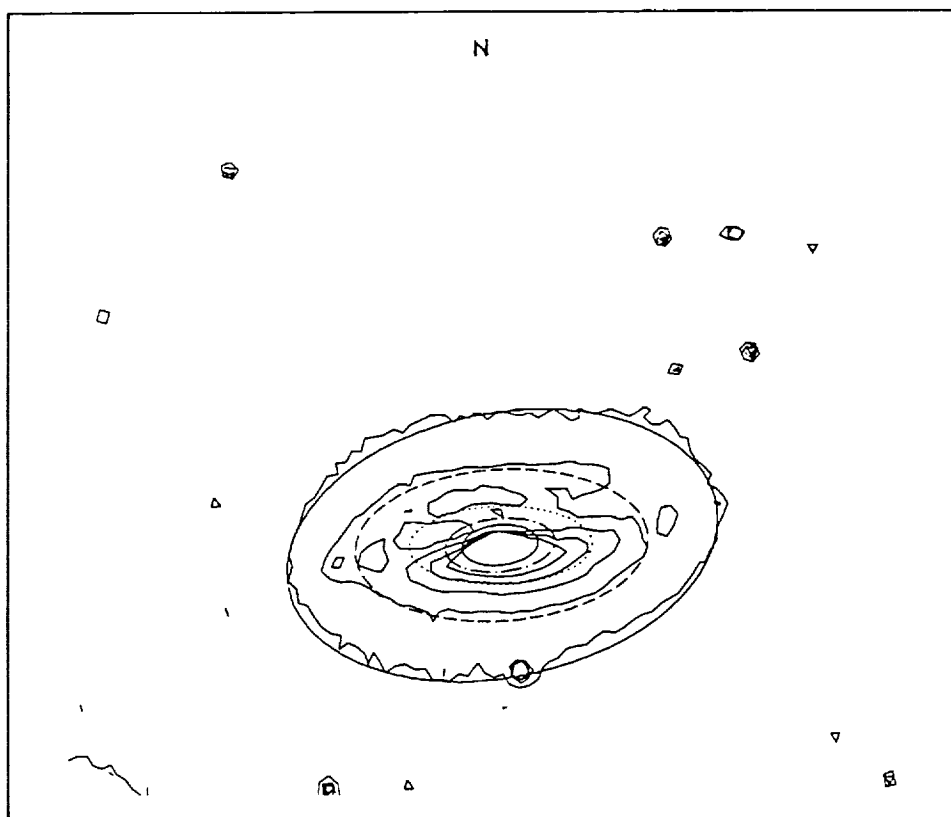


Figure 2. Isophotal contours (full lines) with fitted ellipses (dashed lines).

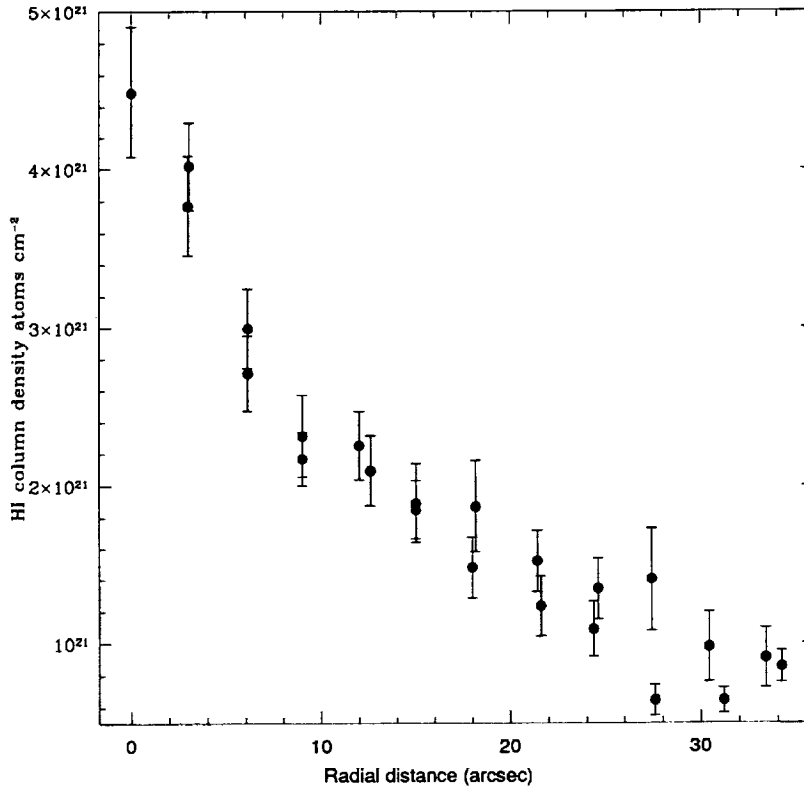


Figure 3. Distribution of $N(\text{HI})$ along the equatorial dust lane plotted as a function of distance from centre.

Table 2. Neutral hydrogen column density.

| $N_{\text{HI}}/10^{21}$ atoms cm^{-2} | Method | Source |
|---|--------------------------------------|---|
| 4 | Balmer decrement | Sharples et al 1984 |
| < 10 | 21 cm line at $z=z(\text{NGC 7172})$ | Bottinelli et al 1980 |
| 90^{+100}_{-90} | X-ray low energy cut-off | Warwick et al 1993, Turner & Pounds 1989 |
| 4.5 ± 0.5 | Optical extinction, $(B - V)$ colour | This work |

dust extinction in our Galaxy (Savage & Mathis 1979). IR spectra of the nucleus (Roche et al. 1991) indicate that the extinction in NGC 7172 is predominantly due to silicate absorption. The dust properties in NGC 7172 may therefore be considered similar to those in our Galaxy.

3.1.2 Neutral hydrogen

The atomic hydrogen column density $N(\text{HI})$ and the total hydrogen column density $N(\text{HI} + \text{H}_2)$ are correlated with the colour excess $E(B - V)$ in our Galaxy (Savage & Mathis 1979). Assuming homogeneous distribution of gas and a dust-to-gas ratio in NGC 7172 similar to that in our Galaxy, we have (Burstein & Heiles 1978)

$$N(\text{HI})/E(B - V) = 5.0 \times 10^{21} \text{ atom cm}^{-2} \text{ mag}^{-1}.$$

We have obtained the distribution of the colour excess $E(B - V)$ along the dust lane using the same $3 \times 9 \text{ arcsec}^2$

aperture as above, and converted this to a distribution of HI column density using the above equation; this is shown in Fig. 3. The column density around the nucleus is estimated to be $4.5 \times 10^{21} \text{ atom cm}^{-2}$. In Table 2 we list the estimate of N_{HI} , along with the estimates based on 21-cm line, spectroscopy and X-ray observations. The N_{HI} estimate from the Balmer decrement and the optical extinction are similar and also consistent with the upper limit estimated from 21-cm line measurements. X-ray observations give a much higher value.

The total HI content in the dust lane ($34 \times 9 \text{ arcsec}^2$) is

$$N_{\text{HI}}^{\text{tot}} = D^2 \int_{\text{dust}} N_{\text{HI}} d\Omega,$$

where D is the distance to the galaxy used to convert the angular sizes in arcsec to the physical sizes in kpc, and the integration is performed over the dust lane with a beam size $d\Omega$, which in this case is the size of the aperture used. Using $D = 33.9 \text{ Mpc}$ (Tully 1988) and the estimate of N_{HI} obtained from the map, we get for the total number of HI atoms and mass,

$$N_{\text{HI}}^{\text{tot}} = 3 \times 10^{65} \text{ atom}, \quad M_{\text{HI}}^{\text{tot}} = 2.6 \times 10^8 M_{\odot}.$$

Using the Galactic dust-to-gas ratio of ~ 100 (Burstein & Heiles 1978), the dust mass $M_d = 2.6 \times 10^6 M_{\odot}$. Table 3 lists the hydrogen and dust mass estimates. The mass of HI estimated here is a lower limit, since we are unable to estimate the HI in regions beyond the dust lane. The

Table 3. Hydrogen and dust masses (in M_\odot).

| M_{HI} | M_{dust} | M_{H_2} | Method |
|-------------------|-------------------|-------------------|--|
| $< 7 \times 10^8$ | | | 21 cm line emission |
| 2.6×10^8 | | | dust lane ($B - V$) colour |
| | 2.6×10^6 | | M_{HI} and Galactic dust-to-gas ratio |
| | 2.1×10^6 | | 100 μm flux |
| | | 2.6×10^9 | L_{CO} and Galactic L_{CO} to M_{H_2} ratio |
| | | 1.6×10^9 | M_{dust} and dust to M_{H_2} ratio for spirals |

estimated mass is consistent with the upper limit $M_{\text{HI}}^{\text{tot}} < 7 \times 10^8 M_\odot$ obtained from 21-cm observations (Bottinelli et al. 1980; Sharples et al. 1984). Using $\log L_B = 10.23$ (Tully 1988), and our estimate of M_{H_2} , we get a neutral hydrogen content of $\log(M_{\text{HI}}/L_B) = -1.8$, which is much lower than the value -0.55 ± 0.41 expected for an S-type galaxy (Haynes & Giovanelli 1984).

3.2 Radial luminosity profiles

The light distribution of normal spiral galaxies can be divided into two distinct components, a bulge and a disc. The

radial luminosity profile across the bulge can usually be represented by a de Vaucouleurs model with the intensity distribution $I_{\text{bulge}} \propto 10^{-(r/r_b)^{1/4}}$, where r_b is the effective radius. The radial profile across the disc is taken to be exponential with scalelength r_d , so that $I_{\text{disc}} \propto e^{-r/r_d}$ (Mihalas & Binney 1981). Spiral arms in the galaxy induce fluctuations about the mean value in the profile, which average out when one goes far out in radial distance. In the case of Seyferts, the active nucleus at the centre contributes an unresolved source to the profile.

We have modelled the observed radial profile of NGC 7172 with bulge, disc and point-source components by constructing model galaxies with the three components, and convolving these with a PSF estimated from foreground stars in the frame of the galaxy. The intensity profile of such a model galaxy is defined by seven parameters: the effective radius of the bulge r_b , the disc scalelength r_d , the central bulge luminosity per square arcsec $\mu_B(0)$, the ratio of the disc luminosity to bulge luminosity D/B , the ratio of the point source luminosity to the bulge luminosity P/B , and the ellipticity e_b and e_d of the bulge and disc respectively. The best-fitting values for the seven parameters were obtained from the observed intensities along the major axis, using the method of least squares.

The observed profile and the best fits in B filter are shown in Fig. 4, and the values of the fitted parameters are tabulated in Table 4. The χ^2 values are 1.8 for the B profile and 2.0 for

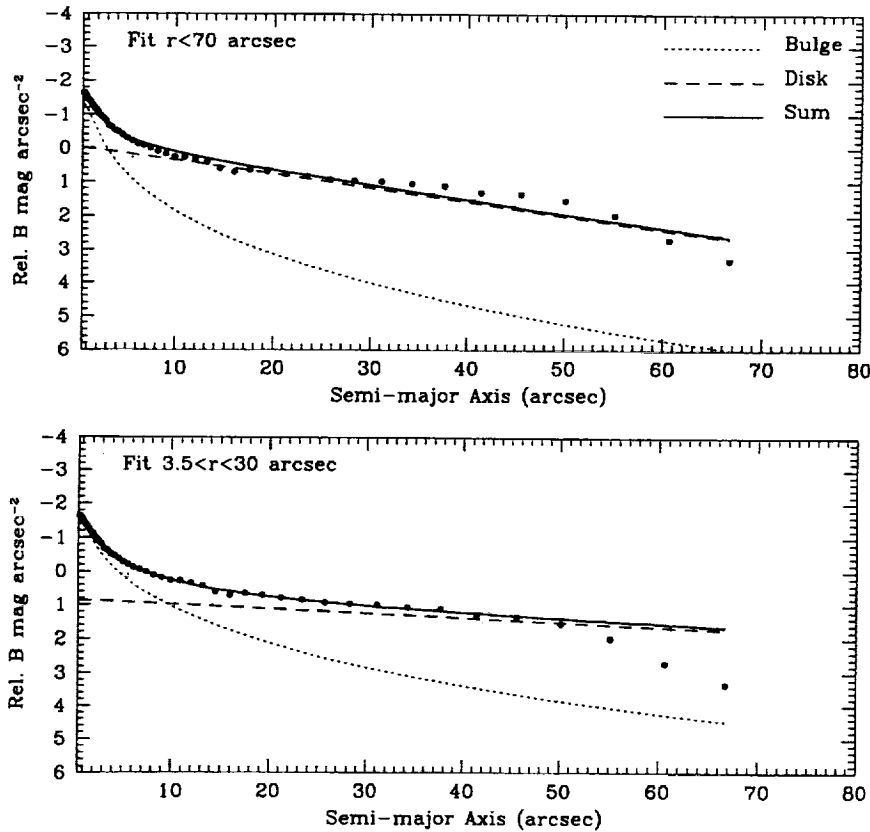


Figure 4. Radial luminosity profiles in B filter, with the best fits to the bulge and disc components. Top panel: fit range $r < 70$ arcsec. Bottom panel: fit range $3.5 < r < 30$ arcsec.

Table 4. Best-fitting parameters for radial luminosity profile.

| Filter | r_b'' | r_d'' | $\mu_b(0)^\dagger$ | D/B | P/B^* | e_b | e_d | Source |
|--------|---------|---------|--------------------|-------|---------|-------|-------|------------------------|
| B | 22.6 | 26.5 | 17.3 | 9.2 | | 0.04 | 0.45 | This Work ¹ |
| V | 18.9 | 23.7 | 15.9 | 7.2 | | 0.04 | 0.45 | |
| B | 29.0 | 9.1 | | 4.4 | 33.5 | | | KWW |
| V | 23.5 | 10.3 | | 5.9 | 35.8 | | | |
| B | 29.0 | 53.6 | 17.6 | 11.1 | | 0.04 | 0.47 | This Work ² |

[†]mag arcsec⁻².^{*}< 3 arcsec.¹Fit range $r < 70$ arcsec.²Fit range $3.5 < r < 30$ arcsec.

the V profile. The nuclear point source is not detected by the fitting routine. This is probably due to obscuration of the nucleus by the dust lane, and also poor seeing conditions. The fit was repeated with only five parameters, keeping e_b and e_d fixed. This does not change either the χ^2 or the values of the fitted parameters significantly, and the nuclear source still remains undetected. We also give in Table 4 the best-fitting values obtained by KWW.

The disc scalelength estimated by us is a factor 2–3 larger than the estimate of KWW, while the bulge scalelength is comparable. Also, the D/B obtained by us is higher than their value due to the fact that we estimate a larger disc. We note that the disc length obtained by us is dominated by the outer radii beyond 30 arcsec, and this region is not used in the profile fit made by KWW. To see whether we can reproduce the bulge and disc parameters obtained by them, we have obtained a fit using the observed radial profile for $3.5 < r < 30$ arcsec, which omits the central region influenced by a possible point source, and at the large- r end extends only to the limit covered by KWW. We omit the central region since the point source is undetected, and also because the bulge scalelength is dominated by points at $r > 3.5$ arcsec. The fit, which has a χ^2 value 0.07, is shown in Fig. 4. While it is excellent over the range of points used, the observed points at larger radii lie substantially below the fit. This produces a bulge scalelength similar to the previous estimate as well as KWW, while the disc scalelength is different. The reason for this discrepancy is not clear to us, and it could indicate that the model used by us (and KWW) is not applicable.

4 DISCUSSION

NGC 7172 appears as a far-infrared (FIR) source in the *IRAS* catalogue (Knapp et al. 1989). Also, CO emission has been detected by Heckman et al. (1989). We discuss in this section the properties of the dust based on the published FIR and CO fluxes. We also discuss the morphology of the galaxy based on the estimates of neutral and molecular hydrogen content, and the bulge and disc scalelengths obtained from surface photometry.

4.1 Far-infrared emission and dust content

The FIR fluxes at 12-, 25-, 60- and 100- μ m bands are 0.4374 ± 0.03 , 0.7612 ± 0.05 , 5.712 ± 0.3 and 12.29 ± 0.61

Jy respectively (Knapp et al. 1989). The FIR ratio F_{60}/F_{100} implies a dust temperature $T_d \sim 36$ K. The total FIR flux, estimated from the fluxes in 60 and 100 μ m using

$$F_{\text{FIR}} = 1.26(2.58F_{60} + F_{100}) \times 10^{-14} \text{ W m}^{-2}$$

(Heckman et al. 1989), is $F_{\text{FIR}} = 3.4 \times 10^{-13} \text{ W m}^{-2}$, and the total FIR luminosity is $L_{\text{FIR}} = 1.2 \times 10^{10} L_\odot$.

The dust temperature in NGC 7172 is similar to that of the general population of dust lane E/S0 galaxies (Brosch 1987). Furthermore, the FIR ratios $\log(F_{12}/F_{25}) = -0.24$ and $\log(F_{60}/F_{100}) = -0.33$ place the galaxy at an intermediate position between galaxies in which the cool component is important and those where OB star formation is responsible for heating the dust. This implies that a minor fraction of the FIR emission is due to Galactic cirrus, while a major fraction of the emission is due to heating of dust by young stars, indicating ongoing star formation, and also due to heating of dust by the central active nucleus.

The total dust mass estimated from the 100- μ m flux and using the relation by Bothun, Lonsdale & Rice (1989),

$$M_d = 5D_{\text{Mpc}}^2 F_{100} [\exp(144/T_d) - 1] M_\odot,$$

is $M_d = 3.8 \times 10^6 M_\odot$. Using the relation by Thronson et al. (1988),

$$M_d = 11D_{\text{Mpc}}^2 F_{100} [\exp(96/T_d) - 1] M_\odot,$$

we estimate $M_d = 2.1 \times 10^6 M_\odot$. These estimates are similar to the dust mass estimated using our optical data, in Section 3.1.1, and are listed in Table 3.

Young et al. (1986) find the molecular hydrogen to dust mass ratio to be ~ 500 for spiral galaxies. Using this, we have

$$M_{\text{H}_2} = 1.6 \times 10^9 M_\odot.$$

The molecular hydrogen mass may be obtained independently from CO luminosity (Young et al. 1986):

$$M_{\text{H}_2} = 6 \times 10^6 L_{\text{CO}} M_\odot,$$

where L_{CO} is in $\text{K km s}^{-1} \text{ kpc}^2$. With this relation and $L_{\text{CO}} = 0.44 \times 10^3 \text{ K km s}^{-1} \text{ kpc}^2$ (Heckman et al. 1989), we have

$$M_{\text{H}_2} = 2.6 \times 10^9 M_\odot.$$

This is in good agreement with the *IRAS*-derived M_{H_2} . The total gas content in NGC 7172, $M_{\text{H}_1} + M_{\text{H}_2}$, is therefore $M_{\text{gas}} \sim 2.3 \times 10^9 M_\odot$, with M_{H_1} from Section 3.1.2 and M_{H_2} taken to be the mean of the values obtained from *IRAS* and CO measurements.

4.2 Morphology

NGC 7172 is classified as Sa(pec) (de Vaucouleurs et al. 1976). The neutral hydrogen mass estimated from 21-cm line observations and the optical extinction give a neutral hydrogen content $-1.8 \leq \log(M_{\text{H}_1}/L_B) \leq -1.4$. The neutral hydrogen content in Sa galaxies is $\log(M_{\text{H}_1}/L_B) = -0.55 \pm 0.41$, while in E and S0 galaxies it is $\log(M_{\text{H}_1}/L_B) = -0.74 \pm 0.37$ (Haynes & Giovanelli 1984). The estimated value of $\log(M_{\text{H}_1}/L_B)$ in NGC 7172 is much less than the observed values for S0 galaxies, which implies that the galaxy could be an elliptical. However, radial luminosity profile fits give a bulge scalelength $r_b = 3.0 \pm 0.3 \text{ kpc}$, and a disc scalelength $r_d = 4.0 \pm 0.3 \text{ kpc}$. These values fall well within the range of scalelengths of

S0/Sa galaxies (Mihalas & Binney 1981). It thus appears that NGC 7172 is H_I-depleted.

The molecular hydrogen in atomic hydrogen mass ratio is $M_{\text{H}_2}/M_{\text{H}_1} \sim 3-8$. This value is similar to that seen in S0/Sa galaxies, for which $M_{\text{H}_2}/M_{\text{H}_1} = 4.0 \pm 1.9$ (Young & Scoville 1991).

5 CONCLUSIONS

We draw the following conclusions.

(1) The neutral hydrogen mass in NGC 7172 estimated based on the optical extinction in the dust lane is $M_{\text{H}_1} = 2.6 \times 10^8 M_\odot$. This value is consistent with the upper limits obtained from 21-cm line estimates.

(2) The FIR fluxes imply a dust temperature $T_d \sim 36$ K, and a dust mass $M_d = 3.0 \times 10^6 M_\odot$. The mass of molecular hydrogen estimated based on the dust mass, and also using the CO luminosity, is $M_{\text{H}_2} = 2.1 \times 10^9 M_\odot$.

(3) The total gas content in NGC 7172, $M_{\text{H}_1} + M_{\text{H}_2}$, is $\sim 2.3 \times 10^9 M_\odot$.

(4) The neutral hydrogen content $-1.8 \leq \log(M_{\text{H}_1}/L_B) \leq -1.4$, molecular hydrogen to atomic hydrogen mass ratio $M_{\text{H}_2}/M_{\text{H}_1} \sim 3-8$ and the bulge and disc scalelengths $r_b = 3.0 \pm 0.3$ kpc, $r_d = 4.0 \pm 0.3$ kpc, together indicate a morphological type S0-Sa for the galaxy.

ACKNOWLEDGMENTS

We thank M. Ward and A. Lawrence for assistance in taking CCD data. We are also grateful to T. P. Prabhu, K. P. Singh and M. Valluri for several valuable discussions. IRAF is distributed by the National Optical Astronomy Observatories, which is operated by the Association of Universities, Inc. (AURA) under cooperative agreement with the National Science Foundation. The Space Telescope Science Data Analysis System STSDAS is distributed by the Space Telescope Science Institute. This research has made use of the NASA/IPAC Extragalactic Database (NED), which is operated by the Jet Propulsion Laboratory, Caltech, under contract with the National Aeronautics and Space Administration.

REFERENCES

- Adams T. F., 1977, *ApJS*, 33, 19
 Baum S., Heckman T. M., 1989, *ApJ*, 336, 681
 Begelman M. C., 1985, *ApJ*, 297, 492
 Bothun G. D., Lonsdale C. J., Rice W., 1989, *ApJ*, 341, 129
 Bottinelli L., Gouguenheim L., Paturel G., 1980, *A&A*, 88, 32
 Brindle C., Hough J. H., Baily J. A., Axon D. J., Ward M. J., Sparks W. B., Mclean I. S., 1990, *MNRAS*, 244, 604
 Brosch N., 1987, *MNRAS*, 225, 40
 Burstein D., Heiles C., 1978, *ApJ*, 251
 de Vaucouleurs G., de Vaucouleurs A., Corwin H. G., 1976, Second Reference Catalogue of Bright Galaxies. Univ. Texas, Austin
 Elvis M., Lockman F. J., Wilkes B. J., 1989, *AJ*, 97, 777
 Graham J. A., 1982, *PASP*, 92, 244
 Hamuy M., Maza J., 1987, *A&AS*, 68, 283
 Haynes M. P., Giovanelli R., 1984, *AJ*, 89, 758
 Heckman T. M., Blitz L., Wilson A. S., Armus L., Miley G. K., 1989, *ApJ*, 342, 735
 Hickson P., 1982, *ApJ*, 255, 382
 Jedrzejewski R. I., 1987, *MNRAS*, 226, 747
 Knapp G. R., Guhathakurta P., Kim D.-W., Jura M., 1989, *ApJS*, 70, 329
 Kotilainen J. K., Ward M. J., 1994, *MNRAS*, 266, 953
 Kotilainen J. K., Boisson C., Depoy D. L., Bryant L. R., Smith M. G., 1992a, *MNRAS*, 256, 125
 Kotilainen J. K., Ward M. J., Boisson C., Depoy D. L., Smith M. G., 1992b, *MNRAS*, 256, 149
 Kotilainen J. K., Ward M. J., Williger G. M., 1993, *MNRAS*, 263, 655 (KWW)
 MacKenty J. W., 1990, *ApJS*, 72, 231
 Mayya Y. D., 1993, PhD thesis, Indian Institute of Science, Bangalore
 Mihalas D., Binney J., 1981, *Galactic Astronomy*, 2nd edn. W. H. Freeman & Co., San Francisco
 Piccinotti G., Mushotzky R. F., Boldt E. A., Holt S. S., Marshall E. E., Serlemitsos R. J., Shafer R. A., 1982, *ApJ*, 253, 485
 Roche P. F., Aitken D. K., Smith C. H., Ward M. J., 1991, *MNRAS*, 248, 606
 Savage B. D. & Mathis J. S., 1979, *ARA&A*, 17, 73
 Shanbhag S., Kembhavi A. K., 1988, *ApJ*, 334, 34
 Sharples R. M., Longmore A. J., Hawarden T. G., Carter D., 1984, *MNRAS*, 208, 15
 Simkin S. M., Su H. J., Schwarz M. P., 1980, *ApJ*, 237, 404
 Storchi-Bergmann T., Mulchaey J. S., Wilson A. S., 1992, *ApJ*, 395, L73
 Thronson H., Hunter D. A., Telesco C., Greenhouse M., Harper D., 1988, *ApJ*, 334, 605
 Tully B., 1988, *Nearby Galaxies Catalog*. Cambridge Univ. Press, Cambridge
 Turner T. J., Pounds K. A., 1989, *MNRAS*, 240, 833
 Unger S. W., Pedlar A., Axon D. J., Whittle M., Meurs E. J. A., Ward M. J., 1987, *MNRAS*, 228, 671
 Warwick R. S., Sembay S., Yaqoob T., Makishima K., Ohashi T., Tashiro M., Kohmura Y., 1993, *MNRAS*, 265, 412
 Wilson A. S., 1992, in Duschl W. J., Wagner S. J., eds, *Physics of Active Galactic Nuclei*. Springer-Verlag, Berlin, p. 307
 Yee H. K. C., 1983, *ApJ*, 272, 473
 Young J. S., Scoville N. Z., 1991, *ARA&A*, 29, 581
 Young J. S., Schloerb F. P., Kenney J. D., Lord S. D., 1986, *ApJ*, 304, 445

AN ASCA GIS SPECTRUM OF S5 0014+813 AT $z = 3.384$

MARTIN ELVIS,¹ M. MATSUOKA,² A. SIEMIGINOWSKA,¹ F. FIORE,^{1,3} T. MIHARA,² AND W. BRINKMANN⁴

Received 1994 May 27; accepted 1994 August 26

ABSTRACT

ASCA has detected the $z = 3.384$ quasar S5 0014+813 up to energies of 34 keV in the quasar rest frame using the two GIS instruments. The combined X-ray spectrum has a signal-to-noise ratio of over 50σ and is consistent with a single power law of energy slope 0.63 ± 0.03 over the 0.8–8 keV (observed) energy range. The spectrum is also well fitted with a simple thermal bremsstrahlung model of $kT = 40 \pm 4$ keV (in the quasar frame), which raises obvious possibilities for contributions to the diffuse X-ray background.

A maximum solid angle of $\Omega_d/2\pi = 0.4$ (90% confidence) can be placed on the strength of a Compton reflection component above the energy of the Fe K-edge. The Fe K 6.4 keV fluorescence line has a rest frame equivalent width < 120 eV (90% confidence) at its redshifted energy of 1.46 keV. The weakness of these features differentiates this high-luminosity, high-redshift quasar from the majority of Seyfert galaxies using its X-ray spectrum alone. The GIS slope is consistent with the slope derived by the *ROSAT* PSPC. The normalization at 1 keV in the *ASCA* observation is, however, a factor 30%–40% higher than in the *ROSAT* observation, suggesting a significant increase in the 1 keV (observed) flux over the 31.5 months between the two observations (7.2 months, rest frame).

Subject headings: diffuse radiation — galaxies: active — quasars: general —
 quasars: individual (S5 0014+813)

1. INTRODUCTION

X-ray observations of AGNs are heavily biased toward X-ray-loud objects of low redshift and moderate luminosity (Elvis 1991). Moreover, these X-ray spectra tend to be taken at low energies, less than ~ 3 keV for *Einstein* (Shastri et al. 1993) and *ROSAT* spectra (Walter & Fink 1993; Fiore et al. 1994; Laor et al. 1994), and less than ~ 10 keV for *Ginga* spectra (Williams et al. 1992; Lawson et al. 1992). Naturally we would like to know the form of AGN spectra at higher energies and how the many features seen in the low-redshift, low-luminosity AGNs extrapolate to extreme examples of the AGN population.

ROSAT PSPC spectra have allowed some determination of spectral slopes for quasars at high redshift and luminosity (Elvis et al. 1994a; Bechtold et al. 1994) in the 1–10 keV emitted range. Unfortunately, the common low-energy cutoff discovered with the PSPC, due possibly to absorption, leads to poorly determined slopes (Elvis et al. 1994a).

ASCA (Tanaka, Holt, & Inoue 1994) now provides the sensitivity to explore higher energies for the brightest quasars at $z \sim 3$. The *ASCA* Gas Imaging Spectrometer (GIS; Maki-shima et al. 1994) instruments, in particular, are able to determine spectral slopes over the 3–8 keV and 8–30 keV emitted energy ranges to good accuracy. These energy ranges are optimal for setting constraints on Fe K fluorescence emission and on Compton reflection components (Lightman & White 1988; Guilbert & Rees 1988) which begin above 8 keV in the rest frame.

Accordingly we observed S5 0014+813 with *ASCA*. This is a $z = 3.384$ quasar (Kühr et al. 1983) and is among the highest X-ray flux quasars known with $z \sim 3$. Indeed, it is the only $z \sim 3$ quasar to have a 2–10 keV spectrum reported by *EXOSAT* (Lawson et al. 1992).

2. ASCA GIS OBSERVATIONS OF S5 0014+813

The quasar was observed on 1993 October 29 for a total good exposure time of 31.5 ks in both GIS2 and GIS3. We applied the standard conservative data filters: a minimum elevation angle of 15° above Earth's limb, and a minimum cutoff rigidity of $8 \text{ GeV } c^{-1}$. We also excluded data acquired in the first 60 s following each passage through the SAA. The source was readily apparent in the center of the GIS field of view, and the source centroid is $1.5'$ from the optical position, an offset typical of *ASCA* data at present. A total of 2904 and 3244 counts were recorded within a $6'$ radius circle centered on the quasar in GIS2 and GIS3, respectively.

The background within the source extraction region was estimated in two ways:

1. The backgrounds were taken from annuli of inner and outer radii between $10'$ and $17'$.

2. Background events were extracted from the same region as the source events in blank sky background event files, provided by the *ASCA* Guest Observer Facility (the files being a superposition of 15 blank sky fields observed during the *ASCA* PV phase [1993 May–1994 March] with a total exposure time of 350 ksec), for the same values of cutoff rigidity ($> 8 \text{ GeV } c^{-1}$) used for the source events.

The former background was significantly smaller than the latter (by a factor ~ 0.75) as expected due to the vignetting of the XRT. In the following we present the results obtained with the second background subtraction method. We point out, however, that the shapes of the spectra obtained with the two

¹ Harvard-Smithsonian Center for Astrophysics, 60 Garden Street, Cambridge, MA 02138. E-mail: elvis@cfa.harvard.edu

² RIKEN, the Institute of Physical and Chemical Research, Wako, Saitama, Japan.

³ Osservatorio Astronomico di Roma, via dell'Osservatorio 5, Monteporzio-Catone (RM), I00040 Italy.

⁴ Max-Planck Institut für Extraterrestrische Physik, W-8046, Garching bei München, Germany.

TABLE 1
ASCA OBSERVATIONS OF S5 0014+813

| Instrument | Counts | Exposure (s) | Background (counts) | Net Counts s^{-1} |
|------------|--------|--------------|---------------------|---------------------|
| GIS2 | 2904 | 31635 | 800 | 0.066 |
| GIS3 | 3244 | 31500 | 860 | 0.075 |

methods agree to within $\sim 3\%$. The total background is $\sim 40\%$ of the source counts, leading to a total of about 2200 net counts and a 40σ spectrum of S5 0014+813 in each GIS (Table 1). The ASCA point-spread function (PSF) in the GIS puts $\sim 10\%$ of the flux of a point source with a spectrum similar to that of S5 0014+813 outside the $6'$ radius used here. All reported fluxes are corrected for this. Fluxes are not corrected for dead-time effects. The highest energy at which the quasar is detected at the 3σ level is 7.7 keV (bin width of 0.3 keV), which corresponds to 34 keV in the emitted frame.

A complication is the presence of two sources in the ROSAT PSPC image within $6'$ of the quasar. In the ROSAT band, the count rate of these sources represents 90% of that of the quasar. The brighter source (80% of S5 0014+813), $5'$ from the quasar, is probably identified with a $V = 8.8$ K0 star (HD 1165, SAO 44, PSPC offset = $9''$). The fainter source (10% of S5 0014+813), only $1.5'$ from the quasar, is unidentified. It has a PSPC hardness ratio $[R = (H - S)/(H + S) = 0.76 \pm 0.36]$, where S is the 0.1–0.4 keV band and H is the 0.4–2.4 keV band] similar to the quasar, suggesting that it is outside the substantial Galactic N_H (14.4×10^{20} atoms cm^{-2} ; Stark et al. 1989) in this direction. HD 1165 is detected in the ASCA SIS0 image of the field (Elvis et al. 1994b). Its count rate is about 10% of that of the quasar in the 0.8–2 keV band and is only 2% in the 2–8 keV band. We shall assume the contribution from

these two sources is negligible, but this caveat should be borne in mind.

3. SPECTRAL FITS

In all spectral fits we used the response matrices “g2v3_1_4c” (1994 April 20) provided by the ASCA Guest Observer Facility. Note that, because of the small count rates, statistical errors dominate over systematic errors from the two instrumental responses. The results of all fits are given in Table 2.

A single power-law fit gave no significant evidence of excess absorption in either GIS, so we fixed N_H to the Galactic value. The GISs are not sensitive to column densities smaller than 10^{21} atoms cm^{-2} in any case. For a power law, the two instruments agree well (to 20% in normalization, 2% in slope), and both give good χ^2 , so we made a simultaneous joint fit (letting the normalization in the two instruments be free to vary). This gave an energy slope of 0.63 ± 0.05 , consistent with the ROSAT PSPC slope of 0.8 ± 0.2 (assuming Galactic N_H). Adding the PSPC spectra simultaneously gives the same results. Allowing an extra absorption component at the quasar redshift gives a 90% upper limit to the intrinsic absorption is 2.6×10^{22} atoms cm^{-2} . Figures 1 and 2 show the fit and residuals to all three data sets.

A thermal bremsstrahlung spectrum fitted the joint GIS data just as well as a power law. Such a fit is constrained on both sides and gives a rest frame temperature of 39 ± 4 keV. This is a temperature of some interest.

More complex spectra are not required. To investigate the presence of curvature we fitted a power law to the PSPC-GIS data above and below 2 keV (8.8 keV in the quasar frame) separately. No slope change is seen greater than 0.2 (1 σ). A complete Compton reflection model fit to the GIS data using a cold flat disk for the reflector gave a 90% upper limit (for two

TABLE 2
GIS ASCA POWER-LAW SPECTRAL FITS FOR S5 0014+813

| Instruments | Energy range (keV) | N_H (10^{22} atoms cm^{-2}) | α_E , or kT^a [$\Omega_e/2\pi$] | Normalization (10^{-4} keV s^{-1} cm^{-2} keV $^{-1}$) | $\chi^2(dof)$ |
|------------------------|--------------------|-------------------------------------|--|--|---------------|
| Power-Law | | | | | |
| GIS2 | 0.8–8 | 0.22 ± 0.12 | 0.69 ± 0.14 | 6.1 ± 1.0 | 78.1 (58) |
| GIS2 | 0.8–8 | 0.144FIX | 0.62 ± 0.05 | 5.5 ± 0.3 | 79.1 (59) |
| GIS3 | 0.8–8 | 0.23 ± 0.12 | 0.72 ± 0.13 | 7.3 ± 1.2 | 49.2 (67) |
| GIS3 | 0.8–8 | 0.144FIX | 0.63 ± 0.05 | 6.5 ± 0.3 | 50.4 (68) |
| GIS2+3 | 0.8–8 | 0.22 ± 0.09 | 0.70 ± 0.09 | ... | 127.5 (127) |
| GIS2+3 | 0.8–8 | 0.144FIX | 0.63 ± 0.03 | ... | 129.5 (128) |
| PSPC+GIS2+3 | 0.2–8 | 0.144FIX | 0.63 ± 0.05 | ... | 149.8 (147) |
| | | $0+2.0^b$ | | | |
| PSPC+GIS2+3 | 0.2–2 | 0.144FIX | 0.67 ± 0.17 | ... | 65.0 (55) |
| GIS2+3 | 2–8 | 0.144FIX | 0.68 ± 0.05 | ... | 81.9 (88) |
| Thermal Bremsstrahlung | | | | | |
| PSPC+GIS2+3 | 0.2–8 | 0.144FIX | $38.9^{+4.1}_{-3.5}$ | ... | 149.6 (148) |
| GIS2+3 | 0.8–8 | 0.144FIX | $39.6^{+4.3}_{-3.6}$ | ... | 125.6 (128) |
| Reflection | | | | | |
| PSPC+GIS2+3 | 0.8–8 | 0.144FIX | 0.63 ± 0.03 [0.0 + 0.3] | ... | 149.8 (147) |
| GIS2+3 | 0.2–8 | 0.144FIX | 0.62 ± 0.03 [0.0 + 0.4] | ... | 129.5 (127) |

^a In keV, in quasar rest frame, for thermal Bremsstrahlung fits.

^b Column at $z = 3.38$.

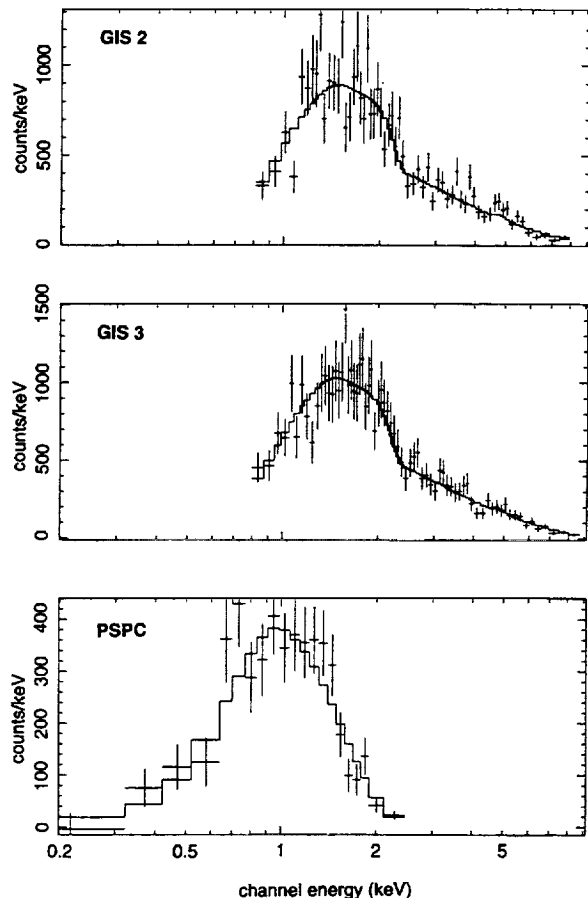


FIG. 1.—*ASCA* GIS + PSPC X-ray spectra of S5 0014+813. The solid line shows the best-fit single power-law model fitted from 0.2 to 8 keV. Energies are in the observed frame.

interesting parameters) of $\Omega_d/2\pi = 0.4$ to the solid angle subtended by the disk. (Adding the PSPC data tightened this limit slightly to 0.3.) None of the fits is improved by an Fe K fluorescence line at 6.4 or 6.7 keV (emitted, 1.46 keV; 1.53 keV, observed, respectively; $\Delta\chi^2 < 1$). A 90% upper limit to the equivalent width for an intrinsically narrow line at 1.46 keV is 27 eV (observed frame, 120 eV emitted). The 90% limit for a narrow line at 1.53 keV is EW = 31 eV (EW = 140 eV, quasar frame).

The mean GIS normalization for a power-law fit, when corrected for the PSF loss, is a factor 1.4 above that of the *ROSAT* data and suggests variability in the 31.5 months between the two observations (7.2 months in the quasar frame). If this light-travel time radius corresponds to 10 Schwarzschild radii, then $M < 4 \times 10^{11} M_\odot$. The *EXOSAT* 1 keV normalization is close to the PSPC value and the *EXOSAT* slope (0.9 ± 0.4) is fully consistent with both the *ASCA* GIS and PSPC values (see Bechtold et al. 1994).

The flux of S5 0014+813 in the 1–8 keV observed band is 3.2×10^{-12} ergs s $^{-1}$ cm $^{-2}$, which corresponds to a 4–30 keV luminosity of 1.1×10^{48} ergs s $^{-1}$, about 2.5 times greater than the inferred *ROSAT* rest frame luminosity of 4.4×10^{47} ergs s $^{-1}$, (the GIS 2–10 keV luminosity is 6.2×10^{47} ergs s $^{-1}$) for $H_0 = 50$ km s $^{-1}$ Mpc $^{-1}$, and $\Omega = 0$. The GIS X-ray luminosity requires a central black hole mass $\sim 10^{10} M_\odot$ in order

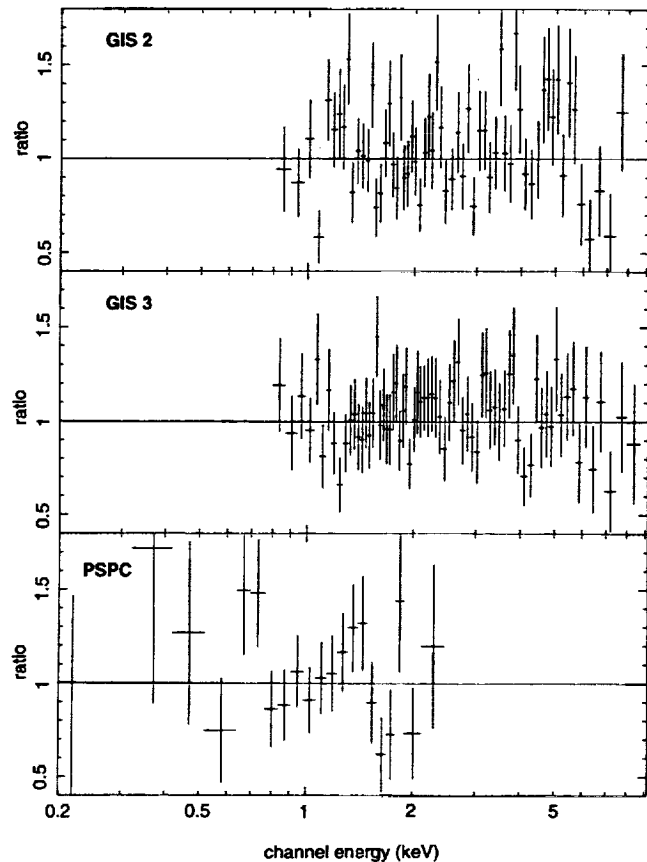


FIG. 2.—Residuals after subtracting the best-fitting 0.2–8 keV power law from the *ASCA* GIS and PSPC spectra of S5 0014+813. Energies are in the observed frame.

not to violate the Eddington limit, which does not conflict with the variability limit. If the bolometric luminosity could be used, then the two limits would become very close.

4. DISCUSSION AND CONCLUSIONS

We have detected a $z = 3.384$ quasar up to 34 keV in the quasar frame with the *ASCA* GIS. With a S/N of $\sim 50 \sigma$ the GIS measurements of high-redshift quasars currently give us, paradoxically, our best measurements of quasar spectra above 10 keV⁵ and approach the quality of spectra for bright Seyfert galaxies from *Ginga*.

A thermal bremsstrahlung fit gives a temperature of 39 ± 4 keV (quasar frame). Similar temperatures were reported to two other high- z quasars by Serlemitsos et al. (1994), unfortunately without quoted uncertainties. The closeness of these three temperatures to the X-ray background temperature (40 ± 5 keV; Marshall et al. 1980) is remarkable. Superficially it suggests that AGNs produce the X-ray background. Radio-loud, $z = 3$

⁵ The only other quasar with a high S/N spectrum above 10 keV (emitted) was 3C 273 (Turner et al. 1990). However, an observation of a transient source of equal or greater strength to 3C 273 at 60 keV only 15' from 3C 273 (GRS 1227+025; Bassani et al. 1991) puts in doubt the reliability of the large-beam *Ginga* measurement.

quasars such as those observed with *ASCA* cannot themselves produce the XRB, being too rare and redshifted down to $kT \sim 10$ keV. However, *OSSE* also gives a temperature of ~ 45 keV (Johnson et al. 1994) for low- z AGNs. That AGNs from opposite ends of the luminosity, redshift, and radio-loudness scales gives the same temperature suggests a remarkably uniform process at work, such as the Klein-Nishina cross section, and may allow the background spectrum to be produced by AGNs.

A power-law fit gives a slope $\alpha_E = 0.63 \pm 0.03$ and needs no additional components down to quite tight limits: a Lightman & White (1988) Compton reflection component is not required and the 90% limit to the solid angle subtended by the disk is $\Omega_d/2\pi = 0.4$; a narrow 6.4 keV (rest frame) iron line is not required by the fit either, and the 90% limit on its rest frame equivalent width is 120 eV. This is strikingly similar to the unusual Seyfert NGC 4151 (Yaqoob et al. 1993) and differentiates S5 0014+813 from typical low-redshift Seyfert galaxies which have strong iron K-lines ($EW = 100\text{--}300$ eV), and a strong Compton hump ($\Omega_d/2\pi \approx 1$; Nandra & Pounds 1994 and references therein). Williams et al. (1992) found these features to be weak in high-luminosity, radio-loud AGNs. S5

0014+813 strengthens this trend. Zdziarski, Życki, & Krolik (1993) use a strong reflection component in AGNs to integrate over redshift to produce the X-ray background. Not seeing a reflection hump in S5 0014+813 detracts from this model.

ASCA has demonstrated an ability to produce good spectra of quite faint quasars. This should be exploited for more high-redshift quasars, particularly radio-quiet quasars and quasars at redshifts more likely to dominate the X-ray background. We also note that even in the lower (rest frame) energy range of 2–10 keV there are only about 20 good S/N quasar spectra, all from *Ginga* (Williams et al. 1992). Here *ASCA* is ideally placed to obtain high-quality spectra. Even short *ASCA* observations of bright low-redshift quasars will dramatically improve our basic knowledge of quasars.

We thank Smita Mathur for identifying the K0 star. We thank Keith Gendreau and the staff of the *ASCA* GOF at GSFC for their assistance with the data reduction. The spectral analysis was performed using XSPEC, and the data were extracted using XSELECT; both packages were provided by the *ASCA* GOF. This work was supported by NASA grants NAGW-2201 (LTSA) and NAG 5-2563 (*ASCA*).

REFERENCES

- Bassani, L., et al. 1991, 22d Internat. Cosmic-Ray Conference (Dublin), 1, 173
 Bechtold, J., et al. 1994, *AJ*, 108, 374
 Elvis, M. 1991, in *Frontiers of X-Ray Astronomy*, ed. Y. Tanaka & K. Koyama (Tokyo: Universal Academic), 567
 Elvis, M., Fiore, F., Wilkes, B. J., McDowell, J. C. M., & Bechtold, J. 1994a, *ApJ*, 422, 60
 Elvis, M., et al. 1994b, in preparation
 Fiore, F., Elvis, E., Siemiginowska, A., Wilkes, B. J., & McDowell, J. C. 1994, *ApJ*, 431, 515
 Guilbert, P. W., & Rees, M. J. 1988, *MNRAS*, 233, 475
 Johnson, W. N., et al. 1994, in *Proc. 2nd Compton Symp.*, ed. C. E. Fichtel, N. Gehrels, & J. P. Norris (New York: AIP), 515
 Kühr, H., Witzel, A., Pauliny-Toth, I. I. K., & Nauber, U. 1981, *A&AS*, 45, 367
 Laor, A., Fiore, F., Elvis, E., Wilkes, B. J., & McDowell, J. C. 1994, *ApJ*, 435, 611
 Lawson, A. J., Turner, M. J. L., Williams, O. R., Stewart, G. C., & Saxton, R. D. 1992, *MNRAS*, 259, 743
 Lightman, A. P., & White, T. R. 1988, *ApJ*, 335, 57
 Makishima, K., et al. 1994, *PASJ*, in press
 Marshall, F. E., et al. 1980, *ApJ*, 235, 4
 Nandra, K., & Pounds, K. A. 1992, *Nature*, 356, 215
 ———. 1994, *MNRAS*, 268, 405
 Serlemitsos, P., Yaqoob, T., Ricker, G., Woo, J., Kunieda, H., Terashima, Y., & Iwasawa, K. 1994, *PASJ*, 46, L43
 Shastri, P., Wilkes, B. J., Elvis, M., & McDowell, J. C. 1993, *ApJ*, 410, 29
 Stark, A. A., Gammie, C. F., Wilson, R. W., Bally, J., Linke, R., Heiles, C., & Hurwitz, M. 1989, *ApJS*, 79, 77
 Tanaka, Y., Holt, S. S., & Inoue, H. 1994, *PASJ*, 46, L37
 Turner, M. J. L., et al. 1990, *MNRAS*, 244, 310
 Williams, O. R., et al. 1992, *ApJ*, 389, 157
 Walter, R., & Fink, H. H. 1993, *A&A*, 274, 105
 Yaqoob, T., Warwick, R. S., Makino, F., Otani, C., Sokoloski, J. L., Bond, I. A., & Yamauchi, M. 1993, *MNRAS*, 262, 435
 Zdziarski, A. A., Życki, P. T., & Krolik, J. H. 1993, *ApJ*, 414, L81

GALACTIC H I COLUMN DENSITIES TOWARD QUASARS AND ACTIVE GALACTIC NUCLEI

EDWARD M. MURPHY

University of Virginia and National Radio Astronomy Observatory,¹ 520 Edgemont Road, Charlottesville, VA 22903

FELIX J. LOCKMAN

National Radio Astronomy Observatory, Green Bank, WV 24944

ARI LAOR

Physics Department, Technion, Haifa 32000, Israel

AND

MARTIN ELVIS

Harvard-Smithsonian Center for Astrophysics, Cambridge, MA 02138

Received 1995 November 16; accepted 1996 January 5

ABSTRACT

We have determined accurate values of the Galactic neutral hydrogen column density, N_{H} , toward 220 quasars and active galactic nuclei from 21 cm H I measurements made on the 140 Foot Telescope (42.7 m). Accurate values of N_{H} have now been obtained for the whole PG bright quasar sample and most quasars that have been observed by *ROSAT* and the *Hubble Space Telescope* through mid-1993. The spectra were corrected for stray 21 cm radiation yielding values of N_{H} with a typical uncertainty of $1 \times 10^{19} \text{ cm}^{-2}$ for high Galactic latitude directions. The H I column densities will be useful for correcting for interstellar opacity at UV and soft X-ray wavelengths, and for estimating the reddening and extinction toward these objects.

Subject headings: Galaxy: structure — radio lines: ISM — X-rays: general

1. INTRODUCTION

It is crucial to make an accurate correction for absorption in the interstellar medium (ISM) of the Milky Way when interpreting soft X-ray and ultraviolet observations of active galactic nuclei (AGNs) and quasars. The spectral shape of the X-ray “soft excess” seen in the spectra of quasars, for example, depends heavily on the amount of Galactic absorption. In fact, the uncertainty in Galactic absorption limits the extent to which models of accretion disk emission can be tested. For most high Galactic latitude directions, the absorption at soft X-ray and UV wavelengths is proportional to the H I column density, N_{H} , which can be measured through the 21 cm line. For a typical high Galactic latitude column of $3 \times 10^{20} \text{ cm}^{-2}$, the ISM becomes optically thick below 0.3 keV, increasing to $\tau = 10$ at 0.12 keV (Morrison & McCammon 1983). Knowledge of N_{H} can also be used to establish the Galactic interstellar reddening and the strength of ISM absorption lines toward distant objects (e.g., Lockman & Savage 1995).

Previous projects have derived accurate 21 cm H I column densities toward more than 300 quasars and AGNs (Elvis, Lockman, & Wilkes 1989, hereafter ELW; Lockman & Savage 1995; Danly, Lockman, & Savage 1996), and in the widely observed region around the north ecliptic pole (Elvis, Lockman, & Fasnacht 1994). We report here on an additional 220 measurements, which together with the other surveys, expand the list of objects with accurate measurements of the Galactic absorption to include (1) most quasars that have been observed by the *ROSAT* PSPC; (2) most quasars that have been observed by *HST* through mid-1993; (3) all quasars that are in the bright PG quasar

sample (Schmidt & Green 1983) which have not been previously observed with the 140 Foot Telescope; (4) extragalactic sources which have been detected or tentatively detected by the *Extreme-Ultraviolet Explorer* (*EUVE*).

2. OBSERVATIONS

The 21 cm H I measurements were made with the 140 Foot Telescope (42.7 m) of the NRAO at Green Bank, West Virginia during observing sessions in 1993 November and in the spring of 1995. At the frequency of the H I 21 cm line, the telescope has an angular resolution of 21'. The receiver was dual polarization with a system temperature of 19 K in each channel at zenith. The spectra have a velocity resolution of 1 km s^{-1} and cover the range -250 km s^{-1} to $+175 \text{ km s}^{-1}$. Each object was observed for typically 12 minutes, the spectra were combined and calibrated, an instrumental baseline was removed, and a correction was made for stray radiation. Table 1 gives a summary of the new measurements. Columns (1)–(5) contain the name, right ascension and declination (B1950), and the Galactic longitude and Galactic latitude of each object.

Stray radiation is 21 cm H I emission which enters through the far sidelobes of the telescope and contributes to the signal entering the main beam (e.g., Kalberla, Mebold, & Reich 1980). At high Galactic latitudes, stray radiation can comprise a significant fraction of an observed 21 cm spectrum. The observations reported here were corrected for stray radiation in the manner described by Lockman, Jahoda, & McCammon (1986, hereafter LJM). This method consists of “bootstrapping” stray radiation contaminated spectra to spectra that have little or no stray radiation. The latter were taken from the Stark et al. (1992) survey of 21 cm emission that was made using the Bell Laboratories horn reflector, an antenna which has few far sidelobes but poor angular resolution ($\sim 2^\circ \times 3^\circ$). The technique used to

¹ The National Radio Astronomy Observatory is a facility of the National Science Foundation, operated under cooperative agreement by Associated Universities, Inc.

TABLE 1
SUMMARY OF 21 cm H I OBSERVATIONS

| Object | α_{1950} h m s | δ_{1950} d m s | ℓ (deg) | b (deg) | N_H (10^{19} cm $^{-2}$) (thin) | Notes | Object | α_{1950} h m s | δ_{1950} d m s | ℓ (deg) | b (deg) | N_H (10^{19} cm $^{-2}$) (thin) | Notes |
|--------------|--------------------------|--------------------------|-----------------|------------|--|-------|-----------------|--------------------------|--------------------------|-----------------|------------|--|-------|
| Q 0000-269 | 000049.5 | -262001 | 35.92 | -79.21 | 14.3 | 14.4 | NGC 1614 | 043135.6 | -084056 | 204.45 | -34.38 | 65.2 | 69.7 |
| MKN 335 | 000245.2 | +195529 | 108.76 | -41.42 | 37.0 | 37.7 | PKS 0438-436 | 043843.1 | -433853 | 248.41 | -41.57 | 13.0 | 13.1 |
| PKS 0008+171 | 000759.4 | +170738 | 109.23 | -44.38 | 36.2 | 37.1 | S5 0454+84 | 045457.3 | +842753 | 128.35 | 24.66 | 56.3 | 57.5 |
| S5 0014+813 | 001404.1 | +811828 | 121.61 | 18.80 | 143.0 | 149.8 | NGC 1808 | 050558.5 | -373436 | 241.21 | -35.90 | 23.4 | 23.7 |
| S5 0016+73 | 001654.0 | +731051 | 120.64 | 10.73 | 199.8 | 211.7 | PKS 0537-441 | 053721.0 | -440645 | 250.08 | -31.09 | 28.8 | 29.1 |
| MC 0042+101 | 004222.6 | +101030 | 120.33 | -52.39 | 52.6 | 55.3 | PKS 0548-322 | 054849.0 | -321701 | 237.57 | -26.14 | 24.9 | 25.1 |
| NGC 247 | 004440.0 | -210200 | 113.95 | -83.56 | 13.7 | 13.8 | S5 0615+82 | 061532.7 | +820356 | 131.74 | 25.97 | 56.5 | 57.9 |
| MKN 348 | 004604.9 | +314104 | 122.28 | -30.91 | 59.0 | 60.8 | S4 0636+680 | 063647.3 | +680136 | 147.17 | 24.15 | 51.1 | 52.4 |
| 0055-2659 | 005532.6 | -265926 | 197.66 | -88.49 | 18.6 | 18.8 | S5 0716+71 | 071612.5 | +712614 | 143.98 | 28.02 | 30.2 | 30.5 |
| PHL 923 | 005631.8 | -000918 | 127.11 | -62.70 | 27.8 | 28.2 | MKN 10 | 074307.3 | +610324 | 155.99 | 30.21 | 44.3 | 45.4 |
| B2 0110+29 | 011038.6 | +294223 | 128.58 | -32.66 | 60.4 | 62.1 | IRAS 07598+6508 | 075953.1 | +650821 | 151.21 | 32.08 | 45.2 | 46.2 |
| 3C 37 | 011543.6 | +242220 | 136.12 | -59.21 | 35.1 | 35.8 | 3C 192 | 080235.5 | +241827 | 197.92 | 26.41 | 49.4 | 50.6 |
| NGC 507 | 012051.0 | +325944 | 130.64 | -29.13 | 54.3 | 55.7 | B2 0827+24 | 082754.4 | +242108 | 200.02 | 31.88 | 30.6 | 31.0 |
| MKN 359 | 012450.2 | +185511 | 134.60 | -42.87 | 47.1 | 48.7 | MKN 1218 | 083513.0 | +250416 | 199.81 | 33.68 | 33.0 | 33.6 |
| Q 0130-403 | 013050.2 | -402151 | 272.00 | -74.42 | 15.9 | 16.0 | S5 0836+71 | 083621.5 | +710422 | 143.54 | 34.43 | 28.0 | 28.3 |
| 3C 47 | 013340.5 | +204209 | 136.83 | -40.70 | 51.2 | 53.4 | PG 0838+770 | 083831.9 | +770358 | 136.66 | 32.68 | 22.7 | 22.9 |
| PKS 0135-247 | 013517.1 | -244608 | 201.39 | -79.28 | 10.4 | 10.5 | NGC 2639 | 084003.0 | +502310 | 168.87 | 38.18 | 27.3 | 27.6 |
| PHL 1092 | 013718.9 | +060410 | 144.03 | -54.55 | 35.3 | 36.1 | E 0844+377 | 084401.0 | +374354 | 185.03 | 38.27 | 29.0 | 29.4 |
| PHL 1093 | 013722.8 | +011636 | 147.04 | -59.05 | 31.9 | 32.4 | 0846+51W1 | 084622.5 | +511939 | 167.61 | 39.14 | 27.8 | 28.2 |
| NGC 660 | 014021.7 | +132339 | 141.61 | -47.35 | 49.5 | 51.1 | LB 8775 | 084853.7 | +162339 | 210.93 | 33.74 | 24.8 | 25.0 |
| MKN 573 | 014122.1 | +020556 | 148.23 | -57.92 | 26.9 | 27.4 | LB 8956 | 085436.4 | +190700 | 208.45 | 36.00 | 32.3 | 32.7 |
| S5 0153+74 | 015304.2 | +742806 | 127.34 | 12.41 | 225.2 | 247.4 | 3C 212 | 085555.6 | +142134 | 214.00 | 34.50 | 40.0 | 40.9 |
| MKN 1014 | 015715.8 | +000909 | 156.56 | -57.94 | 24.6 | 24.9 | PKS 0859-14 | 085954.8 | -140338 | 242.25 | 20.72 | 59.2 | 61.2 |
| MKN 1018 | 020342.5 | -003146 | 159.82 | -57.70 | 25.7 | 26.1 | 3C 216 | 090617.2 | +430559 | 178.33 | 42.84 | 13.9 | 14.0 |
| Q 0207-398 | 020724.4 | -395348 | 255.62 | -69.53 | 13.0 | 13.1 | IRAS 09104+4109 | 091032.9 | +410853 | 181.01 | 43.63 | 18.1 | 18.2 |
| S5 0212+73 | 021249.9 | +733540 | 128.93 | 11.96 | 266.1 | 302.3 | MKN 110 | 092144.3 | +523007 | 165.01 | 44.36 | 12.1 | 12.1 |
| PKS 0214+10 | 021426.7 | +105018 | 154.32 | -46.51 | 64.9 | 68.4 | B2 0923+39 | 092355.3 | +391523 | 183.71 | 46.16 | 16.1 | 16.2 |
| 3C 66B | 022001.7 | +424553 | 140.25 | -16.77 | 80.8 | 83.6 | 3C 220.3 | 093110.9 | +832855 | 128.81 | 31.52 | 23.9 | 24.0 |
| MKN 1044 | 022738.2 | -091311 | 179.69 | -60.48 | 30.1 | 30.6 | 3C 223 | 093650.5 | +360805 | 188.39 | 48.66 | 12.0 | 12.0 |
| PKS 0229+13 | 022902.4 | +130940 | 157.09 | -42.74 | 83.1 | 88.9 | 4C 73.08 | 094509.9 | +732822 | 138.06 | 38.08 | 22.2 | 22.4 |
| NGC 1044 | 023825.8 | +083127 | 163.30 | -45.36 | 85.6 | 89.9 | ESO 434-G40 | 094528.4 | -304257 | 262.74 | 17.23 | 84.2 | 87.5 |
| NGC 1052 | 023837.3 | -082809 | 182.02 | -57.93 | 29.9 | 30.4 | 4C 40.24 | 094550.1 | +405343 | 180.99 | 50.28 | 13.7 | 13.7 |
| NGC 1068 | 024007.0 | -001331 | 172.10 | -51.93 | 29.5 | 29.9 | PG 0946+301 | 094646.3 | +300919 | 197.83 | 50.24 | 16.3 | 16.4 |
| NGC 1097 | 024410.8 | -302905 | 226.92 | -64.68 | 18.6 | 18.8 | PG 0947+396 | 094744.8 | +394054 | 182.85 | 50.75 | 19.1 | 19.2 |
| MKN 372 | 024631.4 | +190550 | 157.71 | -35.48 | 86.1 | 91.5 | MKN 1239 | 094946.1 | -012234 | 239.27 | 38.22 | 43.4 | 44.9 |
| MKN 609 | 032257.2 | -061909 | 190.18 | -47.85 | 42.3 | 43.8 | 4C 09.35 | 095217.2 | +094408 | 227.31 | 44.86 | 31.4 | 32.1 |
| NGC 1365 | 033142.0 | -361818 | 237.95 | -54.60 | 12.6 | 12.6 | 4C 55.17 | 095414.3 | +553717 | 158.60 | 47.93 | 8.8 | 8.8 |
| NGC 1399 | 033634.0 | -353642 | 236.71 | -53.64 | 15.2 | 15.3 | 0957+561A/B | 095757.2 | +560819 | 157.57 | 48.19 | 7.7 | 7.7 |
| DW 0400+25 | 040003.6 | +255147 | 168.03 | -19.65 | 79.6 | 83.3 | PKS 1001+22 | 100158.5 | +223954 | 210.64 | 52.04 | 31.7 | 32.2 |
| PKS 0403-13 | 040314.0 | -131618 | 205.76 | -42.65 | 42.4 | 43.2 | IRAS 10026+4347 | 100238.9 | +434710 | 175.64 | 59.92 | 10.5 | 10.5 |

TABLE 1—Continued

| Object | α_{1950} h m s s | δ_{1950} d m s | ℓ (deg) | b (deg) | N_H (10^{19} cm^{-2}) (thin) | Notes | Object | α_{1950} h m s s | δ_{1950} d m s | ℓ (deg) | b (deg) | N_H (10^{19} cm^{-2}) (thin) | Notes |
|-----------------|----------------------------|--------------------------|-----------------|------------|---|-------|--------------|----------------------------|--------------------------|-----------------|------------|---|-------|
| PKS 1004+13 | 100445.1 | +130337 | 225.12 | 49.12 | 39.3 | 40.1 | NGC 4151 | 120801.0 | +394101 | 155.08 | 75.06 | 21.7 | 21.9 |
| PG 1008+133 | 100830.0 | +131902 | 225.40 | 50.05 | 37.2 | 38.0 | 1208+101 | 120823.6 | +101108 | 272.01 | 70.31 | 15.9 | 15.9 |
| PG 1011-040 | 101149.2 | -040343 | 246.50 | 40.75 | 37.8 | 38.7 | NGC 4235 | 121436.7 | +072809 | 279.18 | 68.47 | 14.6 | 14.7 |
| GB 1011+496 | 101155.3 | +494057 | 165.53 | 52.71 | 7.4 | 7.4 | 4C 64.15 | 121517.1 | +642347 | 128.99 | 52.61 | 23.8 | 23.9 |
| NGC 3227 | 102046.7 | +200705 | 216.99 | 55.45 | 20.7 | 20.9 | MKN 766 | 121555.7 | +300525 | 190.68 | 82.27 | 17.6 | 17.7 |
| IRAS 10214+4724 | 102131.0 | +472423 | 168.12 | 55.03 | 14.3 | 14.4 | NGC 4258 | 121629.4 | +473453 | 138.32 | 68.84 | 11.9 | 11.9 |
| PG 1022+519 | 102223.0 | +515550 | 160.99 | 53.27 | 12.1 | 12.1 | NGC 4278 | 121736.5 | +293325 | 193.79 | 82.77 | 20.1 | 20.2 |
| ZWG 212 025 | 103144.3 | +395359 | 180.28 | 59.06 | 14.3 | 14.3 | 3C 270.1 | 121803.8 | +335950 | 166.31 | 80.64 | 11.4 | 11.4 |
| PKS 1034-293 | 103455.7 | -291827 | 270.95 | 24.85 | 38.8 | 39.4 | PKS 1219+04 | 121949.4 | +042950 | 284.82 | 66.06 | 16.2 | 16.4 |
| NGC 3310 | 103540.3 | +534545 | 156.61 | 54.06 | 14.0 | 14.0 | NGC 4365 | 122155.8 | +073542 | 283.81 | 69.18 | 17.1 | 17.2 |
| S5 1039+81 | 103927.7 | +811023 | 128.74 | 34.74 | 25.0 | 25.2 | NGC 4382 | 122252.8 | +182800 | 267.72 | 79.24 | 26.0 | 26.3 |
| PG 1048+342 | 104856.1 | +341523 | 190.60 | 63.44 | 17.4 | 17.5 | TON 1530 | 122256.6 | +225149 | 249.14 | 82.56 | 16.4 | 16.4 |
| PKS 1055+201 | 105537.6 | +200755 | 222.52 | 63.13 | 18.9 | 19.0 | B2 1223+25 | 122309.1 | +251512 | 231.88 | 83.82 | 17.9 | 18.0 |
| PKS 1055+01 | 105555.3 | +015003 | 251.51 | 52.77 | 34.0 | 34.5 | NGC 4388 | 122315.0 | +125617 | 279.13 | 74.34 | 25.4 | 25.6 |
| NGC 3516 | 110322.7 | +725020 | 133.24 | 42.40 | 29.1 | 29.4 | NGC 4395 | 122320.0 | +334924 | 162.09 | 81.53 | 14.3 | 14.3 |
| Q 1107+487 | 110748.2 | +484730 | 158.56 | 61.05 | 15.5 | 15.6 | NGC 4450 | 122559.0 | +172142 | 273.92 | 78.64 | 23.3 | 23.6 |
| PG 1114+445 | 111420.5 | +443001 | 164.67 | 64.49 | 19.3 | 19.3 | 1E 12270+140 | 122702.4 | +140303 | 280.92 | 75.70 | 25.2 | 25.5 |
| NGC 3610 | 111531.4 | +590338 | 143.54 | 54.46 | 7.1 | 7.1 | TON 83 | 123113.6 | +311742 | 166.77 | 84.51 | 13.3 | 13.3 |
| PG 1115+080 | 111541.6 | +080224 | 249.89 | 60.65 | 35.6 | 36.2 | NGC 4569 | 123418.7 | +132618 | 288.47 | 75.62 | 28.7 | 29.4 |
| PG 1115+407 | 111546.1 | +404213 | 172.24 | 66.67 | 17.4 | 17.4 | IC 3599 | 123506.0 | +265900 | 219.88 | 86.88 | 12.3 | 12.3 |
| NGC 3628 | 111739.6 | +135115 | 240.86 | 64.77 | 22.2 | 22.3 | NGC 4579 | 123512.0 | +120534 | 290.40 | 74.36 | 30.2 | 30.9 |
| MC 1118+128 | 111853.4 | +125245 | 243.10 | 64.42 | 23.1 | 23.3 | NGC 4594 | 123723.3 | -112055 | 298.46 | 51.15 | 37.7 | 38.3 |
| MKN 423 | 112407.5 | +353133 | 183.49 | 70.22 | 19.9 | 20.0 | NGC 4636 | 124017.4 | +025742 | 297.76 | 65.47 | 18.7 | 18.9 |
| MKN 1298 | 112643.6 | -040736 | 267.63 | 52.75 | 44.4 | 45.0 | NGC 4639 | 124021.7 | +133155 | 294.30 | 75.99 | 22.7 | 23.0 |
| PKS 1127-14 | 112735.6 | -143254 | 275.28 | 43.64 | 38.3 | 38.9 | NGC 4649 | 124109.0 | +114930 | 295.88 | 74.32 | 21.4 | 21.7 |
| MKN 739 | 113353.3 | +215222 | 226.84 | 72.08 | 20.4 | 20.5 | 3C 275.1 | 124127.6 | +163918 | 293.39 | 79.11 | 18.8 | 18.9 |
| NGC 3783 | 113633.0 | -372741 | 287.46 | 22.95 | 95.9 | 101.3 | Q 1246-057 | 124638.7 | -054257 | 301.93 | 56.88 | 22.3 | 22.5 |
| MKN 744 | 113704.8 | +321110 | 191.59 | 73.70 | 22.2 | 22.4 | PG 1247+268 | 124738.9 | +264728 | 276.63 | 89.32 | 8.6 | 8.6 |
| 4C 58 | 114006.4 | +582435 | 139.43 | 56.74 | 8.3 | 8.3 | B2 1248+30 | 124800.1 | +303259 | 126.90 | 86.84 | 11.8 | 11.9 |
| MC 1146+111 | 114613.4 | +111139 | 257.66 | 68.09 | 36.3 | 36.8 | 3C 280 | 125443.4 | +473646 | 120.21 | 69.76 | 12.4 | 12.5 |
| PG 1149-110 | 114930.3 | -110542 | 280.47 | 48.89 | 32.6 | 33.2 | 3C 281 | 130522.5 | +065814 | 314.51 | 69.20 | 22.1 | 22.5 |
| S5 1150+81 | 115023.6 | +811510 | 125.72 | 35.84 | 52.0 | 53.4 | NGC 5005 | 130838.5 | +371922 | 101.60 | 79.25 | 11.1 | 11.2 |
| LB 2136 | 115048.0 | +494750 | 145.55 | 64.98 | 21.1 | 21.2 | Q 1309-056 | 130900.7 | -053642 | 312.08 | 56.64 | 25.3 | 25.5 |
| PG 1151+117 | 115115.7 | +114510 | 259.31 | 69.31 | 19.9 | 20.0 | PG 1309+355 | 130958.5 | +353115 | 95.49 | 80.73 | 10.0 | 10.0 |
| NGC 3982 | 115352.2 | +552409 | 138.83 | 60.27 | 10.0 | 10.0 | PG 1310-108 | 131028.0 | +105148 | 311.46 | 51.38 | 30.0 | 30.4 |
| NGC 3998 | 115520.9 | +554355 | 138.17 | 60.06 | 9.7 | 9.7 | PG 1322+659 | 132210.0 | +655722 | 117.63 | 51.10 | 18.8 | 18.9 |
| TEX 1156+213 | 115652.2 | +212338 | 237.03 | 76.71 | 22.6 | 22.8 | NGC 5135 | 132256.9 | -293423 | 311.75 | 32.45 | 43.7 | 45.0 |
| Q 1159+123 | 115914.1 | +122312 | 282.74 | 71.00 | 20.4 | 20.5 | PG 1329+412 | 132929.9 | +411723 | 94.71 | 73.82 | 7.9 | 7.9 |
| NGC 4125 | 120534.8 | +652718 | 130.19 | 51.34 | 19.0 | 19.1 | MKN 789 | 132955.3 | +112143 | 335.91 | 71.31 | 20.8 | 21.1 |
| PKS 1207-399 | 120659.6 | -395931 | 294.34 | 21.90 | 78.9 | 82.1 | 4C 55.27 | 133215.8 | +551645 | 110.25 | 61.04 | 9.1 | 9.1 |

TABLE 1—Continued

| Object | α_{1950} h m s.s | δ_{1950} d m s | ℓ (deg) | b (deg) | N_H (10^{19} cm $^{-2}$) (thin) | Notes | Object | α_{1950} h m s.s | δ_{1950} d m s | ℓ (deg) | b (deg) | N_H (10^{19} cm $^{-2}$) (thin) | Notes |
|-----------------|----------------------------|--------------------------|-----------------|--------------|--|-------|-----------------|----------------------------|--------------------------|-----------------|--------------|--|-------|
| IRAS 13349+2438 | 133457.3 | +243818 | 20.60 | 79.32 | 10.7 | 10.8 | PG 1626+554 | 162651.4 | +552904 | 84.51 | 42.19 | 15.5 | 15.5 |
| MKN 266 | 133615.2 | +483153 | 102.72 | 66.97 | 15.2 | 15.3 | MKN 883 | 162747.0 | +243307 | 42.71 | 41.14 | 38.7 | 39.6 |
| PG 1341+258 | 134136.8 | +255355 | 28.71 | 78.15 | 10.1 | 10.2 | B2 1633+38 | 163330.6 | +381409 | 61.09 | 42.34 | 10.1 | 10.2 |
| MKN 273 | 134251.5 | +560812 | 108.11 | 59.68 | 9.7 | 9.8 | 3C 343 | 163401.0 | +625141 | 93.61 | 39.38 | 24.4 | 24.5 |
| PKS 1351-018 | 135132.0 | -015120 | 332.73 | 57.10 | 31.7 | 32.5 | OS 562 | 163717.3 | +572616 | 86.64 | 40.36 | 17.7 | 17.8 |
| PG 1351+236 | 135146.1 | +234030 | 21.75 | 75.37 | 15.2 | 15.3 | NGC 6251 | 163756.7 | +823818 | 115.76 | 31.20 | 56.8 | 58.2 |
| B2 1351+318 | 135151.2 | +315345 | 55.02 | 75.64 | 12.9 | 13.0 | NGC 6240 | 165027.9 | +022855 | 20.73 | 27.29 | 53.1 | 55.0 |
| MKN 464 | 135345.5 | +384907 | 77.33 | 72.32 | 15.7 | 15.8 | PKS 1656+053 | 165605.7 | +051947 | 24.30 | 27.44 | 61.1 | 64.0 |
| PG 1354+213 | 135411.6 | +211829 | 14.23 | 73.97 | 22.0 | 22.2 | PG 1715+535 | 171530.7 | +533124 | 80.97 | 35.41 | 24.4 | 24.6 |
| 4C 58.29 | 135636.2 | +580638 | 106.58 | 57.09 | 12.9 | 12.9 | NGC 6500 | 175348.3 | +182040 | 43.76 | 20.23 | 69.5 | 71.9 |
| IRAS 14026+4341 | 140237.6 | +434127 | 85.50 | 67.97 | 12.7 | 12.7 | S5 1803+78 | 180339.2 | +782755 | 110.04 | 29.07 | 36.4 | 37.0 |
| NGC 5506 | 141039.0 | -025826 | 339.15 | 53.81 | 43.1 | 44.7 | 3C 371 | 180718.0 | +694859 | 100.13 | 29.17 | 43.8 | 44.2 |
| H 1413+117 | 141320.0 | +114336 | 358.73 | 64.77 | 16.9 | 17.1 | 3C 382 | 183311.7 | +323918 | 61.30 | 17.45 | 65.0 | 67.0 |
| PG 1415+451 | 141504.2 | +450956 | 84.72 | 65.32 | 9.6 | 9.6 | 3C 390.3 | 184536.6 | +794308 | 111.44 | 27.07 | 36.8 | 37.4 |
| MKN 673 | 141506.1 | +270515 | 37.05 | 70.88 | 14.8 | 14.9 | OV -236 | 192142.3 | -292027 | 9.34 | -19.61 | 73.9 | 77.6 |
| NGC 5548 | 141543.4 | +252200 | 31.96 | 70.50 | 16.1 | 16.3 | HS 1946+7658 | 194641.0 | +765826 | 109.23 | 23.49 | 72.0 | 74.2 |
| MKN 471 | 142046.6 | +330439 | 54.62 | 69.43 | 10.2 | 10.3 | PKS 2000-330 | 200012.8 | -330014 | 8.40 | -28.58 | 74.4 | 78.3 |
| H 1426+428 | 142635.9 | +425346 | 77.49 | 64.90 | 13.6 | 13.7 | S5 2007+77 | 200720.5 | +774358 | 110.46 | 22.73 | 90.7 | 94.2 |
| PG 1427+480 | 142753.9 | +480046 | 86.65 | 61.83 | 16.8 | 16.9 | MKN 509 | 204125.5 | -105417 | 35.97 | -29.85 | 44.4 | 45.2 |
| PG 1435-067 | 143537.5 | -064522 | 343.98 | 47.21 | 52.5 | 54.9 | MKN 896 | 204344.4 | -025946 | 44.25 | -26.72 | 38.2 | 38.9 |
| MKN 478 | 144004.6 | +353907 | 59.24 | 65.03 | 9.6 | 9.7 | 3C 433 | 212130.6 | +245118 | 74.48 | -17.69 | 86.9 | 91.5 |
| PG 1448+273 | 144858.6 | +272142 | 39.94 | 63.43 | 28.6 | 29.4 | PKS 2143-156 | 214338.8 | -153937 | 38.44 | -45.60 | 45.8 | 47.1 |
| MKN 841 | 150136.4 | +103758 | 11.21 | 54.63 | 21.7 | 21.9 | MKN 516 | 215352.8 | +070742 | 65.65 | -35.38 | 45.8 | 46.8 |
| PKS 1504-167 | 150416.4 | -164058 | 343.64 | 35.06 | 70.2 | 73.0 | 3C 445 | 222114.8 | 022126 | 61.87 | -46.71 | 51.2 | 53.3 |
| PG 1535+547 | 153520.7 | +544322 | 86.92 | 49.39 | 13.5 | 13.6 | PKS 2223+21 | 222314.6 | +210250 | 83.16 | -30.09 | 42.5 | 43.2 |
| MC 1549+114 | 154821.2 | +112947 | 21.32 | 45.12 | 37.2 | 38.1 | PKS 2305+18 | 230517.1 | +184506 | 91.56 | -37.45 | 48.8 | 50.5 |
| B2 1555+33 | 155533.7 | +331320 | 53.06 | 49.65 | 25.7 | 26.2 | IRAS 23060+0505 | 230601.6 | +050514 | 81.65 | -49.09 | 48.5 | 50.2 |
| GC 1556+33 | 155659.4 | +333147 | 53.57 | 49.37 | 24.1 | 24.4 | NGC 7603 | 231621.9 | -090147 | 80.06 | -54.74 | 40.0 | 41.2 |
| MKN 493 | 155716.3 | +351015 | 56.09 | 49.41 | 20.4 | 20.8 | UM 164 | 232902.3 | -020440 | 82.50 | -58.26 | 43.6 | 45.0 |
| PKS 1623+26 | 162311.4 | +265713 | 45.48 | 42.75 | 26.4 | 26.8 | PKS 2351-154 | 235155.7 | -152953 | 72.03 | 72.20 | 23.9 | 24.2 |

NOTES.—(1). Data not corrected for stray radiation. (2). The listed value of N_H includes emission only between LSR velocities -60 km s $^{-1}$ and $+28$ km s $^{-1}$. The H I in NGC 247 itself appears in the spectrum at $V_{LSR} > +28$ km s $^{-1}$. Table 1 will appear in computer-readable form in the AAS CD-ROM Series, Vol. 7.

remove stray radiation from 140 Foot Telescope data requires observation of an additional ~ 75 spectra around the direction of interest, but it results in an H I spectrum with the adequately high angular resolution of the 140 Foot Telescope ($21''$), but with greatly reduced stray radiation (see LJM for details).

In directions in which the H I emission is especially strong, the stray radiation correction becomes unreliable, but in these directions stray radiation is expected to be a small component of the total N_{H} , and its neglect should not introduce a substantial error compared to other uncertainties. In these cases, noted with a footnote to Table 1, no stray radiation correction was made.

3. DETERMINATION OF N_{H} AND ITS UNCERTAINTY

The derivation of N_{H} from 21 cm spectra is reviewed in Dickey & Lockman (1990). All the H I emission over the full range of observed velocities was used to derive the Galactic N_{H} , except in the direction of the galaxy NGC 247, where emission from that galaxy itself is in our spectrum and is excluded from the calculated N_{H} .

The uncertainties in the final values of N_{H} derive from several sources that are discussed more fully in Lockman (1993) and in Elvis et al. (1994). There may be an overall calibration error of a few percent. Noise and baseline uncertainties may each contribute several 10^{18} cm^{-2} . The stray radiation correction can contribute an uncertainty in the range $0.5\text{--}1.0 \times 10^{19} \text{ cm}^{-2}$. For high N_{H} directions, the uncertain opacity correction can also produce a substantial uncertainty in N_{H} .

The H I excitation temperature toward most of these objects is not known. Therefore, columns (6) and (7) of Table 1 give the measured N_{H} for two assumptions: that the H I is optically thin, and that it has a uniform temperature of 150 K. In most directions, the results differ by less than 10^{19} cm^{-2} . For objects that show a significant difference, the larger value (from the 150 K case) will be the more accurate. However, differences between columns (6) and (7) of greater than $2 \times 10^{19} \text{ cm}^{-2}$ occur exclusively for directions with $N_{\text{H}} > 5 \times 10^{20} \text{ cm}^{-2}$, and these sight lines almost certainly intersect clouds containing some molecular hydrogen (Savage et al. 1977). Thus, when the opacity cor-

rection is significant, it indicates that N_{H} is not a complete measure of the ISM in these directions, and thus the use of N_{H} alone will underestimate the total Galactic interstellar opacity.

4. ESTIMATED UNCERTAINTIES IN DERIVED X-RAY OPACITIES

The typical high-latitude objects observed here should have a 1σ uncertainty in N_{H} of no more than $1.0 \times 10^{19} \text{ cm}^{-2}$. For intermediate-latitude and low-latitude objects, the uncertainties are larger and are typically dominated by the uncertain opacity correction. An estimate of this can be obtained from comparison of columns (6) and (7). For objects with $N_{\text{H}} > 5 \times 10^{20} \text{ cm}^{-2}$, one must consider that some H_2 might be present along the line of sight, and for objects with N_{H} of more than a few times 10^{21} cm^{-2} , the values given here are certainly a significant underestimate to the total Galactic interstellar opacity.

In addition to absorption by H I and H_2 , any neutral He in the ionized interstellar medium can contribute to the opacity in the soft X-ray bands. A discussion of this component relevant to the question of its effect on Galactic opacity is in Elvis et al. (1994) and in Snowden et al. (1994).

5. SUMMARY

We have derived the Galactic N_{H} in the direction of 220 quasars and AGNs. Most of the values of N_{H} have uncertainties $\sim 10^{19} \text{ cm}^{-2}$ and are about 10 times more accurate than other currently available estimates. The error estimates are dominated by baseline uncertainties, opacity corrections, and the stray radiation correction. The current data set as well as a compilation of the more than 500 N_{H} measurements made with the 140 foot telescope will be available on the World Wide Web at <http://info.gb.nrao.edu>. Files containing Table 1 and all the H I spectra will appear in the AAS CD-ROM Series, Vol. 7.

This work was supported in part by NASA grant NAGW-2201 (LTSA) and NASA contract NAS 8-39073 to M. E. and by NASA grant NAG 5-2496 to A. L.

REFERENCES

- Danly, L., Lockman, F. J., & Savage, B. D. 1996, in preparation
 Dickey, J. M., & Lockman, F. J. 1990, *ARA&A*, 28, 215
 Elvis, M., Lockman, F. J., & Fassnacht, C. 1994, *ApJS*, 95, 413
 Elvis, M., Lockman, F. J., & Wilkes, B. J. 1989, *AJ*, 97, 777 (ELW)
 Kalberla, P. M. W., Mebold, U., & Reich, W. 1980, *A&A*, 82, 275
 Lockman, F. J. 1993, in *Workshop on Databases for Galactic Structure*, ed. A. G. D. Philip, B. Hauck, & A. R. Upgren (Schenectady: L. Davis Press), 181
 Lockman, F. J., Jahoda, K., & McCammon, D. 1986, *ApJ*, 302, 432 (LJM)
 Lockman, F. J., & Savage, B. D. 1995, *ApJS*, 97, 1
 Morrison, R., & McCammon, D. 1983, *ApJ*, 270, 119
 Savage, B. D., Bohlin, R. C., Drake, J. F., & Budich, W. 1977, *ApJ*, 216, 291
 Schmidt, M., & Green R. F. 1983, *ApJ*, 269, 352
 Snowden, S. L., Hasinger, G., Jahoda, K., Lockman, F. J., McCammon, D., & Sanders, W. T. 1994, *ApJ*, 430, 601
 Stark, A. A., Gammie, C. F., Wilson, R. W., Bally, J., Linke, R., Heiles, C., & Hurwitz, M. 1992, *ApJS*, 79, 77

7

8

9

10